Université Paris-Sud

Ecole doctorale STITS

Dossier des Travaux Scientifiques
2 - Annexes

présenté pour l'obtention du diplôme
d' HABILITATION A DIRIGER DES RECHERCHES
en Electronique

Structures périodiques et métamatériaux. Antennes et dispositifs électromagnétiques.

Shah Nawaz BUROKUR

Soutenue publiquement le 09/12/2013 devant un jury composé de :

Rapporteurs	Ronan Sauleau	Professeur, Université de Rennes 1
	Eric Lheurette	Professeur, Université de Lille
	Robert Staraj	Professeur, Université de Nice
Examinateurs	Xavier Begaud	Professeur, Télécom ParisTech
	André de Lustrac	Professeur, Université Paris Ouest
Invité	Gérard-Pascal Piau	Senior Expert, EADS IW

Institut d'Electronique Fondamentale, UMR 8622

Annexe 1 : Principaux travaux relatifs au chapitre 1

Annexe 1.1

A. Ourir, S. N. Burokur, A. de Lustrac

« Phase-varying metamaterial for compact steerable directive antennas »

Electronics Letters, vol. 43, no. 9, pp. 493-494, April 2007

Phase-varying metamaterial for compact steerable directive antennas

A. Ourir, S.N. Burokur and A. de Lustrac

The design of a locally phase-varying one-dimensional metamaterial working near 10 GHz is reported. It is made from a capacitive and an inductive grid. The phase-varying behaviour is obtained with a regular incrementation of the spacing between each unit cell of the capacitive grid in one direction. This composite metamaterial is then used as a partially reflecting surface in a resonant Fabry-Pérot type cavity together with a patch antenna to constitute a compact steerable directive printed antenna. A $\pm 20^\circ$ deflection of the antenna beam is obtained.

Introduction: Recently, Feresidis *et al.* [1] and Zhou *et al.* [2] showed that the half wavelength restriction of a Fabry-Perot cavity antenna can be reduced to respectively a quarter wavelength and a tenth (10th) wavelength by using a novel type of metamaterial-based resonant cavity in order to design compact directive electromagnetic sources based on a single radiating antenna. The latter consists of an artificial magnetic conductor (AMC) surface with reflection phase zero instead of a perfect electric conductor (PEC) surface and a partially reflective surface (PRS) with a frequency dependent reflection phase. Using a novel 2D composite metamaterial, made of capacitive and inductive grids, our group has lately further reduced the cavity thickness up to $\lambda/60$ for applications to ultra-thin directive antennas [3]. In this Letter, we present the modelling and characterisation of an optimised resonant cavity for a passive steerable directive beam antenna near 10 GHz using a phase-varying metamaterial. The cavity is composed of a PEC surface and a new 1D composite metamaterial acting as a PRS with a locally variable reflection and transmission phase. The cavity resonance is presently shown to occur for a cavity thickness as small as $\lambda/30$. Furthermore, a drastic enhancement of the antenna directivity is obtained and a deflection of the antenna beam of about $\pm 20^\circ$ is observed in simulation and verified in experiments.

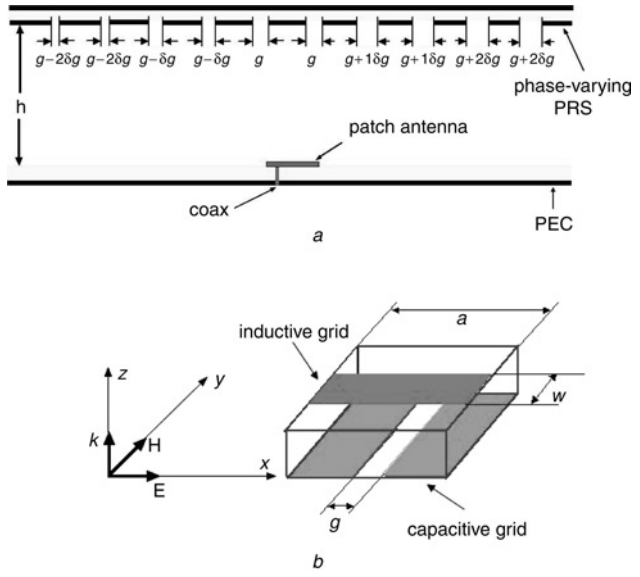

Fig. 1 *Schematic view of cavity composed of PEC and phase-varying PRS, and elementary cell of composite metamaterial, showing capacitive and inductive grids*

a Schematic view of cavity
b Elementary cell of composite metamaterial

Design of phase varying metamaterial and PRS: The cavity considered here is composed of the patch antenna's metallic ground plane and the PRS reflector placed at a distance h above the antenna (Fig. 1*a*). The PRS reflector consists of a periodic array of copper strips mechanically etched on each face of a 1.4 mm-thick FR3-epoxy ($\varepsilon_r = 3.9$ and $\tan\delta = 0.0197$) substrate as shown in Fig. 1*b*. The periodicity a and the width w of the strips are 5 and 2.2 mm, respectively, optimised to have a resonance near 10 GHz and to provide a sufficiently high reflectance. The upper array where the strips are oriented parallel to the electric field E of the antenna plays the role of the inductive grid, whereas the lower array where the strips are oriented parallel to the magnetic field H acts as the capacitive grid. By changing the gap spacing g between the metallic strips of the capacitive grid of the PRS in only the direction parallel to E (x-direction is chosen here) and keeping all the other geometric parameters unchanged, the capacitance of the metamaterial will also vary along this same direction. As a consequence, the phases of the computed reflection and transmission coefficients vary. This behaviour is illustrated by the simulation results of the transmission coefficient phase shown in Fig. 2. The numerical simulations were run using the finite element method (FEM) based HFSS software for the 5 to 15 GHz frequency band. Owing to the different gap spacing g, each PRS has a different transmission phase characteristic. From Fig. 2, we can note that the variation of g accounts for the shift of the resonance frequency. An increase in the value of g causes a decrease in the value of the capacitance created between two cells, and finally a shift of the resonance towards higher frequencies. At a particular frequency the phase of the PRS increases with an increase in the gap spacing. This phase shift especially for the transmission coefficient is very important since it will help to control the radiated beam direction of the antenna.

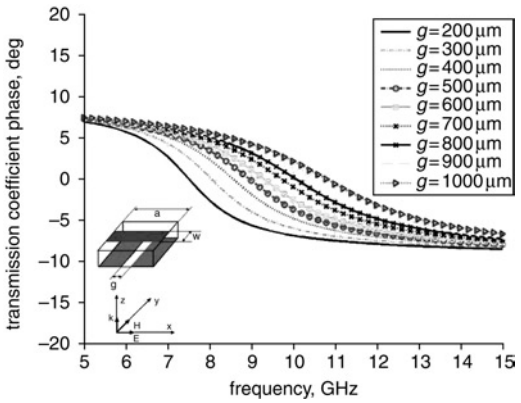

Fig. 2 *Transmission coefficient phase of PRS (shown in inset) with different gap spacing g*

A shift towards high frequencies noted when g increases

Steerable directive antenna: To make the antenna beam steerable, the PRS of the cavity must be designed in such a manner that there exists a continuous phase variation. The precedent study on the variation of g leads us to a new design of the PRS (Fig. 1) with a continuous variation of the gap g. As illustrated by the antenna cavity system shown in Fig. 1, the proposed PRS is now divided into five different regions, where each has a specific gap spacing. The basic gap spacing g ($g = 400$ μm) in the centre of the PRS is taken as a reference and a double variation of $\pm n\ \delta g$ (with $n = 0, 1, 2$) is imposed on each side of the central region. The gap spacing is thus incremented regularly when moving from left to right along the PRS. If we consider each gap as a slot antenna, an analogy can then be made with an array of seven antennas with a regular phase difference. Note that here the resonance frequency of the central region of the metamaterial corresponds to that of the PRS without gap spacing variation ($g = 400$ μm and $\delta g = 0$), i.e. 8.7 GHz, as shown in Fig. 2. Several prototypes of the subwavelength cavity have been simulated and fabricated. Concerning the PRS, 11×11 unit cells have been used and therefore the overall dimensions of the prototypes are $55 \times 55 \times 3.8$ mm. The first one consists of the metamaterial PRS with the same gap spacing g between the metallic strips of the capacitive grid ($\delta g = 0$). This prototype will ensure no deflection of the beam since there exists no phase variation of the metamaterial. The second and third ones are the prototypes incorporating a variation of $\delta g = 50$ μm and $\delta g = 100$ μm, respectively, along the positive x-direction. The cases where the variation δg is negative (180° rotation of the PRS around the z-axis) have also been considered. The resonance frequency of the proposed cavity which depends on the phase of the reflection coefficient of the PRS and also the height is found to be 10.5 GHz. Fig. 3 show the gain patterns of the antenna in the E ($\phi = 90^\circ$) plane at 10.5 GHz for an optimised cavity thickness

$h = 1$ mm, $a = 5$ mm, $w = 2.2$ mm, $g = 400$ μm, $\delta g = 0$. The beam is normal to the plane of the antenna and shows no deflection, which confirms our prediction on the constant phase metamaterial. However, in the case of a regular variation of 50 μm, a deflection of the antenna beam of about 10° can be observed either in the forward (clockwise) or backward (anticlockwise) direction depending if δg is, respectively, negative or positive. Similar observations and a higher deflection can be noted for, respectively, $\delta g = 100$ μm and $\delta g = -100$ μm. This Figure illustrates very clearly the control of the direction of the radiation beam when the gap spacing, and consequently the phase, vary locally along the PRS surface. However, a sidelobe, which is mainly due to the asymmetrical feeding of the microstrip antenna, appears on the gain pattern for the case $\delta g = -100$ μm. The directivity of the cavity antenna can be calculated using the following expression: $D = 41253/(\theta_1 \times \theta_2)$ where θ_1 and θ_2 are, respectively, the half-power widths (in degrees) for the H-plane and E-plane patterns. In our case, the directivity is found to be approximately equal to 14.8 dB.

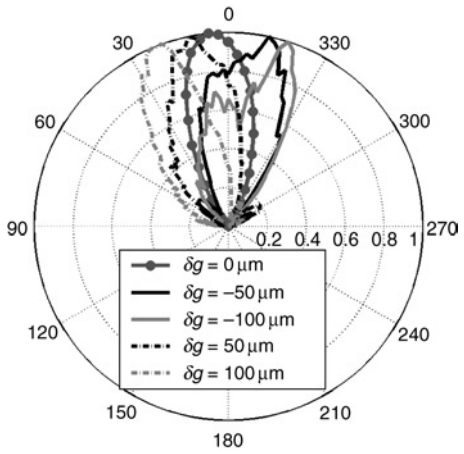

Fig. 3 *Measured gain patterns of antenna in E-plane ($\phi = 90°$) at 10.5 GHz for $\delta g = 0$, $\delta g = \pm 50$ μm and $\delta g = \pm 100$ μm*

Conclusions: We have demonstrated that a compact steerable directive antenna with a thickness equal to $\lambda/30$ can be fabricated using a metamaterial-based Fabry-Pérot cavity with a minimal reflection phase of the reflectors. So as to make the antenna steerable, the cavity is based on the use of a PEC and a phase-varying metamaterial composed of constant inductive and locally variable capacitive strips. A deflection of the antenna beam of $\pm 20°$ has been observed.

29 January 2007
Electronics Letters online no: 20070298
doi: 10.1049/el:20070298

A. Ourir, S. N. Burokur and A. de Lustrac (*IEF, Université Paris-Sud, UMR, 8622 CNRS, Orsay, France*)

E-mail: andre.delustrac@ief.u-psud.fr

References

1 Feresidis, A.P., Goussetis, G., Wang, S., and Vardaxoglou, J.C.: 'Artificial magnetic conductor surfaces and their application to low-profile high-gain planar antennas', *IEEE Trans. Antennas Propag.*, 2005, **53**, (1), pp. 209–215
2 Zhou, L., Li, H., Qin, Y., Wei, Z., and Chan, C.T.: 'Directive emissions from subwavelength metamaterial-based cavities', *Appl. Phys. Lett.*, 2005, **86**, pp. 101101-1–101101-3
3 Ourir, A., de Lustrac, A., and Lourtioz, J.-M.: 'All-metamaterial-based sub-wavelength cavities ($\lambda/60$) for ultrathin directive antennas', *Appl. Phys. Lett.*, 2006, **88**, pp. 084103-1–084103-3

Annexe 1.2

S. Haché, S. N. Burokur, A. de Lustrac, F. Gadot, P. Cailleu, G.-P. Piau

« Principles and applications of a controllable electromagnetic band gap material to a conformable spherical radome »

EPJ Applied Physics, vol. 46, no. 3 (32611), June 2009

Eur. Phys. J. Appl. Phys. **46**, 32611 (2009)
DOI: 10.1051/epjap/2009040

THE EUROPEAN PHYSICAL JOURNAL APPLIED PHYSICS

Principles and applications of a controllable electromagnetic band gap material to a conformable spherical radome

S. Haché[1], S.N. Burokur[1], A. de Lustrac[1,a], F. Gadot[1], P. Cailleu[2], and G.-P. Piau[2]

[1] IEF, Université Paris-Sud, 91405 Orsay, France
[2] EADS Research Center, 92000 Suresnes, France

Received: 10 March 2008 / Accepted: 2 February 2009
Published online: 3 April 2009 –

Abstract. This paper presents the principle of two types of conformable and controllable spherical radome based on Electromagnetic Band Gap (EBG) materials operating at around 10 GHz. The EBG structure is composed of a grid of metallic wires conformed on a hollow spherical object. Two switching control configurations are considered: (1) between an EBG structure made of electrically continuous wires and another one made of discontinuous wires, and (2) between two EBG structures made of discontinuous wires where each has a different period of discontinuities. Both switching configurations are simulated and experimentally characterized on passive prototypes. An excellent agreement is observed between simulations and measurements. The radiation patterns of two types of antennas, a horn antenna and a meteorological antenna, are also measured in the presence of the radome.

PACS. 41.20.Jb Electromagnetic wave propagation; radiowave propagation – 42.70.Qs Photonic bandgap materials – 84.40.Ba Antennas: theory, components and accessories

1 Introduction

Controllable Electromagnetic Band Gap (EBG) structures can find a variety of applications to antennas, RF screens, signature control and filters... [1,2]. Several studies have been made on electronically active planar EBG structures in the microwave domain where their applications to electromagnetic windows and antennas have been demonstrated [3,4]. The main advantage of these structures resides in the large easiness of continuous directional control of transmission and of frequency adjustment, which depends on the structure's periodic parameters.

In this paper we use a controllable EBG to design an electronically controllable radome working around 10 GHz. In the open literature, Frequency Selective Surfaces (FSS) have been proposed to design radomes [5–11]. Patents covering the use of active FSS to design controllable radomes can also be found [12,13]. However to the best of our knowledge it is the first time that a controllable radome is made of a conformed EBG material. The application of controllable EBG material to a radome implies that the classical properties of a radome will be satisfied, i.e. a transmission close to unity. Then we have optimized the radome structure to meet this criterion.

The EBG structures considered in this paper are composed of periodically organized copper strips on a conformal spherical shape. The final aim of this study is to achieve an electronic commutation of the transmission from an allowed state to a forbidden one at around 10 GHz. The structure must then consist of discontinuous parallel copper strips incorporating fast switching elements such as PIN diodes or photoconductors, necessary to obtain the commutation of the metallic wires from a discontinuous electrical state to a continuous one. In this present work, we consider the spherical radome only in a passive mode. This study on passive structures is the starting point to demonstrate the principle of the commutation before going towards electronically active structures. EBG structures are characterized by an alternation of forbidden frequency and allowed frequency bands depending on the geometrical and electromagnetic parameters of the structure, and also on the polarization of the incident wave. If the EBG structure is made of continuous metallic wires parallel to the electrical field of the incident wave, the first band at low frequencies is a forbidden band. In a pioneering work, Pendry has studied metallic electromagnetic band gap materials and has shown that a continuous metallic lattice may be considered like a diluted metal with a first forbidden frequency band from 0 Hz to a plasma frequency ω_p [14]. This plasma frequency depends on the geometrical parameters of the metallic lattice and on the used metal:

$$\omega_p^2 = \frac{ne^2\pi r^2}{\varepsilon_0 a^2 m_{eff}} \quad \text{with} \quad m_{eff} = \ln\left(\frac{a}{r}\right)\mu_0 e^2 r^2 n/2$$

[a] e-mail: andre.delustrac@ief.u-psud.fr

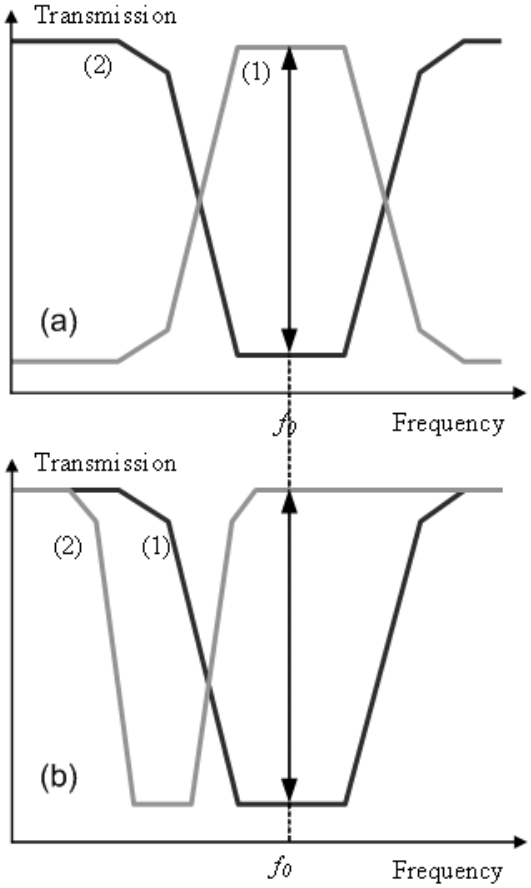

Fig. 1. (a) First operating mode: switching between an EBG structure composed of continuous metallic wires (1: grey curve) and one made of discontinuous metallic wires with a period p_1 of discontinuities (2: black curve). (b) Second operating mode: switching between an EBG structure composed of discontinuous metallic wires with a period p_1 of discontinuities (1: black curve) and another one with a period p_2 of discontinuities (2: grey curve). At the frequency f_0 both operating modes allow the switching from a transmitting state of the EBG structure to a reflecting one.

where a is the period of the lattice, r is the radius of the wire, n is the electron density and m_{eff} the effective electron mass.

When the continuous metallic wires are replaced by discontinuous ones with discontinuities periodically inserted along the wires with a period p, an allowed band is observed at low frequencies. The bandwidth of this allowed band depends on the capacitance and the period of the discontinuities [15]. If we can control the switching of the metallic wires from a discontinuous electrical state to a continuous one, then we can obtain the switching of the structure from a transmitting state to a reflecting one. This is the first control configuration investigated in this paper (Fig. 1a). However it is possible to use another mode. If we can control not only the electrical state of all the discontinuities, but also the periodicity of these discontinuities, we can then control the switching from a set of frequency bands, alternating forbidden and allowed bands, to a different set. If these periodicities are well chosen, an allowed band in the first set may be replaced by a forbidden band in the second set (Fig. 1b). This constitutes the second control configuration under study. We can see in Figure 1 that at the frequency f_0 both control modes allow the switching from a transmitting state of the EBG material to a reflecting one. Several conformed prototypes have been simulated, fabricated and characterized to illustrate both control modes on a real scale spherical radome. The results obtained from both configurations show that the switching of the transmission is observed in both cases in simulations and measurements with a very good agreement. The first configuration is more suitable to the use of electronic switching components biased by DC current whereas the second one corresponds much better to the use of photoconductive components.

In this study we present calculated and measured results obtained on only passive prototypes. These prototypes have been fabricated and characterized to demonstrate the feasibility of the electrical state switching concept. To further validate this concept, the radome has been tested with a meteorological radar antenna actually used in airplanes.

2 Design and simulation of the EBG structures

The radome considered here is a conformable one on a spherical shape. This shape corresponds to the vertex of the real radome of an ATR 42 airplane, with a maximum radius $R = 16.5$ cm. The studied EBG structures are all composed of a one-dimensional grid of parallel copper strips of width $w = 1$ mm (Fig. 2a) regularly disposed on the spherical shape with a projection period $a = 1$ cm on the horizontal plane (xOy plane). This structure has two symmetry planes (xOz and yOz) that allow simplifying its simulation. The calculation is performed using Flomerics' Microstripes commercial software based on the Transmission Line Matrix method [16]. The software allows reducing the calculation time by simulating the wires using a wire model. The horn antenna used in the experimental characterizations of the radome is also included in the calculation to increase its accuracy. This type of excitation acts as a Transverse Electromagnetic (TEM) plane wave propagating towards the EBG structure in the $+z$ direction with its electric field $\mathbf{E}$ oriented along the y-axis and its magnetic field $\mathbf{H}$ oriented along the x-axis. The two switching control configurations are tested using structures with either continuous wires or discontinuous wires.

2.1 Configuration 1: commutation between continuous and discontinuous wires

The first spherical EBG structure is composed of continuous metallic wires of width $w = 1$ mm. The continuous

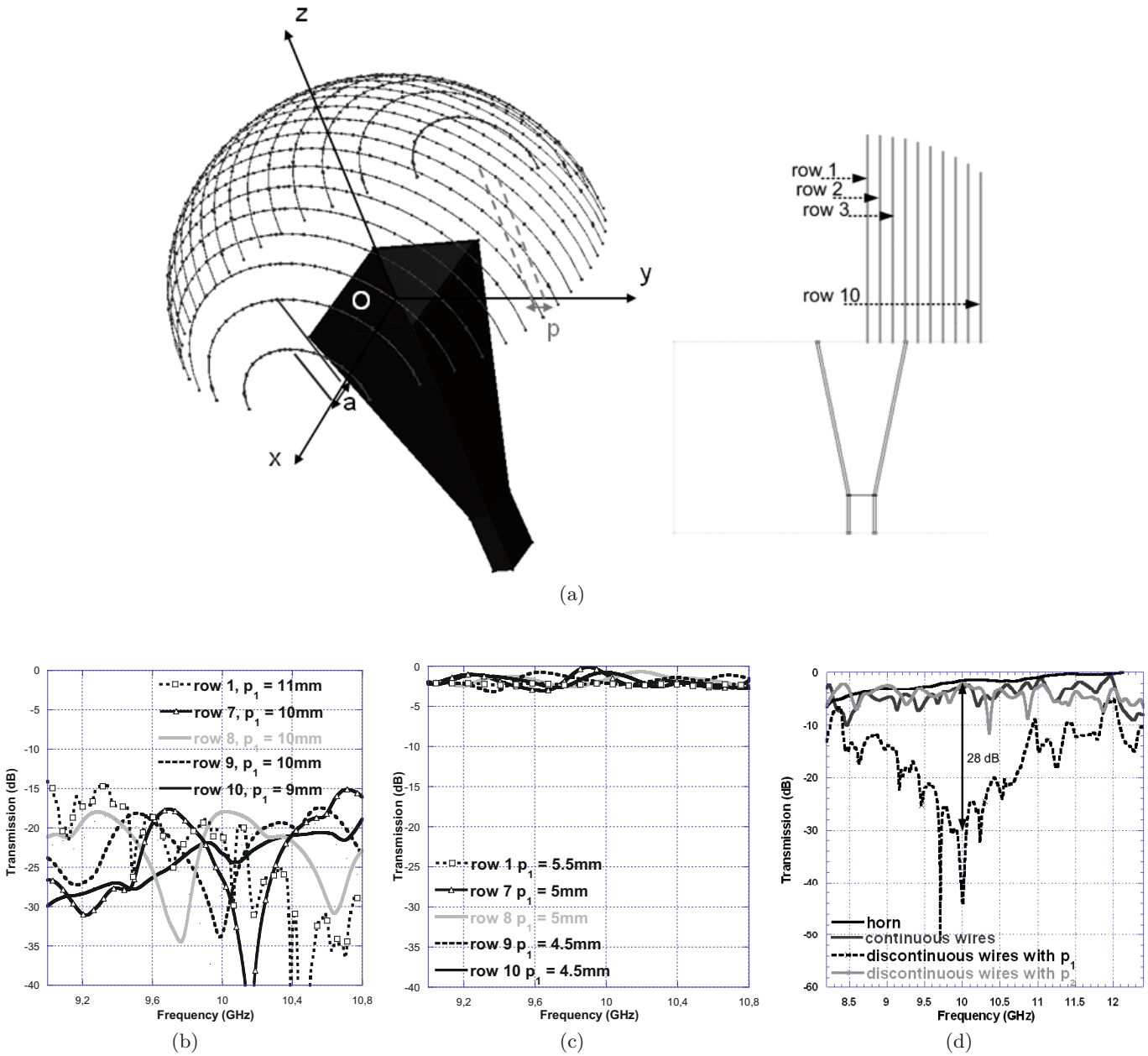

Fig. 2. (a) Schematic figure of the simulated structure with Microstripes. The inset shows half of the simulated radome in the xOz plane with the position of the different rows of wires. (b) Calculated transmission response for different row of wires with different periods p_1. (c) Calculated transmission response for different row of wires with different periods p_2. (d) Calculated frequency response for both configurations of wires. The radome is transmitting when the wires are continuous (grey curve) and when they are discontinuous with a discontinuity period p_2 (solid light grey curve). The radome is reflecting when the wires are discontinuous with a period p_1 (dark dashed curve). The commutation reaches more than 28 dB at 10 GHz between the transmitting and the reflecting state. The transmission of the horn antenna alone is given by the black curve.

wires are supposed to present an allowed band at 10 GHz. For the second structure composed of discontinuous wires, the discontinuities are placed along each row of wires in such a manner that their projections on the y-axis are equally spaced with a period p. The width of the discontinuities in all the rows is 0.1 mm. For the simulation, the **E**-field is polarised parallel to the wires. Here, we have tested only this polarization, but it is also possible to design a structure operating for two perpendicular linear polarizations with the use of crossed grids at 90°. The wires are considered to be perfect conductors in the various simulations. The EBG structures are designed so as to obtain a switching between an allowed and a forbidden transmission band at around 10 GHz. In this first configuration,

a commutation between the allowed band of the continuous wire strips structure and the forbidden band of discontinuous wire strips structure is desired. The position of the forbidden band depends on the discontinuities' periodicity and on the bend radius of the structure.

On the sphere, each row of wires has a different bend radius. Since the transmission level through the EBG structure depends on this bend radius, a different discontinuities' periodicity p_1 must be applied to each row of wires in order to obtain a forbidden band at 10 GHz. The period p_1 for each row is determined separately from a cylindrical periodical structure, so as to obtain a commutation at the desired frequency. The cylindrical EBG structure has been previously presented and investigated in [17]. The different parameters of the structure for a forbidden band at around 10 GHz are as follows: $p_1 = 11$ mm (discontinuities' periodicity) for the first six rows of wires, near of the summit of the radome, $p_1 = 10$ mm for the seventh (7th) to ninth (9th) rows and $p_1 = 9$ mm for the last row (10th). This set of wires will be referred to as having a discontinuities' periodicity p_1 in the rest of the text.

Figure 2b presents the transmission responses calculated for each row of wires separately on a cylindrical structure having a different specified radius. These rows of wires will then be applied on the spherical radome of variable radius. The responses show a very low transmission level for each row at 10 GHz ($\pm 10\%$), indicating that the different optimized periods can be applied to the discontinuities in order to have a forbidden band with the spherical radome.

2.2 Configuration 2: commutation between two structures of discontinuous wires

In the second configuration a commutation between the allowed band of a structure composed of discontinuous wires with a projection period p_2 and the forbidden band of the structure composed of discontinuous wires with the projection period p_1 previously used in configuration 1. For this second structure composed of discontinuous wires, the same study to optimize the different values of p_2 has been done so to obtain an allowed band at 10 GHz. For the six first rows, the discontinuities periodicity is $p_2 = 5.5$ mm, for the 7th to 9th rows $p_2 = 5$ mm, and for the last row $p_2 = 4.5$ mm. This set of wires will be referred to as having a discontinuities' periodicity p_2 in the rest of the text. The simulated transmission responses are presented in Figure 2c. We can observe that the transmission level is high and close to 0 dB for each row of wires, indicating an allowed band at 10 GHz. These rows of wires will then be applied on the spherical radome to exhibit an allowed band.

The transmissions through the three EBG-based radomes normalized to that of the horn antenna are presented in Figure 2d. For both configurations, a commutation of the transmitted signal can be observed at 10 GHz. This commutation reaches a level of more than 28 dB. In the first configuration this switching occurs between the EBG structure made of continuous wires (solid grey curve) and the structure made of discontinuous wires with periods p_1 (dashed black curve). In the second configuration, the commutation is observed between the EBG structure made of discontinuous wires with periods p_1 and an EBG structure made of discontinuous wires with periods p_2 (solid light grey curve). The main difference between these two commutation configurations is the transmission level when the radome is transparent to the horn antenna. In the first configuration, this level is weaker (–1.6 dB at 10 GHz) for the EBG structure made of continuous wires than for the second one made of discontinuous wires with periods p_2 (–0.6 dB).

3 Measurements

3.1 Gain versus frequency

Three different passive prototypes of the spherical EBG-based radome are fabricated according to the parameters mentioned above for the two switching control configurations. The first prototype is composed of continuous wire strips and the second one is composed of discontinuous wires with the periods of discontinuities p_1. Finally, the last prototype has the periods of discontinuities p_2 for the rows of wires. The wires made of copper are printed on a flexible support and are disposed on the hollow conformable spherical object made of low loss foam having a relative permittivity close to 1 and a thickness $h = 17$ mm. The maximum radius of the sphere is 16.5 cm. The widths of the wires and of the discontinuities are respectively 1 mm and 0.1 mm. A first set of transmission measurements are done using a horn antenna working in the X band (8.2 GHz–12.4 GHz) and having a angular beam width of 30° at –3 dB. It is placed at the centre inside the hollow foam sphere at a distance of 20 cm of the EBG structure. A picture of the EBG-based spherical radome with the emitting horn antenna inside is shown in Figure 3a. A receiving horn antenna is placed at a distance of 8 m from the radome. The measurements are done in the EADS Innovation Works' anechoic chamber at Suresnes (France) as illustrated by the experimental setup shown in Figure 3b. The gains of the emitting horn antenna alone and in the presence of the three different EBG-based radomes are measured versus frequency and the results are presented in Figure 4a.

The black curve represents the gain of the horn antenna alone in free space (without the use of the radome). For both configurations, a switching occurs at about 9.3 GHz. Compared to the simulation results, the measured commutation is shifted towards lower frequencies of about 0.7 GHz. This frequency shift between the simulated and the measured responses can be explained by the fabrication accuracy of the structures. The grey curve represents the gain response for the EBG structure with continuous wires. We can note that there is an average loss of 1.5 dB compared to the gain of the antenna alone, as it has been observed in simulations. In the first configuration, the switching between the EBG structures made

(a)

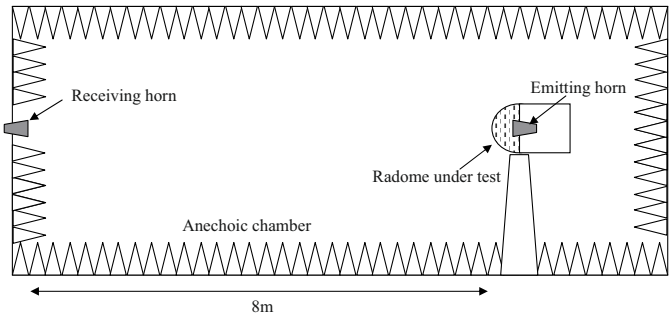

(b)

Fig. 3. (a) EBG structure under test in the anechoic chamber of EADS (Suresnes, France). (b) Schematic view of the anechoic chamber with the radome under test.

of continuous wires and discontinuous wires with periods p_1 reaches 24.5 dB, slightly weaker than the simulated one. The light grey curve represents the gain response for the radome made of discontinuous wires with periods p_2. Compared to the gain of the horn antenna alone, the transmission is quite lossless at 9.3 GHz. In the second configuration, the switching between the two EBG structures composed of discontinuous wires reaches a level of more than 26 dB.

A second set of measurements are done using as emitter a meteorological radar antenna array working at a centre frequency of 9.3 GHz with a bandwidth of about 10% (8.8 GHz–9.8 GHz) and having a angular beam width of 12° at –3 dB. This antenna is composed of an array of 256 elementary slot antennas. This type of antenna is used in the modern aircraft for weather forecasts and corresponds much better to the antenna associated really with this radome. In this case, the switching reaches a level of

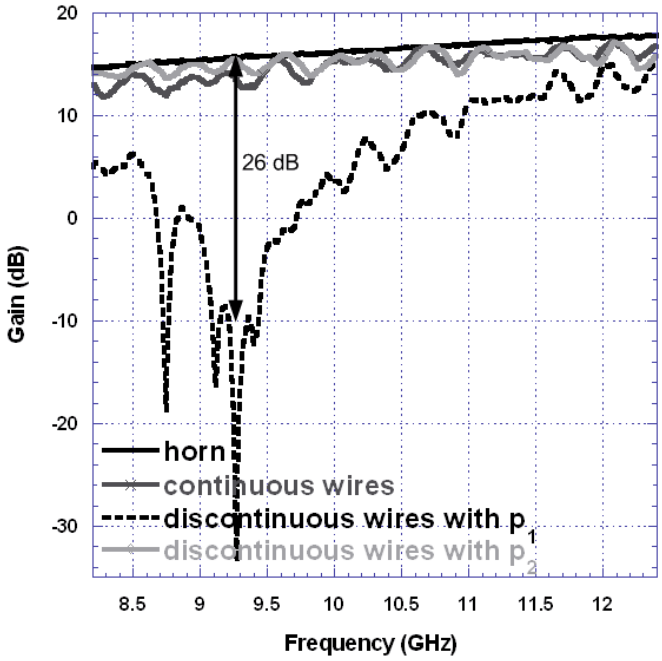

(a)

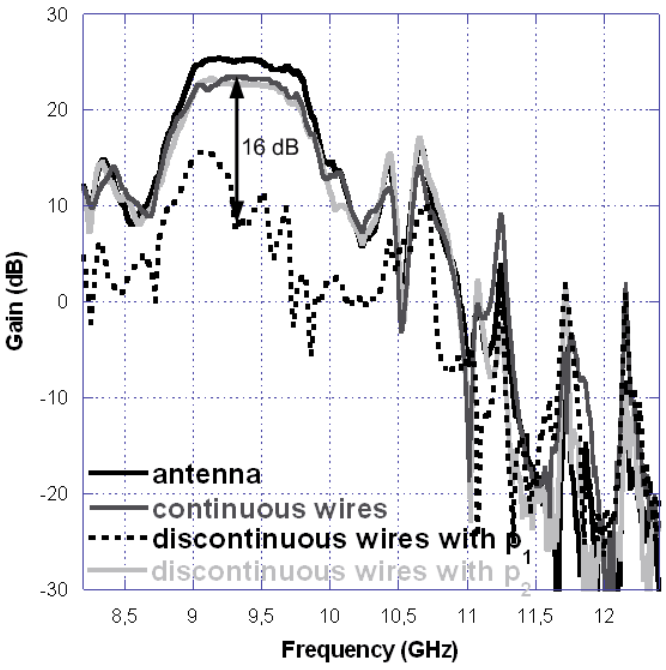

(b)

Fig. 4. (a) Measured transmission responses for the two commutation configurations with the horn antenna. (b) Measured transmission responses for the two commutation configurations with the meteorological antenna. The EBG radome is transmitting when the wires are continuous (solid grey curve) and when they are discontinuous with a discontinuity period p_2 (light grey curve). The radome is reflecting when the wires are discontinuous with a period p_1 (dashed black curve). The solid black curve illustrates the gain of the horn antenna alone.

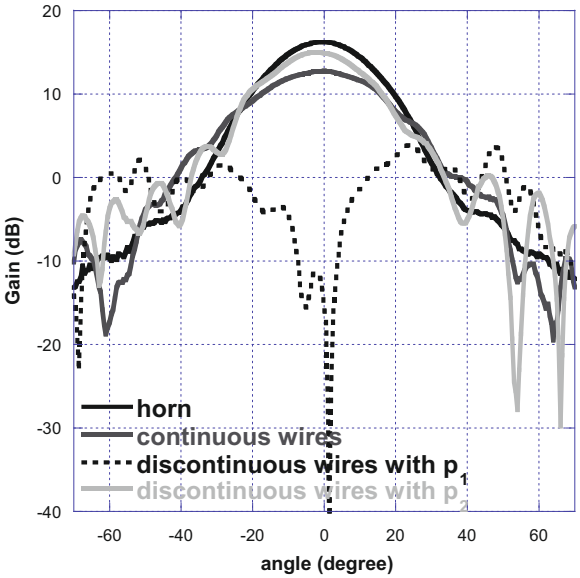

(a)

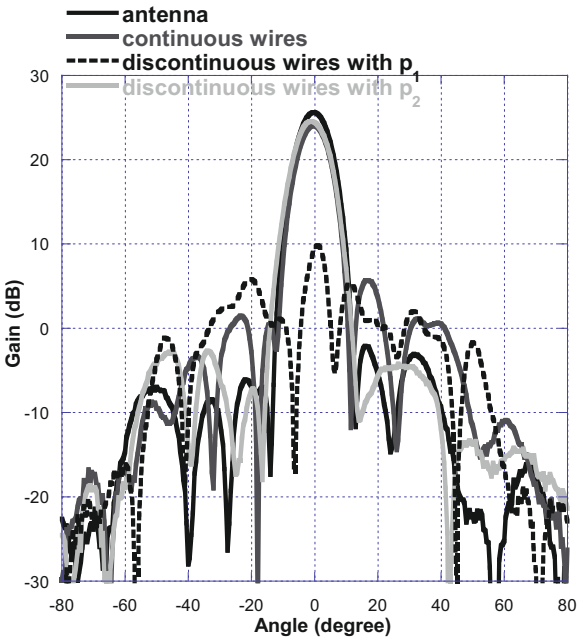

(b)

Fig. 5. (a) Radiation patterns for the three EBG radomes and the horn antenna alone at 9.3 GHz. (b) Radiation patterns for the three EBG radomes and the meteorological antenna alone at 9.3 GHz. The color code is the same as in Figure 4.

about 16 dB as shown in Figure 4b. Compared to the gain of the meteorological antenna alone, there is an average loss of 2 dB when the EBG-based radome is transparent.

3.2 Radiation patterns

The **E**-plane radiation patterns are also measured at the frequency corresponding to the commutation (f = 9.3 GHz) for the horn antenna alone and in presence of the three EBG-based radomes. The diagrams are shown in Figure 5a where the same color code of Figure 4 holds. In these measurements, the radome is rotated from –120° to 120° with respect to the position of the horn antenna which remains fixed. From Figure 5a, we can observe that the primary lobes of the continuous wires and the discontinuous wires with period p_2 have the same aperture angle at –3 dB as that of the horn antenna alone. However the secondary lobes reaching a level of –12 dB are higher for the EBG structure with period p_2. This may be due to the large number of discontinuities in this structure.

As for the horn antenna, measurements are done with the three EBG structures associated with the meteorological antenna array in order to show the commutation of the transmitted signal. The radiation patterns of the antenna alone and in presence of the EBG-based radomes at 9.3 GHz are presented in Figure 5b. Concerning the first commutation configuration, i.e. between the continuous wires and the discontinuous ones with periods p_1, we can observe a maximum level of commutation in transmission at 9.3 GHz of about 16 dB. For the second configuration between the EBG structure composed of discontinuous wires with periods p_2 and the one with p_1, the commutation level is quite identical. We can also observe an increase in the level of the secondary lobes in the presence of the radome. But the level of these lobes lies under –20 dB, which is better than those observed in the measurements using the horn antenna as emitter.

4 Conclusion

This paper presents the principle of two types of conformable and controllable spherical radomes based on an Electromagnetic Band Gap (EBG) material operating at around 9.3 GHz. The EBG structures are composed of a grid of metallic wires conformed on a hollow spherical object. Two configurations corresponding to two different operating modes have been tested: (1) an EBG structure made of electrically continuous wires and a structure made of discontinuous wires with periods p_1, (2) two EBG structures made of discontinuous wires with different periods of discontinuity, p_1 and p_2. Calculations and measurements performed on passive prototypes are in good agreement. A switching of the transmission is observed in simulations at 10 GHz and in measurements at 9.3 GHz. These EBG-based radomes have been tested with a horn antenna and a meteorological antenna array composed of 256 elementary slot antennas. The radiation patterns of both configurations of radomes have been measured and presented. A switching of about 26 dB is observed for the horn antenna, with an increase of the secondary lobes at a level of –12 dB. For the second antenna, which corresponds better to the real antenna used with this type of radome, we obtain a switching of 16 dB, with secondary lobes lying under –20 dB.

The authors would like to thank the EADS Foundation and DGA for its financial support.

References

1. M. Hook, J. Vardaxoglou, K. Ward, *Proc. 27th ESA Antenna Technology Workshop Innovative Periodic Antennas, Santiago de Compostela, Spain, 2004*, pp. 273–283
2. S. Maci, M. Caiazzo, A. Cucini, M. Casaletti, IEEE Trans. Antennas Propag. **53**, 70 (2005)
3. A. de Lustrac, F. Gadot, S. Cabaret, J.-M. Lourtioz, T. Brillat, A. Priou, E. Akmansoy, Appl. Phys. Lett. **75**, 1625 (1999)
4. A. de Lustrac, F. Gadot, E. Akmansoy, T. Brillat, Appl. Phys. Lett. **78**, 4196 (2001)
5. B.A. Munk, *Frequency selective surfaces, Theory and design* (Wiley-Interscience, 2000), p. 259
6. T.K. Chang, R.J. Langley, E. Parker, IEEE Microw. Guid. Wave Lett. **3**, 387 (1993)
7. B. Philips, E.A. Parker, R.J. Langley, Electron. Lett. **31**, 1 (1995)
8. T.K. Chang, R.J. Langley, E.A. Parker, IEE Proc. Microw. Antennas Propag. **143**, 62 (1996)
9. J.C. Vardaxoglou, Electron. Lett. **32**, 2345 (1996)
10. B.M. Cahill, E.A. Parker, Electron. Lett. **37**, 244 (2001)
11. G.I. Kiani, K.L. Ford, K.P. Esselle, A.R. Weily, C. Panagamuwa, J.C. Batchelor, Microw. Opt. Technol. Lett. **50**, 2149 (2008)
12. D.A. Whelan, J. Fraschilla, B.M. Pierce, *Ferro-electric frequency selective surface radome*, United States Patent 5600325 (1997)
13. W.S. Arceneaux, R.D. Akins, W.B. May, *Absorptive/transmissive radome*, United States Patent 5400043 (1995)
14. J.B. Pendry, A. Holden, W. Stewart, I. Youngs, Phys. Rev. Lett. **76**, 4773 (1996)
15. A. de Lustrac, T. Brillat, F. Gadot, E. Akmansoy, Opt. Quant. Electron. **34**, 265 (2002)
16. Microstripes, Microstripes Reference Manual Release 7.0, FLOMERICS Ltd., 2005
17. S. Haché, S.N. Burokur, F. Gadot, P. Cailleu, G.-P. Piau, A. de Lustrac, *Proc. Loughborough Antennas and Propagation Conference (LAPC 2007), Loughborough, UK, 2007*, p. 305

Annexe 1.3

S. N. Burokur, A. Ourir, J.-P. Daniel, P. Ratajczak, A. de Lustrac

« Highly directive ISM band cavity antenna using a bi-layered metasurface reflector »

Microwave and Optical Technology Letters, vol. 51, no. 6, pp. 1393-1396, June 2009

high passband selectivity. The proposed compact dual-wideband BPF is useful for mobile wideband wireless transmitting system.

REFERENCES

1. M.H. Weng, H.W. Wu, and Y.K. Su, Compact and low loss dual-band bandpass filter using pseudo-interdigital stepped impedance resonators for WLANs, IEEE Microwave Wireless Compon Lett 17 (2007), 187–189.
2. M.H. Weng, Y.C. Chang, H.W. Wu, and C.Y. Huang, Design of multi-layered dual-band bandpass filter using cross-coupled stepped impedance resonators, Microwave Opt Technol Lett 49 (2007), 2713–2717.
3. J.T. Kuo, T.H. Yeh, and C.C. Yeh, Design of microstrip bandpass filters with a dual-passband response, IEEE Trans Microwave Theory Tech 53 (2005), 1331–1337.
4. C.F. Chen, T.Y. Huang, C.P. Chou, and R.B. Wu, Microstrip diplexers design with common resonator sections for compact size, but high isolation, IEEE Trans Microwave Theory Tech 54 (2006), 1945–1952.
5. K. Li, D. Kurita, and T. Matsui, A novel UWB bandpass filter and its a application to UWB Pulse Generation, In: European Microwave Conference, Manchester, England, 2006, pp. 591–594.
6. H. Shaman, J.S. Hong, Ultra-wideband (UWB) bandpass filter with embedded band notch structures, IEEE Microwave Wireless Compon Lett 17 (2007), 193–195.
7. J.S. Hong and M.J. Lancaster, Microstrip filters for RF/microwave application, Wiley, New York, NY, 2001.
8. IE3D Simulator, Zeland Software, Inc., Fremont, CA, 1997.

HIGHLY DIRECTIVE ISM BAND CAVITY ANTENNA USING A BI-LAYERED METASURFACE REFLECTOR

Shah Nawaz Burokur,[1] Abdelwaheb Ourir,[1] Jean-Pierre Daniel,[2] Philippe Ratajczak,[3] and André de Lustrac[1]

[1] Institut d'Electronique Fondamentale (IEF), Université Paris-Sud, CNRS, UMR 8622, Orsay, France; Corresponding author: andre.de-lustrac@u-psud.fr

[2] Advanten, Rennes, France

[3] Orange Labs-Recherche et Développement, La Turbie, France

Received 15-Sep-2008

ABSTRACT: *The design of a highly directive metamaterial-based cavity antenna for a 2.46 GHz application is reported. The proposed structure is evolved from a Fabry-Perot (FP) cavity with a patch antenna acting as the feed and four metallic walls on the lateral sides. One of the two reflectors is the antenna's ground plane and the other is made from a bilayered metamaterial-based partially reflecting surface (PRS) constituted by a capacitive and an inductive grid. Calculations together with experimental results obtained from the fabricated prototype are presented. The results show a high directivity and low levels for the secondary lobes compared to a 2 × 2 patch antenna array.* © 2009 Wiley Periodicals, Inc. Microwave Opt Technol Lett 51: 1393–1396, 2009; Published online in Wiley InterScience (www.interscience.wiley.com). DOI 10.1002/mop.24391

Key words: *metamaterials; highly directive; Fabry-Perot (FP) cavity; microstrip patch antenna*

1. INTRODUCTION

There have been different solutions proposed recently in literature concerning the design of compact directive electromagnetic sources based on a single feeding point. The most common method to produce a highly directive antenna is obviously based on the Fabry-Perot (FP) cavity [1]. Such cavities can be considered quite bulky because a thickness of half of the working wavelength is required. But recently, Feresidis et al. showed that the half wavelength restriction can be reduced to a quarter wavelength by using a novel type of metamaterial-based resonant cavity in which a microstrip patch antenna was embedded [2]. The latter requires the use of artificial magnetic conductor (AMC) surfaces introducing a zero degree reflection phase shift to incident waves. The cavity of thickness $\lambda/4$ proposed by Feresidis is composed of two planar AMC surfaces. The first one is used as a perfect magnetic conductor (PMC) surface with 0° reflection phase so as to replace the perfect electric conductor (PEC) ground plane with 180° reflection phase of the antenna. The second one acts as a partially reflective surface (PRS) with a 180° reflection phase. This idea has been pushed further by Zhou et al. by taking advantage of the dispersive characteristics of metamaterials, designing a subwavelength cavity [3]. Compared with Feresidis, Zhou made use of a nonplanar mushroom structure with a dipole acting as the feeding source.

Using a novel type of composite metamaterial made of inductive and capacitive grids as a partially reflecting surface (PRS) and an AMC surface as antenna substrate, our group has further reduced the cavity thickness to $\lambda/60$ for applications to ultra-thin directive antennas [4]. Another cavity of thickness $\lambda/30$ using a PEC reflector and the composite metamaterial has been proposed [5]. Recently, we have also designed a frequency reconfigurable cavity antenna based on the use of a composite phase varying metamaterial by the incorporation of varactors [6].

In this article, we report the design of a highly directive and compact cavity antenna at 2.46 GHz for point to point radio communication links. The metallic cavity is composed of the feeding antenna's ground plane and a metamaterial-based PRS as reflectors. Furthermore, four metallic walls are also fixed on the lateral sides, so as to enhance the directivity of the cavity antenna while keeping low lateral dimensions. A numerical analysis using the transmission line matrix (TLM) method software *Micro-Stripes* [7] together with discussions on the fabrication process and the characterization results are presented for the proposed cavity. The performances of the metallic cavity are further compared with those obtained from microstrip patch arrays.

2. DESIGN AND OPTIMIZATION OF THE CAVITY ANTENNA

2.1. Feeding Patch Antenna

The frequency of the feeding patch antenna must lie at a slightly higher frequency than that of the desired 2.46 GHz for the cavity. This is because the whole structure (cavity + feeding antenna) always shows a resonance at a lower frequency than that of the feeding patch alone because we are in presence of two highly coupled cavities, i.e. the patch antenna and the FP cavity. The frequency found after optimization for the antenna alone is 2.63 GHz and the dielectric board used in simulations is made of foam having a relative permittivity $\varepsilon_r = 1.45$, a tangential loss of 0.0058 and a thickness $d = 5$ mm. The lateral dimensions of the dielectric board is 200 mm ×200 mm, corresponding to $1.64\lambda_0 \times 1.64\lambda_0$, where λ_0 is the free space wavelength. The dimensions calculated for the square patch are 43 mm ×43 mm. The patch antenna is simulated with a coaxial feed placed at 10 mm offset from the centre of the patch for a very good matching.

A return loss of 24 dB and a directivity of 8.38 dB are observed at 2.63 GHz for the antenna alone. At 2.46 GHz, a directivity of 7.99 dB is noted.

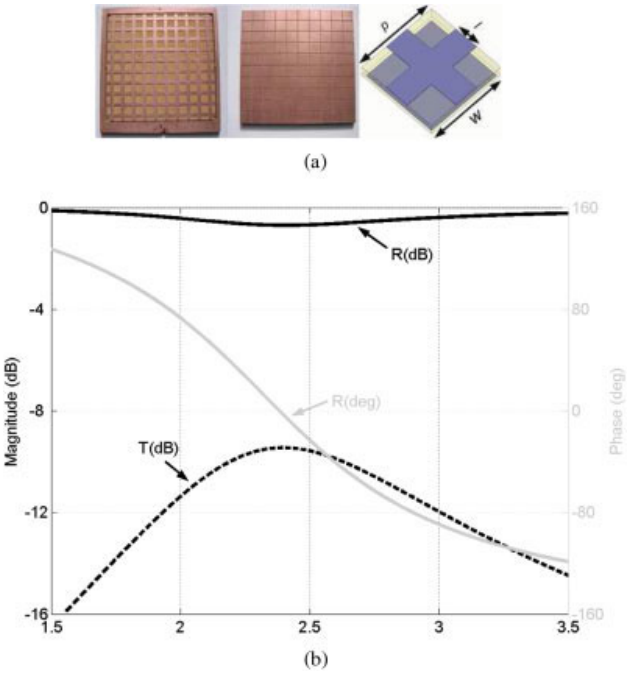

Figure 1 (a) Unit cell (right) of the metamaterial-based PRS composed of an inductive (left) and a capacitive grid (middle). (b) Calculated reflection phase (solid grey), reflection (solid dark), and transmission (dashed dark) magnitudes for the PRS reflector. [Color figure can be viewed in the online issue, which is available at www.interscience.wiley.com]

2.2. *Metamaterial-Based PRS*

In this section, we design the planar bilayered metamaterial-based surface for operations near 2.46 GHz. The surface used by our group for the PRS of the cavity is made of a composite metamaterial consisting of simultaneously a capacitive and an inductive grid on the two faces of an 8 mm thick foam dielectric substrate. This thickness is sufficient enough to provide a relatively smooth slope of the phase response, hence rendering the metamaterial less sensitive to fabrication tolerances. The capacitive grid is formed by 2-D periodic metallic patches lattice (period $p = 20$ mm and width $w = 18.8$ mm), whereas the inductive grid is formed by a 2-D periodic mesh (line width $l = 6$ mm, period $p = 20$ mm) as shown by the unit cell in Figure 1(a). The composite metamaterial acts as a resonant filter, which presents a reflection phase between 180° and −180°, depending on the frequency. The size of the different patterns has been chosen in order to have the phase of the reflection coefficient below 0° near 2.46 GHz while providing a sufficiently high reflectance (∼90%). A numerical analysis is performed on one unit cell together with appropriate boundary conditions. The results presented in Figure 1(b) show firstly a resonance frequency of 2.38 GHz, i.e. where the phase crosses 0°. Secondly, we can also note a pass-band behavior where the transmission level is relatively low (about −9.5 dB). Finally, this figure shows a reflection phase of −15° at 2.46 GHz. This phase value is very important because it will help to determine the thickness of the cavity as it will be described in the next section. Compared with the PRS used in [2] by Feresidis et al., which is composed uniquely of a capacitive grid exhibiting a slow variation of the reflection phase over a wide frequency band, our composite metamaterial-based one proposes a reflection phase coefficient varying from 180° to −180° over a lower frequency range. This variation helps to be more flexible in designing thin cavities by choosing reflection phase values below 0°.

2.3. *Optimization of the Metallic Cavity Antenna*

Now that the feeding patch antenna and the PRS have been properly defined, we can proceed with the design of the cavity antenna. The cavity proposed here is composed of two reflectors; the first one being the feeding antenna's PEC ground plane and the other one is the metamaterial-based PRS. Figure 2(a) illustrates the design of the cavity. Following the early work of Trentini [1], a

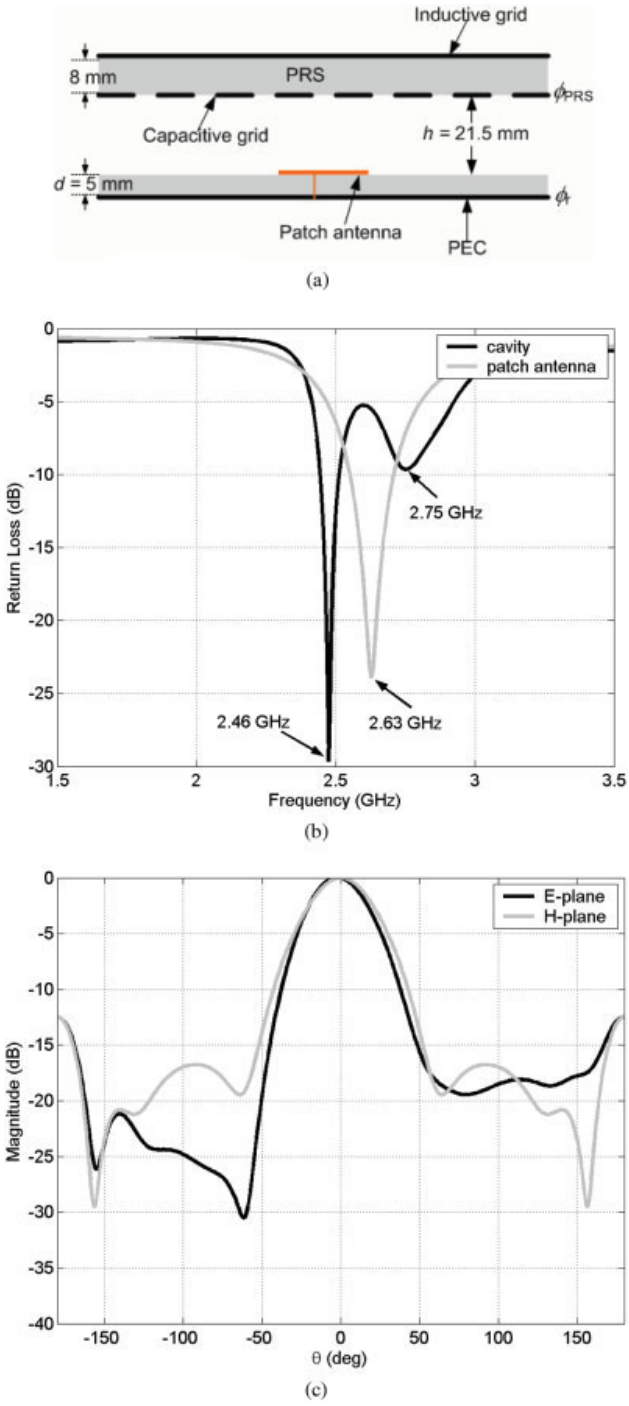

Figure 2 (a) Cavity composed of the patch antenna's PEC ground plane and the metamaterial-based PRS. (b) Return losses of the cavity antenna and the feeding patch antenna. (c) **E**- and **H**-plane radiation patterns at 2.46 GHz. [Color figure can be viewed in the online issue, which is available at www.interscience.wiley.com]

simple optical ray model can be used to describe the resonant cavity modes. This model is used to theoretically predict the existence of a low-profile high-directivity metamaterial-based subwavelength cavity antenna, which is formed by a feeding antenna placed between two reflectors separated by a distance h. Phase shifts are introduced by these two reflectors and also by the path length of the wave traveling inside the cavity. With the multiple reflections of the wave emitted by the antenna, a resonance is achieved when the reflected waves are in phase after one cavity roundtrip. The resonance condition can then be written as:

$$h + d\sqrt{\varepsilon_r} = (\phi_{PRS} + \phi_r)\frac{\lambda}{4\pi} \pm N\frac{\lambda}{2}. \quad (1)$$

where ϕ_{PRS} is the reflection phase of the PRS reflector, ϕ_r is the reflection phase of the reflector near the antenna (PEC in our case), and N is an integer corresponding to the order of the cavity's electromagnetic mode. d and ε_r are respectively the thickness and the relative permittivity of the antenna's dielectric board. If the cavity thickness h is fixed, the resonant wavelength is determined by the sum of the reflection phases $\phi_{PRS} + \phi_r$. Conversely, for a given wavelength, the thickness h can be minimized by minimizing the total phase shift $\phi_{PRS} + \phi_r$. The use of our composite metamaterial-based surface answers this purpose because it provides a low reflection phase around the frequency of maximum surface impedance. If the reflector near the feeding antenna is composed of a PEC surface, then ϕ_r will be very close to 180°.

So with a $\phi_{PRS} = -15°$, the thickness of the cavity is found to be $h = 21.5$ mm ($< \lambda/5$). The simulated cavity presents a return loss of 22.8 dB at 2.46 GHz [Fig. 2(b)]. A second resonance is observed at 2.75 GHz corresponding to the resonance of the feeding antenna. These two resonances are situated at each side of that of the feeding patch alone due to the coupling between the patch antenna and the FP cavity. The **E**- and **H**-plane radiation patterns [Fig. 2(c)] show a directivity of 12.27 dB, corresponding to an enhancement of about 4 dB compared with the patch antenna alone. The secondary lobes reach a level of −16.8 dB in the **H**-plane. Moreover, we can also observe backward radiations with a level approaching −12.5 dB because of the small lateral dimensions.

To reach a higher directivity, a better confinement of the electromagnetic energy must be reached in the cavity. For this purpose, two solutions can be considered. The first one is to increase the lateral dimensions of the cavity, leading to a larger surface of the PRS. The innovative second solution studied here is to shield the cavity by four metallic walls, while keeping the lateral dimensions of the cavity close to $2\lambda_0 \times 2\lambda_0$. This is the maximum lateral dimensions of the foam that can be chemically processed for the metallization by Advanten. A schematic view of the metallic cavity antenna is proposed in Figure 3(a).

The surface of the inductive and capacitive grids forming the PRS remains the same (200 mm ×200 mm), whereas the lateral dimensions of the dielectric board supporting the grids as well as that of the cavity have been increased to 250 mm ×250 mm. However, the metallic walls are separated by a distance of 240 mm. The calculated results [Figs. 3(b) and 3(c)] for the **E**- and **H**-plane radiation patterns show lower secondary lobes and a directivity of 15.21 dB, indicating clearly an enhancement of about 3 dB compared with the case without the metallic walls. To reach this same directivity without metallic walls, we should have used a cavity with lateral dimensions close to 400 mm × 400 mm. Also, the metallic cavity presents very low backward radiations (−24.3 dB) because of the energy confinement by the lateral walls.

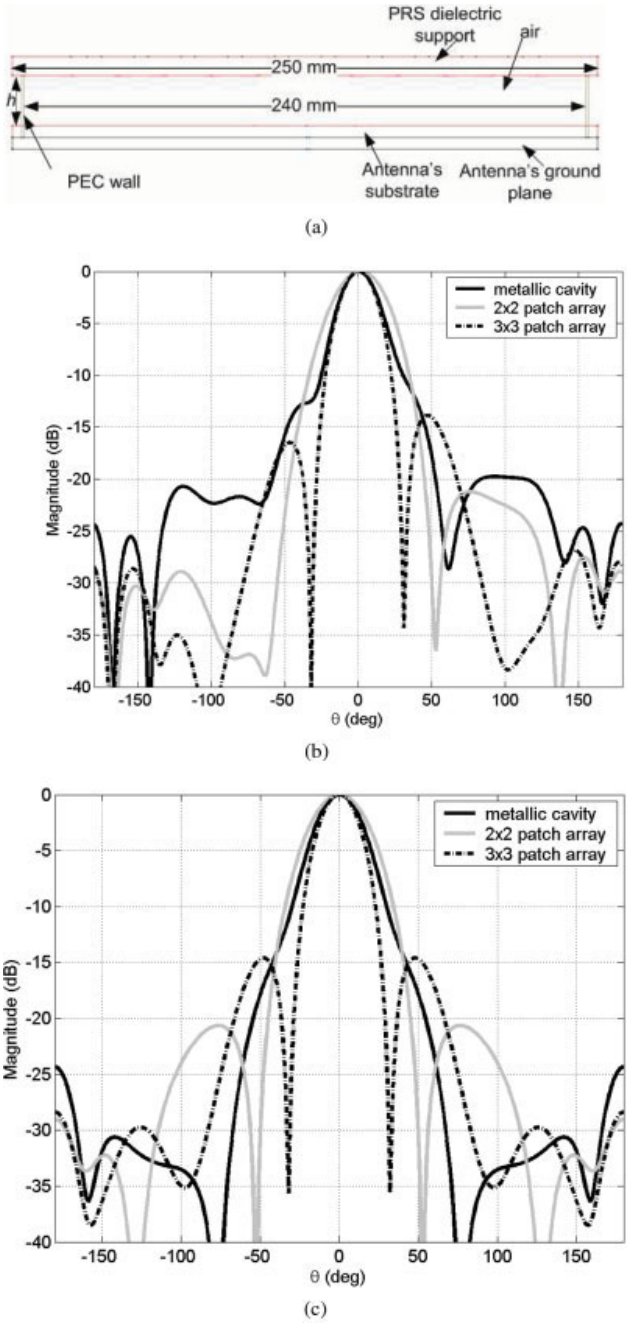

Figure 3 (a) Schematic view of the metallic cavity antenna. (b) Comparison of the **E**-plane radiation pattern between the metallic cavity and patch arrays at 2.46 GHz. (c) Comparison of the **H**-plane radiation pattern between the metallic cavity and patch arrays at 2.46 GHz. [Color figure can be viewed in the online issue, which is available at www.interscience.wiley.com]

2.4. Comparison with Microstrip Patch Arrays

These results are further compared with those obtained for a 2 × 2 and 3 × 3 patch antenna arrays operating at 2.46 GHz, where all the elements are excited simultaneously. The dimensions of the square patches are 46 mm × 46 mm and the distance between each patch is 30.5 mm corresponding to $\lambda/4$ at 2.46 GHz. 13.9 dB and 16.8 dB are respectively observed for the directivities of the 2 × 2 and 3 × 3 patch arrays. Compared with the 2 × 2 patch array, the metallic cavity presents a higher directivity but a slightly

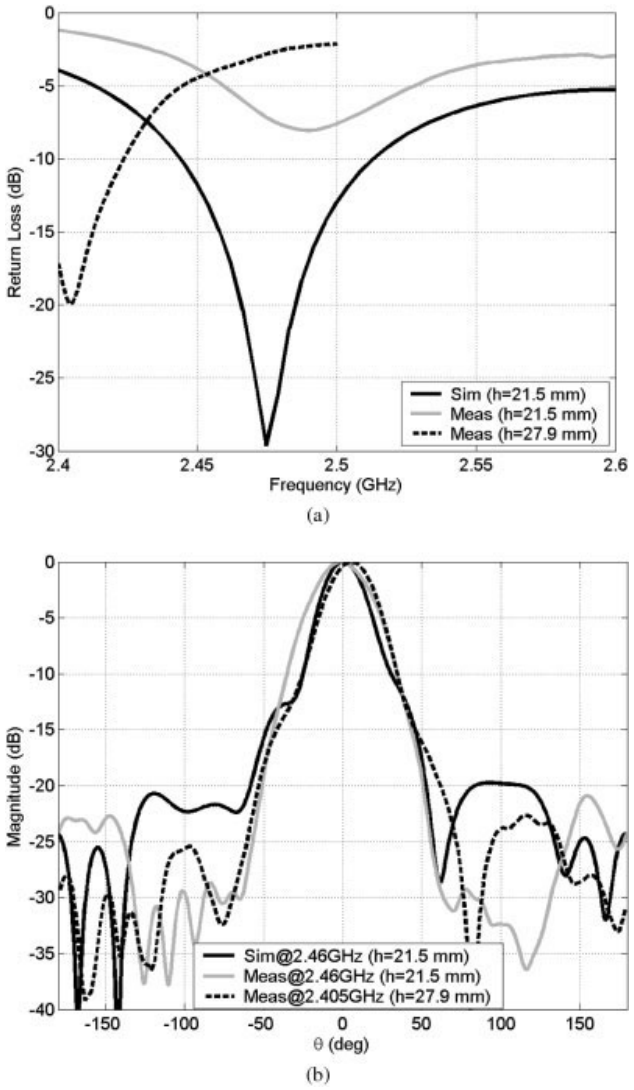

Figure 4 (a) Measured return loss of the metallic cavity antenna. (b) Comparison between simulated and measured **E**-plane radiation patterns.

higher level of secondary lobes in the E-plane. The 3 × 3 patch array not only proposes a slightly higher directivity but also higher secondary lobes than the metallic cavity, due to the restricted lateral dimensions of the ground plane. In the **H**-plane, the secondary lobes of the cavity are very low compared with the two patch arrays. We must note that with a conventional antenna array, we should have used power dividers for the complicated feeding of each element, whereas the cavity antenna presents only a single feeding point.

2.5. Measurements and Discussions

A prototype of the proposed cavity has been fabricated and measured (Figure 4). However, the responses measured with $h = 21.5$ mm have not shown a resonance as expected at 2.46 GHz but at 2.49 GHz. This is due to the matching of the fabricated feeding patch antenna which does not occur at 2.63 GHz as in simulation. Moreover, the responses of the PRS may also present a shift in frequency, which can be attributed to the manufacturing tolerances. A modification on the thickness of the cavity has then been undertaken to achieve as close as possible the calculated resonance frequency. Three other different thicknesses ($h = 25$ mm, $h = 27.9$ mm, and $h = 28.5$ mm) have shown remarkable performances. The different results are summarized in Table 1.

TABLE 1 Performances of the Metallic Cavity Antenna

h (mm)	Resonant Frequency (GHZ)	Return LOSS (DB)	Directivity (dB)	Secondary Lobes Level (dB)
21.5 (sim)	2.46	29.5	15.3	−19.7
21.5 (meas)	2.49	8	12.36	−28.7
25 (meas)	2.46	11	12.79	−26.5
27.9 (meas)	2.405	20	13.4	−22.7
28.5 (meas)	2.4	21.5	12.4	−24.4

As the thickness increases, the resonance of the cavity antenna tends to lower frequencies. For $h = 25$ mm, the measurements show a return loss of 11 dB and a directivity of 12.79 dB with secondary lobes reaching a level of −26.5 dB. For $h = 28.5$ mm, the return loss is enhanced to 21.5 dB at 2.405 GHz but the directivity falls to 12.4 dB. The best directivity (13.4 dB) is observed at 2.405 GHz for $h = 27.9$ mm with secondary lobes level of −22.7 dB.

3. CONCLUSION

A highly directive metallic cavity antenna has been proposed for point to point radio communication links at 2.46 GHz in the ISM band. The metallic cavity is composed of the feeding patch antenna's ground plane and a bilayered metamaterial-based PRS acting as reflectors and four metallic walls on the lateral sides. A single patch antenna is used as radiating source. The calculated directivity reaches 15.21 dB and presents lower secondary lobes than a 3 × 3 patch array. The radiation measurements have shown a maximum directivity of 13.4 dB with secondary lobes level less than −22.7 dB at 2.405 GHz.

REFERENCES

1. G.V. Trentini, Partially reflecting sheet arrays, IRE Trans Antennas Propag AP-4 (1956), 666–671.
2. A.P. Feresidis, G. Goussetis, S. Wang, and J.C. Vardaxoglou, Artificial magnetic conductor surfaces and their application to low-profile high-gain planar antennas, IEEE Trans Antennas Propag 53 (2005), 209–215.
3. L. Zhou, H. Li, Y. Qin, Z. Wei, and C.T. Chan, Directive emissions from subwavelength metamaterial-based cavities, Appl Phys Lett 86 (2005), 101101–1–101101–3.
4. A. Ourir, A. de Lustrac, and J.-M. Lourtioz, All-metamaterial-based sub-wavelength cavities (λ/60) for ultrathin directive antennas, Appl Phys Lett 88 (2006), 084103–1–084103–3.
5. A. Ourir, A. de Lustrac, and J.-M. Lourtioz, Optimization of metamaterial based subwavelength cavities for ultracompact directive antennas, Microwave Opt Technol Lett 48 (2006), 2573–2577.
6. A. Ourir, S.N. Burokur, and A. de Lustrac, Electronically reconfigurable metamaterial for compact directive cavity antennas, Electron Lett43 (2007), 698–700.
7. Micro-Stripes Reference Manual Release 7.0, FLOMERICS Ltd., 2005.

Annexe 1.4

S. N. Burokur, R. Yahiaoui, A. de Lustrac

« Subwavelength metamaterial-based resonant cavities fed by multiple sources for high directivity »

Microwave and Optical Technology Letters, vol. 51, no. 8, pp. 1883-1888, August 2009

mm. It is observed that the lower resonance shift to lower side, whereas upper resonance frequency shift to higher side with increasing value of P_s. This shift in resonances causes considerable increases in bandwidth with P_s.

Theoretical and simulated plots of return loss are shown in Figure 9 for given value of $w_s = 2$ mm, $L_s = 11$ mm, and $P_s = 5$ mm. It is found that proposed theoretical results are in close agreement with the simulated results obtained from IE3D. The deviation in the proposed results is due to some approximations made in the analysis.

5. CONCLUSIONS

From the analysis, it is found that the resonances and bandwidth of the antenna depend on the parameters of the notches cut in the patch which results into controllable bandwidth of the antenna.

REFERENCES

1. S.D. Targonski, R.B. Waterhouse, and D.M. Pozar, Design of wideband aperture stacked patch microstrip antennas, IEEE Trans Antennas Propoag 14 (1998), 1245–1251.
2. S.N. Mulgi, R.M. Vani, P.V. Hunagund, and P.M. Hadalgi, A compact broadband gap-coupled microstrip antenna, Indian J Radio Space Phys 33 (2004), 139–141.
3. J.A. Ansari, S.K. Dubey, P. Singh, R.U. Khan, and B.R. Vishvakarma, Analysis of V-slot loaded patch antenna for wideband operation, Microwave Opt Technol Lett 50 (2008), 3069–3075.
4. J.A. Ansari and R.B. Ram, Analysis of broadband U-slot microstrip patch antenna, Microwave Opt Technol Lett 50 (2008), 1069–1073.
5. R.B. Waterhouse, Broadband stacked shorted patch, Electron Lett 35 (1999), 98–100.
6. Y.J. Wang and C.K. Lee, Versatile semi-disk microstrip antennas: Study and application, J Electromagn Waves Appl 15 (2001), 1595–1613.
7. J.-H. Lu, C.-L. Tang, and K.-L. Wong, Novel dual-frequency and broadband designs of slot-loaded equilateral triangular microstrip antennas, IEEE Trans Antennas Propag 48 (2000), 1048–1054.
8. T.K. Lo, Miniature aperture-coupled microstrip antenna of very high permittivity, Electron Lett 33 (1997), 9–10.
9. S. Pinhas and S. Shtrikman, Comparison between computed and measured bandwidth of quarter-wave microstrip radiators, IEEE Trans Antennas Propoag 36 (1988), 1615–1616.
10. R.B. Waterhouse, Small microstrip patch antenna, Electron Lett 31 (1995), 604–605.
11. J.A. Ansari, P. Singh, S.K. Dubey, R.U. Khan, and B.R. Vishvakarma, Analysis of symmetrically notch loaded stacked disk patch antenna for wideband application, Microwave Opt Technol Lett, in press.
12. IE3D simulation software, Zeland, version 14.05, Zeland Inc., USA, 2008.
13. G. Kumar and K.P. Ray, Broadband microstrip antennas, Artech House, Boston, London, 2003, pp. 74–79.
14. K.P. Ray and G. Kumar, Determination of resonant frequency of microstrip antennas, Microwave Opt Technol Lett 23 (1999), 114–117.
15. I.J. Bahal and P. Bhartia, Microstrip antennas, Artech House, Boston, MA, 1985.
16. L.C. Shen, et al., Resonant frequency of a circular disk printed circuit antenna, IEEE Trans Antennas Propoag 25 (1997), 595–596.
17. V.K. Pandey and B.R. Vishvakarma, Analysis of an E-shaped patch antenna, Microwave Opt Technol Lett 18 (2006), 297–300.
18. F. Yang, X.X. Zhang, X. Ye, and R.S. Yahya, Wide-band E-shaped patch antennas for wireless communications, IEEE Trans Antennas Propag 49 (2001), 1094–1100.
19. X.X. Zhang and F.N. Yang, Study of slit cut on microstrip antenna and its application, Microwave Opt Technol Lett 18 (1998), 297–300.
20. I.J. Bahal, Lumped elements for RF and microwave circuit, Artech House, Norwood, MA 2003, pp. 456–459.
21. C.A. Balanis, Antenna theory analysis and design, 2nd ed., Wiley, New York, 1997.

SUBWAVELENGTH METAMATERIAL-BASED RESONANT CAVITIES FED BY MULTIPLE SOURCES FOR HIGH DIRECTIVITY

Shah Nawaz Burokur, Riad Yahiaoui, and André de Lustrac
Institut d'Electronique Fondamentale (IEF), Univ. Paris-Sud, CNRS, UMR 8622, Orsay, France; Corresponding author: nawaz.burokur@u-psud.fr

Received 6 November 2008

ABSTRACT: *The analysis and design of subwavelength metamaterial-based resonant cavity antennas are presented. The antennas under investigation are formed by embedding a feeding source in a Fabry-Perot (FP) cavity composed of a Perfect Electrical Conductor (PEC) surface and a metasurface reflector. The embedded feeding source used in this study is a 2 × 2 microstrip patch array. The influence of the interelement spacing of the patch array feed on the radiation patterns is investigated and reported. The effect of the cavity thickness is also considered. Finally, the design of highly directive subwavelength cavity antennas is presented.* © 2009 Wiley Periodicals, Inc. Microwave Opt Technol Lett 51: 1883–1888, 2009; Published online in Wiley InterScience (www.interscience.wiley.com). DOI 10.1002/mop.24485

Key words: *metamaterials; highly directive antenna; Fabry-Perot cavity; microstrip patch antenna; subwavelength antenna*

1. INTRODUCTION

According to the earlier work of Trentini [1], a highly directive antenna can be obtained by using a Fabry-Perot (FP) cavity. The latter cavity is composed of an embedded source between two reflecting or semireflecting mirrors. The thickness h of a Fabry-Perot (FP) cavity antenna is given by the resonance condition which is written as follows:

$$h + d\sqrt{\varepsilon_r} = (\phi_{PRS} + \phi_r)\frac{\lambda}{4\pi} \pm N\frac{\lambda}{2} \quad (1)$$

where ϕ_{PRS} is the reflection phase of the PRS reflector, ϕ_r is the reflection phase of the reflector near the antenna, and N is an integer corresponding to the order of the cavity's electromagnetic mode. d and ε_r are, respectively, the thickness and the dielectric constant of the antenna's substrate. Such cavities can be considered quite bulky since a thickness of half of the working wavelength is generally required when metallic mirrors are used with a total reflection phase shift $\phi_{PRS} + \phi_r = 2\pi$. However, recent developments on Fabry-Perot type antennas have shown the possibility to design subwavelength resonant cavities by minimizing the total reflection phase shift $\phi_{PRS} + \phi_r$ [2–5]. Indeed, Artificial Magnetic Conductor (AMC) surfaces and metasurfaces have been proposed for applications as Partially Reflective Surface (PRS) in the design of compact and highly directive cavity antennas. These surfaces present a tailored reflection phase varying from +180° to −180° and crossing 0° at the resonance frequency. In Ref. 2, two planar AMC surfaces have been used to achieve a cavity of thickness λ/4. By taking advantage of the dispersive characteristics of metamaterials, Zhou et al. [3] made use of a nonplanar mushroom structure with a dipole acting as the feeding source to design a subwavelength cavity. Using a novel type of composite metamaterial made of inductive and capacitive grids as a Partially Reflecting Surface (PRS) and an AMC surface as antenna substrate, our group has further reduced the cavity thickness to λ/60 for applications to ultrathin directive antennas [4]. Another cavity

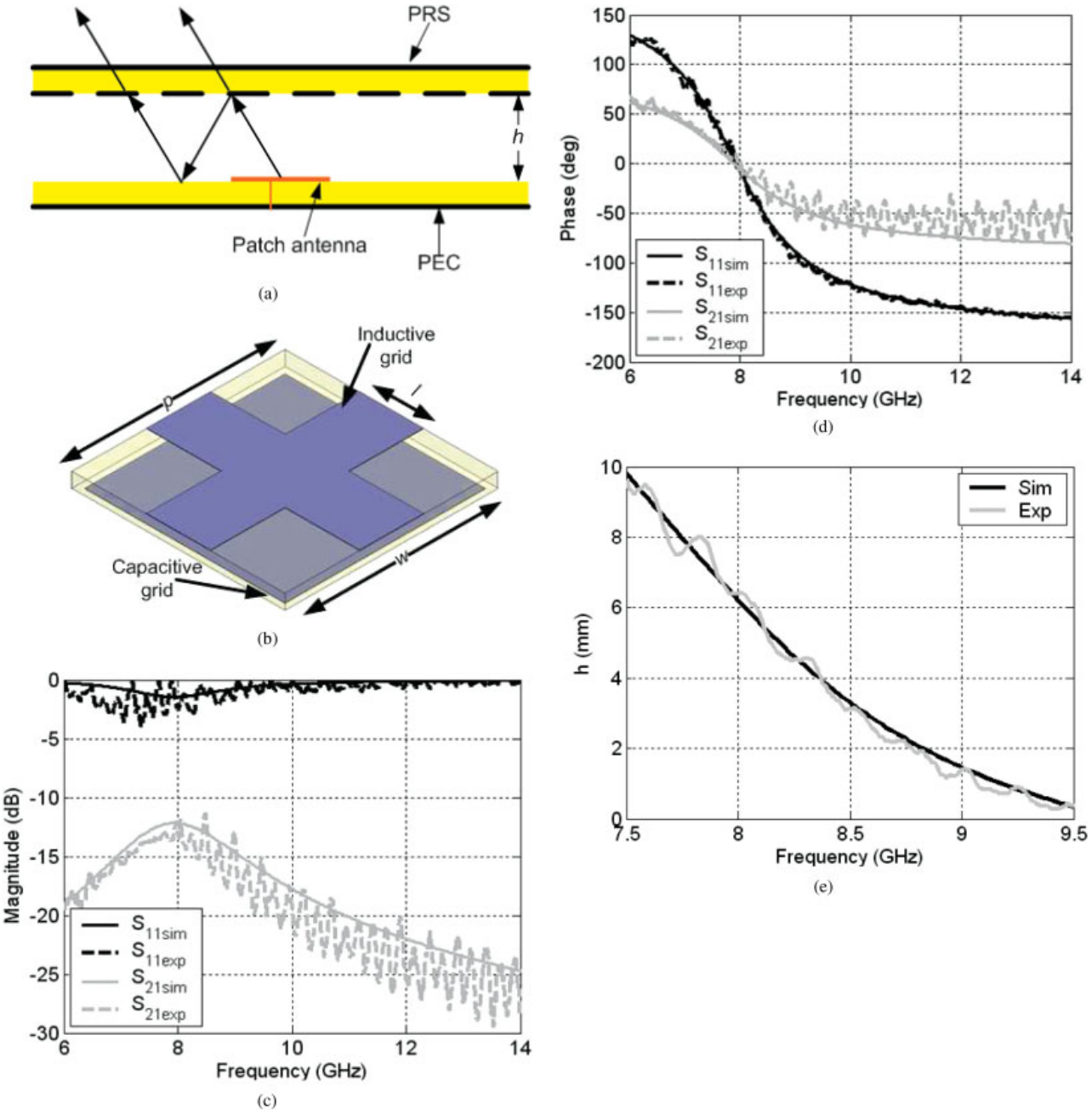

Figure 1 (a) Schematic of the metamaterial-based subwavelength cavity antenna, (b) unit cell of the metasurface reflector used as PRS with $l = 2.4$ mm, $w = 4.8$ mm, and $p = 5$ mm, (c)–(d) magnitude and phase of the reflection and transmission coefficients, and (e) thickness h of the cavity versus frequency. [Color figure can be viewed in the online issue, which is available at www.interscience.wiley.com]

of thickness $\lambda/30$ using a PEC reflector and the composite metamaterial has been proposed in Ref. 5. The cavities presented in Refs. 2–5 are all based on the use of a single feeding source.

In this work, we report the numerical analysis of metamaterial-based resonant cavities fed by multiple microstrip sources using the Transmission Line Matrix (TLM) method software Microstripes [6]. A 2×2 microstrip patch array feed is considered and the influence of its interelement spacing on the radiation characteristics is studied. Prototypes are fabricated and radiation measurements are performed in an anechoic chamber. The performances are compared with those of a single source fed cavity. The influence of the cavity thickness is also investigated and the practical design of subwavelength antennas exhibiting high-directivity is proposed.

2. OPERATING PRINCIPLE OF THE SUBWAVELENGTH METAMATERIAL-BASED CAVITY ANTENNA

Cavity antennas are formed by placing a feeding source between two reflectors as shown in Figure 1(a). For our convenience, one of the two reflectors is a PEC surface so as to prevent undesired backward radiation. The second reflector must present a high reflectivity to act as the so-called Partially Reflective Surface (PRS). This PRS is used to confine the electromagnetic waves in the cavity. Our recent works [4, 5] have shown that metasurfaces

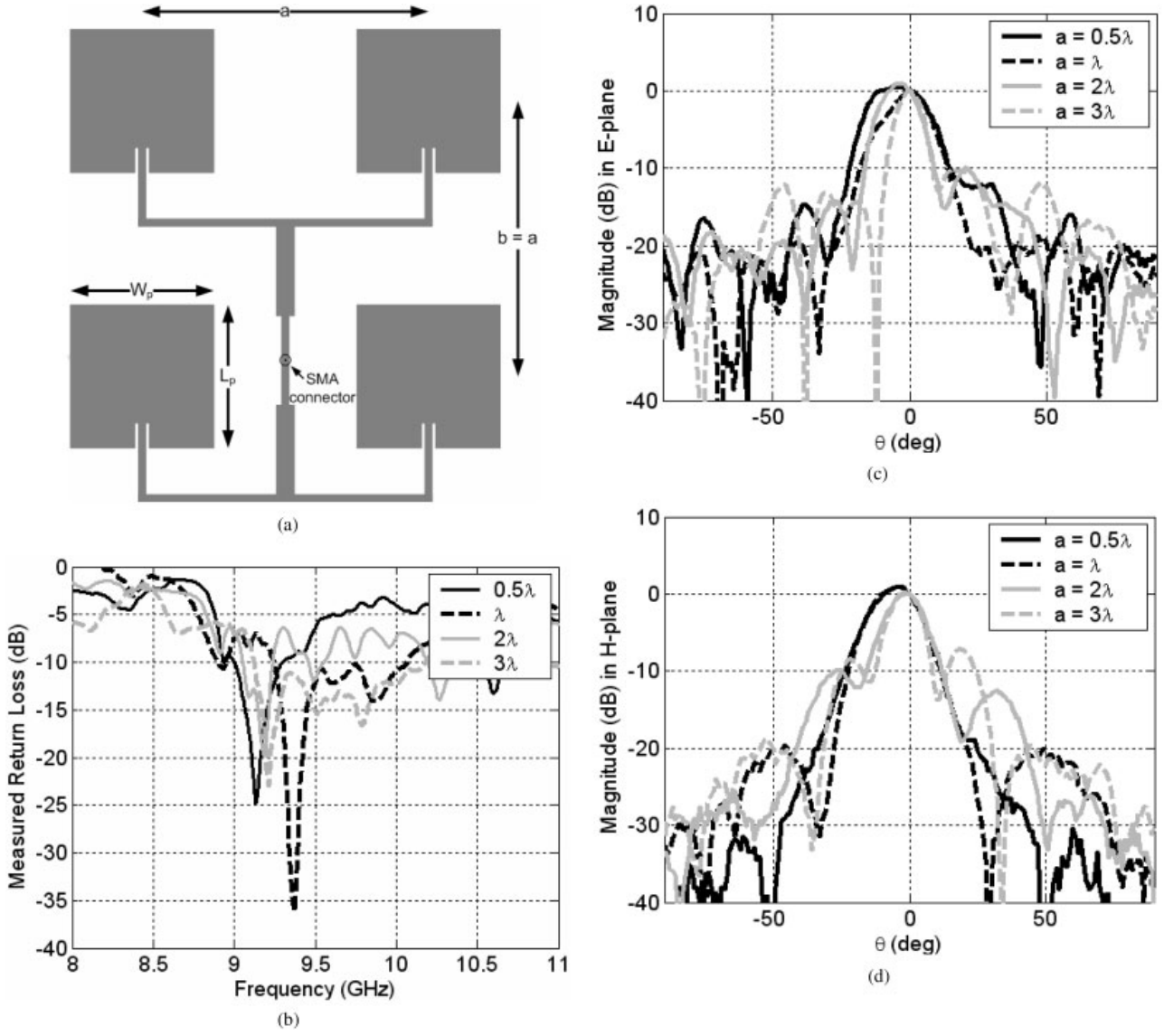

Figure 2 (a) 2 × 2 patch array used as a multisource, (b) measured return losses of the cavities, (c) measured **E**-plane radiation patterns, and (d) measured **H**-plane radiation patterns for $a = 0.5\lambda$, λ, and 2λ for a cavity thickness $h = 1.5$ mm

composed simultaneously of an inductive and capacitive grid are suitable for this purpose. The inductive grid and capacitive grid are, respectively, made of a periodic array of copper mesh and square patches. The grids are patterned on the two faces of a 1.47 mm thick Arlon 25FR substrate ($\varepsilon_r = 3.58$ and $\tan(\delta) = 0.0035$) as illustrated by the unit cell in Figure 1(b). This metasurface presents an LC resonance where the reflection phase varies from $+180°$ to $-180°$ and crosses $0°$ at the resonance. The different dimensions of the metasurface unit cell are optimized for an X-band operation. The width of the strip constituting the mesh of the inductive grid is $l = 2.4$ mm, the side of the square patches of the capacitive grid is $w = 4.8$ mm, and the lattice period is $p = 5$ mm. A prototype consisting of 36 × 36 cells on a 180 mm × 180 mm dielectric substrate is fabricated using chemical etching. The computed and measured *S*-parameters are compared in Figures 1(c) and 1(d). There is a good qualitative agreement between the simulations and measurements. The PRS exhibits a resonance frequency of 8 GHz ($\phi_{PRS} = 0°$) and a high reflectivity with low phase values ($< -90°$) at 9 GHz. As it can be seen in Eq. (1), the reflection phase values of the PRS (ϕ_{PRS}) are needed to calculate the thickness h of the cavity versus the frequency at which maximum boresight directivity can be obtained. The traces representing h obtained from the calculated and measured ϕ_{PRS} are plotted in Figure 1(e). Subwavelength thicknesses ($h < \lambda/10$) can therefore be expected at 8.5 GHz and above.

3. EFFECT OF THE INTERELEMENT SPACING

This section deals with the design of subwavelength cavity antennas based on the use of the metasurface reported above. Compared with the previous works in this field [2-5], here, we use a microstrip patch array as feeding source instead of a single patch antenna. A 2 × 2 microstrip patch array is designed on a 180 mm × 180 mm Arlon 25FR substrate, where each square patch element has lateral dimensions $W_p = L_p = 7.5$ mm as shown in Figure 2(a). The four patches are fed simultaneously via microstrip transmission lines acting as $\lambda/4$ impedance transformers and excited by a 50 Ω SMA connector [Fig. 2(a)]. The interelement spacing a of the

TABLE 1 Performances of the Cavity Antennas for $h = 1.5$ mm

a (mm)	Calculated Resonance Frequency (GHz)	Measured Resonance Frequency (GHz)	Calculated Maximum Directivity (dB)	Measured Maximum Directivity (dB)	Measured Sidelobes Level (dB)
0.5λ	9.51	9.13	18.2 @ 9.7GHz	19 @ 8.93GHz	−12
λ	10.15	9.37	21.1 @ 9.65GHz	20.9 @ 9.07GHz	−19
2λ	9.44	9.18	23.7 @ 9.85GHz	23.21 @ 8.94GHz	−10
3λ	9.49	9.21	25.35 @ 9.6GHz	25.35 @ 8.96GHz	−8

microstrip patch array feed plays an important role in the directivity of the cavity antenna. For this reason, the influence of this latter parameter is studied for a fixed cavity thickness $h = 1.5$ mm. The interelement spacing a is varied from 0.5λ to 3λ. The PRS used in this section is the same as reported in the previous section. Numerical calculations using the full-wave solver Microstripes are run and measurements are done in an anechoic chamber using a wideband (2–18 GHz) horn as receiving antenna. The return losses of the cavities are plotted in Figure 2(b). We can note a very good matching (< -10 dB) around 9.25 GHz for the four different cases.

The measured **E**- and **H**-plane radiation patterns of the cavity antennas are presented in Figures 2(c) and 2(d). For $a = 0.5\lambda$, a measured directivity of 19 dB is obtained at 8.93 GHz. This value is very close to that of a cavity fed by a single source (for e.g., Ref. 4). So, it is worth to note that conversely to classical antenna arrays, the directivity is not doubled each time that the number of sources is doubled. For $a = \lambda$, a measured directivity of 20.9 dB is noted at 9.07 GHz, showing clearly an enhancement of 1.9 dB with regard to the case $a = 0.5\lambda$. It is also very important to note that the sidelobes level of the patch array is considerably reduced when embedded in the cavity. This effect is highlighted in Table 1 where calculations and measurements data are compared. From the measured planes for $a = 2\lambda$ and $a = 3\lambda$, 23.21 dB and 25.35 dB is deduced, respectively. When the case $a = 3\lambda$ is compared with $a = 0.5\lambda$, an increase of 6.35 dB is obtained for the directivity, which is comparable to an increase from a single patch element to a 2×2 patch array. The measured sidelobes level are higher (~ -8 dB in the **H**-plane) for the case $a = 3\lambda$. However, this sidelobes level is still low compared with the sidelobes level of the source alone. It is well known that an interelement spacing of an array higher than λ leads to high-sidelobes level and also to the apparition of grating lobes.

The directivity D of the cavity antennas can be calculated using the following expression: $D = 41253/(\theta_1 \times \theta_2)$, where θ_1 and θ_2 are, respectively, the half-power widths (in degrees) for the **H**-plane and **E**-plane patterns. The directivity values are given in Table 1, where we can observe that an increase in the interelement

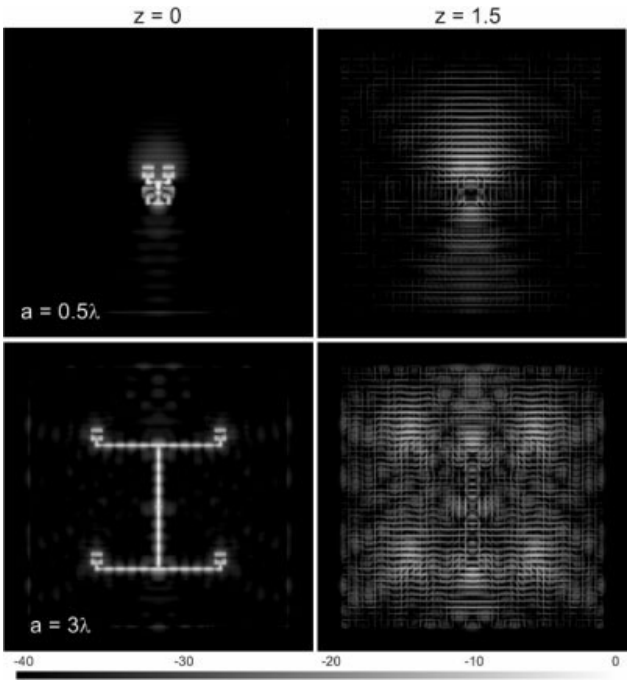

Figure 3 E-field distribution in a horizontal plane in the cavity antenna for $a = 0.5\lambda$ and $a = 3\lambda$

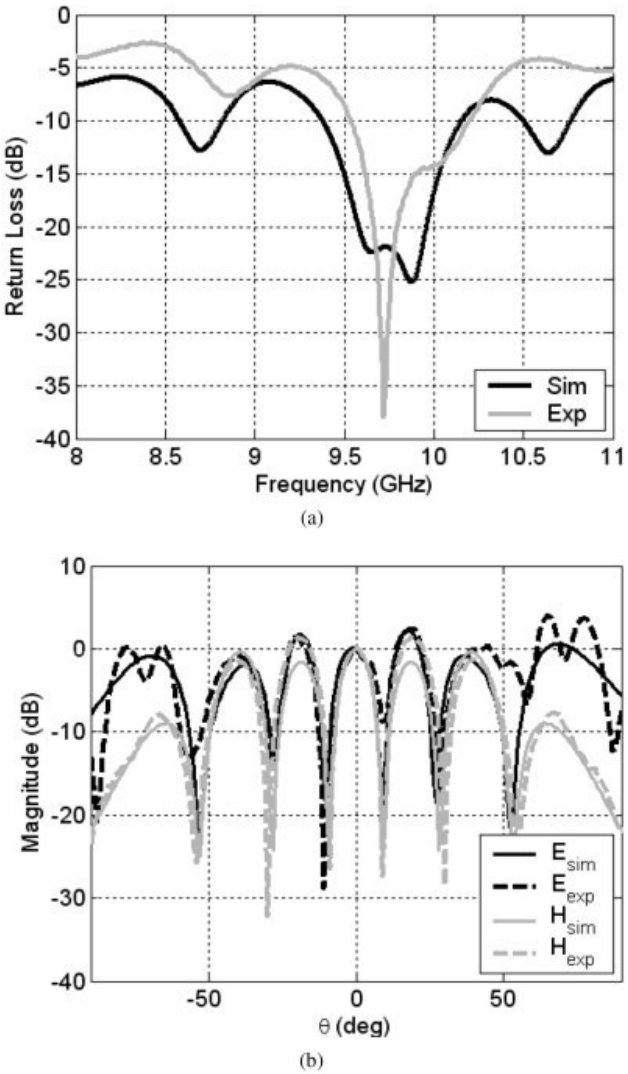

Figure 4 2×2 patch array source with $a = 3\lambda$. (a) Calculated and measured return losses and (b) radiation patterns of the array

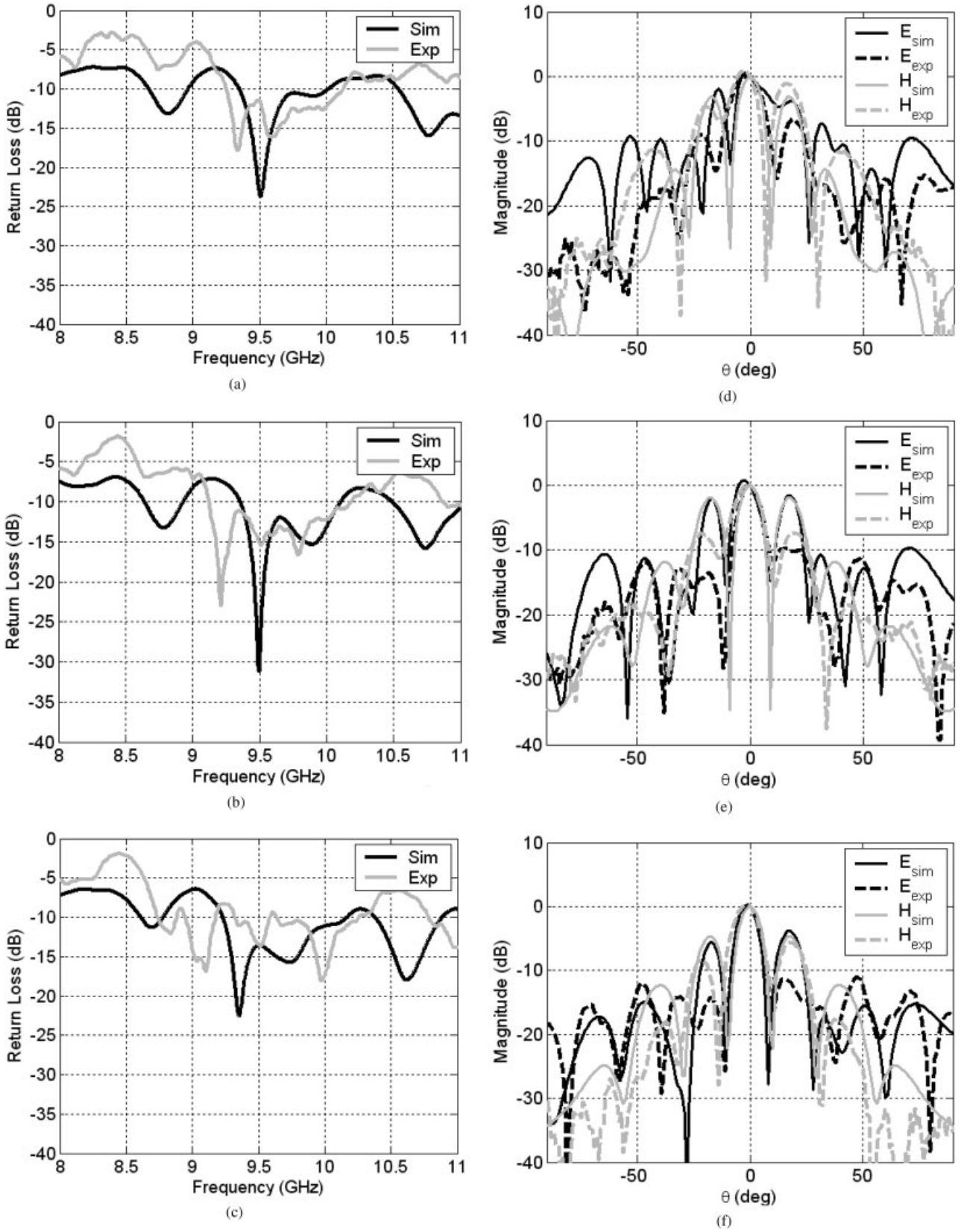

Figure 5 Cavities fed by 2 × 2 patch array ($a = 3\lambda$). (a)–(c) Calculated and measured return losses, and (d)–(f) Calculated and measured radiation diagrams for, respectively, $h = 1$, 1.5, and 2 mm

TABLE 2 Performances of the Cavity Antennas for $a = 3\lambda$

h (mm)	Calculated Resonance Frequency (GHz)	Measured Resonance Frequency (GHz)	Calculated Maximum Directivity (dB)	Measured Maximum Directivity (dB)	Measured Sidelobes Level (dB)
1	9.51	9.34	24.4 @ 10.1GHz	24.2 @ 9.27GHz	−1
1.5	9.49	9.21	25.35 @ 9.6 GHz	25.35 @ 8.96GHz	−8
2	9.35	9.10	26.15 @ 9.4 GHz	25.35 @ 8.84GHz	−6

spacing a in the cavity antenna gives rise to a higher directivity. This is because the radiation area at the surface of the source is bigger when a increases and therefore, a larger surface of the PRS is illuminated by the radiation source. This phenomenon is illustrated in Figure 3, where the E-field distribution is plotted in a horizontal plane at two different locations z in the cavity antenna. $z = 0$ and $z = 1.5$ corresponds, respectively, to the plane of the radiating patch array source and to the thickness $h = 1.5$ mm at the inner surface of the PRS (location of the capacitive grid). This figure shows that the radiation area at the surface of the feed source in the case $a = 3\lambda$ is bigger than in the case $a = 0.5\lambda$ and therefore, a larger surface of the PRS is illuminated leading to a higher directivity. On the counter part, the side lobes level also increases.

4. EFFECT OF THE CAVITY THICKNESS

From the previous study made on the influence of the interelement spacing, a is now taken to be 3λ for the study on the effect of the cavity thickness. The simulated and measured performances of the patch array are given in Figures 4(a) and 4(b), where a good agreement is obtained between simulations and measurements.

The best matching is observed at around 9.7 GHz with a measured return loss level close to 38 dB as shown in Figure 4(a). The **E**- and **H**-plane radiation patterns of Figure 4(b) shows firstly a directive primary lobe but also sidelobes with high levels. The sidelobes levels are even higher than the main beam. This physical phenomenon is due to the large interelement spacing used in the array.

This microstrip patch array is embedded in the cavity comprising the metasurface reflector. Different thicknesses h are considered as follows: 1, 1.5, and 2 mm. We shall note that the $h = 1.5$ mm case has been already studied in section III. Full-wave simulations are performed and experimental tests are done on the fabricated prototypes. The simulated and measured performances are plotted in the various parts of Figure 5. The return losses for the three cavities [Fig. 5(a) for $h = 1$ mm, Fig. 5(b) for $h = 1.5$ mm, and Fig. 5(c) for $h = 2$ mm] show the best matching at a frequency lower than that of the microstrip patch array alone. This phenomenon is due to the coupling between the two cavities, i.e., the FP cavity and the feeding patch array. The measured best matching frequencies are also lower than the simulated ones and when the thickness of the cavity increases, the best matching tends toward lower frequencies. This observation is in good agreement with Figure 1(e) where we can note that the thickness of the cavity decreases with an increase in frequency since the total reflection phase shift $\phi_{PRS} + \phi_r$ decreases.

The measured radiation patterns plotted in Figures 5(d)–(f) for the different thicknesses show a good qualitative agreement with the calculated ones. These patterns corresponds to the frequency where the directivity is maximum but not where the resonance frequency lies. This is so, because the maximum directivity is often obtained outside the resonance frequency of the cavity antenna. We can note that as the thickness increases, the primary lobe becomes more directive but also the sidelobes level, particularly in the **E**-plane, tends to decrease. The different characteristics of the cavities (frequencies of resonance and maximum directivity and also the directivity values) observed in simulations and measurements are summarized in Table 2.

Table 2 shows that the frequency of the measured maximum directivity for the three cases corresponds to the value predicted by the trace in Figure 1(e). According to this trace, for $h = 1$, 1.5, and 2 mm, a frequency close to 9.2 GHz, 8.9 GHz, and 8.75 GHz is, respectively, expected for the maximum boresight directivity. We can note that the measured characteristics correspond better to the predicted h values compared with the calculations. A maximum directivity of 25.35 dB is observed from the measurements. This value is more than 6 dB higher than the directivity observed for a single source fed cavity as reported in Ref. 4.

5. CONCLUSIONS

A metamaterial-based cavity fed by a 2×2 microstrip patch array antenna acting as a multisource has been proposed to enhance the directivity of ultrathin cavity antennas. We have shown that an increase in interelement spacing leads to a higher directivity since a larger surface of the PRS is illuminated. When the thickness of the cavity is increased, an enhancement in the directivity has also been observed. The radiation measurements have shown a maximum directivity of 25.35 dB at, respectively, 8.96 GHz and 8.84 GHz for a thickness of 1.5 mm ($\lambda/22$) and 2 mm ($\lambda/17$) and for a spacing between the radiating elements equal to 3λ. The multisource fed cavity therefore constitutes a highly directive antenna. It can be easily fabricated and constitutes an interesting alternative for large antenna arrays where a complicated feeding network is necessary. However, in some cases the sidelobes level may be too high for certain applications.

REFERENCES

1. G.V. Trentini, Partially reflecting sheet arrays, IRE Trans Antennas Propag AP-4 (1956), 666–671.
2. A.P. Feresidis, G. Goussetis, S. Wang, and J.C. Vardaxoglou, Artificial magnetic conductor surfaces and their application to low-profile high-gain planar antennas, IEEE Trans Antennas Propag 53 (2005), 209–215.
3. L. Zhou, H. Li, Y. Qin, Z. Wei, and C.T. Chan, Directive emissions from subwavelength metamaterial-based cavities, Appl Phys Lett 86 (2005), 101101-1-101101–3.
4. A. Ourir, A. de Lustrac, and J.-M. Lourtioz, All-metamaterial-based sub-wavelength cavities ($\lambda/60$) for ultrathin directive antennas, Appl Phys Lett 88 (2006), 084103-1–084103-3.
5. A. Ourir, A. de Lustrac, and J.-M. Lourtioz, Optimization of metamaterial based subwavelength cavities for ultracompact directive antennas, Microwave Opt Technol Lett 48 (2006), 2573–2577.
6. FLOMERICS, Micro-Stripes Reference Manual Release 7.0, FLOMERICS Ltd., 2005.

Annexe 1.5

S. N. Burokur, J.-P. Daniel, P. Ratajczak, A. de Lustrac

« Tunable bi-layered metasurface for frequency reconfigurable directive emissions »

Applied Physics Letters, vol. 97, no. 6 (064101), August 2010

Tunable bilayered metasurface for frequency reconfigurable directive emissions

S. N. Burokur,[1,a)] J.-P. Daniel,[2] P. Ratajczak,[3] and A. de Lustrac[1,b)]
[1]*IEF, CNRS, UMR 8622, Univ. Paris-Sud, 91405 Orsay Cedex, France*
[2]*Advanten, 35510 Cesson-Sévigné, France*
[3]*Orange Labs–R&D, 06320 LaTurbie, France*

(Received 7 March 2010; accepted 18 July 2010; published online 9 August 2010)

The directive emission from a bilayered metamaterial surface is numerically and experimentally reported. The LC-resonant metasurface is composed of both a capacitive and an inductive grid constituted by copper strips printed on both sides of a dielectric board. By the incorporation of varactor diodes in the capacitive grid, resonance frequency and phase characteristics of the metamaterial can be tuned. The tunable phase metasurface is used as a partially reflecting surface in a Fabry–Perot resonance cavity. Far field radiation patterns obtained by direct measurements show the reconfigurability of emission frequency while maintaining an enhanced directivity. © *2010 American Institute of Physics*. [doi:10.1063/1.3478214]

Metamaterials are artificial materials typically fabricated via suitable periodic arrangement of microstructured metallic or dielectric inclusions. Due to their unusual electromagnetic properties,[1] these microstructured metamaterials have made relevant a wide array of interesting applications such as invisibility cloaks,[2–6] perfect lenses,[7] directive antennas,[8–10] and waveguide tapers.[11] Planar versions of metamaterials, also known as metasurfaces, have been used for microwave filtering[12] and antenna's coupling reduction.[13] However, the use of metasurfaces is not been limited to decoupling purposes in antenna applications. They are intensely used as reflectors in Fabry–Perot (FP) cavity systems[14] for the design of directive emissions. Feresidis *et al.*[15] reduced a half wavelength thick cavity to a quarter wavelength one by using a artificial magnetic conductor (Ref. 16) metasurface reflector with 0° phase at reflection instead of a perfect electric conductor (PEC) with 180° phase. The other cavity reflector consisted of a metasurface acting as a partially reflective surface (PRS) with a reflection phase equal to 180°. This idea has been pushed further by Zhou *et al.*[17] who fabricated a subwavelength cavity with a thickness smaller than tenth of the wavelength. Another interesting achievement from Ourir *et al.*[18] consisted in using a novel type of composite metasurface made of simultaneously inductive and capacitive grids allowing the realization of even more compact cavity antenna systems with thickness reaching $\lambda/60$. Such a low thickness has been made possible by considering low phase values close to zero from LC resonant metasurface. Recently, we have also shown that the emission from the cavity antenna system could be oriented in an oblique direction by locally changing the periodicity of copper strips constituting the capacitive grid, thereby adjusting phase characteristics of the metasurface.[19] In a previous work,[20] a reconfigurable metamaterial-based cavity antenna has been tested but due to the use of a narrowband microstrip patch as primary source, the emission was reconfigured only over a frequency bandwidth $\Delta f/f_0$ of about 3.6%.

In this paper, we show that a tunable metasurface associated to an array of wideband sources in a FP cavity leads to a reconfigurable directive emission on a wide frequency range. We deal with the modeling and characterization of an electronically tunable bilayered metasurface composed of periodic resonant LC cells. By incorporating varactor diodes in the capacitive grid, the capacitance of the grid can be tuned when applying different bias voltage. Reflection and transmission characteristics can then be electronically adjusted. By equipping a FP cavity with this metasurface reflector as shown in Fig. 1(a), we show that not only a low profile high antenna gain can be achieved with a narrow beam profile, but also the emission can be electronically controlled over a frequency bandwidth $\Delta f/f_0$ as much as 20%. The design of the cavity antenna system is made through numerical analysis using transmission line matrix method simulations done with CST's commercial electromagnetic solver MICROSTRIPES.[21] Reported experimental measurements agree qualitatively with simulations.

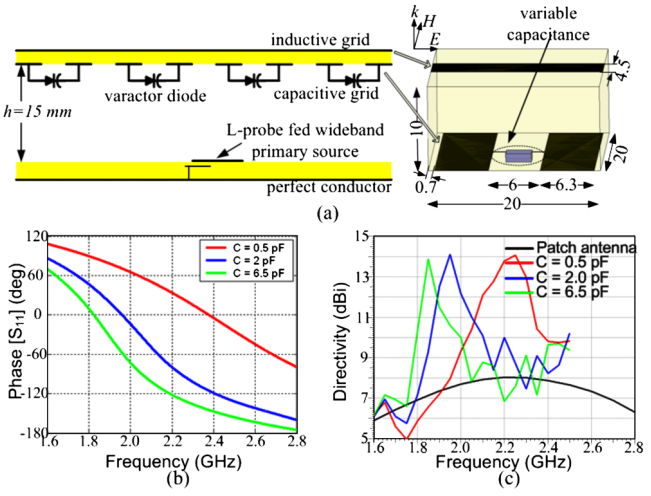

FIG. 1. (Color online) (a) Schematic view of the cavity composed of a PEC and an electronically tunable metasurface reflector used as PRS. Inset shows the composite metasurface's unit cell where physical dimensions are given in millimeter. (b) Reflection phase of the PRS for capacitance values C =0.5 pF, C=2.0 pF, and C=6.5 pF. (c) Directivity vs frequency for different capacitance values with the black trace corresponding to the wideband patch source.

[a)]Present address: LEME EA 4416, Université Paris-Ouest, 50 rue de Sèvres, 92410 Ville d'Avray, France. Electronic mail: sburokur@u-paris10.fr.
[b)]Electronic mail: andre.de-lustrac@u-psud.fr.

The metasurface consists of a periodic array of resonant cells made of copper strips mechanically etched on each face of a 10 mm thick foam (ε_r=1.23 and tan δ=0.0058) substrate. The unit cell with physical dimensions optimized for a working frequency around 2 GHz is depicted in Fig. 1(a). The upper array where the strips are oriented parallel to the electric field ***E*** of the antenna plays the role of the inductive grid, whereas the lower array where the strips are oriented parallel to the magnetic field ***H*** acts as the capacitive grid. Active components are inserted between the strips to model the reconfigurable capacitive grid so that resonance characteristics can be tuned. The use of variable capacitance in split ring resonators has previously shown the possibility of tuning resonance frequency.[22] For our simulation purposes, a capacitance where the value can be changed is thus incorporated into the capacitive grid between two adjacent metallic strips and depending on its value, the phase of the PRS varies with frequency. This variable capacitance will be in fact replaced by a varactor diode biased by a dc voltage on the fabricated prototype.

By changing all capacitance values of the metasurface similarly, phases of reflection coefficient also vary. This behavior is illustrated by calculated results of reflection coefficient phase of the PRS shown in Fig. 1(b) for three capacitance values. The value range corresponds to 0.52–6.6 pF, the typical tuning range of a BB857 varactor diode from Infineon Technologies that will be used in experimental tests. We shall note that capacitance is inversely proportional to applied dc bias voltage in a varactor diode. As observed in Fig. 1(b), a decrease in capacitance value leads to a resonance shift toward higher frequencies.

The tunable phase metasurface is used as a PRS in the FP cavity. A conventional FP cavity is composed of a primary source embedded between two parallel reflectors, separated by a distance h [Fig. 1(a)]. One of the two reflectors is the PEC ground plane of the primary source and the other one is the electronically tunable metasurface PRS. The primary source is a wideband microstrip patch antenna designed on the foam dielectric substrate to cover 1.8–2.7 GHz frequency range and therefore to illuminate the PRS at any frequency within this range. This patch antenna is electromagnetically coupled to an L-probe which itself is connected to an coaxial connector. Simulations have shown a good matching (return loss $<$ 10 dB) from 1.8 to 2.7 GHz. Resonance modes are given at frequencies f satisfying the condition

$$f = (\phi_{\mathrm{PRS}} + \phi_r)\frac{c}{4\pi(h + d\sqrt{\varepsilon_r})}, \tag{1}$$

where ϕ_{PRS} and ϕ_r denote, respectively, the reflection phases of the PRS and the PEC ground plane of the wideband microstrip patch antenna. d is the thickness of the dielectric support used for the patch antenna (d=20 mm) and ε_r is the relative permittivity of the foam dielectric. A relatively high value is needed for d in order to achieve wide bandwidth operation with a microstrip patch antenna. In (1) we consider only the zeroth order of the cavity's electromagnetic mode. As it can be observed from the above expression, the thickness h is directly proportional to the sum of phases ($\phi_{\mathrm{PRS}} + \phi_r$) and to the frequency f. From the calculated reflection phases for different capacitance values in Fig. 1(b), a thickness h=15 mm corresponding to $\lambda_0/10$ at 2 GHz is applied.

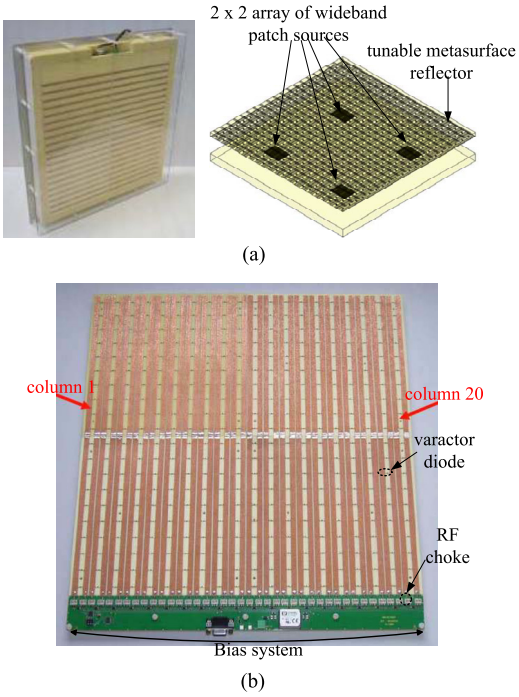

FIG. 2. (Color online) (a) Photography and perspective view of the cavity antenna. (b) Electronically tunable metasurface reflector incorporating varactor diodes, RF chokes, and bias system.

According to (1), to obtain a frequency change, ϕ_{PRS} has to be necessarily tuned in order to maintain a fixed thickness from 1.8 to 2.7 GHz.

A cavity with lateral dimensions 200$\times$200 mm^2 is considered for simulation. These lateral dimensions (approximately 1.5$\lambda\times$1.5λ) are sufficient enough to show the reconfigurability concept and also to avoid secondary lobes occurring from lateral radiations of the cavity. Calculated directivities of the cavity for different capacitance values of the PRS are presented in Fig. 1(c) with the black trace corresponding to that of the wideband primary source. A maximum directivity reaching 14 dBi for each case can be noted. For C=0.5 pF, the maximum directivity is obtained at 2.25 GHz and for C=2.0 pF, the directivity peak occurs at 1.95 GHz. The maximum directivity is observed at 1.85 GHz for C=6.5 pF. These data show the reconfigurability of emission frequency of the FP cavity from 1.85 to 2.25 GHz by using a tunable metasurface reflector that allows tailoring desired phase characteristics. The phase shift is very important since it helps to tune the frequency of the maximum directivity of the cavity antenna.

To demonstrate experimentally the mechanism for reconfigurable directive emissions from a metamaterial-based FP cavity, a prototype having dimensions 400$\times$400 mm^2 (approximately 3$\lambda\times$3λ) has been fabricated and tested. Since the fabricated prototype is four times bigger in surface area than the simulated model, four elementary sources constituting a 2$\times$2 wideband patch array are used as primary source; the interelement spacing between the different sources being 200 mm. The metasurface is then composed of 20 columns, each containing 20 resonant cells. Figures 2(a) and 2(b) show, respectively, photography of the prototype and the capacitive grid of the tunable metasurface reflector incorporating voltage controlled varactor diodes and RF chokes which prevent high frequency currents going to the dc bias system. In order to experimentally estimate directiv-

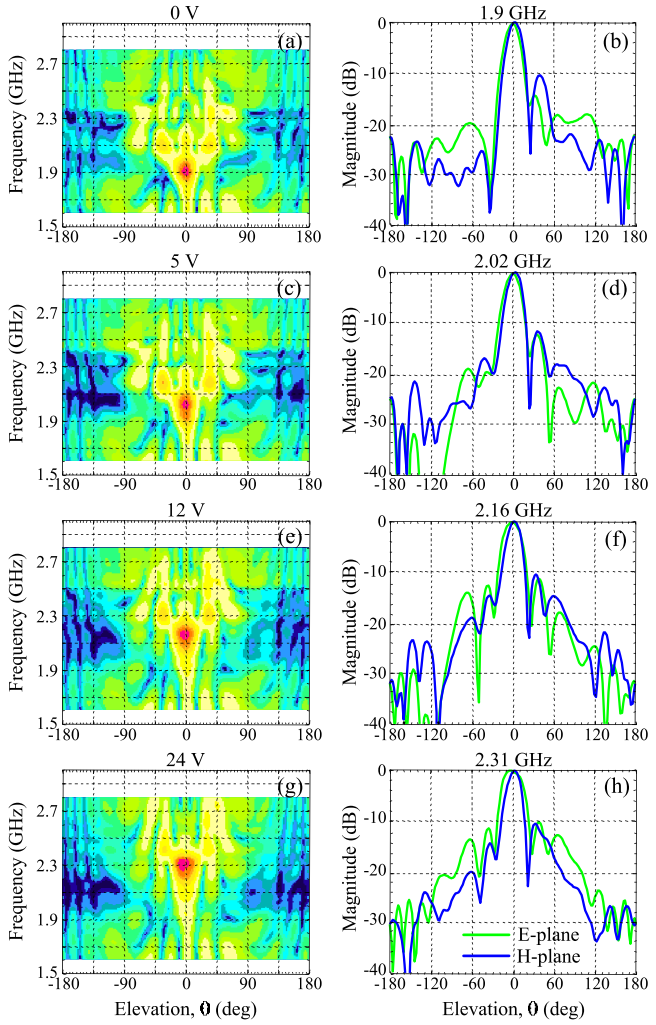

FIG. 3. (Color online) Far field intensity maps vs frequency and elevation angle θ in E-plane and measured radiation patterns in E- and H-planes at maximum gain frequency for different bias voltage applied: [(a) and (b)] 0 V, 1.9 GHz; [(c) and (d)] 5 V, 2.02 GHz; [(e) and (f)] 12 V, 2.16 GHz; and [(g) and (h)] 24 V, 2.31 GHz.

ity and gain of the cavity's radiated beam, direct far field measurements are performed using a SATIMO STARLAB and the different characteristics are shown in Fig. 3. When capacitance of the metasurface reflector is changed by varying bias voltage of varactor diodes, the frequency of maximum gain is tuned as clearly shown in the different diagrams of Fig. 3. When 0 V is applied, maximum gain is observed at 1.9 GHz corresponding approximately to the simulated case with C=6.5 pF. When dc bias voltage is increased, the capacitance value is decreased, resulting in an increase in maximum gain frequency. For 24 V, maximum gain occurs at 2.31 GHz, corresponding to lowest capacitance value. To gain more insight in the electromagnetic properties of the metamaterial-based FP cavity, intensity maps of scanned far field versus frequency and elevation angle θ, in E-plane are presented. The emission frequency represented by the red spot varies from 1.9 to 2.31 GHz from 0 to 24 V as shown in Figs. 3(a), 3(c), 3(e), and 3(g). These figures demonstrate clearly the frequency reconfigurability property of the FP cavity. We shall also note that for each frequency the spot is situated at an elevation angle of 0°, indicating a radiated beam normal to the cavity metasurface reflector. Figures 3(b), 3(d), 3(f), and 3(h) show radiation patterns in E- and H-planes at, respectively, 1.9 GHz, 2.02 GHz, 2.16 GHz, and 2.31 GHz, corresponding to maximum gain frequency for 0 V, 5 V, 12 V, and 24 V. The tuning range of maximum gain frequency results in an effective operation bandwidth close to 20%. A wider frequency bandwidth is achieved compared to previous work in Ref. 20 due to the use of a higher cavity thickness. With $h=15$ mm, reflection phase values around 0° are needed in the 1.85–2.25 GHz frequency band. A lower h would lead to phase values approaching –180° and the possible frequency bandwidth from the capacitance tuning range would be narrow. Actually, a greater directivity (approximately 18 dBi) is obtained experimentally due to larger lateral dimensions of the fabricated cavity and also to the use of four elementary sources instead of only one. Compared to Ref. 20, lower sidelobes level of less than –10 dB are observed.

In conclusion, electronically tunable metasurface incorporating varactor diodes has been proposed to act as a PRS in a subwavelength ($\lambda/10$) FP cavity for 1.9–2.31 GHz frequency range. The metasurface presenting tunable resonance characteristics when dc bias voltage is varied similarly along the surface, allows achieving a frequency reconfigurable directive emission. Direct far field measurements and field intensity mappings have been performed to experimentally demonstrate the reconfigurability mechanism. Due to its simplicity, this cavity antenna system could be an interesting low-cost alternative to electrically reconfigurable antennas.

This work was supported by the French National Research Agency (ANR) through the METABIP project.

[1] V. G. Veselago, Sov. Phys. Usp. **10**, 509 (1968).
[2] U. Leonhardt, Science **312**, 1777 (2006).
[3] J. B. Pendry, D. Schurig, and D. R. Smith, Science **312**, 1780 (2006).
[4] D. Schurig, J. J. Mock, B. J. Justice, S. A. Cummer, J. B. Pendry, A. F. Starr, and D. R. Smith, Science **314**, 977 (2006).
[5] W. Cai, U. K. Chettiar, A. V. Kildishev, and V. M. Shalaev, Nat. Photonics **1**, 224 (2007).
[6] B. Kanté, A. de Lustrac, J.-M. Lourtioz, and S. N. Burokur, Opt. Express **16**, 9191 (2008).
[7] J. B. Pendry, Phys. Rev. Lett. **85**, 3966 (2000).
[8] S. N. Burokur, M. Latrach, and S. Toutain, IEEE Antennas Wireless Propag. Lett. **4**, 183 (2005).
[9] R. W. Ziolkowski, IEICE Trans. Electron. **E89-C**, 1267 (2006).
[10] P.-H. Tichit, S. N. Burokur, and A. de Lustrac, J. Appl. Phys. **105**, 104912 (2009).
[11] P.-H. Tichit, S. N. Burokur, and A. de Lustrac, Opt. Express **18**, 767 (2010).
[12] F. Falcone, T. Lopetegi, M. A. G. Laso, J. D. Baena, J. Bonache, M. Beruete, R. Marqués, F. Martín, and M. Sorolla, Phys. Rev. Lett. **93**, 197401 (2004).
[13] E. Saenz, I. Ederra, R. Gonzalo, S. Pivnenko, O. Breinbjerg, and P. de Maagt, IEEE Trans. Antennas Propag. **57**, 383 (2009).
[14] G. V. Trentini, IRE Trans. Antennas Propag. **4**, 666 (1956).
[15] A. P. Feresidis, G. Goussetis, S. Wang, and J. C. Vardaxoglou, IEEE Trans. Antennas Propag. **53**, 209 (2005).
[16] D. Sievenpiper, L. Zhang, R. F. J. Broas, N. G. Alexópoulos, and E. Yablonovitch, IEEE Trans. Microwave Theory Tech. **47**, 2059 (1999).
[17] L. Zhou, H. Li, Y. Qin, Z. Wei, and C. T. Chan, Appl. Phys. Lett. **86**, 101101 (2005).
[18] A. Ourir, A. de Lustrac, and J.-M. Lourtioz, Appl. Phys. Lett. **88**, 084103 (2006).
[19] A. Ourir, S. N. Burokur, and A. de Lustrac, Electron. Lett. **43**, 493 (2007).
[20] A. Ourir, S. N. Burokur, and A. de Lustrac, Electron. Lett. **43**, 698 (2007).
[21] MICROSTRIPES Reference Manual Release v7.5, CST (2007).
[22] K. Aydin and E. Ozbay, J. Appl. Phys. **101**, 024911 (2007).

Annexe 1.6

A. Ghasemi, S. N. Burokur, A. Dhouibi, A. de Lustrac

« High beam steering in Fabry-Pérot leaky-wave antennas »

IEEE Antennas and Wireless Propagation Letters, vol. 12, pp. 261-264, 2013

High Beam Steering in Fabry–Pérot Leaky-Wave Antennas

Amirhossein Ghasemi, Shah Nawaz Burokur, Abdallah Dhouibi, and André de Lustrac, *Member, IEEE*

***Abstract*—A high-gain low-profile Fabry–Pérot (FP) leaky-wave antenna (LWA) presenting one-dimensional high beam steering properties is proposed in this letter. The structure consists of a ground plane and a varying inductive partially reflective surface (PRS). A microstrip patch antenna is embedded into the cavity to act as the primary feed. As design examples, antennas are designed to operate at 9.5 GHz. Subwavelength FP cavities with fixed overall thickness of $\lambda_0/6$ (where λ_0 is the free-space operating wavelength) are fabricated and measured. The impact of varying the PRS inductance is analyzed. It is shown that a high beam steering angle from broadside toward endfire direction close to 60° can be obtained when judiciously designing the inductive grid of the PRS.**

***Index Terms*—Beam steering, leaky-wave antennas (LWAs), varying inductance.**

I. Introduction

OVER the last few years, periodic structures organized on dielectric substrates have been intensely integrated in antenna systems in order to enhance their performances. For example, nonplanar high impedance surfaces (HISs) have been used to suppress the propagation of surface currents [1] and to minimize the distance between the radiating element and ground plane [2]. High-gain low-profile antenna designs have also inherited the unique properties of periodic structures. The interesting feature of partial reflection has contributed to the design of superstrate layers so as to significantly enhance the directivity of radiating sources at boresight [3], [4]. The structure is based on a parallel-plate configuration, enclosing a resonant Fabry–Pérot (FP) cavity. In a conventional FP leaky-wave antenna (LWA), the partially reflecting surface (PRS) is placed half a wavelength above the perfect electric conductor (PEC) ground plane of the primary radiating source [3], [4]. Replacing the PEC surface by an artificial magnetic conductor (AMC) that presents 0° reflection phase shift allows reducing the antenna profile to a quarter wavelength [5], [6]. Further thickness reduction is possible thanks to the dispersion characteristics of metamaterial surfaces also referred to as metasurfaces [7]–[10]. Furthermore, electronically reconfigurable structures have been introduced to achieve frequency agility [11]–[13]. Beam-steering characteristics from such FP antennas have also been shown by utilizing a passive phase-varying metasurface as PRS [14]. Recently, varactor diode-tuned elements integrated in periodic structures have been proposed to realize electrically scanned antennas [15]–[17]. We shall note that in [14]–[17], beam steering is achieved through varying capacitance.

In this letter, we present a new configuration of phase-varying metasurface for a one-dimensional (1-D) steerable FP LWA. The inductance of the LC-resonant PRS is varied in order to control the reflection phase and thus the pointing angle. Several prototypes have been fabricated for an operation in X-band near 9.5 GHz. Far-field measured radiation patterns agree very well with the simulated ones.

Manuscript received December 06, 2012; accepted February 12, 2013. Date of publication February 20, 2013; date of current version March 14, 2013.

A. Ghasemi is with the IEF, CNRS, UMR 8622, Univ. Paris-Sud, 91405 Orsay cedex, France.

S. N. Burokur and A. de Lustrac are with the IEF, CNRS, UMR 8622, Univ. Paris-Sud, 91405 Orsay cedex, France, and also with the Université Paris Ouest, 92410 Ville d'Avray, France (e-mail: shah-nawaz.burokur@u-psud.fr).

A. Dhouibi is with the LEME, EA 4416, Université Paris Ouest, 92410 Ville d'Avray, France.

Color versions of one or more of the figures in this letter are available online at http://ieeexplore.ieee.org.

Digital Object Identifier 10.1109/LAWP.2013.2248052

II. Steered-Beam Fabry–Pérot LWA Geometry

The proposed structure is depicted in Fig. 1(a). This configuration is inspired by an earlier design presented in [14], where the LWA is composed of a perfect metallic reflector and a 2-D PRS reflector. The lateral dimensions of the reflectors are 180×180 mm^2, corresponding to $5.7\lambda \times 5.7\lambda$ at 9.5 GHz. A patch antenna fed by a coaxial probe is chosen as the primary source. The PRS surface is composed of a composite metamaterial consisting simultaneously of a capacitive and an inductive grid on the two faces of a dielectric substrate. For a proof of concept, we restricted ourselves to inexpensive (but lossy) 35 μm copper clad FR4 material ($\varepsilon_{\rm r} = 3.9$ and $\tan\delta = 0.0197$) of thickness $t = 1.6$ mm. The capacitive grid is formed by a row of metallic strips oriented perpendicular to the polarized electric field (period $p = 5$ mm and gap $g = 0.4$ mm), whereas the strips of the inductive grid are oriented parallel to the electric field with similar period p. The PRS is composed of 36×36 cells, each cell having an elementary capacitance and inductance. The inductive grid is made variable by changing the line width w. A numerical analysis is performed on the unit cell together with appropriate periodic boundary conditions. The results presented in Fig. 1(b) first show a resonance frequency lying between 6.1 and 8.6 GHz for w ranging from 0.5 to 4.5 mm. The size of the different patterns has been chosen in order to have the phase of the reflection coefficient below 0° near 9.5 GHz while providing a sufficiently high reflectance ($\rho_{\rm PRS} \sim 90\%$). Compared to the PRS used in [4]–[6], composed uniquely of a capacitive grid exhibiting a slow variation of the reflection phase over a wide frequency band, our composite metamaterial-based one proposes a reflection phase coefficient varying from 180° to $-180°$ over a lower frequency range. This variation helps to be more flexible

TABLE I
ANTENNA DIMENSIONS AND SUMMARY OF THE SIMULATION RESULTS

Antenna type	Fixed LWA @ 9.5 GHz	Steered LWA 1 @ 9.5 GHz	Steered LWA 2 @ 9.55 GHz	Steered LWA 3 @ 9.7 GHz	Steered LWA 4 @ 9.8 GHz
w_i (w of the ith row)	w_1 to w_{36} = 2.4 mm	w_1 = 0.4 mm w_2 = 0.5 mm ⋮ w_{16} = 1.9 mm w_{17} = 2.2 mm w_{18} = 2.5 mm w_{19} = 2.8 mm w_{20} = 3.1 mm w_{21} = 3.2 mm ⋮ w_{35} = 4.6 mm w_{36} = 4.7 mm	w_1 to w_{16} = 0.4 mm w_{17} = 1.7 mm w_{18} = 2.3 mm w_{19} = 2.9 mm w_{20} = 3.5 mm w_{21} to w_{36} = 4.3 mm	w_1 to w_{16} = 0.4 mm w_{17} = 1.7 mm w_{18} = 2.3 mm w_{19} = 2.9 mm w_{20} = 3.5 mm w_{21} to w_{36} = 0.4 mm	w_1 to w_{16} = 1.1 mm w_{17} = 1.7 mm w_{18} = 2.3 mm w_{19} = 2.9 mm w_{20} = 3.5 mm w_{21} to w_{36} = 1.1 mm
Return loss (dB)	18.7	12.1	15.1	14.2	12.2
Directivity (dBi)	15.8	14.96	13.3	12.635	12.81
Steered angle (°)	0	36	56	59	51

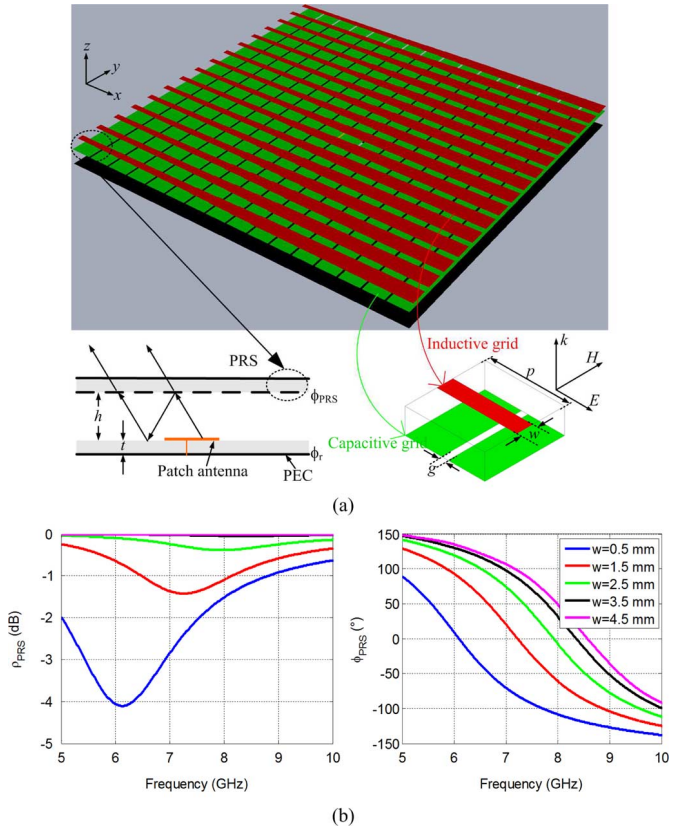

Fig. 1. (a) Proposed Fabry–Pérot LWA composed of the patch antenna's ground plane and a metamaterial-based PRS. Calculated reflection phase of the PRS for different values of w.

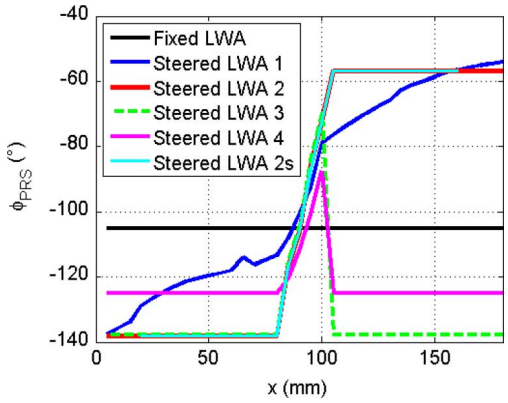

Fig. 2. Reflection phase variation along the PRS surface for the LWA described in Section III. The source is located at $x = 90$ mm.

in designing cavities with low thickness by choosing reflection phase values below 0°.

III. NUMERICAL RESULTS

Several antenna configurations are studied and compared here. This allows demonstrating the impact of each PRS on the steering performance. We only give the main geometrical parameters of the studied configuration, and we present the main numerical results obtained from the commercial TLM solver of CST Studio Suite [18]. Detailed comparisons to experimental data are provided in Section IV.

A. Constant $-105°$ Phase PRS (Fixed LWA)

A nonsteered-beam conventional subwavelength PRS-based FP cavity is designed first in order to better highlight the role of the phase-varying PRS. The operating frequency of the antenna being related to the cavity height and reflection phase of the two reflectors (PEC and PRS), h is calculated by [3]

$$h + t\sqrt{\varepsilon_r} = (\phi_{\mathrm{PRS}} + \phi_r)\frac{\lambda}{4\pi}. \quad (1)$$

A cavity denoted by "Fixed LWA" with $h = 2$ mm ($\approx \lambda/16$) is therefore designed to operate near 9.5 GHz. A summary of the optimized geometrical parameters and numerical results is provided in Table I. No beam deviation is obtained due to the constant phase along the PRS as shown in Fig. 2.

B. $-138°$ to $-54°$ Incremented Phase PRS (Steered LWA 1)

In this section and the following ones, phase-varying PRS is used. Here, the width w of the inductive grid varies from 0.4 to 4.7 mm along the surface. From left to right, w varies by 0.1 mm for the first 16 rows, then by 0.3 mm for the four middle rows

and by 0.1 mm for the last 16 rows. w of the four middle rows is therefore 2.2, 2.5, 2.8, and 3.1 mm. This structure is referred to as "Steered LWA 1." The reflection phase (ϕ_{PRS}) variation along the PRS surface is shown in Fig. 2. The variation is made bigger in the middle from 80 to 100 mm since a single primary source in a subwavelength cavity illuminates mainly the central region of the PRS. Such observations have been made in [19] and [20]. Table I shows that this configuration enables a beam steering of 36° at 9.5 GHz.

C. $-138°$ *Constant Phase–Incrementing Phase–*$-57°$ *Constant Phase PRS (Steered LWA 2)*

Our intention to improve the steering angle has led us to increase the variation of w in the middle of the surface to 0.6 mm, such that the four middle rows have a width equal to 1.7, 2.3, 2.9, and 3.5 mm. In this configuration denoted by "Steered LWA 2," w is kept fixed to 0.4 and 4.3 mm in, respectively, the first and the last 16 rows. Final numerical results show a beam steering of 56° with low sidelobes at 9.55 GHz. As illustrated in Fig. 2, even though the phase is constant on both sides of the high gradient-phase central region, a high beam steering can be obtained.

D. $-138°$ *Constant Phase–Incrementing Phase to* $-57°$*–*$-138°$ *Constant Phase PRS (Steered LWA 3)*

Another studied configuration consists in having the same phase on both sides of the central phase-varying region. Here, the central region is the same as in "Steered LWA 2," and we focus on the case with $w = 0.4$ mm on the other 32 rows. Table I shows that this antenna referred to as "Steered LWA 3" produces a beam steering of 59° at 9.7 GHz, with a high reflected lobe pointing in the opposite direction. Compared to the case "Steered LWA 2," the main difference here is that the phase goes down to a low value instead of having a high one on the right side of the central region. This important phase discontinuity is responsible of the high reflected lobe.

E. $-125°$ *Constant Phase–Incrementing Phase to* $-87°$*–*$-125°$ *Constant Phase PRS (Steered LWA 4)*

This configuration labeled "Steered LWA 4" keeps the same phase-varying central region as above, but utilizes $w = 1.1$ mm on the other 32 rows. In this case, simulations show a 51° beam steering at 9.8 GHz, with also a high reflected lobe pointing in the opposite direction. A lower steering is observed since the gradient phase is smaller. We shall note that the phase variation is not the same in each case even if the variation of w is the same since the phases are plotted at the corresponding operating frequency of each LWA.

F. $-138°$ *to* $-54°$ *Incremented Phase PRS With Smaller Lateral Dimensions (Steered LWA 2s)*

This antenna denoted by "Steered LWA 2s" obeys the same configuration as "Steered LWA 2," but possesses smaller lateral dimensions. Here, we use a 140×140-mm^2 cavity, with 12 rows on each side of the central phase-varying region. This structure shows a beam steering of 52° and a secondary lobe having a magnitude of -10 dB with respect to the main beam at 9.55 GHz.

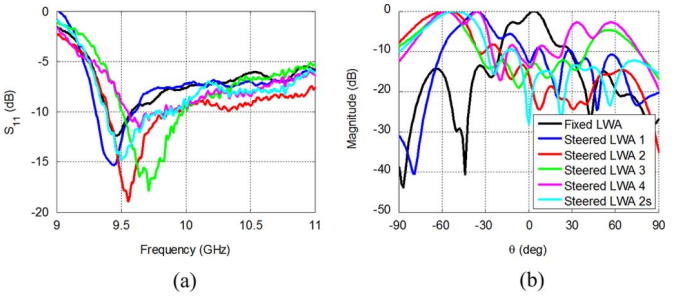

Fig. 3. (a) Measured S_{11} plots for the Fabry–Pérot LWA described in Section III. (b) Normalized simulated E-plane radiation patterns at 9.5 GHz.

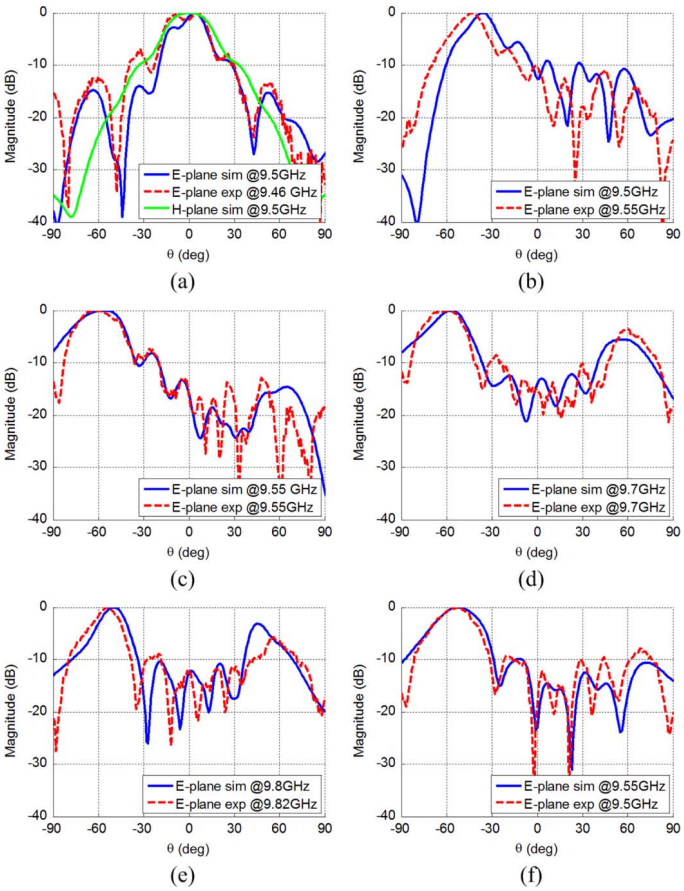

Fig. 4. Normalized radiation patterns for the Fabry–Pérot LWA. (a) Fixed LWA. (b) Steered LWA 1. (c) Steered LWA 2. (d) Steered LWA 3. (e) Steered LWA 4. (f) Steered LWA 2s.

IV. Experimental Results

Prototypes corresponding to the antenna configurations studied in Section III have been fabricated and measured to validate the numerical results. In all cases, the primary source is a 6.1×6.1 mm^2 microstrip patch with a 1.45-mm offset coaxial feed. The measured reflection coefficients are plotted in Fig. 3(a). A good matching can be observed ($S_{11} < -10$ dB) for all configurations at slightly different frequencies around

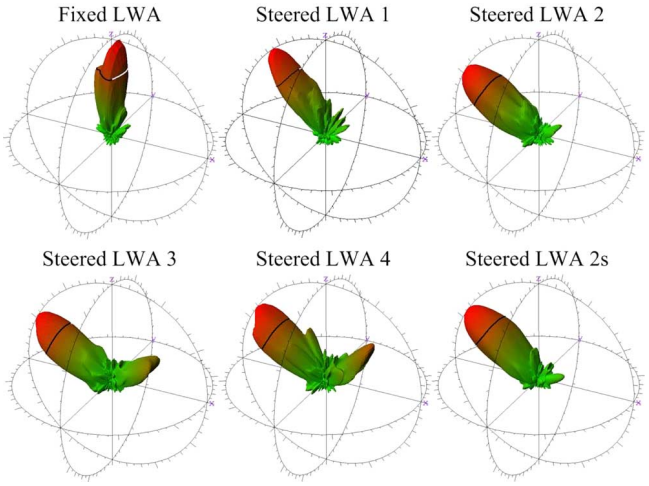

Fig. 5. 3-D radiation patterns of the Fabry–Pérot LWA.

9.5 GHz. The simulated E-plane radiation patterns are plotted at 9.5 GHz to show the beam deflection in the different configurations [Fig. 3(b)].

The radiation and beam steering characteristics have been measured in an anechoic chamber. Fig. 4 depicts the normalized E-plane radiation patterns of the different antennas, and Fig. 5 shows the simulated 3-D radiation patterns. As expected, no beam steering is observed when the reflection phase is constant along the PRS [Fig. 4(a)]. However, as reflection phase varies due to a change in w along the PRS, a steered pencil beam is created. Fig. 4 shows a good agreement between simulations and measurements and illustrates clearly the steering mechanism. Several clear observations can be made. First, when the phase varies from low values to high values along the PRS as in the case of "Steered LWA 1," "Steered LWA 2," and "Steered LWA 2s" [Figs. 4(b), (c), and (f)], the level of parasitic lobes remains low. Even when the lateral dimensions of the LWA are reduced to 140×140 mm^2, a high beam steering is produced. However, when phase increases and then gets down to low values [Fig. 4(d)–(e)], beam deviation is still conserved, but a high reflected lobe arises due to the important phase discontinuity, which results in poor radiation efficiency. Therefore, a large amount of energy is reflected at the far end of the antenna. Second, it is very important to note that to achieve beam steering, phase variation is not needed along the entire surface. Indeed in such subwavelength cavities, the region of the PRS located above the primary source is mainly illuminated. Therefore, a phase variation in this specific illuminated region is sufficient to create a steering mechanism.

V. Conclusion

A new topology of steerable Fabry–Pérot LWA is presented as a proof of concept. The configuration is based on a varying inductive and constant capacitive 2-D PRS combined with a perfect metallic reflector. The introduction of the varying inductive grid allows a beam steering of the LWA. It has been found that a variation of the phase in the central region just above the location of the feeding source is sufficient to produce a high beam steering approaching 60°. However, in a configuration where the phase values are the same on both sides of this central region, a high reflected lobe arises, degrading the performances of the antenna.

References

[1] D. Sievenpiper, L. Zhang, R. F. J. Broas, N. G. Alexópoulos, and E. Yablonovitch, "High-impedance electromagnetic surfaces with a forbidden frequency band," *IEEE Trans. Microw. Theory Tech.*, vol. 47, no. 11, pp. 2059–2074, Nov. 1999.

[2] R. F. J. Broas, D. Sievenpiper, and E. Yablonovitch, "A high-impedance ground plane applied to a cellphone handset geometry," *IEEE Trans. Microw. Theory Tech.*, vol. 49, no. 7, pp. 262–1265, Jul. 2001.

[3] G. V. Trentini, "Partially reflecting sheet arrays," *IRE Trans. Antennas Propag.*, vol. AP-4, no. 4, pp. 666–671, Oct. 1956.

[4] A. P. Feresidis and J. C. Vardaxoglou, "High gain planar antenna using optimized partially reflective surfaces," *Proc. Inst. Elect. Eng. Microw. Antennas Propag.*, vol. 148, no. 6, pp. 345–350, Dec. 2001.

[5] A. P. Feresidis, G. Goussetis, S. Wang, and J. C. Vardaxoglou, "Artificial magnetic conductor surfaces and their application to low-profile high-gain planar antennas," *IEEE Trans. Antennas Propag.*, vol. 53, no. 1, pp. 209–215, Jan. 2005.

[6] S. Wang, A. P. Feresidis, G. Goussetis, and J. C. Vardaxoglou, "High-gain subwavelength resonant cavity antenna based on metamaterial ground planes," *Inst. Elect. Eng. Proc. Microw. Antennas Propag.*, vol. 153, no. 1, pp. 1–6, Feb. 2006.

[7] L. Zhou, H. Li, Y. Qin, Z. Wei, and C. T. Chan, "Directive emissions from subwavelength metamaterial-based cavities," *Appl. Phys. Lett.*, vol. 86, no. 10, p. 101101, Feb. 2005.

[8] A. Ourir, A. de Lustrac, and J.-M. Lourtioz, "All-metamaterial-based sub-wavelength cavities ($\lambda/60$) for ultrathin directive antennas," *Appl. Phys. Lett.*, vol. 88, no. 8, p. 084103, Feb. 2006.

[9] A. Ourir, A. de Lustrac, and J.-M. Lourtioz, "Optimization of metamaterial based subwavelength cavities for ultracompact directive antennas," *Microw. Opt. Technol. Lett.*, vol. 48, no. 12, pp. 2573–2577, Dec. 2006.

[10] Y. Sun, Z. N. Chen, Y. Zhang, H. Chen, and T. S. P. See, "Subwavelength substrate-integrated Fabry-Pérot cavity antennas using artificial magnetic conductor," *IEEE Trans. Antennas Propag.*, vol. 60, no. 1, pp. 30–35, Jan. 2012.

[11] A. Ourir, S. N. Burokur, and A. de Lustrac, "Electronically reconfigurable metamaterial for compact directive cavity antennas," *Electron. Lett.*, vol. 43, no. 13, pp. 698–700, June 2007.

[12] A. R. Weily, T. S. Bird, and Y. J. Guo, "A reconfigurable high-gain partially reflecting surface antenna," *IEEE Trans. Antennas Propag.*, vol. 56, no. 11, pp. 3382–3390, Nov. 2008.

[13] S. N. Burokur, J.-P. Daniel, P. Ratajczak, and A. de Lustrac, "Tunable bi-layered metasurface for frequency reconfigurable directive emissions," *Appl. Phys. Lett.*, vol. 97, no. 6, p. 064101, Aug. 2010.

[14] A. Ourir, S. N. Burokur, and A. de Lustrac, "Phase-varying metamaterial for compact steerable directive antennas," *Electron. Lett.*, vol. 43, no. 9, pp. 493–494, Apr. 2007.

[15] A. Ourir, S. N. Burokur, and A. de Lustrac, "Electronic beam steering of an active metamaterial-based directive subwavelength cavity," in *Proc. 2nd Eur. Conf. Antennas Propag.*, Nov. 11–16, 2007, pp. 1–4.

[16] A. Ourir, S. N. Burokur, R. Yahiaoui, and A. de Lustrac, "Directive metamaterial-based subwavelength resonant cavity antennas—Applications for beam steering," *Comptes Rendus Phys.*, vol. 10, no. 5, pp. 414–422, Jun. 2009.

[17] R. Guzman-Quiros, J. L. Gomez-Tornero, A. R. Weily, and Y. J. Guo, "Electronic full-space scanning with 1-D Fabry-Pérot LWA using electromagnetic band-gap," *IEEE Antennas Wireless Propag. Lett.*, vol. 11, pp. 1426–1429, 2012.

[18] CST Studio Suite 2012. Computer Simulation Technology, Framingham, MA, USA, 2012 [Online]. Available: http://www.cst.com

[19] R. Yahiaoui, S. N. Burokur, and A. de Lustrac, "Enhanced directivity of an ultra-thin metamaterial-based cavity antenna fed by a multisource," *Electron. Lett.*, vol. 45, no. 16, pp. 814–816, July 2009.

[20] S. N. Burokur, R. Yahiaoui, and A. de Lustrac, "Subwavelength metamaterial-based resonant cavities fed by multiple sources for high directivity," *Microw. Opt. Technol. Lett.*, vol. 51, no. 8, pp. 1883–1888, Aug. 2009.

Annexe 1.7

D. Germain, D. Seetharamdoo, S. N. Burokur, A. de Lustrac

« Thin conformal directive Fabry-Pérot cavity antenna »

IEEE Antennas and Wireless Propagation Letters, vol. 12, pp. 926-929, 2013

Thin Conformal Directive Fabry–Pérot Cavity Antenna

Dylan Germain, Divitha Seetharamdoo, Shah Nawaz Burokur, and André de Lustrac, *Member, IEEE*

***Abstract*—A compensated-phase partially reflective surface (PRS) is proposed in this letter. It is used together with a metallic ground plane to form a low-profile Fabry–Pérot (FP) cavity antenna conformed on a cylindrical surface. A microstrip patch antenna is embedded inside the cavity to act as the primary feed. To validate the proposed PRS, an antenna is designed to operate at the 5.7-GHz Wi-Fi frequency. The subwavelength FP cavity with a fixed overall thickness of $\lambda_0/10$ (where λ_0 is the free-space operating wavelength) is fabricated and measured. The impact of compensating the PRS phase is analyzed.**

***Index Terms*—Cavity antenna, conformal, phase compensation.**

I. Introduction

OVER the last few years, periodic structures patterned on dielectric substrates have been intensely integrated in antenna systems so as to enhance their performances. High-gain low-profile antenna designs have inherited the unique properties of periodic structures. The interesting feature of partial reflection has contributed to the design of superstrate layers so as to significantly enhance the directivity of single radiating sources at boresight [1], [2]. Such structures are based on a parallel-plate configuration, enclosing a resonant Fabry–Pérot (FP) cavity. In a conventional FP cavity antenna, a partially reflecting surface (PRS) presenting a 180° reflection phase is placed a half-wavelength above the perfect electric conductor (PEC) ground plane of the primary radiating source [1], [2]. Replacing the PEC surface by an artificial magnetic conductor (AMC) presenting 0° reflection phase shift allows reducing the antenna profile to a quarter-wavelength [3]. Further thickness reduction is possible thanks to the dispersion characteristics of metamaterial surfaces also known as metasurfaces [4]–[6]. Furthermore, varactor diode-tuned elements integrated in periodic structures have been introduced to achieve frequency agility [7]–[9]. Beam-steering characteristics from such FP antennas have also been shown by utilizing a passive phase-varying metasurface as PRS [10]. Recently, electronically reconfigurable structures have been proposed to realize electrically scanned antennas [11]–[13]. All these previously proposed designs have shown their good efficiencies in planar configurations.

Recently, conformal antennas have received a lot of attention [14]–[17]. Antennas on conformal structures play considerable roles in modern communication systems such as the spatial domain multiple access (SDMA), smart antennas, beam-steering array antennas, radar systems, and aerospace applications. Due to aerodynamic constraints, high-speed vehicles and missiles require antennas conformed to their surfaces. Generally, a conformal antenna is cylindrical or spherical, with the radiating elements mounted on or integrated into the curved surface. Such conformal antennas offer various advantages such as a potential of 360° coverage so as to secure continuous communications, a minimal level of unwanted radiations, low weight, and the possibility of obtaining significant gains. When the curved surface has a large radius compared to the operating wavelength, analyses can omit the influence of curvature on the radiating element. However, when the curvature radius is small compared to wavelength, the influence of curvature on the radiating element needs to be considered and integrated in the design.

In this letter, we consider a conformal cavity antenna and present a new configuration of compensated phase PRS for such a configuration. The inductance and capacitance of the LC-resonant metasurface reflector is varied in order to control the phase characteristics and thus to compensate the distance from a curved surface to a planar one. The design of the conformal cavity antenna is made through numerical analyses. To validate the proposed concept, experimental measurements are performed on a fabricated prototype, and a good agreement is obtained between simulations and measurements.

II. Design Principle of the Conformal Cavity Antenna

The proposed principle is depicted by the schematic in Fig. 1(a). When illuminated by the primary feed in an FP cavity antenna, the LC resonant cells of the planar PRS can be viewed as an array of microantenna elements radiating in phase. However, resonant cells of a curved reflector do not produce in-phase radiation. In order to show how the in-phase emission from a curved PRS can be restored, we first consider an array of micro wire antennas placed on a metallic quarter-cylinder of radius $r = 152$ mm (approximately 3λ), as shown in Fig. 1(a). The working frequency is set to 5.7 GHz, and 25 sources are considered. Each wire antenna acts as a Hertzian dipole and has a length $l = \lambda_0/10$. The array is distant from the surface of the cylinder by $h = 3.5$ mm ($\lambda_0/15$). To assure an in-phase emission, the curved array

Manuscript received April 02, 2013; revised June 09, 2013; accepted June 10, 2013. Date of publication July 18, 2013; date of current version August 07, 2013.

D. Germain is with the IEF, CNRS, UMR 8622, Université Paris-Sud, 91405 Orsay cedex, France.

D. Seetharamdoo is with IFSTTAR-LEOST, 59666 Villeneuve d'Ascq cedex, France.

S. N. Burokur and A. de Lustrac are with the IEF, CNRS, UMR 8622, Université Paris-Sud, 91405 Orsay cedex, France, and also with Université Paris Ouest, 92410 Ville d'Avray, France (e-mail: shah-nawaz.burokur@u-psud.fr).

Color versions of one or more of the figures in this letter are available online at http://ieeexplore.ieee.org.

Digital Object Identifier 10.1109/LAWP.2013.2273972

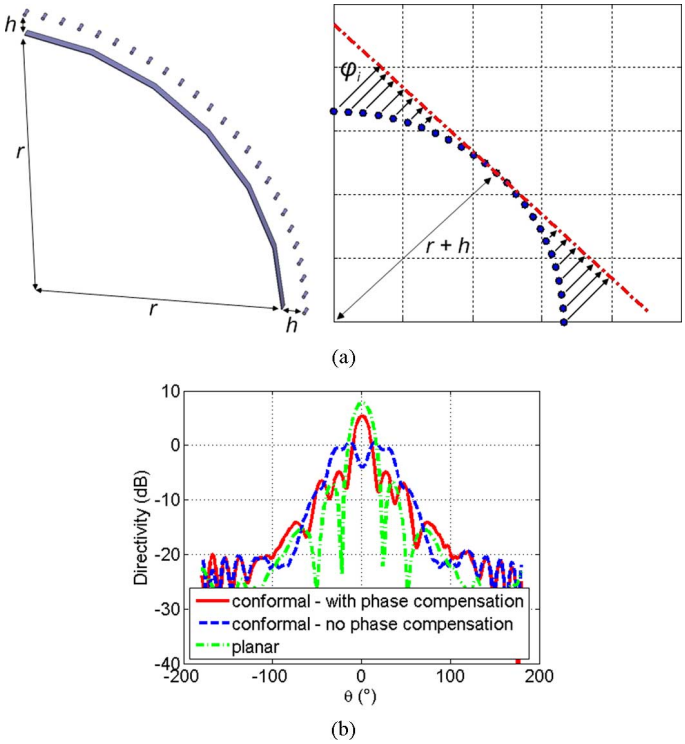

Fig. 1. (a) Schematic principle of the conformal FP cavity antenna. (b) Directivity of the conformal array with and without phase compensation and of an ideal rectilinear array.

must be able to exhibit a phase distribution such that it radiates like a rectilinear one. Each microantenna must then be fed with a phase shift that compensates the distance of the latter antenna from a planar surface, as illustrated in Fig. 1(a). The positions of the antennas are given by (x_i, y_i) coordinates in the plane with an origin O at the center of the cylinder, where the index i ($1 \leq i \leq 25$) denotes the different microantennas. θ is the angular step of the curved antenna array, and in our case, $\theta = 90/24 = 3.75°$. The positions x_i and y_i are respectively given by $x_i = R\cos((i-1) * \theta)$ and $y_i = R\sin((i-1) * \theta)$ with $R = r + h = 155.5$ mm. The general equation of the planar surface is expressed as: $ax + by + c = 0$. The phase is then given by the general expression

$$\varphi_i = \frac{2\pi}{\lambda} \frac{|ax_i + by_i + c|}{\sqrt{a^2 + b^2}}. \tag{1}$$

To validate the proposed compensated phase distribution, the antenna array is simulated using the commercial finite element software HFSS. The calculated phase compensation is applied to each antenna element according to its position. The obtained far-field radiation pattern is illustrated by the continuous trace in Fig. 1(b). A directive emission is observed with secondary parasitic lobes having levels lower than -10 dB compared to the primary lobe. In the case of a conformal antenna array without compensated phase (dashed trace), a broader primary lobe is observed with a lower magnitude. When comparing the proposed conformal antenna array to an ideal rectilinear one, a good qualitative agreement can be observed. The shapes of the emitted beam are similar in both cases, even though the magnitude is higher by 2.4 dB. The performances obtained from the conformal antenna array show the usefulness of the phase compensation.

III. Curved Phase Compensated Metasurface

In order to achieve the compensated phase distribution, the metamaterial cell shown in the inset of Fig. 2(a), simultaneously composed of a capacitive and an inductive grid, is used. By tuning the geometrical dimensions w and g and keeping the others fixed, the phase characteristics can be easily tailored. The reflection and transmission characteristics are presented in Fig. 2(b) for $w = 1.5$ mm, $g = 0.4$ mm, $l = 10$ mm, $p_x = 10$ mm, and $p_y = 10.8$ mm. The dielectric support used is the 0.75-mm-thick RO 3003 with a relative permittivity $\varepsilon_r = 3$ and loss tangent $\tan\delta = 0.0013$. To realize the desired phase distribution given by (1), w and g are varied respectively from 1.5 to 5 mm and 0.4 to 6.4 mm. Since the metamaterial cell presents transmission phase values varying from $+90°$ to $-90°$, we restricted ourselves to respectively $+80°$ and $-80°$ on the edges and in the center of the metamaterial reflector. A good agreement is observed between the theoretical and realized phase profile as shown in Fig. 2(c). The theoretical profile of the phase distribution necessary to restore the in-phase emission from the conformal array has a parabolic shape.

The proposed phase compensation principle is applied to a low-profile antenna using the concept of Fabry–Pérot reflex-cavity. A conventional FP cavity is composed of a primary source embedded between two parallel reflectors, separated by a distance h. The other reflector is the cylindrical PEC ground plane of the primary source. The primary source used to illuminate the PRS at 5.7 GHz is a microstrip patch antenna designed on an RO 3003 substrate. Resonance is obtained at the frequency f satisfying the condition

$$f = (\phi_{\mathrm{PRS}} + \phi_{\mathrm{r}}) \frac{c}{4\pi h} \tag{2}$$

where ϕ_{PRS} and ϕ_{r} denote respectively the reflection phases of the PRS and the PEC ground plane of the microstrip patch feed. In (2), we consider only the zeroth order of the cavity's electromagnetic mode. The thickness h is directly proportional to sum of phases $(\phi_{\mathrm{PRS}} + \phi_{\mathrm{r}})$ and to frequency f. From the calculated reflection phase of the metamaterial cell located just above the feed, h is found to be equal to 3.5 mm corresponding to approximately $\lambda_0/15$ at 5.7 GHz.

A metasurface composed of a tapered array of the resonant cells presented in Fig. 2(a) is designed to obey the phase characteristics plotted in Fig. 2(c). The phase compensated metasurface is then used as a PRS in the FP cavity antenna. With such a nonuniform array for the phase compensation, and even though physically curved, the PRS behaves electromagnetically as a rectilinear one, with a constant reflection phase along the whole surface. Therefore, the reflection phase shown by the unit cell at the center of the metasurface reflector is taken as reference for the calculation of the cavity thickness h at resonance. Also, as pointed out in [18] and [19], in such a subwavelength $(\lambda_0/15)$ cavity antenna fed by a single primary source, the PRS is mainly illuminated at the central region, which justifies the use of the reflection phase of the central unit cell for the resonance condition.

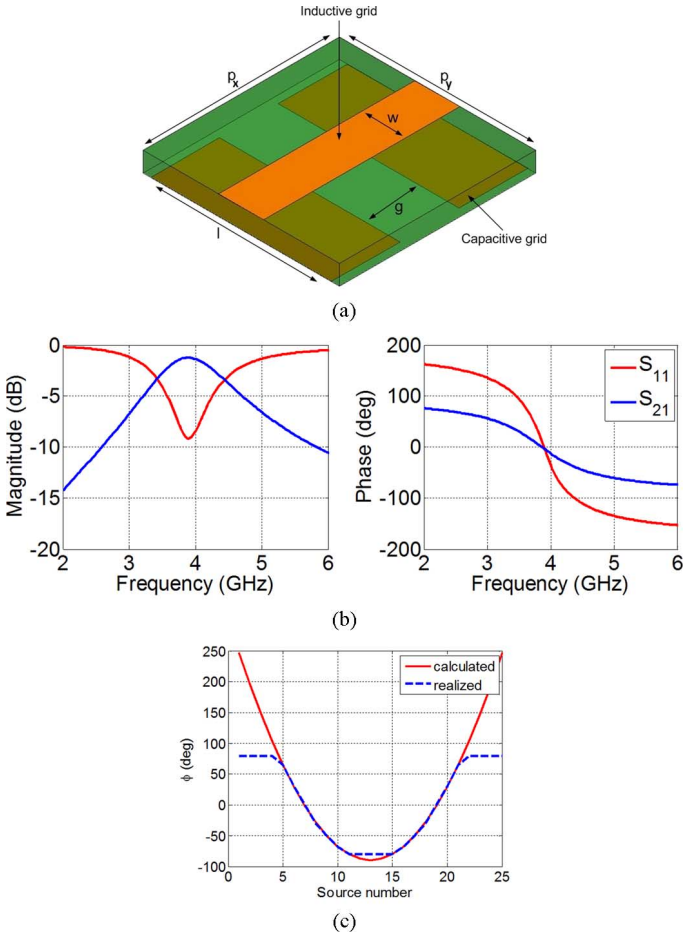

Fig. 2. (a) Metamaterial unit cell used to realize the phase compensated surface. (b) Magnitude and phase of the reflection and transmission coefficients of the unit cell. (c) Theoretical and realized phase distribution for position compensation.

IV. Conformal Metamaterial-Based FP Cavity Antenna

Fig. 3(a) and (b) shows respectively the design principle and the photograph of the fabricated conformal FP cavity antenna. The conformed metasurface reflector has lateral dimensions 250×50 mm^2, which are sufficient enough to validate the proposed concept and also to avoid secondary lobes occurring from lateral radiations of the cavity. The primary source is a 13.95×13 mm^2 microstrip patch with a 2.3-mm offset coaxial feed. The simulated and measured reflection coefficients are plotted in Fig. 3(c). A good matching can be observed at 5.7 GHz. Fig. 3(d) shows the calculated emitted electric field distributions of the cavity antenna without and with phase compensation. A clearly narrower beamwidth is observed from the antenna where the phase compensated PRS is used.

The radiation characteristics have been measured in an anechoic chamber. Fig. 4 depicts the normalized $\boldsymbol{E}$- and $\boldsymbol{H}$-plane radiation patterns of the conformal antenna. A good qualitative agreement is observed between simulations and experiments. The H-plane diagrams are consistent with those obtained from the antenna array in Fig. 1(b) and also with the field distributions of Fig. 3(d).

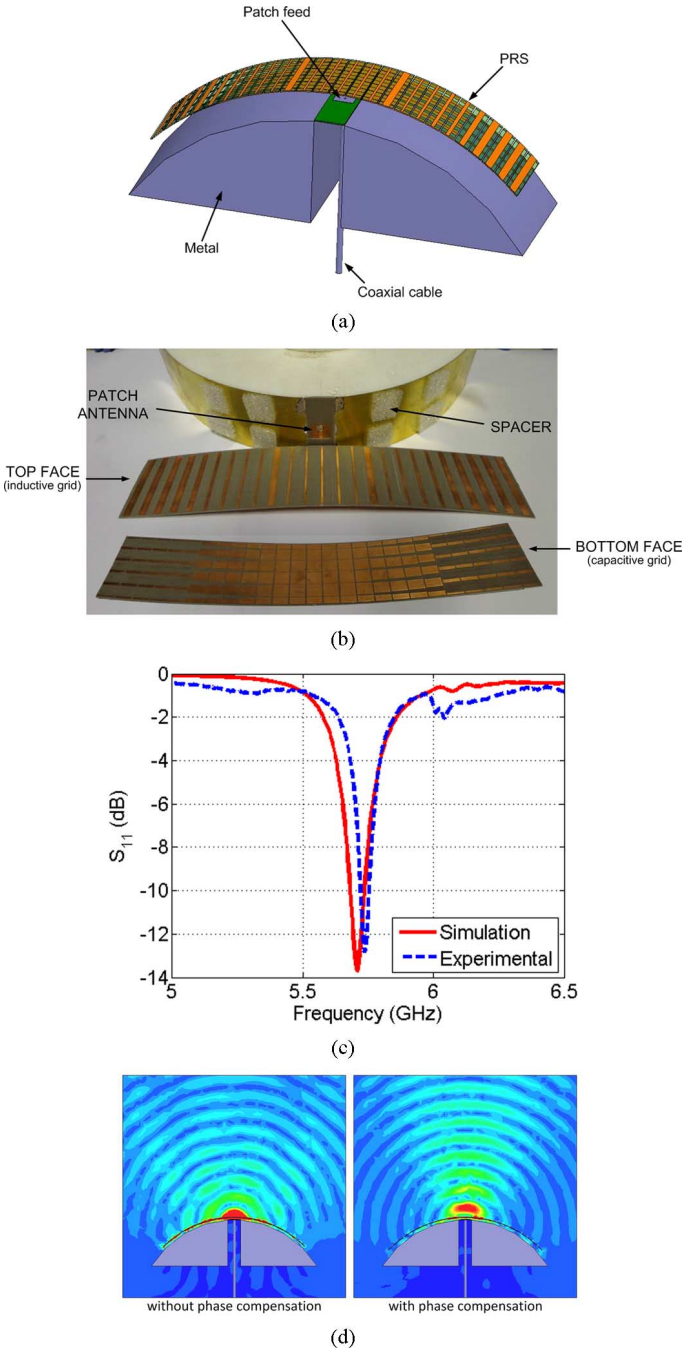

Fig. 3. (a) Design principle of the conformal FP cavity antenna. (b) Photograph of the fabricated prototype. (c) Return losses of the conformal antenna. (d) Calculated electric field distributions in the $\boldsymbol{H}$-plane in the case of the PRS respectively without phase compensation and with the phase compensation.

As expected, without phase compensation, the PRS produces a distorted beam in both radiation planes due to the out-of-phase emission. However, the proposed phase compensation allows restoring in-phase emission. Furthermore, when compared to a planar FP cavity antenna of similar thickness, similar radiation patterns are obtained, validating the proper functioning of the phase compensated metasurface.

V. Conclusion

A conformal topology of the Fabry–Pérot cavity antenna is presented. The configuration is based on a phase-compensated

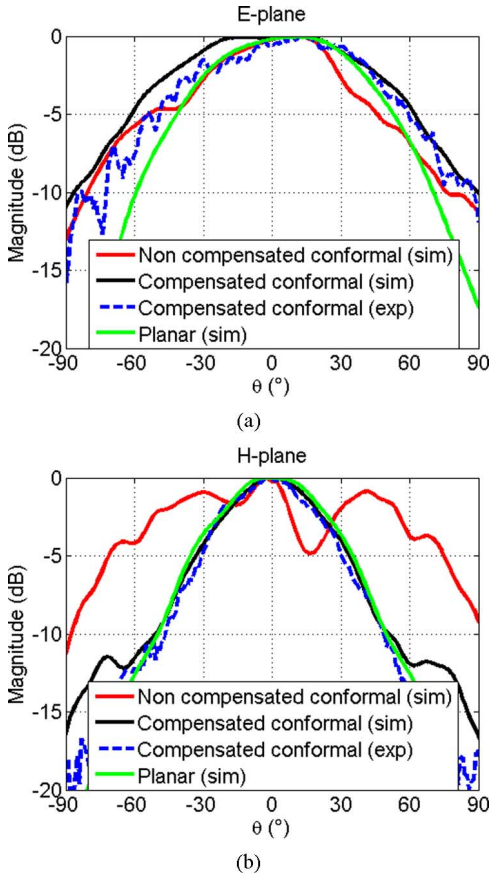

Fig. 4. Far-field radiation patterns. (a) $\boldsymbol{E}$-plane. (b) $\boldsymbol{H}$-plane.

2-D PRS combined with a perfect metallic reflector. The introduction of the phase compensation allows to restore the in-phase directive emission from the curved antenna. The presented concept can be generalized to other shaped surfaces defined or not by analytical expressions.

REFERENCES

[1] G. V. Trentini, "Partially reflecting sheet arrays," *IRE Trans. Antennas Propag.*, vol. AP-4, no. 4, pp. 666–671, Oct. 1956.

[2] A. P. Feresidis and J. C. Vardaxoglou, "High gain planar antenna using optimized partially reflective surfaces," *Proc. Inst. Elect. Eng., Microw. Antennas Propag.*, vol. 148, no. 6, pp. 345–350, Dec. 2001.

[3] A. P. Feresidis, G. Goussetis, S. Wang, and J. C. Vardaxoglou, "Artificial magnetic conductor surfaces and their application to low-profile high-gain planar antennas," *IEEE Trans. Antennas Propag.*, vol. 53, no. 1, pp. 209–215, Jan. 2005.

[4] L. Zhou, H. Li, Y. Qin, Z. Wei, and C. T. Chan, "Directive emissions from subwavelength metamaterial-based cavities," *Appl. Phys. Lett.*, vol. 86, no. 10, p. 101101, Feb. 2005.

[5] A. Ourir, A. de Lustrac, and J.-M. Lourtioz, "All-metamaterial-based sub-wavelength cavities ($\lambda/60$) for ultrathin directive antennas," *Appl. Phys. Lett.*, vol. 88, no. 8, p. 084103, Feb. 2006.

[6] A. Ourir, A. de Lustrac, and J.-M. Lourtioz, "Optimization of metamaterial based subwavelength cavities for ultracompact directive antennas," *Microw. Opt. Technol. Lett.*, vol. 48, no. 12, pp. 2573–2577, Dec. 2006.

[7] A. Ourir, S. N. Burokur, and A. de Lustrac, "Electronically reconfigurable metamaterial for compact directive cavity antennas," *Electron. Lett.*, vol. 43, no. 13, pp. 698–700, Jun. 2007.

[8] A. R. Weily, T. S. Bird, and Y. J. Guo, "A reconfigurable high-gain partially reflecting surface antenna," *IEEE Trans. Antennas Propag.*, vol. 56, no. 11, pp. 3382–3390, Nov. 2008.

[9] S. N. Burokur, J.-P. Daniel, P. Ratajczak, and A. de Lustrac, "Tunable bi-layered metasurface for frequency reconfigurable directive emissions," *Appl. Phys. Lett.*, vol. 97, no. 6, p. 064101, Aug. 2010.

[10] A. Ourir, S. N. Burokur, and A. de Lustrac, "Phase-varying metamaterial for compact steerable directive antennas," *Electron. Lett.*, vol. 43, no. 9, pp. 493–494, Apr. 2007.

[11] A. Ourir, S. N. Burokur, and A. de Lustrac, "Electronic beam steering of an active metamaterial-based directive subwavelength cavity," in *Proc. 2nd Eur. Conf. Antennas Propag.*, Nov. 11–16, 2007, pp. 1–4.

[12] A. Ourir, S. N. Burokur, R. Yahiaoui, and A. d. Lustrac, "Directive metamaterial-based subwavelength resonant cavity antennas – Applications for beam steering," *Comptes Rendus Phys.*, vol. 10, no. 5, pp. 414–422, Jun. 2009.

[13] R. Guzman-Quiros, J. L. Gomez-Tornero, A. R. Weily, and Y. J. Guo, "Electronic full-space scanning with 1-D Fabry–Pérot LWA using electromagnetic band-gap," *IEEE Antennas Wireless Propag. Lett.*, vol. 11, pp. 1426–1429, 2012.

[14] J.-W. Niu and S.-S. Zhong, "Cylindrical conformal bow-tie microstrip antennas with small curvature radius," *Microw. Opt. Technol. Lett.*, vol. 39, no. 6, pp. 511–514, Dec. 2003.

[15] J. L. Gomez-Tornero, "Analysis and design of conformal tapered leaky-wave antennas," *IEEE Antennas Wireless Propag. Lett.*, vol. 10, pp. 1068–1071, 2011.

[16] D. Gaetano, M. J. Ammann, P. McEvoy, M. John, L. Keating, and F. Horgan, "Proximity study of a conformal UWB directional antenna on water pipe," *Microw. Opt. Technol. Lett.*, vol. 54, no. 8, pp. 1982–1986, Aug. 2012.

[17] Z.-Q. Liu, Y.-S. Zhang, Z. Qian, Z. P. Han, and W. Ni, "A novel broad beamwidth conformal antenna on unmanned aerial vehicle," *IEEE Antennas Wireless Propag. Lett.*, vol. 11, pp. 196–199, 2012.

[18] R. Yahiaoui, S. N. Burokur, and A. de Lustrac, "Enhanced directivity of an ultra-thin metamaterial-based cavity antenna fed by a multisource," *Electron. Lett.*, vol. 45, no. 16, pp. 814–816, Jul. 2009.

[19] S. N. Burokur, R. Yahiaoui, and A. de Lustrac, "Subwavelength metamaterial-based resonant cavities fed by multiple sources for high directivity," *Microw. Opt. Technol. Lett.*, vol. 51, no. 8, pp. 1883–1888, Aug. 2009.

Annexe 1.8

S. N. Burokur, A. Ourir, A. de Lustrac, R. Yahiaoui

« Metasurfaces for high directivity antenna applications »

pp. 533-556 in book *Metamaterial*, edited by X.-Y. Jiang, ISBN 978-953-51-0591-6,
InTech, 2012

20

Metasurfaces for High Directivity Antenna Applications

Shah Nawaz Burokur, Abdelwaheb Ourir,
André de Lustrac and Riad Yahiaoui
Institut d'Electronique Fondamentale,
Univ. Paris-Sud, CNRS UMR 8622,
France

1. Introduction

There has been a lot of study published in literature on the improvement of the performances of microstrip patch antennas. Most of the solutions proposed in the past were to use an array of several antennas. The particular disadvantage of this method comes from the feeding of each antenna and also from the coupling between each element. Other interesting solutions have then been suggested: the first one (Jackson & Alexópoulos, 1985) was to make use of a superstrate of either high permittivity or permeability above the patch antenna and the second one proposed (Nakano et al., 2004), is to sandwich the antenna by dielectric layers of the same permittivity. A Left-Handed Medium (LHM) superstrate where both permittivity and permeability are simultaneously negative has also been suggested (Burokur et al., 2005). The numerical study of a patch antenna where a Left-Handed Medium (LHM) is placed above has been done and in this case a gain enhancement of about 3 dB has been observed. However, these solutions are all based on non-planar designs which are bulky for novel telecommunication systems requiring compact low-profile and environment friendly directive antennas.

To overcome the major problem of complex feeding systems in antenna arrays, the design of compact directive electromagnetic sources based on a single feeding point has become an important and interesting research field. Different interesting solutions based on this concept have been proposed. At first, resonant cavities in one-dimensional (1-D) dielectric photonic crystals have been used (Cheype et al., 2002). Afterwards, three dimensional (3-D) structures have been used, leading to better performances (Temelkuran et al., 2000). Another interesting solution proposed by Enoch *et al*. was to use the refractive properties of a low optical index material interface in order to achieve a directive emission (Enoch et al., 2002). The authors have shown how a simple stack of metallic grids can lead to ultra-refraction. Because the resulting metamaterial structure has an index of refraction, n, which is positive, but near zero, all of the rays emanating from a point source within such a slab of zero index material would refract, by Snell's Law, almost parallel to the normal of every radiating aperture. We shall note that these solutions are all also based on the use of a bulky 3-D material.

Otherwise, the most common method to reach directive emission is obviously based on the Fabry-Pérot reflex-cavity mechanism (Trentini, 1956). Such cavities have first been considered quite bulky too since a thickness of half of the working wavelength is required (Akalin et al., 2002). But recently, the introduction of composite metasurfaces has shown that the half wavelength thickness restriction in a Fabry-Pérot cavity can be judiciously avoided. For example, Feresidis *et al*. showed that a quarter wavelength thick Fabry-Pérot cavity can be designed by using Artificial Magnetic Conductor (AMC) surfaces introducing a zero degree reflection phase shift to incident waves (Feresidis et al., 2005). Assuming no losses and exactly 0° reflection phase, the surface is referred to as a Perfect Magnetic Conductor (PMC), which is the complementary of a Perfect Electric Conductor (PEC). The latter AMC surfaces have been first proposed in order to act as the so called High Impedance Surface (HIS) (Sievenpiper et al., 1999). This HIS is composed of metallic patches periodically organized on a dielectric substrate and shorted to the metallic ground plane with vias, appearing as "mushroom" structures. In a particular frequency band where reflection phase is comprised between -90° and +90°, this surface creates image currents and reflections in-phase with the emitting source instead of out of phase reflections as the case of conventional metallic ground plane. The HIS allows also the suppression of surface waves which travel on conventional ground plane. However, the HIS of Sievenpiper needs a non-planar fabrication process, which is not suitable for implementation in lots of microwave and millimetric circuits.

The reflex-cavity antenna proposed by Feresidis was composed of two planar AMC surfaces and a microstrip patch antenna acting as the primary (feeding) source. The first AMC surface was used as the feeding source's ground plane so as to replace the PEC surface and hence, to achieve a 0° reflection phase. The second one acted as a Partially Reflective Surface (PRS) with a reflection phase equal to 180°. This idea has then been pushed further by Zhou *et al*. (Zhou et al., 2005). By taking advantage of the dispersive characteristics of metamaterials, the authors designed a subwavelength cavity with a thickness smaller than a 10^{th} of the wavelength. Compared to Feresidis, Zhou made use of a non-planar mushroom structure with a dipole acting as the feeding source.

In this chapter, using a novel composite metamaterial, made of both capacitive and inductive grids, we review our recent works in the fields of low-profile and high-gain metamaterial-based reflex-cavity type antennas. First, we will show how our group has lately further reduced the cavity thickness by $\lambda/30$ for applications to ultra-thin directive antennas by using a PEC surface as the source's ground plane and one subwavelength metamaterial-based composite surface as the PRS. We will also present how an optimization of the cavity has also been undertaken in order to reduce the thickness to $\lambda/60$ by using an AMC surface instead of the PEC ground plane and a metasurface as PRS. We will then present the modeling and characterization of resonant cavities for enhancing the directivity. Finally, a phase controlled metasurface will be proposed for applications to beam steerable and frequency reconfigurable cavity antennas. Numerical analyses using Finite Element Method (FEM) based software *HFSS* and CST's Transmission Line Modeling (TLM) solver *MICROSTRIPES* together with discussions on the fabrication process and the experimental results will be presented for the different cavities mentioned above.

2. Operating principle of the Fabry-Pérot reflex-cavity

A cavity antenna is formed by a feeding source placed between two reflecting surfaces as shown in Fig. 1. In this paper, different cavities based on the schematic model presented in Fig. 1 will be discussed and used. The cavity is composed of a PEC surface acting as a conventional ground plane for the feeding source and a metamaterial-based surface (metasurface) playing the role of a transmitting window known as a PRS. Following the earlier work of Trentini, a simple optical ray model can be used to describe the resonant cavity modes (Trentini, 1956). This model is used to theoretically predict the operating mode of a low-profile high-directivity metamaterial-based subwavelength reflex-cavity antenna. Let us consider the cavity presented in Fig. 1(a). It is formed by a feeding antenna placed between two reflectors separated by a distance *h*. Phase shifts are introduced by these two reflectors and also by the path length of the wave travelling inside the cavity. With the multiple reflections of the wave emitted by the antenna, a resonance is achieved when the reflected waves are in phase after one cavity roundtrip. The resonance condition, for waves propagating vertically, can then be written as:

$$h + t\sqrt{\varepsilon_r} = (\phi_{PRS} + \phi_r)\frac{\lambda}{4\pi} \pm N\frac{\lambda}{2} \tag{1}$$

where ϕ_{PRS} is the reflection phase of the PRS reflector, ϕ_r is the reflection phase of the feeding source's ground plane, ε_r is the relative permittivity of the substrate supporting the primary source and *t* is its thickness. N is an integer qualifying the electromagnetic mode of the cavity. If the cavity and the substrate thicknesses *t* and *h* are fixed, the resonant wavelength is determined by the sum of the reflection phases $\phi_{PRS} + \phi_r$ for a fixed N. Conversely, for a given wavelength, the thickness *h* can be minimized by reducing the total phase shift $\phi_{PRS} + \phi_r$. The use of metasurfaces answers this purpose since they can exhibit an LC resonance. This resonance helps to have a reflection phase response varying from 180° to -180°, passing through 0° at the resonance frequency. By choosing a desired operating cavity frequency above the metasurface resonance where the reflection phase is negative, the sum $\phi_{PRS} + \phi_r$ can be very small leading to a very low cavity thickness. Since the reflector near the feeding antenna in Fig. 1(a) is composed of a PEC surface, then ϕ_r will be very close to 180°. On the other side, an AMC ground plane is used in Fig. 1(b) and in such case ϕ_r will show frequency dependent phase characteristics.

Therefore, taking advantage of the phase dispersive characteristics of metasurfaces, we will present several models of reflex-cavity antennas, each designed for a specific task. We will first present a λ/30 (1 mm @ 10 GHz) thick cavity antenna by using a PRS reflection phase value around -120°. This cavity antenna has a narrow beam profile in both E- and H-planes, producing a directivity of 160 (22 dBi). To further reduce the cavity thickness, we will emphasize on the use of two metasurfaces as illustrated in Fig. 1 (b), one as a PRS reflector and the other one as AMC ground plane of the primary source. The combination of these two metasurfaces, particularly the low phase values above their resonance, allows to design very low profile cavity antennas. For e.g., a λ/60 thickness has been achieved and the latter cavity presents a directivity of 78 (19 dBi).

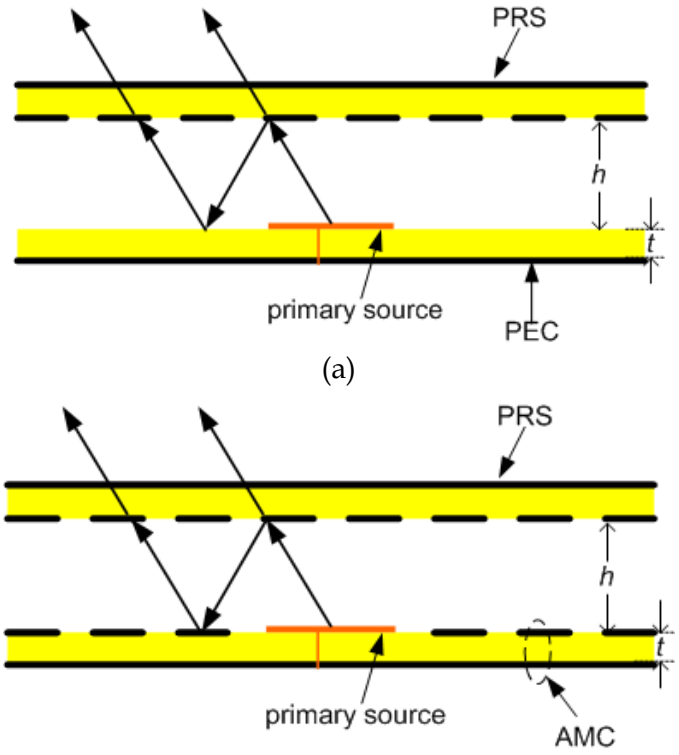

Fig. 1. Resonant cavity formed by a PEC ground plane and a metamaterial-based PRS (a) and, an AMC ground plane and a metamaterial-based PRS (b).

Since directivity depends strongly on the radiating aperture which is defined by the field distribution illuminating the PRS, we will present two ways on how we can manipulate the directivity of such reflex-cavity antennas. First, we will present the use of lateral PEC walls in the cavity antenna to form what we will refer to as metallic cavity. This method allows to enhance the directivity by 3 dB compared to the case where the cavity is open on the lateral sides. Also, the metallic cavity presents lower backward radiations due to the confinement of electromagnetic radiation, therefore increasing the front-to-back (FBR) ratio. Secondly, in order to optimize the field distribution illuminating the PRS, we will study the use of several primary sources inside the cavity. We will show how judiciously placing the different sources in the cavity helps to increase the directivity to more than 6 dB compared to single source fed cavity.

Finally, we will present beam steerable and frequency reconfigurable cavity antennas. For the beam steering, we will in a first step study a cavity where the PRS presents a locally variable phase. The latter PRS then acts as a phased array of micro-antennas, thus allowing to achieve beam steering. This concept has been pushed further by designing an electronically tunable metasurface via the incorporation of lumped elements (varactor diodes). This active metasurface can be used as PRS for two different tasks. Firstly, by applying different bias voltage along the PRS, a locally variable phase is obtained and is fully compatible for beam steering. On the other side, if we change the bias voltage of all the lumped elements similarly, then we can tune the operation frequency of the PRS so as to achieve a frequency reconfigurable reflex-cavity antenna.

3. Analysis of the planar metasurfaces

The cavity presented in Fig. 1 requires the application of a metamaterial-based surface. So in this section, we will design planar metamaterial-based surfaces for operation near 10 GHz.

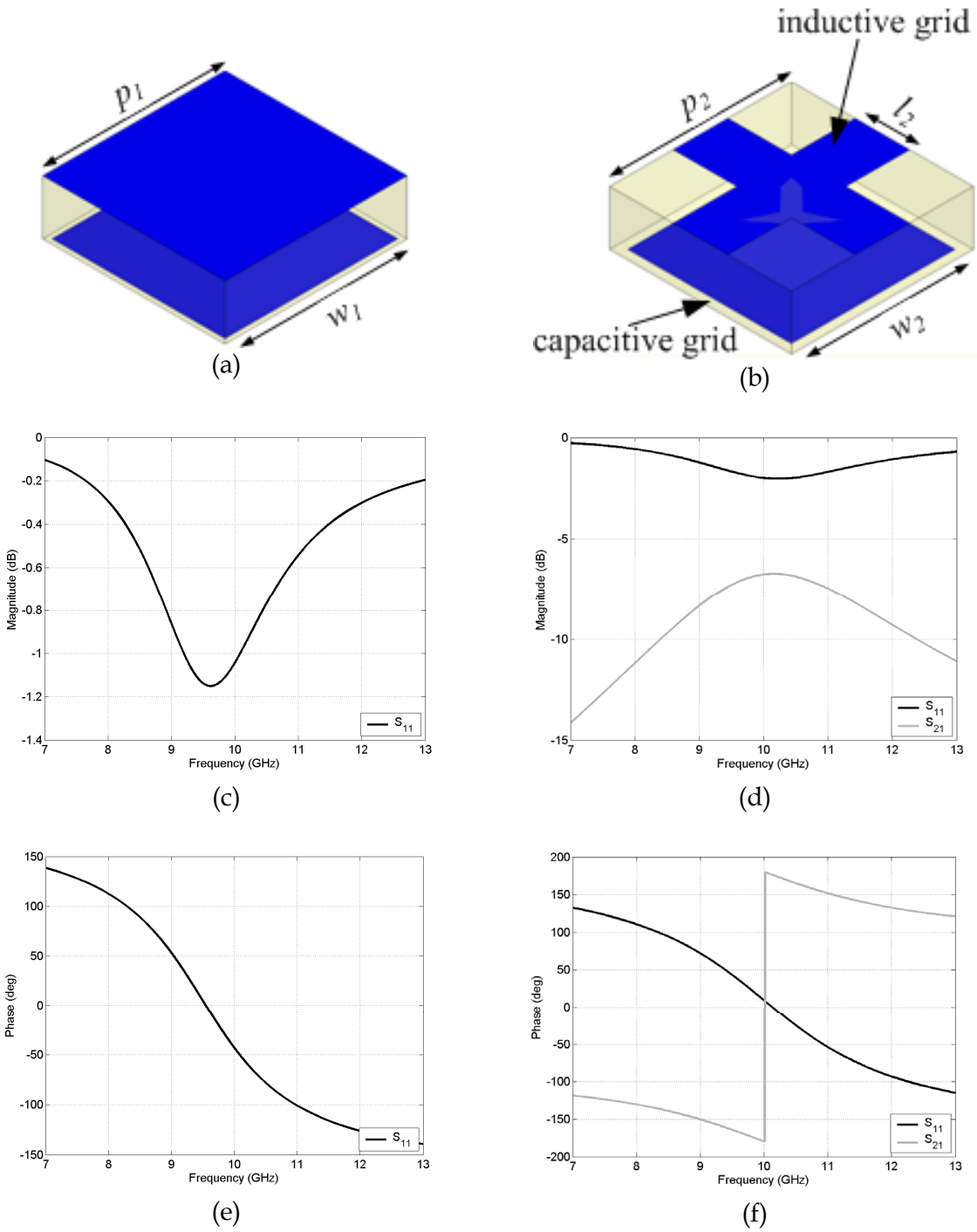

Fig. 2. Unit cell of AMC ground plane (a) and metamaterial-based PRS (b). Calculated reflection magnitude and phase of the AMC ground plane (c), (e) and reflection and transmission magnitudes and phases of the metamaterial-based PRS (d), (f).

The surface used by our group in order to achieve the AMC ground plane is made of a metamaterial composed of 2-D periodically subwavelength metallic square patches organized on one face of a dielectric substrate as illustrated in Fig. 2(a). The different dimensions of the patches are as follows: period p_1 = 4 mm and width w_1 = 3.8 mm. Another surface which we are going to use for the PRS of the cavity is made of a composite metamaterial consisting of simultaneously a capacitive and an inductive grid on the two faces of a dielectric substrate. The capacitive grid is also formed by 2-D periodic metallic patches (period p_2 = 4 mm and width w_2 = 3.6 mm) whereas the inductive grid is formed by a 2-D periodic mesh (line width l_2 = 1.2 mm) as shown in Fig. 2(b). Concerning the substrate, we have used the double copper cladded epoxy substrate of relative permittivity ε_r = 3.9, of tangential loss $\tan\delta$ = 0.0197 and having a thickness of 1.2 mm. The size of the different patterns has been chosen in order to minimize the phase of the reflection coefficient near 10 GHz while providing a sufficiently high reflectance (~90%).

The metasurfaces are analyzed numerically using the finite element software *HFSS* so as to present its characteristics in terms of reflection and transmission. Simulations are performed on a unit cell together with appropriate periodic boundary conditions. The results are presented in Fig. 2(c) and Fig. 2(d). As shown, the calculated resonance frequency of the AMC surface and PRS reflector is respectively 10.4 GHz and 9.7 GHz. At resonance, phase crosses 0° as illustrated in Fig. 2(e) and Fig. 2(f).

The composite metamaterial acts as a resonant filter which presents a reflection phase varying from 180° to –180°, depending on the frequency. This variation helps to be more flexible in designing thin cavities by choosing reflection phase values below 0°.

4. Metamaterial-based low-profile highly directive cavity antenna

In this section, we discuss about the design, implementation and characterization of low profile and highly directive cavity antennas. Two different models are presented; an AMC-PRS cavity and a PEC-PRS cavity.

4.1 AMC-PRS cavity antenna

The AMC-PRS cavity antenna is formed by the AMC reflector and the metasurface reflector used as PRS together with a patch antenna designed to operate near 10 GHz (Ourir et al., 2006a). The patch antenna of dimensions 6.8 × 7 mm² is placed on the AMC in the cavity as shown in Fig. 1(b). The reflectors used are those presented in Fig. 2. The different phases (simulated and measured) are used to estimate the thickness h of the AMC-PRS cavity as given by Eq. (1). Fig. 3(a) shows that h first decreases with increasing frequency of the first resonant mode (N = 0) to the point where a cavity zero thickness is reached at around 10.2 GHz. Then a jump in the mode occurs leading to an abrupt variation of h and the value decreases again for N = 1. A cavity thickness h = 0.5 mm is chosen for the cavity. The thickness h of the Fabry-Perot cavity formed by the two reflectors is adjusted mechanically. The lateral dimensions of the reflector plates are 17 × 17 cm². This thickness leads to a good matching of the cavity at 10.1 GHz (Fig. 3(b)) corresponding to the design of a $\lambda/60$ cavity. This frequency is in good agreement with the resonance frequency calculated from the optical ray model. The directive emission of the subwavelength cavity antenna at 10.1 GHz

is illustrated from the calculated and measured E-plane (ϕ = 90°) and H-plane (ϕ = 0°) radiation patterns in Fig. 3(c) and 3(d).

Using the formulation proposed in (Temelkuran et al., 2000), the directivity of the cavity antenna is written as:

$$D = \frac{4\pi}{\theta_1 \theta_2} \tag{2}$$

where θ_1 and θ_2 are respectively the half-power widths for the E-plane and H-plane radiation patterns. The antenna directivity is then found to be equal to 78 (19 dB) for $\theta_1 = 22°$ and $\theta_2 = 24°$.

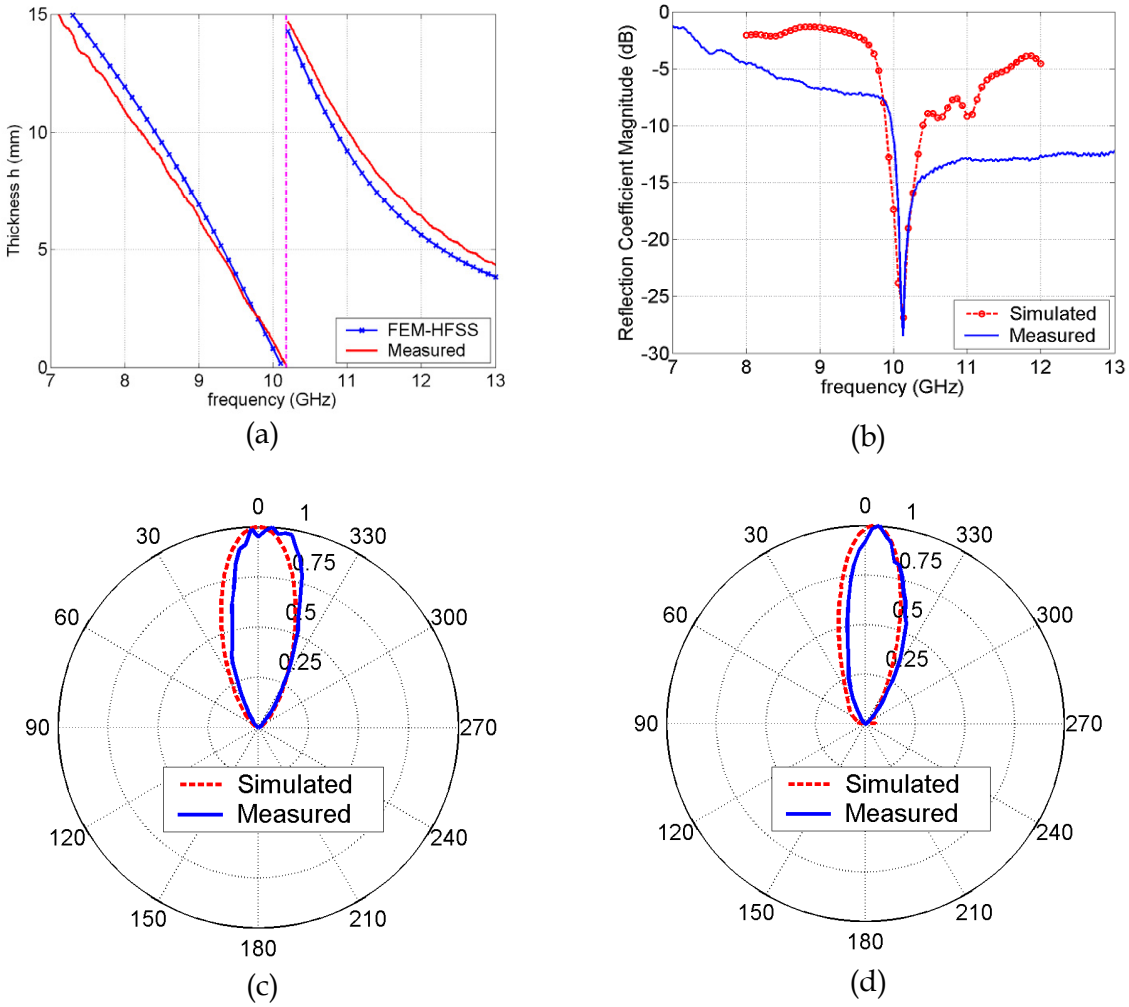

Fig. 3. (a) Evolution of the cavity thickness *h* versus frequency, this evolution being estimated from Eq. (1) by the calculated and measured reflection phases of the two reflectors used in the AMC-PRS cavity. (b) Calculated and measured matching of the cavity antenna. (c) E-plane (ϕ = 90°) radiation pattern at 10.1 GHz. (d) H-plane (ϕ = 0°) radiation pattern at 10.1 GHz.

4.2 PEC-PRS cavity antenna

In order to simplify the fabrication of the cavity antenna, another one using only one metamaterial-based surface reflector acting as the PRS and a PEC reflector (similar to the cavity shown in Fig. 1(a)) is designed (Ourir et al., 2006b). As we have seen from the reflection coefficients in Fig. 2(c) and 2(d), losses are maximum at the resonance frequency of the metamaterial-based surfaces. Thus using only one reflector has also the advantage of presenting lower losses. The PRS composed of simultaneously a capacitive and an inductive grid on the two faces of a dielectric substrate as presented in Fig. 2(b) has been designed for this purpose. Concerning the metallic patches of the capacitive grid, a period p_2 = 5 mm and a width w_2 = 4.8 mm are used. A line width l_2 = 2.2 mm is considered for the mesh of the inductive grid. This PRS having a resonance frequency of about 8 GHz presents a reflection phase close to -150° for frequencies higher than 10 GHz. The use of such a reflector in conjunction with a PEC leads also to a subwavelength cavity since the sum ($\phi_{PRS} + \phi_r$) is very close to zero between 9 GHz and 11 GHz.

A 1 mm (λ/30) thick cavity is designed with lateral dimensions of 10 × 10 cm² where the resonance is achieved at around 9.7 GHz. The antenna gain patterns in the E- and H-planes obtained from simulation and measurements are presented in Fig. 4(a) and 4(b).

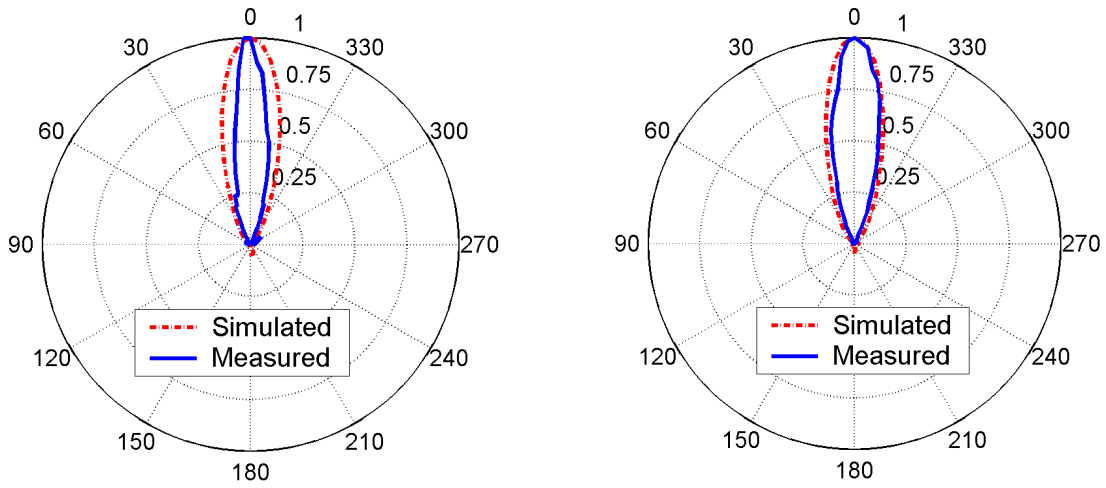

Fig. 4. (a) Calculated and measured reflection phases of the PRS reflector used in the PEC-PRS cavity. (b) Calculated and measured matching of the cavity antenna. (c) E-plane (ϕ = 90°) radiation pattern at 9.7 GHz. (d) H-plane (ϕ = 0°) radiation pattern at 9.7 GHz.

In this case, despite the use of only one metamaterial-based surface as the PRS and the use of smaller lateral dimensions than the two metamaterial-based cavity, the antenna directivity is found to be twice and equal to 160 (22 dB).

5. Directivity enhancement in Fabry-Pérot cavity antennas

This section deals with the enhancement of directivity in Fabry-Pérot cavity antennas. Two different approaches are presented to achieve higher performances in terms of directivity and beamwidths. In order to reach a higher directivity, a larger surface of the

PRS must be illuminated. Therefore, a better distribution and confinement of the electromagnetic energy must be produced in the cavity. For this purpose, two innovative solutions can be considered. The first one is to shield the cavity by four metallic walls and the second one is to feed the cavity by multiple primary sources. The two methods are detailed below.

5.1 Metallic cavity antenna

The cavity antenna proposed in this section was designed at 2.46 GHz for point to point radio communication links. The metallic cavity is composed of the feeding antenna's PEC ground plane and a metamaterial-based PRS as reflectors. Furthermore, four metallic walls are also fixed on the lateral sides so as to enhance the directivity of the cavity antenna while keeping low lateral dimensions (Burokur et al., 2009a).

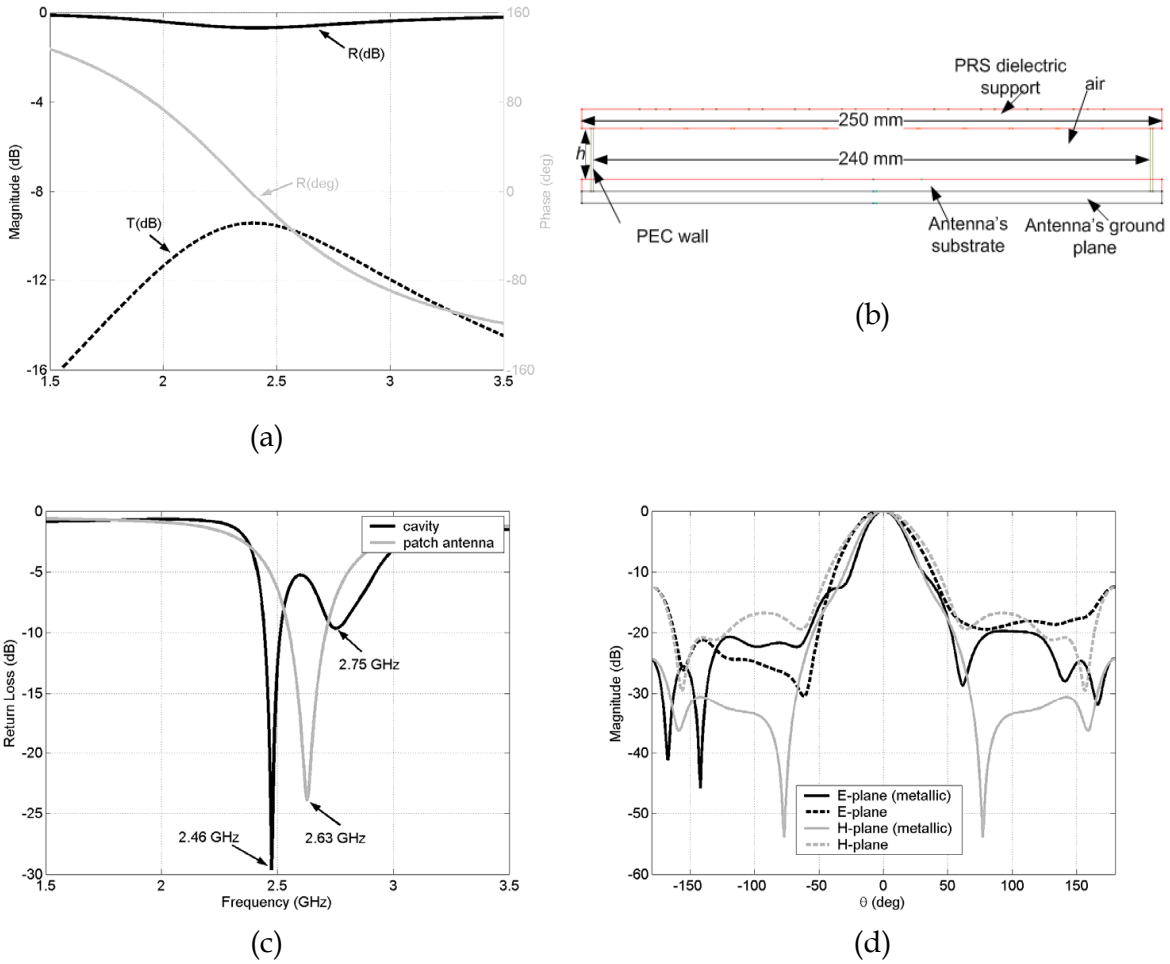

Fig. 5. (a) Calculated reflection phase (solid grey), reflection (solid dark) and transmission (dashed dark) magnitudes for the PRS reflector. (b) Schematic view of the metallic cavity antenna with h = 21.5 mm. (c) Return losses of the cavity antenna and the feeding patch antenna. (d) E- (ϕ = 90°) and H-plane (ϕ = 0°) radiation patterns at 2.46 GHz for the metallic and conventional cavity antennas.

The inductive and capacitive grids of the metasurface are printed on the faces of an 8 mm thick foam dielectric substrate (ε_r = 1.45, tanδ = 0.0058). This thickness is sufficient enough to provide a relatively smooth slope of the phase response, hence rendering the metamaterial less sensitive to fabrication tolerances. The capacitive grid is formed by 2-D periodic metallic patches lattice (period p_2 = 20 mm and width w_2 = 18.8 mm) whereas the inductive grid is formed by a 2-D periodic mesh (line width l_2 = 6 mm). The size of the different patterns has been chosen in order to have the phase of the reflection coefficient below 0° near 2.46 GHz while providing a sufficiently high reflectance (~90%). The numerical results presented in Fig. 5(a) show firstly a resonance frequency of 2.38 GHz, i.e. where the phase crosses 0°. Secondly, we can also note a pass-band behavior where the transmission level is relatively low (about –9.5 dB). Finally this figure shows a reflection phase of –15° at 2.46 GHz.

The microstrip patch feeding source having dimensions 43 mm x 43 mm is designed on a similar foam dielectric substrate of thickness 5 mm. The surface of the inductive and capacitive grids forming the PRS has dimensions 200 mm × 200 mm, while the lateral dimensions of the dielectric board supporting the grids as well as that of the cavity have been increased to 250 mm × 250 mm. However the lateral metallic walls are separated by a distance of 240 mm, as illustrated by the side view of the cavity antenna in Fig. 5(b). So with a ϕ_{PRS} = –15°, the thickness of the cavity is found to be h = 21.5 mm (< λ/5).The simulated metallic cavity presents a return loss of 22.8 dB at 2.46 GHz [Fig. 5(c)]. A second resonance is observed at 2.75 GHz corresponding to the resonance of the feeding antenna. These two resonances are situated at each side of that of the feeding patch alone due to the coupling between the patch antenna and the FP cavity.

The calculated results [Fig. 5(d)] for the E- and H-plane radiation patterns show a directivity of 15.21 dB. Compared to a similar cavity without metallic walls, an enhancement of about 3 dB and lower secondary lobes are achieved. To reach this same directivity without metallic walls, we should have used a cavity with lateral dimensions close to 400 mm × 400 mm. Also, the metallic cavity presents very low backward radiations (–24.3 dB) due to the energy confinement by the lateral walls.

A prototype of the proposed cavity has been fabricated and measured (Fig. 6). However, the responses measured with h = 21.5 mm have not shown a resonance as expected at 2.46 GHz but at 2.49 GHz. This is due to the matching of the fabricated feeding patch antenna which does not occur at 2.63 GHz as in simulation. Moreover, the responses of the PRS may also present a shift in frequency which can be attributed to the manufacturing tolerances. A modification on the thickness of the cavity has then been undertaken in order to achieve as close as possible the calculated resonance frequency. Three other different thicknesses (h = 25 mm, h = 27.9 mm and h = 28.5 mm) have shown remarkable performances. The different results are summarized in Table 1.

As the thickness increases, the resonance of the cavity antenna tends to lower frequencies. For h = 25 mm, the measurements show a return loss of 11 dB and a directivity of 12.79 dB with secondary lobes reaching a level of –26.5 dB. For h = 28.5 mm, the return loss is enhanced to 21.5 dB at 2.405 GHz but the directivity falls to 12.4 dB. The best directivity (13.4 dB) is observed at 2.405 GHz for h = 27.9 mm with secondary lobes level of -22.7 dB.

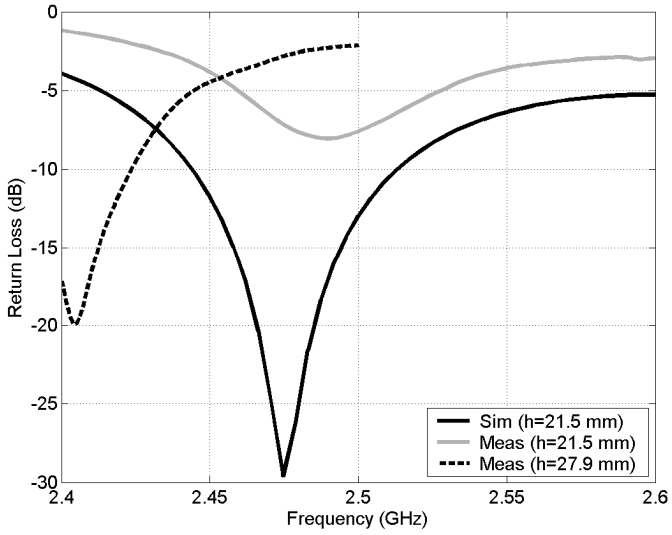

(a)

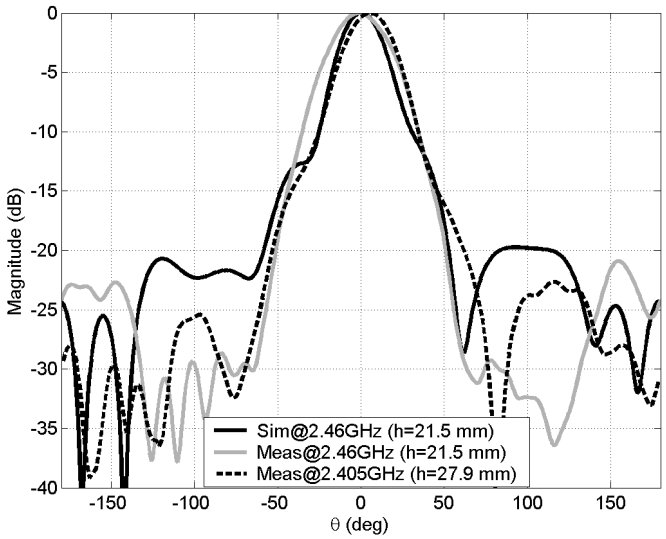

(b)

Fig. 6. (a) Measured return loss of the metallic cavity antenna. (b) Comparison between simulated and measured E-plane radiation patterns.

h (mm)	Resonant frequency (GHz)	Return loss (dB)	Directivity (dB)	Secondary lobes level (dB)
21.5 (sim)	2.46	29.5	15.3	-19.7
21.5 (meas)	2.49	8	12.36	-28.7
25 (meas)	2.46	11	12.79	-26.5
27.9 (meas)	2.405	20	13.4	-22.7
28.5 (meas)	2.4	21.5	12.4	-24.4

Table 1. Performances of the metallic cavity antenna.

5.2 Multisource-fed cavity antenna

As stated earlier, the second method to reach higher directivity is based on the use of multiple primary sources in the cavity. Therefore in this section, the cavities operating near 10 GHz are fed with a 2 x 2 microstrip patch array (Yahiaoui et al. 2009, Burokur et al., 2009b). The four patches with dimensions W_p = L_p = 7.5 mm are fed simultaneously via microstrip transmission lines acting as λ/4 impedance transformers and excited by a 50Ω SMA connector as shown in Fig. 7(a). The inter-element spacing *a* of the microstrip patch array feed plays an important role in the directivity of the cavity antenna. For this reason, the influence of this latter parameter is studied for a fixed cavity thickness *h* = 1.5 mm. The inter-element spacing *a* is varied from 0.5λ to 3λ. The return losses of the cavities are plotted in Fig. 7(b). We can note a very good matching (< –10 dB) around 9.25 GHz for the four different cases.

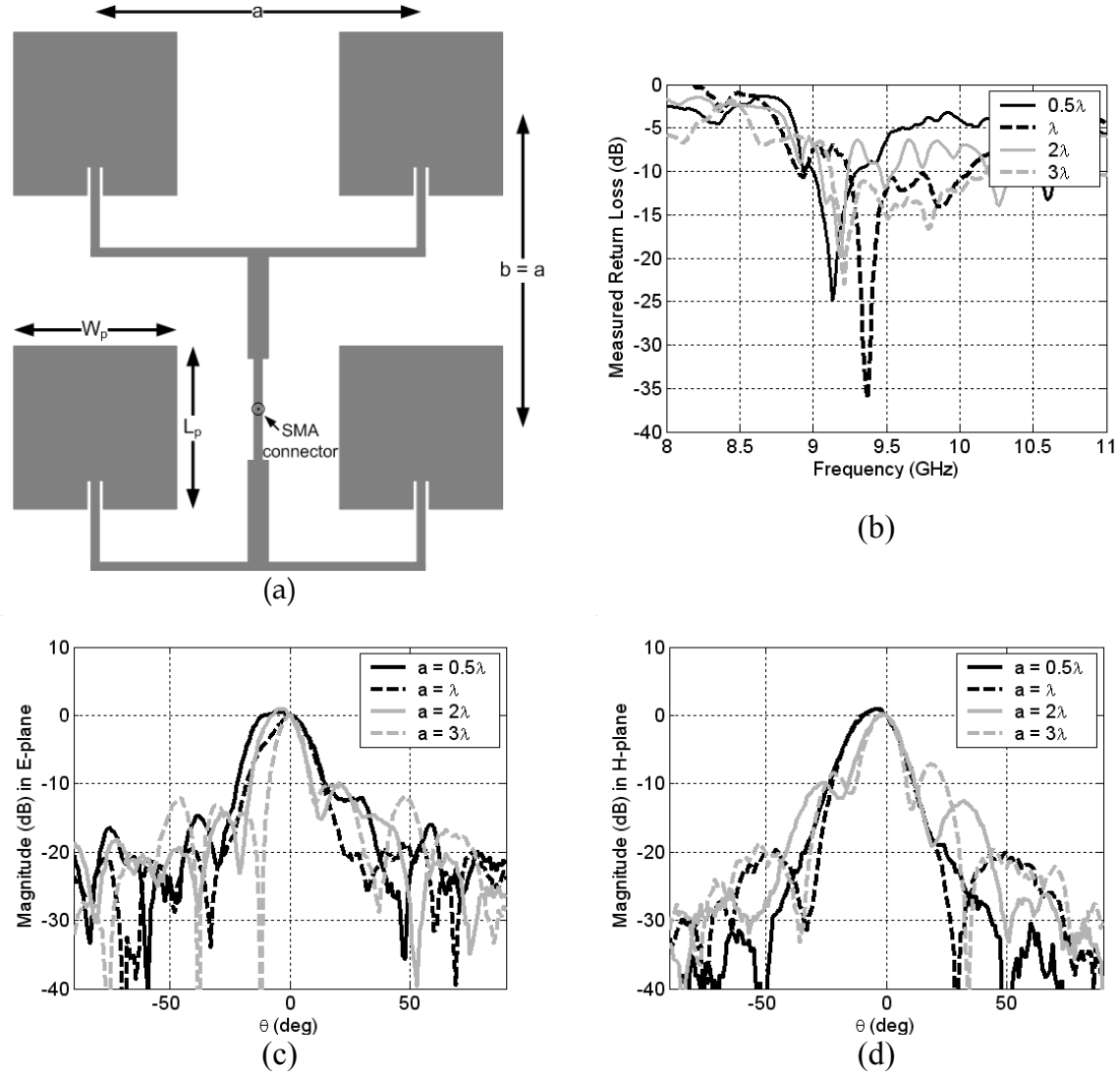

Fig. 7. (a) 2 × 2 patch array used as a multi-source. (b) Measured return losses of the cavities. (c)-(d) Measured E-plane and H-plane radiation patterns with *a* = 0.5λ, λ, 2λ and 3λ for a cavity thickness *h* = 1.5 mm.

The measured E- and H-plane radiation patterns of the cavity antennas are presented in Fig. 7(c) and 7(d). For $a = 0.5\lambda$, a measured directivity of 19 dB is obtained at 8.93 GHz. This value is very close to that of a cavity fed by a single source (see for *e.g*. Ourir et al., 2006a, 2006b). So, it is worth to note that conversely to classical antenna arrays, the directivity is not doubled each time that the number of sources is doubled. For $a = \lambda$, a measured directivity of 20.9 dB is noted at 9.07 GHz, showing clearly an enhancement of 1.9 dB with regard to the case $a = 0.5\lambda$. It is also very important to note that the sidelobes level of the patch array is considerably reduced when embedded in the cavity. This effect is highlighted in Table 2 where the performances of cavities for the different inter-element spacing are presented. 23.21 dB and 25.35 dB is respectively deduced from the measured planes for $a = 2\lambda$ and $a = 3\lambda$. When the case $a = 3\lambda$ is compared to $a = 0.5\lambda$, an increase of 6.35 dB is obtained for the directivity, which is comparable to an increase from a single patch element to a 2×2 patch array. The measured sidelobes level are higher (~ –8dB in the H-plane) for the case $a = 3\lambda$. However, this sidelobes level is still low compared to the sidelobes level of the source alone. It is well known that an inter-element spacing of an array higher than λ leads to high sidelobes level and also to the apparition of grating lobes.

The directivity D of the cavity antennas can be calculated using $D = 41253/(\theta_1 \times \theta_2)$ where θ_1 and θ_2 are respectively the half-power widths (in degrees) for the H-plane and E-plane patterns. The directivity values are given in Table 2 where we can observe that an increase in the inter-element spacing a in the cavity antenna gives rise to a higher directivity. This is because the radiation area at the surface of the source is bigger when a increases and therefore, a larger surface of the PRS is illuminated by the radiation source. This phenomenon is illustrated in Fig. 8 where the E-field distribution is plotted in a horizontal plane at two different locations z in the cavity antenna. $z = 0$ and $z = 1.5$ corresponds respectively to the plane of the radiating patch array source and to the thickness $h = 1.5$ mm at the inner surface of the PRS (location of the capacitive grid). This figure shows that the radiation area at the surface of the feed source in the case $a = 3\lambda$ is bigger than in the case $a = 0.5\lambda$ and therefore, a larger surface of the PRS is illuminated leading to a higher directivity. On the counter part, the side lobes level also increases.

a (mm)	Resonance frequency (GHz)	Maximum directivity (dB)	Secondary lobes level (dB)
0.5λ	9.13	19 @ 8.93 GHz	-12
λ	9.37	20.9 @ 9.07 GHz	-19
2λ	9.18	23.21 @ 8.94 GHz	-10
3λ	9.21	25.35 @ 8.96 GHz	-8

Table 2. Performances of the cavity antennas with $a = 0.5\lambda$, λ, 2λ and 3λ for a cavity thickness $h = 1.5$ mm.

6. Beam steering in Fabry-Pérot cavity antennas

In this section, we present the modeling and characterization of optimized resonant cavities for beam steering applications. Firstly, the design principle is presented for a passive cavity. The idea is then pushed further to achieve controllable beam steering by incorporating lumped elements in the metasurface reflector.

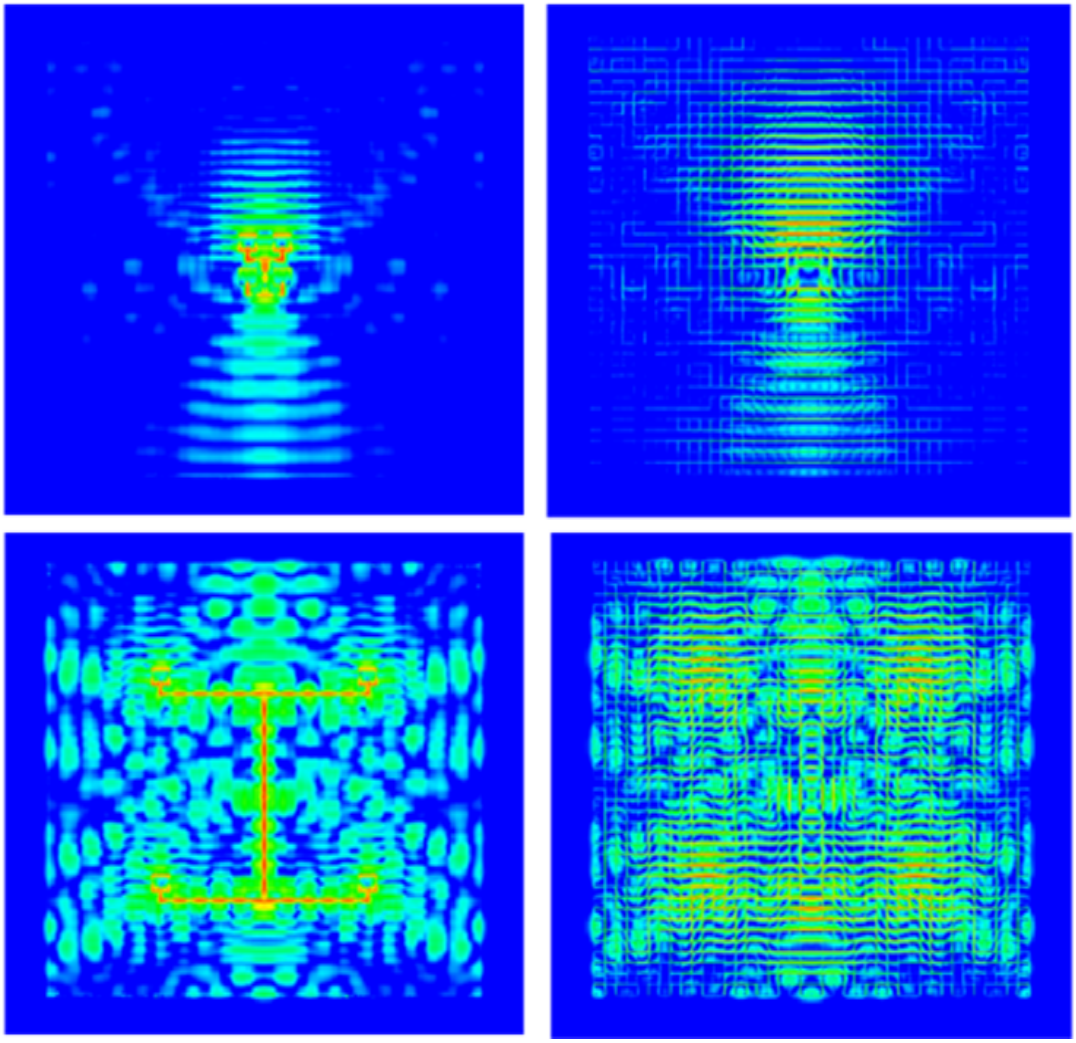

Fig. 8. E-field distribution in a horizontal plane in the cavity antenna for a = 0.5λ and a = 3λ.

6.1 Passive beam steering

Since the beam steering operation is presented in only one radiation plane, the metasurface used is composed of a 1-D array of copper strips etched on each face of a dielectric substrate as shown in Fig. 9(a).

We shall note that the gap spacing *g* in the capacitive grid plays a crucial role in determining the capacitance and therefore the resonance frequency of the metasurface. By changing *g* and keeping all the other geometric parameters unchanged, the capacitance of the metamaterial will also vary. As a consequence, the phases of the computed reflection coefficients vary. This behavior is illustrated by the numerical results shown in Fig. 9(b). We can note that the variation of *g* accounts for the shift of the resonance frequency. An increase in the value of *g* causes a decrease in the value of the capacitance created between two cells, and finally a shift of the resonance towards higher frequencies. At a particular frequency, the phase of the metasurface increases with an increase in the gap spacing. The study on the variation of *g* shows that it is possible to design a PRS with a continuous variation of the gap *g*, resulting in a local variation of the phase characteristics (Fig. 9(c)). If we consider each gap

as a slot antenna, an analogy can then be made with an array of several antennas with a regular phase difference. The locally variable phase metasurface can then be applied for passive beam steering (Ourir et al. 2007a, 2009).

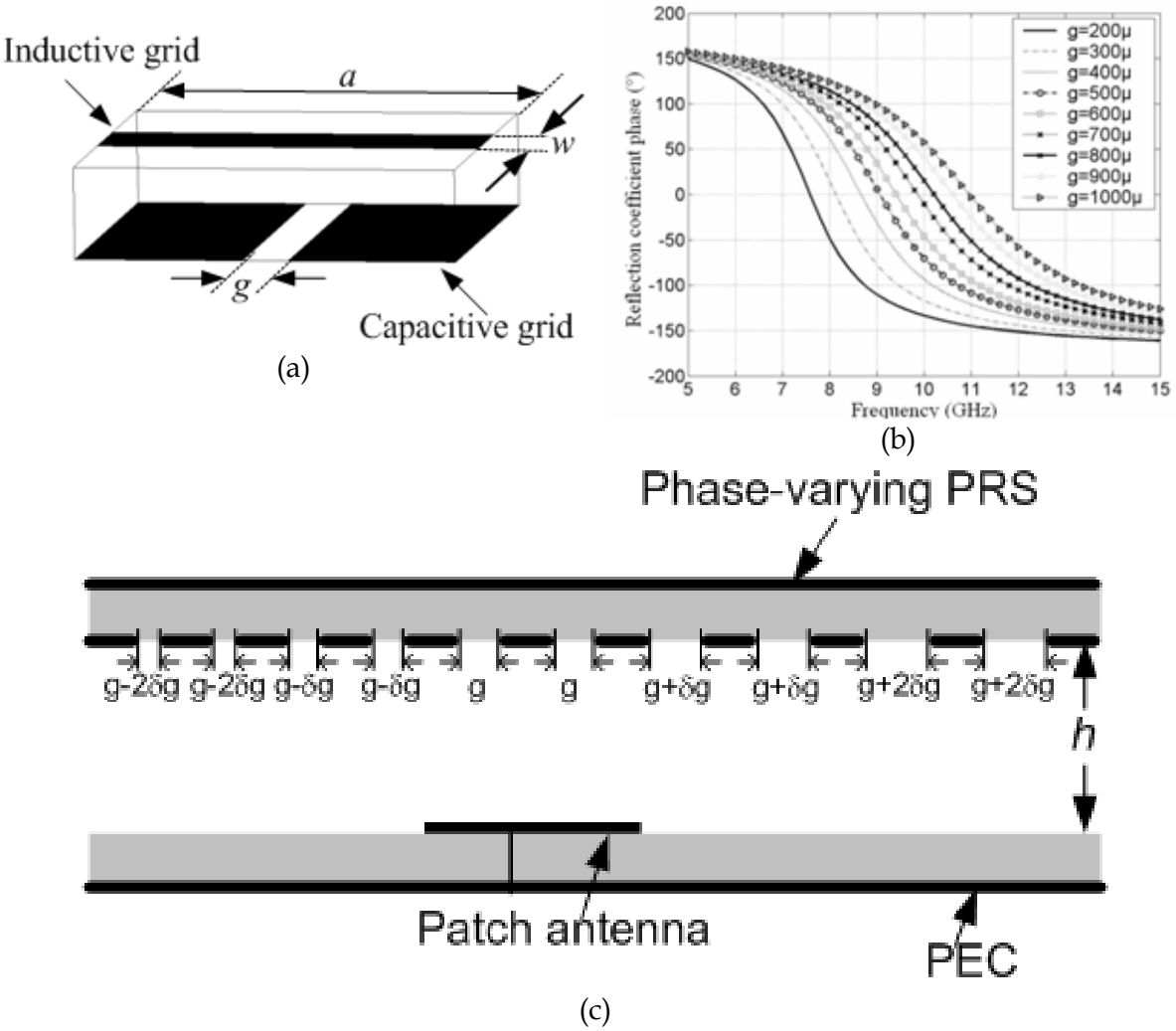

Fig. 9. (a) Elementary cell of the metamaterial composed of an inductive and capacitive grid, which is proposed for the PRS. (b) Reflection phase coefficient of the metasurface versus the gap width g. (c) Schematic view of the cavity composed of a PEC and a métasurface with a variable gap width.

To show the performances in terms of beam steering, several subwavelength cavities have been simulated and fabricated using the 1-D metasurface as PRS. The first one consists of the metamaterial PRS with the same gap spacing g = 400 µm between the metallic strips of the capacitive grid (δg = 0). This prototype will assure no deflection of the beam since it exists no phase variation of the metamaterial. The second and third ones are the prototypes incorporating respectively a variation of δg = 50 µm and δg = 100 µm along the positive x-direction. The cases where the variation δg is negative (180° rotation of the PRS around the z-axis) have also been considered. Note that here the resonance frequency of the central region of the metamaterial corresponds to that of the PRS without gap spacing

variation (g = 400 µm and δg = 0), i.e. 8.7 GHz as shown in Fig. 9(b). The resonance frequency of the cavity is found to be ~10.5 GHz for the three prototypes as shown in Fig. 10(a). Best matching is observed when the metallic gap of the PRS capacitive grid increases. However, the resonance frequency remains the same for the three configurations since it depends on the gap spacing of the central region of the PRS, which is the same for the three prototypes.

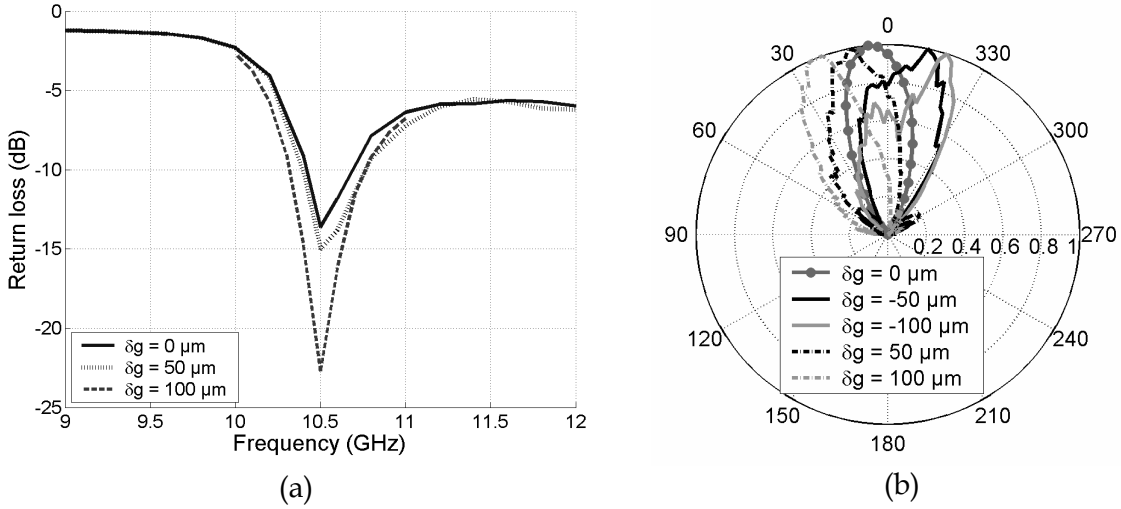

(a) (b)

Fig. 10. (a) Return loss of the antennas with different variation of gap width. (b) Measured gain patterns of the cavity antennas versus the gap width variation.

Fig. 10(b) shows the measured gain patterns of the antenna in the E (ϕ = 90°) plane at 10.5 GHz for an optimized cavity thickness h = 1 mm. For δg = 0, the beam is normal to the plane of the antenna and shows no deflection, which confirms our prediction on the constant phase metamaterial. However, in the case of a regular variation of 50 µm, a deflection of the antenna beam of about 10° can be observed either in the forward (clockwise) or backward (anti-clockwise) direction depending if δg is respectively negative or positive. Similar observations and a higher deflection of ±20° can be noted for δg = ±100 µm. The directivity of the cavity antenna can be calculated using the following expression: D = 41253/($\theta_1 \times \theta_2$) where θ_1 and θ_2 are respectively the half-power widths (in degrees) for the **H**-plane and **E**-plane patterns. In this case, the directivity is found to be approximately equal to 14.8 dB.

6.2 Active beam steering

The cavity antenna proposed in this section includes the use of lumped elements such as varactor diodes so as to be able to control electronically the phase of the metasurface. As a preliminary step in the design of such cavities, we present firstly the design of the active metasurface.

6.2.1 Electronically controlled metasurface

The metasurface used in this section is based on the same principle as the one illustrated in Fig. 9. But, instead of applying a linear variation of the gap spacing g in order to create a

locally variable phase, we now use active components to make the phase of the metasurface shift in frequency. Varactor diodes having a capacitance value ranging from 0.5 pF to 1.0 pF are thus incorporated into the capacitive grid between two adjacent metallic strips (Fig. 11(a)) and depending on the applied bias voltage, the phase of the metasurface varies with frequency (Ourir et al. 2007b). The variable capacitive grid of the tunable phase PRS used for an operating frequency around 8 GHz consists of a lattice of metallic strips with varactor diodes connected each 6 mm (s = 6 mm) between two adjacent strips. The width of the strips and the spacing between two strips of the capacitive grid is respectively w = 1 mm and g = 2 mm.

Concerning the inductive grid, the width of the strips and the spacing between two strips are respectively w_1 = 2 mm and g_1 = 4 mm (Fig. 11(b)). Note that the inductive grid is not made tunable. RF chokes are also used in the microstrip circuit in order to prevent high frequency signals going to the DC bias system. Potentiometers are implemented in the structure to create a voltage divider circuit so as to be able to bias locally the varactors. The capacitance in each row can then be adjusted according to the bias voltage applied. This capacitance can also be varied from one row to another by the use of the voltage dividers on the prototype. By changing the bias voltage of the varactors of the PRS similarly, the capacitance of the metamaterial will also vary. As a consequence, the reflection and the transmission coefficients also vary. This behavior is illustrated by the measurement results of the reflection coefficient magnitude and phase shown in Fig. 11(c) and 11(d) respectively. These curves are obtained when the same bias voltage is applied to the different rows of varactors along the PRS. The measurements are performed in an anechoic chamber using two horn antennas working in the [2 GHz – 18 GHz] frequency band and an 8722ES network analyzer. From Fig. 11(c), we can note that the variation of the bias voltage accounts for the shift of the resonance frequency of the PRS, *i.e.* the frequency where the phase crosses 0°. An increase in the bias voltage leads to a decrease in the value of the capacitance of the metamaterial, and finally to a shift of the resonance towards higher frequencies. At a particular frequency the phase of the PRS increases with an increase in the bias voltage. This phase shift is very important since it will help to tune the resonance frequency of the cavity antenna and also to control the radiated beam direction of the antenna.

6.2.2 Active beam steering

Instead of applying a uniform variation in the periodicity of the cells composing the capacitive grid so as to create a locally variable phase as in section 6.1, we now use the electronically controlled metasurface as PRS (Ourir et al. 2009). The active components biased differently make the phase of the PRS shifts in frequency locally. As illustrated by the varactors bias system shown in Fig. 12(a), the proposed PRS is now divided into different regions, where each of them has a specific bias voltage bias. We shall note that here the resonance frequency of the cavity is imposed by the resonance frequency of the central region just above the feeding source corresponding to the bias voltage $V_4=V_1+3\delta V$. The bias voltage is thus increased uniformly with a step δV when moving from the left to the right of the metamaterial-based PRS by the use of the potentiometers. This action creates a regular variation of the phase along the PRS.

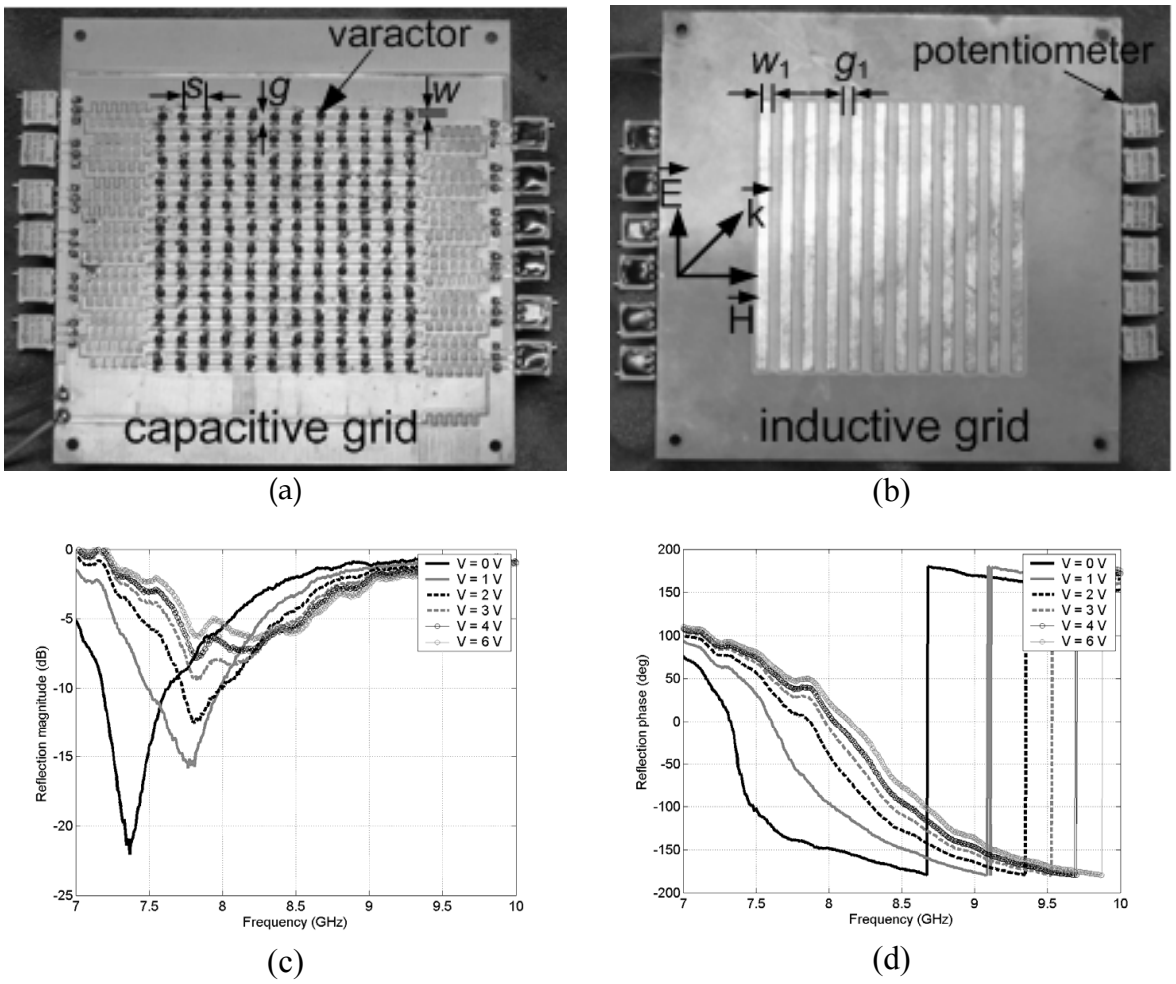

Fig. 11. (a) Electronically phase-varying metasurface. (a) Capacitive grid incorporating varactors and voltage dividers. (b) Inductive grid. (c) Measured magnitude and (d) measured phase of the reflection coefficient versus bias voltage of the varicaps.

The first configuration studied here is the antenna cavity based on the metamaterial PRS with the same null bias voltage for all the varactors. This configuration will assure no deflection of the beam since it exists no phase variation of the metamaterial. The second and third configurations are prototypes incorporating respectively a variation of $\delta V = 0.2$ V and $\delta V = 0.3$ V along the positive x-direction. The cases where the variation δV is negative (180° rotation of the PRS around the z-axis) have also been considered.

Fig. 12(b) shows the gain patterns of the antenna in the **E**-plane ($\phi = 90°$) at 7.9 GHz for the optimized cavity. For $\delta V = 0$ V, the beam is normal to the plane of the antenna and shows no deflection, which confirms our prediction on the constant phase metamaterial. However, in the case of a regular variation of $\delta V = 0.2$ V, a deflection of the antenna beam of about 7° can be observed either in the forward or backward direction depending if δV is respectively negative or positive. Similar observations and a higher deflection can be noted for respectively $\delta V = 0.3$ V and $\delta V = -0.3$ V. This figure illustrates very clearly the control of the radiation pattern of the antenna by the bias voltage of the varactors. The direction of the radiation beam depends of the direction of the variation of the bias of the varactors. If we

inverse the sign of δV, the sign of the deviation changes also. This demonstration opens the door to the realization of very simple electronically beam steering ultra-compact antennas based on active metamaterials.

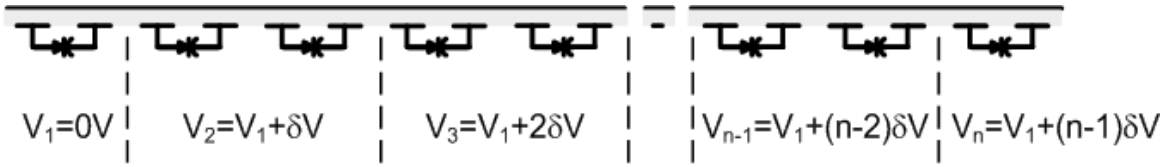

(a)

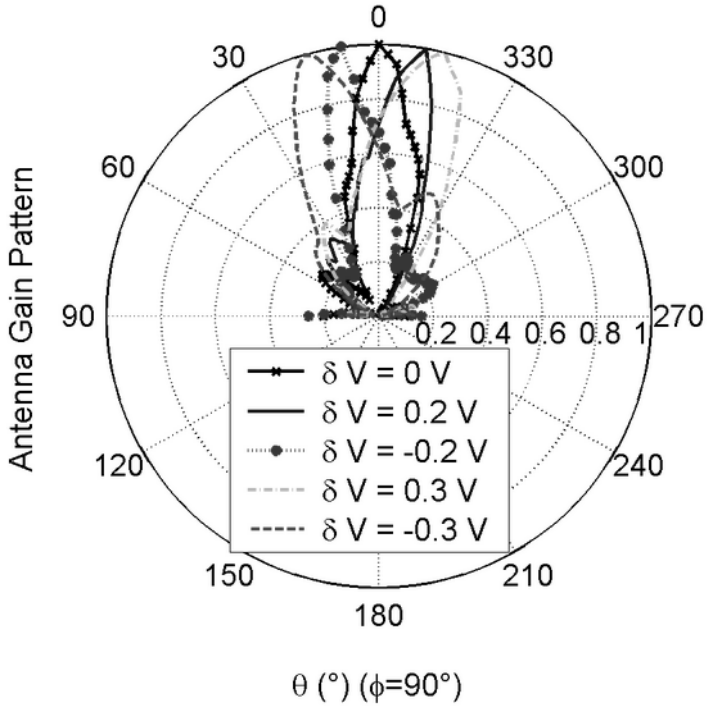

(b)

Fig. 12. (a) Variation of the bias voltage of the varactors along the phase varying PRS. (b) Measured gain patterns in the **E**-plane (ϕ = 90°) at 7.9 GHz for δV = 0 V, δV = 0.2 V and δV = 0.3 V. The steering of the antenna's radiated beam can be clearly observed with a positive steering angle for positive bias and negative one for a negative bias.

7. Frequency agile Fabry-Pérot cavity antennas

Conversely to beam steerable cavity antennas, we do not need a locally phase-varying PRS for frequency agility applications. What we seek is the ability to change the resonance frequency of the PRS and this is possible by changing simultaneously and in the same manner the capacitance value of the varactor diodes. Here, we show that a tunable metasurface associated to an array of wideband sources in a Fabry-Pérot cavity leads to a reconfigurable directive emission on a wide frequency range (Burokur et al. 2010, 2011). A

similar electronically controlled PRS as the one shown in Fig. 11(a) is designed to operate near 2 GHz in base station antennas for mobile phone communication systems. The primary source of the cavity is a wideband microstrip patch antenna designed to cover 1.8 GHz – 2.7 GHz frequency range and therefore to illuminate the PRS at any frequency within this range. This patch antenna is electromagnetically coupled to an L-probe which itself is connected to a coaxial connector. Simulations have shown a good matching (return loss < 10 dB) from 1.8 GHz to 2.7 GHz.

To demonstrate experimentally the mechanism for reconfigurable directive emissions from a metamaterial-based FP cavity, a prototype having dimensions 400*400 mm² (approximately 3λ*3λ) has been fabricated and tested. As it has been shown in section 5.2, the directivity is drastically enhanced when a cavity is fed by judiciously spaced multiple sources since a larger surface of the PRS is illuminated, and therefore the size of the effective radiating aperture of the cavity antenna is increased. Four elementary sources constituting a 2 x 2 wideband patch array are used as primary source; the inter-element spacing between the different sources being 200 mm. Fig. 13(a) and 13(b) shows respectively the photography of the prototype and the capacitive grid of the electronically tunable metasurface In order to experimentally estimate directivity and gain of the cavity's radiated beam, direct far field measurements are performed using a SATIMO STARLAB and the characteristics are shown in Fig. 14.

When capacitance of the metasurface reflector is changed by varying bias voltage of varactor diodes, the frequency of maximum gain is tuned as clearly shown in the different diagrams of Fig. 14. When 0 V is applied, maximum gain is observed at 1.9 GHz corresponding approximately to the simulated case with C = 6.5 pF. When DC bias voltage is increased, the capacitance value is decreased, resulting in an increase of maximum gain frequency. For 24 V, maximum gain occurs at 2.31 GHz, corresponding to lowest capacitance value. To gain more insight in the electromagnetic properties of the metamaterial-based Fabry-Pérot cavity, intensity maps of scanned far field versus frequency and elevation angle θ, in E-plane are presented. The emission frequency represented by the red spot varies from 1.9 GHz to 2.31 GHz from 0 V to 24 V as shown in Figs. 14(a), 14(c), 14(e) and 14(g). These figures demonstrate clearly the frequency reconfigurability property of the cavity. We shall also note that for each frequency the spot is situated at an elevation angle of 0°, indicating a radiated beam normal to the cavity metasurface reflector. Figs. 14(b), 14(d), 14(f) and 14(h) show radiation patterns in E- and H-planes at respectively 1.9 GHz, 2.02 GHz, 2.16 GHz and 2.31 GHz corresponding to maximum gain frequency for 0 V, 5 V, 12 V and 24 V. The tuning range of maximum gain frequency results in an effective operation bandwidth close to 20%. A wide frequency bandwidth is achieved due to the cavity thickness fixed in this particular case. With h = 15 mm, reflection phase values around 0° are needed in the 1.85 GHz – 2.25 GHz frequency band. A lower h would lead to phase values approaching -180° and the possible frequency bandwidth from the capacitance tuning range would be narrow. Actually, a high directivity (approximately 18 dBi) is obtained experimentally due to the large lateral dimensions of the fabricated cavity and also to the use of four elementary sources instead of only one where only 14 dBi is obtained.

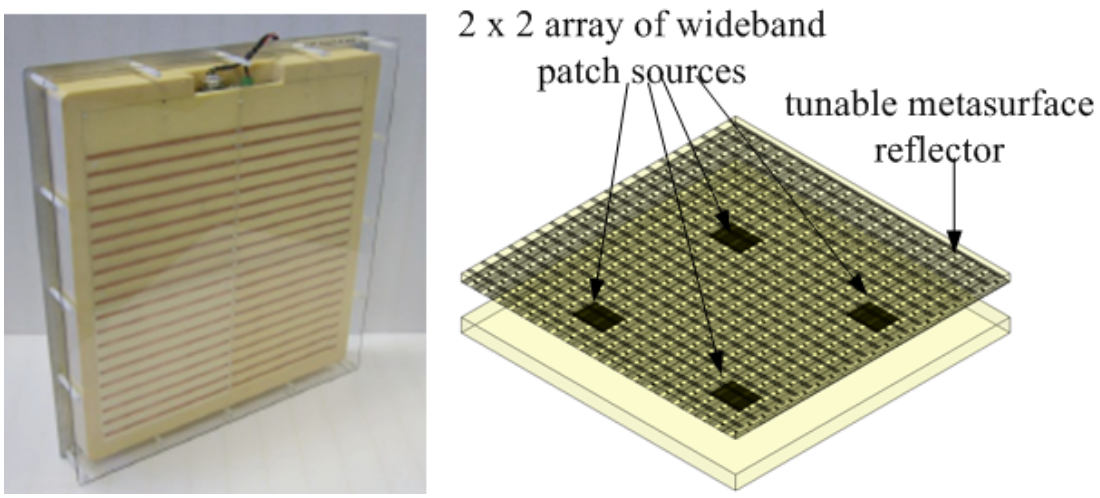

(a)

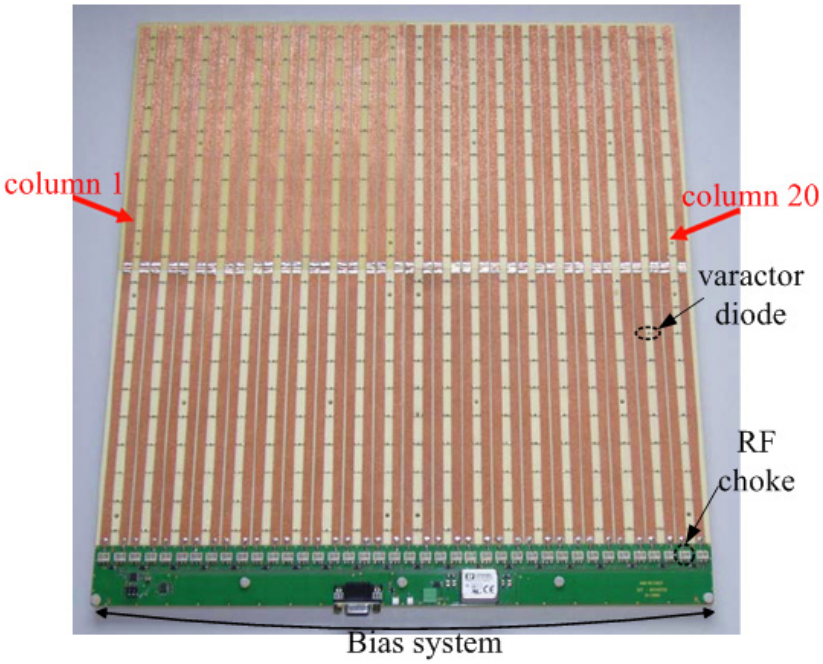

(b)

Fig. 13. (a) Photography and perspective view of the cavity antenna. (b) Electronically tunable metasurface reflector incorporating varactor diodes, RF chokes and bias system.

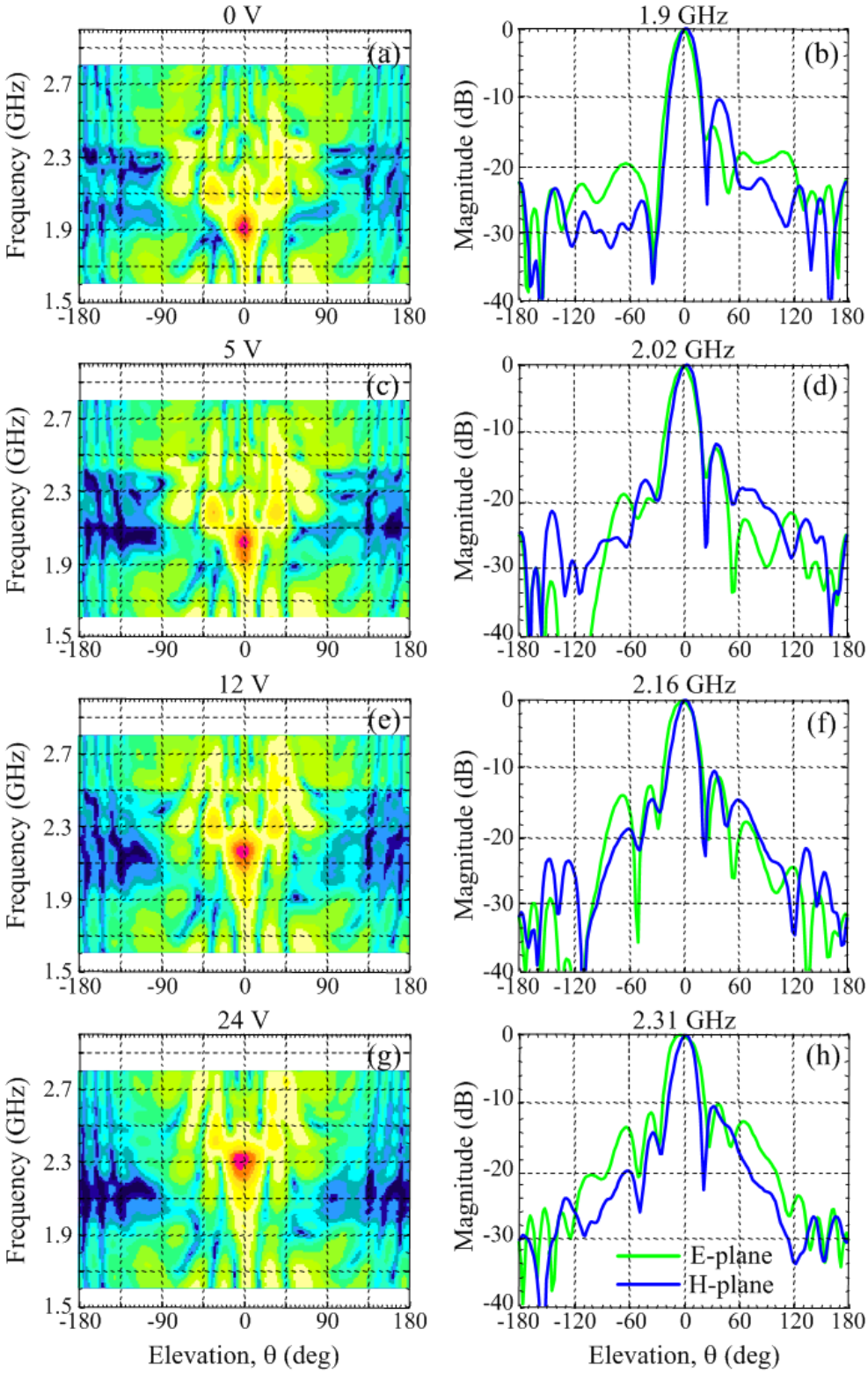

Fig. 14. Far field intensity maps versus frequency and elevation angle in E-plane and measured radiation patterns in E- and H-planes at maximum gain frequency for different bias voltage applied : (a)-(b) 0 V – 1.9 GHz, (c)-(d) 5 V – 2.02 GHz, (e)-(f) 12 V – 2.16 GHz, and (g)-(h) 24 V – 2.31 GHz.

8. Conclusion

To conclude, we have presented various aspects of reflex-cavity antennas: low-profile, high gain, beam steering and frequency agility. For each aspect, numerical calculations together with measurements have been presented. The development of these works has enabled to promote the interesting characteristics of metamaterial-based surfaces. Variable phase metasurfaces compared to conventional PEC and AMC surfaces have also shown their usefulness in reconfigurability applications. Further studies are actually performed to transpose the reflex-cavity antenna concept to industrial applications in various domains such as telecommunications, aeronautical, transport and housing.

9. Acknowledgements

The authors are very grateful to the French National Research Agency (ANR) for the financial support of the METABIP Project. These works have also been made possible by the partial financial support of the Eureka TELEMAC project. We would like also to thank our partners P. Ratajczak and J.-P. Daniel for the fabrication and characterization of antenna prototypes.

10. References

Akalin, T., Danglot, J., Vanbesien, O. & Lippens, D. (2002). A highly directive dipole antenna embedded in a Fabry–Perot-type cavity. *IEEE Microw. Wireless Component Lett.*, Vol.12, No.2, (February 2002), pp. 48-50, ISSN 1531-1309.

Burokur, S.N., Latrach, M. & Toutain, S. (2005). Theoretical investigation of a circular patch antenna in the presence of a Left-Handed Medium. *IEEE Antennas Wireless Propag. Lett.*, Vol.4, (June 2005), pp. 183-186, ISSN 1536-1225.

Burokur, S.N., Ourir, A., Daniel, J.-P., Ratajczak, P. & de Lustrac, A. (2009a). Highly directive ISM band cavity antenna using a bi-layered metasurface reflector. *Microwave Opt. Technol. Lett.*, Vol.51, No.6, (June 2009), pp. 1393-1396, ISSN 0895-2477.

Burokur, S.N., Yahiaoui, R. & de Lustrac, A. (2009b). Subwavelength metamaterial-based resonant cavities fed by multiple sources for high directivity. *Microwave Opt. Technol. Lett.*, Vol.51, No.8, (August 2009), pp. 1883-1888, ISSN 0895-2477.

Burokur, S.N., Daniel, J.-P., Ratajczak, P. & de Lustrac, A. (2010). Tunable bilayered metasurface for frequency reconfigurable directive emissions. *Appl. Phys. Lett.*, Vol.97, No.6, (August 2010), 064101, ISSN 0003-6951.

Burokur, S.N., Daniel, J.-P., Ratajczak, P. & de Lustrac, A. (2011). Low-profile frequency agile directive antenna based on an active metasurface. *Microwave Opt. Technol. Lett.*, Vol.53, No.10, (October 2011), pp. 2291-2295, ISSN 0895-2477.

Cheype, C., Serier, C., Thèvenot, M., Monédière, T., Reinex, A. & Jecko, B. (2002). An electromagnetic bandgap resonator antenna. *IEEE Trans. Antennas Propag.*, Vol.50, No.9, (September 2002), pp. 1285-1290, ISSN 0018-926X.

Enoch, S., Tayeb, G., Sabouroux, P., Guérin, N. & Vincent, P. (2002). A metamaterial for directive emission. *Phys. Rev. Lett.*, Vol.89, No.21, (November 2002), 213902, ISSN 0031-9007.

Feresidis, A.P., Goussetis, G., Wang, S. & Vardaxoglou, J.C. (2005). Artificial Magnetic Conductor Surfaces and their application to low-profile high-gain planar antennas. *IEEE Trans. Antennas Propag*., Vol.53, No.1, (January 2005), pp. 209-215, ISSN 0018-926X.

Jackson, D.R. & Alexópoulos, N.G. (1985). Gain enhancement methods for printed circuit antennas. *IEEE Trans. Antennas Propag*., Vol.AP-33, No.9, (September 1985), pp. 976-987, ISSN 0018-926X.

Nakano, H., Ikeda, M., Hitosugi, K. & Yamauchi, J. (2004). A spiral antenna sandwiched by dielectric layers. *IEEE Trans. Antennas Propag*., Vol.52, No.6, (June 2004), pp. 1417-1423, ISSN 0018-926X.

Ourir, A., de Lustrac, A. & Lourtioz, J.-M. (2006a). All-metamaterial-based subwavelength cavities ($\lambda/60$) for ultrathin directive antennas. *Appl. Phys. Lett*., Vol.88, No.8, (February 2006), 084103, ISSN 0003-6951.

Ourir, A., de Lustrac, A. & Lourtioz, J.-M. (2006b). Optimization of metamaterial based subwavelength cavities for ultracompact directive antennas. *Microwave Opt. Technol. Lett*., Vol.48, No.12, (December 2006), pp. 2573-2577, ISSN 0895-2477.

Ourir, A., Burokur, S.N. & de Lustrac, A. (2007a). Phase-varying metamaterial for compact steerable directive antennas. *Electron. Lett*., Vol.43, No.9, (April 2007), pp. 493-494, ISSN 0013-5194.

Ourir, A., Burokur, S.N. & de Lustrac, A. (2007b). Electronically reconfigurable metamaterial for compact directive cavity antennas. *Electron. Lett*., Vol.43, No.13, (June 2007), pp. 698-700, ISSN 0013-5194.

Ourir, A., Burokur, S.N., Yahiaoui, R. & de Lustrac, A. (2009). Directive metamaterial-based subwavelength resonant cavity antennas – Applications for beam steering. *C. R. Physique*, Vol.10, No.5, (June 2009), pp. 414-422, ISSN 1631-0705.

Sievenpiper, D., Zhang, L., Broas, R.F.J., Alexópoulos, N.G. & Yablonovitch, E. (1999). High-Impedance Electromagnetic Surfaces with a forbidden frequency band. *IEEE Trans. Microw. Theory Tech*., Vol.47, No.11, (November 1999), pp. 2059-2074, ISSN 0018-9480.

Temelkuran, B., Bayindir, M., Ozbay, E., Biswas, R., Sigalas, M.M., Tuttle, G. & Ho, K.M. (2000). Photonic crystal-based resonant antenna with a very high directivity. *J. Appl. Phys*., Vol.87, No.1, (January 2000), pp. 603-605, ISSN 0021-8979.

Trentini, G.V. (1956). Partially reflecting sheet arrays. *IRE Trans. Antennas Propag*., Vol.4, No.4, (October 1956), pp. 666-671, ISSN 0096-1973.

Yahiaoui, R., Burokur, S.N. & de Lustrac, A. (2009). Enhanced directivity of ultra-thin metamaterial-based cavity antenna fed by multisource. *Electron. Lett*., Vol.45, No.16, (July 2009), pp. 814-816, ISSN 0013-5194.

Zhou, L., Li, H., Qin, Y., Wei, Z. & Chan, C.T. (2005). Directive emissions from subwavelength metamaterial-based cavities. *Appl. Phys. Lett*., Vol.86, No.10, (March 2005), 101101, ISSN 0003-6951.

Annexe 2 : Principaux travaux relatifs au chapitre 2

Annexe 2.1

B. Kanté, S. N. Burokur, A. Sellier, A. de Lustrac, J.-M. Lourtioz

« Controlling plasmon hybridization for negative refraction metamaterials »

Physical Review B, vol. 79, no. 7 (075121), February 2009

Controlling plasmon hybridization for negative refraction metamaterials

B. Kanté,* S. N. Burokur, A. Sellier, A. de Lustrac,† and J.-M. Lourtioz
Institut d'Electronique Fondamentale, Université Paris-Sud 11, CNRS UMR 8622, Orsay, F-91405 France
(Received 8 November 2008; revised manuscript received 28 December 2008; published 25 February 2009)

The hybridization scheme of plasmon modes in cut-wire-based left-handed metamaterials is shown to critically depend on the coupling between paired cut wires. We show that an inverted hybridization scheme obtained with an asymmetric alignment of paired cut wires is the most appropriate to negative refraction. This is validated (numerically and experimentally) by the first demonstration of negative refraction in the microwave domain using only periodic ensembles of cut wires.

DOI: 10.1103/PhysRevB.79.075121 PACS number(s): 42.70.Km, 73.20.Mf, 81.05.Zx

I. INTRODUCTION

Metamaterials have attracted considerable interest since the pioneering work by Pendry *et al.*[1,2] and Smith *et al.*[3] While the association of split-ring resonators and continuous wires has been the main architecture of metamaterials in the microwave domain,[3] a periodic array of paired metallic cut wires was the first structure to exhibit negative refractive index in optics.[4] Surprisingly, attempts to reproduce negative refraction with this simple cut-wire structure in the microwave regime failed despite it being easier to fabricate at longer wavelengths.[5,6] In these experimental attempts, the spectral region of negative dielectric permittivity and that of negative magnetic permeability did not overlap. A broadband electric plasma (e.g., a periodic array of continuous wires) has thus been incorporated into the cut-wire structure to obtain negative refraction.[5,6] The resulting structure and its analogs, also called mesh or fishnet structures, are now recognized as universal structures for negative refraction in optics and microwaves.[5–11] Their great potential has been confirmed in recent research where negative refraction was extended for the first time to a three-dimensional optical metamaterial.[11] However, the large fraction of metal contained in fishnet structures is an important drawback because it can lead to high-level losses especially in the optical domain. In addition fishnet structures do not provide an independent control of the magnetic and electric responses of metamaterials as is necessary, for instance, in electromagnetic cloaking.[12,13]

Artificial magnetism in paired cut wires stems from the hybridization of the plasmon modes of each individual cut wire, thus forming two separate eigenmodes with opposite symmetry. The antisymmetric mode provides artificial magnetism, while the symmetric mode mainly contributes to the dielectric permittivity of the effective medium. Figures 1(a) and 1(b) show the hybridization scheme in the case where the degeneracy of cut-wire eigenmodes is lifted due to the strong coupling between vertically aligned cut wires. If the coupling strength between vertically aligned cut wires is very high (for very small spacing between them), the symmetric and antisymmetric bands are split further apart [Fig. 1(c)]. The design of metamaterials with a negative index of refraction consists of preserving a certain overlap between the symmetric and antisymmetric frequency bands.

In this work, we show that true negative index of refraction can be achieved by appropriately controlling the coupling strength between paired cut wires of adjacent layers. The coupling strength is itself controlled by adjusting either the spacing or the alignment of paired cut wires. Using an asymmetric alignment, an inverted hybridization scheme where the asymmetric mode is at higher frequency than the symmetric mode is predicted and thus more favorable for obtaining negative refraction. The first experimental demonstration of a negative refraction metamaterial exclusively based on paired cut wires is reported in the microwave range using such an inverted hybridization scheme. This scheme is also applicable to the optical domain.

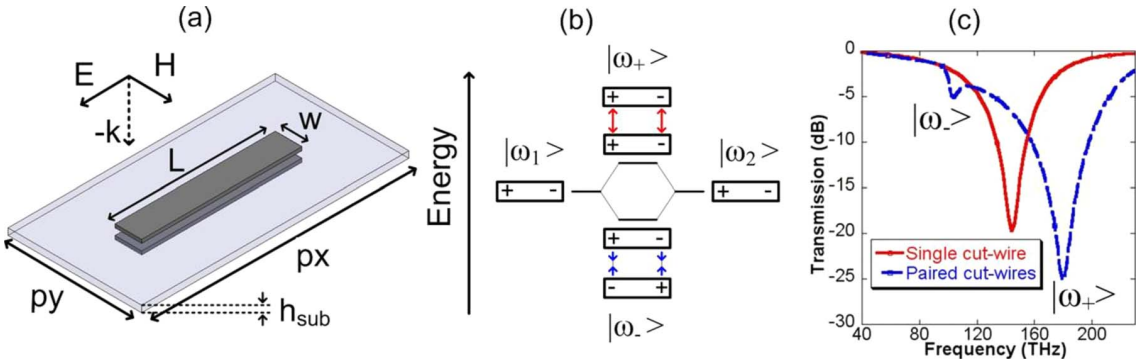

FIG. 1. (Color online) (a) Schematic of the symmetric cut-wire pair. (b) Hybridization scheme of the two coupled dipoles. (c) Transmission spectra calculated at normal incidence for a periodic array of cut wires [red (continuous dark gray)] and of paired cut wires [blue (dashed black)], respectively (px=1.2 μm, py=200 nm, w=30 nm, L=600 nm, and h_{sub}=100 nm). The 30–nm-thick gold cut wires are described using a Drude model whose parameters can be found in Ref. 13. The dielectric spacer (SiO_2) permittivity is ε_{sub}=2.25.

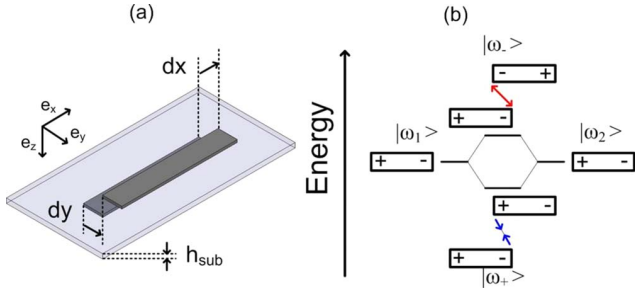

FIG. 2. (Color online) (a) Asymmetric cut-wire pair with the 3 degrees of freedom for the control of the coupling strength: h_{sub}, dx, and dy. (b) Inverted hybridization scheme.

II. MODE ENGINEERING AND COUPLING STRENGTH IN METAMATERIALS BASED ON PAIRED CUT WIRES

The plasmon hybridization scheme as recently introduced in Refs. 14 and 15 gives an intuitive electromagnetic analog of molecular orbital theory. Such a scheme has largely been used by the metamaterial community especially for simplifying metamaterial designs at optical wavelengths.[4,16] The coupling of two electric dipoles facing each other has thus been exploited to mimic magnetic atoms and alter the effective magnetic permeability of metamaterials in the optical range. While a magnetic activity was indeed obtained from metamaterials comprised of metallic dipoles,[4,16] negative refraction was reported only in the pioneering demonstration by Shalaev *et al.*[4] who used a periodic array of cut-wire pairs. In order to unambiguously achieve negative refraction, the magnetic activity must actually occur within a frequency band in which the dielectric permittivity is negative. For this purpose, one solution consists of associating magnetic "atoms" (coupled metallic dipoles) to a broadband "electric plasma" (continuous wires) in the same structure. Many authors have used this solution either in the microwave[5,6] or in the optical regime,[17,18] thereby contributing to the development of the so-called fishnet structure. We propose another solution based on the control of the coupling between metallic dipoles in such a way that the symmetric and antisymmetric bands have a sufficient overlap. The coupling strength is varied either by changing the distance between coupled dipoles or by breaking the symmetry of the structure.

Figure 1(a) shows the rectangular unit cell of the studied two-dimensional (2D) structure in the case where the coupled metallic dipoles (cut wires) are vertically aligned. This structure is henceforth referred to as the symmetric cut-wire structure to distinguish it from the asymmetric structure discussed later (see Fig. 2). Both structures consist of 2D periodic arrays of metallic cut wires separated by a dielectric spacer.[4] The electromagnetic wave should propagate normally to the layers with the electric field parallel to the longest side of dipolar elements. A normal incidence is thus considered. Such structures can be described in terms of effective index as long as the cut-wire width w and spacer thickness h_{sub} are much smaller than the wavelength.[4,7–11] Two series of calculations were carried out using a finite element simulation package (HFSS from Ansoft), one for symmetric structures and the other for asymmetric structures. The effective index was obtained from the calculated transmission and reflection coefficients.[19]

The first series of calculations were performed to compare the electromagnetic response of a symmetric cut-wire bilayer [blue curve (dashed black) in Fig. 1(c)] to that of a cut-wire monolayer [red curve (continuous dark gray) in Fig. 1(c)]. As is evident in the curve, only one resonance is observed for the cut-wire monolayer in the frequency range of interest. This resonance corresponds to the fundamental cut-wire dipolar mode which, in the optical regime, can also be interpreted in terms of a localized plasmon resonance.[20] Collective electronic excitations, also called surface plasmons, are indeed the main mechanism at short wavelengths. For the cut-wire bilayer, the coupling between paired cut wires lifts the degeneracy of the single cut-wire mode, which hybridizes into two plasmon modes. One mode is symmetric and corresponds to in-phase current oscillations, while the other is antisymmetric and corresponds to out-of-phase current oscillations. For a symmetric cut-wire pair with a vertical alignment of the two cut wires, the antisymmetric mode is the low-energy (low-frequency) mode since attractive forces are present in the system. Conversely, repellent forces are produced in the case of the symmetric mode that is therefore the high-frequency mode. The stronger the coupling (the smaller the spacing between the dipoles), the larger the frequency difference between the two modes. The evolution of the transmission spectra with the thickness of the dielectric spacer (or substrate) h_{sub} is illustrated in Fig. 3(a) in the case of a structure designed for operation in the microwave regime. Similar results were obtained for the structure in Fig. 1(c).

A second series of calculations were performed to analyze the influence of a vertical misalignment of metallic dipoles at a fixed spacer (or substrate) thickness. For this purpose, the cut-wire layers were shifted from each other in the horizontal XY plane [Fig. 2(a)] thus breaking the symmetry of the cut-wire structure. The relative displacements dx and dy in the X and Y directions, respectively, were used as parameters. The electromagnetic response of this type of asymmetric structure was studied both in the microwave and optical regimes. Similar evolutions of the hybridization scheme were found whatever the regime was. Results of Fig. 3 correspond to the microwave structure that was fabricated in this work. The substrate thickness was chosen to be equal to that of commercially available epoxy dielectric boards (1.2 mm). For this thickness and a vertical alignment of paired cut wires ($dx=dy=0$), the calculated transmission spectrum in Fig. 3(a) revealed a pronounced frequency separation between the symmetric (electric) and antisymmetric (magnetic) modes. Figures 3(b) and 3(c) show the evolution of the transmission spectrum for nonzero values of the longitudinal (dx) and lateral (dy) displacements, respectively. Quite surprisingly, as previously reported by Christ *et al.*[21] for the control of Fano resonances in a plasmonic lattice of continuous wires, symmetry breaking can invert the hybridization scheme due to modified Coulomb interactions [Fig. 2(b)] resulting in the symmetric resonance occurring at a lower frequency than the antisymmetric one. The Coulomb forces in our system result from the interaction of charges located at the cut-wire ends.

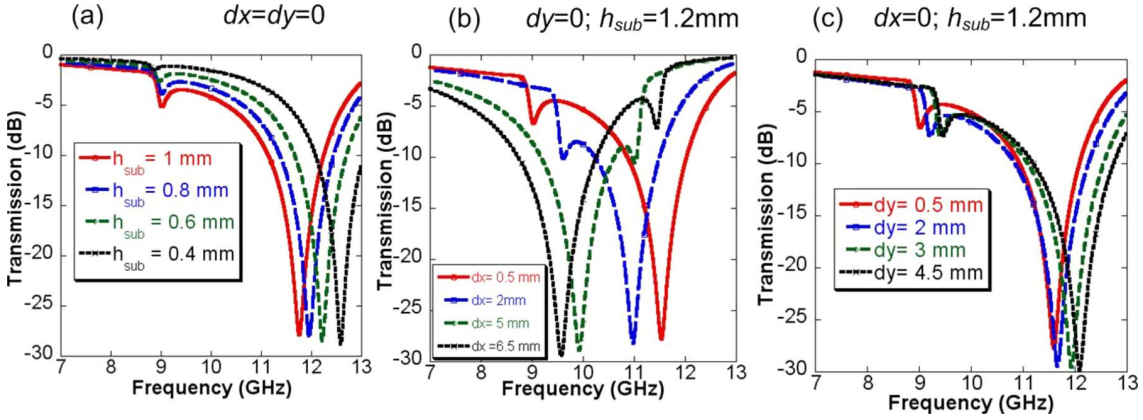

FIG. 3. (Color online) Influence of the coupling strength on the transmission spectra of a bilayer structure (px=19 mm, py=9.5 mm, w=0.3 mm, L=9.5 mm, and h_{sub}=1.2 mm). The substrate permittivity is ε_{sub}=3.9. (a) Variation in the dielectric spacer (or substrate) thickness h_{sub}. (b) Variation in the longitudinal shift dx. (c) Variation in the lateral shift dy.

When the longitudinal shift (dx) is progressively increased, the signs of the charges in close interaction change. As a result the repulsive force becomes attractive and vice versa. Correspondingly, the symmetric mode becomes the low-energy mode while the asymmetric mode is shifted to higher frequencies. It is evident that this inversion process is impossible in the case of a lateral dy displacement of the dipoles [Fig. 3(c)]. Let us notice that another structural asymmetry has recently been reported in Ref. 22 leading to an increase in the antiphase resonant mode response, but no inverted hybridization scheme was evidenced in that case.

Controlling the coupling between metallic dipoles thus allows the two plasmons resonances to be engineered. When the magnetic and electric modes are very close together, a negative refraction material can be obtained. More generally, the design of true negative index metamaterials can be achieved by appropriate design of the three degrees of freedom h_{sub}, dx, and dy.

III. NEGATIVE INDEX OF REFRACTION IN ASYMMETRIC CUT-WIRE STRUCTURES

Results in Fig. 3(a) clearly show that strong coupling and small spacing between paired dipoles do not favor negative refraction in cut-wire bilayers. In the optical regime, the thickness of dielectric spacers is in general easily controlled using standard layer deposition techniques. However, breaking the symmetry of a multilayer stack (Fig. 2) can be of interest when the use of additional techniques, such as planarization, modifies the thickness of each deposited layer.[16] Moreover, the fact that a strict vertical alignment of cut wires is not required simplifies the fabrication process. In the microwave regime, the thickness of the dielectric spacer or substrate is usually that of commercially available dielectric boards. Figure 3(a) most likely explains why negative refraction was not obtained with standard substrates whose thickness was of the order of $\lambda/25$. Breaking the symmetry of the structure is in this case an attractive solution to provide negative index. Our experiments were carried out to demonstrate the possibility of negative refraction metamaterial in the microwave spectral regime using an asymmetric cut-wire structure.

A photograph of the fabricated cut-wire bilayer is shown in Fig. 4(a). The structure consists of cut-wire pairs with L =9.5 mm, w=0.3 mm, px=19 mm, py=9.5 mm, h_{sub} =1.2 mm, dx=9.5 mm, and dy=0. Measurements were performed in free space with an Agilent 8722ES vectorial network analyzer and two X-band horn antennas. Figure 4(b) shows the measured and calculated transmission/reflection spectra. There is an excellent agreement between experiments and theory. The dips in the transmission spectra near 9.5 and 11.5 GHz correspond to the symmetric and antisymmetric modes, respectively. The real and imaginary parts of effective index, n, retrieved from both experiments and

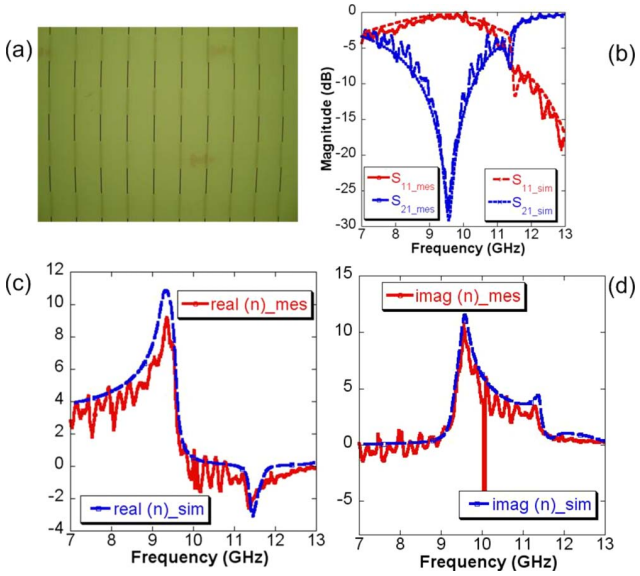

FIG. 4. (Color online) (a) Top photograph of the microwave prototype. Cut wires on the bottom face of the semitransparent substrate appear in light gray. (b) Measured and simulated reflection (S_{11}) and transmission (S_{21}) coefficients. (c) and (d) Retrieved effective index: real and imaginary parts of the relative refractive index.

theory are reported in Figs. 4(c) and 4(d). A negative index of refraction is unambiguously observed around 11.5 GHz. The figure of merit (ratio between the real and imaginary parts of n) at this frequency is found to be as high as 42, which is the highest value reported so far for this kind of metamaterial. We have thus demonstrated a negative refraction metamaterial in the microwave regime using only cut wires as the metallic constituents. Direct measurements of the refractive index using a prism configuration will be published elsewhere. We may notice that the cut-wire length is ~2.75 times smaller than the negative index wavelength, which itself is ~22 times larger than the metamaterial thickness. The propagation of light at normal incidence and within some angular range is mainly dominated by the material thickness, not by the in-plane periodicity.[11] In contrast, because of in-plane dimensions comparable to half the wavelength, the structure should exhibit a "photonic-crystal-like" behavior for plane waves with large in-plane wave-vector component. As for most of the negative-refraction metamaterials published in the literature, our structure suffers from the fact that negative refraction is obtained over a limited range of incident angles. In turn, the present concept of inverted hybridization for negative refraction can be applied to more "compact" structures so as to better satisfy the homogenization rules at all angles of incidence.[23]

IV. CONCLUSION

Design rules have been established for the control of the coupling strength between paired metallic dipoles in cut-wire bilayers, thereby allowing the engineering of the symmetric and antisymmetric modes. An inversion of the hybridization scheme has been shown when an asymmetric alignment of the paired cut wires is used. More generally, the coupling strength can be controlled by adjusting either the spacing or the alignment of the paired cut wires. Negative refraction has been demonstrated in an asymmetric cut-wire structure in the microwave domain. These results open up solutions for the design of metamaterials both in the microwave and optical spectral regimes. Clearly, experimental demonstration in the microwave regime cannot be automatically transferred to the optical regime. However, numerical calculations accounting for finite conductivity and losses of metal at optical frequencies indicate that the inverted hybridization scheme still works for obtaining negative refraction metamaterials in optics.

*boubacar.kante@ief.u-psud.fr
†andre.delustrac@ief.u-psud.fr

[1] J. B. Pendry, A. J. Holden, D. J. Robbins, and W. J. Stewart, J. Phys.: Condens. Matter **10**, 4785 (1998).
[2] J. B. Pendry, A. J. Holden, D. J. Robbins, and W. J. Stewart, IEEE Trans. Microwave Theory Tech. **47**, 2075 (1999).
[3] D. R. Smith, W. J. Padilla, D. C. Vier, S. C. Nemat-Nasser, and S. Schultz, Phys. Rev. Lett. **84**, 4184 (2000).
[4] V. M. Shalaev, W. Cai, U. K. Chettiar, H. K. Yuan, A. K. Sarychev, V. P. Drachev, and A. V. Kildishev, Opt. Lett. **30**, 3356 (2005).
[5] J. Zhou, L. Zhang, G. Tuttle, T. Koschny, and C. M. Soukoulis, Phys. Rev. B **73**, 041101(R) (2006).
[6] K. Guven, M. D. Kaliskan, and E. Ozbay, Opt. Express **14**, 8685 (2006).
[7] M. Kafesaki, I. Tsiapa, N. Katsarakis, T. Koschny, C. M. Soukoulis, and E. N. Economou, Phys. Rev. B **75**, 235114 (2007).
[8] S. Zhang, W. Fan, N. C. Panoiu, K. J. Malloy, R. M. Osgood, and S. R. J. Brueck, Phys. Rev. Lett. **95**, 137404 (2005).
[9] G. Dolling, M. Wegener, C. M. Soukoulis, and S. Linden, Opt. Lett. **32**, 53 (2007).
[10] G. Dolling, C. Enkrich, M. Wegener, C. M. Soukoulis, and S. Linden, Science **312**, 892 (2006).
[11] J. Valentine, S. Zhang, T. Zentgraf, E. U. Avila, D. A. Genov, G. Bartal, and X. Zhang, Nature (London) **455**, 376 (2008).
[12] D. Schurig, J. J. Mock, B. J. Justice, S. A. Cummer, J. B. Pendry, A. F. Starr, and D. R. Smith, Science **314**, 977 (2006).
[13] B. Kanté, A. de Lustrac, J.-M. Lourtioz, and S. N. Burokur, Opt. Express **16**, 9191 (2008).
[14] U. Kreibig, A. Althoff, and H. Pressmann, Surf. Sci. **106**, 308 (1981).
[15] E. Prodan, C. Radloff, N. J. Halas, and P. Nordlander, Science **302**, 419 (2003).
[16] N. Liu, H. Guo, L. Fu, S. Kaiser, H. Schweizer, and H. Giessen, Nature Mater. **7**, 31 (2008).
[17] E. Pshenay-Severin, U. Hübner, J. Petschulat, C. Rockstuhl, T. Pertsch, F. Lederer, and A. Tünnermann, Proceedings of META'08, Marrakech, Morocco, 2008 (unpublished).
[18] T. F. Gundogdu, N. Katsarakis, M. Kafesaki, R. S. Penciu, G. Konstantinidis, A. Kostopoulos, E. N. Economou, and C. M. Soukoulis, Opt. Express **16**, 9173 (2008).
[19] D. R. Smith, S. Schultz, P. Markos, and C. M. Soukoulis, Phys. Rev. B **65**, 195104 (2002).
[20] C. Rockstuhl, F. Lederer, C. Etrich, T. Zentgraf, J. Kuhl, and H. Giessen, Opt. Express **14**, 8827 (2006).
[21] A. Christ, Y. Ekinci, H. H. Solak, N. A. Gippius, S. G. Tikhodeev, and O. J. F. Martin, Phys. Rev. B **76**, 201405(R) (2007).
[22] T. Pakizeh, A. Dmitriev, M. S. Abrishamian, N. Granpayeh, and M. Käll, J. Opt. Soc. Am. B **25**, 659 (2008).
[23] Constantin R. Simovski and S. A. Tretyakov, Phys. Rev. B **75**, 195111 (2007).

Annexe 2.2

A. Sellier, S. N. Burokur, B. Kanté, A. de Lustrac

« Negative refractive index metamaterials using only metallic cut wires »

Optics Express, vol. 17, no. 8, pp. 6301-6310, April 2009

Negative refractive index metamaterials using only metallic cut wires

Alexandre Sellier, Shah Nawaz Burokur, Boubacar Kanté, and André de Lustrac

Institut d'Electronique Fondamentale, Univ. Paris-Sud, CNRS, UMR 8622, 91405 Orsay cedex, France
nawaz.burokur@u-psud.fr, andre.de-lustrac@u-psud.fr

Abstract: We present, design and analyze a novel planar Left-Handed (LH) metamaterial at microwave frequencies. This metamaterial is composed of only metallic cut wires and is used under normal-to-plane incidence. Using Finite Element Method (FEM) based simulations and microwave experiments, we have investigated the material properties of the structure. Simultaneous negative values are observed for the permittivity ε and permeability μ by the inversion method from the transmission and reflection responses. A negative index n is verified in a bulk prism engineered by stacking several layers of the metamaterial. Our work demonstrates the feasibility of a LH metamaterial composed of only cut wires.

OCIS codes: (160.3918) Materials; Metamaterials; (260.2065) Physical optics; Effective medium theory; (260.2110) Physical optics; Electromagnetic optics.

References and links

1. V. G. Veselago, "The electrodynamics of substances with simultaneously negative values of permittivity and permeability," Sov. Phys. Usp. **10**, 509-514 (1968).
2. D. R. Smith, W. J. Padilla, D. C. Vier, S. C. Nemat-Nasser, and S. Schultz, "Composite medium with simultaneously negative permeability and permittivity," Phys. Rev. Lett. **84**, 4184-4187 (2000).
3. J. B. Pendry, A. J. Holden, W. J. Stewart, and I. Youngs, "Extremely low frequency plasmons in metallic mesostructures," Phys. Rev. Lett. **76**, 4773-4776 (1996).
4. J. B. Pendry, A. J. Holden, D. J. Robbins, and W. J. Stewart, "Magnetism from conductors and enhanced nonlinear phenomena," IEEE Trans. Microwave Theory Tech. **47**, 2075-2084 (1999).
5. J. Zhou, T. Koschny, M. Kafesaki, E. N. Economou, J. B. Pendry, and C. M. Soukoulis, "Saturation of magnetic response of split-ring resonators at optical frequencies," Phys. Rev. Lett. **95**, 223902 (2005).
6. V. A. Podolskiy, A. K. Sarychev, and V. M. Shalaev, "Plasmon modes and negative refraction in metal nanowire composites," Opt. Express **11**, 735-745 (2003).
7. V. M. Shalaev, W. Cai, U. K. Chettiar, H. K. Yuan, A. K. Sarychev, V. P. Drachev, and A. V. Kildishev, "Negative index of refraction in optical metamaterials," Opt. Lett. **30**, 3356-3358 (2005).
8. V. M. Shalaev, "Optical negative-index metamaterials," Nature Photonics **1**, 41-48 (2007).
9. G. Dolling, C. Enkrich, M. Wegener, J. F. Zhou, C. M. Soukoulis, and S. Linden, "Cut-wire pairs and plate pairs as magnetic atoms for optical metamaterials," Opt. Lett. **30**, 3198-3200 (2005).
10. J. Zhou, L. Zhang, G. Tuttle, T. Koschny, and C. M. Soukoulis, "Negative index materials using simple short wire pairs," Phys. Rev. B **73**, 041101 (2006).
11. J. Zhou, E. Economou, T. Koschny, and C. M. Soukoulis, "Unifying approach to left-handed material design," Opt. Lett. **31**, 3620-3622 (2006).
12. G. Dolling, M. Wegener, C. M. Soukoulis and S. Linden, "Negative-index metamaterial at 780 nm wavelength," Opt. Lett. **32**, 53-55 (2007).
13. M. Kafesaki, I. Tsiapa, N. Katsarakis, Th. Koschny, C. M. Soukoulis, and E. N. Economou, "Left-handed metamaterials: The fishnet structure and its variations," Phys. Rev. B **75**, 235114 (2007).
14. High Frequency Structure Simulator, HFSS v11.1, Ansoft Ltd.
15. A. M. Nicolson, and G. F. Ross, "Measurement of the intrinsic properties of materials by time-domain techniques," IEEE Trans. Instrum. Meas. **19**, 377-382 (1970).
16. J. Valentine, S. Zhang, T. Zentgraf, E. Ulin-Avila, D. A. Genov, G. Bartal, X. Zhang, "Three Dimensional Optical Metamaterial Exhibiting Negative Refractive Index," Nature **455**, 376 (2008).
17. H. Chen, L. Ran, J. Huangfu, X. Zhang, K. Chen, T. M. Grzegorczyk, and J. A. Kong, "Left-handed materials composed of only S-shaped resonators," Phys. Rev. E **70**, 057605 (2004).

#104790 - $15.00 USD Received 1 Dec 2008; revised 15 Jan 2009; accepted 15 Jan 2009; published 2 Apr 2009

18. K. Aydin, I. Bulu, and E. Ozbay, "Focusing of electromagnetic waves by a left-handed metamaterial flat lens," Opt. Express **13**, 8753-8759 (2005).
19. G. Wang, J. R. Fang, and X. T. Dong, "Refocusing of backscattered microwaves in target detection by using LHM flat lens," Opt. Express **15**, 3312-3317 (2007).
20. R.W. Ziolkowski, and A. Kipple, "Application of double negative metamaterials to increase the power radiated by electrically small antennas," IEEE Trans. Antennas Propag. **51**, 2626-2640 (2003).
21. S. N. Burokur, M. Latrach, and S. Toutain, "Theoretical investigation of a circular patch antenna in the presence of a left-handed medium," IEEE Antennas Wireless Propag. Lett. **4**, 183-186 (2005).
22. R. A. Shelby, D. R. Smith, and S. Schultz, "Experimental verification of a negative index of refraction," Science **292**, 77-79 (2001).

1. Introduction

Left-Handed (LH) metamaterials are in general artificial composite structures exhibiting simultaneously a negative effective permittivity ε_{eff} and permeability μ_{eff} over a common frequency range [1]. Such metamaterials can be constructed from conductive metals and dielectrics. Since the first demonstration of a LH material by Smith *et al*. [2] in 2000, following the work by Pendry *et al*. [3-4], a lot of work has been done and is still in progress in order to simplify the structures for optical wavelengths. Due to the saturation of the magnetic response of Split-Ring Resonators (SRR) at optical frequencies [5], a different topology composed of metal wire pairs with dielectric spacing has been introduced theoretically by Podolskiy *et al*. to exhibit a negative refractive index *n* [6]. Later, Shalaev *et al*. [7] used this configuration to show experimentally a negative index under normal-to-plane incidence (when the wave vector $\boldsymbol{k}$ is perpendicular to the structure) in the optical range at the telecommunication wavelength $\lambda = 1.5\ \mu m$. In a recent review paper [8], Shalaev stated that it is very difficult to achieve a negative refractive index with exclusively wire pairs and the negative index value observed in [7] was accomplished in part because of the significant contribution from the imaginary part of the permeability. Other experiments on short wire pairs by Dolling *et al*. have not shown evidence of negative *n* due to two distinct frequency bands for the negative permeability μ and permittivity ε [9]. In the meantime, Zhou *et al*. emphasized that the condition to obtain simultaneously negative permittivity and permeability by pairs of finite metallic wires is very restrictive [10]. The authors then showed the possibility of obtaining a negative refractive index in the microwave regime from bi-layered structures by combining periodic continuous and cut wires as shown in Fig. 1(a). The continuous wires are used to provide the negative effective permittivity. The negative permeability is obtained by exciting resonant circular currents in the cut wire pair in order to create a strong magnetic resonance. Zhou *et al*. also theoretically demonstrated a left-handed material using only cut wire pairs by increasing the equivalent capacitance between two consecutive short wires on the same face to adjust the electric resonance frequency [11]. However this increase of capacitance can only be achieved by strongly reducing the spacing between two consecutive wires and this is quite difficult to achieve at optical wavelengths. Another bi-layered structure shown in Fig. 1(b) and referred to as "fishnet" has been reported to exhibit a negative index at optical [12] and microwave frequencies [13]. The main drawback of the cut-continuous wires and fishnet topologies is the high level of metallization which is an important source of losses at high frequencies, particularly in the optical domain.

In this paper, we present a systematic study of the novel cut wires structure presented in Fig. 1(c) under normal-to-plane incidence in the microwave domain. This structure is made only of cut-wires on a dielectric substrate. We demonstrate numerically and experimentally that this simplified structure (Fig. 1(c)) using fewer metallic parts compared to the cut-continuous wires (Fig. 1(a)) and the fishnet (Fig. 1(b)) structures, exhibits simultaneously a negative permittivity and a negative permeability. Numerical simulations performed using the FEM based software *HFSS* [14] are run to show and understand the electromagnetic behavior of the design. A single layer of the metamaterial is characterized by reflection and transmission measurements. The retrieved parameters show simultaneous resonances in the permittivity and permeability responses leading to a negative index of refraction. The results

#104790 - $15.00 USD Received 1 Dec 2008; revised 15 Jan 2009; accepted 15 Jan 2009; published 2 Apr 2009

are confirmed by experimental measurements. A prism made of this metamaterial is engineered and used not only to observe a negative refraction, but also to estimate and verify the refractive index.

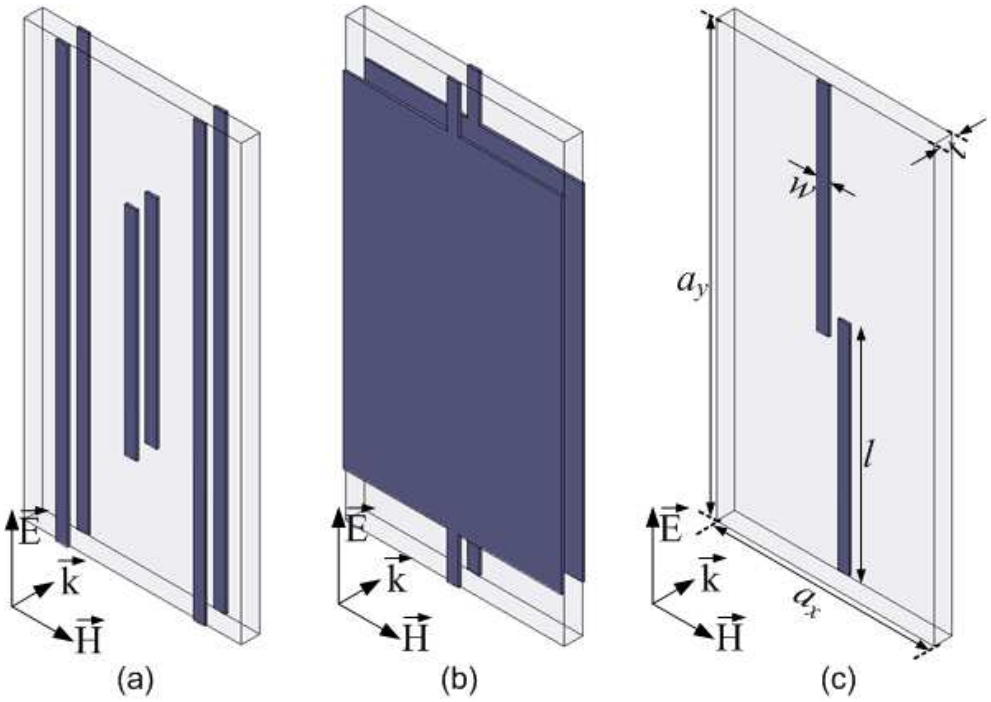

Fig. 1. Unit cell of: (a) cut-continuous wires structure, (b) fishnet structure, and (c) only cut wires structure under normal-to-plane propagation (a_x = 9.5 mm, a_y = 19 mm, w = 0.3 mm, l = 9.5 mm). The inserts show the direction and the polarization of the wave.

2. Material properties of the cut wires metamaterial

In this study, the cut wires metamaterial illustrated by its unit cell in Fig. 1(c) is employed to operate in the microwave regime. It consists of a bi-layered structure composed of periodic cut wires of finite length. Compared to the cut wires structure of ref. [6-8] (Fig. 1(a)), the finite wires in our case do not face each other entirely on the dielectric board. In fact, the wires on one face are laterally shifted along the y-axis by the length l. The structure is printed on both faces of an epoxy dielectric board of thickness t = 1.2 mm and of relative permittivity ε_r = 3.9. For the different samples reported here, the width of the cut wires denoted by w is 0.3 mm. The length of the cut wires is l = 9.5 mm and the unit cell size in the x and y direction is respectively a_x = 9.5 mm and a_y = 19 mm. These dimensions have been optimized to operate around 10 GHz and remain the same throughout the whole paper.

The reflection and transmission spectra of the metamaterial are calculated using *HFSS* by applying the necessary periodic boundary conditions on the unit cell. Several samples of the structure consisting of 10 × 5 cells on a 120 mm × 120 mm epoxy surface are fabricated using conventional commercial chemical etching technique. Measurements are done in an anechoic chamber using an Agilent 8722ES network analyzer and two X-band horn antennas. In the transmission measurements, the plane waves are incident normal to the prototype surface and a calibration to the transmission in free space (the metamaterial sample is removed) between the two horn antennas is done. The reflection measurements are done by placing the emitting and receiving horn antennas on the same side of the prototype and inclined with an angle of

#104790 - $15.00 USD Received 1 Dec 2008; revised 15 Jan 2009; accepted 15 Jan 2009; published 2 Apr 2009

about 5° with respect to the normal on the prototype surface. The calibration for the reflection is done using a sheet of copper as reflecting mirror.

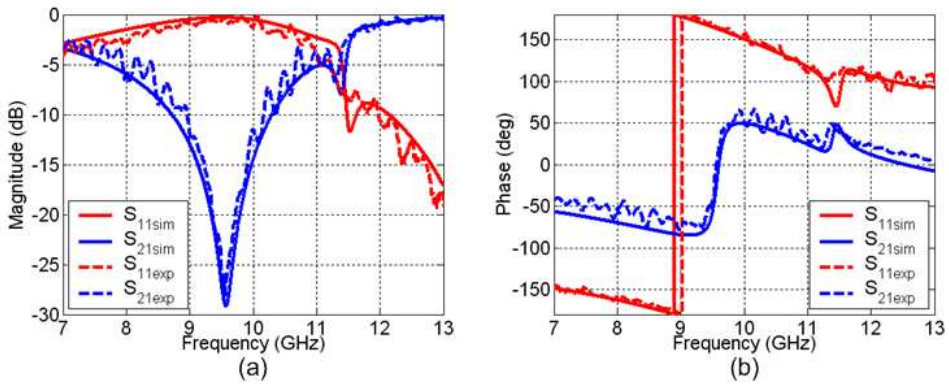

Fig. 2. Calculated and measured reflection (S_{11}) and transmission (S_{21}) responses of the metamaterial for a single layer: (a) magnitude, and (b) phase.

Figure 2 shows the calculated (continuous lines) and measured (dashed lines) *S*-parameters of the metamaterial for a single layer configuration. There is a very good qualitative agreement between simulations and measurements. The calculated and measured magnitudes of S_{21} presented in Fig. 2(a) show clearly two resonance dips, the first one at 9.58 GHz and a second one at 11.39 GHz. We can note in Fig. 2(b) that a change in sign occurs for the transmission phase at the first resonance dip. At the second resonance dip, a peak and a dip is respectively observed in the transmission and reflection phase.

Using the retrieval procedure described in [15], based on the inversion of the reflection and transmission coefficients, the effective parameters of the bi-layered metamaterial structure are extracted. The metamaterial has a period very small compared to the wavelength λ (less than λ/20) in the propagation direction. The propagation of the electromagnetic wave travelling along this direction is dominated by this deep sub-wavelength period and not by the in-plane period a_x or a_y. There is only a single propagating mode in the negative-index frequency region, justifying the description of the cut wires metamaterial with an effective index [16].

The extracted permittivity ε, permeability μ and refractive index n are shown in the various parts of Fig. 3. Two extraction procedures have been performed: the first one uses the calculated *S*-parameters and the second one is based on the measured *S*-parameters. It must be noted that the extraction from the measured spectra are presented without any fitting. As illustrated by the extracted parameters from the calculated and measured *S*-parameters, the cut wires structure shows firstly an electric resonance at the first resonance dip observed at 9.58 GHz in Fig. 2. This electric resonance exhibits values going negative for the real part of the permittivity in the vicinity of the resonance. Secondly a magnetic resonance with negative values appears at the right hand side of the second resonance dip at 11.5 GHz. Around the same frequency, the real part of the permittivity is still negative. The extracted real part of the refractive index is therefore negative around 11.5 GHz which is the frequency of the LH peak. However, we can also notice that the zero value for the ε response is very close to 13 GHz where a full transmission band is observed in Fig. 2(a). This frequency constitutes the frequency of the RH transmission peak. We can therefore deduce that this RH transmission peak is due to an impedance matching between the structure and vacuum.

#104790 - $15.00 USD Received 1 Dec 2008; revised 15 Jan 2009; accepted 15 Jan 2009; published 2 Apr 2009

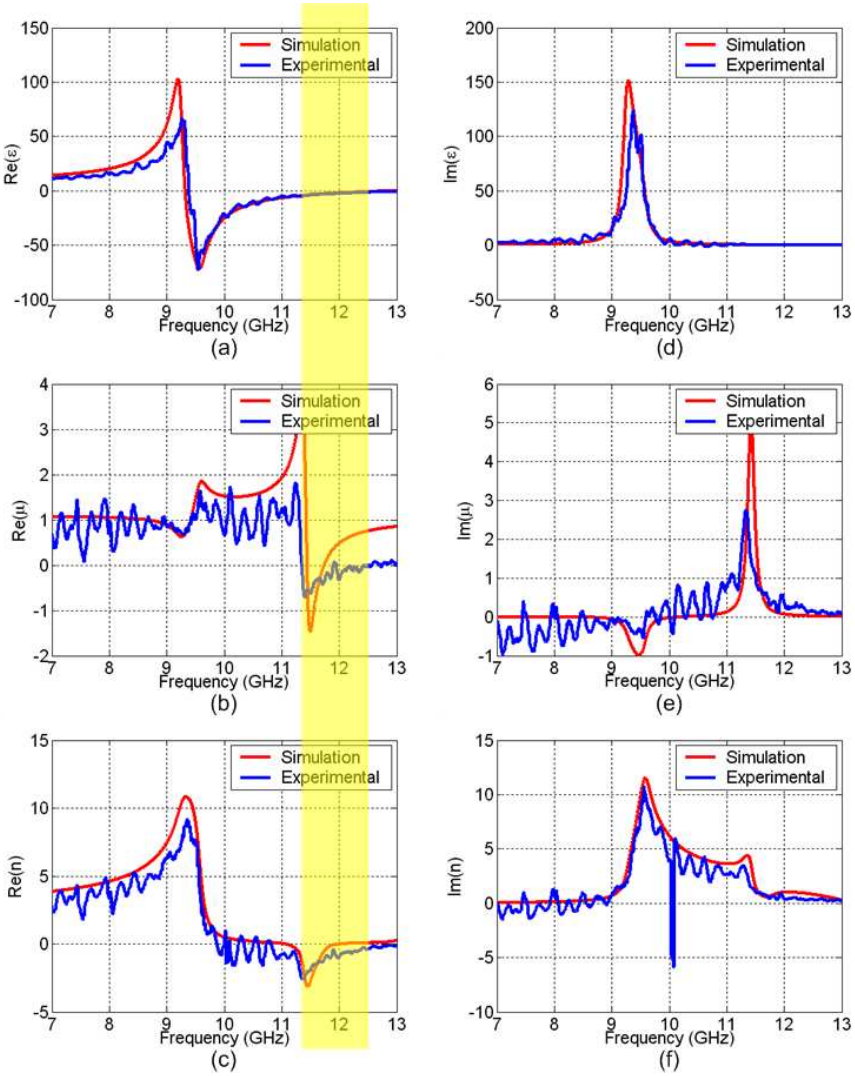

Fig. 3. Extracted electromagnetic properties of the cut wires metamaterial using the simulated and experimental data of Fig. 2: (a)-(c) real parts, and (d)-(f) imaginary parts of the permittivity ε, of the permeability μ and the refraction index n. The shaded yellow area delineates the frequency region where the measured real parts of ε and μ are simultaneously negative.

Since the real part of n (n') is given by $n' = \varepsilon' z' - \varepsilon'' z''$ from $n = \varepsilon z$ and $z = \sqrt{(\mu/\varepsilon)}$, the imaginary parts of the permittivity (ε'') and the permeability (μ'') also accounts for n'. Therefore, a negative real part of n can be accomplished without having ε' and μ' simultaneously negative. This can happen only if ε'' and μ'' are sufficiently large compared to ε' and μ'. A wider negative n' frequency band is observed due to the dispersion of the fabricated prototype. The shaded yellow area in Fig. 3 highlights the frequency region where the measured real parts of the permittivity (ε') and the permeability (μ') are simultaneously negative to emphasize the desired measured negative values of n'. Concerning the imaginary parts, a very good qualitative agreement is observed between calculations and experiments. We shall note that the imaginary part of n (n'') is very low in the negative n' frequency region.

#104790 - $15.00 USD Received 1 Dec 2008; revised 15 Jan 2009; accepted 15 Jan 2009; published 2 Apr 2009

The proposed cut wires structure can be viewed as a simplification of the S-shaped resonator previously presented in [17]. While the face-to-face cut wire pair is issued from the elimination of the horizontal arms of a conventional one loop SRR as described in [9], we can similarly cancel the horizontal arms of a single S-shaped resonator so as to consider only the vertical arms as presented by the proposed cut wire pair in Fig. 1(c). The magnetic coil is still present to produce a negative permeability since a capacitance is created between the ends of the wires on the opposite faces of the dielectric board.

3. Stacking of layers

Stacking multiple layers of LH materials may be useful in many practical applications such as subwavelength imaging [18, 19] and directive antennas [20, 21]. In this paper, the stacking of layers is considered as a preliminary study before the verification of the negative index of refraction from a prism-shaped bulk metamaterial. It is obvious that the effective properties obtained from the inversion method on a single layer give a good idea about the effective properties of the metamaterial. However, other effect such as inter-layer coupling must be taken into account because it affects the material properties of the structure. Therefore, two, three and four layers of the designed bi-layered metamaterial are stacked with a 1 mm air spacing between each layer as presented in Fig. 4(a). Numerical simulations are run to show the expected performances of a bulk metamaterial composed of multiple layers. The transmission spectra for the different number of layers are presented in Fig. 4(b).

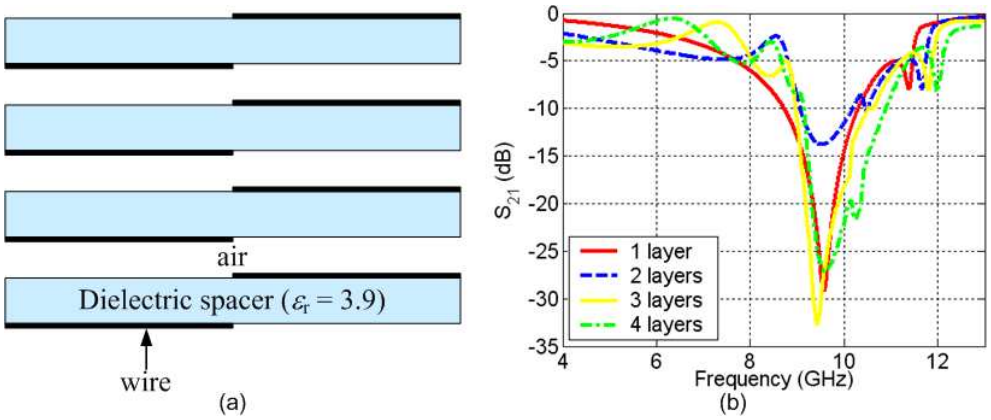

Fig. 4. (a) A bulk metamaterial composed of four layers interleaved with 1 mm air spacing, and (b) transmission spectra for different number of layers.

From the spectra of Fig 4(b), we can note that the frequency of the first transmission dip remains constant with an increasing number of layers while the second dip shifts slightly towards higher frequencies. However, peaks and valleys appear at lower frequencies suggesting a coupling mechanism between consecutive layers. The number of these peaks and valleys increases with an increasing number of layers as shown in Fig. 4(b). The transmission spectra together with the corresponding reflection spectra are used for the extraction of the material properties presented in Fig. 5. It should be noted that the first transmission dip in the single layer case corresponds to an electric resonance where ε' exhibits negative values. However, other $\varepsilon' < 0$ frequency bands can be observed in Fig. 5(a) for the multiple layers cases due to the valleys noted in the transmission spectra. And, since the magnitude of the transmission dips decreases with the number of layers, the magnitude of ε' also decreases as shown in Fig. 5(a). At higher frequencies near 12 GHz, a magnetic resonance is also observed for multiple layers as for the single layer case. However the magnitude tends to decrease while the number of layers increases (Fig. 5(b)). For more than two layers, μ' exhibits only positive values at the resonance near 12 GHz. Besides, another magnetic resonance with $\mu' <$

#104790 - $15.00 USD Received 1 Dec 2008; revised 15 Jan 2009; accepted 15 Jan 2009; published 2 Apr 2009

0 can be observed at lower frequencies with simultaneously $\varepsilon' < 0$ when more than one layer is used. So even if the $\mu' < 0$ frequency band disappears at the second transmission dip due to the $\mu' > 0$, a negative index band is observed at lower frequencies as shown in Fig. 5(c). This negative refractive index results from the coupling mechanism created when several layers of the bi-layered structure are stacked. The negative index frequency band widens when the number of layers increases.

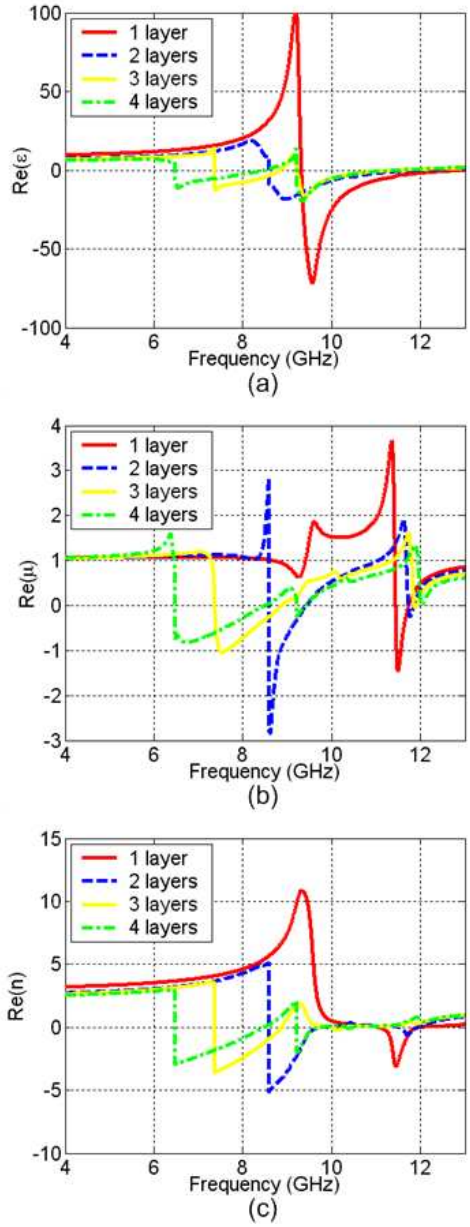

Fig. 5. Extracted material properties for different number of layers. (a) Re(ε), (b) Re(μ), and (c) Re(n).

#104790 - $15.00 USD Received 1 Dec 2008; revised 15 Jan 2009; accepted 15 Jan 2009; published 2 Apr 2009

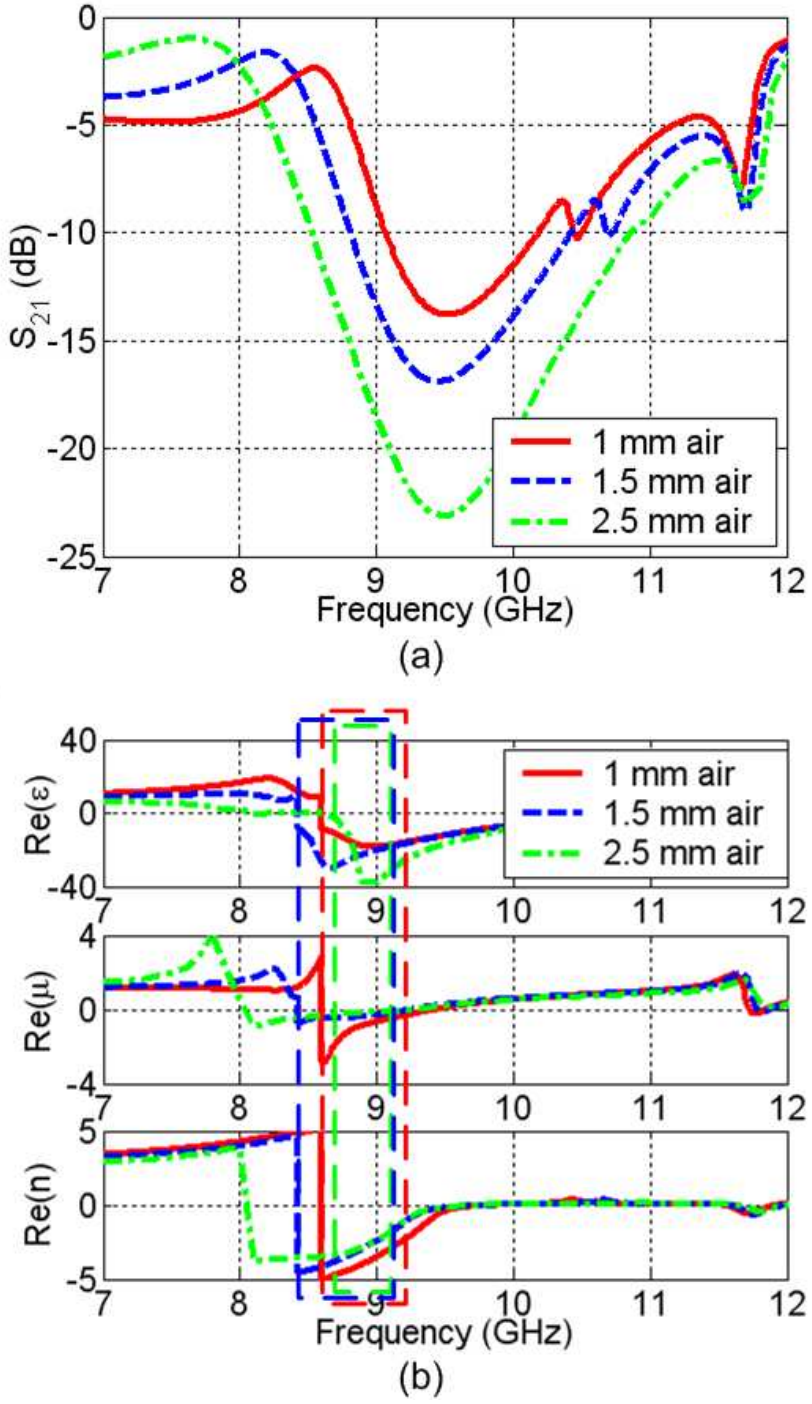

Fig. 6. Different air spacing for the two layers case. (a) S_{21} (dB), and (b) Re(ε), Re(μ), and Re(n). The colored dashed regions highlight the frequency region where Re(ε) and Re(μ) are simultaneously negative for each case.

#104790 - $15.00 USD Received 1 Dec 2008; revised 15 Jan 2009; accepted 15 Jan 2009; published 2 Apr 2009

We shall also note that when a bigger air spacing is left between the layers, the only major change is the shift towards lower frequencies for the transmission peak around 8 GHz. This phenomenon is clearly shown in Fig. 6(a) for a two layers case when the air spacing varies from 1 mm to 2.5 mm. At 12 GHz, a very slight shift in frequency can be noted. The variation in air spacing therefore causes a consequent shift in the $\mu' < 0$ frequency band at 8 GHz as shown in Fig. 6(b). Since the $\varepsilon' < 0$ frequency band presents only a very slight shift, one must be very careful in choosing the right spacing between the different layers so that overlapping of $\varepsilon' < 0$ and $\mu' < 0$ frequency bands is maintained. As it can observed from the colored dashed regions, the frequency region where Re(ε) and Re(μ) are simultaneously negative tends to become narrower when the air spacing is too high.

3. Refraction experiment

The refractive index n can also be scaled by a refraction experiment based on Snell's law where an electromagnetic wave passes through a prism made from a slab of the metamaterial under test [22]. The incident face of the prism is illuminated with a beam of microwaves whose electric field is polarized such that it is parallel to the wires as shown in Fig. 7(a). To determine the refractive index n, the deflection of the beam of microwave radiation as it passes through the prism-shaped metamaterial is measured. Knowing the angle of incidence α, the angle of refraction β is easily determined and used to calculate the index of refraction n at different frequencies by Snell's law. These values are plotted in Fig. 7(b) where a negative index can be observed around 9.7 GHz. This frequency band is different from that obtained from the extraction on one layer but is in good agreement with the one observed from the study made on stacking multiple layers if we consider that the microwave beam passes through several number of layers.

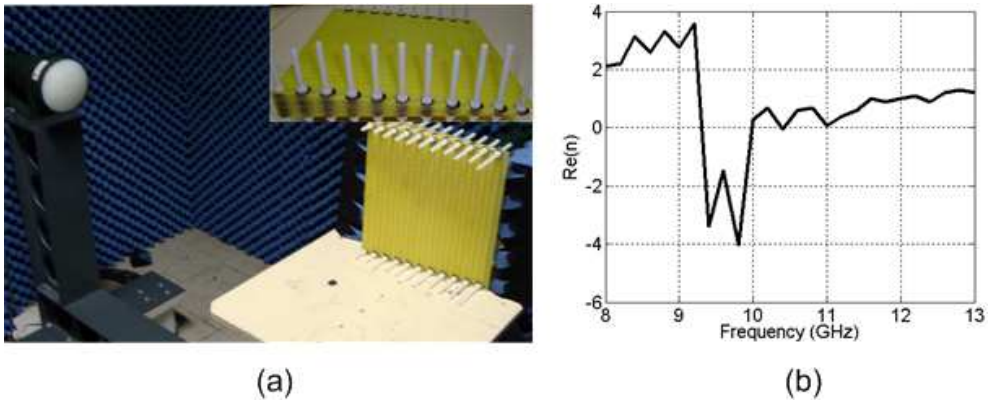

Fig. 7. (a) Experimental setup for the refraction experiment. The inset shows a side view of the fabricated prism shaped metamaterial. (b) Refractive index n obtained by the refraction experiment.

4. Conclusion

In conclusion, we studied the propagation of a normal-to-plane incident electromagnetic wave through a bi-layered cut wires structure and we investigated numerically and experimentally its electromagnetic properties. Numerical simulations have been performed in order to present the reflection and transmission spectra together with the effective parameters responses. The LH structure exhibits two transmission peaks, the first one corresponding to an electric resonance and another one corresponding to a magnetic resonance. Based on these responses, the effective parameters have been extracted to show a negative refractive index. A parameterized study of a material made of a stack of several layers showed that the coupling between layers modifies strongly the LH response of the material and shifts the LH band at

#104790 - $15.00 USD Received 1 Dec 2008; revised 15 Jan 2009; accepted 15 Jan 2009; published 2 Apr 2009

lower frequencies. This result has then been verified by a refraction experiment made on an engineered prism from several layers of the metamaterial.

The results obtained from this metamaterial therefore show the possibility of obtaining a negative index from a judicious tailoring of the cut wires structures without the need for additional continuous wires as proposed in [10]. This reduces strongly the use of metallic parts which is quite advantageous particularly in the optical regime.

#104790 - $15.00 USD Received 1 Dec 2008; revised 15 Jan 2009; accepted 15 Jan 2009; published 2 Apr 2009

Annexe 2.3

S. N. Burokur, A. Sellier, B. Kanté, A. de Lustrac

« Symmetry breaking in metallic cut wire pairs metamaterials for negative refractive index »

Applied Physics Letters, vol. 94, no. 20 (201111), May 2009

Symmetry breaking in metallic cut wire pairs metamaterials for negative refractive index

Shah Nawaz Burokur,[a] Alexandre Sellier, Boubacar Kanté, and André de Lustrac[b]
IEF, Univ. Paris-Sud, CNRS, UMR 8622, 91405 Orsay Cedex, France

(Received 10 December 2008; accepted 3 May 2009; published online 21 May 2009)

Metamaterials made of exclusively metallic cut wire pairs have been experimentally demonstrated to exhibit a negative refractive index at optical frequencies. However, other related works have not shown a negative index. In this paper, we propose an easy way to manipulate the magnetic and electric resonances of these metamaterials to produce a negative index. We show that judiciously breaking the symmetry of the structure allows tuning of both resonances leading to an overlapping between the negative permeability and negative permittivity regions. Numerical and experimental parametric studies of several cut wire pairs metamaterials are presented to validate our method at microwave frequencies. © *2009 American Institute of Physics*. [DOI: 10.1063/1.3141729]

Metamaterials recently attracted considerable interest[1–5] because of their unusual electromagnetic properties[6] and because of their potential applications such as invisibility cloaks[7–11] and the so-called perfect lenses.[12] Lately, pairs of finite-length wires (cut wire pairs)[13] have been shown to be able not only to replace the conventional split-ring resonators[14] (SRRs) to produce negative magnetic permeability μ under normal to plane incidence, but also lead to a negative refractive index n in the optical regime. However in a recent review paper,[15] Shalaev stated that it is very difficult to achieve a negative refractive index with exclusively wire pairs and that the negative index value observed in Ref. 13 was accomplished in part because of the significant contribution from the imaginary part of μ. However, other related works on cut wire and plate pairs (with slightly different structures from those used in Ref. 13) have not shown a negative index.[16] Instead, continuous wires have been combined to the cut wire pairs to produce negative permittivity ε to lead to a negative index in the microwave domain.[17] Zhou *et al.* also theoretically proposed a left-handed material using only cut wire pairs by increasing the equivalent capacitance between two consecutive short wire pairs so as to adjust the electric resonance frequency.[18] This increase in capacitance can only be obtained by strongly reducing the spacing between two consecutive wires, which will be limited according to the fabrication technology.

It is our aim in this letter to investigate numerically and experimentally the electromagnetic properties of cut wire pairs metamaterials, where the symmetry between the wires on opposite faces is voluntarily broken along the **E**-field direction. It is reported that in this case the electric resonance can occur at lower frequencies than the magnetic resonance, which is in contrast with the symmetrical configuration. A common frequency region where μ and ε are simultaneously negative is then achieved. This claim is verified numerically and experimentally in the microwave domain and indications on designing negative refractive index from structures composed of only cut wire pairs are given. This experimental demonstration of simultaneous negative real parts of μ and ε from only cut wire pairs metamaterials in the microwave domain shows the potential usefulness of such structures as negative index materials.

The basic structure of a single unit cell of our cut wire pairs metamaterial is shown in Fig. 1(a). It consists of a pair of metal patches with lateral displacement d_x, separated by a dielectric spacer of thickness t. The dielectric spacer used

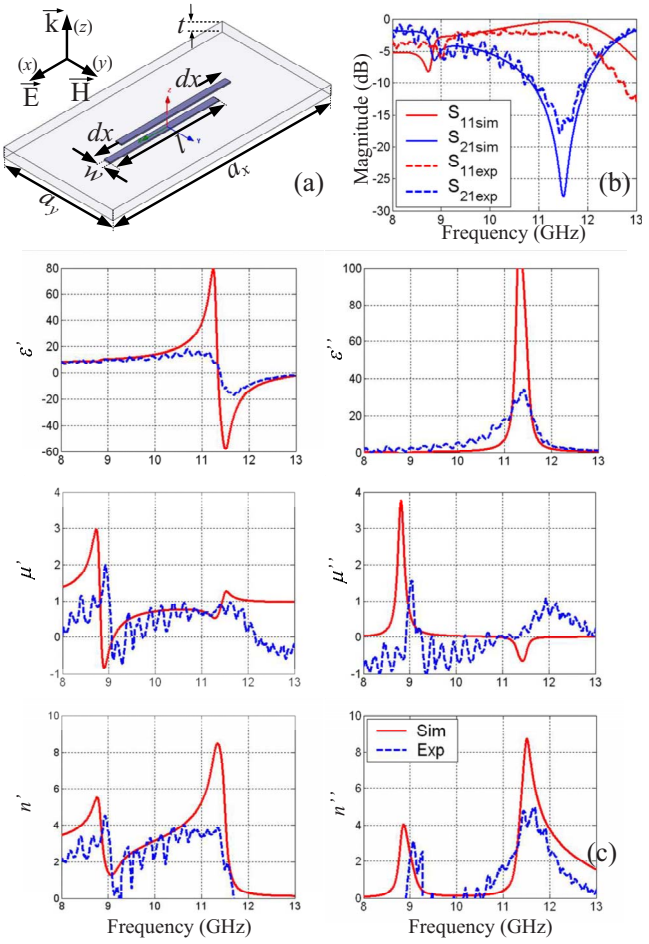

FIG. 1. (Color online) (a) Schematic representing the unit cell of the cut wires metamaterial where d_x denotes the lateral displacement of the wires. (b) Computed and measured reflection and transmission coefficients for symmetrical cut wire pairs materials (d_x=0). (c) Computed and measured effective parameters for d_x=0.

[a]Electronic mail: nawaz.burokur@u-psud.fr.
[b]Electronic mail: andre.de-lustrac@u-psud.fr.

throughout this study is epoxy with a relative dielectric constant of 3.9, a tangential loss of 0.02, and a thickness of 1.2 mm. For the samples reported in this letter, the length of the 35 μm thick copper wires is l=9.5 mm and the width is w=0.3 mm in both simulations and experiments. For the unit cell, a_x=19 mm and a_y=9.5 mm. Total sample size is 10×5 cells on a 120×120 mm^2 dielectric board. These dimensions have been optimized to operate around 10 GHz. To examine the performances of cut wire pairs, the properties of the structure of Fig. 1(a) are characterized numerically using finite element method simulations done with Ansoft's commercial electromagnetic solver HFSS.[19] For an electromagnetic wave incident with a wave vector and field polarization of Fig. 1(a), cut wire pairs will exhibit a magnetic resonance at the frequency f_m as well as an electric resonance at the frequency f_e. However, it is difficult to obtain a negative n with the symmetrical configuration (d_x=0 mm), since in this case f_e is well above f_m,[17,18] thus preventing ε and μ from being simultaneously negative. This is the main reason why the authors of Ref. 17 added the extra continuous wires so as to provide a Drude-model-like permittivity response.

Calculated reflection and transmission spectra of a single layer structure with lateral displacement d_x=0 mm are presented in Fig. 1(b). Microwave measurements based on the experimental setup described in Ref. 17 have been done on a fabricated prototype in an anechoic chamber using an Agilent 8722ES network analyzer and two 2–18 GHz wideband band horn antennas. Phase referencing and normalization have been performed in transmission by removing the sample from the signal path and, in reflection, by replacing the sample with a copper plate. Measured reflection and transmission coefficients are compared to the simulated ones in Fig. 1(b). There is very good qualitative agreement between simulations and measurements. Calculated and measured magnitudes of S_{21} show clearly two resonance dips, one at 8.9 GHz and another one at 11.5 GHz.

Using reflection and transmission responses from a single bilayered sample, effective parameters can be extracted using the retrieval procedure described elsewhere.[20] This is possible since the structure period along the propagation direction is very small compared to the working wavelength. In performing the retrieval, we assume a z-direction size a_z=1.27 mm corresponding to the total thickness of the dielectric spacer and the copper wires. Extracted permittivity ε, permeability μ, and refractive index n are shown in the various parts of Fig. 1(c). The lower resonance dip corresponds to the magnetic resonance at f_m=8.9 GHz, whereas the higher one corresponds to the electric resonance at f_e =11.5 GHz. At the magnetic resonance the two wires sustain antiparallel currents, producing a magnetic field mainly confined between the wires, which is directed opposite to the external one and exhibiting negative values for μ. As can be observed, f_m is well below the electric resonance f_e and the frequency bands of the two resonances do not overlap to produce a negative index. In order to observe a negative index, the magnetic resonance must lie at a frequency equal to or slightly above the electric resonance so that μ and ε are simultaneously negative. With the bilayered cut wire pairs acting as an LC resonator, the magnetic resonance frequency can then be expressed as $f_m=1/2\pi\sqrt{LC_m}$, while the electric resonance frequency is expressed as $f_e=1/2\pi\sqrt{LC_e}$.[18] L is the total inductance of the parallel wires, C_m corresponds to the capacitance created between the upper and lower halves of the cut wire pairs, and C_e is the equivalent capacitance between two neighboring wire pairs. Both resonances correspond to different electric charge configurations as shown in Figs. 2(a) and 2(b). For the magnetic resonance, the upper and lower wires carry electrical charge with opposite signs and the equivalent capacitance C_m is then concentrated between the overlapping section of the wires. At the electrical resonance, upper and lower wires carry electrical charge with the same sign leading to an equivalent capacitance C_e between neighboring cells. Thus, C_m depends strongly on wires overlapping surface on each face of the dielectric spacer. To increase the magnetic resonance frequency, one must necessarily decrease the capacitance C_m. The simplest way to do so is to displace laterally the wires and hence break the symmetry of the structure such that a smaller overlapping surface of the wires is considered for the calculation of C_m. However, the lateral displacement leads also to an increase in C_e since the distance d_1 between neighboring wire pairs on two consecutive cells decreases [Fig. 2(b)]. Consequently, breaking the symmetry of the cut wire pairs causes a shift toward higher and lower frequencies for, respectively, the magnetic and electric resonances. The impact of breaking the symmetry of cut wires pairs on the magnetic and electric resonances is clearly shown in Fig. 2(c) by calculations performed for d_x=0, 0.5, 1, and 2 mm. A shift toward high and low frequencies can be observed for f_m and f_e, respectively, when d_x increases. For d_x=0, 0.5, and 1 mm, it can be noted that f_m, corresponding to the lower frequency dip, is still lower than f_e, indicating that no negative refractive index will be ob-

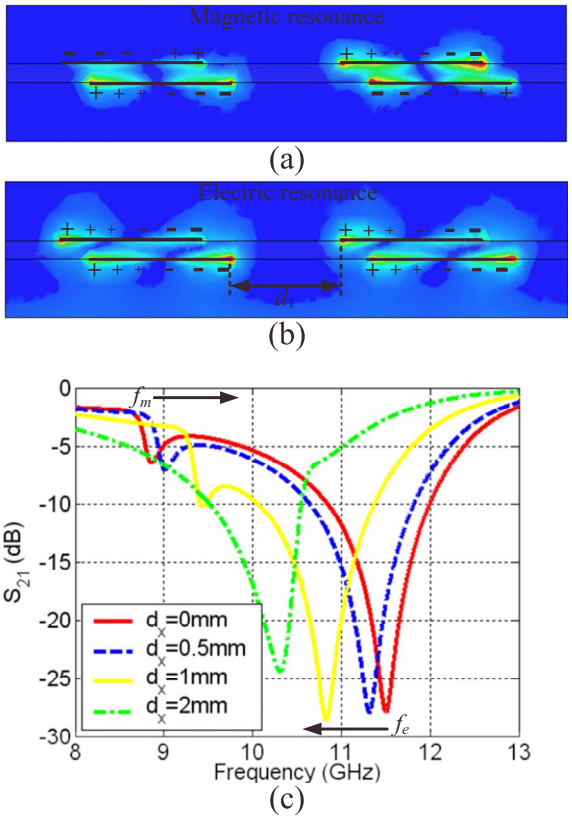

FIG. 2. (Color online) **E**-field cartography at the magnetic (a) and electric (b) resonances. (c) Computed transmission coefficients of the cut wire pairs materials for d_x=0, 0.5, 1, and 2 mm. The arrows show the shift of f_m and f_e when d_x increases.

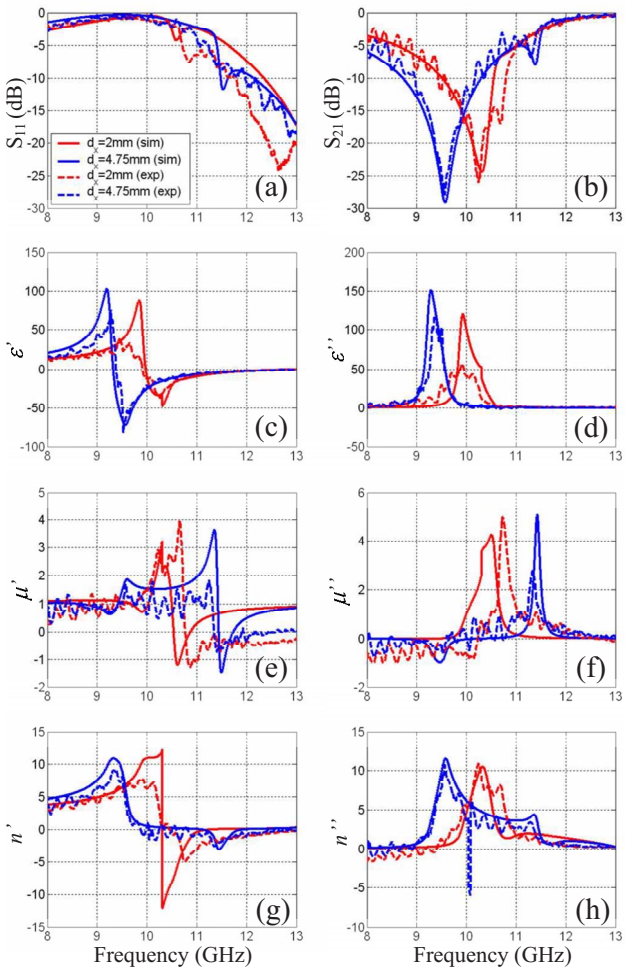

FIG. 3. (Color online) Computed and measured performances of asymmetrical cut wire pairs metamaterials for d_x=2 mm and d_x=4.75 mm. (a) S_{11} (dB). (b) S_{21} (dB). [(c)–(h)] Effective parameters.

tained. Conversely for d_x=2 mm, we can observe that the electric resonance is lower in frequency than the magnetic one though the two resonances are very close. In this case and also for higher values of d_x, a negative n can then be expected.

To validate this interpretation, various samples of different $d_x \geq 2$ mm have been simulated, fabricated, and measured. We shall note that in the symmetry breaking procedure each wire is laterally displaced by d_x in antiparallel directions. Therefore, the maximum value of d_x, when l=9.5 mm while keeping a_x=19 mm, is $(a_x - l)/2$ =4.75 mm. Chosen values for d_x are 2 and 4.75 mm. The performances are plotted in the various parts of Fig. 3.

As the symmetry of the metamaterial structure is broken, the overlapping surface of the wires decreases leading to a decrease in the capacitance C_m created between the upper and lower halves of the wire pairs. As can be observed from the computations and measurements of the reflection and transmission spectra in Figs. 3(a) and 3(b), respectively, this reduced capacitance results in a shift of the magnetic resonance dip toward high frequencies. Hence, the negative permeability frequency band is shifted toward higher frequencies as can be seen in Figs. 3(e) and 3(f). With the lateral displacement, the distance d_1 between the wires on opposite faces from two consecutive unit cells [Fig. 2(b)] tends to decrease. Therefore, the capacitance C_e at the edges of the wires on the two faces increases. This capacitance C_e accounts mainly for the electric resonance which then shifts toward lower frequencies [Figs. 3(a)–3(d)]. The electric resonances are then located at lower frequencies than the magnetic ones leading to a frequency band where ε and μ are simultaneously negative. The performances obtained from the microwave measurements agree very well with the numerical simulations. For these two configurations of d_x presented, a negative refractive index is obtained [Figs. 3(g) and 3(h)] since the magnetic resonance lies in the frequency region where the permittivity ε is negative.

In summary, we presented an experimental demonstration of a negative refractive index from metamaterials composed of only cut wire pairs in the microwave domain. The $n<0$ can only be achieved under the condition that the magnetic resonance lies at a frequency equal to or slightly above the electric resonance. This condition has been made possible by breaking the symmetry of the conventional cut wire pairs metamaterials previously presented in literature. An overlap between the frequency regions corresponding to a negative permittivity and a negative permeability is then accomplished.

[1]R. A. Shelby, D. R. Smith, and S. Schultz, Science **292**, 77 (2001).
[2]T. J. Yen, W. J. Padilla, N. Fang, D. C. Vier, D. R. Smith, J. B. Pendry, D. N. Basov, and X. Zhang, Science **303**, 1494 (2004).
[3]D. R. Smith, J. B. Pendry, and M. C. K. Wiltshire, Science **305**, 788 (2004).
[4]S. Linden, C. Enkrich, M. Wegener, J. Zhou, T. Koschny, and C. M. Soukoulis, Science **306**, 1351 (2004).
[5]S. Zhang, W. Fan, B. K. Minhas, A. Frauenglass, K. J. Malloy, and S. R. J. Brueck, Phys. Rev. Lett. **94**, 037402 (2005).
[6]V. G. Veselago, Sov. Phys. Usp. **10**, 509 (1968).
[7]U. Leonhardt, Science **312**, 1777 (2006).
[8]J. B. Pendry, D. Schurig, and D. R. Smith, Science **312**, 1780 (2006).
[9]D. Schurig, J. J. Mock, B. J. Justice, S. A. Cummer, J. B. Pendry, A. F. Starr, and D. R. Smith, Science **314**, 977 (2006).
[10]W. Cai, U. K. Chettiar, A. V. Kildishev, and V. M. Shalaev, Nat. Photonics **1**, 224 (2007).
[11]B. Kanté, A. de Lustrac, J.-M. Lourtioz, and S. Burokur, Opt. Express **16**, 9191 (2008).
[12]J. B. Pendry, Phys. Rev. Lett. **85**, 3966 (2000).
[13]V. M. Shalaev, W. Cai, U. K. Chettiar, H. K. Yuan, A. K. Sarychev, V. P. Drachev, and A. V. Kildishev, Opt. Lett. **30**, 3356 (2005).
[14]J. B. Pendry, A. J. Holden, D. J. Robbins, and W. J. Stewart, IEEE Trans. Microwave Theory Tech. **47**, 2075 (1999).
[15]V. M. Shalaev, Nat. Photonics **1**, 41 (2007).
[16]G. Dolling, C. Enkrich, M. Wegener, J. F. Zhou, C. M. Soukoulis, and S. Linden, Opt. Lett. **30**, 3198 (2005).
[17]J. Zhou, L. Zhang, G. Tuttle, T. Koschny, and C. M. Soukoulis, Phys. Rev. B **73**, 041101(R) (2006).
[18]J. Zhou, E. Economou, T. Koschny, and C. M. Soukoulis, Opt. Lett. **31**, 3620 (2006).
[19]High Frequency Structure Simulator v. 11, Ansoft Ltd.
[20]D. R. Smith, S. Schultz, P. Markos, and C. M. Soukoulis, Phys. Rev. B **65**, 195104 (2002).

Annexe 2.4

S. N. Burokur, T. Lepetit, A. de Lustrac

« Incidence dependence of negative index in asymmetric cut wire pairs metamaterials »

Applied Physics Letters, vol. 95, no. 19 (191114), November 2009

Incidence dependence of negative index in asymmetric cut wire pairs metamaterials

Shah Nawaz Burokur,[a] Thomas Lepetit,[b] and André de Lustrac[c]
IEF, Univ. Paris-Sud, CNRS, UMR 8622, 91405 Orsay Cedex, France

(Received 17 July 2009; accepted 23 October 2009; published online 12 November 2009)

Metamaterials made of asymmetric cut wire pairs have experimentally demonstrated a negative refractive index at microwave frequencies. In this letter, we begin by presenting the analogy between asymmetric cut wire pairs and S-shaped metamaterials by a simple unifying approach. Then, using simulations and experiments in the microwave domain, we investigate the dependence of resonances and retrieved effective index on the incident angle in asymmetric cut wire pairs. While it is found that resonances shift in frequency with increasing oblique incidence in the E-plane, it is shown that the structure is angle-independent in the H-plane. © *2009 American Institute of Physics*. [doi:10.1063/1.3263730]

In the past few years there has been ample experimental proof of the existence of negative index metamaterials (NIMs) in the gigahertz frequency range.[1–3] Due to their unusual electromagnetic properties[4] these microstructured metamaterials have made relevant a wide array of interesting applications such as invisibility cloaks,[5–9] perfect lenses,[10] and directive antennas.[11–13] However, despite the boom in metamaterial research, most NIM implementations so far have relied on the topology proposed by Pendry, namely, split ring resonators[14] (SRRs), providing the negative permeability μ and continuous wires,[15] providing the negative ε. Lately, symmetric pairs of finite-length wires or cut wire pairs[16] working under normal to plane propagation, unlike SRRs, have been shown to be able not only to replace conventional SRRs but also to lead to a negative refractive index n in the optical regime. In other related works on slightly different cut wire pairs, continuous wires have been added to obtain a negative index in the microwave domain.[17] Zhou *et al.*[18] also theoretically proposed a left-handed material using only cut wire pairs by increasing the equivalent capacitance between two consecutive short wire pairs so as to adjust the electric resonance frequency. Very recently, we have experimentally demonstrated in the microwave domain that breaking the symmetry of cut wire pairs leads to a detuning of the resonances such that there is overlapping between negative μ and ε.[19] A negative refractive index has been experimentally verified from a prism-shaped bulk metamaterial made of asymmetric cut wire pairs.[20] Another structure composed of asymmetric cut wires[21] has been proposed for negative index by considering the fact that displacement currents inside a dielectric resonator[22,23] can be imitated by conductive currents.

It is our aim in this letter to show the similarity between previously proposed S-shaped resonator[24] and asymmetric cut wire pairs, presented in Refs. 19 and 20, by a simple unifying approach. These two structures constitute good alternatives to conventional SRR-based NIMs. Then, we investigate numerically and experimentally the reflection and transmission spectra for an obliquely incident plane wave on the asymmetric structure. It is reported that a diffraction threshold appears in E-plane (plane containing vectors E and k), that is the $(-1,0)$ mode starts to propagate. Besides, resonances in E-plane shift in frequency with increasing oblique incidence. However in H-plane (plane containing vectors H and k), the structure is diffractionless and independent of the incidence, and therefore the negative index is maintained in a wide angular range. These statements are verified numerically and experimentally in the microwave domain.

The unit cell structure of the S-shaped resonator is shown in Fig. 1(a). In contrast to Ref. 24 where double-sided S is used, here we study only single-sided resonator, which is also different from the single-sided S-rings pair presented in Ref. 25. By continuous transformation, diminishing the length of the z-oriented wires, it can be reduced to a pair of asymmetric metal cut wire separated by a dielectric spacer of thickness t.[19,20] In Figs. 1(b) and 1(c) the view in the (E,k) plane of this structure is shown. Besides its simplicity, the design shown in Figs. 1(b) and 1(c) has distinct advantages over conventional SRR-based NIMs. The incident electromagnetic wave is normal to the structure enabling the fabrication of NIMs with a single layer of sample. Conventional SRRs, although they exhibit magnetic resonance that may lead to negative μ, fail to give negative ε at the same frequency range; hence they are unable of producing NIMs by themselves. Extra continuous wires are needed to obtain negative ε via a plasmonic response.[1,15] In contrast, pairs of cut wires in Fig. 1(c) are expected to exhibit not only a magnetic resonance (antisymmetric mode) but also an elec-

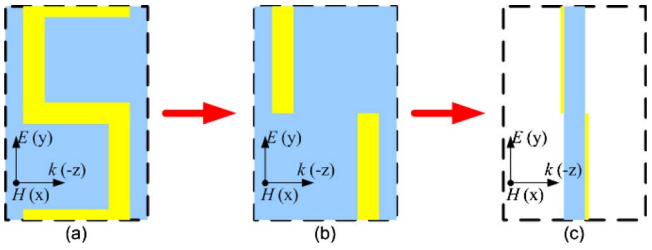

FIG. 1. (Color online) The S-shaped resonator (a) can be transformed to a pair of asymmetric parallel metallic cut wires separated by a dielectric; (b) and (c) view in (E,k) plane.

[a]Present address: LEME EA 4416, Université Paris-Ouest, 50 rue de Sèvres, 92410 Ville d'Avray, France. Electronic mail: sburokur@u-paris10.fr.
[b]Present address: Institut Langevin, ESPCI ParisTech, 10 rue Vauquelin, 75005 Paris. Electronic mail: thomas.lepetit@espci.fr.
[c]Electronic mail: andre.de-lustrac@u-psud.fr.

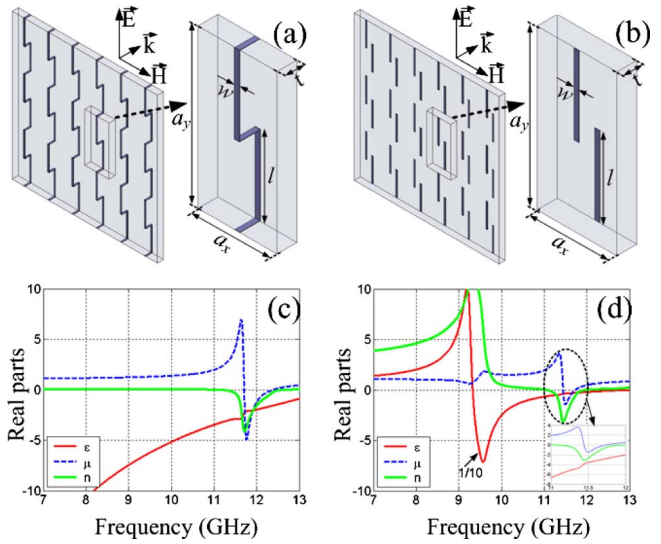

FIG. 2. (Color online) Schematic representing the unit cell of (a) S-shaped resonator, and (b) asymmetric cut wire pairs metamaterial arranged in a square lattice. [(c) and (d)] Computed effective ε, μ and n.

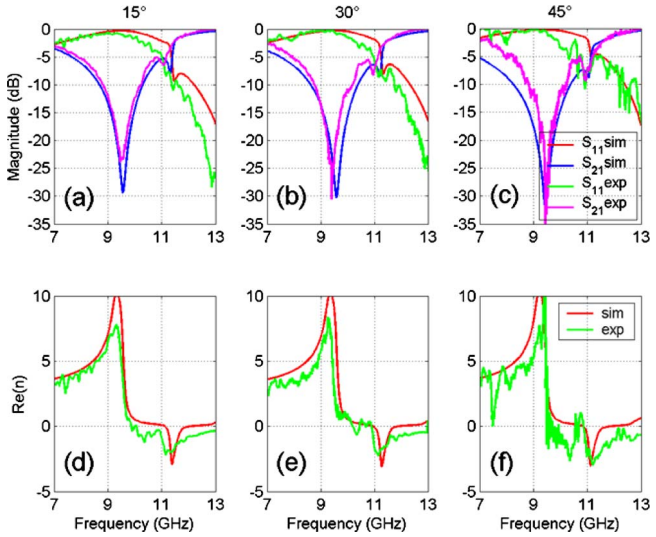

FIG. 3. (Color online) Oblique incidence (15°, 30°, and 45°) in H-plane. (a)-(c) Computed and measured reflection and transmission coefficients. (d)-(f) Real part of effective index n.

tric resonance (symmetric mode), which when properly designed, result in a frequency overlap of negative μ and ε.[19,20]

The dielectric spacer used throughout this study is epoxy with a relative dielectric constant of 3.9, a loss tangent of 0.02, and a thickness of 1.2 mm. For samples reported in this letter, the length of the 35 μm thick copper wires is l =9.5 mm and the width is w=0.3 mm, in both simulations and experiments. For the unit cell, periods along x and y are, respectively, a_x=4.75 mm for the S resonator and 9.5 mm for the cut wire pairs and a_y=9.5 mm for both, as shown in Figs. 2(a) and 2(b). These dimensions have been designed to operate around 10 GHz. To analyze performances of cut wire pairs, properties of the structure are characterized numerically using finite element method simulations done with Ansoft's commercial electromagnetic solver HFSS.[26] Reflection and transmission spectra of S-shaped resonators and asymmetric cut wire pairs arranged in a square lattice with their respective polarization as shown in Figs. 2(a) and 2(b) are calculated from a single bilayered sample. Effective parameters can then be extracted from these responses using a retrieval procedure described elsewhere.[27] This is possible since the period along the propagation direction is very small compared to the working wavelength. Extracted permittivity ε, permeability μ, and index n are shown in Figs. 2(c) and 2(d). These results show the similarity between S-shaped resonator and our asymmetric cut wire pairs. To compare with the S-shaped metamaterial, the cut wire pairs present a strong resonance instead of a Drude-model-like permittivity response since there exists no electrical contact between consecutive wires.

Further investigations on asymmetric cut wire pairs, particularly on the dependence of resonances and retrieved parameters on the incident angle θ, are performed in this study. Three different angles, namely, 15°, 30°, and 45° in both H- and E-planes of the square lattice, are studied in simulations and experiments. Microwave measurements based on the experimental setup described in Ref. 17 are done on a fabricated prototype in an anechoic chamber using an Agilent 8722ES network analyzer and two 2–18 GHz wideband horn antennas. Phase referencing and normalization are performed in transmission by removing the sample from the signal path, and in reflection, by replacing the sample with a perfectly reflecting copper plate of similar size.

Measured reflection and transmission coefficients are compared to simulated ones in Fig. 3 for the H-plane. There is qualitative agreement between simulations and measurements. Calculated and measured magnitudes of S_{21} show clearly two resonance dips, an electric one at 9.5 GHz and a magnetic one at 11.5 GHz. These two resonances are found to be independent of the incidence angle in the H-plane as shown in Figs. 3(a)–3(c).

To retrieve effective parameters at oblique incidence, the retrieval procedure in Ref. 27 has to be modified and anisotropy has to be addressed. Indeed cut wire pairs represent a biaxial anisotropic media whose principal axis are along x, y, and z. Consequently 2×2 transfer matrices used in normal incidence are no longer sufficient and the full 4×4 transfer matrix accounting for coupling of s- and p-waves should be considered.[28] However, since the electric field in our case is always along y independently of θ, cross-polarization terms do not arise and therefore we only use one 2×2 transfer matrix for s-waves. In this case the effective index is given by $\varepsilon_y\mu_x\mu_z/\mu_z\cos^2\theta+\mu_x\sin^2\theta$. We shall note that this is similar to the waveguide procedure presented in Ref. 29 where the μ_z component is also retrieved. Figures 3(d)–3(f) show that n responses remain mostly unchanged compared to the 0° case studied in Refs. 19 and 20.

Measured reflection and transmission coefficients are compared to simulated ones in Figs. 4(a)–4(c) for the E-plane. Apart from one sharp feature on each spectrum, simulations and measurements agree qualitatively. This peak, which is much sharper than either the antisymmetric or the symmetric resonance, shifts with incidence angles from 12.47 GHz at 15° to 10.5 GHz at 30° and 9.22 GHz at 45°. It is the manifestation on the specular order (0,0) of a diffraction threshold, namely, that of the (0,−1) diffracted order.[30] At these frequencies the (0,−1) diffracted order transits from evanescent to propagating, appearing at grazing incidence. Diffraction thresholds frequencies are calculated in two ways, with HFSS and using Eq. (1) from grating theory taking into account the fact that there is no wave vector component along x in E-plane,[30]

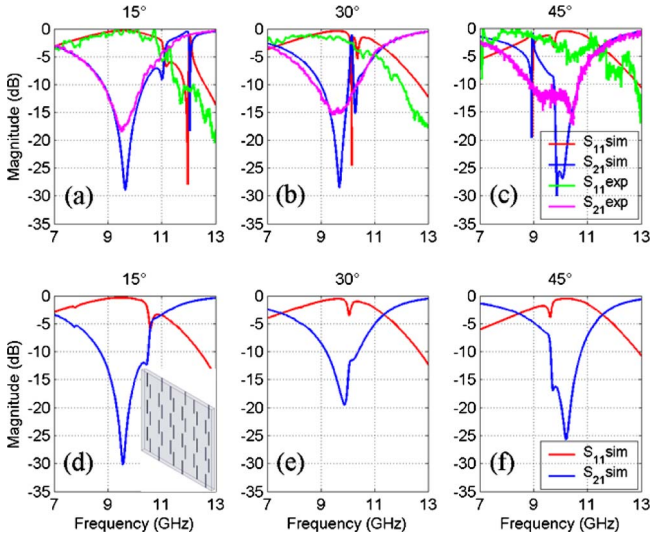

FIG. 4. (Color online) Oblique incidence (15°, 30° and 45°) in E-plane. [(a)–(c)] Computed and measured reflection and transmission coefficients for the square lattice. [(d)–(f)] Computed reflection and transmission coefficients for the triangular lattice. The inset in (d) shows the triangular lattice.

$$k_{\perp} = \pm \sqrt{\frac{\omega^2}{c^2}\varepsilon_r - k_{\parallel}^2} = \pm \sqrt{\frac{\omega^2}{c^2}\varepsilon_r - \left(m\frac{2\pi}{a_x}\right)^2 - \left(\frac{\omega}{c}\sin\theta + n\frac{2\pi}{a_y}\right)^2} \quad m,n \in Z. \tag{1}$$

Due to respective values of $a_x = 9.5$ mm and $a_y = 19$ mm, it can be seen that the $(0,-1)$ order is the first diffracted order to become propagating. Results for diffraction thresholds frequencies are summarized in Table I. By comparison, in the H-plane even at an angle of 45° the $(0,-1)$ diffracted order is above 18 GHz. To overcome the appearance of a diffraction threshold, a triangular lattice as shown in the inset of Fig. 4(d) is proposed to replace the square one presented in Fig. 2(b). In the triangular lattice, every other cell along x is laterally displaced by 4.75 mm along y. In this lattice, diffraction thresholds frequencies are given by Eq. (2),

$$k_{\perp} = \pm \sqrt{\frac{\omega^2}{c^2}\varepsilon_r - k_{\parallel}^2} = \pm \sqrt{\frac{\omega^2}{c^2}\varepsilon_r - \left((2m-n)\frac{2\pi}{a_x}\right)^2 - \left(\frac{\omega}{c}\sin\theta + n\frac{2\pi}{a_y}\right)^2} \quad m,n \in Z. \tag{2}$$

Computed reflection and transmission spectra presented in Figs. 4(d)–4(f) confirm the rejection of the diffraction threshold above 13 GHz. Besides, a shift in frequency can be noted for both antisymmetric and symmetric resonances. This shift is seen to be much stronger than for any resonances in the H-plane and the detuning of both electric and magnetic resonances with respect to the incidence angle θ leads to a loss of the frequency overlap, hence the negative index, above 20°. As it can be noted particularly for $\theta = 15°$, the magnetic resonance shifts toward lower frequencies for the triangular lattice (10.43 GHz) compared to the square one (11.02 GHz). This is most probably due to extra capacitive coupling between y-displaced wires on same face of the dielectric board.

TABLE I. Computed numerical and analytical diffraction threshold frequencies (GHz).

	HFSS (square lattice)	Grating (square lattice)	HFSS (triangular lattice)	Grating (triangular lattice)
	Mode (0, −1)	Mode (0, −1)	Mode (0, −1)	Mode (0, −1)
$\theta=0°$	15.78	15.79	22.31	22.33
$\theta=15°$	12.58	12.54	19.15	19.15
$\theta=30°$	10.54	10.53	17.31	17.32
$\theta=45°$	9.24	9.25	16.35	16.35

In summary, we presented the dependence of resonances and retrieved effective index on the incident angle in recently proposed asymmetric cut wire pairs. No change has been observed for oblique incidence in the H-plane. However for the E-plane, a diffraction threshold appears for the square lattice rendering the introduction of effective parameters meaningless. A triangular lattice has therefore been proposed to avoid having the diffraction threshold below the electric and magnetic resonances. A detuning of both resonances has been observed leading to a lack of resonance frequencies overlap above 20°. In conclusion, asymmetric cut wire pairs have been shown to possess a negative index in a wide angular range around normal incidence.

[1] D. R. Smith, W. J. Padilla, D. C. Vier, S. C. Nemat-Nasser, and S. Schultz, Phys. Rev. Lett. **84**, 4184 (2000).
[2] D. R. Smith and N. Kroll, Phys. Rev. Lett. **85**, 2933 (2000).
[3] R. A. Shelby, D. R. Smith, and S. Schultz, Science **292**, 77 (2001).
[4] V. G. Veselago, Sov. Phys. Usp. **10**, 509 (1968).
[5] U. Leonhardt, Science **312**, 1777 (2006).
[6] J. B. Pendry, D. Schurig, and D. R. Smith, Science **312**, 1780 (2006).
[7] D. Schurig, J. J. Mock, B. J. Justice, S. A. Cummer, J. B. Pendry, A. F. Starr, and D. R. Smith, Science **314**, 977 (2006).
[8] W. Cai, U. K. Chettiar, A. V. Kildishev, and V. M. Shalaev, Nat. Photonics **1**, 224 (2007).
[9] B. Kanté, A. de Lustrac, J.-M. Lourtioz, and S. Burokur, Opt. Express **16**, 9191 (2008).
[10] J. B. Pendry, Phys. Rev. Lett. **85**, 3966 (2000).
[11] S. N. Burokur, M. Latrach, and S. Toutain, IEEE Antennas Wireless Propag. Lett. **4**, 183 (2005).
[12] R. W. Ziolkowski, IEICE Trans. Electron. **E89-C**, 1267 (2006).
[13] P.-H. Tichit, S. N. Burokur, and A. de Lustrac, J. Appl. Phys. **105**, 104912 (2009).
[14] J. B. Pendry, A. J. Holden, D. J. Robbins, and W. J. Stewart, IEEE Trans. Microwave Theory Tech. **47**, 2075 (1999).
[15] J. B. Pendry, A. J. Holden, W. J. Stewart, and I. Youngs, Phys. Rev. Lett. **76**, 4773 (1996).
[16] V. M. Shalaev, W. Cai, U. K. Chettiar, H. K. Yuan, A. K. Sarychev, V. P. Drachev, and A. V. Kildishev, Opt. Lett. **30**, 3356 (2005).
[17] J. Zhou, L. Zhang, G. Tuttle, T. Koschny, and C. M. Soukoulis, Phys. Rev. B **73**, 041101(R) (2006).
[18] J. Zhou, E. Economou, T. Koschny, and C. M. Soukoulis, Opt. Lett. **31**, 3620 (2006).
[19] S. N. Burokur, A. Sellier, B. Kanté, and A. de Lustrac, Appl. Phys. Lett. **94**, 201111 (2009).
[20] A. Sellier, S. N. Burokur, B. Kanté, and A. de Lustrac, Opt. Express **17**, 6301 (2009).
[21] Z. Wang, D. Wang, T. Jiang, L. Peng, J. Huangfu, and L. Ran, Appl. Phys. Lett. **94**, 231905 (2009).
[22] L. Peng, L. Ran, H. Chen, H. Zhang, J. A. Kong, and T. M. Grzegorczyk, Phys. Rev. Lett. **98**, 157403 (2007).
[23] T. Lepetit, E. Akmansoy, M. Paté, and J.-P. Ganne, Electron. Lett. **44**, 1119 (2008).
[24] H. Chen, L. Ran, J. Huangfu, X. Zhang, K. Chen, T. M. Grzegorczyk, and J. A. Kong, Phys. Rev. E **70**, 057605 (2004).
[25] D. Wang, L. Ran, H. Chen, M. Mu, J. A. Kong, and B.-I. Wu, Appl. Phys. Lett. **90**, 254103 (2007).
[26] High Frequency Structure Simulator v11, Ansoft Ltd.
[27] D. R. Smith, S. Schultz, P. Markos, and C. M. Soukoulis, Phys. Rev. B **65**, 195104 (2002).
[28] P. Yeh, *Optical Waves in Layered Media* (Wiley, New York, 1998).
[29] H. Chen, J. Zhang, Y. Bai, Y. Luo, L. Ran, Q. Jiang, and J. A. Kong, Opt. Express **14**, 12944 (2006).
[30] R. Petit, *Electromagnetic Theory of Gratings* (Springer, Berlin, 1980).

Annexe 2.5

A. Dhouibi, S. N. Burokur, A. de Lustrac, A. Priou

« Z-shaped meta-atom for negative permittivity metamaterials »

Applied Physics A : Materials Science & Processsing, vol. 106, no. 1, pp. 47-51, January 2012

Appl Phys A (2012) 106:47–51
DOI 10.1007/s00339-011-6673-9

Applied Physics A
Materials Science & Processing

Z-shaped meta-atom for negative permittivity metamaterials

Abdallah Dhouibi · Shah Nawaz Burokur · André de Lustrac · Alain Priou

Received: 4 August 2011 / Accepted: 3 November 2011 / Published online: 1 December 2011

Abstract A printed Z-shaped electric meta-atom is presented as an alternative design to the conventional electric-LC (ELC) resonator. We propose an easy way to redesign the ELC resonator pattern to get a compact and a low cost electric resonator exhibiting a strong electric response. Our approach involves, in the effective medium regime, redressing the resonator shape to accommodate higher inductance and lead to a lower resonance frequency without being limited by fabrication tolerances. The electromagnetic behaviour of the meta-atom has been investigated through both simulations and experiments in the microwave regime. Our results show that the Z meta-atom exhibits an electric response to normally incident radiation and can be used very effectively in producing materials with negative permittivity. The proposed planar meta-atom can find various applications in high frequency passive circuits which are designed in planar technology. Moreover, the proposed structure can be scaled to much higher frequencies via appropriate lithographic scaling.

1 Introduction

Metamaterials have recently attracted considerable interests [1–3] because of their capabilities which go beyond conventional materials [4] and because of their applications in novel class coordinate transformation based devices such as invisibility cloaks [5–9], rotators [10], retroreflectors, [11] Luneberg lenses [12, 13] and directive antennas [14–16]. A typical metamaterial is an artificial composite material made of a periodic array of subwavelength inclusions called meta-atoms. These inclusions are equivalent to LC resonant elements with the inductance and capacitance greatly influenced by the geometrical shape and dimensions. Various forms of meta-atoms such as Split Ring Resonator [17] or electric-LC (ELC) resonator [18] have been shown to be able to produce, respectively, a wide range of permeability or permittivity values in the vicinity of the resonance. In order to use such resonators in the effective medium regime, the ratio between the operating wavelength and the unit cell size must be greater than 4 [19]. Different approaches have been proposed to increase the latter ratio with the main goal to shift downwards the resonance frequency of the meta-atoms. For example, a classic method consists of changing the feature dimensions of the structure, i.e., shorten the gaps or lengthen the wires so as to increase the capacitance and inductance. However, such attempt is very limited according to the fabrication technology and can be a severe problem when we move to higher frequencies.

It is our aim in this paper to investigate numerically and experimentally the electromagnetic properties of a Z-shaped meta-atom in the microwave regime. It is reported that the structure presents an electric resonance which occurs at a lower frequency than that presented by the ELC resonator for similar geometrical dimensions. This experimental demonstration of negative real part of ε from the proposed structure shows the potential usefulness of such structures in media with desired positive or negative permittivity. The simplicity of the design also suggests the practical feasibility of such resonators at much higher frequencies.

A. Dhouibi · S.N. Burokur (✉) · A. Priou
LEME, Univ. Paris-Ouest, EA 4416, 92410 Ville d'Avray, France
e-mail: sburokur@u-paris10.fr

A. Dhouibi
e-mail: a.dhouibi@u-paris10.fr

A. de Lustrac
IEF, Univ. Paris-Sud, CNRS, UMR 8622, 91405 Orsay Cedex, France

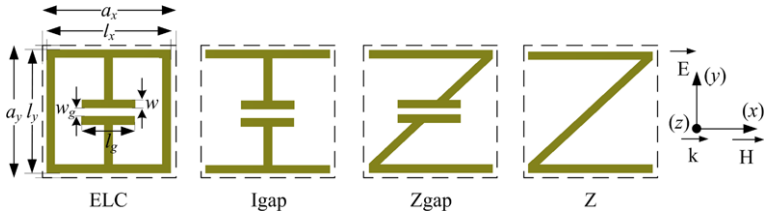

Fig. 1 (**a**) The ELC resonator. (**b**) Igap is derived from ELC by cancelling the side arms. (**c**) Zgap is obtained by using slant lines on each side of the gap. (**d**) Z-shaped resonator designed by removing the middle gap. For all the resonators, the geometrical dimensions are: $a_x = a_y = 6$ mm, $l_x = 5.7$ mm, $l_y = 5.8$ mm, $w = 0.3$ mm, $w_g = 0.45$ mm and $l_g = 2$ mm

2 Transformation of the ELC meta-atom

Let us first consider the unit cell of the ELC resonator introduced in Ref. [18] and presented in Fig. 1(a). This resonator has both inductive and capacitive elements, where only the capacitive element couples strongly to the electric field, inversely to Pendry's SRR where the inductive element couples to the external magnetic field. By continuous transformation, eliminating the y-oriented lateral wires, it can be reduced to an I-shaped resonator with a capacitive gap referred to as Igap resonator, as shown in Fig. 1(b). We shall note that by removing these two side arms, we reduce the inductance of the element. On the counterpart, we add a lateral gap on both sides of the initial middle one. However, the parallel capacitances created by the two lateral gaps are supposed to be negligible compared to the middle one, which suggests that the Igap resonator will show a higher resonant frequency than the ELC one. Furthermore, as shown in Fig. 1(c), without changing the lattice constant we compensate a part of the reduced inductance by transforming the Igap into a Zgap resonator. Adding physical length when passing from Igap to Zgap structure produces a higher phase delay and increases the total inductance of the metamaterial without requiring additional fabrication steps. Due to this increase in inductance, the Zgap resonator will present a resonance at a lower frequency. To facilitate the metamaterial fabrication process, we further transform the Zgap resonator into a Z-shaped one (Fig. 1(d)) by removing the capacitive gap.

3 Simulations and experimental verifications

To examine the performances of resonators presented in Fig. 1, the properties of the structures are characterized numerically using a Finite Difference Time Domain (FDTD) Maxwell's equations solver, Microwave Studio Suite by CST. A single unit cell is simulated together with necessary periodic boundary conditions. Floquet mode ports are used to launch an incident plane wave on the different resonators. This simulation method implies that an infinite array of resonators along x and y directions is simulated. However, fabricated prototypes will have finite dimensions and therefore small discrepancies can arise between calculations and measurements. The dielectric spacer used throughout this study is single face copper-cladded epoxy with a relative dielectric constant of 3.9, a tangential loss of 0.02 and a thickness $t_s = 0.4$ mm. For the samples reported in this paper, the length of the 17 μm thick copper wires along the x- and y-direction is, respectively, $l_x = 5.7$ mm and $l_y = 5.8$ mm and the width is $w = 0.3$ mm in both simulations and experiments. For the gaps present in the ELC, Igap and Zgap resonators, the width and length are, respectively, $w_g = 0.45$ mm and $l_g = 2$ mm. For the unit cell, $a_x = a_y = 6$ mm. Total sample size is 18×18 cells on a 120 mm $\times$ 120 mm dielectric board. For an electromagnetic wave incident with a wave vector and field polarization of Fig. 1, the different resonators will exhibit an electric resonance.

Calculated reflection and transmission spectra of a single layer structure are presented in Fig. 2. Microwave measurements based on the experimental setup described in Ref. [20] have been done on fabricated prototypes in an anechoic chamber using an Agilent 8722ES network analyzer and two standard FLANN® 2–18 GHz wideband band horn antennas serving as the source and the receiver. Phase referencing and normalization have been performed in transmission and reflection. In the transmission measurements, the microwaves are incident normal to the sample surface. Transmission measurements are calibrated to the transmission between the horns with the sample removed. The reflection measurements are done by placing the source and receiving horns on the same side of the sample and bouncing the microwave signal off the sample. The source and receiver horns are each inclined with an angle of about 4–5° with respect to normal on the sample surface. The reflection measurement is calibrated using a sample-sized sheet of copper as a reflecting mirror. In all measurements, the fields polarization illustrated in Fig. 1 is used. Measured reflection and transmission coefficients are compared to the simulated ones. There is a very good qualitative agreement between simulations and measurements. Calculated and measured magnitudes of S_{21} show clearly a resonance dip for each type of resonator, as

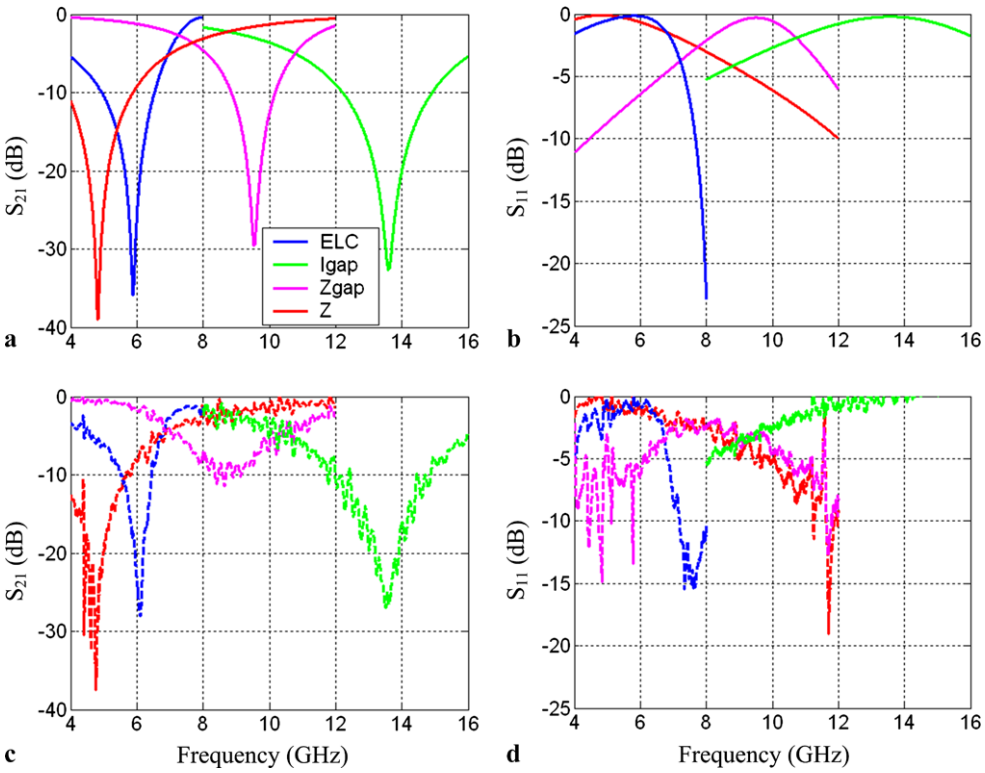

Fig. 2 Computed (**a**)–(**b**) and measured (**c**)–(**d**) transmission and reflection coefficients of the different resonators

Table 1 Computed and measured resonance frequencies of the resonators (GHz)

Resonator	Simulated f_0	Measured f_0	Effective medium ratio λ/a
ELC	5.9	6.0	8.3
Igap	13.6	13.6	3.7
Zgap	9.5	9.1	5.5
Z	4.9	4.9	10.2

summarized in Table 1. The Igap resonator presents a resonance frequency at 13.6 GHz, compared to 6.0 GHz for ELC. This shift toward higher frequencies was predictable since the inductance is greatly reduced when transforming ELC into Igap. To decrease the resonance frequency of Igap, we therefore increase its inductance by using slant lines on each side of the gap instead of vertical ones, therefore converting it to Zgap. This procedure causes a frequency downward shift of approximately 33%, which suggests that the capacitance created by the gap acts mainly to drive the LC resonance and that the LC resonance frequency is mainly based on the inductance of the structure. When cancelling the middle capacitive gap to design the Z-shaped resonator, the resonance frequency is considerably decreased. This is because two capacitances are connected in series in the Zgap structure as shown in Fig. 3. The first one noted C_1 is created between two consecutive cells due to the periodicity of the structure and the second one noted C_2 is formed by

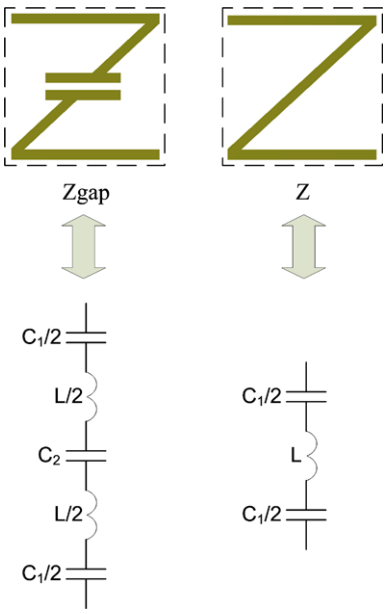

Fig. 3 An equivalent LC circuit model for the Zgap and Z meta-atoms where the capacitances created by the lateral gaps are neglected. C_1 and C_2 denote, respectively, the capacitance created due to the periodicity of the structure and the capacitance created by the gap. L is the inductance of the structure

the gap in the middle of the Z. We shall note that here, the capacitances created by the lateral gaps are neglected and therefore do not appear in the LC circuit model. The equivalent capacitance in the Zgap structure is then given

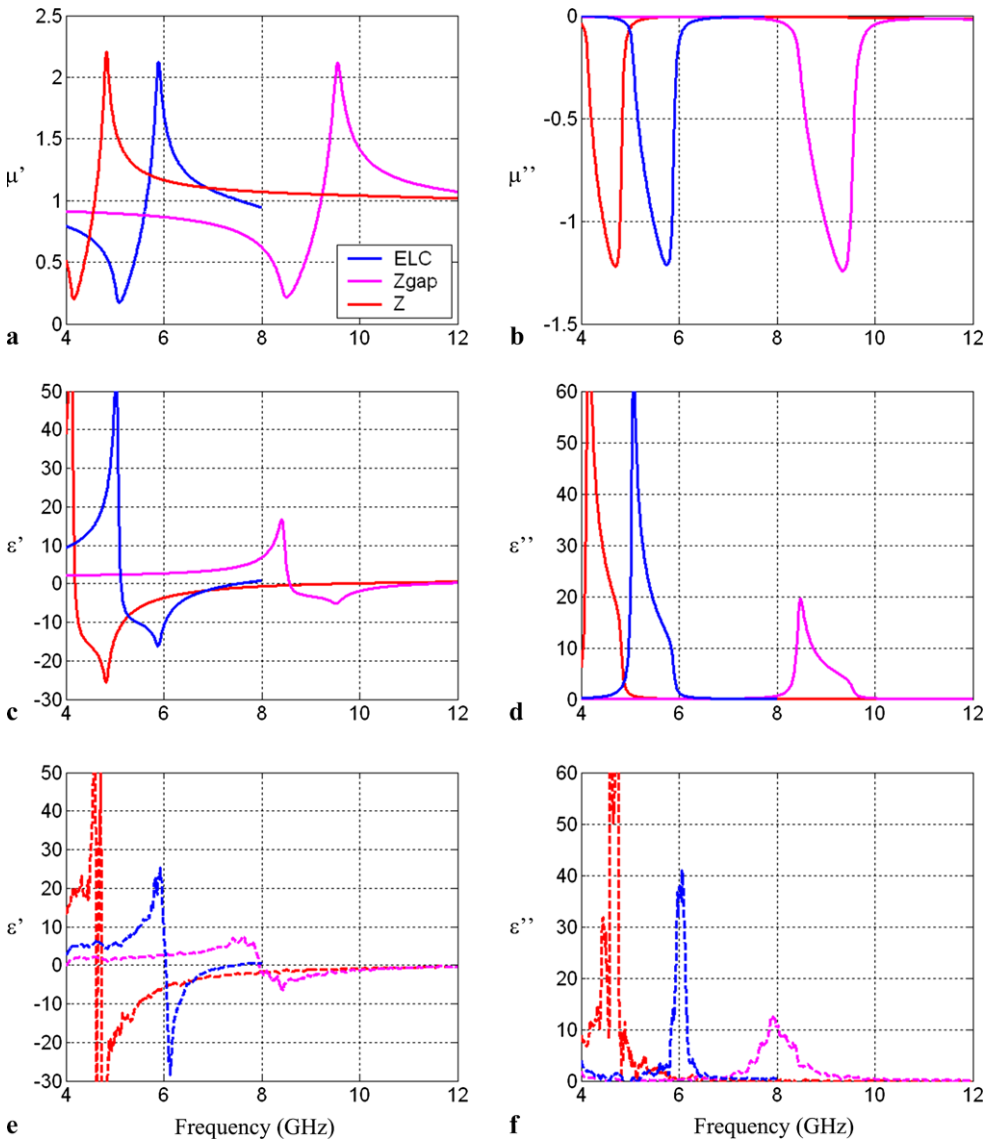

Fig. 4 Computed effective parameters: (**a**) Re(μ), (**b**) Im(μ), (**c**) Re(ε), and (**d**) Im(ε). Measured effective parameters: (**e**) Re(ε) and (**f**) Im(ε)

by $C_1C_2/(C_1+C_2)$. In the Z-shaped structure, only the capacitance C_1 between two consecutive cells is present. According to the dimensions w_g and l_g used for the gap, the capacitance of the latter (C_2) is almost half of the one created by the periodicity (C_1). Thus the resonance frequency of the Z is 1.8 times smaller than that of the Zgap, if we consider similar inductance in both structures. And finally, in terms of effective medium ratio λ/a, an improvement of 1.9 can be observed for the Z-shaped resonator compared to the conventional ELC.

The resonance frequency of the Z-shaped resonator is expressed as $f_r = \frac{1}{2\pi\sqrt{LC_1}}$ where the inductance [21] is approximated by $L \approx \mu_0 t_s(\frac{2w}{l_x} + \frac{\sqrt{l_x^2+l_y^2}}{w})$ and the inter-cell capacitance [17, 21] by $C_1 \approx \frac{\varepsilon l_x}{\pi} \ln(\frac{2w}{a_y - l_y})$. Circuit theory then predicts a resonance frequency equal to 5.2 GHz, which is in good agreement with the simulated and measured values. Further simulations performed on an ELC resonator with the capacitive gap removed have shown a resonance frequency of 13 GHz. This increase in frequency is explained by the fact the resonator becomes quasi-purely inductive and no current flows in the two loops conversely to the conventional ELC. Therefore, $\sqrt{LC}$ is smaller in the case of ELC without gap and thus its resonance frequency is higher. This trend in frequency is found to be opposite when comparing Zgap and Z resonators. This is because inter-cell capacitance plays an important role in the resonance of the Z-type resonators, but not in the ELC type resonators.

4 Parameters extraction

Using reflection and transmission responses from a single layer of the sample, effective parameters can be extracted

using the retrieval procedure described elsewhere [22]. This is possible since the structure period along the propagation direction is very small compared to the working wavelength. In performing the retrieval, we assume a z-direction size $a_z = 6$ mm corresponding to a cubic unit cell as proposed in Ref. [18]. Extracted permittivity ε and permeability μ are shown for ELC, Zgap and Z resonators in the various parts of Fig. 4. Concerning Igap resonator, parameters extraction is not possible since the ratio between the operating wavelength and the unit cell size, i.e. the effective medium ratio λ/a is low ($\sim$3.7). Real and imaginary parts of μ are, respectively, shown in Fig. 4(a) and 4(b). As stated above, the ELC resonator presents an electric response but no magnetic response, i.e., the real part of μ is close to unity over the frequencies of interest. However, the retrieved parameters do not strictly comply with this principle. As shown in Fig. 4(a), the real part of μ becomes anti-resonant. In fact, this anomaly is an artifact introduced during parameter extraction in a frequency range where the medium is highly spatially dispersive [18]. The Z and Zgap resonators present similar responses at, respectively, a lower and a higher resonant frequency. From Figs. 4(c)–4(f), we see a strong electric resonance, with the real part of the permittivity ranging from positive to negative values in the vicinity of the resonance. The values issued from measurement data agree very well with those calculated from numerical simulations. It must be noted that the extraction from the measured spectra are presented without any fitting. From the simulated and measured real parts of ε, it can also be noted that both Z-shaped meta-atoms (with and without gap) present a wider frequency band where the values are negative compared to the ELC resonator. The proposed Z-shaped resonator can be combined with a negative permeability metamaterial such as the SRR or MSRR [23, 24] in order to produce a negative index of refraction. It can also be very useful in applications where permittivity gradient is desired, such as in devices designed from transformation optics concept [5–16].

5 Conclusion

In summary, we have presented an experimental demonstration of a negative permittivity from a Z-shaped meta-atom in the microwave domain. This proposed electric resonator allows to considerably improve the effective medium ratio λ/a observed from a conventional electric LC (ELC) resonator. Due to the simplicity of the structure and the absence of capacitive gap, a transposition of geometrical parameters can be considered for the optical regime.

Acknowledgements This work was supported by the EADS Company Foundation through the METAQOPT project, contract No. 090-AO09-1006. One of the authors (A.D.) would like to acknowledge support for his PhD scholarship from EADS Company Foundation.

References

1. R.A. Shelby, D.R. Smith, S. Schultz, Science **292**, 77 (2001)
2. T.J. Yen, W.J. Padilla, N. Fang, D.C. Vier, D.R. Smith, J.B. Pendry, D.N. Basov, X. Zhang, Science **303**, 1494 (2004)
3. D.R. Smith, J.B. Pendry, M.C.K. Wiltshire, Science **305**, 788 (2004)
4. V.G. Veselago, Sov. Phys. Usp. **10**, 509 (1968)
5. U. Leonhardt, Science **312**, 1777–1780 (2006)
6. J.B. Pendry, D. Schurig, D.R. Smith, Science **312**, 1780 (2006)
7. D. Schurig, J.J. Mock, B.J. Justice, S.A. Cummer, J.B. Pendry, A.F. Starr, D.R. Smith, Science **314**, 977 (2006)
8. W. Cai, U.K. Chettiar, A.V. Kildishev, V.M. Shalaev, Nat. Photonics **1**, 224 (2007)
9. B. Kanté, A. de Lustrac, J.-M. Lourtioz, S. Burokur, Opt. Express **16**, 9191 (2008)
10. H. Chen, B. Hou, S. Chen, X. Ao, W. Wen, C.T. Chan, Phys. Rev. Lett. **102**, 183903 (2009)
11. Y.G. Ma, C.K. Ong, T. Tyc, U. Leonhardt, Nat. Mater. **8**, 639 (2009)
12. N. Kundtz, D.R. Smith, Nat. Mater. **9**, 129 (2010)
13. H.F. Ma, T.J. Cui, Nat. Commun. **1**, 21 (2010)
14. P.-H. Tichit, S.N. Burokur, A. de Lustrac, J. Appl. Phys. **105**, 104912 (2009)
15. P.-H. Tichit, S.N. Burokur, D. Germain, A. de Lustrac, Phys. Rev. B **83**, 155108 (2011)
16. P.-H. Tichit, S.N. Burokur, D. Germain, A. de Lustrac, Electron. Lett. **47**, 580 (2011)
17. J.B. Pendry, A.J. Holden, D.J. Robbins, W.J. Stewart, IEEE Trans. Microw. Theory Tech. **47**, 2075 (1999)
18. D. Schurig, J.J. Mock, D.R. Smith, Appl. Phys. Lett. **88**, 041109 (2006)
19. T. Koschny, P. Markos, E.N. Economou, D.R. Smith, D.C. Vier, C.M. Soukoulis, Phys. Rev. B, Condens. Matter **71**, 245105 (2005)
20. J. Zhou, L. Zhang, G. Tuttle, T. Koschny, C.M. Soukoulis, Phys. Rev. B **73**, 041101(R) (2006)
21. J. Wang, S. Qu, Z. Xu, J. Zhang, H. Ma, Y. Yang, C. Gu, Photonics Nanostruct. Fundam. Appl. **7**, 108 (2009)
22. D.R. Smith, S. Schultz, P. Markos, C.M. Soukoulis, Phys. Rev. B **65**, 195104 (2002)
23. R. Marqués, F. Medina, R. Rafii-El-Idrissi, Phys. Rev. B **65**, 144440 (2002)
24. F.-Y. Meng, Q. Wu, Y. Liang, K. Zhang, L.-W. Li, IEEE Trans. Magn. **45**, 4329 (2009)

Annexe 2.6

A. Dhouibi, S. N. Burokur, A. de Lustrac, A. Priou

« Comparison of compact electric-LC resonators for negative permittivity metamaterials »

Microwave and Optical Technology Letters, vol. 54, no. 10, pp. 2287-2295, October 2012

12. H. Zheng and H. C. Luong, Ultra-low-voltage 20-GHz frequency dividers using transformer feedback in 0.18-μm CMOS process, IEEE J Solid-State Circuits 43 (2008), 2293–2302.

COMPARISON OF COMPACT ELECTRIC-LC RESONATORS FOR NEGATIVE PERMITTIVITY METAMATERIALS

Abdallah Dhouibi,[1] Shah Nawaz Burokur,[1] André de Lustrac,[2] and Alain Priou[1]
[1] LEME, University Paris-Ouest, EA 4416, 92410 Ville d'Avray, France; Corresponding author: sburokur@u-paris10.fr
[2] IEF, University Paris-Sud, CNRS, UMR 8622, 91405 Orsay Cedex, France

Received 12 January 2012

ABSTRACT: *Various easy made planar electric meta-atoms are presented as alternative designs to the conventional electric-LC resonator for achieving negative permittivity. Transforming the LC topology of the resonator helps to facilitate transposition of geometrical parameters for the optical regime and also to improve the metamaterial homogeneity. Our approach aims to simplify the resonator design and achieve a lower resonance frequency without being limited by fabrication techniques. A parametric sweep is performed to evaluate the influence of the different geometrical parameters on the resonance frequencies of the meta-atoms. The electromagnetic behavior is investigated through both simulations and experiments in the microwave regime. Our results show that the developed meta-atoms exhibit a purely strong electric response to normally incident radiation and can be used very effectively in producing materials with negative permittivity. For instance, a Z-shaped structure is shown to present a higher effective medium ratio. The proposed meta-atoms can find various applications in planar high-frequency passive circuits due the simplicity of fabrication.* © 2012 Wiley Periodicals, Inc. Microwave Opt Technol Lett 54:2287–2295, 2012; View this article online at wileyonlinelibrary.com. DOI 10.1002/mop.27050

Key words: *metamaterials; electric-LC resonators; negative permittivity*

1. INTRODUCTION

Metamaterials has gained lots of attention within the scientific community over the past decade [1–3] because of their capabilities that go beyond conventional materials [4] and because of their applications in novel class coordinate transformation-based devices such as invisibility cloaks [5–9], rotators [10], retroreflectors [11], Luneburg lenses [12], waveguide tapers [13], and directive antennas [14–16]. A typical metamaterial is an artificially engineered structure made of a periodic array of subwavelength metallic or dielectric inclusions called meta-atoms. These inclusions can be presented as LC resonant elements with the inductance and capacitance defined by the shape and geometrical dimensions of the latter resonator. These resonators can exhibit of permittivity and/or permeability values in the effective medium regime where the ratio between the operating wavelength and the unit cell size λ/a must be greater than 4 [17]. With typical designs incorporating resonant and dispersive elements much smaller than the operating wavelength, a homogenization scheme is possible, which leads to meaningful interpretation of the effective permittivity ε, permeability μ, and index n.

Different approaches based on the common idea of increasing the total capacitance or inductance of a single unit cell were proposed to improve the ratio between the operating wavelength and the lattice constant of a unit cell. A classic and well-known method consists in changing the feature dimensions of the structure, that is, shorten the gaps or lengthen the wires so as to increase the capacitance or inductance. Other specific solutions such as integrating interdigital capacitors [18] or using high permittivity or permeability host substrates [19] were presented. However, such attempts are very limited according to the fabrication technology when frequency shifts upward.

In this article, we propose a practical way to change the LC equivalent circuit topology of the conventional electric-LC (ELC) resonator [20] in the effective medium regime. It is reported that our transformation can lead to a better metamaterial homogeneity; in other words, we can observe resonance at a lower frequency for similar geometrical dimensions. We investigate numerically and experimentally the electromagnetic behavior of different structures evolved from the transformation and negative real parts of ε are demonstrated in the microwave domain. Moreover, we perform a detailed analysis of the different geometrical parameters' influence on the resonance frequency. Equivalent circuit models are used to explain the parameters' dependence. Owing to the simplicity of designs, the resulting structures may pave the way to realistic practical applications in the optical regime.

We first consider the unit cell of the ELC resonator introduced in Ref. 20 and presented in Figure 1(a). In the effective medium regime, where resonator size is much smaller than the operating wavelength, the ELC resonator can be described qualitatively in terms of its equivalent circuit as illustrated in Figure 1(b). A capacitor-like structure couples to the electric field and is connected in parallel to two loops providing inductance to the circuit. To increase the ratio between the operating wavelength and the ELC unit cell size, it has been suggested that the resonance frequency of the LC circuit expressed as $f_r = \frac{1}{2\pi\sqrt{LC}}$, can be tuned downward by introducing additional inductive loops to accommodate more inductance. Similar to interdigital capacitors, adding inductive loops can be a difficult technological task at optical frequencies.

2. GEOMETRICAL TRANSFORMATION OF THE ELC RESONATOR

On our part, we propose to transform the LC topology of the ELC resonator with the main goal to lower the resonance frequency. This transformation presents also the advantage of facilitating the metamaterial fabrication process. Thus, the ELC resonator is reduced to an I-shaped resonator with a capacitive gap referred to as Igap resonator, as shown in Figure 1(c). As for the ELC, the capacitance created by the gap accounts for the LC resonance. By removing the two side arms, the inductance of the element is considerably decreased. On the counterpart, a new capacitance is created between the two Igap's lateral arms as shown by the equivalent circuit model in Figure 1(d). However, this capacitance C is very weak compared to that of the gap C_g in the middle of the structure, which suggests that the Igap resonator will show a higher resonant frequency than the ELC. Removing the gap in the middle of the resonator (Igap) changes the LC circuit topology and the resulting I-shaped resonator presented in Figure 1(e) is equivalent to the circuit given in Figure 1(f). In this case, without the gap, the capacitance needed for the LC resonance is given by C_p created between two consecutive unit cells.

Another practical shape transformation aiming to decrease the resonance frequency of the ELC resonator without changing the lattice constant consists in adding physical length to both inductive loops by using a slant line as presented in Figure 1(g).

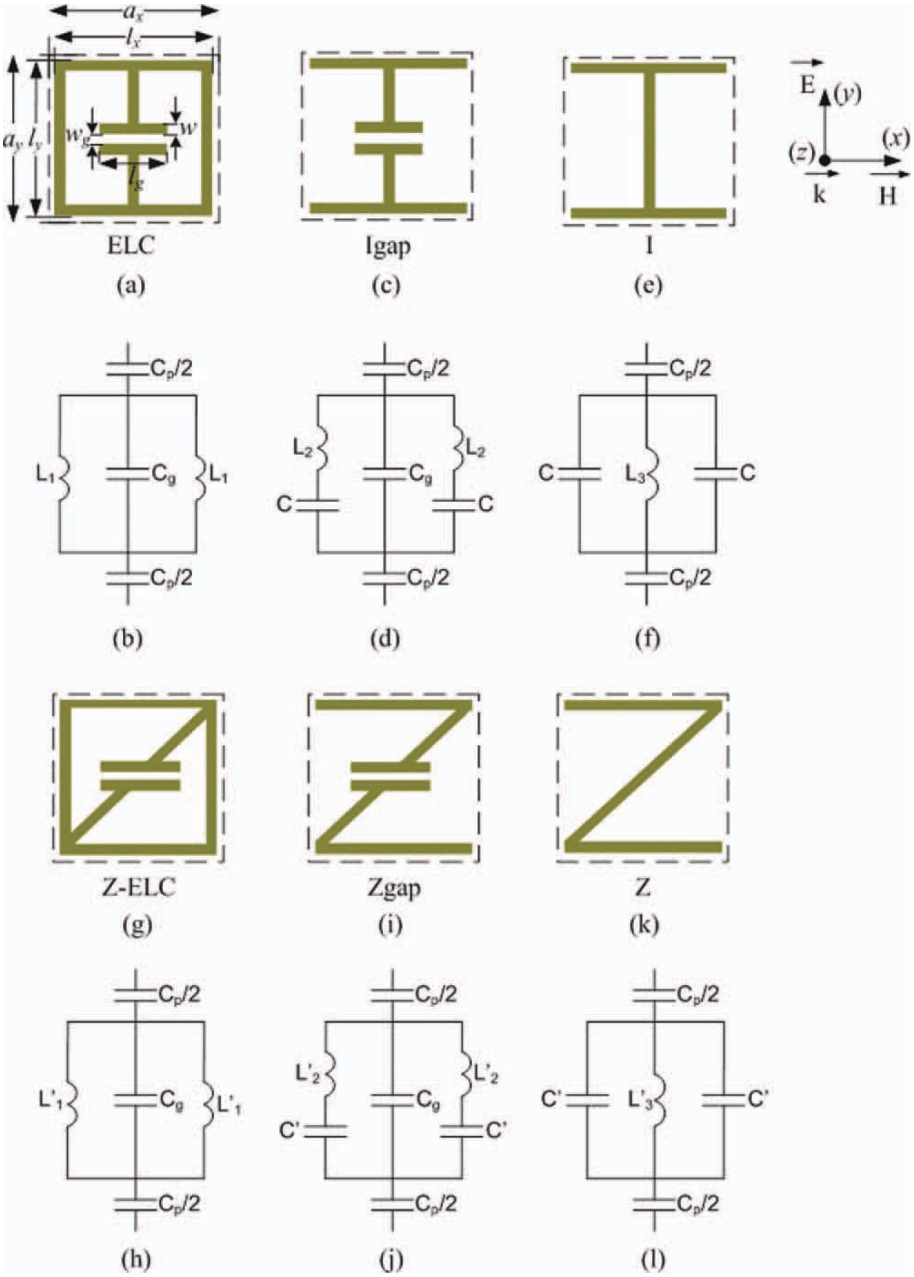

Figure 1 Unit cells and equivalent LC circuit models. (a)-(b) ELC resonator. (c)-(d) Igap resonator. (e)-(f) I-shaped resonator. (g)-(h) Z-ELC resonator. (i)-(j) Zgap resonator. (k)-(l) Z-shaped resonator. For all the resonators, the geometrical dimensions are: $a_x = a_y = 6$ mm, $l_x = 5.7$ mm, $l_y = 5.8$ mm, $w = 0.3$ mm, $w_g = 0.45$ mm and $l_g = 2.$mm. [Color figure can be viewed in the online issue, which is available at wileyonlinelibrary.com]

Adding physical length when passing from ELC to Z-ELC structure shall produce a larger phase delay and increases the total inductance of the metamaterial without requiring additional fabrication steps. Due to this increase in inductance, the Z-ELC resonator shall present resonance at a lower frequency. By continuous transformation, eliminating the *y*-oriented lateral wires, the Z-ELC resonator can be reduced to a Zgap resonator, as shown in Figure 1(i). The decrease in inductance must be less important here than the one observed in the Igap structure, and the resonance frequency of Zgap is expected to be lower than the Igap. As for Igap, removing the gap in the middle of the Zgap resonator changes the LC circuit topology. The equivalent circuit model of the resulting Z-shaped structure [Fig. 1(k)] is given in Figure 1(l).

3. PARAMETRIC STUDY OF THE ELECTRIC META-ATOMS

To examine and compare the performances of the different resonators presented in Figure 1, the properties of the structures are characterized numerically using a finite difference time domain Maxwell's equations solver, Microwave Studio Suite by CST. The dielectric spacer used throughout this study is single face copper-cladded epoxy with a relative dielectric constant of 3.9, a tangential loss of 0.02, and a thickness of 0.4 mm. For the samples reported in this article, the nominal length of the 17 μm

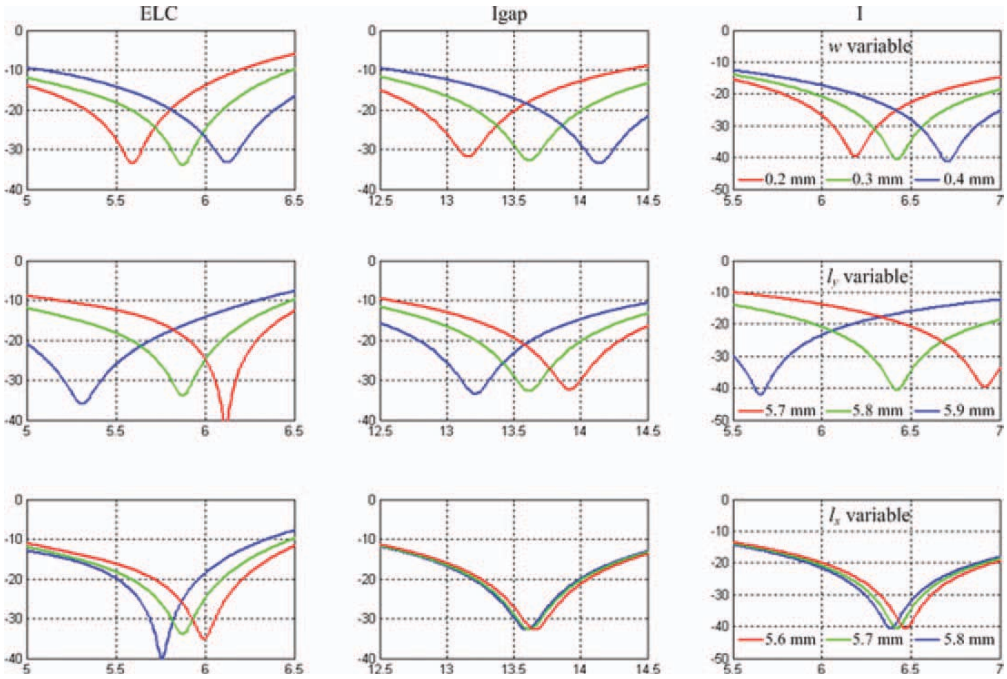

Figure 2 Parametric study of ELC, Igap, and I-shaped resonators. Variation of w, l_y, and l_x. [Color figure can be viewed in the online issue, which is available at wileyonlinelibrary.com]

thick copper wires along the x- and y-direction is $l_x = 5.7$ mm and $l_y = 5.8$ mm, respectively, and the nominal width is $w = 0.3$ mm in both simulations and experiments. For the capacitive gaps present in the ELC, Z-ELC, Igap, and Zgap resonators, the nominal width and length is $w_g = 0.45$ mm and $l_g = 2$ mm, respectively. For the unit cell, $a_x = a_y = 6$ mm. For an electromagnetic wave incident with a wave vector and field polarization of Figure 1, the different resonators will exhibit a strong electric response.

A parametric study of the resonators is performed to point out the importance of the different geometric parameters in the LC resonance frequency and to provide a guideline for design of such metamaterials. Three series of calculations are performed for each resonator; the first one concerns the width of the strip lines w, the second one for the length l_y, and the third one concerns the length l_x. The transmission spectra under normal incidence are shown for each configuration. For the structures evolved from the ELC resonator, i.e., ELC, Igap, and I, the parametric study is presented in the various parts of Figure 2. Each column corresponds to a specific resonator and each row corresponds to the study of a physical parameter. In all subplots, the green traces correspond to the nominal values and the red and blue traces correspond to upper and lower values, respectively. When considering only the resonance corresponding to nominal parameters (green traces), a resonance is clearly observed for each type of meta-atom. The Igap resonator presents a resonance frequency of 13.6 GHz, compared with 5.9 GHz for ELC. This shift toward higher frequencies was predictable as the inductance is greatly reduced when transforming ELC into Igap. When canceling the middle capacitive gap of the Igap to design the I-shaped resonator, the resonance frequency is considerably decreased to 6.4 GHz. The shape transformation induces a change on the LC topology. In a quasi-static approximation, where resonator size is very small compared to operating wavelength, the Igap and I-shaped structures can be modeled in the form of the LC resonance circuit presented in Figures 1(d) and 1(f), respectively. We can consider quasi-similar inductance in both structures and neglect the capacitance C. The equivalent capacitance in the Igap structure is then given by $C_pC_g/(C_p+C_g)$, whereas that of the I-shaped structure is C_p. According to the dimensions w_g and l_g used for the gap, the capacitance of the latter (C_g) is almost half of the one created by the periodicity (C_p). Thus, the resonance frequency of the I-shaped resonator should be $\sqrt{3}$ times smaller than that of the Igap. Actually, a ratio of 2.13 is observed when comparing the resonance frequencies as the inductance in the two resonators is not exactly the same though very close and also because $C_g \neq C_p/2$. The effective medium ratio λ/a, that is, the ratio between the operating wavelength and the unit cell size, is given for each meta-atom in Table 1. We can clearly observe that parameters extraction cannot be performed with the Igap resonator as λ/a is very low (<4).

Commenting on the parametric sweep, the first series of calculation given in Figure 2(a) illustrate the influence of the strip lines width, w. We observe a shift toward higher frequencies for

TABLE 1 Computed and Measured Resonance Frequencies of the Resonators (GHz)

Resonator	Simulated f_0	Measured f_0	Simulated Effective Medium Ratio λ/a
ELC	5.9	6.0	8.5
Igap	13.6	13.6	3.7
I	6.4	7	7.8
Z-ELC	6.2	6.8	8.1
Zgap	9.5	9.1	5.3
Z	4.9	4.9	10.2

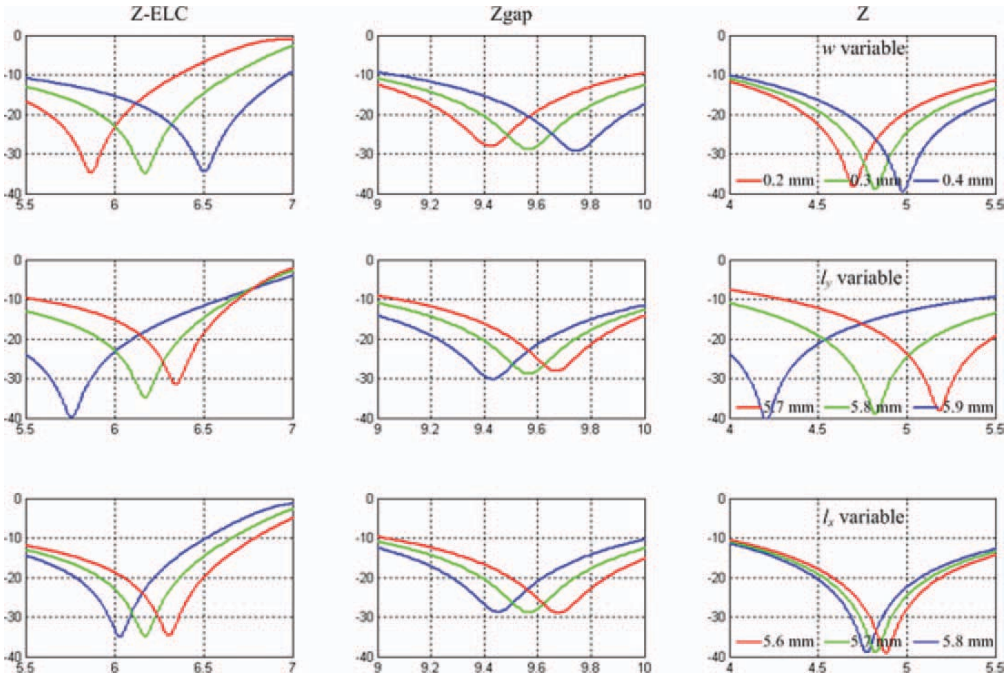

Figure 3 Parametric study of Z-ELC, Zgap, and Z-shaped resonators. Variation of w, l_y, and l_x. [Color figure can be viewed in the online issue, which is available at wileyonlinelibrary.com]

the three resonators when increasing w, as the inductance involved in the LC resonance is reduced. The second series of calculation is based on the variation of the vertical length l_y, and keeping a_y fixed to 6 mm. As l_y is increased, the resonance frequency of each meta-atom is decreased. This is because a higher capacitance value C_p is present between consecutive cells in the y-direction and also to higher inductance in the circuits. The third parametric sweep concerns the horizontal length l_x while keeping a_x fixed to 6 mm. An increase in l_x causes a decrease in resonance frequency for the different resonators. However, this decrease is more important in the ELC meta-atom as vertical arms are present in the structure and therefore, a capacitance is created between consecutive cells in the x-direction. In the Igap and I-shaped resonators, the decrease is only very slight due to the absence of vertical arms.

For the structures evolved from the Z-ELC resonator, that is, Z-ELC, Zgap, and Z, the parametric study is presented in the various parts of Figure 3. For the nominal parameters (green traces), the Z-ELC presents a resonance frequency of 6.2 GHz. This frequency is higher than that of the conventional ELC, which is counterintuitive as the slant lines induce a higher inductance in the circuit. However, simulations have shown a difference in E-field cartography at the capacitive gap location. Indeed, the distribution of the E-field covers a smaller space around the gap in the case of the Z-ELC, suggesting a lower capacitance and therefore a higher resonance frequency. When transforming a Z-ELC to Zgap resonator, the evolution in resonance frequency is similar to that observed in the transformation from ELC to Igap. The Zgap resonator presents a resonance frequency at 9.5 GHz, compared with 13.6 GHz for Igap. Finally, the Z-shaped resonator has a resonance frequency of 4.9 GHz, which is about 1.94 times smaller than that of the Zgap. The same reasoning as for the difference between Igap and I-shaped resonators can be applied to explain such ratio. As shown in Table 1, the effective medium ratio of the three meta-atoms (Z-ELC, Zgap and Z) is greater than 4, indicating that parameters extraction is possible.

Concerning the parametric study performed on the structures evolved from the Z-ELC, similar observations to Figure 2 are made. A shift toward higher frequencies is obtained for the three resonators when increasing w, as the inductance involved in the LC resonance is reduced. An increase in l_y and l_x causes a decrease in resonance frequency. For a change in l_y, the frequency shift is smaller in the case of the Z-type resonators though the change in capacitance C_p is the same. This is because of the physical length of the slant line which causes a smaller variation in inductance and therefore smaller change in resonance frequency. A variation in l_x causes inherently a variation in the length of the slant lines. On the other side, the length of the vertical lines does not vary in the structures evolved from the ELC. Therefore, a greater change in inductance is noted with the Z-type resonators and this explains why the Z-type resonators present a larger shift in frequency when l_x varies.

Two other dominant parameters for ELC, ZELC, Igap, and Zgap resonators are investigated and presented in Figure 4. Indeed, the capacitive gap in the middle of these resonators plays a crucial role in the LC resonance. A parametric study is thus performed to show the influence of the length l_g and width w_g of the gap. As l_g increases, the capacitance created by the gap increases causing the resonance frequency to shift downward. Conversely, when w_g increases, the capacitance decreases and therefore, the resonance frequency increases.

4. STUDY OF CROSS-POLARIZING BEHAVIOR IN Z-SHAPED META-ATOM

It can be clearly observed that the structures evolved from the ELC resonator possess a high level of symmetry, implying both an electric coupling to an electric field and a magnetic coupling to a magnetic field. However, due to the symmetric configuration, the two inductive loops are equivalent but opposite,

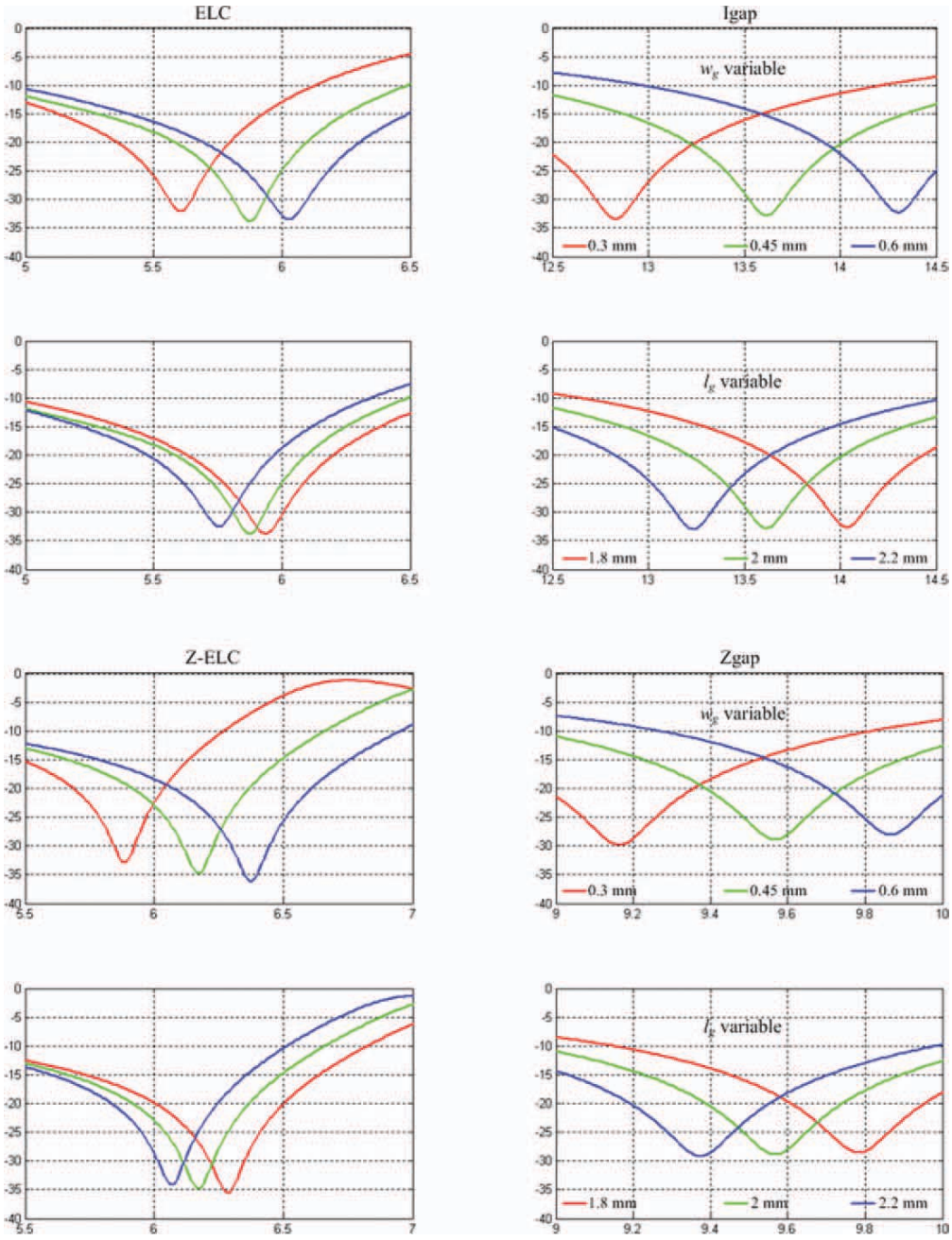

Figure 4 Parametric study of ELC, Igap, Z-ELC, and Zgap resonators. Variation of w_g and l_g. [Color figure can be viewed in the online issue, which is available at wileyonlinelibrary.com]

canceling the magnetic coupling in the structure [20]. Thus, a purely electric response is obtained from such structures. In the case of the structures evolved from the Z-ELC resonator, the only apparent symmetry is a rotation of 180° around the z-axis. Because of the lack of mirror symmetry plane in the Z-type designs, the eigenwave in such structures is not as simple as the y-direction linear polarized wave defined in Figure 1. For this reason, cross-polarizing behavior and magnetoelectric coupling study need to be addressed.

We first start by verifying the electromagnetic (EM) wave polarization of the Z-shaped structure. Two linear eigenmodes corresponding to x-polarized and y-polarized waves are considered in the numerical simulations. Therefore, four linear transmission coefficients T_{xx}, T_{yx}, T_{xy}, and T_{yy} are obtained and used to calculate circular transmission coefficients T_{++}, T_{-+}, T_{+-} and T_{--} using the following equation [21]:

$$\begin{pmatrix} T_{++} & T_{+-} \\ T_{-+} & T_{--} \end{pmatrix} = \frac{1}{2}\begin{pmatrix} (T_{xx}+T_{yy})+i(T_{xy}-T_{yx}) & (T_{xx}-T_{yy})-i(T_{xy}+T_{yx}) \\ (T_{xx}-T_{yy})+i(T_{xy}+T_{yx}) & (T_{xx}+T_{yy})-i(T_{xy}-T_{yx}) \end{pmatrix} \quad (1)$$

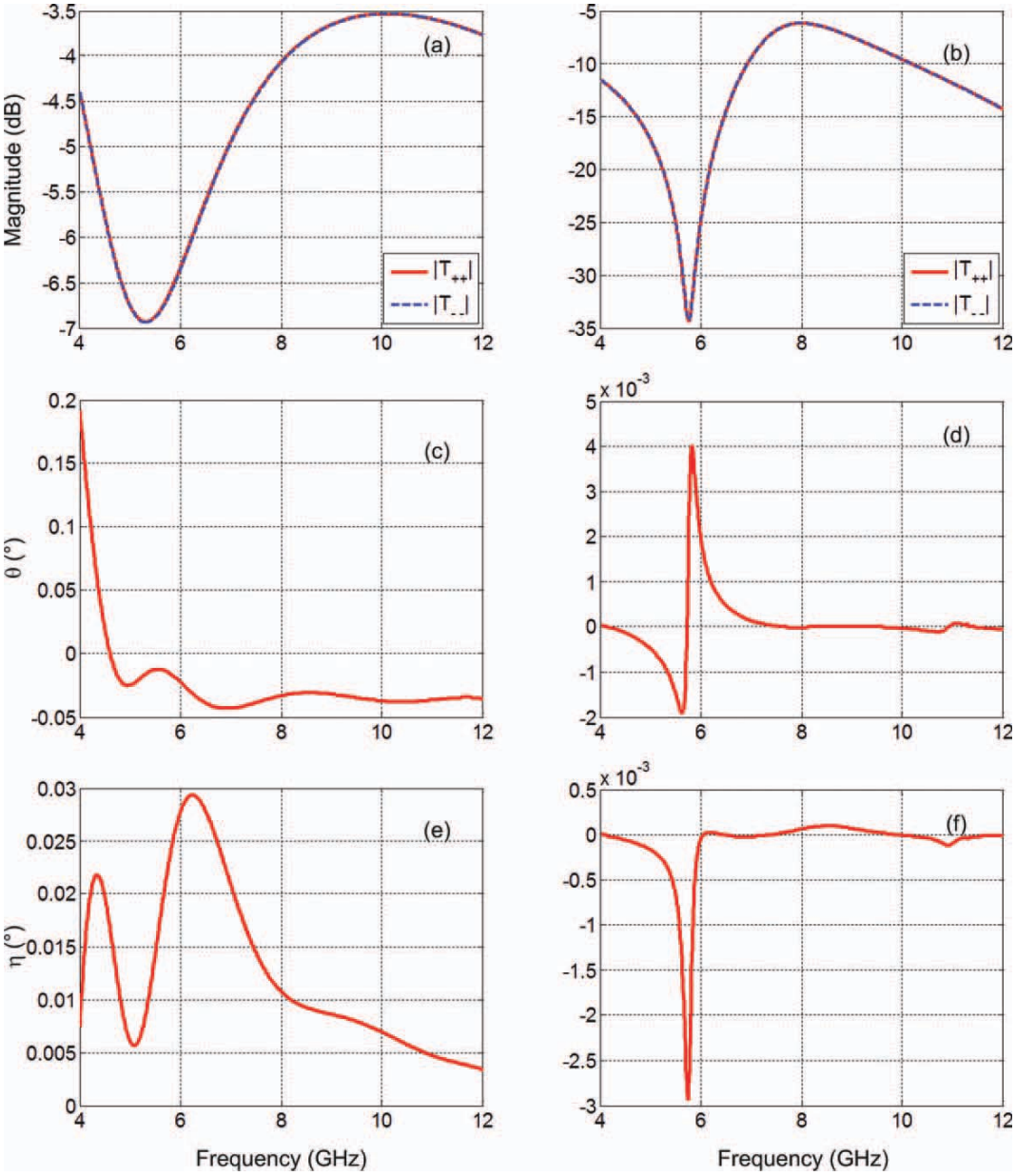

Figure 5 (a)-(b) Computed magnitude of transmission coefficient for the circularly polarized EM wave, (c)-(d) Computed polarization azimuth rotation (θ), (e)-(f) Computed ellipticity angle (η) for the Z-shaped and ELC resonators, respectively. [Color figure can be viewed in the online issue, which is available at wileyonlinelibrary.com]

Figure 5(a) shows the calculated T_{++} and T_{--} coefficients for the Z-shaped meta-atom. We can note that conversely to the chiral metamaterial presented in Ref. 21, the right-handed and left-handed circularly polarized EM waves are similar in this case. The same behavior is observed for the ELC resonator as illustrated in Figure 5(b). The polarization azimuth rotation $\theta = [\arg(T_{++}) - \arg(T_{--})]/2$ and the ellipticity $\eta = \frac{1}{2}\arcsin\left(\frac{|T_{++}|-|T_{--}|}{|T_{++}|+|T_{--}|}\right)$ of elliptically polarized light are presented in Figures 5(c) and 5(e) and Figures 5(d) and 5(f) for the Z-shaped and ELC resonator, respectively. Compared to Ref. 21, the polarization rotation and the ellipticity present very low values close to zero for both the Z-shaped and the ELC resonators, suggesting that the structures do not possess chiral properties.

Further investigations about magnetoelectric coupling are performed by comparing the magnetic field vector distribution in the Z-shaped and ELC resonators at resonance. As it can be observed in Figure 6, a magnetic loop is formed on each side of the central line in both resonators. The magnetic field vectors of the loops point in opposite directions, canceling the magnetic coupling in the resonators. It can therefore be deduced that similarly to the ELC resonator, a purely electric response is obtained from the Z-shaped meta-atom.

5. EXPERIMENTAL RESULTS

Prototypes based on the nominal dimensions have been fabricated for each resonator using standard lithography techniques. Total sample size is 18 × 18 cells on a 120 × 120 mm^2 dielectric

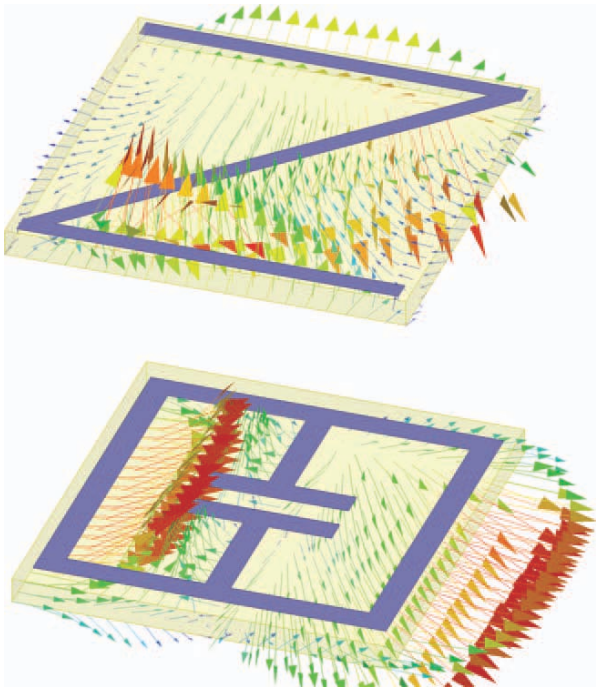

Figure 6 Magnetic field vector distribution at resonance in the Z-shaped and ELC resonators. [Color figure can be viewed in the online issue, which is available at wileyonlinelibrary.com]

board. Microwave measurements based on the experimental setup described in Ref. 22 have been done on the fabricated prototypes in an anechoic chamber using an Agilent 8722ES network analyzer and two 2–18 GHz wideband horn antennas. Phase referencing and normalization have been performed in transmission by removing the sample from the signal path, and in reflection, by replacing the sample with a copper plate. Measured reflection and transmission coefficients are compared to the simulated ones in Figure 7. Calculated and measured magnitudes of S_{21} show clearly a resonance dip for each type of resonator. There is a very good qualitative agreement between simulations and measurements, except for I-shaped and Z-ELC resonators. This discrepancy is due to the fact that the dimensions obtained with the fabricated prototypes of the I-shaped and Z-ELC structures do not correspond exactly to those used in simulations. Table 1 summarizes the numerical and experimental resonance frequencies.

Using reflection and transmission responses from a single layer of the sample and considering a *y*-direction linear polarized wave, effective parameters can be extracted using the retrieval procedure described elsewhere [23]. This is possible as the structure period along the propagation direction is very small compared to the working wavelength. In performing the retrieval, we assume a *z*-direction size $a_z = 6$ mm corresponding to a cubic unit cell as proposed in Ref. 20. Extracted permittivity ε and permeability μ are shown for ELC, I, ZELC, Zgap, and Z resonators in the various parts of Figure 8. Concerning Igap resonator, parameters extraction is not possible with the nominal dimensions as the ratio between the operating wavelength and the unit cell size is low ($\lambda/a \approx 3.7$). Real and imaginary parts of μ are shown in Figures 8(a) and 8(b), respectively. As stated above, the ELC resonator presents an electric response but no magnetic response, that is, the real part of μ is close to unity over the frequencies of interest. However, the retrieved parameters do not strictly comply with this principle. As shown in Figure 8(a), the real part of μ becomes anti-resonant. In fact, this anomaly is an artifact introduced during parameter extraction in a frequency range where the medium is highly spatially dispersive [20]. The other resonators present

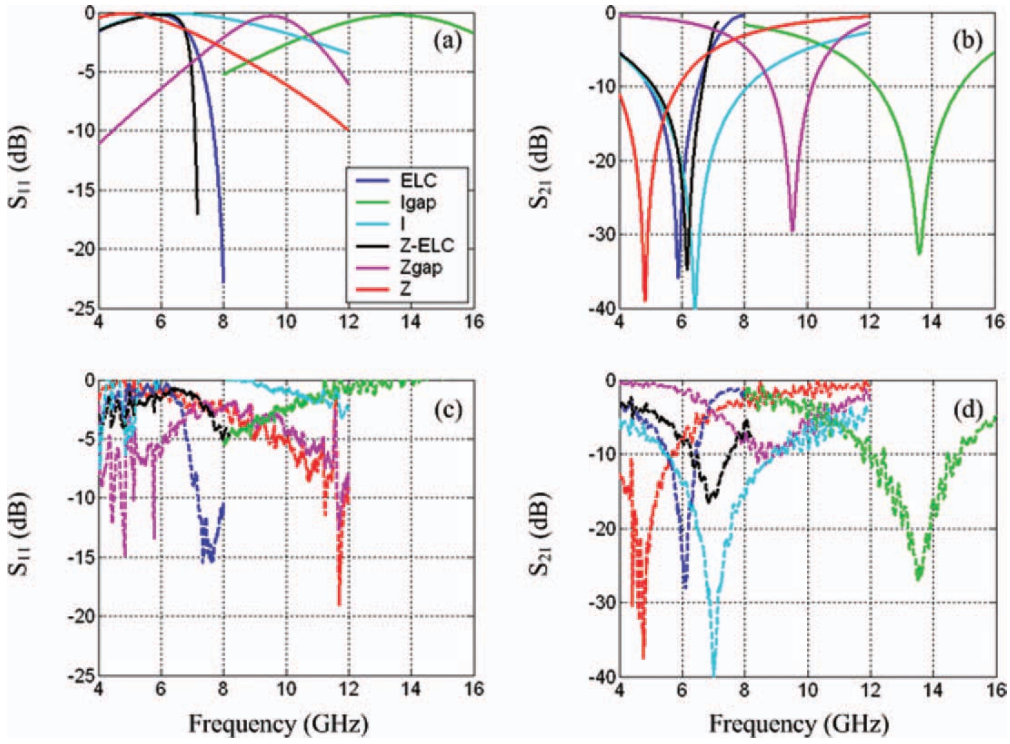

Figure 7 Computed (a)-(b) and measured (c)-(d) reflection and transmission responses of the different resonators. [Color figure can be viewed in the online issue, which is available at wileyonlinelibrary.com]

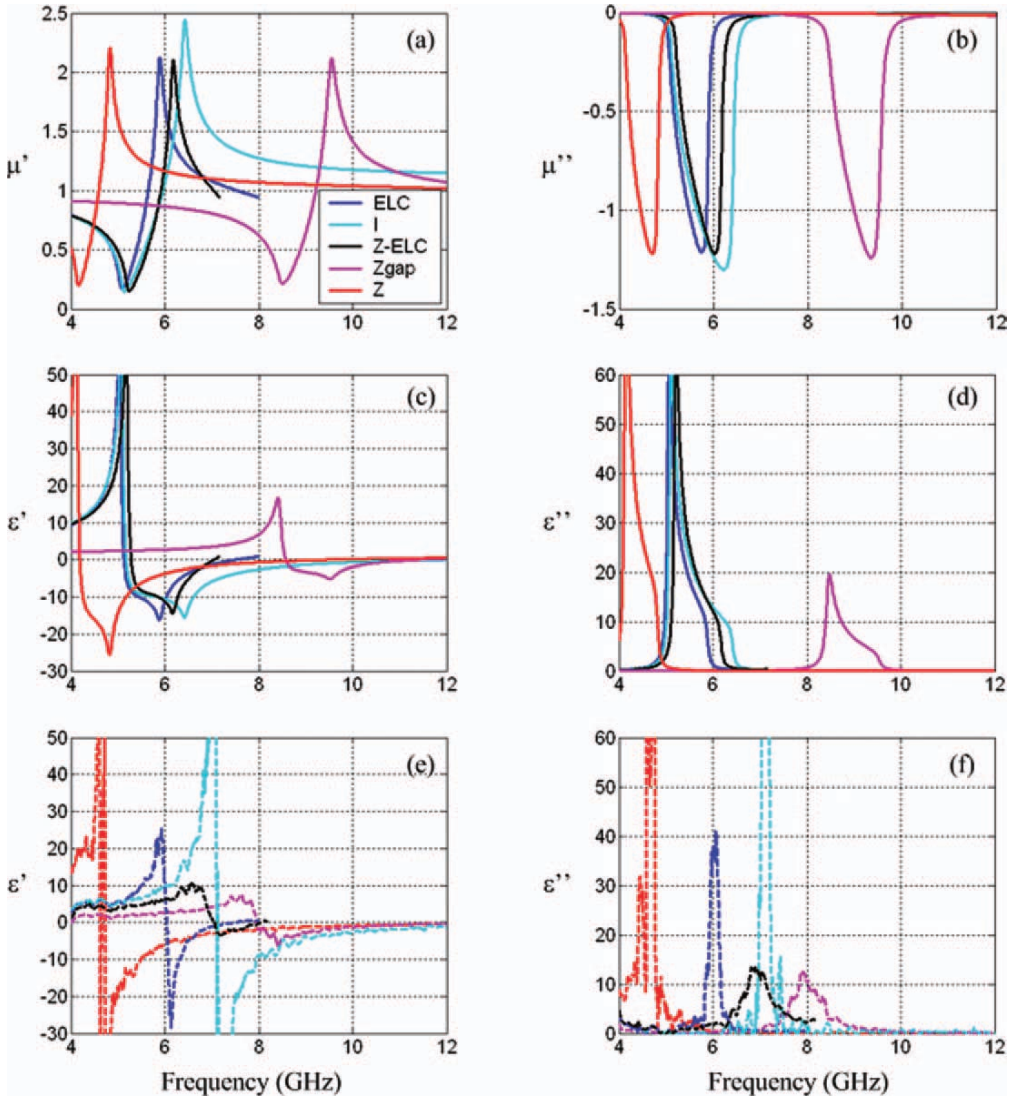

Figure 8 Computed effective parameters: (a) Re(μ), (b) Im(μ), (c) Re(ε), and (d) Im(ε). Measured effective parameters: (e) Re(ε) and (f) Im(ε). [Color figure can be viewed in the online issue, which is available at wileyonlinelibrary.com]

similar responses. From Figures 8(c)–8(f), we see a strong electric resonance, with the real part of the permittivity ranging from positive to negative values in the vicinity of the resonance. The values issued from measurement data agree very well with those calculated from numerical simulations. It must be noted that the extraction from the measured spectra is presented without any fitting. From the simulated and measured real parts of ε, it can also be noted that both Z-shaped meta-atoms (with and without gap) present a wider frequency band where the values are negative compared to the ELC resonator.

6. CONCLUSION

We have presented an experimental demonstration of a negative permittivity from various meta-atoms in the microwave domain. The proposed structures, evolved from the transformation of conventional ELC resonator, are simple to design and can be easily fabricated with standard techniques. A parametric study on the different parameters has also been presented so as to show the influence on the resonance frequency of the different resonators. In particular, a Z-shaped meta-atom has been shown to be an interesting alternative to the conventional ELC. This proposed electric resonator allows to considerably improve the effective medium ratio λ/a. Due to the simplicity of the structure geometry and to the absence of capacitive gap, a transposition of geometrical parameters can be considered for the optical regime.

ACKNOWLEDGMENTS

This work was supported by the EADS Company Foundation through the METAQOPT project, contract No. 090-AO09-1006. One of the authors (A.D.) would like to acknowledge support for his PhD scholarship from EADS Company Foundation. The authors thank T. Lepetit and A. Degiron for fruitful discussions on magnetoelectric coupling.

REFERENCES

1. R.A. Shelby, D.R. Smith, and S. Schultz, Experimental verification of a negative index of refraction, Science 292 (2001), 77–79.
2. T.J. Yen, W.J. Padilla, N. Fang, D.C. Vier, D.R. Smith, J.B. Pendry, D.N. Basov, and X. Zhang, Terahertz magnetic response from artificial materials, Science 303 (2004), 1494–1496.
3. D.R. Smith, J.B. Pendry, and M.C.K. Wiltshire, Metamaterials and negative refractive index, Science 305 (2004), 788–792.

4. V.G. Veselago, The electrodynamics of substances with simultaneously negative values of ε and μ, Sov Phys Usp 10 (1968), 509–514.
5. U. Leonhardt, Optical conformal mapping, Science 312 (2006), 1777–1780.
6. J.B. Pendry, D. Schurig, and D.R. Smith, Controlling electromagnetic fields, Science 312 (2006), 1780–1782.
7. D. Schurig, J.J. Mock, B.J. Justice, S.A. Cummer, J.B. Pendry, A.F. Starr, and D.R. Smith, Metamaterial electromagnetic cloak at microwave frequencies, Science 314 (2006), 977–980.
8. W. Cai, U.K. Chettiar, A.V. Kildishev, and V.M. Shalaev, Optical cloaking with metamaterials, Nat Photon 1 (2007), 224–227.
9. B. Kanté, A. de Lustrac, J.-M. Lourtioz, and S. Burokur, Infrared cloaking based on the electric response of split ring resonators, Opt Express 16 (2008), 9191–9198.
10. H. Chen, B. Hou, S. Chen, X. Ao, W. Wen, and C.T. Chan, Design and experimental realization of a broadband transformation media field rotator at microwave frequencies, Phys Rev Lett 102 (2009), 183903.
11. Y.G. Ma, C.K. Ong, T. Tyc, and U. Leonhardt, An omnidirectional retroreflector based on the transmutation of dielectric singularities, Nat Mater 8 (2009), 639–642.
12. N. Kundtz and D. R. Smith, Extreme-angle broadband metamaterial lens, Nat Mater 9 (2010), 129–132.
13. P.-H. Tichit, S.N. Burokur, and A. de Lustrac, Waveguide taper engineering using coordinate transformation technology, Opt Express 18 (2010), 767–772.
14. P.-H. Tichit, S.N. Burokur, and A. de Lustrac, Ultradirective antenna via transformation optics, J Appl Phys 105 (2009), 104912.
15. P.-H. Tichit, S.N. Burokur, D. Germain, and A. de Lustrac, Design and experimental demonstration of a high-directive emission with transformation optics, Phys Rev B 83 (2011), 155108.
16. P.-H. Tichit, S.N. Burokur, D. Germain, and A. de Lustrac, Coordinate transformation based ultra-directive emission, Electron Lett 47 (2011), 580–582.
17. T. Koschny, P. Markos, E.N. Economou, D.R. Smith, D.C. Vier, and C.M. Soukoulis, Phys Rev B 71 (2005), 245105.
18. W. Withayachumnankul, C. Fumeaux, and D. Abbott, Compact electric-LC resonators for metamaterials, Opt Express 18 (2010), 25912–25921.
19. C. Caloz, A. Lai, and T. Itoh, The challenge of homogenization in metamaterials, New J Phys 7 (2005), 167.
20. D. Schurig, J.J. Mock, and D.R. Smith, Electric-field-coupled resonators for negative permittivity metamaterials, Appl Phys Lett 88 (2006), 041109.
21. J. Zhou, J. Dong, B. Wang, T. Koschny, M. Kafesaki, and C.M. Soukoulis, Negative refractive index due to chirality, Phys Rev B 79 (2009), 121104.
22. J. Zhou, L. Zhang, G. Tuttle, T. Koschny, and C.M. Soukoulis, Negative index materials using simple short wire pairs, Phys Rev B 73 (2006), 041101.
23. D.R. Smith, S. Schultz, P. Markos, and C.M. Soukoulis, Determination of effective permittivity and permeability of metamaterials from reflection and transmission coefficients, Phys Rev B 65 (2002), 195104.

A LOW-CHIP AREA AND LOW-PHASE NOISE HYBRID PHASE-LOCKED LOOP

Jhin-Fang Huang,[1] Chien-Ming Hsu,[1] and Kuo-Lung Chen[2]
[1] Department of Electronic Engineering, National Taiwan University of Science and Technology, Taipei 10672, Taiwan; Corresponding author: jfhuang@mail.ntust.edu.tw
[2] National Communication Committee, Taipei, Taiwan

Received 1 January 2012

ABSTRACT: *A low-chip area and low-phase noise phase-locked loop (PLL) combining fractional-N and integer-N modes operating at 2.4 GHz band is proposed and fabricated in TSMC 0.18-μm CMOS process. The proposed PLL with a Gm-boosted Colpitts voltage-controlled oscillator improves phase noise and a hybrid design of different divider loops achieves fast lock. At 1.8 V supply voltage, the proposed PLL shows a wide tuning range from 2.14 to 2.36 GHz, corresponding to 9.7%, a phase noise of −119.3 dBc/Hz at an offset frequency of 1 MHz from the carrier frequency of 2.14 GHz, a power consumption of 17.3 mW, and an output power of −15.37 dBm. Including pads, the chip area only occupies 0.588 (0.87 × 0.67) mm^2.* © 2012 Wiley Periodicals, Inc. Microwave Opt Technol Lett 54:2295–2300, 2012; View this article online at wileyonlinelibrary.com. DOI 10.1002/mop.27082

Key words: *voltage-controlled oscillator; LC-tank voltage-controlled oscillator; phase-locked loop*

1. INTRODUCTION

Phase-locked loop (PLL) is a critical component used in a RF wireless receiver. Numerous designs of 2.4 GHz PLLs are found in standard CMOS process and performed much growth in recent years [1–3]. In Ref. 1, the authors adopt hybrid technique to achieve a locking time of 20 μs, but at the expenses of a high power consumption of 29.6 mW and a chip area of 2.08 mm^2. Literature [2] uses a low power technique to reduce power consumption, but suffers from long locking time of 55 μs. A low voltage design to reduce power consumption is published and attractive, but with a degraded phase noise of −110.5 dBc/Hz and with a bigger chip area of 1.68 mm^2 [3].

With those factors of power consumption, phase noise and chip area, and so forth, a high performance of PLL under 1.8 V supply voltage is proposed and fabricated in TSMC 0.18-μm CMOS process. The features of this proposed PLL include using Gm-boosted Colpitts LC-tank voltage-controlled oscillator (VCO) to improve phase noise and increase setup, adopting hybrid technique with combining integer-N and fractional-N advantages, using pulse swallow counter as a frequency divider to reduce locking time and deliberate and compact layout to lower chip area. Measured results of the proposed PLL achieve good performances and are very comparable to other published works.

2. HYBRID PHASE-LOCKED LOOP ARCHITECTURE

A fractional-N PLL is adopted to overcome the disadvantages of integer-N PLLs and is especially a PLL where the frequency divider is divided by an integer plus a fraction. The proposed PLL mainly contains a phase/frequency detector (PFD), a charge pump (CP) working in tandem with an on-chip third-order low-pass RC filter and a Gm-boosted Colpitts VCO in the feed-forward path and a pulse swallow divider in the feedback path, as shown in Figure 1, which combines the advantages of both integer mode and fractional mode. External signals, MC0–MC5 control on-and-off functions of Mux. When Mux = 1, the circuit operates on the fractional mode. The PFD compares the inputs of reference $F_{\mathrm{REF}} = 64$ MHz and frequency divider output $F_{\mathrm{div\_Fractional}} = 64$ MHz to achieve fast lock as the loop

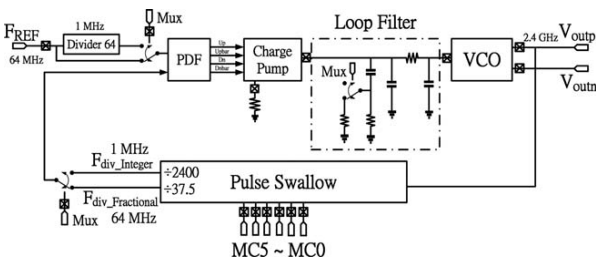

Figure 1 Architecture of the proposed hybrid PLL

Annexe 2.7

A. Dhouibi, S. N. Burokur, A. Lupu, A. de Lustrac, A. Priou

« Excitation of trapped modes from a metasurface composed of only Z-shaped meta-atoms »

Applied Physics Letters, vol. 103, no. 18 (184103), October 2013

Excitation of trapped modes from a metasurface composed of only Z-shaped meta-atoms

Abdallah Dhouibi,[1] Shah Nawaz Burokur,[2,3,a)] Anatole Lupu,[2] André de Lustrac,[2,3] and Alain Priou[1]
[1]*LEME, Univ. Paris-Ouest, EA 4416, 92410 Ville d'Avray, France*
[2]*IEF, Univ. Paris-Sud, CNRS, UMR 8622, 91405 Orsay Cedex, France*
[3]*Univ. Paris-Ouest, 92410 Ville d'Avray, France*

(Received 26 June 2013; accepted 16 October 2013; published online 31 October 2013)

A printed planar Z-shaped meta-atom has recently been proposed as an alternative design to the conventional electric-LC resonator for achieving negative permittivity. Transforming the LC topology of the resonator helps to facilitate transposition of geometrical parameters for the optical regime and also to improve the metamaterial homogeneity. In this work, we discuss about the excitation of a dark or trapped mode in such Z-shaped meta-atom. The electromagnetic behavior of the meta-atom has been investigated through both simulations and experiments in the microwave regime. Our results show that the Z meta-atom exhibits a trapped mode resonance. Depending on the orientation of the polarized electromagnetic field with respect to the Z atom topology and the incident plane, the excitation of the dark mode can lead either to a narrowband resonance in reflection or to a very asymmetric Fano-like resonance in transmission, analog of electromagnetically induced transparency. Compared to other structures, the Z meta-atom presents the advantage of having the dark mode resonance spectrally spaced with respect to the bright mode resonances, which could simplify the observation of the dark mode at much shorter wavelengths. © *2013 AIP Publishing LLC*. [http://dx.doi.org/10.1063/1.4827880]

Metamaterials made of a periodic array of subwavelength inclusions have recently attracted considerable interests because of their capabilities which go beyond conventional materials.[1] Their potential applications in novel class transformation optics based devices such as invisibility cloaks,[2] rotators,[3] retroreflectors,[4] Luneburg lenses,[5,6] and directive antennas.[7,8] Various forms of inclusions such as Split Ring Resonator (SRR)[9] or electric-LC (ELC) resonator[10] have been shown to be able to produce, respectively, a wide range of permeability or permittivity values in the vicinity of the resonance.

Recently, we have proposed a practical way to change the LC equivalent circuit topology in the effective medium regime of the conventional ELC resonator. It has been reported that our geometrical transformation can lead to a better material homogeneity;[11] in other words, we can observe resonance at a lower frequency for similar geometrical dimensions. We investigated numerically and experimentally the electromagnetic behavior of a Z-shaped resonator, and we have shown that the latter resonator exhibits an electric resonance, with the real part of the permittivity ranging from positive to negative values in the vicinity of the resonance.

It is our aim in this letter to show that the Z-shaped meta-atom can demonstrate a trapped mode resonance that is associated with a Fano-type line shape.[12–14] Indeed, the asymmetric Fano resonance has initially been observed in an array of asymmetrically split rings, consisting of two wire arcs of different electrical lengths.[15] The idea has been pushed further by applying metamaterial surfaces, also referred to as metasurfaces to mimick characteristic electromagnetically induced transparency (EIT) responses.[16,17] EIT is an optical phenomenon which turns an originally opaque medium into a transparent one by means of destructive quantum interference between two excitation channels and is linked to the existence of a dark mode (or trapped mode) decoupled from the incident light.[18] Establishing such a phenomenon needs the use of a pumping laser. However, trapped modes, where current distribution is similar in magnitude but with opposite directions, have been observed either in metamaterial structures involving two different geometries that are asymmetric[16] or in structures with a broken symmetry.[17,19–25] And more recently, such high Q-factor modes have also been observed in double-layered symmetric structures.[26] Furthermore, a single symmetric U-shaped resonator has been used under off-normal incidence to demonstrate an EIT-like transmission behavior.[27] Conversely to all these previous studies, our work deals with the excitation of a trapped mode from a surface composed of a planar array of only Z-shaped resonant structures possessing an inversion symmetry geometry. This study is highly motivated by the prospects of the slow light effect associated with EIT and index sensing applications. Working with only one type of meta-atom could facilitate the fabrication process at small wavelengths such as in the terahertz (THz) or optical domains. Here, we validate the Z meta-atom design for the excitation of the trapped mode at microwave frequencies due to the easiness of experimental verification. However, the structural design and associated behaviors remain valid for much shorter wavelengths.

To examine the performances of the Z-shaped resonator presented in Fig. 1, the properties of the structure are characterized numerically using the Finite Integral Technique (FIT) Maxwell's equations solver, Microwave Studio Suite by CST. The dielectric spacer used throughout this study is single face copper-cladded epoxy with a relative dielectric constant of 3.9, a tangential loss of 0.02, and a thickness of 0.4 mm. For the samples reported in this letter, the length of

[a)]Electronic mail: shah-nawaz.burokur@u-psud.fr

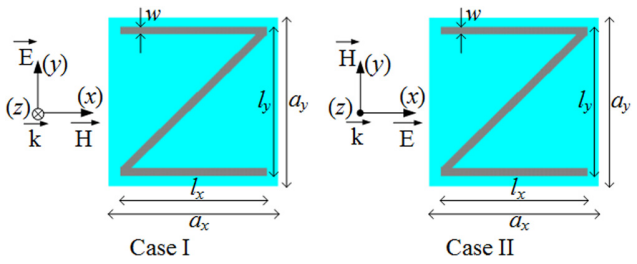

FIG. 1. Incident field polarizations for the Z-shaped resonator. The geometrical dimensions are $a_x = a_y = 6$ mm, $l_x = 5.7$ mm, $l_y = 5.8$ mm, and $w = 0.3$ mm.

the 17 μm thick copper wires along the x- and y-direction is, respectively, $l_x = 5.7$ mm and $l_y = 5.8$ mm, and the width is $w = 0.3$ mm in both simulations and experiments. For the unit cell, $a_x = a_y = 6$ mm and the total sample size is 19×19 cells on a 114 mm $\times$ 114 mm dielectric substrate. Two different types of field polarizations are considered as shown in Fig. 1, and for each case, we explore the characteristics of the resonator under normal incidence and also off-normal incidence in both E-plane (plane containing vectors E and k) and H-plane (plane containing vectors H and k).

Calculated reflection and transmission spectra of a single layer structure with the field polarization of case I are presented in Fig. 2. For all incidence angles, a resonance is obtained around 4.6 GHz. The instantaneous current distribution shown in Fig. 3(a) indicates that it indeed corresponds to the lowest LC frequency of the Z-shaped meta-atom. Also, for off-normal incidence the excitation of an additional resonance can be observed in the reflection response around 13.8 GHz. Its origin is related to the excitation of a dark (or trapped) mode occurring at this frequency. To explain the excitation of the trapped mode, the Z atom is considered as an arrangement of two V-like antennas.[28] Due to the Z atom inversion symmetry, the dipolar moments of the anti-symmetric modes of the two V-like antennas are oppositely directed and perfectly cancel each other at normal incidence. As confirmed by the snapshot of the instantaneous current distribution shown in Fig. 3(b) for normal incidence, the current flow is extremely weak at 13.8 GHz, meaning that the mode is not excited and remains dark at this frequency.

The excitation of the dark mode becomes possible under off-normal incidence. It is highly efficient under the H-plane oblique incidence and much less under the E-plane incidence. To understand such a behavior, from the snapshot of the current distribution displayed in Fig. 3(c) at 13.8 GHz under 45° H-plane oblique incidence, we can infer the presence of an allowed dipole magnetic momentum induced in the loops formed by the capacitance between the coupled arms of two adjacent Z meta-atoms, as illustrated by the blue dashed line. As already highlighted in previous studies, the interaction between a forbidden dark mode resonance and an allowed bright mode gives rise to the Fano resonance.[13,14] The interference of such two modes may result either in a strong enhancement (constructive interference) or strong suppression (destructive interference) of the electromagnetic field. The balance of the electric field induced oppositely flowing currents is broken for a destructive interference and gives rise to the excitation of the V antenna anti-symmetric mode that otherwise is forbidden under normal incidence. The excitation of the dark mode in this case results in the appearance of a narrowband resonance in reflection, named by analogy Electromagnetically Induced Reflection (EIR).[29] As it can observed in the reflection responses under H-plane incidence in Fig. 2, the magnitude of the resonance varies from −12.3 dB for 15° to −2.5 dB for 60°.

There is no such kind of allowed magnetic and forbidden electric dipolar momentums interaction under E-plane oblique incidence. The direction of the electric field component induced magnetic momentums is always orthogonal to the magnetic component of the incident field. We attribute the weak excitation of the resonance at 13.8 GHz to the phase delay caused by the different spatial location of the two V antennas. The excitation of the dark mode is mainly forbidden for E-plane oblique incidence.

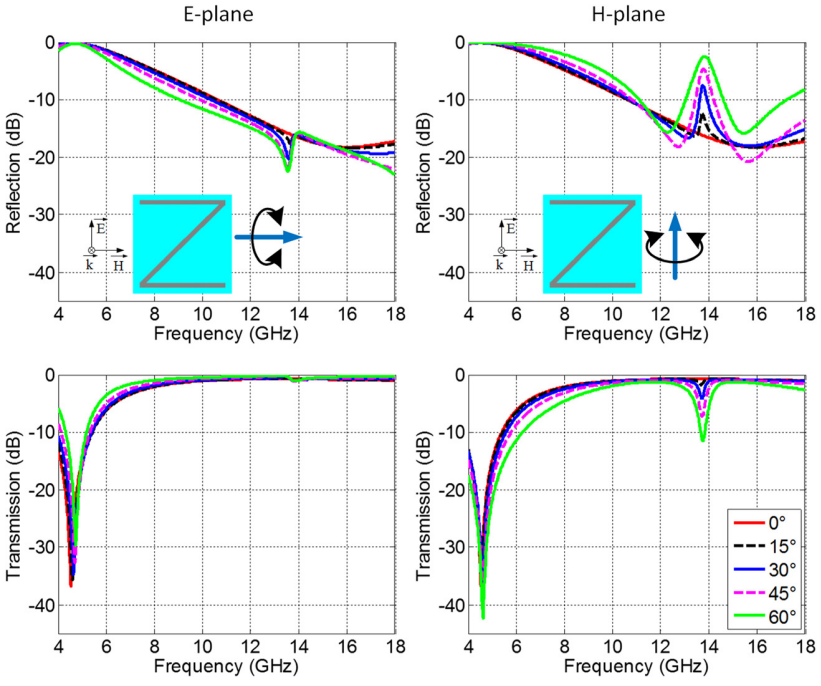

FIG. 2. Computed reflection and transmission coefficients for the field polarization of case I and for incidence radiation varying from 0° to 60°.

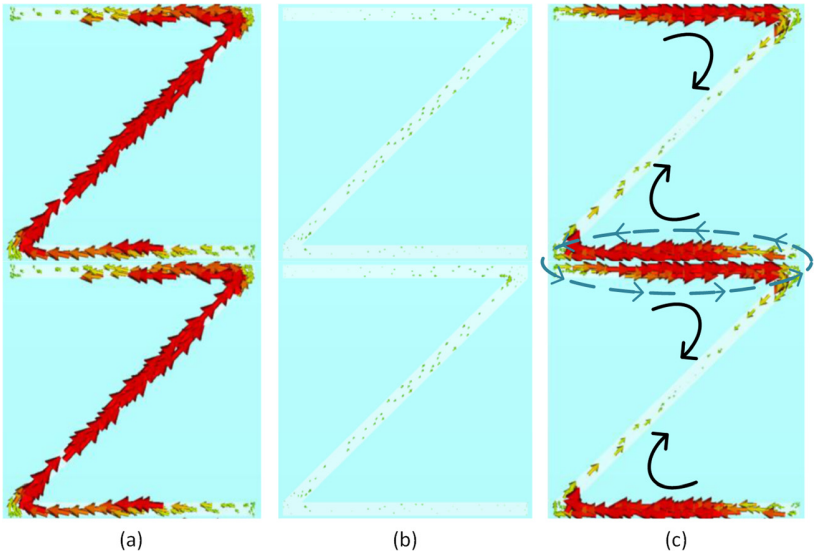

FIG. 3. Computed current distributions for case I. (a) Normal incidence at 4.6 GHz. (b) Normal incidence at 13.8 GHz. (c) 45° oblique incidence at 13.8 GHz.

The calculated reflection and transmission spectra of a single layer structure with the field polarization of case II are presented in Fig. 4. For normal incidence, a resonance in transmission is observed at 20 GHz (not shown in the Figure) corresponding to the excitation of the symmetric mode of the V antenna. As previously explained, the V antenna antisymmetric mode at 13.8 GHz is dark and is excited only at oblique incidence. Similar to the case of case I, dark mode excitation is very efficient under H-plane oblique incidence and much less efficient for E-plane oblique incidence. The underlying mechanism responsible for the excitation of the dark mode under H-plane oblique incidence is the same as for case I. It is due to the contribution of the magnetic component of the incident field. However in contrast to case I, the excitation of the dark mode leads now to the appearance of the peak in transmission in a narrow frequency range, analog of the EIT. As illustrated by the transmission responses under H-plane incidence, the resonance dip present for off-normal incidence varies from −9 dB for 15° to −26 dB for 60°. For E-plane oblique incidence, the calculated results show a very weak excitation of the dark mode that we attribute to the phase delay caused by the different spatial location of the two V antennas.

Microwave measurements based on the experimental setup described in Ref. 11 have been done on fabricated prototypes in an anechoic chamber using an Agilent 8722ES network analyzer and two 2–18 GHz wideband horn antennas, as illustrated in Fig. 5(a). Phase referencing and normalization have been performed in transmission by removing the sample from the signal path, and in reflection, by replacing the sample with a copper plate. Measured reflection and transmission coefficients are compared to the simulated ones, as represented in Figs. 5(b) and 5(c). A good qualitative agreement between simulations and measurements is found.

The above results have confirmed the excitation of a dark mode under off-normal incidence. However, a method

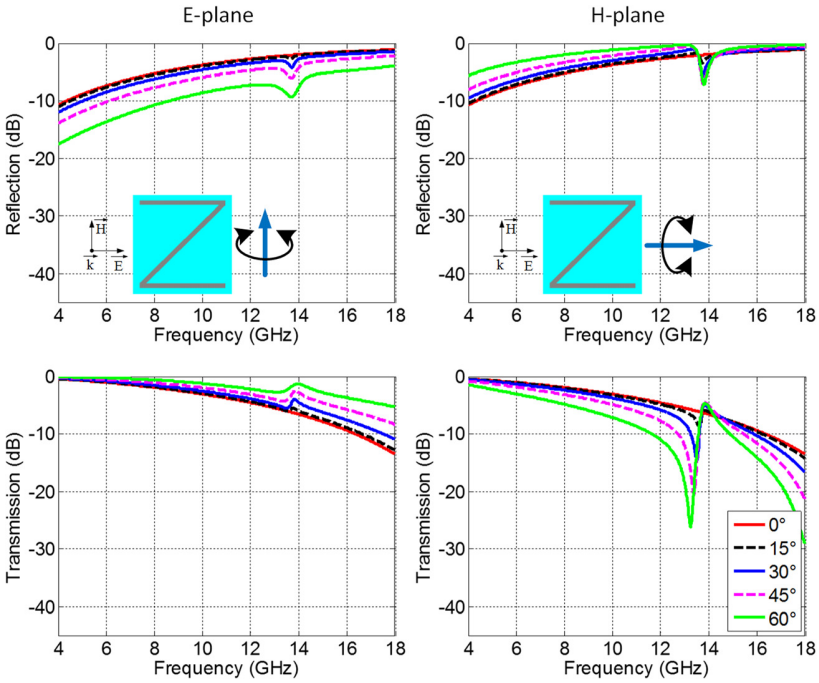

FIG. 4. Computed reflection and transmission coefficients for the field polarization of case II and for incidence radiation varying from 0° to 60°.

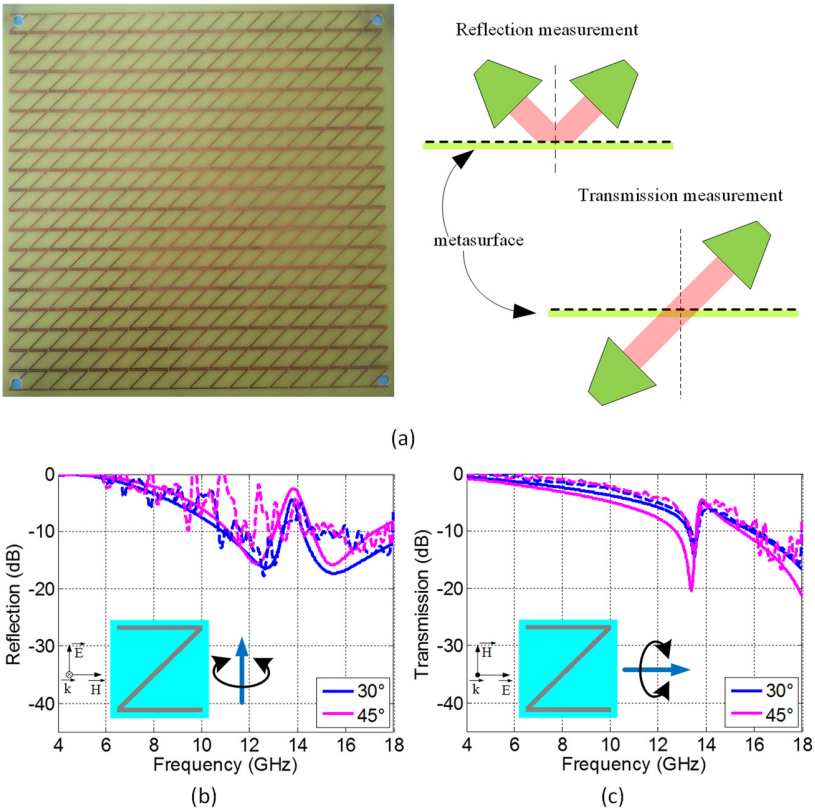

FIG. 5. Experimental measurements (dashed traces) compared to simulations (continuous traces). (a) Photography of the fabricated prototype and diagrams showing how reflection and transmission measurements are performed. (b) Reflection coefficient for the field polarization of case I under 30° and 45° H-plane oblique incidence. (c) Transmission coefficient for the field polarization of case II under 30° and 45° H-plane oblique incidence.

also exists to excite the dark mode in the Z-shaped meta-atom under normal incidence. It consists in applying different lengths to the horizontal arms. When l_2 is different from l_1 which is fixed to 5.7 mm as shown in Fig. 6, the orientation of the two V antennas dipolar momentums are not collinear anymore and do not mutually cancel each other. The balance of the electric field induced oppositely flowing currents is now broken. As it is clearly illustrated in Fig. 6, similar current distribution as for off-normal incidence is observed. It results in the excitation of the V antenna anti-symmetric mode that otherwise is forbidden for $l_2 = l_1$ and leads to the appearance of a narrowband resonance as shown in Fig. 7. We can also note the shift towards higher frequencies due to lower inductance with shorter l_2 in the structure. The EIR

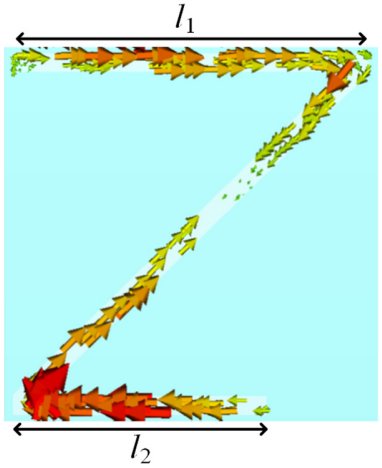

FIG. 6. Computed current distribution at dark mode resonance when $l_2 = 4.066$ mm.

observed for the incident field polarization of case I shows a well pronounced asymmetric Fano resonance shape. However the excitation of the dark mode resonance in such case is not as efficient as for the original Z meta-atom under H-plane oblique incidence.

In contrast, the excitation of the EIT under normal incidence caused by the symmetry breaking is more efficient as compared to the H-plane oblique incidence excitation mechanism. The degree of asymmetry of the Z meta-atom and the polarization of the incident wave provide the means for the control and selective excitation of either EIR or EIT depending of the target applications. The downscale of the considered design makes possible to achieve a similar operation of Z-shaped atoms in the THz or near infra-red (IR) or even visible domain. The use of the narrow band resonances in these spectral domains can be of great interests for refractive index sensing applications where the Z meta-atoms are promising candidates due to the relative simplicity of their design composed of a single element, which allows a simpler technological realization.

In conclusion, we have presented the experimental demonstration of a dark (trapped) mode from an asymmetric Z-shaped meta-atom in the microwave domain. Indeed, depending on how the incident field is polarized, such resonator exhibits a resonant peak in either the reflection or transmission response, leading to a dark mode excitation or even the demonstration of an EIT-like transmission peak. In the microwave domain the slow wave properties of dark resonances can be used for pulse delay or dispersion compensation applications.[16,17,30] The association with active magnetic[31,32] or optic substrates[33,34] opens avenues for agile frequency tuning antennas with highly selective bandwidth. Due to the design simplicity of the metamaterial surface composed of only one kind of resonator structure, a

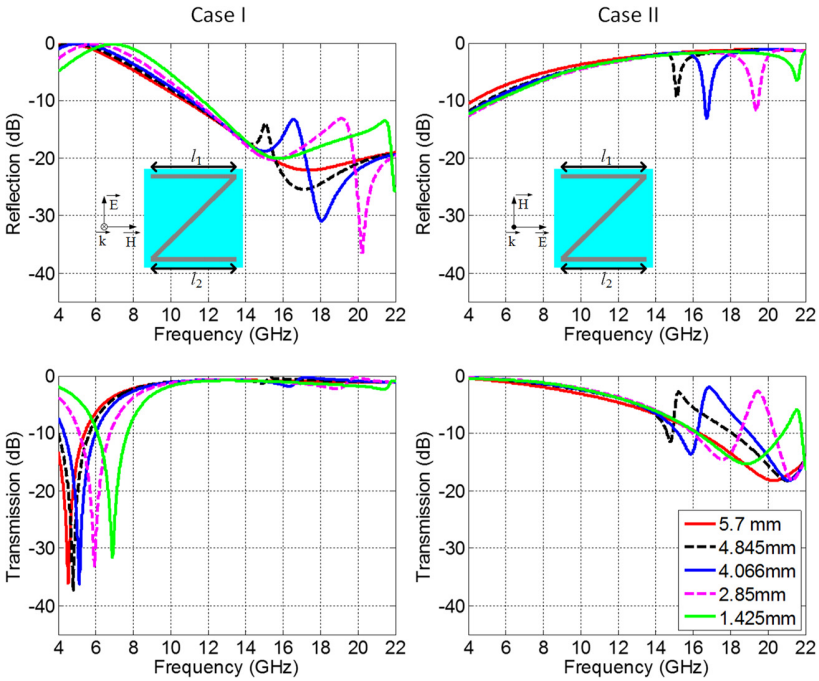

FIG. 7. Reflection and transmission coefficients for varying l_2 under normal incidence.

transposition of geometrical parameters can be considered for the optical regime in view of sensing applications or tuning of light tunneling effects.[35] Indeed, compared to the structures reported in literature, the Z meta-atom dark mode does not rely on coupling effects between two or more closely spaced elements. The excitation of the dark mode is uniquely determined by the symmetry properties and the geometry of the Z atom. This leads to a dark mode resonance which is spectrally spaced to the bright mode resonances, rendering its observation in the optical domain much easier. Furthermore, the control of the asymmetry of the Z-shaped atom and the incidence wave polarization allow a preferential excitation of either EIR or EIT bringing an additional versatility to the considered structure. The concomitant use of both EIT and EIR effects would allow to further improve detection sensitivity by means of correlation techniques.

This work was supported by the EADS Company Foundation through the METAQOPT project (Contract No. 090-AO09-1006). A.D. would like to acknowledge support for his Ph.D. scholarship from EADS Company Foundation.

[1]R. A. Shelby, D. R. Smith, and S. Schultz, Science **292**, 77 (2001).
[2]D. Schurig, J. J. Mock, B. J. Justice, S. A. Cummer, J. B. Pendry, A. F. Starr, and D. R. Smith, Science **314**, 977 (2006).
[3]H. Chen, B. Hou, S. Chen, X. Ao, W. Wen, and C. T. Chan, Phys. Rev. Lett. **102**, 183903 (2009).
[4]Y. G. Ma, C. K. Ong, T. Tyc, and U. Leonhardt, Nature Mater. **8**, 639 (2009).
[5]N. Kundtz and D. R. Smith, Nature Mater. **9**, 129 (2010).
[6]H. F. Ma and T. J. Cui, Nat. Commun. **1**, 21 (2010).
[7]P.-H. Tichit, S. N. Burokur, D. Germain, and A. de Lustrac, Phys. Rev. B **83**, 155108 (2011).
[8]Z. H. Jiang, M. D. Gregory, and D. H. Werner, Phys. Rev. B **84**, 165111 (2011).
[9]J. B. Pendry, A. J. Holden, D. J. Robbins, and W. J. Stewart, IEEE Trans. Microwave Theory Tech. **47**, 2075 (1999).
[10]D. Schurig, J. J. Mock, and D. R. Smith, Appl. Phys. Lett. **88**, 041109 (2006).
[11]A. Dhouibi, S. N. Burokur, A. de Lustrac, and A. Priou, Appl. Phys. A **106**, 47 (2012).
[12]H. Benisty, J. Opt. Soc. Am. B **26**, 718 (2009).
[13]A. E. Miroshnichenko, S. Flach, and Y. S. Kivshar, Rev. Mod. Phys. **82**, 2257 (2010).
[14]B. Luk'yanchuk, N. I. Zheludev, S. A. Maier, N. J. Halas, P. Nordlander, H. Giessen, and C. T. Chong, Nature Mater. **9**, 707 (2010).
[15]V. A. Fedotov, M. Rose, S. L. Prosvirnin, N. Papasimakis, and N. I. Zheludev, Phys. Rev. Lett. **99**, 147401 (2007).
[16]N. Papasimakis, Y. H. Fu, V. A. Fedotov, S. L. Prosvirnin, D. P. Tsai, and N. I. Zheludev, Appl. Phys. Lett. **94**, 211902 (2009).
[17]N. Papasimakis, V. A. Fedotov, N. I. Zheludev, and S. L. Prosvirnin, Phys. Rev. Lett. **101**, 253903 (2008).
[18]M. Fleischhauer, A. Imamoglu, and J. P. Marangos, Rev. Mod. Phys. **77**, 633 (2005).
[19]Z.-G. Dong, H. Liu, M.-X. Xu, T. Li, S.-M. Wang, J.-X. Cao, S.-N. Zhu, and X. Zhang, Opt. Express **18**, 22412 (2010).
[20]A. Christ, O. J. F. Martin, Y. Ekinci, N. A. Gippius, and S. G. Tikhodeev, Nano Lett. **8**, 2171 (2008).
[21]R. Singh, I. A. I. Al-Naib, Y. Yang, D. R. Chowdhury, and W. Cao, Appl. Phys. Lett. **99**, 201107 (2011).
[22]S.-D. Liu, Z. Yang, R.-P. Liu, and X.-Y. Li, Opt. Express **19**, 15363 (2011).
[23]K. Aydin, I. M. Pryce, and H. A. Atwater, Opt. Express **18**, 13407 (2010).
[24]R. Singh, I. A. I. Al-Naib, M. Koch, and W. L. Zhang, Opt. Express **19**, 6312 (2011).
[25]W. Cao, R. Singh, I. A. I. Al-Naib, M. He, A. J. Taylor, and W. Zhang, Opt. Lett. **37**, 3366 (2012).
[26]B.-J. Seo, K. Kim, S. G. Kim, A. Kim, H. Cho, and E. Choi, J. Appl. Phys. **111**, 113106 (2012).
[27]J. Shao, J. Li, J. Li, Y.-K. Wang, Z.-G. Dong, P. Chen, R.-X. Wu, and Y. Zhai, Appl. Phys. Lett. **102**, 034106 (2013).
[28]N. Yu, P. Genevet, M. A. Kats, F. Aieta, J.-P. Tetienne, F. Capasso, and Z. Gaburro, Science **334**, 333 (2011).
[29]N. Liu, T. Weiss, M. Mesch, L. Langguth, U. Eigenthaler, M. Hirscher, C. Soünnichsen, and H. Giessen, Nano Lett. **10**, 1103 (2010).
[30]V. Yannopapas, E. Paspalakis, and N. V. Vitanov, Phys. Rev. B **80**, 035104 (2009).
[31]V. Dmitriev, S. Prosvirnin, V. Tuz, and M. N. Kawakatsu, Adv. Electromagn. **1**, 89 (2012).
[32]S. Prosvirnin and V. Dmitriev, Eur. Phys. J.: Appl. Phys. **49**, 33005 (2010).
[33]C. H. Lee, P. S. Mak, and A. P. De Fonzo, IEEE J. Quantum Electron. **16**, 277 (1980).
[34]V. Tuz and S. Prosvirnin, Eur. Phys. J.: Appl. Phys. **56**, 30401 (2011).
[35]T. Feng, F. Yang, Y. Li, Y. Sun, H. Lu, H. Jiang, Y. Zhang, and H. Chen, Appl. Phys. Lett. **102**, 251908 (2013).

Annexe 2.8

A. de Lustrac, S. N. Burokur, B. Kanté, A. Sellier, D. Germain

« Design and characterization of metamaterials for optical and radio communications »

pp. 269-302 in book *Metamaterial*, edited by X.-Y. Jiang, ISBN 978-953-51-0591-6,
InTech, 2012

11

Design and Characterization of Metamaterials for Optical and Radio Communications

André de Lustrac, Shah Nawaz Burokur, Boubacar Kanté,
Alexandre Sellier and Dylan Germain
Institut d'Electronique Fondamentale,
Univ. Paris-Sud, CNRS UMR 8622, Orsay,
France

1. Introduction

Metamaterials have attracted considerable interests (Shelby, 2001, Yen, 2004, Smith, 2004, Linden, 2004, Zhang, 2004) because of their unusual electromagnetic properties (Veselago, 1968) and because of their potential applications such as invisibility cloaks (Leonhardt, 2006, Pendry, 2006, Schurig, 2006, Cai, 2007, Gaillot, 2008, Kante, 2008), the so-called perfect lenses (Pendry, 2000) and gradient index (GRIN) lenses. For example, perfect lenses require the use of Left-Handed (LH) metamaterials (Smith, 2000) having a negative refractive index, which can be produced by a simultaneously negative electric permittivity ε and magnetic permeability μ. Invisibility cloaks require adjustable positive permeability and permittivity from near zero values to several tenths. Traditionally, these properties are achieved by the use of a combination of split-ring resonators (Pendry, 1999) and metallic wires (Pendry, 1996), with periods much smaller than the wavelength of the electromagnetic wave, such that the medium can be considered homogeneous. Lately, pairs of finite-length wires (cut wires pairs) (Shalaev, 2005) have been proposed not only to replace the conventional split-ring resonators (SRRs) to produce a negative magnetic permeability under normal to plane incidence, but also lead to a negative refractive index n in the optical regime. However in a recent review paper (Shalaev, 2007), Shalaev stated that it is very difficult to achieve a negative refractive index with exclusively wire pairs and that the negative index value observed in the ref. (Shalaev, 2005), was accomplished in part because of the significant contribution from the imaginary part of the permeability. Nevertheless, the negative index from only cut wire and plate pairs has never been verified elsewhere (Dolling, 2005). Instead, continuous wires have been combined to the cut wire pairs to produce simultaneously a negative permittivity to lead to a negative index in the microwave domain (Zhou, 2006a). Zhou *et al*. also theoretically proposed a left-handed material using only cut wire pairs by increasing the equivalent capacitance between two consecutive short wire pairs so as to adjust the electric resonance frequency (Zhou, 2006b) This increase of capacitance can only be obtained by strongly reducing the spacing between two consecutive wires, which is quite difficult to achieve at high frequencies. These cited results concern mainly the microwave domain. In the optical regime, infrared and visible domains, the main problem concern the design and the characterization of metamaterials made of unit cells

with nanometric dimensions. At this scale, the control and the engineering of the electromagnetic properties of metamaterials are closely linked to the easiness of the fabrication. This easiness is more and more important with the simplicity of the geometrical shapes of the unit cell of the metamaterials. We show that we can change the conventional shape of the split ring resonator of J. Pendry to simple coupled nanowires, keeping the same electromagnetic properties (Linden, 2004, Enkrich, 2005, Kante, 2008a, Burokur, 2009a).

In the first part of this chapter we investigate numerically and experimentally the electromagnetic properties of cut wire pairs metamaterials where the symmetry between the wires on opposite faces is voluntarily broken along the **E**-field direction (Sellier, 2009, Kante, 2009a, Burokur, 2009a). It is reported that in this case the electric resonance of the cut wire pairs can occur at lower frequencies than the magnetic resonance, which is in contrast with the symmetrical configuration. This lower electrical resonance frequency allows realizing a common frequency region where the permeability and the permittivity are simultaneously negative. This claim is verified numerically and experimentally in the microwave domain and indications on designing negative refractive index from structures composed of only cut wire pairs are given.

Then, we investigate numerically and experimentally the reflection and transmission spectra for an obliquely incident plane wave on the asymmetric structure. It is reported that a diffraction threshold appears in E-plane (plane containing vectors E and k), that is the (-1,0) mode starts to propagate (Burokur, 2009b). Besides, resonances in E-plane shift in frequency with increasing oblique incidence. However in H-plane (plane containing vectors H and k), the structure is diffractionless and independent of the incidence and therefore the negative index is maintained in a wide angular range. These statements are verified numerically and experimentally in the microwave domain.

On the other hand, we show that it is possible to engineer the resonances of metamaterial in the infrared domain (Kante, 2008b, Kante, 2009b). We present an experimental and numerical analysis of the infrared response of metamaterials made of split ring resonators (SRR) and continuous nanowires deposited on silicon when the geometry of the SRRs is gradually altered. The impact of the geometric transformation of the SRRs on the spectra of the composite metamaterial is measured in the 1.5-15 μm wavelength range for the two field polarizations under normal to plane propagation. We show experimentally and numerically that tuning the SRRs towards elementary cut wires translates in a predictable manner the wavelength response of the artificial material. We also analyze coupling effects between the SRRs and the continuous nanowires for different spacing between them. The results of our study are expected to provide useful guidelines for the design of optical devices using metamaterials on silicon.

2. Cut wire pairs metamaterials with broken symmetry at microwave frequencies

2.1 Plasmon hybrization

In this chapter, we show that negative dielectric permittivity and negative magnetic permeability can be simultaneously achieved by appropriately controlling the coupling strength between paired cut-wires of adjacent layers. The coupling strength is itself

controlled by adjusting either the spacing or the alignment of paired cut-wires. Using an asymmetric alignment, an inverted hybridization scheme, where the asymmetric mode is at a higher frequency than the symmetric mode, is predicted and thus more favorable for obtaining negative refraction. The first experimental demonstration of a negative refraction metamaterial exclusively based on paired cut-wires in the microwave range is reported.

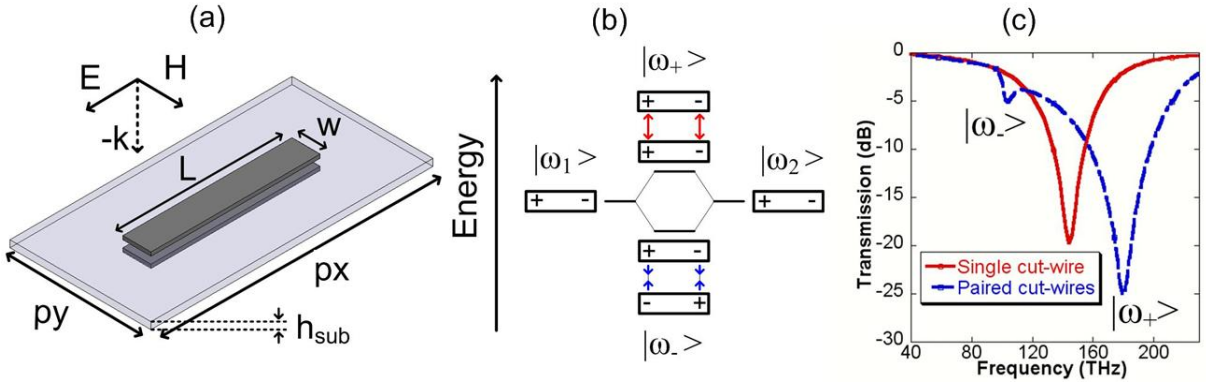

Fig. 1. (a) Schematic of the symmetric cut-wire pair. (b) Hybridization scheme of the two coupled dipoles. (c) Transmission spectra calculated at normal incidence for a periodic array of cut-wires (red) and of paired cut-wires (blue), respectively (px= 1.2 μm; py= 200 nm; w= 30 nm; L= 600 nm; hsub= 100 nm). The 30 nm thick gold cut-wires are described using a Drude model whose parameters can be found in [Kante, 2008a]. The dielectric spacer (SiO2) permittivity is ε_{sub}=2.25.

The plasmon hybridization scheme was introduced by Prodan et al. [Prodan, 2003] who gave an intuitive electromagnetic analogue of molecular orbital theory. Such a scheme has largely been used by the metamaterial community especially for simplifying metamaterial designs at optical wavelengths [Shalaev, 2005, Liu, 2008]. The coupling of two electric dipoles facing each other has thus been exploited to mimic magnetic atoms and alter the effective magnetic permeability of metamaterials in the optical range. While a magnetic activity was indeed obtained from metamaterials comprised of metallic dipoles [Shalaev, 2005, Liu, 2008], negative refraction was reported only in the pioneering demonstration by Shalaev et al. [Shalaev, 2005] who used a periodic array of cut-wire pairs. In order to unambiguously achieve negative refraction, the magnetic activity must actually occur within a frequency band in which the electric permittivity is negative. For this purpose, one solution consists of associating magnetic "atoms" (coupled metallic dipoles) to a broadband "electric plasma" (continuous wires) in the same structure. Many authors have used this solution either in the microwave [Zhou, 2006, Guven, 2006] or in the optical regime [Liu, 2008], thereby contributing to the development of the so-called fishnet structure. We propose another solution based on the control of the coupling between metallic dipoles in such a way that the symmetric and anti-symmetric bands have a sufficient overlap. The coupling strength is varied either by changing the distance between coupled dipoles or by breaking the symmetry of the structure.

Fig. 1(a) shows the rectangular unit cell of the studied 2D structure in the case where the coupled metallic dipoles (cut-wires) are vertically aligned. This structure is henceforth referred to as the symmetric cut-wire structure to distinguish it from the asymmetric

structure discussed later (see fig. 2). Both structures consist of 2D periodic arrays of metallic cut-wires separated by a dielectric spacer [Shalaev, 2005]. The electromagnetic wave should propagate normally to the layers with the electric field parallel to the longest side of dipolar elements. The structure can be described in terms of effective parameters as long as the cut-wire width w and spacer thickness hsub are much smaller than the wavelength [Shalaev, 2005]. Two series of calculations were carried out using a finite element simulation package (HFSS from Ansys), one for symmetric structures and the other for asymmetric structures. The effective parameters were obtained from the calculated transmission and reflection coefficients [Gundogdu, 2008].

The first series of calculations were performed to compare the electromagnetic response of a symmetric cut-wire bi-layer (blue curve in Fig. 1(c)) to that of a cut-wire monolayer (red curve in Fig. 1(c)). As it is evident in the figure, only one resonance is observed for the single-face cut-wire structure in the frequency range of interest. This resonance corresponds to the fundamental cut-wire dipolar mode, which in the optical regime can also be interpreted in terms of a localized plasmon resonance [Smith, 2002]. Collective electronic excitations, also called surface plasmons, are indeed the main mechanism at short wavelengths. For the double-face cut-wire structure, the coupling between paired cut-wires lifts the degeneracy of the single cut-wire mode, which hybridizes into two plasmon modes. One mode is symmetric and corresponds to in-phase current oscillations, while the other is anti-symmetric and corresponds to out-of-phase current oscillations. For a symmetric cut-wire pair with a vertical alignment of the two cut-wires, the anti-symmetric mode is the low-energy (-frequency) mode since attractive forces are present in the system. Conversely, repellent forces are produced in the case of the symmetric mode that is therefore the high-frequency mode. The stronger the coupling (the smaller the spacing between the dipoles), the larger the frequency difference between the two modes. The evolution of the transmission spectra with the thickness of the dielectric spacer (or substrate) h_{sub} is illustrated in Fig. 3(a) in the case of a structure designed to operate in the microwave regime. Similar results were obtained for the structure in Fig. 1(c).

A second series of calculations was performed to analyze the influence of a vertical misalignment of metallic dipoles at a fixed spacer (or substrate) thickness. For this purpose, the cut-wire layers were shifted from each other in the horizontal XY plane (Fig. 2(a)) thus breaking the symmetry of the cut-wire structure. The relative displacements dx and dy in the X and Y directions respectively were used as parameters. In the example in the microwave regime, the substrate thickness was chosen to be equal to that of commercially available epoxy dielectric boards (1.2 mm). For this thickness and a vertical alignment of paired cut-wires (dx = dy = 0), the calculated transmission spectrum in Fig. 3(a) revealed a pronounced frequency separation between the symmetric (electric) and anti-symmetric (magnetic) modes. Figs. 3(b) and 3(c) show the evolution of the transmission spectrum for non-zero values of the longitudinal (dx) and lateral (dy) displacements, respectively. Quite surprisingly, as previously reported by A. Christ et al. [Christ, 2007] for the control of Fano resonances in a plasmonic lattice of continuous wires, symmetry breaking can invert the hybridization scheme due to modified Coulomb interactions (Fig. 2(b)) resulting in the symmetric resonance occurring at a lower frequency than the anti-symmetric one. The Coulomb forces in our system result from the interaction of charges located at the cut-wire ends. When the longitudinal shift (dx) is progressively increased, the signs of the charges in

close interaction change. As a result the repulsive force becomes attractive and vice versa. Correspondingly, the symmetric mode becomes the low-energy mode while the asymmetric mode is shifted to higher frequencies. It is evident that this inversion process is impossible in the case of a lateral dy displacement of the dipoles (Fig. 3(c)).

Controlling the coupling between metallic dipoles thus allows the two plasmon resonances to be engineered. When the magnetic and electric modes are very close together, the bands of negative permeability and negative permittivity overlap, and a negative refraction material is obtained. More generally, the design of true negative index metamaterials can be achieved by appropriate design of the three degrees of freedom h_{sub}, dx and dy.

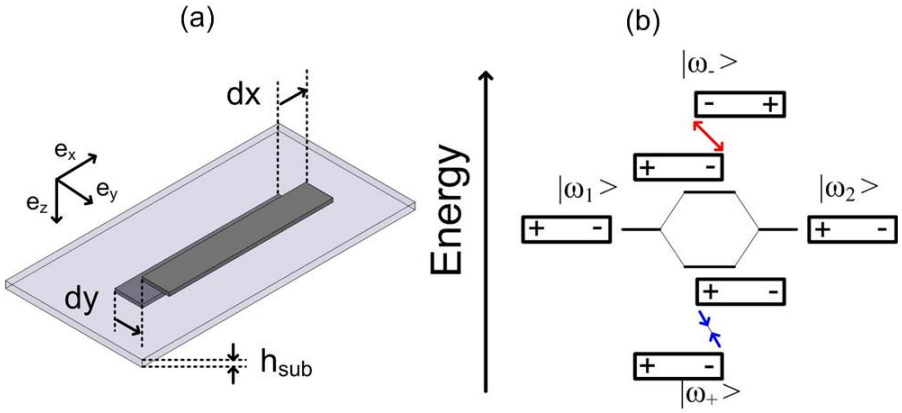

Fig. 2. (a) Asymmetric cut-wire pair with the three degrees of freedom for the control of the coupling strength: hsub, dx and dy. (b) Inverted hybridization scheme.

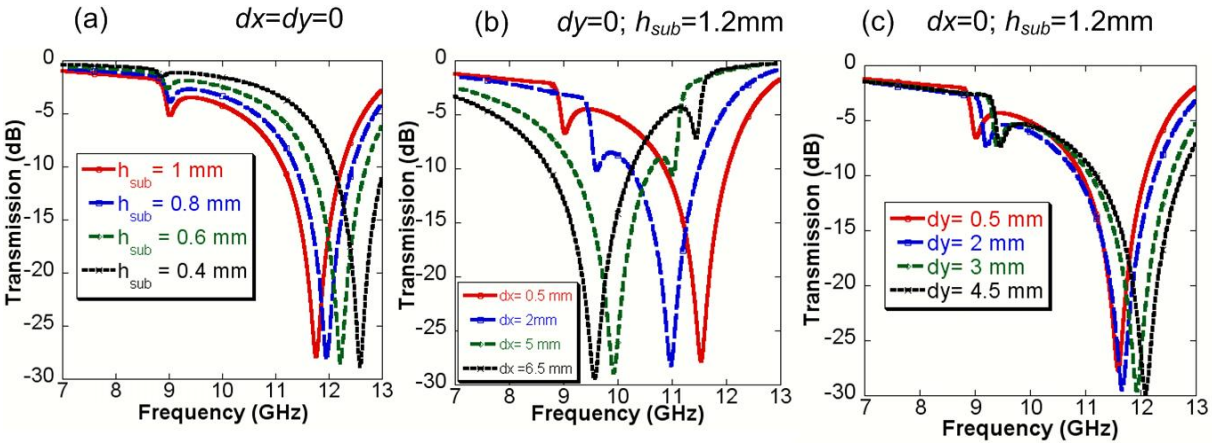

Fig. 3. Influence of the coupling strength on the transmission spectra of a bi-layer structure (px = 19 mm; py = 9.5 mm; w = 0.3 mm; L = 9.5 mm; h_{sub} = 1.2 mm). The substrate permittivity is ε_{sub} = 3.9. (a) variation of the dielectric spacer (or substrate) thickness h_{sub}; (b) variation of the longitudinal shift dx; (c) variation of the lateral shift dy.

2.2 Monolayer double-face structure

In this part, we present a systematic study of the cut wires structure presented in Fig. 4, derived from the previous structures, under normal-to-plane incidence in the microwave domain. Numerical simulations performed using the FEM based software HFSS are run to

show and understand the electromagnetic behavior of the design. A single layer of the metamaterial is characterized by reflection and transmission measurements. The retrieved parameters show simultaneous resonances in the permittivity and permeability responses leading to a negative index of refraction.

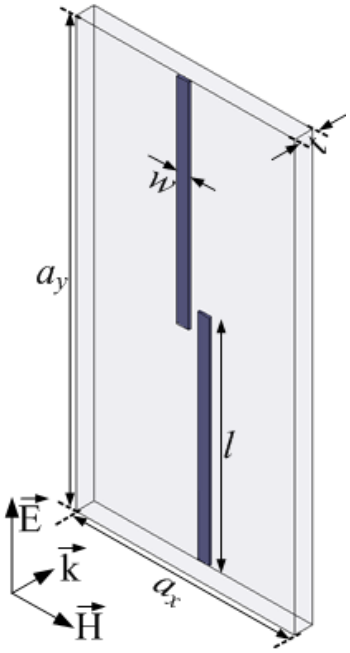

Fig. 4. Unit cell of: cut wires structure under normal-to-plane propagation (ax = 9.5 mm, ay = 19 mm, w = 0.3 mm, l = 9.5 mm). The inserts show the direction and the polarization of the wave.

The cut wires metamaterial illustrated by its unit cell in Fig. 4 is employed to operate in the microwave regime. It consists of a double-face structure composed of periodic cut wires of finite length. The structure is printed on both faces of an epoxy dielectric board of thickness t = 1.2 mm and of relative permittivity ε_r = 3.9. For the different samples reported here, the width of the cut wires denoted by w is 0.3 mm. The length of the cut wires is l = 9.5 mm and the unit cell size in the x and y direction is respectively ax = 9.5 mm and ay = 19 mm. These dimensions have been optimized to operate around 10 GHz and remain the same throughout the section.

The reflection and transmission spectra of the metamaterial are calculated using HFSS by applying the necessary periodic boundary conditions on the unit cell. Several samples of the structure consisting of 10 × 5 cells on a 120 mm × 120 mm epoxy surface are fabricated using conventional commercial chemical etching technique. Measurements are done in an anechoic chamber using an Agilent 8722ES network analyzer and two X-band horn antennas. In the transmission measurements, the plane waves are incident normal to the prototype surface and a calibration to the transmission in free space (the metamaterial sample is removed) between the two horn antennas is done. The reflection measurements are done by placing the emitting and receiving horn antennas on the same side of the prototype and inclined with an angle of about 5° with respect to the normal on the prototype surface. The calibration for the reflection is done using a sheet of copper as reflecting mirror.

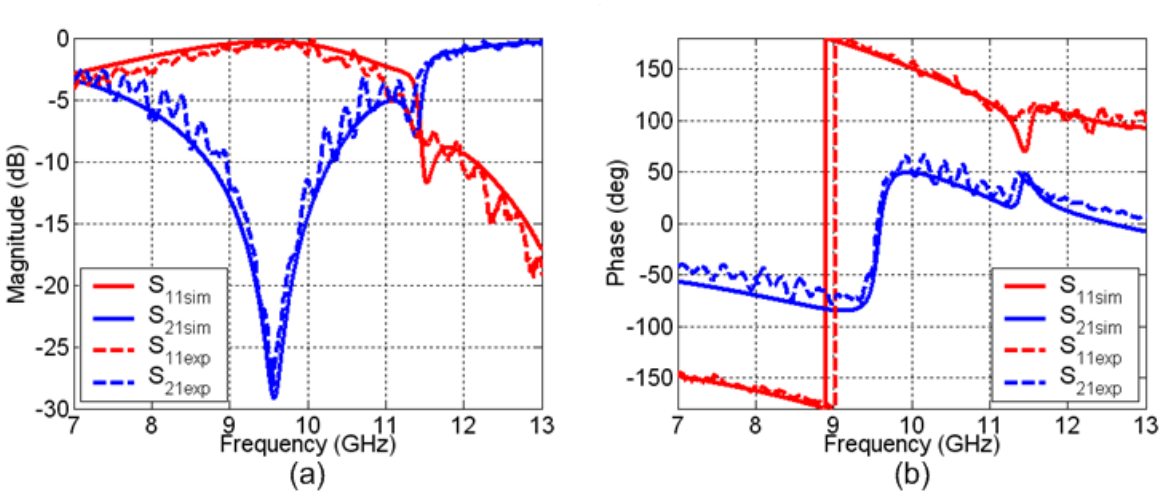

Fig. 5. Calculated and measured reflection (S11) and transmission (S21) responses of the metamaterial for a single layer: (a) magnitude, and (b) phase.

Figure 5 shows the calculated (continuous lines) and measured (dashed lines) S-parameters of the metamaterial for a monolayer configuration. There is a very good qualitative agreement between simulations and measurements. The calculated and measured magnitudes of S21 presented in Fig. 5(a) show clearly two resonance dips, the first one at 9.58 GHz and a second one at 11.39 GHz. We can note in Fig. 5(b) that a change in sign occurs for the transmission phase at the first resonance dip. At the second resonance dip, a peak and a dip is respectively observed in the transmission and reflection phase.

Using the retrieval procedure described in [Nicholson, 1970], based on the inversion of the reflection and transmission coefficients, the effective parameters of the double-face metamaterial structure are extracted. The metamaterial has a period very small compared to the wavelength λ (less than $\lambda/20$) in the propagation direction. The propagation of the electromagnetic wave travelling along this direction is dominated by this deep sub-wavelength period and not by the in-plane period ax or ay. There is only a single propagating mode in the negative-index frequency region, justifying the description of the cut wires metamaterial with an effective index [Valentine, 2008].

The extracted permittivity ε, permeability μ and refractive index n are shown in the various parts of Fig. 6. Two extraction procedures have been performed: the first one uses the calculated S-parameters and the second one is based on the measured S-parameters. As illustrated by the extracted parameters from the calculated and measured S-parameters, the cut wires structure shows firstly an electric resonance at the first resonance dip observed at 9.58 GHz in Fig. 6. This electric resonance exhibits values going negative for the real part of the permittivity in the vicinity of the resonance. Secondly a magnetic resonance with negative values appears at the right hand side of the second resonance dip at 11.5 GHz. Around the same frequency, the real part of the permittivity is still negative. The extracted real part of the refractive index is therefore negative around 11.5 GHz which is the frequency of the LH peak. However, we can also notice that the zero value for the ε response is very close to 13 GHz where a full transmission band is observed in Fig. 6(a). This frequency constitutes the frequency of the RH transmission peak. We can therefore deduce that this RH transmission peak is due to an impedance matching between the structure and vacuum.

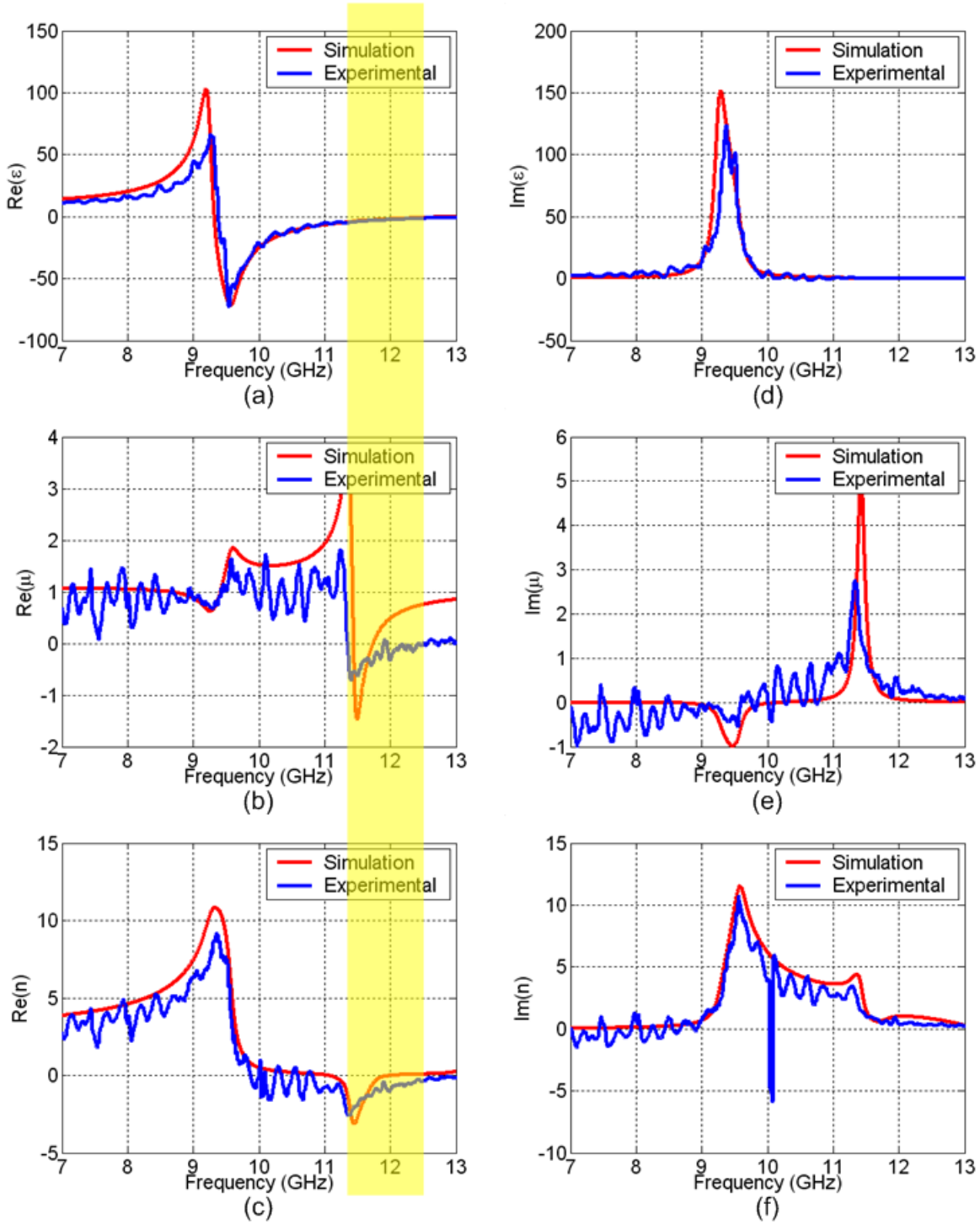
Simulation
Experimental
Re(ε)
Frequency (GHz)
(a)
Im(ε)
(d)
Re(μ)
(b)
Im(μ)
(e)
Re(n)
(c)
Im(n)
(f)

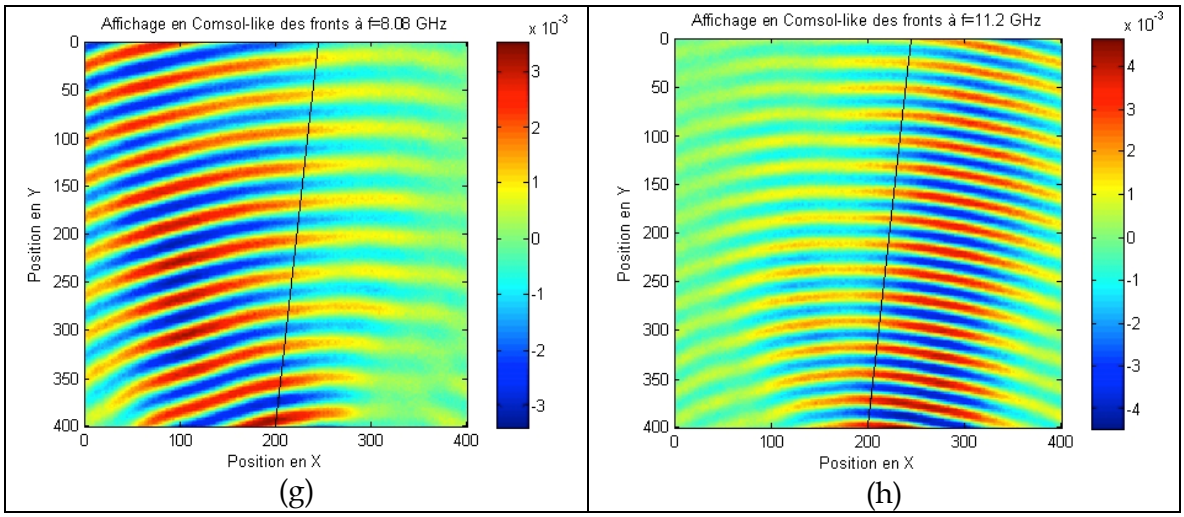

Fig. 6. Extracted electromagnetic properties of the cut wires metamaterial using the simulated and experimental data of Fig. 4: (a)-(c) real parts, and (d)-(f) imaginary parts of the permittivity ε, of the permeability μ and the refraction index n. The shaded yellow area delineates the frequency region where the measured real parts of ε and μ are simultaneously negative. Measurement of the wave propagation trough a prism of 6.3°: (g) E field cartography at 8.08GHz: the optical index is positive, around 5.6 (h) E field cartography at 11.2GHz: the optical index is negative, around -2.3.

Since the real part of n (n′) is given by $n' = \varepsilon' z' - \varepsilon'' z''$ from $n = \varepsilon z$ and $z = \sqrt{(\mu/\varepsilon)}$, the imaginary parts of the permittivity (ε′′) and the permeability (μ′′) also accounts for n′. Therefore, a negative real part of n can be accomplished without having ε′ and μ′ simultaneously negative. This can happen only if ε′′ and μ′′ are sufficiently large compared to ε′ and μ′. A wider negative n′ frequency band is observed due to the dispersion of the fabricated prototype. The shaded yellow area in Fig. 6 highlights the frequency region where the measured real parts of the permittivity (ε′) and the permeability (μ′) are simultaneously negative to emphasize the desired measured negative values of n′. Concerning the imaginary parts, a very good qualitative agreement is observed between calculations and experiments. We shall note that the imaginary part of n (n′′) is very low in the negative n′ frequency region. Figures 6(g) and 6(h) show the measurements of the near electric field through a prism with an angle of 6.3°. Figure 6(g) shows the E field cartography at 8.08 GHz: the optical index is positive and found to be around 5.6. Figure 6(h) shows the E field cartography at 11.2 GHz: the optical index is negative and calculated to be around -2.3. These values agree very well with the extracted values of the optical index calculated from the measurements of the reflexion and transmission coefficients of the figure 6(c) using the retrieval procedure described in [Nicholson, 1970].

2.3 Stacking of layers

Stacking multiple layers of LH materials may be useful in many practical applications such as subwavelength imaging [Wang, 2007, Ziolkowski, 2003] and directive antennas [Burokur, 2005, Shelby, 2001]. It is obvious that the effective properties obtained from the inversion method on a monolayer give a good idea about the effective properties of the metamaterial. However, other effect such as inter-layer coupling must be taken into account because it

affects the material properties of the structure. Therefore, two, three and four layers of the designed bi-layered metamaterial are stacked with a 1 mm air spacing between each layer as presented in Fig. 7(a). Numerical simulations are run to show the expected performances of a bulk metamaterial composed of multiple layers. The transmission spectra for the different number of layers are presented in Fig. 7(b).

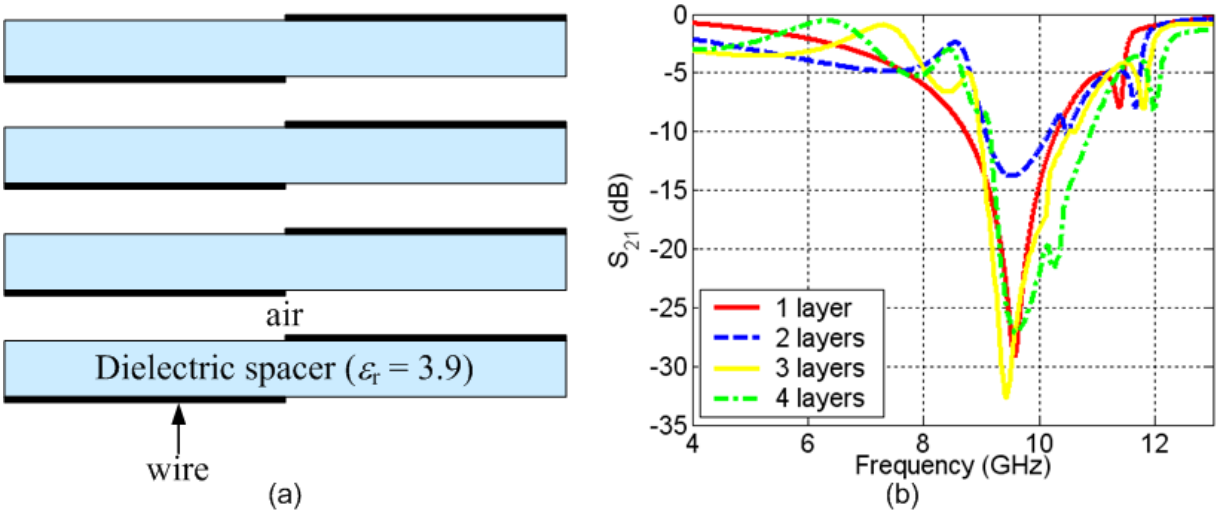

Fig. 7. (a) A bulk metamaterial composed of four layers interleaved with 1 mm air spacing, and (b) transmission spectra for different number of layers.

From the spectra of Fig 7(b), we can note that the frequency of the first transmission dip remains constant with an increasing number of layers while the second dip shifts slightly towards higher frequencies. However, peaks and valleys appear at lower frequencies suggesting a coupling mechanism between consecutive layers. The number of these peaks and valleys increases with an increasing number of layers as shown in Fig. 7(b). The transmission spectra together with the corresponding reflection spectra are used for the extraction of the material properties presented in Fig. 8. It should be noted that the first transmission dip in the single layer case corresponds to an electric resonance where ε' exhibits negative values. However, other $\varepsilon' < 0$ frequency bands can be observed in Fig. 8(a) for the multiple layers cases due to the valleys noted in the transmission spectra. And, since the magnitude of the transmission dips decreases with the number of layers, the magnitude of ε' also decreases as shown in Fig. 8(a). At higher frequencies near 12 GHz, a magnetic resonance is also observed for multiple layers as for the single layer case. However the magnitude tends to decrease while the number of layers increases (Fig. 8(b)). For more than two layers, μ' exhibits only positive values at the resonance near 12 GHz. Besides, another magnetic resonance with $\mu' < 0$ can be observed at lower frequencies with simultaneously $\varepsilon' < 0$ when more than one layer is used. So even if the $\mu' < 0$ frequency band disappears at the second transmission dip due to the $\mu' > 0$, a negative index band is observed at lower frequencies as shown in Fig. 8(c). This negative refractive index results from the coupling mechanism created when several layers of the double-face structure are stacked. The negative index frequency band widens when the number of layers increases.

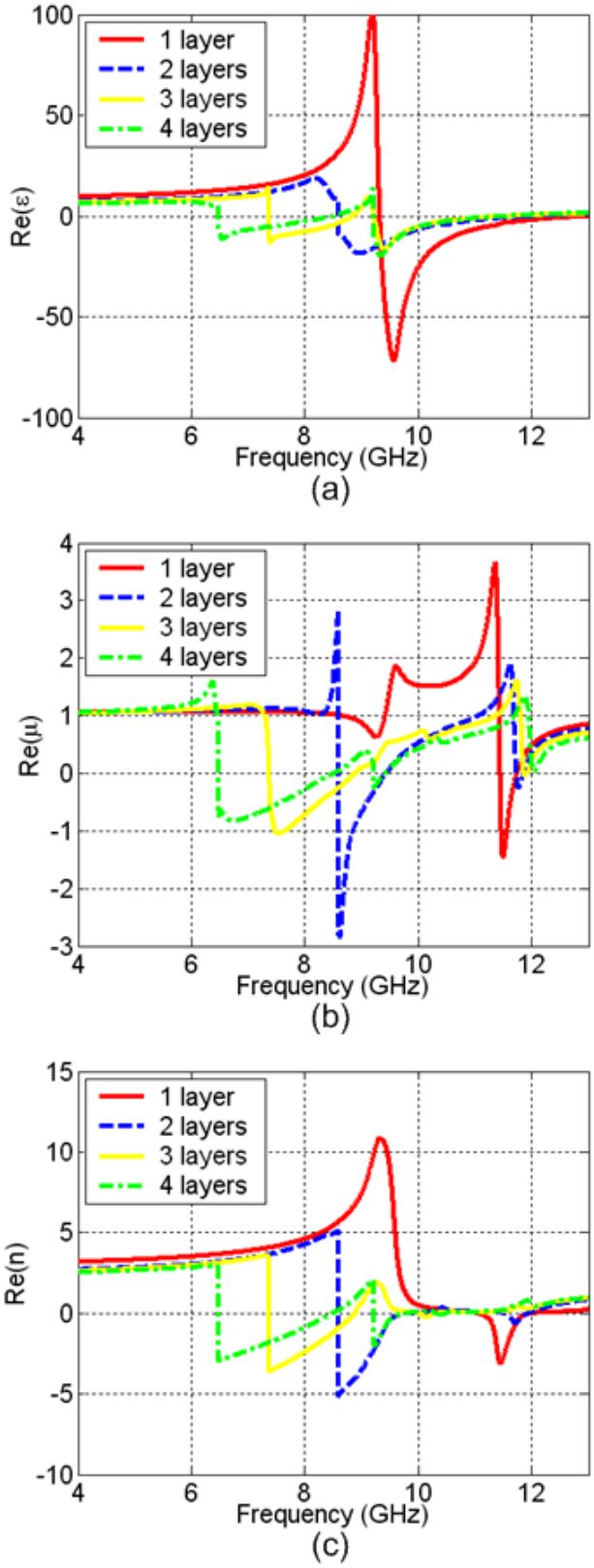

Fig. 8. Extracted material properties for different number of layers. (a) Re(ε), (b) Re(μ), and (c) Re(n).

2.4 Incidence dependence of the negative index

Finally, we investigate numerically and experimentally the reflection and transmission spectra for an obliquely incident plane wave on the asymmetric structure. Three different angles, namely 15°, 30° and 45° in both H- and E-planes of the square lattice are studied in simulations and experiments. Measured reflection and transmission coefficients are compared to simulated ones in Fig. 9 for the H-plane. There is qualitative agreement between simulations and measurements. Calculated and measured magnitudes of S_{21} show clearly two resonance dips, an electric one at 9.5 GHz and a magnetic one at 11.5 GHz. These two resonances are found to be independent of the incidence angle in the H-plane as shown in Figs. 9(a)-(c).

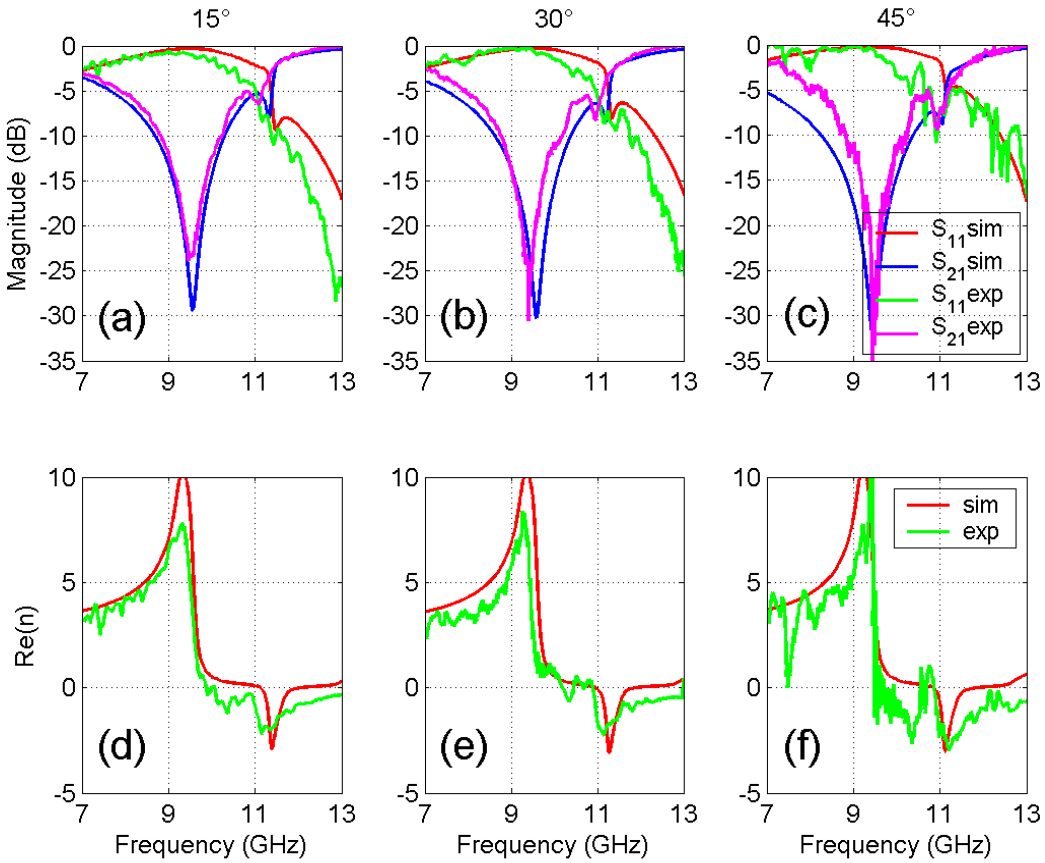

Fig. 9. Oblique incidence (15°, 30° and 45°) in H-plane. (a)-(c) Computed and measured reflection and transmission coefficients. (d)-(f) Real part of effective index n.

To retrieve effective parameters at oblique incidence, the retrieval procedure in [Smith, 2002] has to be modified and anisotropy has to be addressed [Burokur, 2009b]. Indeed cut wire pairs represent a biaxial anisotropic media whose principal axis are along x, y and z. Consequently 2x2 transfer matrices used in normal incidence are no longer sufficient and the full 4x4 transfer matrix accounting for coupling of s- and p-waves should be considered [Yeh, 1998]. However, since the electric field in our case is always along y independently of θ, cross-polarization terms do not arise and therefore we only use one 2x2 matrix for s-waves. In this case the effective index is given by

$$\frac{\varepsilon_y \mu_x \mu_z}{\mu_z \cos^2\theta + \mu_x \sin^2\theta} \tag{1}$$

Figures 9(d)-(f) show that n responses remain mostly unchanged compared to the 0° case studied in [Burokur, 2009, Sellier, 2009].

Measured reflection and transmission coefficients are compared to simulated ones in Fig. 10 for the E-plane. Apart from one sharp feature on each spectrum, simulations and measurements agree qualitatively. This peak which is much sharper than either the anti-symmetric or the symmetric resonance, shifts with incidence angles from 12.47 GHz at 15° to 10.5 GHz at 30° and 9.22 GHz at 45°. It is the manifestation on the specular order (0,0) of a diffraction threshold, namely that of the (0,-1) diffracted order. At these frequencies the (0,-1) diffracted order transits from evanescent to propagating, appearing at grazing incidence. Diffraction thresholds frequencies are calculated in two ways, with HFSS and using (2) from grating theory taking into account the fact that there is no wave vector component along x in E-plane.

$$k_\perp = \pm\sqrt{\frac{\omega^2}{c^2}\varepsilon_r - k_{//}^2} = \pm\sqrt{\frac{\omega^2}{c^2}\varepsilon_r - \left(m\frac{2\pi}{a_x}\right)^2 - \left(\frac{\omega}{c}\sin\theta + n\frac{2\pi}{a_y}\right)^2} \quad m,n \in Z \tag{2}$$

Due to respective values of ax = 9.5 mm and ay = 19 mm, it can be seen that the (0,-1) order is the first diffracted order to become propagating. Results for diffraction thresholds frequencies are summarized in Table I. By comparison, in the H-plane even at an angle of 45° the (0,-1) diffracted order is above 18 GHz. To overcome the appearance of a diffraction threshold, a triangular lattice as shown in the inset of Fig. 10(d) is proposed to replace the square one used in the figure 10(a-c). In the triangular lattice, every other cell along x is laterally displaced by 4.75 mm along y. In this lattice, diffraction threshold frequencies are given by (3):

$$k_\perp = \pm\sqrt{\frac{\omega^2}{c^2}\varepsilon_r - k_{//}^2} = \pm\sqrt{\frac{\omega^2}{c^2}\varepsilon_r - \left((2m-n)\frac{2\pi}{a_x}\right)^2 - \left(\frac{\omega}{c}\sin\theta + n\frac{2\pi}{a_y}\right)^2} \quad m,n \in Z \tag{3}$$

Computed reflection and transmission spectra presented in Figs. 10(d)-(f) confirm the rejection of the diffraction threshold above 13 GHz. Besides, a shift in frequency can be noted for both anti-symmetric and symmetric resonances. This shift is seen to be much stronger than for any resonances in the H-plane and the detuning of both electric and magnetic resonances with respect to the incidence angle θ leads to a loss of the frequency overlap, hence the negative index, above 20°. As it can be noted particularly for θ = 15°, the magnetic resonance shifts towards lower frequencies for the triangular lattice (10.43 GHz) compared to the square one (11.02 GHz). This is most probably due to extra capacitive coupling between y-displaced wires on same face of the dielectric board.

In summary, we presented the dependence of resonances and retrieved effective index on the incident angle in recently proposed asymmetric cut wire pairs. No change has been observed for oblique incidence in the H-plane. However for the E-plane, a diffraction threshold appears for the square lattice rendering the introduction of effective parameters

meaningless. A triangular lattice has therefore been proposed to avoid having the diffraction threshold below the electric and magnetic resonances. A detuning of both resonances has been observed leading to a lack of resonance frequencies overlap above 20°.

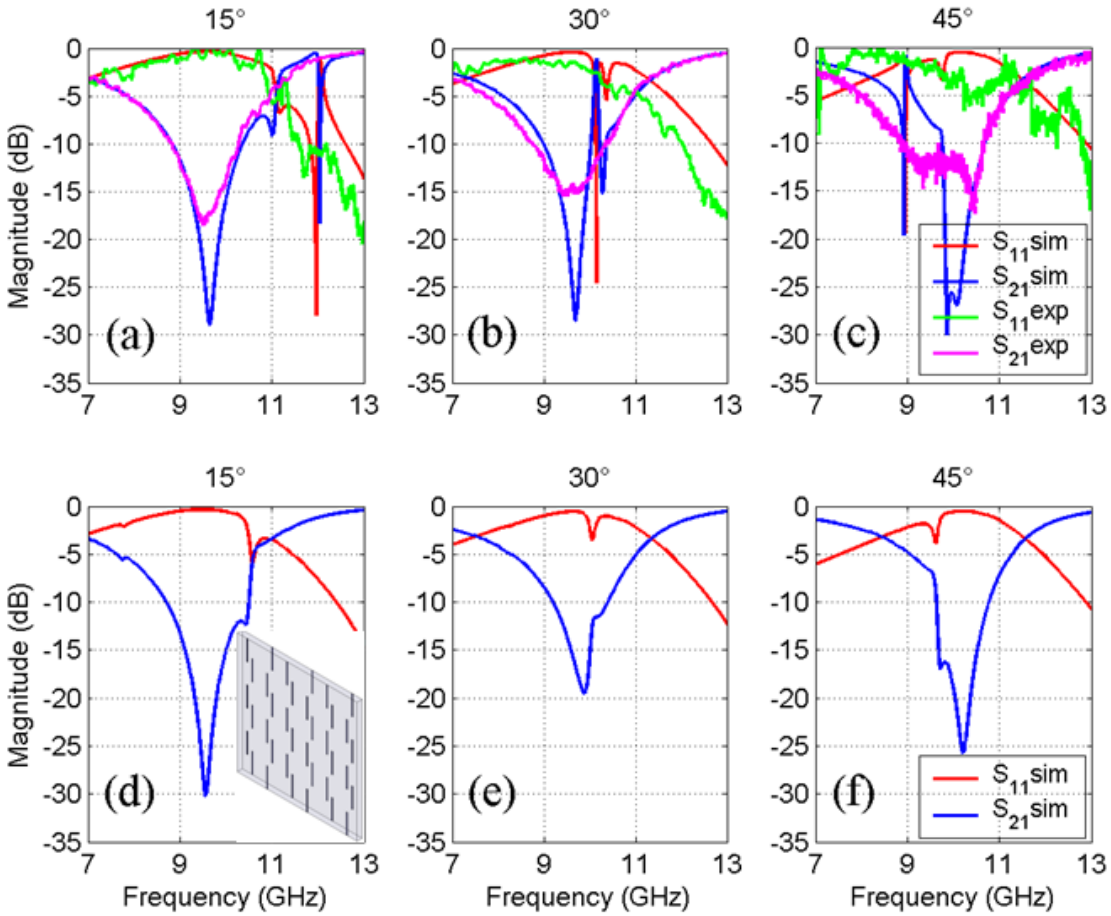

Fig. 10. Oblique incidence (15°, 30° and 45°) in E-plane. (a)-(c) Computed and measured reflection and transmission coefficients for the square lattice. (d)-(f) Computed and measured reflection and transmission coefficients for the triangular lattice.

	HFSS (square lattice) Mode (0,-1)	Grating (square lattice) Mode (0,-1)	HFSS (triangular lattice) Mode (0,-1)	Grating (triangular lattice) Mode (0,-1)
$\theta = 0°$	15.78	15.79	22.31	22.33
$\theta = 15°$	12.58	12.54	19.15	19.15
$\theta = 30°$	10.54	10.53	17.31	17.32
$\theta = 45°$	9.24	9.25	16.35	16.35

Table 1. Computed numerical and analytical diffraction threshold frequencies (GHz)

3. Infrared metamaterials and plasmons hybridization

3.1 Engineering resonances in infrared metamaterials

Recently, a theoretical study showed that optical resonances in both SRR arrays and cut wire arrays could be interpreted in terms of plasmon resonances [Rockstuhl, 2006]. A gradual shift in the SRR resonance frequencies was predicted when reducing the length of SRR legs to the point where each SRR was transformed into a single wire piece. The magnetic and electric properties of these modified versions of SRRs were theoretically investigated in [Zhou, 2007]. Following these theoretical studies, we present here an experimental and numerical analysis of the infrared response of metamaterials made of continuous nanowires and split ring resonators where the geometry is gradually altered. The metamaterial structure is fabricated on low-doped silicon. The impact of the geometric transformation of the SRRs on the spectra of the composite metamaterial is measured in the 20-400 THz frequency range (i.e., in the 1.5 - 15 μm wavelength range) for the two field polarizations under normal to plane propagation. Coupling effects between the SRRs and the continuous nanowires are analyzed for different spacings between them. The results of our study are expected to provide useful guidelines for the design and engineering of negative index metamaterials on silicon.

3.1.1 Design, fabrication, characterization and modeling of metamaterial structures

Four structures consisting of a two-dimensional periodic array of gold nanowires and gold SRRs were fabricated on a 280μm thick silicon substrate (Fig. 11). The fabrication steps included e-beam lithography, high vacuum electron beam evaporation of 5 nm thick titanium and 40 nm thick gold films, and a lift-off process. It is worthwhile noticing that all structures were fabricated in the same run, thereby allowing a meaningful comparison of their optical characteristics. As seen in Fig. 11, the four structures only differ in the shape of SRRs, which are gradually transformed into simple cut wires from structure 1 to structure 4. In the intermediate cases of structures 2 and 3, SRRs appear to be U-shaped with smaller legs than in the standard case of structure 1. Except for this resonator shape, all the other geometrical parameters of the four structures are identical. In each case, the lattice period is ~ 600nm, the width of all wires (continuous and discontinuous) is ~ 50nm, and the continuous wires are parallel to the SRR bases with a separation of 115 ± 20 nm between each continuous wire and the closest SRR base. The SRR gap width in structure 1 is ~100 nm while the length of the two SRR legs is ~ 280nm. This length is reduced to ~190 and 110 nm in structures 2 and 3, respectively. The scanning electron microscope (SEM) images reported in Fig. 11 (middle row) illustrate the excellent regularity of the four fabricated structures.

The transmission and reflection spectra of the fabricated structures were measured under normal-to-plane incidence with a FTIR (Fourier Transformed InfraRed spectrometer) BioRad FTS 60 equipped with a Cassegrain microscope. The FTIR beam was polarized using a KRS5 polarizer adapted to the wavelength region from ~ 1.5 to 15μm (i.e. to frequencies varying from 20 to 200 THz). A diaphragm was used in such a way as to produce a light spot smaller than 100 × 100 μm2 onto the sample (i.e. smaller than the surface of each periodic structure). Measurements were performed for two field polarizations of the incident beam, the parallel polarization with the illuminating electric field parallel to both the continuous wires and the SRR gaps and the perpendicular polarization with the electric field perpendicular to the

continuous wires and SRR gaps. The measured transmission spectra were normalized versus the transmission of an unprocessed part of the silicon substrate. The measured reflection spectra were normalized versus the reflection of a 40 nm thick gold film deposited on silicon.

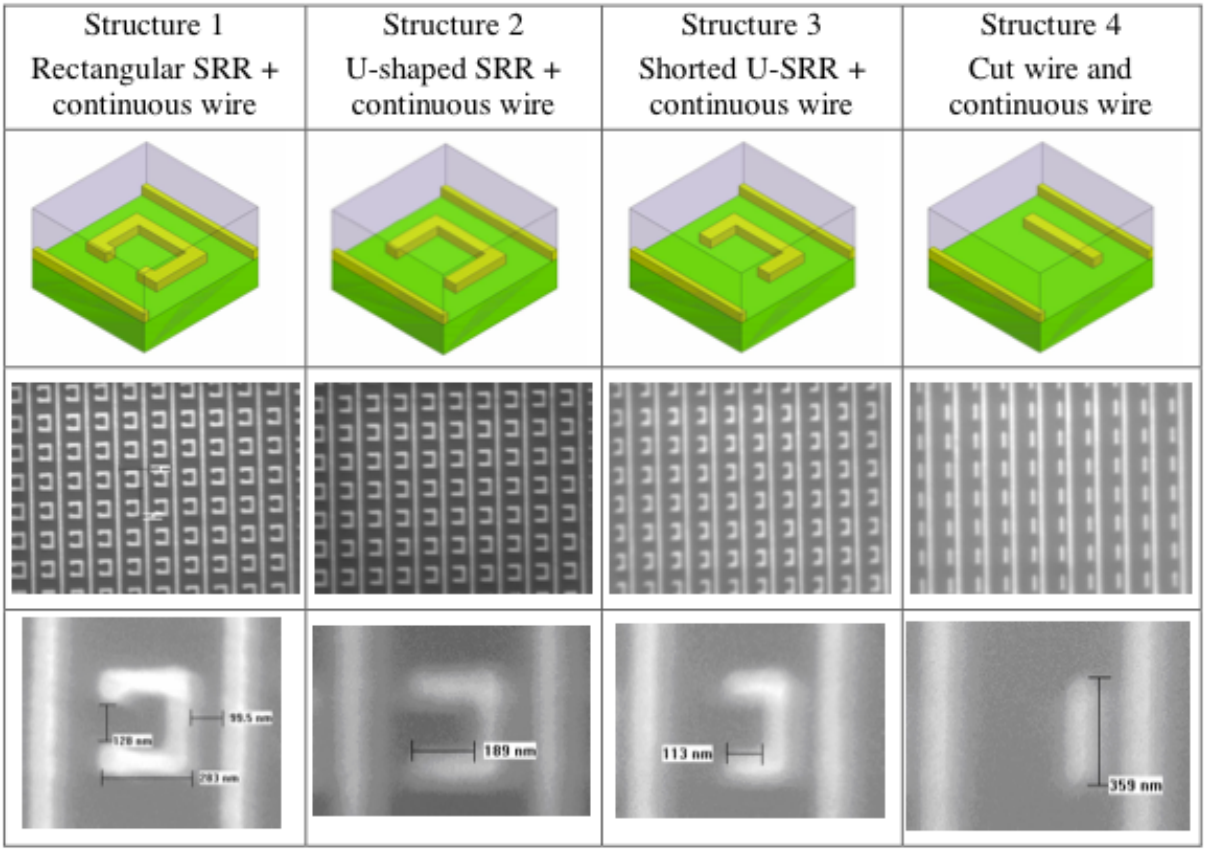

Fig. 11. Schematic representations (top) and scanning electron microscope images (middle and bottom) of the four metamaterial structures fabricated on silicon. The top and bottom pictures show the elementary unit cell of each structure. From left to right, the length of SRR legs is reduced to the point where the SRR is transformed into a single wire piece. The middle pictures show the regularity achieved in the fabrication of the periodic arrays of nanowires and split ring resonators

Numerical simulations of the spectral responses of the four structures were performed with a finite element software (HFSS, 2006). Periodic boundary conditions were applied to the lateral sides of the elementary lattice cell (Fig. 11). The silicon substrate was assumed to be lossless with a constant permittivity equal to 11.9. A Drude model was used to simulate the permittivity and loss tangent of the gold wires:

$$\varepsilon(\omega) = 1 - \frac{\omega_p^2}{\omega(\omega + i\omega_c)} \tag{4}$$

where ω_p and ω_c are the plasma and collision frequency of the gold film, respectively. The values of ω_p and ω_c chosen in the simulations were: ω_p =1.367 x 10^{16}s^{-1} (f_p =2176 THz) and ω_c

= 6.478 x 10^{13} s^{-1} (f_c =10.3 THz). Actually, the collision frequency can be considered to a certain extent as a fit parameter. An increase of the collision frequency results in higher absorption losses of the structures, while it does not change the spectral positions of resonances. The value reported above for ω_c is 2.6 times larger than in bulk gold. This increase is supposed to account for additional scattering experienced by electrons at the metal surfaces.

3.1.2 Results of measurements and simulations

The results of our measurements and simulations are shown in Fig. 12 for the four structures. Results for the parallel polarization are gathered in the series of figures from (a) to (d). Those for the perpendicular polarization are gathered in the series of figures from (e) to (h). In all these figures, resonances manifest themselves as reflection maxima correlated with transmission minima. A slow decrease (resp. increase) of the transmission level (resp. reflection level) is also observed at low frequencies for the parallel polarization. This latter evolution can be readily attributed to the plasmon-like band associated to the periodic array of continuous wires [Pendry, 1998].

For the parallel polarization and the structures with the SRRs of larger sizes (structures 1 and 2), two resonances are observed within the spectral window of measurements [Figs. 12(a) and 12(b)]. Only the first resonance is experimentally observed for structures 3 and 4. The SRR resonances actually shift towards higher and higher frequencies as the whole SRR length is decreased. In the same time, their amplitude becomes smaller and smaller. For the first resonance, the maximum reflection R_{max} decreases from ~0.63 to ~0.5 while the minimum reflection R_{min} remains close to ~0.35 [Fig. 11(b)]. Accordingly, the minimum transmission T_{min} increases from ~0.12 to ~0.25 while the maximum transmission T_{max} remains close to ~0.6 [Fig. 11(a)]. It is worthwhile noticing that the values of R and T out of resonance correspond to those expected for a single face of silicon wafer partially covered with ~10-15% of highly reflecting metal. Whereas (R+T) approaches unity in this case ($R_{min}+T_{max}$~0.95), its smaller value at resonance ($R_{max}+T_{min}$~0.75) clearly indicates the presence of dissipative losses in metallic elements. The frequency positions of resonances, the values of R and T out of resonance, the values of (R+T) in general as well as the shapes of experimental curves in Figs. 12(a) and 12(b) are very well reproduced by numerical simulations [Figs. 12(c) and 12(d)]. The only discrepancy between experiments and simulations stems from the smaller amplitudes of resonances measured in experiments, especially those at high frequencies. The second resonance predicted at ~180 THz (λ ~ 1.7μm) for structure 3 is even not resolved in the experiments. Actually, minute deviations of the geometry from unit cell to unit cell and particularly residual surface roughness of the SRRs and continuous wires can explain the damping and inhomogeneous broadening of resonances as well as the increasing importance of these effects at high frequencies.

For the perpendicular polarization and for structures 1, 2 and 3, a single resonance is observed within the spectral range of measurements [Figs. 12(e) and 12(f)]. In contrast, no resonance is detected for the structure with cut wires. The evolution of the SRR resonance with the SRR length is actually similar to that observed for the parallel polarization. Smaller SRR lengths simultaneously lead to higher resonance frequencies and smaller resonance amplitudes. A good agreement is found between experimental results and numerical simulations [Figs. 12(g) and 12(h)]. Previous remarks made for the parallel polarization

apply to the perpendicular polarization. Minute deviations from unit cell to unit cell and surface roughness of metallic elements are likely to explain the broader resonances with smaller amplitudes observed in the experiments. The second resonances predicted for structures 1, 2 and 3 in the frequency region from 170 to 200 THz [Figs. 12(g) and 12(h) manifest themselves only as smooth maxima (resp. minima) in the measured reflection (resp. transmission) spectra of Fig. 12(f) (resp. Fig. 12(e)]. Supplementary measurements between 200 and 250 THz (not shown here) did not reveal any other resonance.

Figure 13 shows the distribution of the electric field calculated at the bottom surface of metallic elements for each of the resonant modes observed in Fig. 12. These results are in agreement with previous calculations reported by Rockstuhl et al. [Rockstuhl, 2006]. When the incident field is polarized parallel to the SRR gap, resonant modes possess an odd number of nodes along the entire SRR. This number is equal to one for the first resonance, while it is equal to three for the second resonance. The first resonance also identifies to the so-called LC resonance as defined in previous studies at microwave and far infrared frequencies [Katsarakis, 2004, Katsarakis, 2005]. It simply identifies to the dipolar mode in the case of the cut wire. When the incident field is polarized perpendicular to the gap, resonant plasmon modes possess an even number of nodes. The first resonant mode in this polarization thus exhibits one additional node as compared to the first resonance in the parallel polarization. This in turn requires higher energies of the light field to excite this mode. The frequency of the first resonant mode in the perpendicular polarization is typically two times higher than that of the first resonant mode in the parallel polarization.

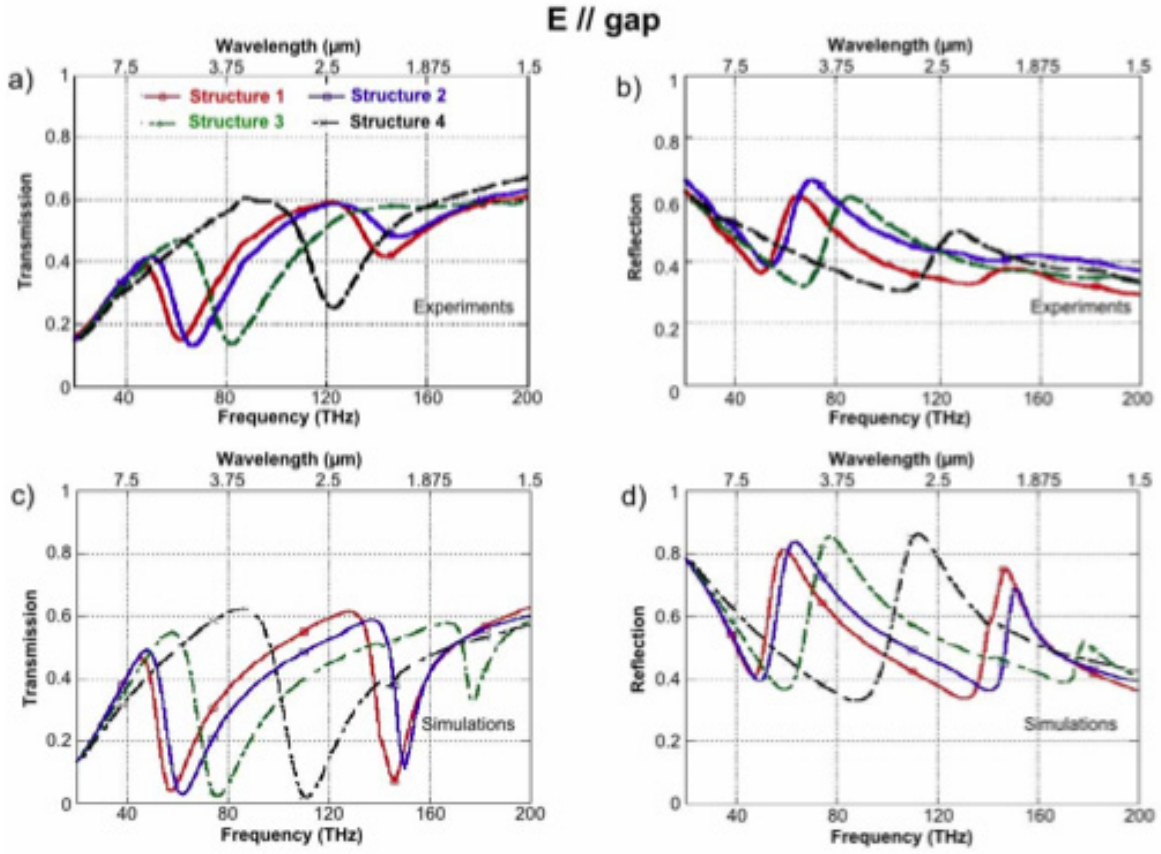

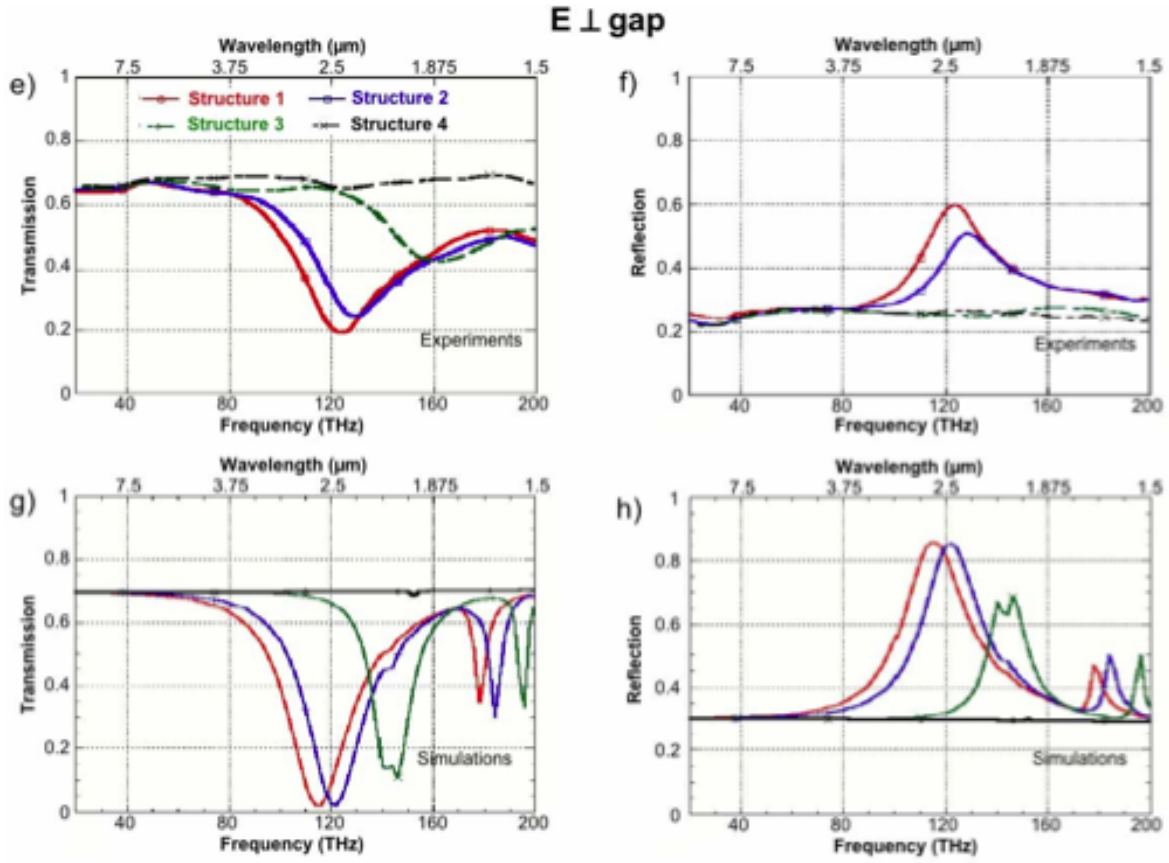

Fig. 12. Measured and simulated transmission/reflection spectra of the four structures depicted in Fig. 10. Curves in red, blue, green and black are for the 1st, 2nd, 3rd and 4th structures, respectively. – (a) and (b): transmission and reflection spectra measured for the parallel polarization (incident electric field parallel to the SRR gap). – (c) and (d): numerical simulations corresponding to (a) and (b), respectively. – (e) and (f): transmission and reflection spectra measured for the perpendicular polarization (incident electric field perpendicular to the SRR gap). – (g) and (h): numerical simulations corresponding to (e) and (f), respectively.

3.1.3 Frequency positions of resonances

At this stage, it is interesting to compare the frequency positions of resonances reported in Figs. 12 to those reported in previous works for similar structures with gold SRRs on glass substrate. For instance, the first resonance calculated in [Rockstuhl, 2006] for the parallel polarization and U–shaped SRRs with 400 nm long base and 190 nm long legs was found to be close to 3800 cm^{-1}, i.e. close to 115 THz instead of 65 THz measured in our experiments for U-shaped SRRs with similar sizes [Figs. 12(a), 12(b), and Fig. 13(b)]. The first resonance calculated in [15] for the parallel polarization and U-shaped SRRs with the same base but with 110 nm legs was found to be near 4800 cm^{-1}, i.e. near 144 THz instead of 80 THz measured in our experiments [Figs. 12(a), 12(b) and Fig. 13(c)]. Actually, all the mode frequencies calculated in [15] are 1.7- 1.9 times higher than those reported in this work, whatever the resonance order and the field polarization are. Approximately the same ratio is obtained when comparing the first resonance measured in [10] for SRRs of standard shape

(~100 THz) to that reported in Fig. 12(a) (~60 THz) for standard SRRs with the same total length (lm ~960 nm). This ratio is actually of the same order of magnitude than the ratio between the refractive index of glass and that of silicon. This suggests that in our case the electromagnetic field at resonance largely extends into the silicon substrate.

3.1.4 Coupling effects between continuous wires and SRRs

In the previous sections, it has been implicitly assumed that the presence of continuous wires had no influence on the resonant response of the structures except for a slow decrease of the transmission observed at low frequencies for the parallel polarization. However, a careful examination of the field distributions in Fig. 13 indicates that, at least for the second resonance, the electromagnetic field extends well in the region comprised between the SRR and the closest wire. We thus performed a numerical analysis to investigate in more detail the possible existence of coupling effects between the SRRs and continuous wires. For this purpose, the spectral responses of the four structures were calculated for different distances d between the SRR base and the closest wire. They were also compared to the spectral response of a periodic array of SRRs only.

Results of our calculations are shown in Figs. 14(a) and 14(b) for structure 1 with three values of d, for a periodic array of SRRs without continuous wires and for a periodic array of wires without SRRs. The dimensions of SRRs are the same for the first four structures. The lattice period is identical for all the structures. Calculations are performed within the same spectral range as in Fig. 12, and the incident electric field is polarized parallel to the continuous wires and/or to the SRR gaps. Figure 14(a) represents the transmission spectra calculated for the different structures. Figure 14(b) shows the electric field distributions calculated for the different resonances observed in Fig. 14(a). As seen in Fig. 14(a), the position of the first SRR resonance is not modified by the presence of the continuous wires whatever the separation between SRRs and wires is. Only the shape of the resonance is modified, and it becomes asymmetric with the presence of the wires.

This asymmetry mainly results from the fact that the optical response of the wires [pink dashed curve in Fig. 14(a)] adds to that of the SRRs. A weak coupling between SRRs and wires only occurs at the smallest separations between the two metallic elements as shown from the calculated distribution of the electric field at the first SRR resonance (Fig. 14(b), second column).

The evolution of the second SRR resonance is quite different. For a sufficiently large separation between the SRRs and wires ($d \geq 100$ nm), the frequency position of this second resonance is still rather independent of the presence of the wires. This justifies our previous interpretations concerning the results of Fig. 12, where the different spectra were obtained for $d \approx 130$ nm. However, for small separations between the SRRs and wires, strong coupling effects exist, which lead to a splitting of the second SRR resonance into two components [Fig. 14(a)]. These components are well separated for the smallest value of d (black dashed curve in Fig. 14(a), $d = 10$ nm). As seen in Fig. 14(b) (second and third columns), the modal field of the low frequency component is found to be concentrated in the region between the SRR base and the closest wire. That of the high frequency component is rather concentrated in the SRR legs.

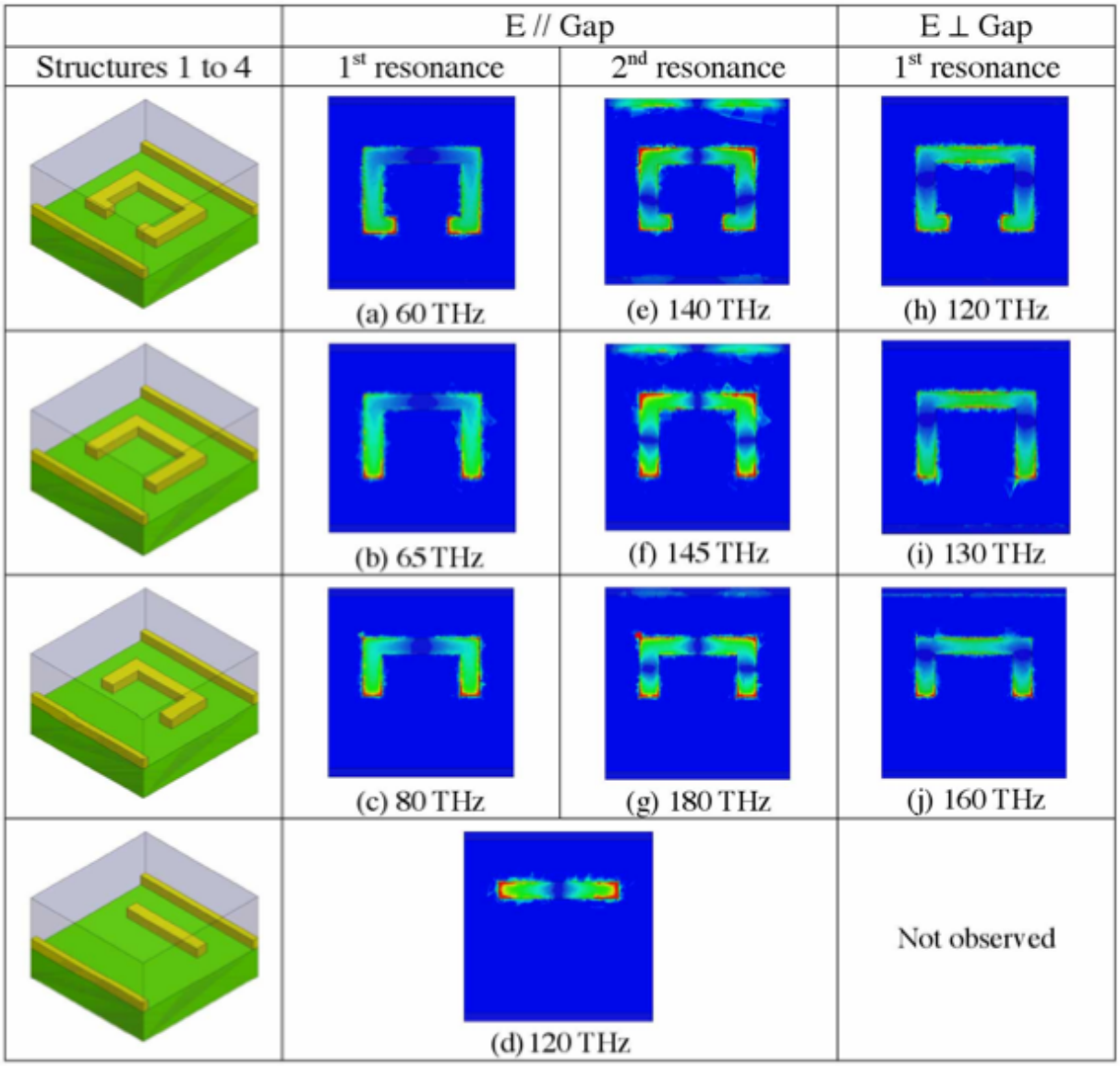

Fig. 13. Magnitude of the normal electric field component (|Ez|) calculated at the bottom surface of the metallic elements for each of the resonant plasmon modes observed in the different spectra of Fig. 11. The different colours, from blue to red correspond to increasing magnitudes of the field component. Modes are classified according to the resonance order and to the polarization of the incident electric field. As expected, both the energy and the number of field nodes increase with the resonance order.

Calculations above were repeated for structures with U-shaped SRRs as structures 2 and 3 and for structures with cut wires as structure 4 (Fig. 11). The same behavior was found in the case of structures with U-shaped SRRs. The frequency position of the first resonance was not modified when the distance between SRRs and continuous wires was varied. The second resonance split into two components for small values of d. In contrast, the structures with cut wires did not exhibit the same "robustness" of the first resonance against coupling effects.

The resonant mode split into two distinct components when the separation between cut wires and continuous wires was smaller than 50 nm. This different behavior can be simply explained by the fact that unlike structures with true SRRs, the field of the first resonant mode is obviously concentrated in the close neighbourhood of the continuous wires, i.e. in the cut wires themselves.

Coupling effects were also investigated from numerical simulations for the perpendicular polarization. We only considered the first SRR resonance since it was the only one clearly observed in the experiments (Fig. 12). The frequency position of this resonance was found to be rather independent of the presence of continuous wires whatever the separation between the SRRs and wires was. However, a small splitting of the resonance was observed for very small separations (d = 10 nm) in the case of U-shaped SRRs with small legs (structure 3).

3.1.5 Metamaterials with negative refraction on silicon

It is now well established that the use of an array of continuous metallic wires allows obtaining a negative permittivity over the whole plasmon-like band when the electric field is polarized parallel to the wires [Pendry, 1998]. Figures 12 and 14(a) presently show that this band can extend well up to near-infrared frequencies for a sufficiently small period of the wire lattice. On the other hand, it has been demonstrated that an array of metallic SRRs can exhibit a magnetic response in the optical domain with a negative permeability at certain frequencies [Enkrich, 2005]. However, this situation only occurs at SRR resonances and for an oblique or grazing incidence, i.e. for an incident magnetic field with a non-zero component along the SRR axis. An additional condition is that the resonant plasmon mode must possess an odd number of field nodes along the SRR [Shalaev, 2005]. Concerning this latter aspect, our experimental results confirm that the first resonant mode, the so-called LC resonance, is by far the most exploitable due both to its strength and to its robustness against parasitic coupling effects. They also show that its frequency position can be finely tuned by adjusting the total length of SRRs and using for instance U-shaped SRRs. One solution to achieve a magnetic response at normal incidence with respect to the sample plane consists in using a stack of SRR layers [Liu, 2008] or simpler, a stack of cut-wires as originally proposed in [Shalaev, 2005]. Coupling between adjacent SRRs or between adjacent cut-wires leads to the formation of hybridized plasmon modes of opposite symmetry. Anti-symmetric plasmon modes can exhibit a magnetic response, and lead to a negative permeability in certain frequency regions. Our experimental results in Fig. 12 show that the resonance associated to the dipolar mode of cut-wires is well pronounced for the fabricated structures. Coupling between two such modes in a multilayer stack should thus allow obtaining a magnetic response at normal incidence. One advantage in using stacked cut-wires instead of stacked SRRs stems from the possibility of achieving more easily a magnetic response at (high) near- infrared frequencies. This is all the more true when metallic nanostructures are fabricated on a high permittivity substrate such as silicon. All the plasmon resonances are shifted to low frequencies, and the realization of very-small-size SRRs operating at telecommunication wavelengths on silicon would require pushing the lithographic techniques to their present limits.

3.2 Optical asymmetric cut-wire pairs

3.2.1 Negative refractive index in optical asymmetric cut-wire pairs

In the previous structures, SRRs were associated with continuous wires to obtain negative index at infrared wavelengths. In this chapter we will study asymmetric cut-wire pairs to obtain also negative index. Metallic nanostructures can be regarded as elementary circuits including nano-capacitors, inductors or resistors [Engheta, 2007]. The simplest resonator that can be imagined is a dipole consisting of a simple metallic cut-wire. Coupling two such oscillators lead to two eigenmodes with opposite symmetry. The virtual current loop of the anti- symmetric mode is now recognized as a mean to create artificial magnetism at optical frequencies [Grigorenko, 2005, Shalaev, 2005]. Fig. 15 shows the structure under consideration. It consists of a periodic array of paired cut-wires separated by a dielectric layer. For simplicity the spacer has been taken to be silicon dioxide (SiO2) with a dielectric permittivity $\varepsilon_r = 2.25$ and a thickness of 100 nm. The surrounding medium is air with $\varepsilon_r = 1$. The relevant polarization of the impinging light is given in Fig. 15(a) with the electric field parallel to the longest side of the cut- wires. Transmission spectra are presented in Fig. 15(b). All the simulations are done using a commercial finite element code (HFSS, 2006). An array of isolated cut-wires is actually found when the separation distance between cut-wires is large: only one resonance (the dipolar mode) is observed in this case (red curve in Fig. 15(b)). This response can be interpreted in terms of a localized plasmon resonance [Rockstuhl, 2006, Kante, 2008]. When the separation distance between cut-wire pairs is progressively diminished, the response of the paired system is modified due to the interaction between its elementary constituents.

Following the plasmon hybridization concept [Kreibig, 1981, Prodan, 2003], coupling effects lift the degeneracy of the single cut-wire mode, thus leading to two distinct plasmons modes [Liu, 2007, Kante 2009], the anti-symmetric and symmetric modes as shown in Fig. 15(b) (blue curve). The symmetric mode with larger restoring force is at a higher energy than the anti-symmetric mode. The main idea of our work is to invert this process. The symmetric mode, which easily couples to incident light, corresponds to a wide rejection band with negative permittivity. The anti-symmetric mode, which is difficult to excite due to the opposite contributions of the two dipoles, manifests itself as a small transmission dip with negative permeability. Achieving such a resonance at a higher frequency than the symmetric mode will ease the overlap condition as proposed recently in [Kante, 2009, Sellier, 2009]. For this purpose, one solution is to break the symmetry of the cut-wire pair. This is achieved in Fig. 15(d) by displacing one of two cut-wires in the direction of the electric field.

Fig. 16(a) and (b) shows the evolutions of the resonant modes and transmission spectra with the longitudinal shift dx between the two cut-wires of each pair. Simulations are performed in the infrared domain. As a major result, for a sufficiently large displacement dx (here dx > 350 nm), the hybridization scheme is inverted with the symmetric mode at a lower frequency than the anti-symmetric mode. The two hybridization schemes are presented in Fig. 15(c) and (e), respectively. Fig. 16(d) clearly shows that a negative refraction regime is obtained (between 145 and 160 THz for dx = 600 nm) for the inverted scheme while the index of refraction remains always positive (dx = 0 nm) for the normal hybridization case (Fig. 16(c)). This extends to infrared frequencies previous results reported by the authors at

microwave frequencies [Kante, 2009, Sellier, 2009]. As seen in Fig. 16(d), negative refraction corresponds to an overlap between the region with negative permittivity and that with negative permeability. It is worthwhile noticing that the domain of overlap with negative permittivity and permeability can be controlled through the different degrees of freedom of the structure [Kante, 2009].

3.2.2 Hybridization of the localized plasmons of SRRs

The recipe proposed above for obtaining a negative index with plasmon hybridization can be applied to any structure supporting localized plasmons. The inversion process resulted from a radical change in near field Coulomb interactions between cut-wires in each pair [Kante, 2009, Christ, 2008]. Let us consider for instance a periodic array of paired SRRs, which are fundamental building blocks in the design of metamaterials. Indeed, the use of SRRs has allowed the achievement of negative magnetic permeability, which is impossible with natural materials at high frequencies. However, obtaining a negative magnetic permeability requires the incident wave to possess a magnetic component along the SRR axis. Such a requirement is not easily fulfilled in optics [Dolling, 2006, Liu, 2009]. Moreover, the electromagnetic response of SRRs has been shown to saturate at optical frequencies [O'Brien, 2002]. In most experimental works reported so far in the infrared domain, normal incidence has been used instead of a grazing or oblique incidence [Kante, 2008]. In this situation, only the electric field can couple to the structure. SRR resonances are nothing but plasmonic resonances which can be classified into even and odd modes depending on the polarization the exciting light with respect to the structure [20]. While even modes are excited for an incident electric field perpendicular to the SRR gap, odd modes are excited for an electric field parallel to this gap. It is straightforward to see that only odd modes can lead to a magnetic moment or eventually to a negative permeability under oblique incidence.

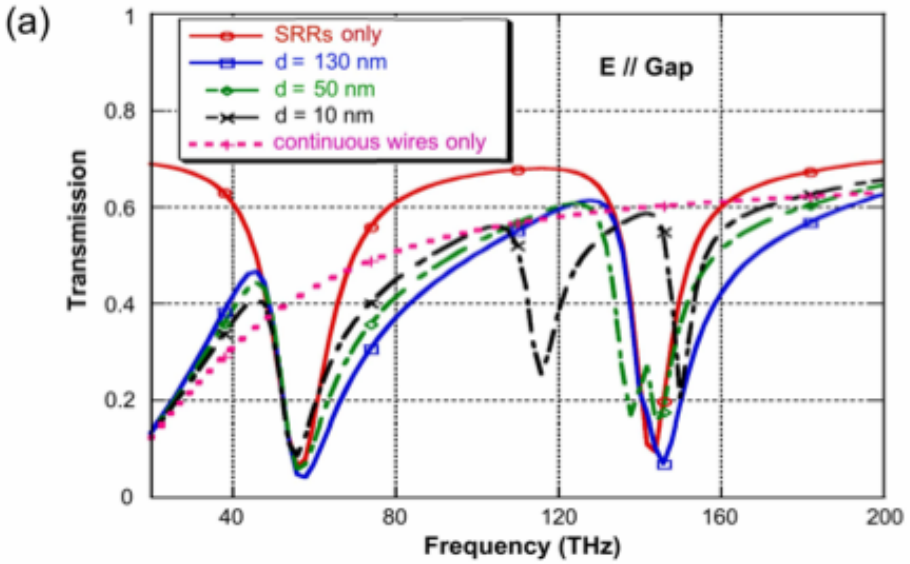

(b)

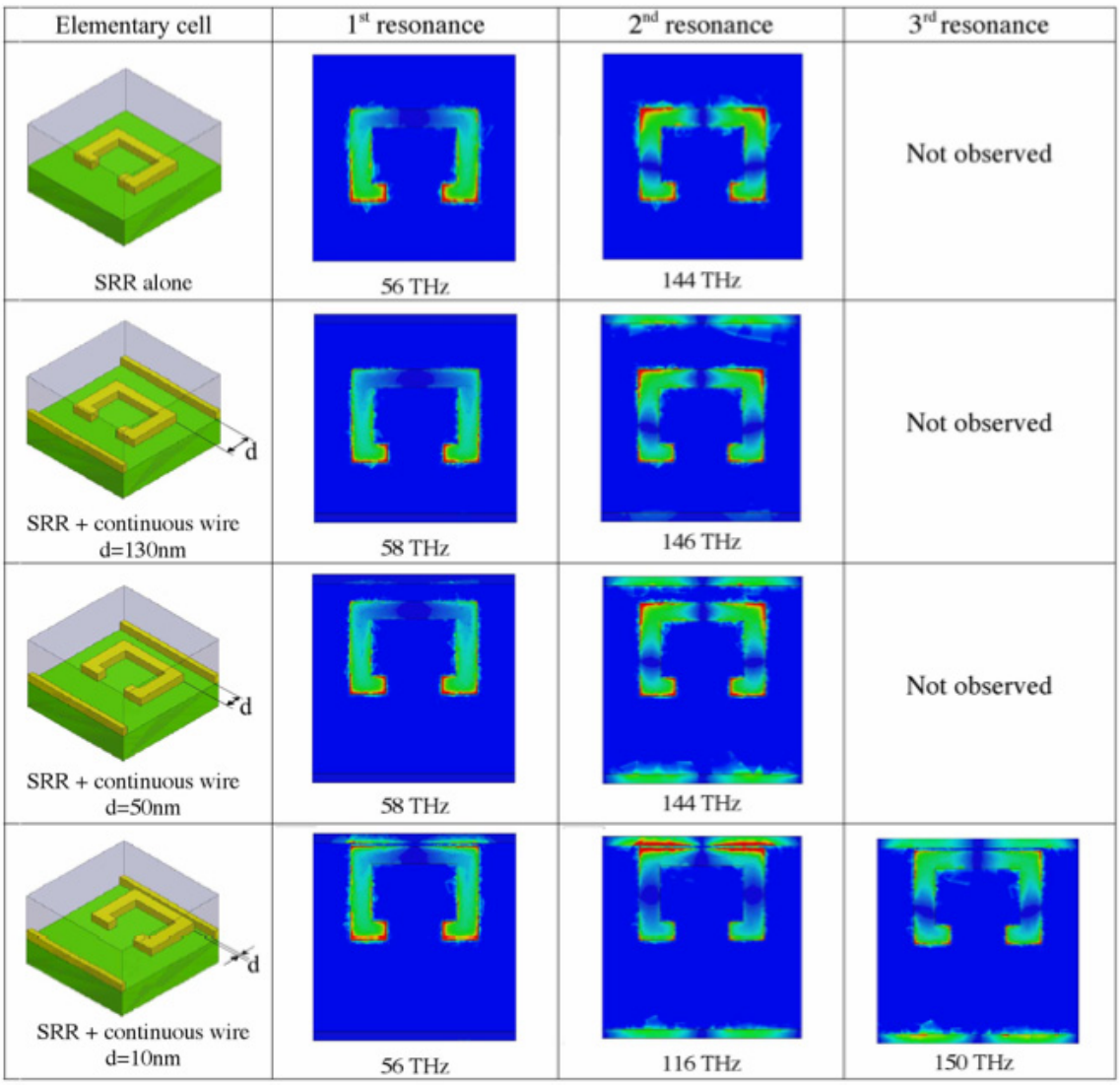

Fig. 14. (a) Transmission spectra calculated for a periodic array of SRRs (red curve), a periodic array of continuous wires (pink dashed curve) and periodic arrays of SRRs and wires with different separations between SRRs and wires: d=130 nm (blue curve), d=50 nm (green dashed curve), d=10 nm (black dashed curve). In each case, the incident electric field is polarized parallel to the gap, the SRR dimensions and lattice period as the same as for structure 1 in Fig. 10. (b) Magnitude of the normal electric field component (|Ez|) calculated at the bottom surface of the metallic elements for each of the resonant modes observed in the transmission spectra of Fig. 14 (a). The different colours, from blue to red correspond to increasing magnitudes of the field component. Modes are classified according to the resonance order and to the separation d between the SRR and the closest wire.

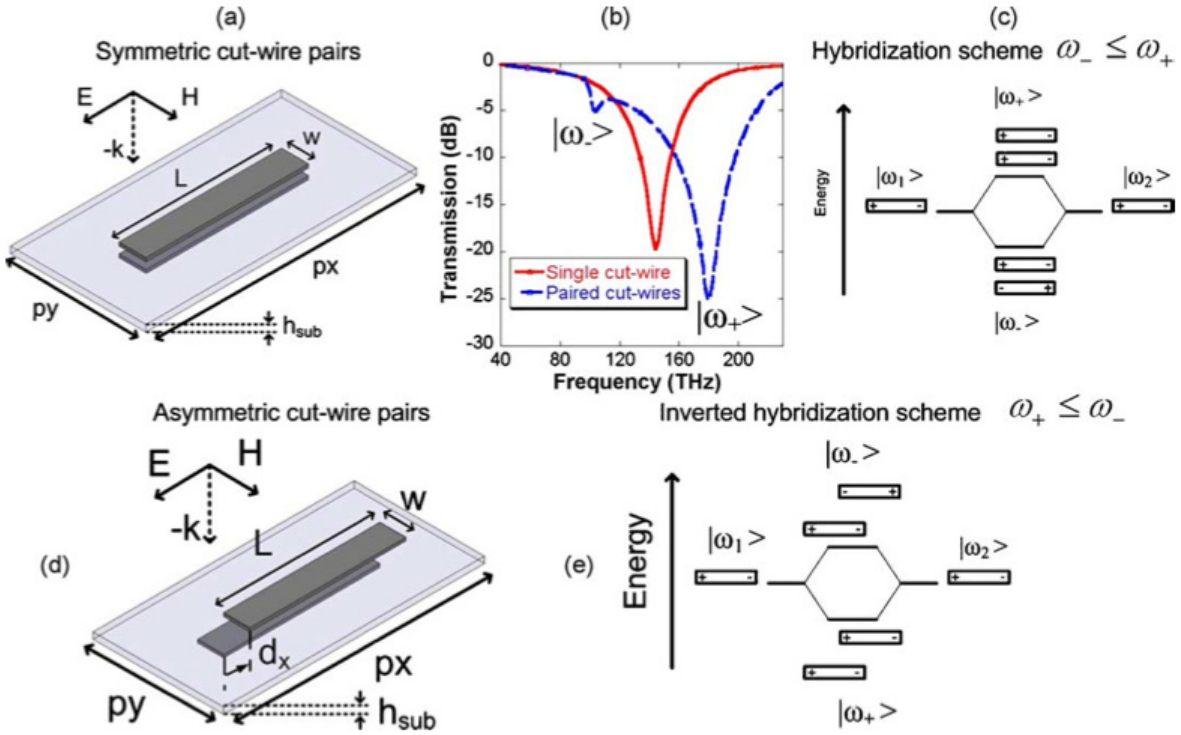

Fig. 15. (a and d) Schematics of the symmetric and asymmetric cut-wire pairs, respectively. (b) Transmission of an array of un-coupled or coupled cut-wires structure with p_x=1.2mm, p_y=200nm, p_z=600nm, w=30nm, L=600nm, h_{sub} =100nm and ε_{sub} =2.25. The pieces of gold metals are described by a Drude model whose parameters can be found in [Kante, 2008]. (c and e) Hybridization scheme and inverted hybridization scheme, respectively.

Fig. 17 (red curves) presents transmission spectra of a single SRR layer designed to operate in the infrared range for two polarizations at normal incidence. When the electric field is perpendicular to the gap, only one resonance (the fundamental even mode) is observed in the frequency range of interest while two resonances are observed for the parallel polarization. These last two resonances respectively correspond to the first and second odd plasmonic modes [Rockstuhl, 2006, Kante, 2008], the fundamental mode being also called LC resonance. When two such SRR structures are brought close to each other, the localized plasmons can hybridize according to a plasmon hybridization scheme similar to the one previously described for cut-wire pairs (Fig. 15). In what follows, the hybridization scheme of an SRR pair is analyzed for both parallel and perpendicular polarization as well as for resonances of different orders. As it will be shown, a negative index of refraction can be obtained at normal incidence for a periodic structure, which is exclusively made of SRRs and based on an inverted hybridization scheme. The SRR pair forming the elementary motif of the periodic structure is depicted in Fig. 17 (left graph). As seen, the lower SRR of the pair is shifted in the x and y directions with respect to the upper one. Following our previous work on cut-wire pairs, this configuration will be simply called ''asymmetric SRR pair''. A system of coupled SRRs has been recently investigated by Liu et al. [Liu, 2009], but in a twisted configuration. These authors showed that the twist angle between vertically coupled SRRs could modify either the electric or magnetic response of the system resulting in what they called a ''stereometamaterial''. Our structure can thus be regarded as a particular

''stereometamaterial''. In contrast, rotating one SRR with respect to another did not produce any inverted hybridization scheme, while this scheme is the most appropriate one for obtaining negative refraction. In fact, split ring resonators are complex structures regarding their responses to an electromagnetic field since they support localized plasmons addressable either by the electric field or the magnetic field. To our knowledge, using the two degrees of freedom (dx, dy) in the design of the SRR pair (Fig. 17 (left graph)) to achieve a negative index of refraction has never been reported so far in the context of SRR-based metamaterials.

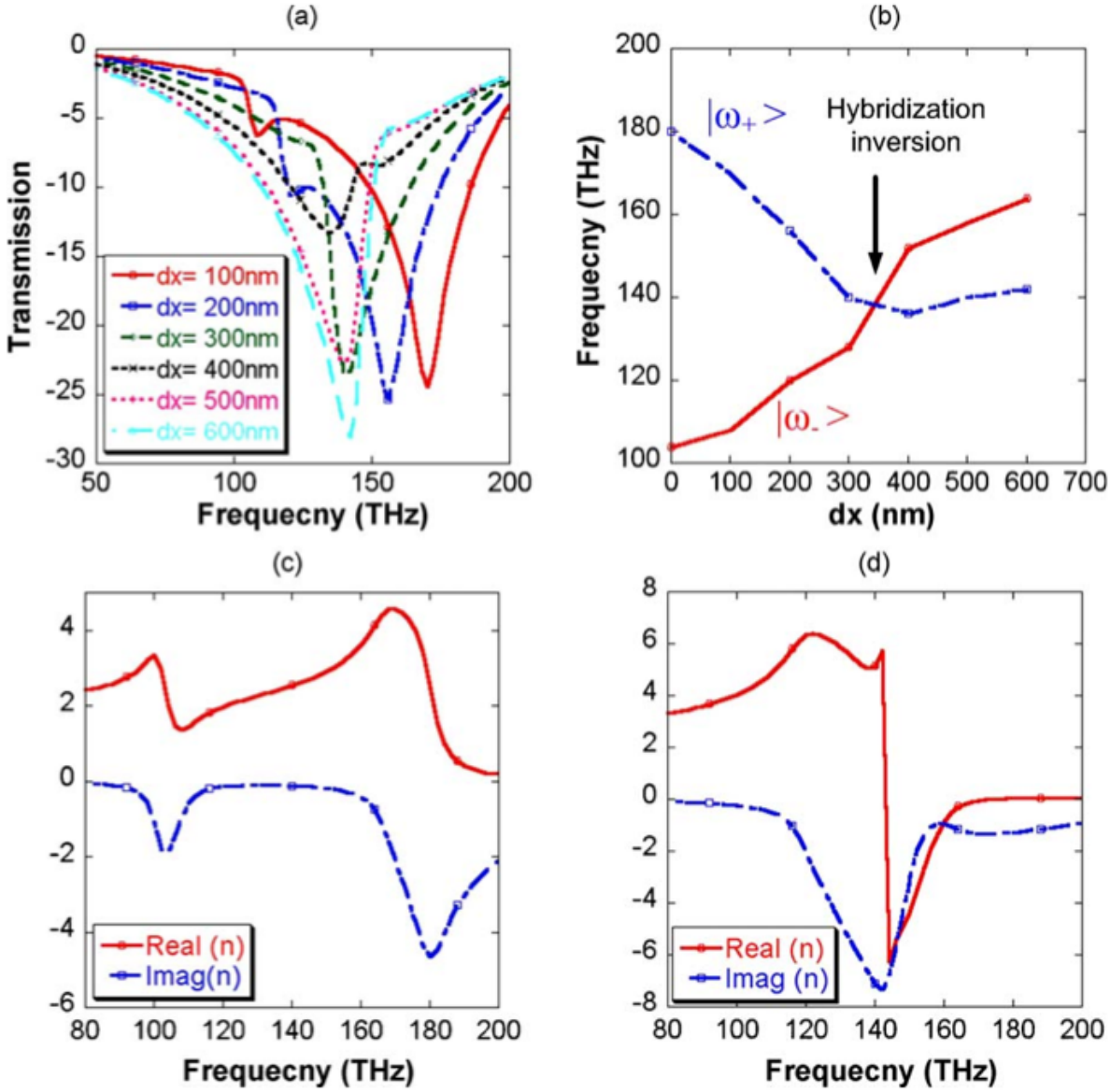

Fig. 16. (a) Transmission spectra of the two-dimensional array of asymmetric cut-wire pairs calculated for different values of the longitudinal shift (dx) between the two cut-wires in each pair. (b) Evolutions of the symmetric and anti-symmetric mode frequencies as a function of the dx shift. (c) Effective index of refraction [30] calculated for dx = 0 with a de-embedding up to the metamaterials interfaces. (d) Same type of calculations for dx = 600 nm.

3.2.3 Hybridization of the LC resonance

The LC resonance (i.e. the fundamental odd mode) is excited at normal incidence when the electric field is parallel to the gap. This resonance has been experimentally observed from microwaves to optics. Electric charges in metallic SRR arms are mainly located near the SRR gap (insert of Fig. 17, middle graph). Fig. 18 shows the modifications of the transmission spectrum when coupling vertically two SRR layers. Curves in the left graph correspond to different values of dx at a fixed dy (dy = 0). Curves in the right graph correspond to different values of dy at fixed dx (dx = 0). As expected, in all cases, coupling between SRRs splits the LC resonance in two eigenmodes. The symmetric mode, which has the largest amplitude, is found at the highest frequency for dx = dy = 0. In principle, a longitudinal magnetic coupling also exists [Liu, 2009], but can be neglected for a qualitative understanding of the hybridization scheme in presence of electric coupling. As seen in the left graph of Fig. 17, a shift of one of the two SRRs in the direction perpendicular to the gap ($dx \neq 0$) has a weak influence. One just observes a small decrease of the mode amplitudes. The evolution is radically different when the shift occurs in the direction parallel to the gap ($dy \neq 0$). An inversion of the hybridization scheme is observed for sufficiently large values of dy. The overall results obtained for the LC mode of SRRs are then very comparable to those reported for the dipolar mode of cut-wires. The LC mode exhibits indeed a dipole-like behavior.

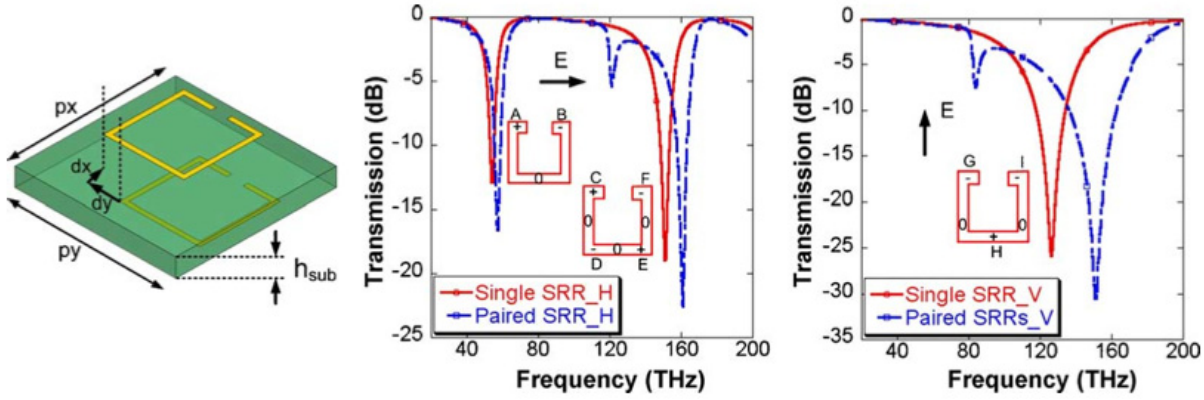

Fig. 17. (Left) Schematics of the asymmetric SRR pair. (Middle) Transmission spectra of periodic SRR arrays at normal incidence for a field polarization parallel to the SRR gap. (Right) Transmission spectra of periodic SRR arrays for a field polarization perpendicular to the SRR gap. In the middle and right graphs, red curves are for one-SRR-layer array while blue curves are for a two-layer array of paired SRRs. Inserts show the distributions of charges and electric field nodes for the different resonances in the one-layer array. Squared SRRs are used with 700 nm side length and 200 nm gap width. The 100 nm wide conducting elements are described using the Drude model reported in [Kante, 2008]. Other parameters are: px = py = 1.4 mm, pz = 1 mm, hsub = 100 nm, εsub = 2.25.

3.2.4 Hybridization of the second odd plasmonic mode

Let us now consider the second odd mode. The corresponding distribution of electric charges and field nodes in SRR arms is shown in the middle graph of Fig. 17 (right insert) for a one-layer SRR array. This picture shows that this mode has a ''dipole activity'' in both the x and y directions. Charges at the extremities of CD and EF arms produce the dipolar activity along the x direction while those at the extremities of the DE arm produce the dipolar activity along the y direction. Correspondingly, in a two-layer SRR array, an inversion of the hybridization occurs whether one of the two layers is displaced along the x or the y direction (Fig. 18). In each case, the inversion stems from the near field interaction between the active dipoles in the corresponding direction. In the case of a displacement along x, the inversion results from the interaction of dipoles CD and EF with dipoles C'D' and E'F'. The primes referring to the second SRR. In the case of a displacement along y, it results from the interaction between DE and D'E'.

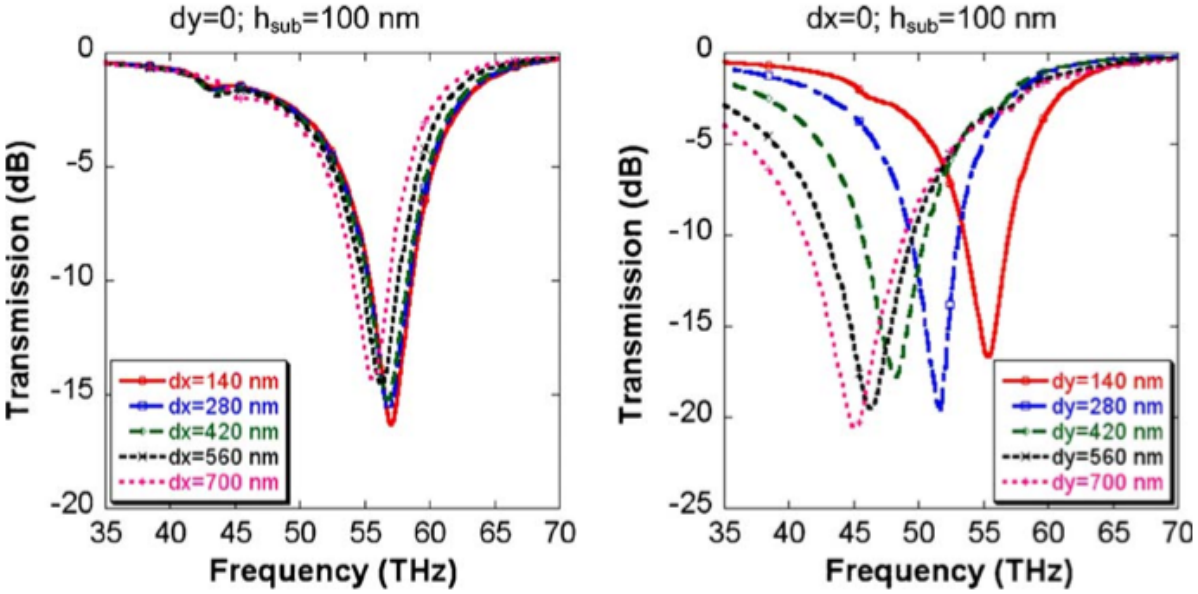

Fig. 18. Transmission spectra of a periodic array of asymmetric SRRs pairs around the LC resonance for different values of dx at dy=0 (left) and for different values of dy at dx = 0 (right)

3.2.5 Hybridization of the fundamental even plasmonic mode (perpendicular polarization)

When the incident electric field is perpendicular to the gap, the SRR can be regarded as two cut-wires in parallel since the charges in the two arms GH and IH oscillate in phase (see insert in the right graph of Fig. 17). In consequence, the hybridization of localized plasmons evolves a priori as in the case of cut-wires pairs [Kante, 2009]. Therefore, only a displacement along the x direction (parallel to the dipoles GH and HI) for one of the SRRs of the asymmetric pair can lead to an inverted hybridization scheme with the possibility of a negative index of refraction.

The inversion of the hybridization scheme for $dx \neq 0$ is illustrated from calculated transmission spectra in Fig. 20(a). Results of calculations for the effective index of refraction

are presented in Fig. 20(c) and (d) for a symmetric SRR pair (dx = dy = 0) and an asymmetric pair (dx = 700 nm, dy = 0), respectively. Results obtained for the symmetric pair are comparable to those reported in [Liu, 2008]. There with no overlap between the regions of negative epsilon and negative mu. In contrast, a negative index of refraction is clearly obtained for the asymmetric SRR pair in Fig. 20(d).

Results obtained for a transversal displacement (dy ≠ 0) of one SRR of the pair may appear to be quite surprising since three peaks are observed in the transmission spectra instead of two (Fig. 20(b)). However, a careful analysis reveals that these peaks have different origins. Three types of dipole–dipole interactions are indeed involved: GH with G'H', GH with I'H' and IH with G' H'. For an intermediate value of dy (i.e. dy = py/2 = 350 nm), the dipole–dipole interactions GH - G'H' and I'H' - IH become degenerate, thereby leading to the disappearance of one of the three peaks.

In conclusion we have numerically demonstrated that the coupling between localized plasmons in periodic arrays of paired cut-wires or SRRs can be controlled by modifying the symmetry of each individual pair. It has been shown that breaking the symmetry of cut-wire or SRR stacks can lead to a negative index of refraction. The scheme proposed here contrasts with previous designs of negative index metamaterials where two kinds of meta-atoms were mixed. Only one type of meta-atom supporting localized plasmons is used. A true negative index band is achieved provided that the coupling between localized plasmons is appropriately controlled.

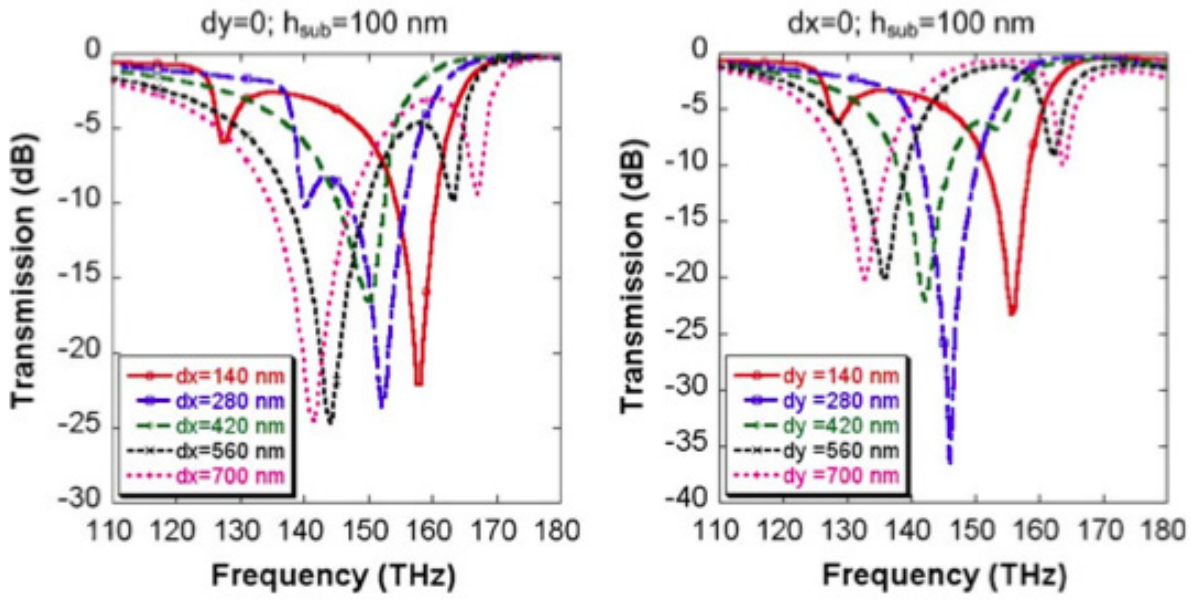

Fig. 19. Transmission spectra of a periodic array of a symmetric SRRs pairs around the second odd SRR mode for different values of dx at dy=0 (left) and for different values of dy at dx = 0 (right).

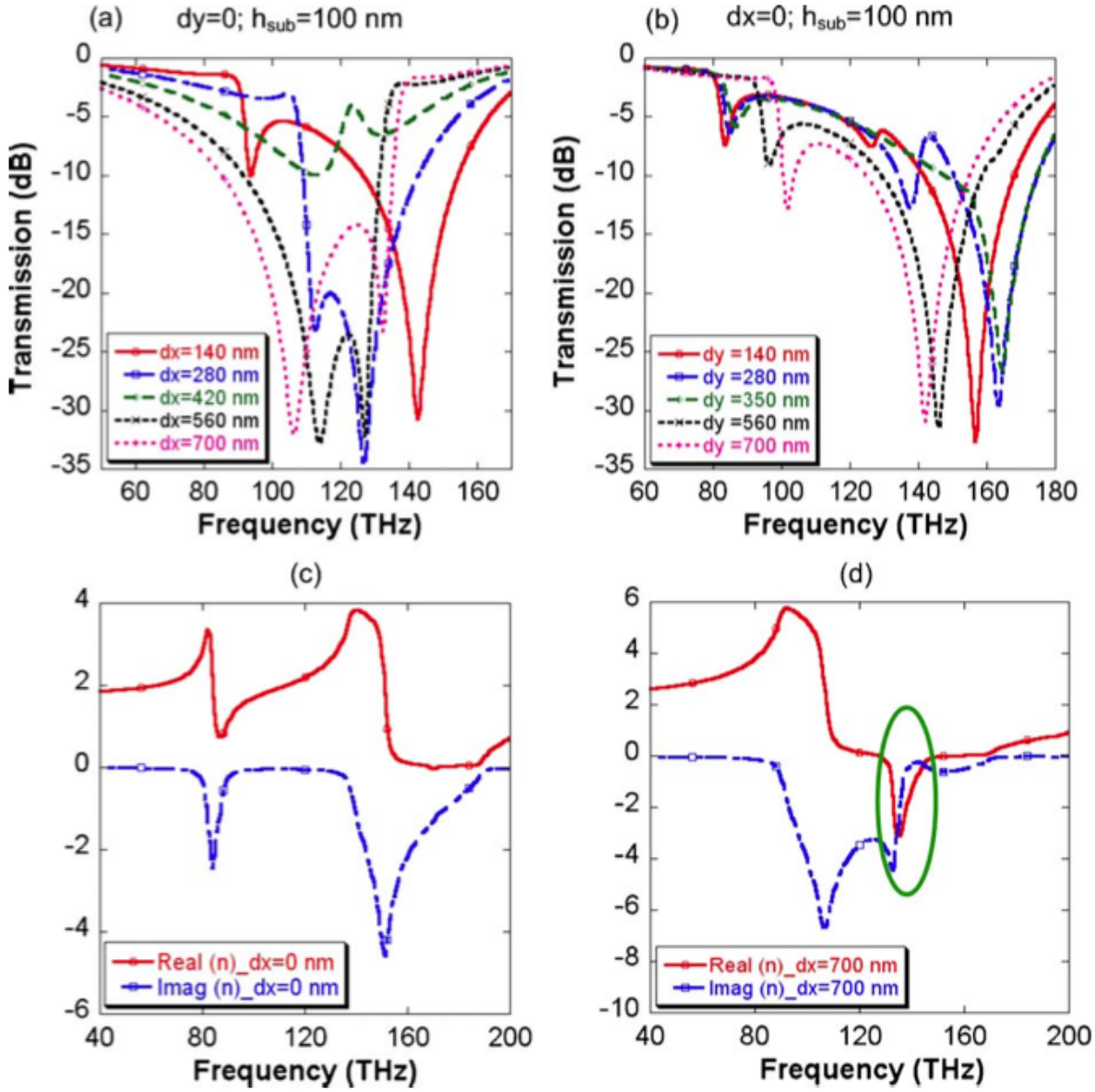

Fig. 20. (Top) Transmission spectra of a periodic array of asymmetric SRRs pairs for vertical polarization and different values of dx at dy=0 (a) and for different values of dy at dx = 0 (b). (Bottom) Effective index of refraction (real and imaginary parts) calculated for dx = 0 and dy = 0 (c) and for dx = 700 nm, dy = 0 (d), pz = 1 mm with a de-embedding up to the metamaterials interfaces.

4. Conclusions

In this chapter, we have presented different metamaterials with a negative index at microwave and optical frequencies. Through numerical simulations and measurements, we have shown that it was possible to obtain a negative index by optimizing the coupling between different layers of metamaterials. We have also shown that this concept can be implemented from microwaves to optics. These works are believed to open a new way for the design of negative refraction metamaterials from microwaves to optics.

5. References

Aydin, K., Bulu, I., Ozbay, E., (2005), Focusing of electromagnetic waves by a left-handed metamaterial flat lens, *Optics Express,* Vol.13, n°22, pp.8753-8759.

Burokur, S. N. , Latrach, M., Toutain, S., (2005), Theoretical investigation of a circular patch antenna in the presence of a left-handed medium, *IEEE Antennas and Wireless Propagation Letters* Vol.4, pp.183-186.

Burokur, S. N., Sellier, A., Kanté, B., de Lustrac, A., (2009a), Symmetry breaking in metallic cut wire pairs metamaterials for negative refractive index, *Applied Physics Letters,* Vol.94, 201111.

Burokur, S. N., Lepetit, T., de Lustrac, A., (2009b), Incidence dependence of negative index in asymmetric cut wire pairs metamaterials, *Applied Physics Letters* Vol.95, 191114.

Cai, W. , Chettiar U. K., Kildishev A. V., Shalaev V. M., (2007), Optical cloaking with metamaterials, *Nature Photonics* Vol.1, pp.224-227.

Christ, A., Ekinci Y., Solak H. H., Gippius N. A., Tikhodeev S. G., Martin O. J. F., (2007), Controlling the Fano interference in a plasmonic lattice, *Physical Review B,* Vol.76, 201405□R.

Christ, A., Marin O.J.F., Ekinci Y., Gippius N. A., Tikhodeev S. G., (2008), Symmetry Breaking in a Plasmonic Metamaterial at Optical Wavelength, *Nano Letters,* Vol.8, pp.2171-2175.

Dolling, G. , Enkrich C., Wegener M., Zhou J. F., Soukoulis C. M., Linden S., (2005), Cut-wire pairs and plate pairs as magnetic atoms for optical metamaterials, *Optics Letters,* Vol.30, n°23, pp.3198-3200.

Dolling, G., Enkrich C., Wegener M., Soukoulis C. M., Linden S., *(2006),* Simultaneous Negative Phase and Group Velocity of Light in a Metamaterial, *Science*, Vol.312, pp. 892-894.

Enkrich, C. , M. Wegener, S. Linden, S. Burger, L. Zschiedrich, F. Schmidt, J. F. Zhou, Koschny, T., Soukoulis, C. M., (2005) , Magnetic Metamaterials at Telecommunication and Visible Frequencies, *Physical Review Letters* Vol.95, 203905.

Gaillot, D. P., Cröenne, C., Lippens, D., (2008), An all-dielectric route for terahertz cloaking, *Optics Express,* Vol.16, n°6, pp.3986-3992

Grigorenko, A.N., Geim A. K., Gleeson H. F., Zhang Y., Firsov A. A., Khrushchev I. H., Petrovic J., (2005), Nanofabricated media with negative permeability at visible frequencies, *Nature,* Vol.438, pp.335–338.

Gundogdu, T., F., Katsarakis N., Kafesaki M., Penciu R. S., Konstantinidis G., Kostopoulos A., Economou E. N., and Soukoulis C. M., (2008), Negative index short-slab pair and continuous wires metamaterials in the far infrared regime, *Optics Express*, Vol.16, n°12, pp. 9173-9180.

Guven, K., M. D. Kaliskan, and E. Ozbay, (2006), Experimental observation of left-handed transmission in a bilayer metamaterial under normal-to-plane propagation, *Optics Express,* Vol.14, n°19, pp. 8685-8693.

HFSS, High-frequency structure simulator version 10.1 Finite-element package, Ansoft Corporation, Pittsburgh, PA (2006).

Kanté, B., Ourir A., Burokur, S. N., Gadot, F., de Lustrac, A., (2008a), Metamaterials for optical and radio communication, *Comptes Rendus Physique,* Vol.9, n°1, pp.31-40.

Kanté, B., de Lustrac, A., Lourtioz, J. M., Burokur, S. N., (2008b), Infrared cloaking based on the electric response of split ring resonators, *Optics Express,* Vol.16, n°12, pp. 9191-9198.

Kanté, B., de Lustrac A., Lourtioz, J.M. , Gadot, F., (2008c), Engineering resonances in infrared metamaterials, *Optics Express*, Vol.16, n°10, pp. 6774-6784.

Kanté, B., Burokur, S. N., Sellier, A. , de Lustrac, A., Lourtioz, J.-M., (2009a), Controlling Plasmon Hybridization for Negative Refraction Metamaterials, *Physical Review B*, Vol.79, 075121.

Kanté, B., de Lustrac, A., Lourtioz, J. M., (2009b), In-plane coupling and field enhancement in infrared metamaterial surfaces, *Physical Review B,* Vol.80, 035108.

Katsarakis, N., Koschny T., Kafesaki M., Economou E. N., and C. M. Soukoulis, (2004), Electric coupling to the magnetic resonance of split ring resonators, *Applied Physics Letters,* Vol.84, pp.2943-2945.

Katsarakis, N., Konstantinidis, G., Kostopoulos, A., Penciu, R. S., Gundogdu, T. F., Kafesaki, M., Economon, E. N., Koschny, T., and Soukoulis, C.M., (2005), Magnetic response of split-ring resonators in the far- infrared frequency regime, *Optics Letters* Vol.30, pp.1348-1350.

Kreibig, U., Althoff, A., Pressmann, H., (1981), Veiling of optical single particle properties in many particle systems by effective medium and clustering effects, *Surface Science* Vol.106 , n°1-3, pp. 308-317.

Leonhardt, U., (2006), Optical Conformal Mapping, *Science,* Vol.312, pp.1777-1780.

Linden, S., Enkrich, C., Wegener, M., Zhou J., Koschny, T., Soukoulis, C. M., (2004), Magnetic Response of Metamaterials at 100 Terahertz, *Science,* Vol.306, pp.1351-1353.

Liu, N., Guo H., Fu L., Kaiser S., Schweizer H., Giessen H., (2007), Plasmon Hybridization in Stacked Cut-Wire Metamaterials, *Advanced Materials*, Vol.19, pp.3628-3632.

Liu, N., Guo H., Fu L., Kaiser S., Schweizer H., and Giessen H., (2008), Three-dimensional photonic metamaterials at optical frequencies, *Nature Materials* Vol.7, pp.31-37.

Liu, N., Liu H., Zhu S., Giessen H., (2009), Stereometamaterials, *Nat. Photon*. Vol.3, pp.157–162

Nicholson, A. M., Ross G.F., (1970), Measurement of the intrinsic properties of materials by time-domain techniques, *IEEE Transactions on Instrumentation And Measusrements* Vol.19, pp.377-382.

O'Brien S, Pendry J.B., (2002), Magnetic Activity at Infra Red Frequencies in Structured Metallic Photonic Crystals, *Journal of Physics Condensed Matter* Vol.14, pp.6383–6394.

Pendry, J. B. , Holden A. J., Stewart W. J., Youngs I, (1996), Extremely Low Frequency Plasmons in Metallic Mesostructures, *Physical Review Letters,* Vol.76, pp.4773-4776.

Pendry, J. B. , Holden A. J., Robbins D. J., Stewart W. J., (1999), Magnetism from conductors and enhanced nonlinear phenomena, *IEEE Trans. Microwave Theory Tech.,* Vol.47, pp.2075-2084.

Pendry, J. B. , (2000), Negative Refraction Makes a Perfect Lens, *Physical Review Letters,* Vol.85, pp.3966-3969.

Pendry, J. B., D. Schurig, and D. R. Smith, (2006), Controlling Electromagnetic Fields, *Science* Vol.312, pp. 1780-1782.

Prodan, E., C. Radloff, N. J. Halas, and P. Nordlander, (2003), A Hybridization Model for the Plasmon Response of Complex Nanostructures, *Science* Vol.302, pp. 419-422.

Rockstuhl, C., F. Lederer, C. Etrich, T. Zentgraf, J. Kuhl, and H. Giessen, (2006), On the reinterpretation of resonances in split-ring-resonators at normal incidence, *Optics Express,* Vol.14, n°19, pp. 8827-8836.

Sellier, A., Burokur S. N., Kanté B., de Lustrac A., (2009), Negative refractive index metamaterials using only metallic cut wires, *Optics Express*, Vol.17, 8, pp. 6301-6310.

Shalaev, V. M., Cai W., Chettiar U. K., Yuan H. K., Sarychev A. K., Drachev V. P., Kildishev A. V., (2005), Negative index of refraction in optical metamaterials, *Optics Letters* Vol.30, pp.3356-3358.

Shalaev, V. M. , (2007), Optical negative-index metamaterials, *Nature Photonics* Vol.1, pp.41-48.

Shelby, R. A. , D. R. Smith, and S. Schultz, (2001), Experimental Verification of a Negative Index of Refraction, *Science* Vol.292, pp.77-79.

Schurig, D., J. J. Mock, B. J. Justice, S. A. Cummer, J. B. Pendry, A. F. Starr, and D. R. Smith, (2006), Metamaterial Electromagnetic Cloak at Microwave Frequencies, *Science,* Vol.314, pp. 977-980.

Smith, D. R., Padilla W.J., Vier D. C., Nemat-Nasser S. C., Schultz S., (2000), Composite Medium with Simultaneously Negative Permeability and Permittivity, *Physical Review Letters,* Vol.84, pp.4184-4187.

Smith, D. R., Schultz S., Markos P., and Soukoulis C. M., (2002), Determination of effective permittivity and permeability of metamaterials from reflection and transmission coefficients, *Physical Review B* Vol.65, 195104.

Smith, D. R. , Pendry J. B., Wiltshire M. C. K., (2004), Metamaterials and Negative Refractive Index, *Science* Vol.305, pp.788-792.

Valentine, J., Zhang S., Zentgraf T., Ulin-Avila E., Genov D.A., Bartal G., Zhang X., (2008), "Three Dimensional Optical Metamaterial Exhibiting Negative Refractive Index," *Nature* Vol.455, pp.376-379.

Veselago, V. G. , (1968), The electrodynamics of substances with simultaneously negative values of e and μ, *Soviet Physics Uspieky* Vol.10, 509.

Wang, G., Fang J. R., Dong X. T., (2007), Refocusing of backscattered microwaves in target detection by using LHM flat lens, *Optics Express,* Vol.15, n°6, pp.3312-3317.

Yeh, P. , (1998), *Optical waves in layered media* (Wiley 1998).

Yen, T. J., Padilla W. J., Fang N., Vier D. C., Smith D. R., Pendry J. B., Basov D. N., Zhang X., (2004), Terahertz Magnetic Response from Artificial Materials, *Science* Vol.303, pp.1494-1496.

Zhang, S. , Fan W., Minhas B. K., Frauenglass A., Malloy K. J., Brueck S. R. J., (2005), Midinfrared Resonant Magnetic Nanostructures Exhibiting a Negative Permeability, *Physical Review Letters,* Vol.94, 37402.

Zhou, J., Zhang L., Tuttle G., Koschny T., Soukoulis C. M., (2006), Negative index materials using simple short wire pairs, *Physical Review B*. Vol. 73, 041101.

Zhou, J., Economon E., Koschny T., Soukoulis C. M., (2006), Unifying approach to left-handed material design, *Optics Letters* Vol.*31,* pp.3620-3622.

Zhou, J., Koschny T., and Soukoulis C. M., (2007), Magnetic and electric excitations in split ring resonators, *Optics Express,* Vol.15, pp.17881-17890 .

Ziolkowski, R.W., Kipple A., (2003), Application of double negative metamaterials to increase the power radiated by electrically small antennas, *IEEE Transaction Antennas Propag*ation Vol.51, pp.2626-2640.

Annexe 3 : Principaux travaux relatifs au chapitre 3

Annexe 3.1

P.-H. Tichit, S. N. Burokur, A. de Lustrac

« Ultra-directive antenna via transformation optics »

Journal of Applied Physics, vol. 105, no. 10 (104912), May 2009

Ultradirective antenna via transformation optics

P.-H. Tichit,[a] S. N. Burokur,[b] and A. de Lustrac[c]
IEF, University of Paris-Sud, CNRS, UMR 8622, 91405 Orsay Cedex, France

(Received 18 February 2009; accepted 14 April 2009; published online 28 May 2009)

Spatial coordinate transformation is used as a reliable tool to control electromagnetic fields. In this paper, we derive the permeability and permittivity tensors of a metamaterial able to transform an isotropically radiating source into a compact ultradirective antenna in the microwave domain. We show that the directivity of this antenna is competitive with regard to conventional directive antennas (horn and reflector antennas), besides its dimensions are smaller. Numerical simulations using finite element method are performed to illustrate these properties. A reduction in the electromagnetic material parameters is also proposed for an easy fabrication of this antenna from existing materials. Following that, the design of the proposed antenna using a layered metamaterial is presented. The different layers are all composed of homogeneous and uniaxial anisotropic metamaterials, which can be obtained from simple metal-dielectric structures. When the radiating source is embedded in the layered metamaterial, a highly directive beam is radiated from the antenna. © *2009 American Institute of Physics*. [DOI: 10.1063/1.3131843]

I. INTRODUCTION

The invariance of Maxwell equations to coordinate transformations has become a hot theme since 2006 and the proposal of a cylindrical invisibility cloak by Pendry *et al.*[1] and Leonhardt.[2] The design and experimental characterization of the first electromagnetic cloak at microwave frequencies have shown that this tool is indeed very efficient.[3,4] After this seminal work, several applications of the transformation optics method have been proposed such as concentrators,[5] electromagnetic wormholes,[6] waveguide transitions and bends,[7–10] rotators,[11] and planar focusing antennas.[12] Transformation optics thus appears as a convenient tool to design devices or components with special properties difficult to obtain from naturally existing materials.

Theoretically, the coordinate transformation method consists in generating a transformed space from an initial one where solutions of Maxwell's equations are known. The first step is to imagine a virtual space with the desired topological properties. As in general relativity, this transformed space will contain the underlying physics which can be gathered in the metric tensor. Although this approach and associated calculations were already well known, Pendry *et al.*[1] have proposed an interpretation where the permeability and permittivity tensor components can be viewed as a material in the original space. It is as if the new material mimics the defined topological space. Moreover the choice of an Euclidean initial space results in devices or components with equal values for the relative permittivity and permeability, and consequently with zero reflection at boundaries with vacuum. These mathematical tools have been intensively used for 2 years in the designing of optical devices and components. However most of the approaches are based on continuous coordinate transformations, which make the calculated electromagnetic parameters complicated, inhomogeneous, and anisotropic. Hence such devices are difficult to realize. To make this fabrication easier, material with simplified parameters has been proposed in the first attempt,[1] with the drawback of an impedance mismatch between the material and vacuum. More recently a discrete optical transformation applied to layered structures has been presented to simplify the realization.[13]

In this paper, following the transformation optics approach, we achieve an ultradirective emission by transforming an initial Euclidean vacuum space described in cylindrical coordinates (cylindrical space) into a space in rectangular coordinates (rectangular space). The medium obtained from this method presents complex anisotropic permittivity and permeability. We thus propose a structure in transverse magnetic (TM) polarization with simplified reduced parameters. Finally a layered structure of the metamaterial is presented in order to facilitate the physical realization process of the ultradirective antenna.

II. TRANSFORMATION FORMULATIONS

We consider here a line source radiating in a cylindrical vacuum space. Wavefronts represented by cylinders at r =constants and polar coordinates (r, θ) are well appropriate to describe such a problem. In order to produce a highly directive emission, a physical space where lines θ=constant become horizontal is generated, as illustrated by the schematic principle in Fig. 1. We can note that each colored circle of the cylindrical space becomes a vertical line having the same color in the Cartesian space, whereas each radial line becomes a horizontal one. Finally the right half cylinder of diameter d is transformed into a rectangular region with width e and length L. The line source in the center of the cylinder becomes the left black vertical radiating surface of the rectangular space.

Mathematically this transformation can be expressed as

[a]Electronic mail: paul-henri.tichit@u-psud.fr.
[b]Electronic mail: nawaz.burokur@u-psud.fr.
[c]Electronic mail: andre.de-lustrac@u-psud.fr.

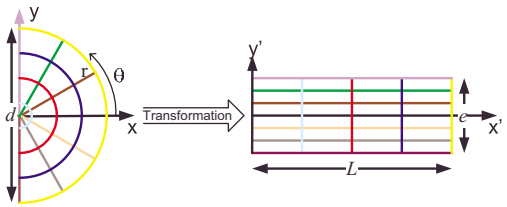

FIG. 1. (Color online) Schematic principle of the coordinate transformation using a color code with the initial cylindrical space (left) and the transformed rectangular space (right).

$$\begin{cases} x' = \dfrac{2L}{d}\sqrt{x^2+y^2}, \\ y' = \dfrac{e}{\pi}\arctan\left(\dfrac{y}{x}\right) \quad \text{with} \quad -\dfrac{\pi}{2} \le \arctan\left(\dfrac{y}{x}\right) \le \dfrac{\pi}{2}, \\ z' = z, \end{cases} \tag{1}$$

where x', y', and z' are the coordinates in the transformed rectangular space, and x, y, and z are those in the initial cylindrical space. In the cylinder we assume free space, with isotropic permeability and permittivity tensors ε_0 and μ_0 and the following transformations are used to obtain the material parameters of the rectangular space:

$$\varepsilon^{i'j'} = \frac{J_i^{i'} J_j^{j'} \varepsilon_0 \delta^{ij}}{\det(J)} \quad \text{and} \quad \mu^{i'j'} = \frac{J_i^{i'} J_j^{j'} \mu_0 \delta^{ij}}{\det(J)}$$

$$\text{with} \quad J_\alpha^{\alpha'} = \frac{\partial x'^{\alpha}}{\partial x^{\alpha}}, \tag{2}$$

where $J_\alpha^{\alpha'}$ and δ^{ij} are, respectively, the Jacobian transformation matrix of the transformation of Eq. (1) and the Kronecker symbol. The Jacobian matrix between the transformed and the original coordinates has four nonzero parameters which depend on the distance from the origin. We assume J_{xx}, J_{yy}, and J_{xy} to be z-independent with $J_{zz}=1$. The divergence of J_{yy} can be explained by the nonbijection of the initial coordinates y-lines transformation. The inverse transformation is obtained from the initial transformation of Eq. (1) and derived by a substitution method, enabling the metamaterial design which leads to anisotropic permittivity and permeability tensors. Both electromagnetic parameters μ and ε have the same behavior. We can also note that the equality of permittivity and permeability tensors implies a perfect impedance matching with no reflection at the interface with vacuum.

By substituting the new coordinate system in the tensor components, and after some simplifications, the following material parameters are derived:

$$\bar{\bar{\varepsilon}} = \begin{pmatrix} \varepsilon_{xx}(x',y') & 0 & 0 \\ 0 & \varepsilon_{yy}(x',y') & 0 \\ 0 & 0 & \varepsilon_{zz}(x',y') \end{pmatrix} \varepsilon_0$$

$$\bar{\bar{\mu}} = \begin{pmatrix} \mu_{xx}(x',y') & 0 & 0 \\ 0 & \mu_{yy}(x',y') & 0 \\ 0 & 0 & \mu_{zz}(x',y') \end{pmatrix} \mu_0, \tag{3}$$

where

$$\varepsilon_{xx}(x',y') = \mu_{xx}(x',y') = \frac{\pi}{e}x' \quad \varepsilon_{yy}(x',y') = \mu_{yy}(x',y')$$

$$= \frac{1}{\varepsilon_{xx}(x',y')} \quad \varepsilon_{zz} = \mu_{zz} = \frac{d^2\pi}{4eL^2}x'. \tag{4}$$

Figure 2 shows the variation in the permittivity tensor components in the transformed rectangular space. The different geometrical dimensions of the initial and transformed spaces are, respectively, $d=15$ cm, $e=15$ cm, and $L=15$ cm. We can note that the three components of the permittivity depend only on the coordinate x'. This is due to the invariance of the initial space with θ with respect to the distance from the source in the cylindrical space. This distance is represented by x' in the transformed rectangular space.

The divergence of ε_{yy} near $x'=0$ creates an "electromagnetic wall" with $\varepsilon_{yy} \to \infty$ on the left side of the rectangular area. This left side also corresponds to the radiating source transformed from the center line source of the cylindrical space. We can note the simplicity of the ε_{xx} and ε_{zz} which present a linear variation.

In the transformed rectangular space the confinement of the electromagnetic field can be controlled and increased by the different parameters d, e, and L, and particularly by the ratio $d/2L$. After the transformation, the electromagnetic en-

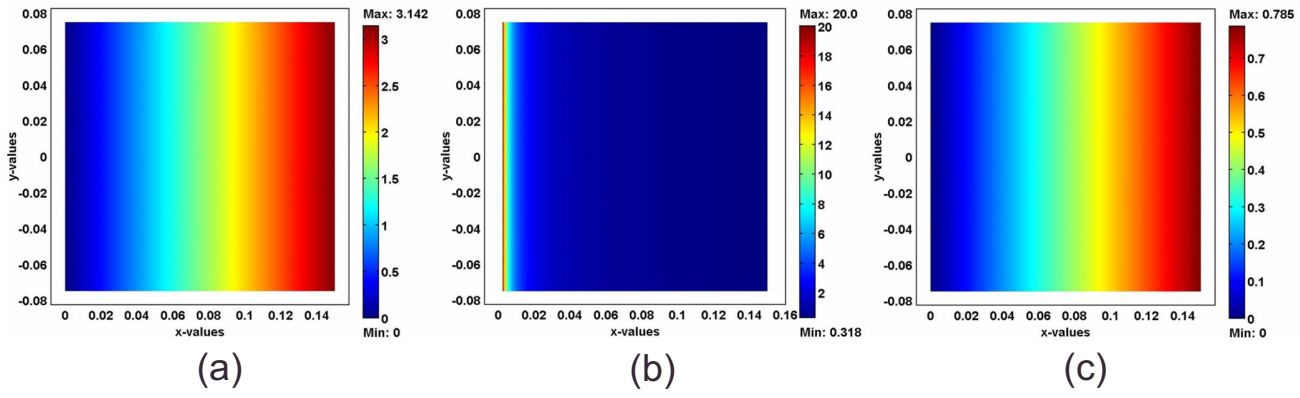

FIG. 2. (Color online) Variation in the permittivity tensor components: (a) ε_{xx}, (b) ε_{yy}, and (c) ε_{zz}.

ergy enclosed in the half cylindrical space is confined in the rectangular space. To characterize the emission directivity realized by the radiating source in the rectangular space, the most important parameter is the ratio between the width e of the aperture and the square of the wavelength λ^2 since the maximum directivity of an antenna is given by

$$D_{\max} = \frac{4\pi A_{\text{eff}}}{\lambda^2} \quad \text{where} \quad A_{\text{eff}} = \frac{\left| \int_A E_a(r) dS \right|^2}{\int_A |E_a(r)|^2 dS}, \tag{5}$$

where A_{eff} is the effective aperture of the antenna and depends on the width e and on the field distribution $E_a(r)$.

III. SIMULATIONS AND RESULTS

In the previous section we have defined the rules transforming an isotropically radiating line source in a cylindrical space into a radiating surface placed on the left side of a rectangular space. We have seen that the variations in the electromagnetic parameters of the transformed space depend on the ratio $d/2L$. In this section, finite element method based numerical simulations with Comsol MULTIPHYSICS (Ref. 14) are used to design and characterize this transformed directive antenna. As the line source of the half right cylindrical space becomes a radiating plane in the transformed rectangular space, an excitation is inserted at the left side of the rectangular space, as shown in Fig. 3(a). This space is delimited by metallic boundaries on the upper and lower sides and at the left side of the rectangular space representing the metamaterial having dimensions 15×15 cm^2. The radiating properties of the antenna are calculated and presented in Fig. 3.

Three operating frequencies have been considered here: 5, 10, and 40 GHz, corresponding, respectively, to $e/\lambda = 2.5$, 5, and 20. A directive emission can be observed as illustrated by the magnetic field radiations of the antenna for a TM wave polarization. A very high directivity is noted and can be calculated using the expression given in[15]

$$D = 41\ 253/(\theta_1 \theta_2), \tag{6}$$

where θ_1 and θ_2 are, respectively, the half-power beamwidths (in degrees) for the H-plane and E-plane patterns. Here we assume $\theta_1 = \theta_2$. Then for a half-power beamwidth of 13.5° at 10 GHz we obtain a directivity of 23.6 dB, implying a ratio $e/\lambda = 5$. This directivity is comparable with that of a parabolic reflector antenna of the same size[15] and is greater than that of a wideband (2–8 GHz) dual polarized FLANN® horn antenna whose directivity varies from 10 to 23 dB.

The far field radiation patterns of the antenna are calculated at different frequencies to assess the variation in the directivity. The dimensions of the rectangular box remain the same as above ($e = 15$ cm and $L = 15$ cm). Figure 4(a) shows the radiation patterns for the cases $e/\lambda = 2.5$ (5 GHz), 5 (10 GHz), and 20 (40 GHz). The directivity strongly increases when we move toward higher frequencies. It goes from 23.6 dB at 5 GHz to 29.5 dB at 10 GHz and 42 dB at 40 GHz. The directivity enhancement is illustrated by the evolution of the half-power beam width versus frequency in Fig. 4(b).

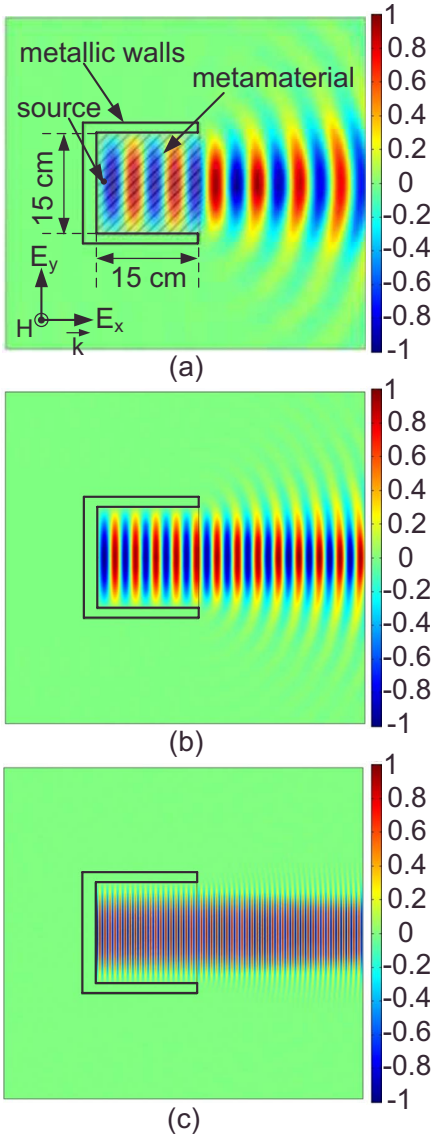

FIG. 3. (Color online) (a) Magnetic field distribution for a TM wave polarization at (a) 5 GHz, (b) 10 GHz, and (c) 40 GHz.

IV. PARAMETER REDUCTION

The metamaterial calculated above shows coordinate dependent electromagnetic parameters following Eq. (4). This dependency is identical for the permittivity and permeability, allowing an exact impedance matching with vacuum. We propose to simplify the calculated parameters of the highly directive antenna for a realistic experimental realization from achievable metamaterial structures. Choosing plane wave solutions for the electric field and magnetic field, with a wave vector $\boldsymbol{k}$ in xy plane, and a TM or a TE polarization with, respectively, the magnetic or electric field polarized along the z axis, we obtain a dispersion equation

$$\det(F) = 0, \tag{7}$$

with

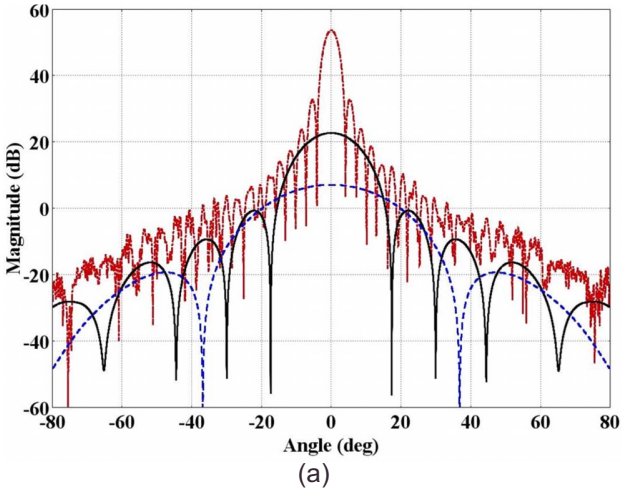

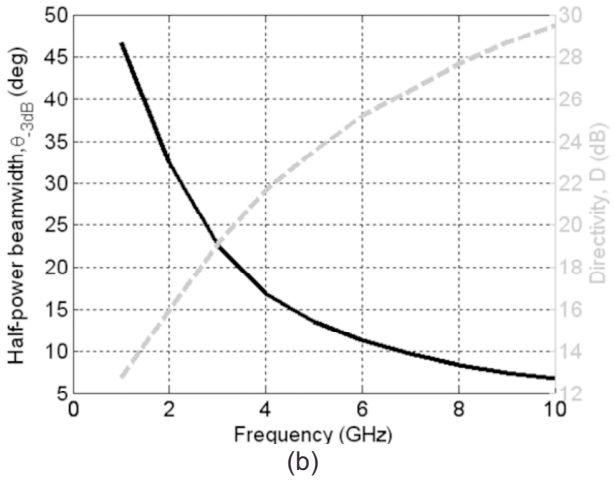

FIG. 4. (Color online) (a) Far field radiation patterns at 5 GHz (dashed), 10 GHz (continuous), and 40 GHz (dashed-dotted). (b) Half-power beamwidth (continuous) and directivity (dashed) vs frequency.

$$F = \begin{pmatrix} \varepsilon_{xx} - \dfrac{k_y^2}{\mu_{zz}} & \dfrac{-k_x k_y}{\mu_{zz}} & 0 \\ \dfrac{-k_x k_y}{\mu_{zz}} & \varepsilon_{yy} - \dfrac{k_x^2}{\mu_{zz}} & 0 \\ 0 & 0 & \varepsilon_{zz} - \dfrac{k_x^2}{\mu_{yy}} - \dfrac{k_y^2}{\mu_{xx}} \end{pmatrix}. \tag{8}$$

The determinant of this equation must be equal to zero. Solving it, we obtain one equation for each polarization. In TE polarization this equation can be written as

$$\varepsilon_{zz} = \frac{k_x^2}{\mu_{yy}} + \frac{k_y^2}{\mu_{xx}}, \tag{9}$$

whereas in TM polarization, it becomes

$$\mu_{zz} = \frac{k_x^2}{\varepsilon_{yy}} + \frac{k_y^2}{\varepsilon_{xx}}. \tag{10}$$

For a possible realization, the TM polarization is considered with, for instance, an inhomogeneous permittivity achievable with existing commercial dielectrics. In this polarization, the electromagnetic behavior is governed by three components: ε_{xx}, ε_{yy}, and μ_{zz} which depend on the x-coordinate values. To simplify these expressions, a simple method consists in dividing the dispersion equation by μ_{zz}. An identification with the initial equation gives $\mu_{zz}=1$, $\varepsilon_{yy}=d^2/4L^2$, and $\varepsilon_{xx}=(d\pi x/2eL)^2$, unaffecting the propagation in the structure. A further simplification is done by choosing $d=2L$, thus giving

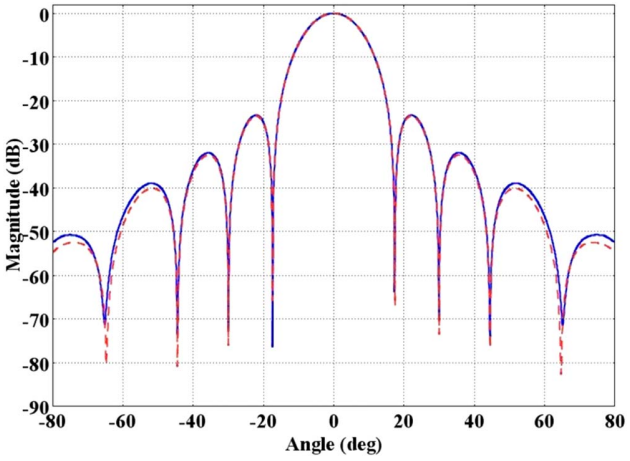

FIG. 5. (Color online) Normalized far field radiation pattern of the antenna with the metamaterial full parameters defined by Eq. (4) (dashed) and with the metamaterial reduced parameters defined by Eq. (11) (continuous) at 10 GHz.

$$\begin{cases} \mu_{zz} = 1. \\ \varepsilon_{yy} = 1. \\ \varepsilon_{xx} = \left(\dfrac{\pi x}{e}\right)^2. \end{cases} \tag{11}$$

Equation (11) describes the material parameters that can be achieved with already existing metamaterial structures, for example, metallic wire lattices with a variable step[16] or periodic array of rectangular resonators operating around their electrical resonance.[17]

Simulations of the antenna with this simplified material are performed and a directive emission is observed at 10 GHz. The radiation pattern obtained with the reduced parameters of Eq. (11) is compared to the one obtained from the continuous material defined by Eq. (4) in Fig. 5. Similar directivity and good overall agreement are observed. The directivity remains the same, 29.5 dB at 10 GHz for an aperture $e=\lambda/2$.

V. LAYERED METAMATERIALS

The previous material has a continuous variation in permittivity along the x-axis (the propagation direction). This is not easy to achieve in practice and in general, it is simpler to carry out a discrete variation. We therefore adopt a method which consists in discretizing the permittivity profile into ten layers of different thicknesses and permittivities. This discretization secures the characteristics of the ε_{xx} response defined by Eq. (11). We assume a constant variation $\Delta\varepsilon=\varepsilon_{\max}/n$ at the end (rear interface) of each layer with $\varepsilon_{\max}=\pi^2$ and $n=10$. Knowing that at the rear interface of layer i $\varepsilon_{xx}=i\Delta\varepsilon$, we can therefore deduce the thickness Δx_i. Then

TABLE I. Discretization of ε_{xx} along the x axis with the thickness of each layer.

Layer	Thickness (mm)	ε_{xx}
1	47.4	0.05
2	19.6	1.44
3	15.1	2.44
4	12.7	3.44
5	11.2	4.42
6	10.1	5.41
7	9.3	6.4
8	8.7	7.4
9	8.1	8.38
10	7.8	9.37

for convenience, we apply to each different layer the value of ε_{xx} corresponding to $x=x_i$ with x_i lying at the middle of each layer. Noting $a=(\pi/e)^2$, the following relations are derived:

$$\Delta x_i = \sqrt{i\frac{\Delta\varepsilon}{a}} - \sqrt{(i-1)\frac{\Delta\varepsilon}{a}} \quad \text{with}$$

$$x_i = \frac{\sqrt{i\frac{\Delta\varepsilon}{a}} + \sqrt{(i-1)\frac{\Delta\varepsilon}{a}}}{2} \quad \text{for} \quad 0 < i < n+1. \tag{12}$$

The values obtained for the thickness and permittivity of each layer are summarized in Table I and plotted in Fig. 6.

Simulations using Comsol MULTIPHYSICS are performed with the different thicknesses and permittivities from Table I and the performances of the antenna are shown in Fig. 7. A highly directive magnetic field distribution can be noted at 10 GHz for the TM wave polarization with the source embedded in the layered metamaterial [Fig. 7(a)]. The normalized far field radiation pattern of the layered metamaterial-based antenna (dashed) agrees very well with the continuous metamaterial-based one (continuous), therefore indicating the easiness of design.

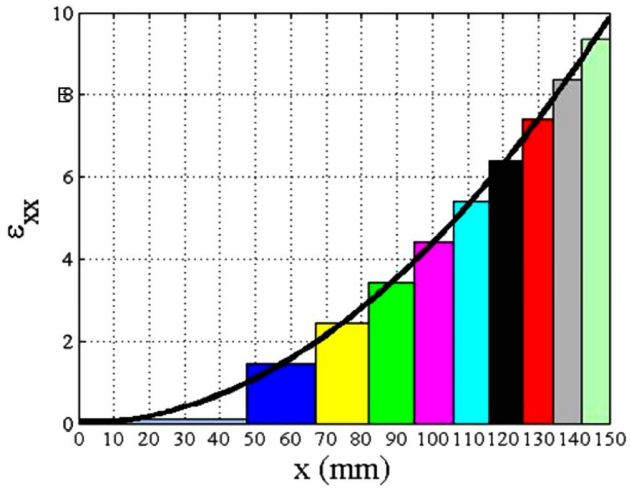

FIG. 6. (Color online) Evolution of the layered permittivity compared to the continuous one defined by Eq. (11).

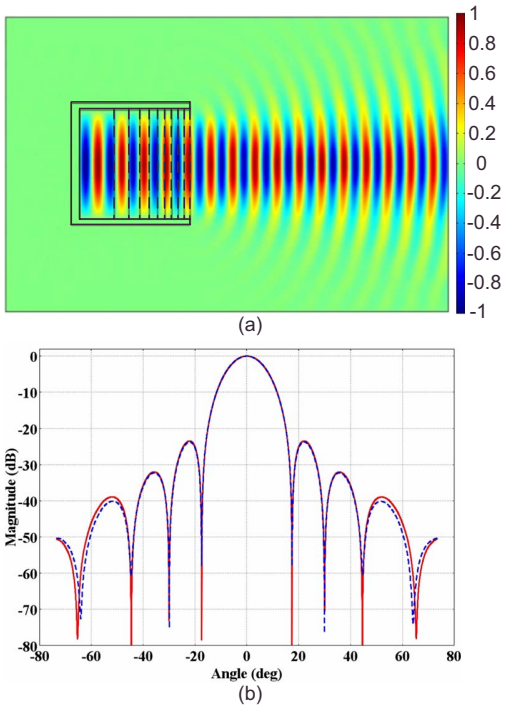

FIG. 7. (Color online) (a) Magnetic field distribution for TM wave polarization with the metamaterial layers at 10 GHz. (b) Normalized far field radiation pattern for the metamaterial layers case (dashed) and for the reduced parameters case (continuous).

VI. CONCLUSION

A metamaterial structure is proposed in an antenna system to achieve the manipulation of directivity via spatial coordinate transformation. Numerical simulations are performed to show that the directivity of this metamaterial-based antenna is competitive with conventional directive antennas such as horn and reflector antennas. By embedding a radiating surface in the optimized metamaterial, a highly directive emission equivalent to parabolic antennas with similar dimensions is generated. The calculated reduced electromagnetic material parameters make the design procedure physically possible. For a practical fabrication with existing commercial dielectrics, a layered structure composed of homogeneous and uniaxial anisotropic metamaterials has been presented. In all the three cases (theoretical, reduced, and layered metamaterials) the directivity of the antenna remains consistent.

[1] J. B. Pendry, D. Schurig, and D. R. Smith, Science **312**, 1780 (2006).
[2] U. Leonhardt, Science **312**, 1777 (2006).
[3] D. Schurig, J. J. Mock, B. J. Justice, S. A. Cummer, J. B. Pendry, A. F. Starr, and D. R. Smith, Science **314**, 403 (2006).
[4] D. Schurig, J. B. Pendry, and D. R. Smith, Opt. Express **14**, 9794 (2006).
[5] M. Rahm, D. Schurig, D. A. Roberts, S. A. Cummer, D. R. Smith, and J. B. Pendry, Photonics Nanostruct. Fundam. Appl. **6**, 87 (2008).
[6] A. Greenleaf, Y. Kurylev, M. Lassas, and G. Uhlmann, Phys. Rev. Lett. **99**, 183901 (2007).
[7] M. Rahm, D. A. Roberts, J. B. Pendry, and D. R. Smith, Opt. Express **16**, 11555 (2008).
[8] M. Rahm, S. A. Cummer, D. Schurig, J. B. Pendry, and D. R. Smith, Phys. Rev. Lett. **100**, 063903 (2008).
[9] L. Lin, W. Wang, J. Cui, C. Du, and X. Luo, Opt. Express **16**, 6815 (2008).
[10] J. Huangfu, S. Xi, F. Kong, J. Zhang, H. Chen, D. Wang, B.-I. Wu, L. Ran, and J. A. Kong, J. Appl. Phys. **104**, 014502 (2008).

[11]H. Chen and C. T. Chan, Appl. Phys. Lett. **90**, 241105 (2007).
[12]F. Kong, B. Wu, J. A. Kong, J. H. Huangfu, and S. Xi, Appl. Phys. Lett. **91**, 253509 (2007).
[13]W. X. Jiang, T. J. Cui, H. F. Ma, X. M. Yang, and Q. Cheng, Appl. Phys. Lett. **93**, 221906 (2008).
[14]Comsol MULTIPHYSICS Modeling (http://www.comsol.com).
[15]C. A. Balanis, *Antenna Theory: Analysis and Design*, 2nd ed. (Wiley, New York, 1997), pp. 46 and 822.
[16]J. B. Pendry, A. J. Holden, W. J. Stewart, and I. Youngs, Phys. Rev. Lett. **76**, 4773 (1996).
[17]B. Kanté, A. de Lustrac, J.-M. Lourtioz, and S. N. Burokur, Opt. Express **16**, 9191 (2008).

Annexe 3.2

P.-H. Tichit, S. N. Burokur, A. de Lustrac

« Waveguide taper engineering using coordinate transformation technology »

Optics Express, vol. 18, no. 2, pp. 767-772, January 2010

Waveguide taper engineering using coordinate transformation technology

Paul-Henri Tichit, Shah Nawaz Burokur, and André de Lustrac

Institut d'Electronique Fondamentale, Univ. Paris-Sud, CNRS, UMR 8622, 91405 Orsay cedex, France
paul-henri.tichit@u-psud.fr, nawaz.burokur@u-psud.fr, andre.de-lustrac@u-psud.fr

Abstract: Spatial coordinate transformation is a suitable tool for the design of complex electromagnetic structures. In this paper, we define three spatial coordinate transformations which show the possibility of designing a taper between two different waveguides. A parametric study is presented for the three transformations and we propose achievable values of permittivity and permeability that can be obtained with existing metamaterials. The performances of such defined structures are demonstrated by finite element numerical simulations.

OCIS codes: (260.2065) Effective medium theory; (260.2110) Electromagnetic optics; (260.2710) Inhomogeneous optical media; (160.1190) Anisotropic optical materials; (160.3918) Metamaterials.

References and links

1. J. B. Pendry, D. Schurig, and D. R. Smith, "Controlling electromagnetic fields," Science **312**(5781), 1780–1782 (2006).
2. U. Leonhardt, "Optical conformal mapping," Science **312**(5781), 1777–1780 (2006).
3. D. Schurig, J. J. Mock, B. J. Justice, S. A. Cummer, J. B. Pendry, A. F. Starr, and D. R. Smith, "Metamaterial electromagnetic cloak at microwave frequencies," Science **314**(5801), 977–980 (2006).
4. D. Schurig, J. B. Pendry, and D. R. Smith, "Calculation of material properties and ray tracing in transformation media," Opt. Express **14**(21), 9794–9804 (2006).
5. M. Rahm, D. Schurig, D. A. Roberts, S. A. Cummer, D. R. Smith, and J. B. Pendry, "Design of electromagnetic cloaks and concentrators using form-invariant coordinate transformations of Maxwell's equations," Photonics and Nanost. Fundam. Appl. **6**(1), 87–95 (2008).
6. M. Rahm, D. A. Roberts, J. B. Pendry, and D. R. Smith, "Transformation-optical design of adaptive beam bends and beam expanders," Opt. Express **16**(15), 11555–11567 (2008).
7. M. Rahm, S. A. Cummer, D. Schurig, J. B. Pendry, and D. R. Smith, "Optical design of reflectionless complex media by finite embedded coordinate transformations," Phys. Rev. Lett. **100**(6), 063903 (2008).
8. L. Lin, W. Wang, J. Cui, C. Du, and X. Luo, "Design of electromagnetic refractor and phase transformer using coordinate transformation theory," Opt. Express **16**(10), 6815–6821 (2008).
9. J. Huangfu, S. Xi, F. Kong, J. Zhang, H. Chen, D. Wang, B.-I. Wu, L. Ran, and J. A. Kong, "Application of coordinate transformation in bent waveguide," J. Appl. Phys. **104**(1), 014502 (2008).
10. D. A. Roberts, M. Rahm, J. B. Pendry, and D. R. Smith, "Transformation-optical design of sharp waveguide bends and corners," Appl. Phys. Lett. **93**(25), 251111 (2008).
11. H. Chen, B. Hou, S. Chen, X. Ao, W. Wen, and C. T. Chan, "Design and experimental realization of a broadband transformation media field rotator at microwave frequencies," Phys. Rev. Lett. **102**(18), 183903 (2009).
12. Z. Wang, Y. Luo, W. Cui, W. Ma, L. Peng, J. Huangfu, H. Chen, and L. Ran, "Controlling the field distribution in waveguides with transformation optics," Appl. Phys. Lett. **94**(23), 234101 (2009).
13. F. Kong, B.-I. Wu, J. A. Kong, J. Huangfu, S. Xi, and H. Chen, "Planar focusing antenna design by using coordinate transformation technology," Appl. Phys. Lett. **91**(25), 253509 (2007).
14. P.-H. Tichit, S. N. Burokur, and A. de Lustrac, "Ultradirective antenna via transformation optics," J. Appl. Phys. **105**(10), 104912 (2009).
15. J. B. Pendry, A. J. Holden, D. J. Robbins, and W. J. Stewart, "Magnetism from conductors and enhanced nonlinear phenomena," IEEE Trans. Microw. Theory Tech. **47**(11), 2075–2084 (1999).
16. J. B. Pendry, A. J. Holden, W. J. Stewart, and I. Youngs, "Extremely low frequency plasmons in metallic mesostructures," Phys. Rev. Lett. **76**(25), 4773–4776 (1996).
17. J. Zhou, L. Zhang, G. Tuttle, T. Koschny, and C. M. Soukoulis, "Negative index materials using simple short wire pairs," Phys. Rev. B **73**(4), 041101 (2006).
18. D. Schurig, J. J. Mock, and D. R. Smith, "Electric-field-coupled resonators for negative permittivity metamaterials," Appl. Phys. Lett. **88**(4), 041109 (2006).
19. S. N. Burokur, A. Sellier, B. Kanté, and A. de Lustrac, "Symmetry breaking in metallic cut wire pairs metamaterials for negative refractive index," Appl. Phys. Lett. **94**(20), 201111 (2009).

#114794 - $15.00 USD Received 27 Jul 2009; revised 26 Aug 2009; accepted 28 Aug 2009; published 6 Jan 2010

20. A. Sellier, S. N. Burokur, B. Kanté, and A. de Lustrac, "Negative refractive index metamaterials using only metallic cut wires," Opt. Express **17**(8), 6301–6310 (2009).

1. Introduction

Although now well-known for 30 years, the invariance of Maxwell's equation has been redesigned since 2006 by J. B. Pendry *et al.* [1] and U. Leonhardt [2]. Some proposals of devices using this method have been presented for cloaking [1, 3, 4], concentrators [5], beam bends and expanders [6-10], rotators [11], channels [12] and ultra-directive antennas [13-14]. Thus transformation optics appears to be a convenient tool to design devices or components with special properties difficult to obtain with naturally occurring materials.

Theoretically, the coordinate transformation method consists in generating a new transformed space from an initial one where solutions of Maxwell's equations are known. First of all, we imagine a virtual space with the desired topological properties. The main goal is to create a new space which contains the underlying physics. We gather all these properties in the metric tensor in order to perform the calculations. Although this approach and associated calculations are now well known, Pendry *et al.* [1] have proposed a new interpretation where the new components tensors of permeability and permittivity can be viewed as a material in the original space. It is as if the new material mimics the defined topological space. Moreover the choice of an Euclidean initial space allows to obtain devices or components with equal values for the permittivity and permeability, and consequently with zero reflection at boundaries with vacuum. These mathematical tools have been intensively used since two years for the design of optical devices and components [5–14].

In this paper, following the transformation optics approach, we design a taper between two waveguides of different cross sections. Three different transformation techniques are presented so as to achieve a reflectionless taper between the two waveguides. The media obtained from these three methods presents complex anisotropic permittivity and permeability. However, we show that using an exponential transformation leads to the design of a taper from a material with physically achievable material parameters.

2. Transformation formulations

Three different formulations are proposed below to achieve a low reflection taper between two waveguides of different cross sections. Each waveguide is represented by black lines in its respective space given in Cartesian coordinates as depicted in Fig. 1. The aim is to connect each horizontal lines of each space to assume transmission of electromagnetic waves. Thus in geometric approximation, each ray of light in the first waveguide is guided into the second one by green lines representing the taper. For the first formulation, we assume a linear transformation by connecting the two spaces with straight lines as shown in Fig. 1(a). The second formulation uses a parabolic transformation to achieve the connection (Fig. 1(b)). For the third one, an exponential transformation is defined as shown in Fig. 1(c). In all three cases, the geometrical properties of the schema under analysis remain unchanged. The width of the input and output waveguides is respectively noted a and b, and the length of the taper in all three cases is taken to be l. Mathematical expressions defining each formulation of the transformation approaches are given in Fig. 1. x', y' and z' are the coordinates in the transformed (new) space and x, y and z are those in the initial space. As it can be observed from the mathematical expressions, the different formulations depend on the geometric parameters (a, b, l).

Each transformation leads to a material with specific properties that can play the role of the desired taper. The transformation approach can be summarized in two main points. First of all we determine the Jacobian matrix of each transformation formulation so as to obtain the properties of the "taper space". Thus we can use the transformation expressed in (1) to obtain the permittivity and permeability tensors in the initial space which are x and y dependent.

$$\varepsilon^{i'j'} = \frac{J_i^{i'} J_j^{j'} \varepsilon_0 \delta^{ij}}{\det(J)} \text{ and } \mu^{i'j'} = \frac{J_i^{i'} J_j^{j'} \mu_0 \delta^{ij}}{\det(J)} \text{ with } \quad J_\alpha^{\alpha'} = \frac{\partial x'^\alpha}{\partial x^\alpha} \tag{1}$$

#114794 - $15.00 USD Received 27 Jul 2009; revised 26 Aug 2009; accepted 28 Aug 2009; published 6 Jan 2010

where $J_{\alpha}^{\alpha'}$ and δ^{ij} are, respectively, the Jacobian transformation matrix of the expressions given in Fig. 1 and the Kronecker symbol.

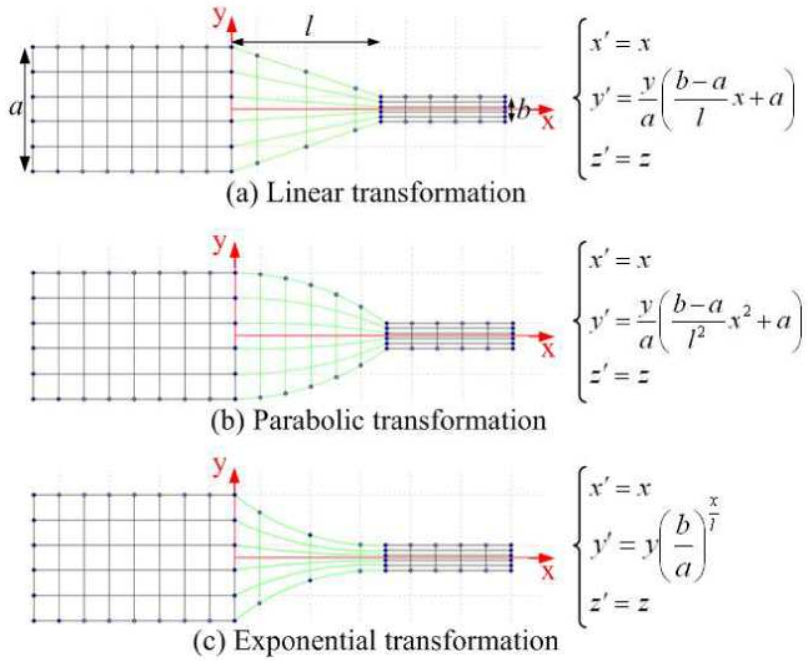

Fig. 1. Transformed taper (green lines) between two waveguides (black lines) with different cross sections. (a) Linear, (b) parabolic, and (c) exponential transformation formulation.

The second step consists in calculating the new permittivity and permeability tensors in the coordinate system (*x*', *y*') so as to mimic the transformed space. At this stage, we have designed a material with specific desired physical properties. This material can then be described by a permeability and permittivity tensors $\overline{\overline{\varepsilon}} = \overline{\overline{\theta}}\varepsilon_0$ and $\overline{\overline{\mu}} = \overline{\overline{\theta}}\mu_0$. In order to simplify the different calculations, we take $\frac{J_i^{i'} J_j^{j'} \delta^{ij}}{\det(J)} = \theta^{i'j'}$ with

$$\overline{\overline{\theta}} = \begin{pmatrix} \theta_{xx}(x') & \theta_{xy}(x', y') & 0 \\ \theta_{xy}(x', y') & \theta_{yy}(x', y') & 0 \\ 0 & 0 & \theta_{zz}(x') \end{pmatrix} \quad (2)$$

The components values of $\overline{\overline{\theta}}$ tensor are given in Table 1 where a nondiagonal term (θ_{xy}) appears. This nondiagonal term is necessary to guide electromagnetic waves in the *x*-*y* plane like it is the case for this taper.

#114794 - $15.00 USD Received 27 Jul 2009; revised 26 Aug 2009; accepted 28 Aug 2009; published 6 Jan 2010

Table 1. Components values of $\overline{\overline{\theta}}$ tensor for the three transformations.

	$\theta_{xx}(x')=\theta_{zz}(x')$	$\theta_{xy}(x',y')$	$\theta_{yy}(x',y')$
Linear transformation	$\frac{al}{a\,(l - x') + b\,x'}$	$\theta_{xx}^2 \frac{b-a}{al} y'$	$\frac{1}{\theta_{xx}} + \frac{\theta_{xy}^2}{\theta_{xx}}$
Parabolic transformation	$\frac{al^2}{(al^2 - a\,x'^2 + b\,x'^2)}$	$\frac{2\theta_{xx}^2\,(b - a)\,x'\,y'}{al^2}$	$\frac{1}{\theta_{xx}} + \frac{\theta_{xy}^2}{\theta_{xx}}$
Exponential transformation	$(\frac{b}{a})^{-\frac{x'}{l}}$	$\frac{\theta_{xx}\,y'\ln(\frac{b}{a})}{l}$	$\frac{1}{\theta_{xx}} + \frac{\theta_{xy}^2}{\theta_{xx}}$

3. Simulations and results

To verify the results expressed in the previous section, finite element method based commercial software Comsol MULTIPHYSICS is used to design the described waveguide taper. Simulations are performed in two-dimensional mode for the validation of the proposed material parameters. Port boundaries are used to excite the first and third Transverse Electric (TE_1 and TE_3) modes of the input waveguide with the E-field directed along the *z*-axis to verify the conservation of modes through the taper. The waveguides boundaries are assumed as Perfect Electric Conductors (PECs) and matched boundaries conditions are applied to the taper. Verifications are done in the microwave domain for a possible future physical prototyping based on the use of metamaterials [15–20], such as Split Ring Resonators (SRRs), Electric LC resonators (ELCs), cut wire pairs and continuous wires. SRRs [15] are known to produce a magnetic resonance where the permeability ranges from negative to positive values and continuous wires [16] have been presented to exhibit a Drude-like permittivity response with negative values below the plasma frequency. Symmetric cut wire pairs presented in [17] produce also a magnetic resonance where as ELCs [18] produce an electric resonance. Asymmetric cut wire pairs recently proposed in [19-20] have experimentally demonstrated both electric and magnetic resonances.

The waveguides widths are chosen to be a = 10 cm and b = 2 cm with respectively 1.5 GHz and 7.5 GHz cutoff frequencies. Length of the taper is chosen as l = 5 cm allowing to generate the entire spatial dependence of the material parameters $\theta_{xx}(x')$, $\theta_{zz}(x')$, $\theta_{xy}(x',y')$ and $\theta_{yy}(x',y')$ as shown in Fig. 2. These distributions are plotted from the expressions given in Table 1. Values of permittivities and permeabilities presented in Fig. 2 account for the control of the electromagnetic field in the taper and the conservation of the propagating modes from waveguide 1 to waveguide 2. Although same spatial distribution profile can be observed for the three different formulations, parameters values are completely different. For linear and parabolic transformations, values of μ_{yy} are too high to be physically achievable with existing metamaterials. However, it is clear that the exponential transformation leads to values more easily achievable with metamaterials. Moreover, the physical realization of such a metamaterial taper will be facilitated by the slow variation of the material parameters, implying a gradual variation of the geometrical parameters of metamaterial inclusions. We shall note that the components are calculated in the Cartesian system and obey the following dispersion relation in the transverse electric (TE) mode:

$$\varepsilon_{zz}\left(\mu_{xy}^{\,2} - \mu_{xx}\mu_{yy}\right) + \mu_{xx}k_x^{\,2} + k_y\left(\mu_{yy}k_y - 2\mu_{xy}k_x\right) = 0 \qquad (3)$$

This equation is obtained from the propagation equation and describes the control of electromagnetic waves in the material. This relation is also important for a future reduction of parameters, which can be done by simplifying the nondiagonal parameter θ_{xy} to a closed interval near zero when choosing appropriately the length of the taper. For example, by

#114794 - $15.00 USD Received 27 Jul 2009; revised 26 Aug 2009; accepted 28 Aug 2009; published 6 Jan 2010

bounding the nondiagonal term of the exponential formulation in Table 1, the condition $l > \frac{a^2}{b}\frac{\left|\ln\left(\frac{b}{a}\right)\right|}{2\Delta}$ leads to $-\Delta < \mu_{xy} < \Delta$ where Δ can be very close to zero.

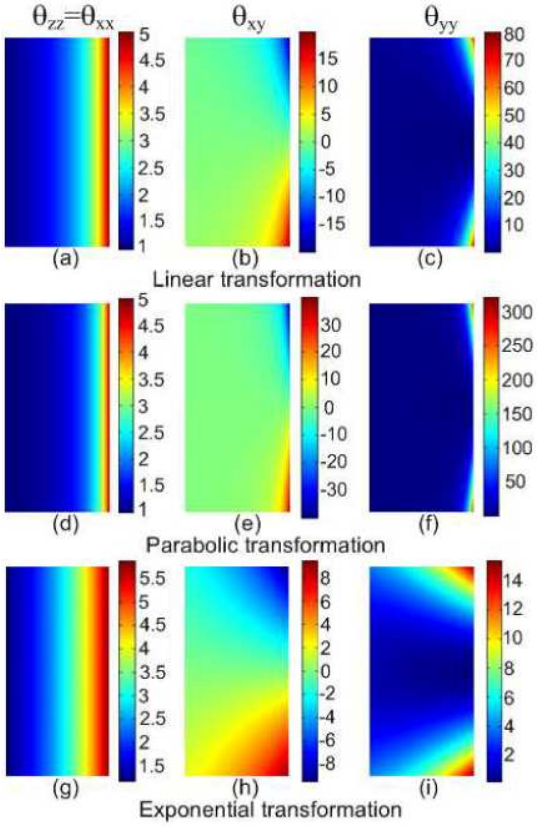

Fig. 2. Components of the permittivity and permeability tensors $\bar{\bar{\theta}}$ for the three transformations with a = 10 cm, b = 2 cm and l = 5 cm.

Simulation results of the E-field distribution of the structure under study for the three transformations are presented in Fig. 3. The distributions in the tapered waveguides are compared to a non tapered case at 10 GHz and 30 GHz for the fundamental (TE_1) excitation mode and at 30 GHz for the third (TE_3) excitation mode. Concerning the non tapered junction waveguides, we can observe phase distortions caused by reflections at the junction from the bigger waveguide to the smaller one (Figs. 3(a)-(c)). These distortions become more severe at higher frequencies (30 GHz). However, simulations performed on the tapered waveguides (Figs. 3(d)-(l)) illustrate that electromagnetic waves are properly guided from one waveguide to the other without any impact on the guided mode when the transformed medium is embedded between the two waveguides. The difference in the transformation formulations indicates a change in the path of electromagnetic waves in the tapered section, highlighted by the shaded gray area in Fig. 3. Increasing the frequency improve the transmission between the two waveguides through the tapered section. This phenomenon can be observed when we compare the E-field distributions at 10 GHz and 30 GHz. At 10 GHz, a slight impedance mismatch between the taper output and the small waveguide input can be observed. This

#114794 - $15.00 USD Received 27 Jul 2009; revised 26 Aug 2009; accepted 28 Aug 2009; published 6 Jan 2010

phenomenon decreases at higher frequencies, as illustrated for 30 GHz. Figure 3 shows the efficiency of the material parameters defined by coordinate transformation technology.

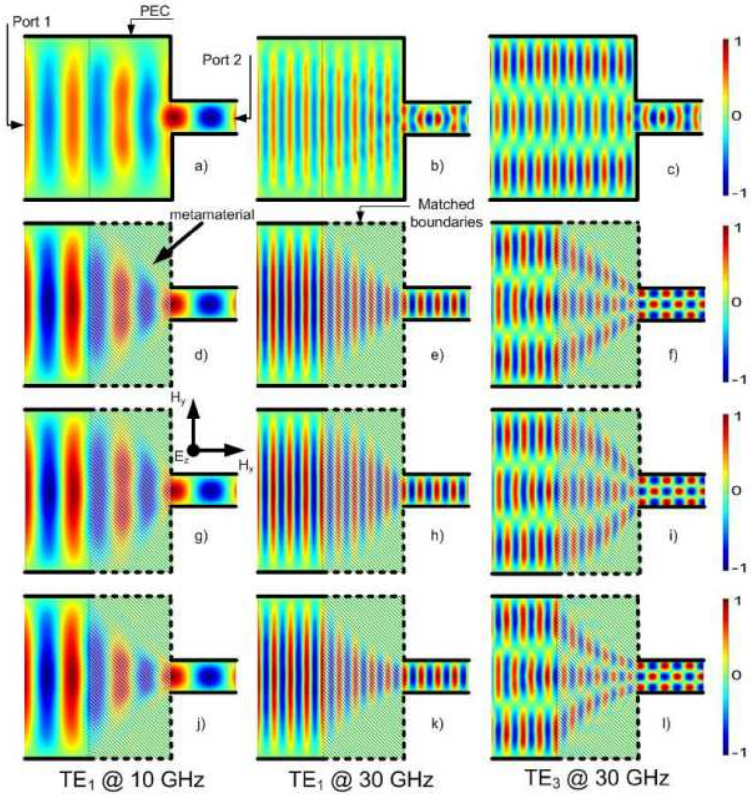

Fig. 3. Normalized E-field distribution for TE polarization. (a)-(c) Non tapered junction waveguides, (d)-(f) Tapered junction waveguides with linear transformation. (g)-(i) Tapered junction waveguides with parabolic transformation. (j)-(l) Tapered junction waveguides with exponential transformation.

4. Conclusion

Spatial coordinate transformation is applied to design a taper between two waveguides with different cross sections. Three transformation formulations have been tested; a linear, a parabolic and an exponential one. Each formulation is used to generate material parameters and it has been observed that the parameters profile depend on the formulation considered. Best tradeoff is obtained with the exponential formulation with a slow variation of the material parameters. This slow variation is very interesting if we consider physical realization of such a structure using metamaterials as SRRs, ELCs, cut and continuous wires. Numerical simulations using the material parameters have been performed to show how electromagnetic waves are guided between two waveguides through the taper. Compared to an abrupt (non tapered) junction where phase distortions appear, transformation optics help to guide properly electromagnetic waves from one waveguide to the other without any impact on the guided propagating modes.

#114794 - $15.00 USD Received 27 Jul 2009; revised 26 Aug 2009; accepted 28 Aug 2009; published 6 Jan 2010

Annexe 3.3

P.-H. Tichit, S. N. Burokur, D. Germain, A. de Lustrac

« Design and experimental demonstration of a high-directive emission with transformation optics »

Physical Review B, vol. 83, no. 15 (155108), April 2011

Design and experimental demonstration of a high-directive emission with transformation optics

P.-H. Tichit, S. N. Burokur, D. Germain, and A. de Lustrac
IEF, Université Paris-Sud, CNRS, UMR 8622, F-91405 Orsay Cedex, France
(Received 21 October 2010; revised manuscript received 5 January 2011; published 11 April 2011)

With the explosion of wireless networks and automotive radar systems, there is an acute need for new materials and technologies that would not only minimize the size of these devices, but also enhance their performance. The technique of transformation optics—an innovative approach to produce artificial metamaterials that control electromagnetic waves as if space itself was transformed—provides unique opportunities to reach this goal. In this paper we design, fabricate, and characterize a new class of metamaterial capable of transforming the source distribution and radiation pattern of an isotropic microwave emitter. Our findings have considerable implications for the development of new ultradirective antennas with superior performances and compactness compared to conventional antennas operating in the same frequency range.

DOI: 10.1103/PhysRevB.83.155108 PACS number(s): 81.05.Xj, 78.67.Pt

The concept of transformation optics was first proposed by J. B. Pendry[1] and U. Leonhardt[2] in 2006. It provides the conceptual design of novel, and otherwise unattainable, electromagnetic and optical devices by controlling the paths of wave propagation. However, practical realization of these structures remains a challenge without the use of an extremely successful second concept, that of artificial metamaterials producing material parameters unobtainable in nature. The first example of this successful merging was the design and experimental characterization of an invisibility cloak in 2006.[3] Later other versions of cloaks have been proposed at microwave[4,5] and optical[6,7] frequencies. Invisibility-cloaking structures can serve as benchmark examples for the much broader ideas of transformation optics. In the last few years, the combination of transformation optics and metamaterials has led to staggering electromagnetic devices.[8–19] Proposals of new electromagnetic devices such as concentrators,[9] wormholes,[10] waveguide transitions and bends,[11–15] and planar focusing antennas[16] have been theoretically submitted. Recently, experimental realizations and demonstrations on several transformation-optics-based devices have been conducted,[17–19] but none in the domain of directive sources. Indeed, practical realization requires design and implementation of anisotropic metamaterials with high accuracy.

Although already known,[20,21] the introduction of transformation optics in 2006 has brought back to mind the correspondence between coordinate transformation and materials parameters. In this way, the material can be viewed as a new geometry,[1,2,22] and information about the coordinate transformation is given by material properties. Based on the reinterpretation of the form-invariance of Maxwell's equation against coordinate transformation, control of the electromagnetic field at will became possible by introducing a specific coordinate transformation that will map an initial space into an imagined one. Among the class of transformation found in literature, several possibilities are available for the design of electromagnetic structures. For example, continuous transformations introduced by Pendry to realize the first electromagnetic cloak[3] led to anisotropic and inhomogeneous permeability and permittivity tensors but present the main advantage of being general. The contribution of these transformations was leveraged in many cases as cited just above. In parallel, Leonhardt proposed the concept of conformal mapping[2] where transformations follow Fermat's principle allowing the design of devices with isotropic dielectric media.[23–26] The main drawback of such transformations is that mathematical requirement is often too complex for realization. Following this idea, quasiconformal transformation,[5–7,27,28] where slight deformation of the transformations can minimize the anisotropy of the material by approximation with an isotropic media, was introduced. Other theoretical works mixed time and space transformations[29–33] and linked these transformations with cosmology and celestial mechanics.[34–36] At the same time, the concept of finite embedded transformation[11,12,37–40] was introduced, adding a significant amount of flexibility and enabling steering or focusing of electromagnetic waves. Finally, techniques of source transformation[41–44] have offered new opportunities for the design of active devices with source distribution included in the transformed space. In this last approach, we design an ultradirective emission by stretching an isotropic source into an extended coherent source.

The design step is very important, first because the values of theoretical electromagnetic parameters calculated by transformation optics are often too extreme to be realized; therefore, a careful design must allow a reduction of these values. Also, in some cases permittivity and permeability tensors have nondiagonal terms that are difficult to implement. To facilitate the realization of structures, it is important to minimize or even cancel these terms. In all cases, for a real device the values of the electromagnetic parameters must be achievable with available metamaterials. Second, a practical realization necessitates a discretization of the theoretical material. This discretization must allow maintaining the performances of the theoretical structure at an acceptable level. For instance, transformation optics has also made it possible to transmute a singular isotropic profile into a regular but anisotropic material, leading to a more practicable device. Dielectric singularities are points where the refractive index n reaches infinity or zero, where electromagnetic waves travel infinitely slow or infinitely fast. Such singularities cannot be made in practice for a broad spectral range, but one can transmute them into topological defects of anisotropic materials.[18] In Ma *et al.*[18] an omnidirectional retroreflector

is implemented thanks to the transformation of a singularity in the index profile into a topological defect. Thus, bounded values of the permittivity and permeability components allow the realization of the device. After the discretization step, tailored composite metal-dielectric metamaterials with optimized electromagnetic properties make it possible to approximate and implement these target distributions. Based on electric and magnetic resonances, these subwavelength structures can be appropriately engineered such that effective electromagnetic parameters can reach desired values.

Besides the transformation optics approach, other interesting techniques have been proposed to achieve directive emissions. Enoch *et al.*[45] have shown how a simple stack of metallic grids can lead to ultrarefraction. Because the resulting metamaterial structure has an index of refraction, n, which is positive, but near zero, all of the rays emanating from a point source within such a slab of zero index material would refract, by Snell's law, almost parallel to the normal of every radiating aperture. Another interesting metamaterial-based directive emission consisted of embedding a feed source between two parallel plate reflectors, forming a resonant cavity antenna system.[46]

In this article we present the practical implementation of a directive emission based on the transformation of an isotropic source at microwaves frequencies. Our aim is to show how a judiciously engineered metamaterial allows us to control the direction of emission of a source in order to collect all the energy in a small angular domain around the normal, with a good impedance matching between the radiating source and the material obtained by transformation optics. Following the theoretical procedure,[1,2] constitutive electromagnetic parameter distributions are obtained for the material surrounding the radiating source. We describe the design of the anisotropic metamaterials used and the implementation of the proposed device. To experimentally demonstrate the directive emission, both the far-field radiation pattern and the near-field distribution are measured. Measurements agree quantitatively and qualitatively with theoretical simulations. The proposed device presents higher performances and compactness, compared to a parabolic reflector antenna with similar dimensions operating in the same frequency range. Our method, though general, is robust and can be easily extended to other frequency ranges and even at optical frequencies. The directive emitter finds important potential interests in communication systems for applications to high-rate data transmission, automotive radar, broadband point-to-point communications, and millimeter wave imaging.

I. DESIGN AND SIMULATION

In a topological approach, transformation optics consists of generating suitable metrics where light follows the geodesics. Here is a brief summary of the theoretical underlying physics of the transformation involved in this present work and the application to our antenna concept[44]: The imagined space of our proposed antenna is obtained by transforming a flat isotropic cylindrical half space with zero Riemann curvature tensor described in polar coordinates $\{r, \theta\}$ into a flat space in squeezed Cartesian coordinates. x', y', and z' are taken to be the coordinates in the virtual transformed rectangular space and x, y, z are those in the initial real cylindrical space, as illustrated by the schematic principle in Fig. 1.

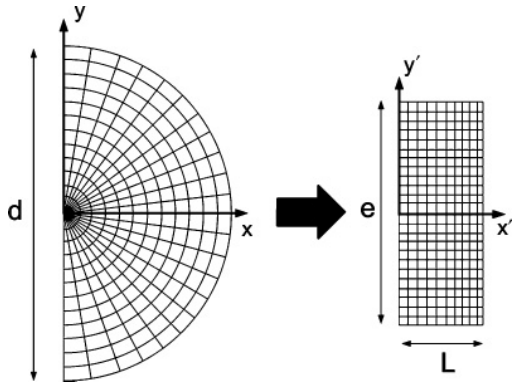

FIG. 1. Representation of the transformation of initial space into desired space. Each radius line of the cylindrical space is transformed into a horizontal line of the right rectangular space.

We assume free space in the cylinder, with isotropic permeability and permittivity tensors ε_0 and μ_0. Theory has shown that the coordinate transformation can be implemented by a material obeying the tensors

$$\theta^{i'j'} = g^{i'j'}|\det(g^{i'j'})|^{-\frac{1}{2}}\theta, \tag{1}$$

where θ represents the permittivity or permeability tensor and g the metric tensor of our designed space. To be implemented the material must be able to produce the following simple dielectric tensors:

$$\varepsilon^{ij} = \mu^{ij} = \mathrm{diag}\left(\varepsilon_{xx}(x'), \frac{1}{\varepsilon_{xx}(x')}, \alpha\varepsilon_{xx}(x')\right), \tag{2}$$

where $\varepsilon_{xx}(x') = \frac{\pi x'}{e}$ and $\alpha = \frac{d^2}{4L^2}$, with d representing the diameter of the initial cylindrical space and e and L, respectively, the width and length of the rectangular target space. The appropriate choice of our transformation thus assures an absence of nondiagonal components, giving rise to a practical implementation using metamaterials. However, this realization needs further simplifications of the material electromagnetic parameters. First, the dimensions of the semicylindrical space must be set so that $\alpha = 4$ in order to obtain achievable values for the electromagnetic parameters. Additional simplification arises from the choice of the polarization of the emitted wave. Here we consider a polarized electromagnetic wave with an electric field pointing in the z direction, which allows modifying the dispersion equation in order to simplify the electromagnetic parameters without changing Maxwell's equations and propagation in the structure. To obtain these electromagnetic parameters values suitable with the manufacturing technology, we use the same method as proposed in Ref. 3. We multiply the dispersion equation by μ_{xx} and our metamaterial is thus simply described by

$$\mu_{xx} = 1, \quad \mu_{yy} = \frac{1}{(\varepsilon_{xx})^2}, \quad \varepsilon_{zz} = 4(\varepsilon_{xx})^2, \quad \text{with } e = 15 \text{ cm and } L = 5 \text{ cm}. \tag{3}$$

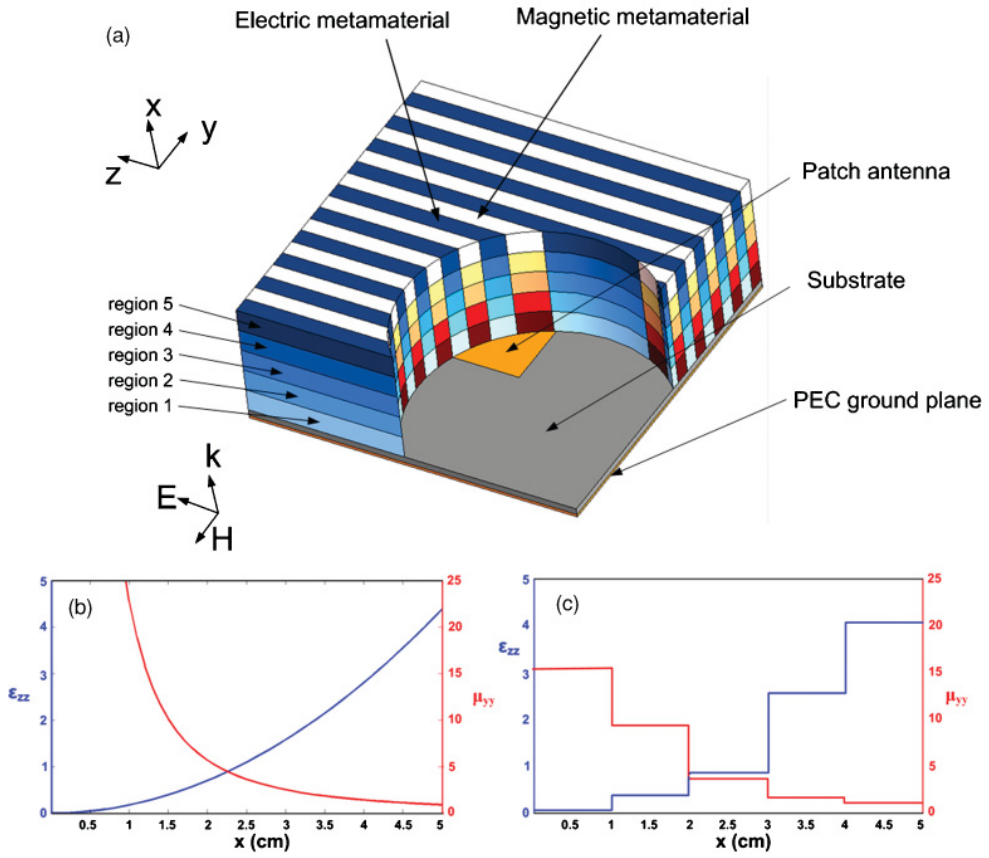

FIG. 2. (Color online) (a) Schematic structure of the proposed antenna with a cylindrical cut to show the internal structure of the material. The emitting source is a microstrip patch antenna on a dielectric substrate. The metamaterial is composed of alternating permittivity and permeability vertical layers. Each layer is made of five different material regions (pale color near the patch to dark color in the x direction). (b) Theoretical material parameters given by relation (3). (c) Discrete values of material parameters used in experimental realization.

The penalty of the above reduction is imperfect impedance matching at the outer boundary of our metamaterial that we can evaluate as $Z = \sqrt{\frac{\mu_{yy}}{\varepsilon_{zz}}}(x = L) = \frac{9}{2\pi^2}$. Thus the transmission at the outer boundary is calculated classically with $T = \frac{4Z}{(1+Z)^2} = 0.85$, which assures a high level of radiated electromagnetic field. Further simplification consists of discretizing the desired variation of the parameters μ_{yy} and ε_{zz} to secure a practical realization producing experimental performances close to theory.

Figure 2(a) shows the schematic structure of the directive emission antenna. A microstrip patch antenna on a dielectric substrate constitutes the radiating source. A surrounding material made of alternating electric metamaterial and magnetic metamaterial layers transforms the isotropic emission of the patch antenna into a directive one. The material is composed of five different regions where permittivity and permeability vary according to the profile of Fig. 2(c). The corresponding reduced magnetic and electric properties of the metamaterial obtained from transformation optics are presented in Figs. 2(b) and 2(c). The distribution of the theoretical material parameters satisfying relation (3) is shown in Fig. 2(b). The distribution in Fig. 2(c) presents the discrete values corresponding to the five regions of the metamaterial used for the experimental validation. To implement the material specifications in Eq. (3) using metamaterials, we must choose the overall dimensions, design the appropriate unit cells, and specify their layout. For our implementation, the metamaterial unit cell is not periodic. It is also advantageous to optimize the three design elements all at once since common parameters are shared. Equation (3) shows that the desired ultradirective emission will have constant μ_{xx}, with ε_{zz} and μ_{yy} varying longitudinally throughout the structure. The axial permittivity ε_{zz} and permeability μ_{yy} show, respectively, values ranging from 0.12 to 4.15 and from 1.58 to 15.3.

As shown by the schematic structure of the antenna in Fig. 2(a), a square copper patch is printed on a 0.787-mm-thick low-loss dielectric substrate (Rogers RT/Duroid 5870^{TM} with 17.5-μm copper cladding, $\varepsilon = 2.33$, and $\tan\delta = 0.0012$) and used as feeding source. The metamaterial covers completely the patch feeding source to capture the emanating isotropic radiation and transform it into a directive one. The metamaterial is a discrete structure composed of alternating layers with anisotropic permeability and permittivity. Figure 3 shows photography of our fabricated antenna device. We built the bulk metamaterial from 56 layers of dielectric boards

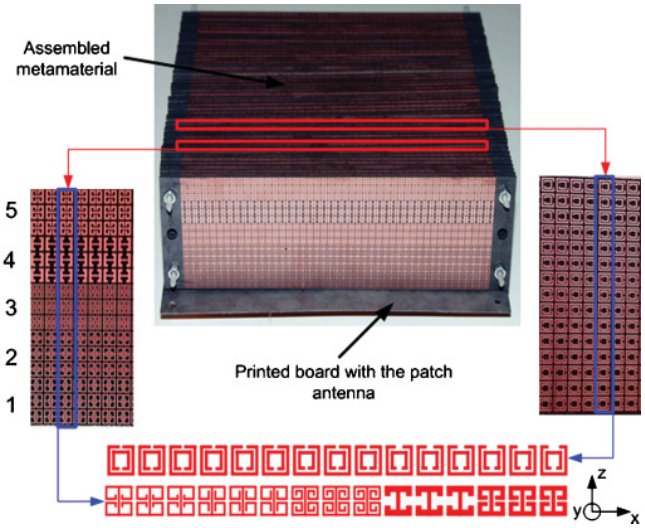

FIG. 3. (Color online) Structure of the antenna. Each magnetic and dielectric layer of the metamaterial is divided into five regions to assure the desired variations of electromagnetic parameters along wave propagation direction. The dimensions of the antenna are 15 × 15 × 5 cm. The operating frequency is 10.6 GHz. Left and right insets show details of the resonators used in the magnetic (right) and electric (left) metamaterial layers. Each level is made of three rows of identical resonators.

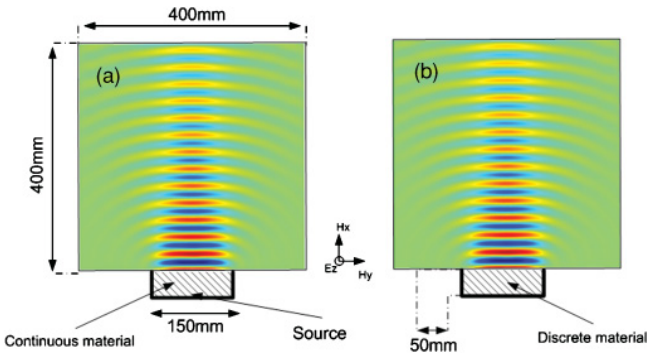

FIG. 4. (Color online) Full-wave finite element simulations of electric fields emitted by the metamaterial antenna. Calculations are performed using the continuous and discrete materials in a 2D configuration using a line source as excitation. (a) Continuous material. (b) Discrete material.

on which subwavelength resonant structures are printed. Twenty-eight layers contain artificial magnetic resonators and 28 contain electric ones. Each layer is made of five regions of metamaterials corresponding to the discretized values of Fig. 2(c). The layers are mounted 2 by 2 with a constant air spacing of 2.2 mm between each, in order to best represent the permeability and permittivity characteristics in the different regions. Overall dimensions of our antenna are 15 × 15 × 5 cm.

The details of the metamaterial cells are illustrated in Fig. 3. The left and right inserts show the designs of the resonators used in the magnetic (right) and electric (left) metamaterial layers. The layers are divided in five regions in the direction of wave propagation. Each region is composed of three rows of resonators with identical geometry and dimensions. Different resonators are used for electric and magnetic layers. Their schematic drawings are depicted at the bottom of Fig. 3.

The permeability (μ_{yy}) and permittivity (ε_{zz}) parameter sets plotted in Fig. 2(c) can be respectively achieved in a composite metamaterial containing Pendry's split-ring resonators (SRRs)[47] and Smith's electric LC resonators (ELCs),[48] known to provide, respectively, a magnetic response and an electric response that can be tailored (Fig. 3). Because of constraints of the layout, we chose a rectangular unit cell with dimensions $p_x = p_z = 10/3$ mm for both resonators. The layout consisted of five regions, each of which was three unit cells long (10 mm). We were able to obtain the desired ε_{zz} and μ_{yy} by tuning the resonators' geometric parameters as illustrated in the supplemental material.[50] Using Ansoft's HFSS commercial full-wave finite-element simulation software, we performed a series of scattering (S) parameter simulations for the SRR and ELC unit cells separately over a discrete set of the geometric parameters covering the range of interest. A normal incident wave impinging on the unit cell is considered for simulations. Electric and magnetic symmetry planes are applied on the unit cell respectively for the faces normal to the electric and magnetic field vector. By calculating the unit cells separately, we therefore assume very low coupling between neighboring ELCs and SRRs. The influence of this coupling is even lower when we consider mounting the electric and magnetic layers 2 by 2. A standard retrieval procedure[49] was then performed to obtain the effective material properties ε_{zz} and μ_{yy} from the S parameters. The discrete set of simulations and extractions was interpolated to obtain the particular values of the geometric parameters that yielded the desired material properties plotted in Fig. 2(c). Simulations were also realized under COMSOL MULTIPHYSICS to assure the functionality of our metamaterial. We chose an operating frequency around 10 GHz, which yields a reasonable effective medium parameter $\lambda/p_x > 10$, where λ is the free space wavelength.

In the designs presented in Figs. 2 and 3, we make use of SRRs and ELCs to realize the continuous-material properties required by the directive antenna. To illustrate the equivalence between continuous materials and actual combination of SRR and ELC metamaterials, we simulated the ideal antenna composed of continuous materials and the experimental antenna composed of SRRs and ELCs metamaterials simultaneously and we compared their electromagnetic properties. However, full-wave simulation of the experimental antenna is impossible using current computer resources owing to the extremely large memory and computing time required. Instead, full-wave simulations were done using the equivalent discrete material having parameters shown in Fig 2(c). The full-wave simulations have been performed using finite-element method based commercial software COMSOL MULTIPHYSICS. Also, the simulations have been made in a two-dimensional (2D) configuration using RF module in a transverse electric wave propagation mode. A surface current having similar dimension as the patch feed is used to model the source. The diagram pattern of our antenna is plotted by inserting match

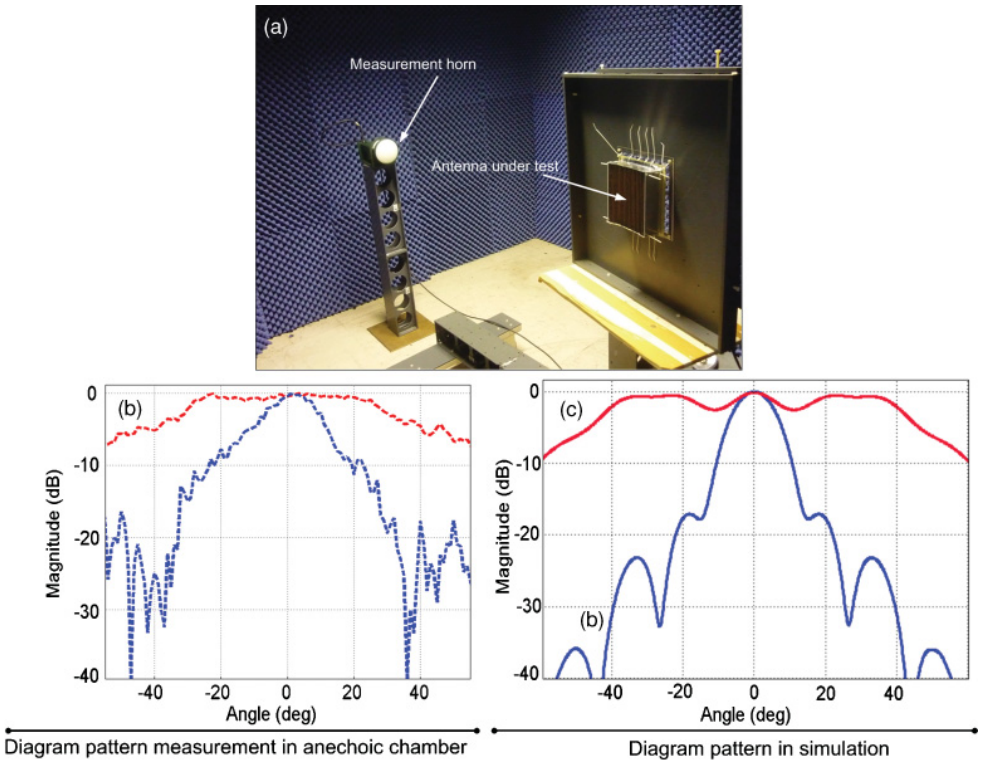

FIG. 5. (Color online) Far-field measurement in a fully anechoic chamber. (a) Experimental setup system. (b) Measurements. (c) Simulations. Radiation patterns of the metamaterial antenna (blue lower trace) and of the feeding microstrip patch antenna alone (red upper trace) are presented at 10.6 GHz.

boundaries with far-field conditions. For the metamaterial, values of permittivity and permeability show in Fig. 2 have been introduced in each of the five layers. Figure 4 shows simulation results of the electric field emanating from the antenna in the continuous and discrete material cases. Excellent qualitative agreement is observed from the simulations, indicating that the SRRs-ELCs combination present nearly the same electromagnetic parameters as the continuous material. As it can observed the intensity of emitted radiation decreases rapidly since the source transformation operates only in the *x*-*y* plane.

II. EXPERIMENTAL SETUPS AND DEMONSTRATION OF ULTRADIRECTIVE

To validate the directive emission device performances, two experiment systems are set up to measure the radiated field. The first method consists of measuring the far-field radiation patterns of the antenna in a fully anechoic chamber. Figure 5(a) shows the far-field measurement system. In such an emission-reception setup, the fabricated metamaterial antenna is used as the emitter and a wideband (2–18 GHz) dual polarized horn antenna is used as the receiver to measure the radiated power level of the emitter. The measurements are done for computer-controlled elevation angle varying from –90° to +90°. The microwave source is a vector network analyzer (Agilent 8722 ES) that we also use for detection. The feeding port is connected to the metamaterial antenna by means of a coaxial cable, whereas the detecting port is connected to the horn antenna also by means of a coaxial cable. The measured far-field radiation pattern in the *E* plane (plane containing the $\boldsymbol{E}$ and $\boldsymbol{k}$ vectors) is presented in Fig. 5(b).

The antenna presents maximum radiated power at 10.6 GHz with a directive main beam and low parasitic secondary lobes, under –15 dB. The main lobe presents 13° half-power beamwidth in the *E* plane (*x*-*y* plane). This narrow beamwidth is less than that of a parabolic reflector antenna having similar dimensions (diameter equal to 15 cm), where the half power beamwidth is around 16°. Measurements are found to be consistent with the predicted radiation patterns shown in Fig. 5(c).

The second experimental setup [Fig. 6(a)] was intended to scan the antenna's near-field microwave radiation. The *E* field is scanned by a field-sensing monopole probe connected to the network analyzer by a coaxial cable. The probe was mounted on two orthogonal linear translation stages (computer-controlled Newport MM4006), so that the probe could be translated with respect to the radiation region of the antenna. By stepping the field sensor in small increments and recording the field amplitude and phase at every step, a full 2D spatial field map of the microwave near-field pattern could be acquired in the free-space radiation region. The total scanning area covers 400 × 400 mm^2 with a step resolution of 2 mm in lateral dimensions shown by red arrows in Fig. 6(a). Microwave absorbers are applied around the measurement stage in order to suppress undesired scattered radiations at the boundaries.

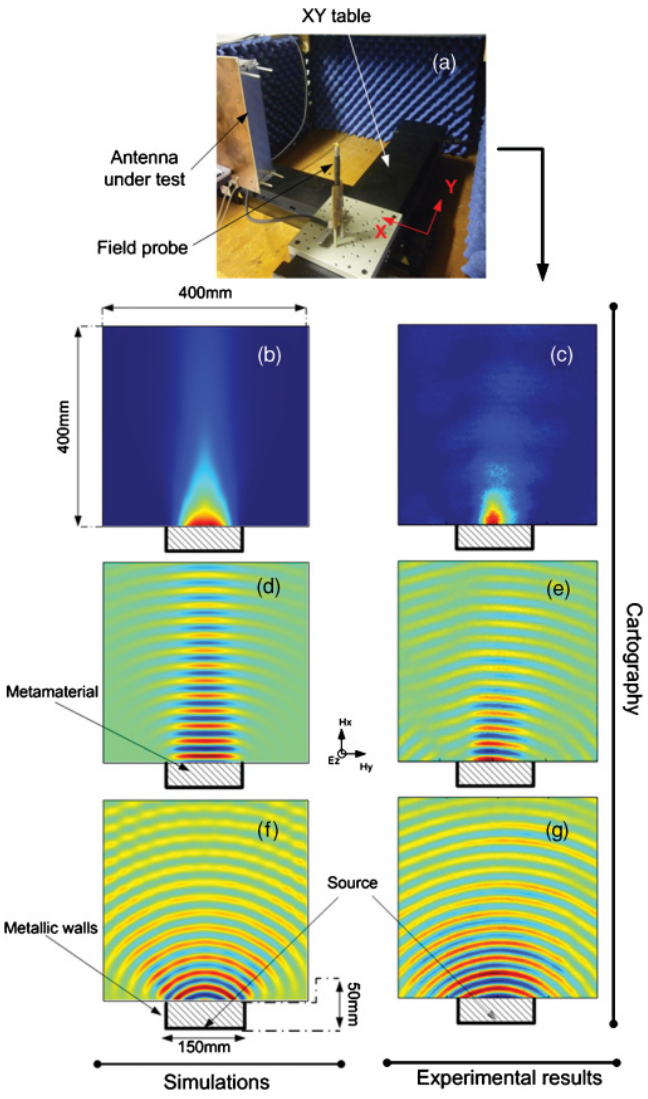

FIG. 6. (Color online) Near-field scanning experiment in comparison with simulations. (a) Experimental setup. (b) Magnitude of the predicted Poynting vector. (c) Magnitude of the experimental Poynting vector. (d) Magnitude of the predicted near field. (e) Mapping of the near field. (f) Magnitude of the excitation source's predicted near field. (g) Mapping of the excitation source's near field. The mappings are shown at 10.6 GHz.

Figure 6 shows the comparison between simulations and experimental results. In Fig. 6(b), the magnitude of the numerical Poynting vector interpreted as an energy flux for the electromagnetic radiation is plotted for the device and compared to measurements in Fig. 6(c). As stated earlier, the emission decreases rapidly since only the *x*-*y* plane has been considered for the source transformation procedure. A clear directive emission is radiated by the antenna as presented by the numerical simulation in Fig. 6(d) and measurement presented in Fig. 6(e) for the electric near field mapping of the antenna's radiation. Also, when compared to the radiation of the patch feed alone shown in Figs. 6(f) and 6(g), we can note of the narrow beam profile of our proposed device.

III. CONCLUSION

In summary, we designed, fabricated, and measured a metamaterial-based ultradirective emission by using the transformation optics approach in the microwave frequency regime. The device is engineered by transforming an isotropic source radiating in a cylindrical space to a directive one radiating in a rectangular space. It is composed of a feeding source covered by an anisotropic composite metamaterial cover. Both electric and magnetic parameters of this metamaterial are finely adjusted to correspond to the calculated parameters given by the transformation. Full-wave simulation results showed that the SRRs-ELCs metamaterials present nearly the same electromagnetic properties as the theoretical continuous materials. As a consequence, the artificial metamaterials used in the experimental device do have the bulk material behaviors that are expected. Calculations and measurements have shown a directive emission making this antenna competitive with conventional parabolic reflector ones. Synthesizing transformation optics through metamaterials appears to be promising and essential in the near future to control emission in a wide range of telecommunication applications.

ACKNOWLEDGMENTS

The authors thank A. Degiron for fruitful discussions and his significant remarks on the manuscript.

[1]J. B. Pendry, D. Schurig, and D. R. Smith, Science **312**, 1780 (2006).
[2]U. Leonhardt, Science **312**, 1777 (2006).
[3]D. Schurig *et al.*, Science **314**, 977 (2006).
[4]B. Kante, D. Germain, and A. de Lustrac, Phys. Rev. B **80**, 201104(R) (2009).
[5]R. Liu *et al.*, Science **323**, 366 (2009).
[6]J. Valentine, J. Li, T. Zentgraf, G. Bartal, and X. Zhang, Nat. Mater. **8**, 568 (2009).
[7]L. H. Gabrielli, J. Cardenas, C. B. Poitras, and M. Lipson, Nat. Photon. **3**, 461 (2009).
[8]H. Chen, C. T. Chan, and P. Sheng, Nat. Mater. **9**, 387 (2010).
[9]M. Rahm *et al.*, Photon. Nanostruct.: Fundam. Appl. **6**, 87 (2008).
[10]A. Greenleaf, Y. Kurylev, M. Lassas, and G. Uhlmann, Phys. Rev. Lett. **99**, 183901 (2007).
[11]M. Rahm, D. A. Roberts, J. B. Pendry, and D. R. Smith, Opt. Express **16**, 11555 (2008).
[12]M. Rahm, S. A. Cummer, D. Schurig, J. B. Pendry and D. R. Smith, Phys. Rev. Lett. **100**, 063903 (2008).
[13]L. Lin, W. Wang, J. Cui, C. Du and X. Luo, Opt. Express **16**, 6815 (2008).

[14]J. Huangfu *et al*., J. Appl. Phys. **104**, 014502 (2008).
[15]P. -H. Tichit, S. N. Burokur, and A. de Lustrac, Opt. Express **18**, 767 (2010).
[16]F. Kong, B. Wu, J. A. Kong, J. H. Huangfu, and S. Xi, Appl. Phys. Lett. **91**, 253509 (2007).
[17]H. Chen, B. Hou, S. Chen, X. Ao, W. Wen, and C. T. Chan, Phys. Rev. Lett. **102,** 183903 (2009).
[18]Y. G. Ma, C. K. Ong, T. Tyc, and U. Leonhardt, Nat. Mater. **8**, 639 (2009).
[19]N. Kundtz and D. R. Smith, Nat. Mater. **9**, 129 (2010).
[20]I. Y. Tamm, J. Russ. Phys. Chem. Soc. **56**, 248 (1924).
[21]J. Plebanski, Phys. Rev. **118**, 1396 (1960).
[22]D. Schurig, J. B. Pendry, and D. R. Smith, Opt. Express **14**, 9794 (2006).
[23]N. I. Landy and W. J. Padilla, Opt Exp. **17**, 14872 (2009).
[24]J. P. Turpin, A. T. Massoud, Z. H. Jiang, P. L. Werner, and D. H. Werner, Opt. Express **18**, 244 (2009).
[25]M. Schmiele, V. S. Varma, C. Rockstuhl, and F. Lederer, Phys. Rev. A **81**, 033837 (2010).
[26]T. Han and C. W. Qiu, Opt. Express **18**, 13038 (2010).
[27]J. Li and J. B. Pendry, Phys. Rev. Lett. **101**, 203901 (2008).
[28]T. Ergin, N. Stenger, P. Brenner, J. B. Pendry, and M. Wegener, Science **328**, 337 (2010).
[29]Z. Chan, X. Zhou, J. Hu, and G. Hu, Opt. Express **18**, 6089 (2010).
[30]U. Leonhardt and T. G. Philbin, Prog. Opt. **53**, 69 (2009).
[31]L. Bergamin, Phys. Rev. A **78**, 043825 (2008).
[32]U. Leonhardt and T. G. Philbin, New J. Phys. **8,** 247 (2006).
[33]R. T. Thompson, S. A. Cummer, and J. Frauendiener, J. Opt. **13**, 024008 (2001).
[34]D. A. Genov, S. Zhang, and X. Zhang, Nat. Phys. **5,** 687 (2009).
[35]E. E. Narimanov and A. V. Kildishev, Appl. Phys. Lett. **95,** 041106 (2009).
[36]Q. Cheng and T. J. Cui, e-print arXiv:0910.2159 (to be published).
[37]D. A. Roberts *et al.,* Appl. Phys. Lett. **93,** 251111 (2008).
[38]T. R. Zhai *et al.,* Opt. Express **17,** 17206 (2009).
[39]W. X. Jiang *et al.,* Appl. Phys. Lett. **92,** 261903 (2008).
[40]N. Kundtz, D. A. Roberts, J. Allen, S. A. Cummer, and D. R. Smith, Opt. Express **16**, 21215 (2008).
[41]Y. Luo, J. Zhang, L. Ran, H. Chen, and J. A. Kong, PIERS Online **4**, 795 (2008).
[42]J. Allen, N. Kundtz, D. A. Roberts, S. A. Cummer, and D. R. Smith, Appl. Phys. Lett. **94**, 194101 (2009).
[43]B. I. Popa, J. Allen, and S. A. Cummer, Appl. Phys. Lett. **94**, 244102 (2009).
[44]P.-H. Tichit, S. N. Burokur, and A. de Lustrac, J. Appl. Phys. **105**, 104912 (2009).
[45]S. Enoch, G. Tayeb, P. Sabouroux, N. Guérin, and P. A. Vincent, Phys. Rev. Lett. **89**, 213902 (2002).
[46]A. Ourir, A. de Lustrac, and J.-M. Lourtioz, Appl. Phys. Lett. **88**, 084103 (2006).
[47]J. B. Pendry, A. J. Holden, D. J. Robbins, and W. J. Stewart, IEEE Trans. Microwave Theory Tech. **47**, 2075 (1999).
[48]D. Schurig, J. J. Mock, and D. R. Smith, Appl. Phys. Lett. **88**, 041109 (2006).
[49]A. M. Nicholson and G. F. Ross, IEEE Trans. Instrum. Meas. **19**, 377 (1970).
[50]See supplemental meterial at [http://link.aps.org/supplemental/10.1103/PhysRevB.83.155108] for on illustration of the resonators' geometric parameters.

Annexe 3.4

P.-H. Tichit, S. N. Burokur, A. de Lustrac

« Transformation media producing quasi-perfect isotropic emission »

Optics Express, vol. 19, no. 21, pp. 20551-20556, October 2011

Transformation media producing quasi-perfect isotropic emission

Paul-Henri Tichit,[1] Shah Nawaz Burokur,[2] and André de Lustrac[1,*]

[1]*IEF, Univ. Paris-Sud, CNRS, UMR 8622, 91405 Orsay Cedex, France*
[2]*LEME, EA 4416, Univ. Paris-Ouest, 92410 Ville d'Avray, France*
[*]*andre.de-lustrac@u-psud.fr*

Abstract: Using the idea of wave manipulation via transformation optics, we propose a way to create a quasi-perfect isotropic emission from a directional one. The manipulation is enabled by composite metamaterials that correspond to a space stretching around the source. It is shown that the directive radiation of a plane source larger than the operating wavelength can be transformed into an isotropic one by modifying the electromagnetic properties of the space around it. A set of parameters allowing practical realization of the proposed device is defined. Numerical simulations using Finite Element Method (FEM) are performed to illustrate the proposed coordinate transformation. This idea, which consists in strongly reducing the apparent size of a radiating source, can find various applications in novel antenna design techniques.

OCIS codes: (260.2065) Effective medium theory; (260.2110) Electromagnetic optics; (260.2710) Inhomogeneous optical media; (160.1190) Anisotropic optical materials; (160.3918) Metamaterials.

References and links

1. J. B. Pendry, D. Schurig, and D. R. Smith, "Controlling electromagnetic fields," Science **312**(5781), 1780–1782 (2006).
2. U. Leonhardt, "Optical conformal mapping," Science **312**(5781), 1777–1780 (2006).
3. D. Schurig, J. J. Mock, B. J. Justice, S. A. Cummer, J. B. Pendry, A. F. Starr, and D. R. Smith, "Metamaterial electromagnetic cloak at microwave frequencies," Science **314**(5801), 977–980 (2006).
4. R. Liu, C. Ji, J. J. Mock, J. Y. Chin, T. J. Cui, and D. R. Smith, "Broadband ground-plane cloak," Science **323**(5912), 366–369 (2009).
5. B. Kanté, D. Germain, and A. de Lustrac, "Experimental demonstration of non-magnetic metamaterial cloak at microwave frequencies," Phys. Rev. B **80**(20), 201104 (2009).
6. W. Cai, U. K. Chettiar, A. V. Kildishev, and V. M. Shalaev, "Optical cloaking with metamaterials," Nat. Photonics **1**(4), 224–227 (2007).
7. J. Valentine, J. Li, T. Zentgraf, G. Bartal, and X. Zhang, "An optical cloak made of dielectrics," Nat. Mater. **8**(7), 568–571 (2009).
8. L. H. Gabrielli, J. Cardenas, C. B. Poitras, and M. Lipson, "Silicon nanostructure cloak operating at optical frequencies," Nat. Photonics **3**(8), 461–463 (2009).
9. M. Rahm, D. Schurig, D. A. Roberts, S. A. Cummer, D. R. Smith, and J. B. Pendry, "Design of electromagnetic cloaks and concentrators using form-invariant coordinate transformations of Maxwell's equations," Photonics Nanostruct. Fundam. Appl. **6**(1), 87–95 (2008).
10. H. Chen, B. Hou, S. Chen, X. Ao, W. Wen, and C. T. Chan, "Design and experimental realization of a broadband transformation media field rotator at microwave frequencies," Phys. Rev. Lett. **102**(18), 183903 (2009).
11. A. Greenleaf, Y. Kurylev, M. Lassas, and G. Uhlmann, "Electromagnetic wormholes and virtual magnetic monopoles from metamaterials," Phys. Rev. Lett. **99**(18), 183901 (2007).
12. M. Rahm, D. A. Roberts, J. B. Pendry, and D. R. Smith, "Transformation-optical design of adaptive beam bends and beam expanders," Opt. Express **16**(15), 11555–11567 (2008).
13. M. Rahm, S. A. Cummer, D. Schurig, J. B. Pendry, and D. R. Smith, "Optical design of reflectionless complex media by finite embedded coordinate transformations," Phys. Rev. Lett. **100**(6), 063903 (2008).
14. L. Lin, W. Wang, J. Cui, C. Du, and X. Luo, "Design of electromagnetic refractor and phase transformer using coordinate transformation theory," Opt. Express **16**(10), 6815–6821 (2008).
15. J. Huangfu, S. Xi, F. Kong, J. Zhang, H. Chen, D. Wang, B.-I. Wu, L. Ran, and J. A. Kong, "Application of coordinate transformation in bent waveguide," J. Appl. Phys. **104**(1), 014502 (2008).
16. P.-H. Tichit, S. N. Burokur, and A. de Lustrac, "Waveguide taper engineering using coordinate transformation technology," Opt. Express **18**(2), 767–772 (2010).

#151938 - $15.00 USD Received 1 Aug 2011; revised 9 Sep 2011; accepted 9 Sep 2011; published 3 Oct 2011

17. W. X. Jiang, T. J. Cui, H. F. Ma, X. M. Yang, and Q. Cheng, "Layered high-gain lens antennas via discrete optical transformation," Appl. Phys. Lett. **93**(22), 221906 (2008).
18. Z. L. Mei, J. Bai, T. M. Niu, and T. J. Cui, "A planar focusing antenna design using quasi-conformal mapping," PIER **13**, 261–273 (2010).
19. Y. G. Ma, C. K. Ong, T. Tyc, and U. Leonhardt, "An omnidirectional retroreflector based on the transmutation of dielectric singularities," Nat. Mater. **8**(8), 639–642 (2009).
20. T. Tyc and U. Leonhardt, "Transmutation of singularities in optical instruments," N. J. Phys. **10**(11), 115038 (2008).
21. N. Kundtz and D. R. Smith, "Extreme-angle broadband metamaterial lens," Nat. Mater. **9**(2), 129–132 (2010).
22. H. F. Ma and T. J. Cui, "Three-dimensional broadband ground-plane cloak made of metamaterials," Nat Commun **1**(3), 1–6 (2010).
23. Y. Luo, J. Zhang, L. Ran, H. Chen, and J. A. Kong, "Controlling the emission of electromagnetic source," PIERS **4**(7), 795–800 (2008).
24. J. Allen, N. Kundtz, D. A. Roberts, S. A. Cummer, and D. R. Smith, "Electromagnetic source transformations using superellipse equations," Appl. Phys. Lett. **94**(19), 194101 (2009).
25. B. I. Popa, J. Allen, and S. A. Cummer, "Conformal array design with transformation electromagnetics," Appl. Phys. Lett. **94**(24), 244102 (2009).
26. P.-H. Tichit, S. N. Burokur, and A. de Lustrac, "Ultradirective antenna via transformation optics," J. Appl. Phys. **105**(10), 104912 (2009).
27. P.-H. Tichit, S. N. Burokur, D. Germain, and A. de Lustrac, "Design and experimental demonstration of a high-directive emission with transformation optics," Phys. Rev. B **83**(15), 155108 (2011).
28. P.-H. Tichit, S. N. Burokur, D. Germain, and A. de Lustrac, "Coordinate transformation based ultra-directive emission," Electron. Lett. **47**(10), 580–582 (2011).
29. U. Leonhardt and T. G. Philbin, "Transformation optics and the geometry of light," Prog. Opt. **53**, 69–152 (2009).
30. Comsol MULTIPHYSICS Modeling, (*http://www.comsol.com*).

1. Introduction

Transformation optics is a mathematical tool that consists in generating a new transformed space from an initial one where solutions of Maxwell's equations are known. As in general relativity, the first step is to imagine a virtual space with the desired topological properties, which will contain the underlying physics. This approach has been revived when J. B. Pendry *et al.* [1] have proposed an interpretation where permeability and permittivity tensors components can be viewed as a material in the original space. It is as if the new material mimicks the defined topological space. Since this pioneering work of J. B. Pendry and that of U. Leonhardt *et al.* [2], transformation optics is an emerging field where Maxwell's equations are form invariant under a coordinate transformation. It offers an unconventional strategy to the design of novel class metamaterial devices. The most intriguing application conceived remains the invisibility cloak whose designs have been presented in microwave [3–5] and optical regimes [6–8]. Other interesting wave manipulation applications such as concentrators [9], rotators [10], wormholes [11], waveguide transitions and bends [12–16] have also been proposed. Concerning antenna applications, focusing lens antennas have been theoretically designed [17,18]. The performances of an omnidirectional retroreflector [19] based on the transmutation of singularities [20] and Luneberg lenses [21,22] have been experimentally demonstrated. Recently, techniques of source transformation [23–28] have offered new opportunities for the design of active devices with source distribution included in the transformed space. Using this last approach, we have designed an ultra-directive emission by stretching a source into an extended coherent radiator [26–28].

2. Transformation formulations

It is our aim in this present work to demonstrate a quasi-perfect isotropic emission from a plane source presenting a directive emission by manipulating the apparent size of the latter source. Such an antenna can be very important in communication systems since it allows designing a reference antenna for measurement setups. To do so, we define a transformation which stretches exponentially the area where the source is located. The wavelength will then be much larger in the vicinity of the source, which makes the latter appear much smaller from outside. To our knowledge, exponential transformation has not been developed in literature. The theoretical analysis devoted to this coordinate transformation is presented and numerical simulations are performed using finite element method to validate the proposed concept.

#151938 - $15.00 USD Received 1 Aug 2011; revised 9 Sep 2011; accepted 9 Sep 2011; published 3 Oct 2011

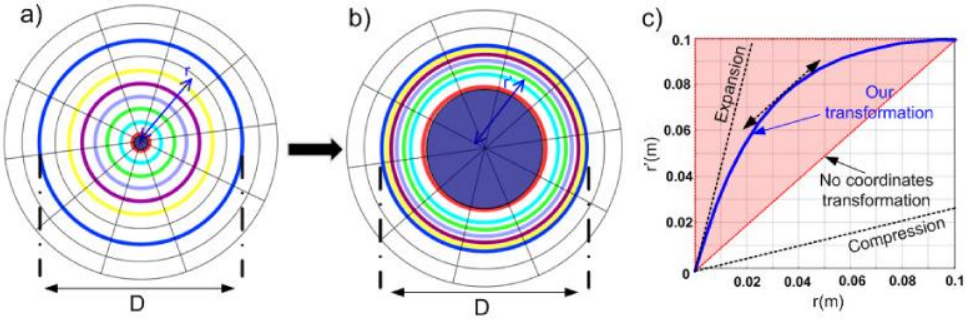

Fig. 1. Space stretching coordinate transformation: (a) the initial space (r, θ, z) is bounded by the blue circle; (b) the transformed space (r', θ', z') is formed by an expansion of the central zone defined by the red circle and a compression of the annular region between the red and blue circles; (c) working principle of the transformation.

In this study, we will focus our attention on the transformation of radiating sources and our plan will be to show how coordinate transformation can be applied to transform directive emissions into isotropic ones. We will start from the basic transformation media approach. An intuitive schematic principle to illustrate the proposed method is presented in Fig. 1. Let us consider a source radiating in a circular space as shown in Fig. 1(a) and a circular region bounded by the blue circle around this source limits the radiation zone. The "space stretching" coordinate transformation consists in stretching exponentially the central zone of this delimited circular region represented by the red circle as illustrated in Fig. 1(b). The expansion procedure is further followed by a compression of the annular region formed between the red and blue circles so as to secure a good impedance matching with free space. Figure 1(c) summarizes the exponential form of our coordinate transformation. The diameter of the transformed, which will be the generated metamaterial circular medium is noted *D*. Mathematically this transformation is expressed as:

$$\begin{cases} r' = \alpha(1-e^{qr}) \\ \theta' = \theta \\ z' = z \end{cases} \quad \text{with} \quad \alpha = \frac{D}{2}\frac{1}{1-e^{\frac{qD}{2}}} \tag{1}$$

where *r'*, *θ'*, and *z'* are the coordinates in the transformed cylindrical space, and *r*, *θ* and *z* are those in the initial cylindrical space. In the initial space, we assume free space, with isotropic permittivity and permeability tensors ε_0 and μ_0. It can be noted that only parameter *q* appears in Eq. (1). *q* (in m^{-1}) must be negative in order to secure the impedance matching condition. This parameter is an expansion factor which can be physically viewed as to what extent space is expanded. A high (negative) value of *q* means a high expansion whereas a low (negative) value of *q* means a nearly zero expansion. The new material can then be described by permeability and permittivity tensors:

$$\overline{\overline{\varepsilon}} = \psi\varepsilon_0 \quad \text{and} \quad \overline{\overline{\mu}} = \psi\mu_0 \quad \text{with} \quad \psi^{i'j'} = \frac{J_i^{i'}J_j^{j'}\delta^{ij}}{\det(J)} \tag{2}$$

where $J_{\alpha}^{\alpha'} = \frac{\partial x'^{\alpha}}{\partial x^{\alpha}}$ represents the Jacobian transformation matrix of Eq. (1) and δ^{ij} is the Kronecker symbol. Both electromagnetic parameters ε and μ have the same behavior, allowing an impedance matching with vacuum outside the transformed space. The inverse transformation is obtained from the initial transformation of Eq. (1) and derived by a substitution method, enabling the circular metamaterial design which leads to anisotropic

#151938 - $15.00 USD Received 1 Aug 2011; revised 9 Sep 2011; accepted 9 Sep 2011; published 3 Oct 2011

permittivity and permeability tensors. More details on similar calculations can be found in [29].

By substituting the new coordinate system in the tensor components, and after some simplifications, the material parameters are derived. Calculations lead to permeability and permittivity tensors given in the diagonal base by:

$$\overline{\overline{\psi}} = \begin{pmatrix} \psi_{rr} & 0 & 0 \\ 0 & \psi_{\theta\theta} & 0 \\ 0 & 0 & \psi_{zz} \end{pmatrix} = \begin{pmatrix} \dfrac{qr(r'-\alpha)}{r'} & 0 & 0 \\ 0 & \dfrac{r'}{qr(r'-\alpha)} & 0 \\ 0 & 0 & \dfrac{r}{r'q(r'-\alpha)} \end{pmatrix} \quad \text{with} \quad r = \frac{\ln\left(1-\dfrac{r'}{\alpha}\right)}{q} \quad (3)$$

The components in the Cartesian coordinate system are calculated and are as follows:

$$\begin{cases} \psi_{xx} = \psi_{rr}\cos^2(\theta) + \psi_{\theta\theta}\sin^2(\theta) \\ \psi_{xy} = \psi_{yx} = (\psi_{rr} - \psi_{\theta\theta})\sin(\theta)\cos(\theta) \\ \psi_{yy} = \psi_{rr}\sin^2(\theta) + \psi_{\theta\theta}\cos^2(\theta) \end{cases} \quad (4)$$

The ε and μ tensors components present the same behavior as given in Eq. (4).

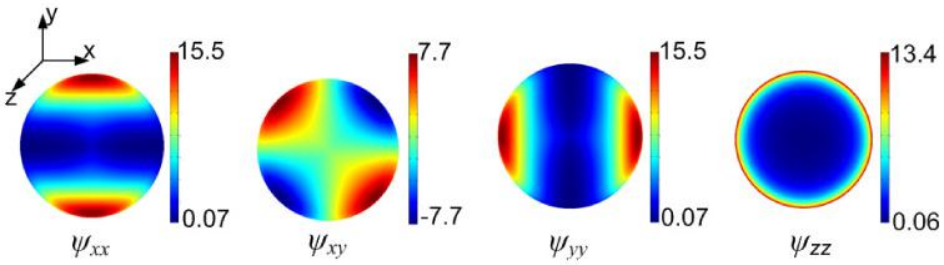

Fig. 2. Variation in the permeability and permittivity tensor components of the transformed space for D = 20 cm and q = –40 m^{-1}.

Figure 2 shows the variation of the permittivity and permeability tensor components in the new generated transformed space. The geometrical dimension D is chosen to be 20 cm and parameter q is fixed to –40 m^{-1}. It can be noted that components ψ_{xx}, ψ_{yy} and ψ_{zz} present variations and an extremum, that are simple to realize with commonly used metamaterials by reducing their inhomogeneous dependence [27]. At the center of the transformed space, ε and μ present very low values (<< 1). Consequently, light velocity and the corresponding wavelength are much higher than in vacuum. The width of the plane source then appears very small compared to wavelength and the source can then be regarded as a radiating wire, which is in fact an isotropic source. The merit of this transformation depends effectively on the expansion factor q value and more generally, it can be applied to a wide range of electromagnetic objects, where the effective size can be reduced compared to a given wavelength.

By fixing the electric field directed along the z-axis and by adjusting the dispersion equation without changing propagation in the structure, the following reduced parameters can be obtained [3]:

#151938 - $15.00 USD Received 1 Aug 2011; revised 9 Sep 2011; accepted 9 Sep 2011; published 3 Oct 2011

$$\begin{cases} \mu_{rr} = 1 \\ \mu_{\theta\theta} = \left(\dfrac{r'}{qr(r'-\alpha)} \right)^2 \\ \varepsilon_{zz} = \left(\dfrac{r}{r'} \right)^2 \end{cases} \tag{5}$$

In Eq. (5), the parameters present positive values which can be easily achieved firstly by discretizing their continuous profile and secondly by using metamaterial resonators where magnetic and electric responses can be tailored and controlled. Such control has been lately performed in [27] with a 200 MHz bandwidth at 10 GHz. A possible prototype of our proposed device is presented in Fig. 3 where permeability and permittivity metamaterial layers are used to assure both $\mu_{\theta\theta}$ and ε_{zz} gradient.

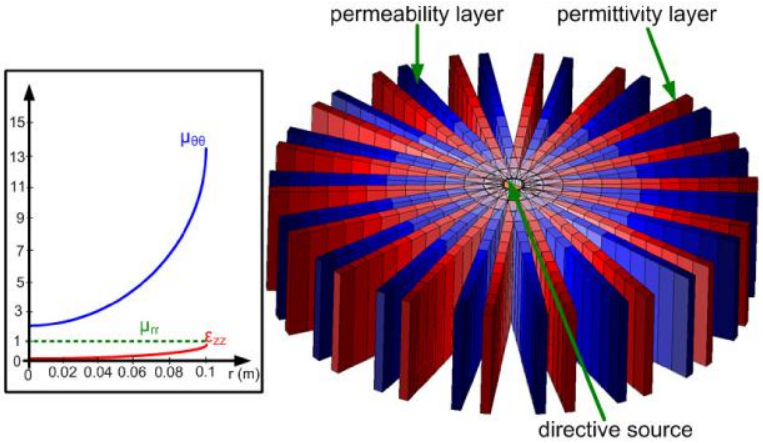

Fig. 3. Schematic of a possible prototype with tailored permittivity and permeability values in a cylindrical configuration.

3. Simulation and results

The theoretical underlying physics of a "space stretching" coordinate transformation involved in this present study having been described, numerical verifications of the method using FEM based commercial solver Comsol Multiphysics [30] are performed to design and characterize the transformed quasi-isotropic emission. A plane current source is used as excitation to validate the concept.

Figure 4 presents simulations results of the source radiating in the initial circular space at an operating frequency of 4 GHz. The current direction of the source is supposed to be along the *z*-axis. Simulations are performed in a Transverse Electric (TE) mode with the electric field polarized along *z*-direction. The surface current source is considered to have a width of 10 cm, which is greater than the 7.5 cm wavelength at 4 GHz. Radiation boundary conditions are placed around the calculation domain in order to plot the radiation properties. Continuity of the field is assured in the interior boundaries. As shown in Fig. 4, different values for the expansion factor q are used in the simulations and as it can be observed, the emission becomes more and more isotropic as the q factor decreases from -5 m^{-1} to -40 m^{-1}. As stated previously and verified from the different electric field distribution patterns, a high negative value of q leads to a quasi-perfect isotropic emission since the space expansion is higher. In Fig. 4(e), we can note the far-field isotropic pattern of our device compared to the directive

#151938 - $15.00 USD Received 1 Aug 2011; revised 9 Sep 2011; accepted 9 Sep 2011; published 3 Oct 2011

source. Figure 4(f) gives an insight of the influence of the q parameter on the proposed coordinate transformation.

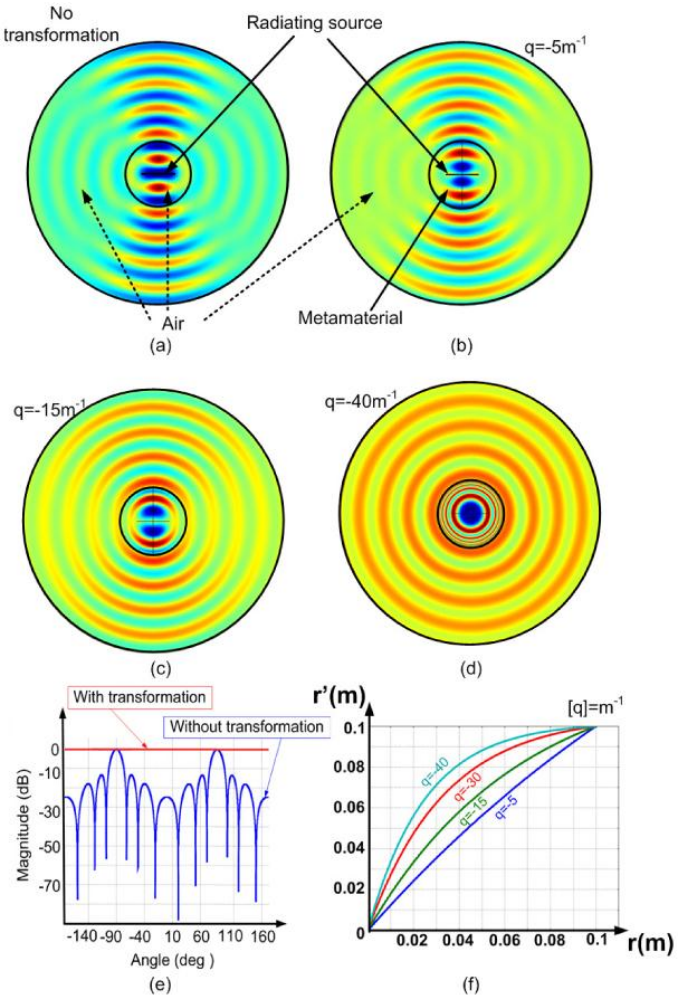

Fig. 4. Simulated electric field distribution for a TE wave polarization at 4 GHz: (a) current plane source used as excitation for the transformation. The current direction is perpendicular to the plane of the figure; [(b)-(d)] verification of the transformation for different values of expansion factor q; (e) Far field radiation pattern of the emission with (q=–40) and without transformation;(f) influence of the q parameter on the proposed coordinate transformation. The emitted radiation is more and more isotropic as q tends to high negative values.

4. Conclusion

In conclusion, using transformation optics, we have proposed a concept to manipulate electromagnetic waves and achieve a quasi-perfect isotropic emission from a directional source. The latter manipulation is enabled by using composite metamaterials corresponding to a space stretching around the source by coordinate transformation. Numerical verifications have been performed where the radiation of a plane source which is directive has been transformed into an isotropic emission by reducing the apparent size of this source. The proposed device can therefore be potentially useful in the reduction of an object's Radar Cross Section (RCS).

#151938 - $15.00 USD Received 1 Aug 2011; revised 9 Sep 2011; accepted 9 Sep 2011; published 3 Oct 2011

Annexe 3.5

X. Wu, P.-H. Tichit, S. N. Burokur, S. Kirouane, A. Sellier, A. de Lustrac

« Numerical and experimental demonstration of a coordinate transformation-based azimuthal directive emission »

Microwave and Optical Technology Letters, vol. 54, no. 11, pp. 2536-2540, November 2012

12. J. Asmussen and D.K. Reinhard, Diamond films handbook, Marcel Dekker, New York, 2002.
13. H. Angus Macleod. Thin-film optical filter, 4th ed., CRC Press, New York, 2010.

NUMERICAL AND EXPERIMENTAL DEMONSTRATION OF A COORDINATE TRANSFORMATION-BASED AZIMUTHAL DIRECTIVE EMISSION

Xinying Wu, Paul-Henri Tichit, Shah Nawaz Burokur, Souad Kirouane, Alexandre Sellier, and André de Lustrac
IEF, Univ. Paris-Sud, CNRS, UMR 8622, 91405 Orsay Cedex, France; Corresponding author: andre.de-lustrac@u-psud.fr

Received 22 January 2012

ABSTRACT: *This article deals with the modeling, practical implementation, and characterization of an azimuthal directive antenna around 10 GHz. The design of the antenna is based on transformation optics concept by transforming the radiation of a plane source into an azimuthal radiation. This coordinate transformation procedure is achieved by modifying the electromagnetic properties of the space around the plane source. Metamaterials presenting electric and magnetic resonances are used to produce the effective material parameters necessary for the transformation. S_{11} parameter and direct far-field measurements are performed on a fabricated prototype to experimentally demonstrate the narrow beam profile and the beam deflection.* © 2012 Wiley Periodicals, Inc. Microwave Opt Technol Lett 54:2536–2540, 2012; View this article online at wileyonlinelibrary.com. DOI 10.1002/mop.27122

Key words: *coordinate transformation; metamaterials; azimuthal; directive emission*

1. INTRODUCTION

Metamaterials are artificial materials typically fabricated via suitable periodic arrangement of microstructured metallic or dielectric inclusions. Because of their unusual electromagnetic properties [1], these microstructured metamaterials have made relevant a wide array of interesting applications. Metamaterials have been proposed for the design of directive antennas [2–4]. In Ref. 2, Enoch et al. proposed to use the refractive properties of a low optical index material interface to achieve the directive emission. Burokur et al. [3] also studied numerically the presence of a left-handed medium with simultaneous negative permittivity and permeability over a patch antenna where a gain enhancement of about 3 dB has been observed. In Ref. 4, Ourir et al. have shown the possibility of using a novel composite metamaterial surface as reflector in a Fabry–Perot cavity system to produce an ultrathin directive antenna. Recently, the concept of transformation optics [5, 6] has revived the interests for man-made metamaterials. As these pioneering works of Leonhardt [5] and that of Pendry [6], transformation optics is an emerging research field where Maxwell's equations are invariant under a coordinate transformation. It generates enormous interest as it offers an unconventional strategy for the design of novel class metamaterial devices. The most intriguing application conceived remains the invisibility cloak [7–9]. Other interesting wave manipulation applications such as waveguide transitions and bends have also been proposed [10–14]. For antenna applications, an omnidirectional retroreflector [15] and a Luneberg lens [16] have been experimentally demonstrated. New techniques of source transformation have offered new opportunities for the design of active devices with source distribution included in the transformed space. This approach has led us to design an ultradirective emission by stretching a source into an extended coherent radiator [17–19] and also a quasi-isotropic emission from a directive source by space expansion [20]. A lens capable of converting the radiation from an embedded isotropic source into multibeam emission has also been experimentally demonstrated [21].

In this letter, we present the design, implementation, and characterization of a metamaterial-based azimuthal directive antenna at 10 GHz using coordinate transformation concept. The latter concept is applied to transform the vertical radiation of a plane source into a directive azimuthal one. The theoretical analysis devoted to this coordinate transformation is presented and numerical simulations are performed using finite element method to confirm the proposed concept. A bulk metamaterial respecting constitutive electric permittivity and magnetic permeability parameters generated by the transformation is used to produce the azimuthal emission. Full-wave numerical simulations and experimental measurements are performed to show the performances of the proposed device. Good quantitative and qualitative agreements are found.

2. DESIGN CONCEPT

In our previous recent works, we have proposed a concept based on coordinate transformation to realize a directive emission from quasi-omnidirectional sources such as microstrip patch antennas or monopoles [17–19]. In this study, our plan is to show how these recent achievements can be extended to transform a broad angular radiation into an azimuthal directive emission. We will start from the basic transformation media approach. The schematic principle of the transformation illustrating the proposed method is presented in Figure 1.

Let us consider a source radiating in a rectangular space. This radiation emitted from the latter source can be transformed into an azimuthal one. The transformation procedure is noted $F(x',y')$ and consists in bending the emission. Figure 1 shows the working principle of this rotational coordinate transformation. Mathematically, $F(x',y')$ can be expressed as:

$$\begin{cases} x' = \text{axcos (by)} \\ y' = \text{axsin (by)} \\ z' = z \end{cases} \tag{1}$$

where x', y', and z' are the coordinates in the bent space, and x, y, and z are those in the initial rectangular space. In the initial space, we assume free space with isotropic permittivity and permeability tensors ε_0 and μ_0. L_2–L_1 and L are, respectively, the width and the length of the rectangular space. The rotational transformation of Figure 1 is defined by parameter a considered as an ''expansion'' parameter and parameter b which controls the rotation angle of the transformation $F(x',y')$.

The new material can then be described by permeability and permittivity tensors:

$$\overline{\overline{\varepsilon}} = \overline{\overline{\psi}}\varepsilon_0 \quad \text{and} \quad \overline{\overline{\mu}} = \overline{\overline{\psi}}\mu_0 \quad \text{with} \quad \psi^{i'j'} = \frac{J_i^{i'} J_j^{j'} \delta^{ij}}{\det(J)} \tag{2}$$

where $J_\alpha^{\alpha'} = \frac{\partial x'^{\alpha}}{\partial x^{\alpha}}$ represents the Jacobian transformation matrix of the transformations of Eq. (1) and δ^{ij} is the Kronecker symbol. Both electromagnetic parameters ε and μ have the same behavior, allowing an impedance matching with vacuum outside the

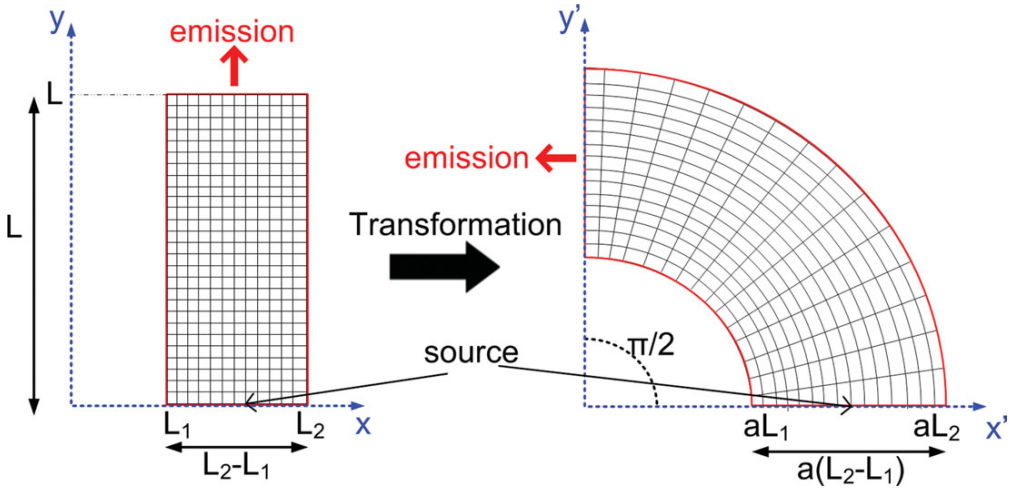

Figure 1 Schematic principle of the 2D rotational coordinate transformation. The emission in a rectangular space is transformed into an azimuthal one. [Color figure can be viewed in the online issue, which is available at wileyonlinelibrary.com]

transformed space. The inverse transformation is obtained from the initial transformation of Eq. (1) and derived by a substitution method, enabling the metamaterial design which leads generally to anisotropic permittivity and permeability tensors.

By substituting the new coordinate system in the tensor components, and after some simplifications, the material parameters are derived. Calculations lead to permeability and permittivity tensors given in the diagonal base by:

$$\overline{\overline{\Psi}} = \begin{pmatrix} \Psi_{xx} & \Psi_{xy} & 0 \\ \Psi_{yx} & \Psi_{yy} & 0 \\ 0 & 0 & \Psi_{zz} \end{pmatrix} \quad \text{with} \quad \begin{cases} \Psi_{xx} = \dfrac{a^2x'^2 + b^2y'^2r^2}{abr^3} \\ \Psi_{xy} = \Psi_{yx} = \dfrac{x'y'(a^2 - b^2r^2)}{abr^3} \\ \Psi_{yy} = \dfrac{a^2y'^2 + b^2x'^2r^2}{abr^3} \\ \Psi_{zz} = \dfrac{1}{abr} \end{cases} \tag{3}$$

Figure 2 shows the variation of the different components of the permeability and the permittivity tensor of the metamaterial structure. The geometrical dimensions are as follows: the width of the source is taken to be 5 cm, and the internal and external radius of the metamaterial structure is 5 and 10 cm, respectively. The working frequency is set to 10 GHz.

After diagonalization, we obtain a more simplified form the tensors:

$$\begin{aligned} \overline{\overline{\varepsilon}} &= \begin{pmatrix} \Psi_{rr} & 0 & 0 \\ 0 & \Psi_{\theta\theta} & 0 \\ 0 & 0 & \Psi_{zz} \end{pmatrix} \varepsilon_0 \ \overline{\overline{\mu}} \\ &= \begin{pmatrix} \Psi_{rr} & 0 & 0 \\ 0 & \Psi_{\theta\theta} & 0 \\ 0 & 0 & \Psi_{zz} \end{pmatrix} \mu_0 \quad \text{with} \quad \begin{cases} \Psi_{rr} = \frac{a}{br} \\ \Psi_{\theta\theta} = \frac{a}{b} r \\ \Psi_{zz} = \frac{1}{abr} \end{cases} \end{aligned} \tag{4}$$

3. NUMERICAL SIMULATIONS

The transformation formulation is implemented using finite-element method (FEM)-based commercial solver Comsol Multiphysics. Figure 3 shows the comparison of two-dimensional (2D) simulations between a plane source made of current lines in yz plane above a limited metallic ground plane [Fig. 3(a)] and the same source surrounded by a metamaterial defined by Eq. (4) [Fig. 3(b)]. Figures 3(c) and 3(d) show respectively the far field patterns of the plane source without and with the metamaterial structure. A finer lobe is observed when the current lines interact with the metamaterial. The left shift of the peak corresponds to a rotation of 76° of the emitted radiation. We shall note that this angular rotation is different from 90° due to the spatial shift of the radiated beam from the symmetry axis.

To have an idea of the expected results from a physically fabricated prototype, we first need to simplify the calculated material parameters through a parameter reduction procedure. We therefore fix a polarization of the electromagnetic field so that we suppose having the magnetic field along the z-direction. In this case, the relevant electromagnetic parameters are μ_{zz}, $\varepsilon_{\theta\theta}$, and ε_{rr}. Thus, we decide to maintain $\varepsilon_{\theta\theta}$ and μ_{zz} constant. Consequently, the new set of coordinates is:

$$\begin{cases} \varepsilon_{rr} = \left(\dfrac{1}{br}\right)^2 \div 1.7 \\ \varepsilon_{\theta\theta} = 2.8 \\ \mu_{zz} = 1.7 \end{cases} \tag{5}$$

The values of ε_{rr} and μ_{zz} have been chosen so that they can be easily achieved from metamaterials. $\varepsilon_{\theta\theta}$ is produced by a host medium, which is a commercially available resin. Physical parameter b allows an optimization of the material parameter ε_{rr}. Figure 4(a) presents the profile of the different material parameters resulting from an optimization for $b = 6$. Figures 4(b) and 4(c) show, respectively, the calculated normalized electric field distribution and the far field pattern where rotation of the beam can be observed.

The previous material obeying Eq. (5) presents a continuous variation in the radial permittivity. As it is not possible to achieve such continuity in practice, we propose to perform a discrete variation of ε_{rr}. Meta-atoms producing electric resonances are designed on the 0.787-mm thick low loss ($\tan\delta = 0.0013$) RO3003™ dielectric substrate to provide the material parameters. A realization of our proposed structure uses a lamellar composite material, as illustrated in Figure 5(a). The proposed structure is then composed of 30 identical layers where

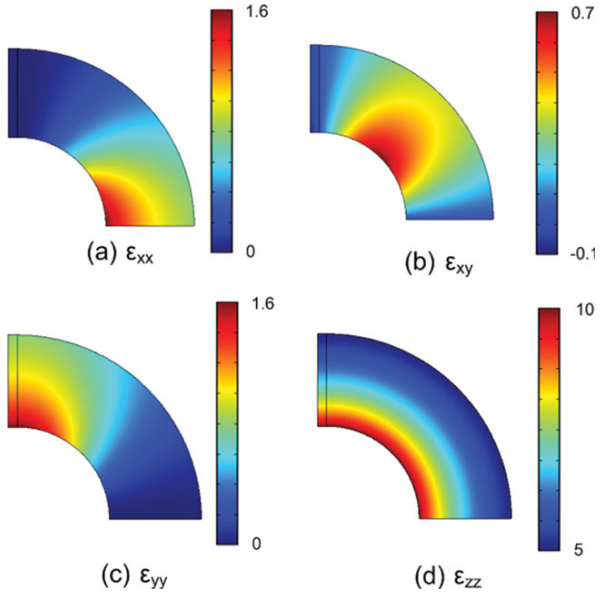

Figure 2 Variation of the permeability and permittivity tensor components: (a) μ_{xx}, (b) μ_{xy}, (c) μ_{yy}, (d) ε_{zz}. [Color figure can be viewed in the online issue, which is available at wileyonlinelibrary.com]

each layer [Fig. 5(b)] is divided in 10 unit cells. Because of constraints of the layout, we choose a rectangular unit cell with dimensions 5 mm for both resonators. We are able to obtain the desired ε_{zz} and μ_{yy} by tuning the resonators' geometric parameters. The 10 cells presented in Figure 5(c) are designed to constitute the discrete variation of ε_{rr}. Table 1 summarizes the corresponding electromagnetic parameters of the cells. The discrete

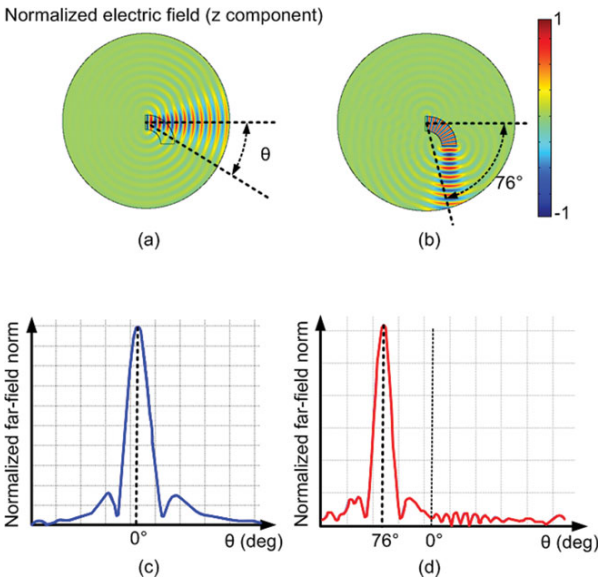

Figure 3 Calculated emission of a plane current source above a limited metallic ground plane (a) without and (b) with the metamaterial structure. Calculated normalized far field of the antenna (c) without and (d) with metamaterial. A 76° rotation of the radiation is clearly observed. [Color figure can be viewed in the online issue, which is available at wileyonlinelibrary.com]

metamaterial antenna simulated with HFSS from Ansys is presented in Figure 6(a).

For the numerical verification, a patch antenna presenting a quasi-omnidirectional radiation is used as the feeding source of the metamaterial antenna. Figure 6(b) shows the calculated magnetic field distribution. We shall note that the metamaterial structure first transforms the quasi-omnidirectional radiation of the patch source into a directive one.

4. EXPERIMENTAL MEASUREMENTS

Figure 7(a) shows a photograph of the fabricated prototype. A microstrip square patch antenna printed on a 1-mm thick epoxy dielectric substrate ($\varepsilon_r = 3.9$ and $\tan\delta = 0.02$) is used as radiating source. A surrounding material made of alternating metamaterial layers transforms the omnidirectional emission of the patch antenna into a directive one steered in an off-normal direction. The metamaterial is a discrete structure composed of 10 different regions where permittivity and permeability vary according to Eq. (5) and to the profile of Figure 6(a). The bulk metamaterial is assembled using 30 layers of RO3003^{TM} dielectric boards on which subwavelength resonant structures are printed. The layers are mounted 1×1 in a molded matrix with a constant angle of 3° between each. A commercially available liquid resin is then flowed into the mold. This resin constitutes the host medium and is an important design parameter which is closely linked to $\varepsilon_{\theta\theta}$. Its measured permittivity has been found to be close to 2.8. The mold is removed after solidification of the resin.

To validate the directive emission device performances, S_{11} parameter measurements are first performed on the fabricated prototype. The measured S_{11} parameter of the metamaterial

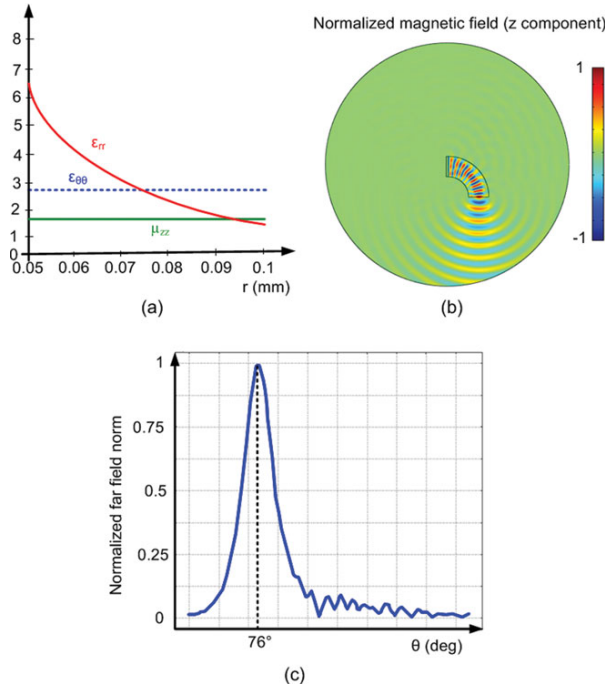

Figure 4 (a) Profile of the different material parameters (ε_{rr}, $\varepsilon_{\theta\theta}$, μ_{zz}). (b) Calculated emission of the plane source associated with the metamaterial defined by the reduced parameters of Eq. (5) for a working frequency of 10 GHz. (c) Calculated far field pattern of the metamaterial antenna. [Color figure can be viewed in the online issue, which is available at wileyonlinelibrary.com]

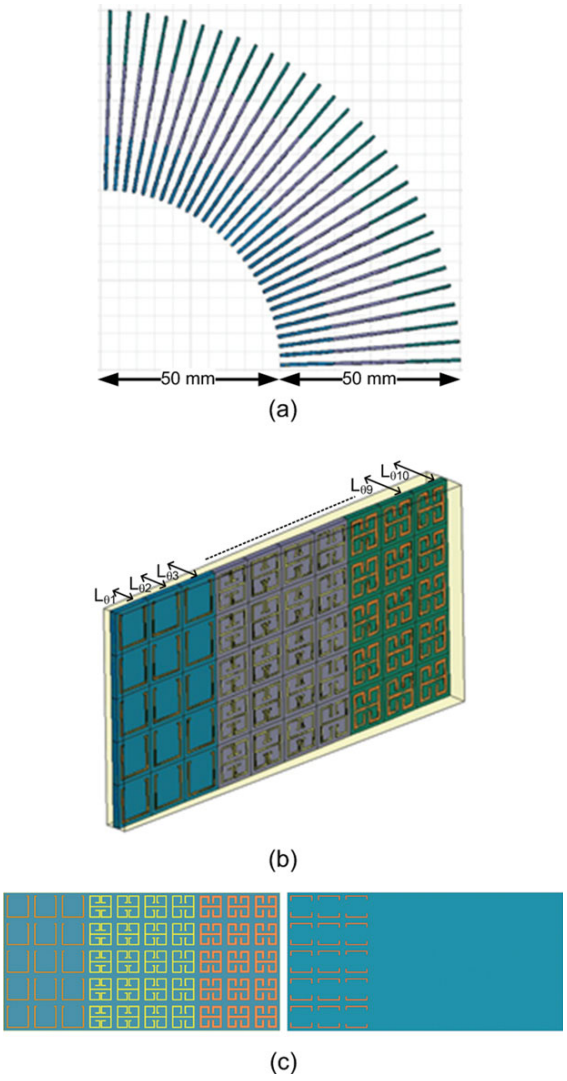

Figure 5 (a) Proposed structure using a lamellar composite material. (b) Single metamaterial layer composed of 10 unit cells providing the material parameters necessary for the coordinate transformation. (c) Front and rear view of the metamaterial cells. [Color figure can be viewed in the online issue, which is available at wileyonlinelibrary.com]

TABLE 1 Electromagnetic Parameters μ_{zz}, and ε_{rr} for the 10 Cells of the Metamaterial Layers

Layer	r_i (mm)	$L_{\theta i}$ (mm)	μ_{zz}	ε_{rr}
1	52.5	2.75	1.7	5.8
2	57.5	3.01	1.7	4.842
3	62.5	3.27	1.7	4.096
4	67.5	3.53	1.7	3.504
5	72.5	3.8	1.7	3.04
6	77.5	4.06	1.7	2.664
7	82.5	4.32	1.7	2.35
8	87.5	4.58	1.7	2.09
9	92.5	4.84	1.7	1.87
10	97.5	5.1	1.7	1.68

The length L_θ of each cell is given as a function of its position along the layer.

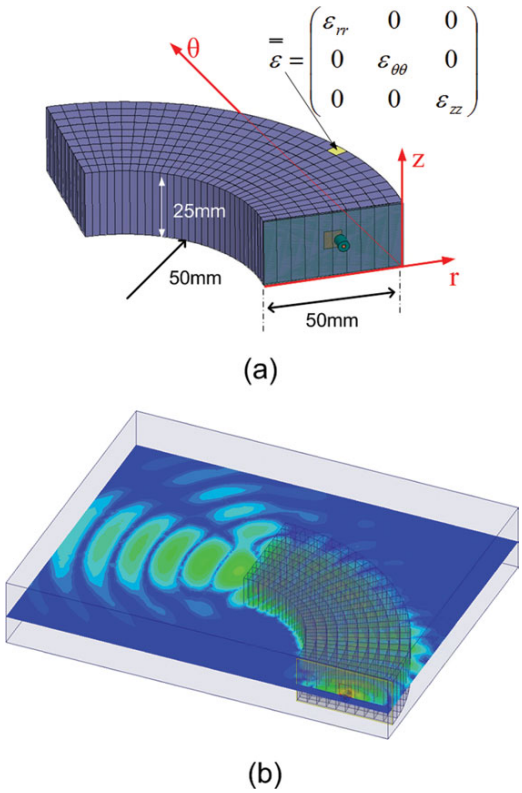

Figure 6 (a) Simulated design consisting of 30 metamaterial layers each composed of 10 cells. (b) Calculated energy distribution at 10 GHz. [Color figure can be viewed in the online issue, which is available at wileyonlinelibrary.com]

antenna is compared with the simulated one using HFSS in Figure 7(b). A good agreement can be observed and return losses reaching 18 dB is observed experimentally at 10.3 GHz compared to 15 dB calculated. This quantity is further compared with that of the feeding patch antenna alone. A better matching can be clearly observed for the metamaterial antenna. The far-field radiation patterns of the antenna have also been measured in a full anechoic chamber to show the beam steering performances. The fabricated prototype is used as emitter and a wide-band (2–18 GHz) dual polarized horn antenna is used as the receiver to measure the radiated power level of the emitter. Measurements are performed for computer-controlled elevation angle varying from $-90°$ to $+90°$. The microwave source is a vector network analyzer (Agilent 8722 ES) that we also use for detection. The simulated and measured far-field radiation patterns in the E-plane (plane containing $\boldsymbol{E}$ and $\boldsymbol{k}$ vectors) are presented in Figure 7(c) for a frequency of 10 and 10.3 GHz, respectively. A directive main beam and low parasitic secondary lobes, around -10 dB are observed experimentally at an angle of 66°. The main lobe presents 18° half-power beamwidth in the E-plane. From the experimental results, we can clearly observe the transformation of the omnidirectional far-field radiation of the patch antenna into a directive one which is further bent at an angle of 66°. The difference in bending angle is due to the fabrication tolerances of the meta-atoms providing the gradient radial permittivity and to the positioning of the patch source. We shall also note that simulations using HFSS [Fig. 7(c)] show 90° beam steering as no spatial shift is considered in the calculation of the far-field pattern.

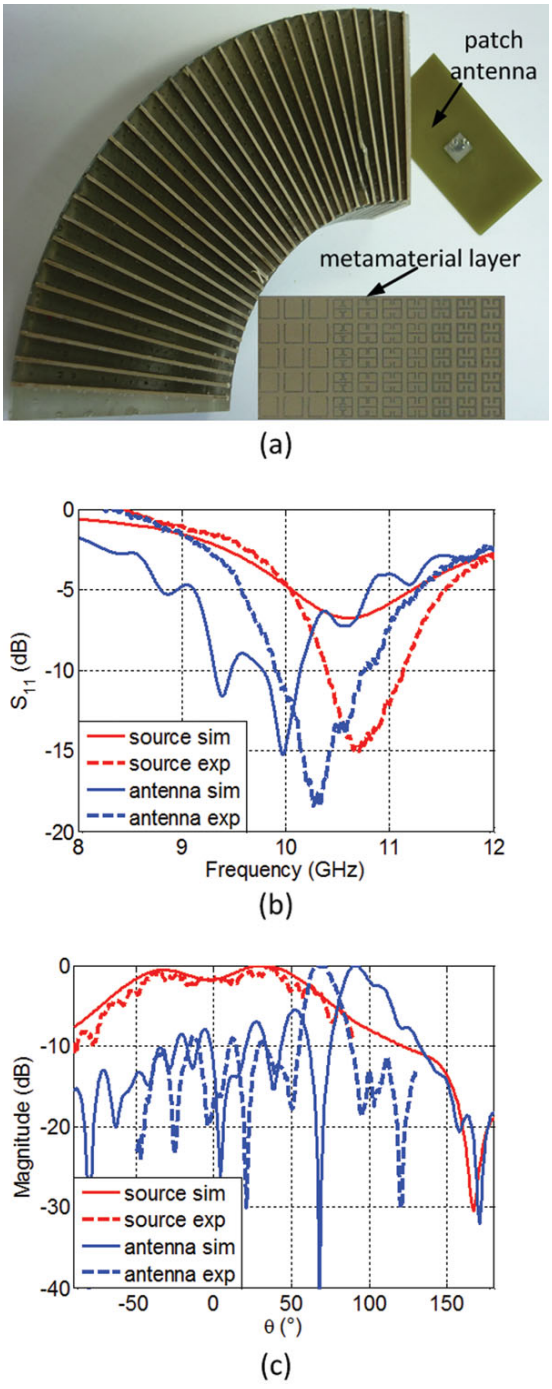

Figure 7 (a) Photography of the fabricated prototype consisting of 30 metamaterial layers each composed of 10 cells. (b) Comparison between simulations and measurements of the S_{11} parameter of the patch source alone and the metamaterial antenna. (c) Far-field *E*-plane radiation patterns of the patch source alone and of the metamaterial antenna. [Color figure can be viewed in the online issue, which is available at wileyonlinelibrary.com]

5. CONCLUSIONS

We have designed and measured a device which was able to transform an omnidirectional radiation into a directive one bent at an angle as much as 66° using the coordinate transformation concept. Metamaterials providing gradient radial permittivity satisfying the transformation are used to fabricate the device. Direct far field measurements have been performed to experimentally demonstrate the directive azimuthal emission, making the proposed device interesting for aeronautical applications.

REFERENCES

1. V.G. Veselago, The electrodynamics of substances with simultaneously negative values of ε and μ, Soviet Phys USPEKHI 10 (1968), 509–514.
2. S. Enoch, G. Tayeb, P. Sabouroux, N. Guérin, and P. Vincent, A metamaterial for directive emission, Phys Rev Lett 89 (2002), 213902.
3. S.N. Burokur, M. Latrach, and S. Toutain, Theoretical investigation of a circular patch antenna in the presence of a left-handed medium, IEEE Antennas Wireless Propag Lett 4 (2005), 183–186.
4. A. Ourir, A. de Lustrac, and J.-M. Lourtioz, Optimization of metamaterial based subwavelength cavities for ultracompact directive antennas, Microwave Opt Technol Lett 48 (2006), 2573–2577.
5. U. Leonhardt, Optical conformal mapping, Science 312 (2006), 1777–1780.
6. J.B. Pendry, D. Schurig, and D.R. Smith, Controlling electromagnetic fields, Science 312 (2006), 1780–1782.
7. D. Schurig, J.J. Mock, B.J. Justice, S.A. Cummer, J.B. Pendry, A.F. Starr, and D.R. Smith, Metamaterial electromagnetic cloak at microwave frequencies, Science 314 (2006), 977–980.
8. W. Cai, U.K. Chettiar, A.V. Kildishev, and V.M. Shalaev, Optical cloaking with non-magnetic metamaterials, Nat Photon 1 (2007), 224–227.
9. B. Kanté, A. de Lustrac, J.-M. Lourtioz, and S.N. Burokur, Infrared cloaking based on the electric response of split ring resonators, Opt Exp 16 (2008), 9191–9198.
10. M. Rahm, D.A. Roberts, J.B. Pendry, and D.R. Smith, Transformation-optical design of adaptive beam bends and beam expanders, Opt Exp 16 (2008), 11555–11567.
11. M. Rahm, S.A. Cummer, D. Schurig, J.B. Pendry, and D.R. Smith, Optical design of reflectionless complex media by finite embedded coordinate transformations, Phys Rev Lett 100 (2008), 063903.
12. L. Lin, W. Wang, J. Cui, C. Du, and X. Luo, Design of electromagnetic refractor and phase transformer using coordinate transformation theory, Opt Exp 16 (2008), 6815–6821.
13. J. Huangfu, S. Xi, F. Kong, J. Zhang, H. Chen, D. Wang, B.-I. Wu, L. Ran, and J.A. Kong, Application of coordinate transformation in bent waveguide, J Appl Phys 104 (2008), 014502.
14. P.-H. Tichit, S.N. Burokur, and A. de Lustrac, Waveguide taper engineering using coordinate transformation technology, Opt Exp 18 (2010), 767–772.
15. Y.G. Ma, C.K. Ong, T. Tyc and U. Leonhardt, An omnidirectional retroreflector based on the transmutation of dielectric singularities, Nat Mater 8 (2009), 639–642.
16. N. Kundtz and D.R. Smith, Extreme-angle broadband metamaterial lens, Nat Mater 9 (2010), 129–132.
17. P.-H. Tichit, S.N. Burokur, and A. de Lustrac, Ultra-directive antenna via transformation optics, J Appl Phys 105 (2009), 104912.
18. P.-H. Tichit, S.N. Burokur, D. Germain, and A. de Lustrac, Design and experimental demonstration of a high-directive emission with transformation optics, Phys Rev B 83 (2011), 155108.
19. P.-H. Tichit, S.N. Burokur, D. Germain, and A. de Lustrac, Coordinate transformation based ultra-directive emission, Electron Lett 47 (2011), 580–582.
20. P.-H. Tichit, S.N. Burokur, and A. de Lustrac, Transformation media producing quasi-perfect isotropic emission, Opt Exp 19 (2011), 20551–20556.
21. Z.H. Jiang, M.D. Gregory, and D.H. Werner, Experimental demonstration of a broadband transformation optics lens for highly directive multibeam emission, Phys Rev B 84 (2011), 165111.

Annexe 3.6

P.-H. Tichit, S. N. Burokur, A. de Lustrac

« Reducing physical appearance of electromagnetic sources »

Optics Express, vol. 21, no. 4, pp. 5053-5062, February 2013

Reducing physical appearance of electromagnetic sources

Paul-Henri Tichit,[1,3] Shah Nawaz Burokur,[1,2,*] and André de Lustrac[1,2,4]

[1]*IEF, Univ. Paris-Sud, CNRS, UMR 8622, 91405 Orsay Cedex, France*
[2]*Univ. Paris-Ouest, 92410 Ville d'Avray, France*
[3]*paul-henri.tichit@u-psud.fr*
[4] *andre.de-lustrac@u-psud.fr*
**shah-nawaz.burokur@u-psud.fr*

Abstract: We propose to use the concept of transformation optics for the design of novel radiating devices. By applying transformations that compress space, and then that match it to the surrounding environment, we show how the electromagnetic appearance of radiating elements can be tailored at will. Our efficient approach allows one to realize a large aperture emission from a small aperture one. We describe transformation of the metric space and the calculation of the material parameters. Full wave simulations are performed to validate the proposed approach on different space compression shapes, factors and impedance matching. The idea paves the way to interesting applications in various domains in microwave and optical regimes, but also in acoustics.

OCIS codes: (260.2065) Effective medium theory; (260.2110) Electromagnetic optics; (260.2710) Inhomogeneous optical media; (160.1190) Anisotropic optical materials; (160.3918) Metamaterials.

References and links

1. J. B. Pendry and S. A. Ramakrishna, "Focusing light using negative refraction," J. Phys. Condens. Matter **15**(37), 6345–6364 (2003).
2. S. Guenneau, B. Gralak, and J. B. Pendry, "Perfect corner reflector," Opt. Lett. **30**(10), 1204–1206 (2005).
3. U. Leonhardt, "Optical conformal mapping," Science **312**(5781), 1777–1780 (2006).
4. J. B. Pendry, D. Schurig, and D. R. Smith, "Controlling electromagnetic fields," Science **312**(5781), 1780–1782 (2006).
5. D. Schurig, J. B. Pendry, and D. R. Smith, "Calculation of material properties and ray tracing in transformation media," Opt. Express **14**(21), 9794–9804 (2006).
6. U. Leonhardt and T. G. Philbin, "General relativity in electrical engineering," New J. Phys. **8**(10), 247 (2006).
7. R. A. Crudo and J. G. O'Brien, "Metric approach to transformation optics," Phys. Rev. A **80**(3), 033824 (2009).
8. U. Leonhardt and T. G. Philbin, "Transformation optics and the geometry of light," Prog. Opt. **53**, 69–152 (2009).
9. D. Schurig, J. J. Mock, B. J. Justice, S. A. Cummer, J. B. Pendry, A. F. Starr, and D. R. Smith, "Metamaterial electromagnetic cloak at microwave frequencies," Science **314**(5801), 977–980 (2006).
10. F. Zolla, S. Guenneau, A. Nicolet, and J. B. Pendry, "Electromagnetic analysis of cylindrical invisibility cloaks and the mirage effect," Opt. Lett. **32**(9), 1069–1071 (2007).
11. M. Rahm, D. Schurig, D. A. Roberts, S. A. Cummer, D. R. Smith, and J. B. Pendry, "Design of electromagnetic cloaks and concentrators using form-invariant coordinate transformations of Maxwell's equations," Photon. Nanostruct.: Fundam. Appl. **6**(1), 87–95 (2008).
12. H. Chen, B. Hou, S. Chen, X. Ao, W. Wen, and C. T. Chan, "Design and experimental realization of a broadband transformation media field rotator at microwave frequencies," Phys. Rev. Lett. **102**(18), 183903 (2009).
13. D.-H. Kwon and D. H. Werner, "Transformation optical designs for wave collimators, flat lenses and right-angle bends," New J. Phys. **10**(11), 115023 (2008).
14. M. Tsang and D. Psaltis, "Magnifying perfect lens and superlens design by coordinate transformation," Phys. Rev. B **77**(3), 035122 (2008).
15. N. Kundtz and D. R. Smith, "Extreme-angle broadband metamaterial lens," Nat. Mater. **9**(2), 129–132 (2010).
16. D. A. Roberts, N. Kundtz, and D. R. Smith, "Optical lens compression via transformation optics," Opt. Express **17**(19), 16535–16542 (2009).
17. A. Greenleaf, Y. Kurylev, M. Lassas, and G. Uhlmann, "Electromagnetic wormholes and virtual magnetic monopoles from metamaterials," Phys. Rev. Lett. **99**(18), 183901 (2007).

#182364 - $15.00 USD Received 27 Dec 2012; revised 8 Feb 2013; accepted 11 Feb 2013; published 21 Feb 2013

18. A. Nicolet, F. Zolla, and S. Guenneau, "A finite element modelling for twisted electromagnetic waveguides," Eur. J. Phys. Appl. Phys. **28**(2), 153–157 (2004).
19. M. Rahm, S. A. Cummer, D. Schurig, J. B. Pendry, and D. R. Smith, "Optical design of reflectionless complex media by finite embedded coordinate transformations," Phys. Rev. Lett. **100**(6), 063903 (2008).
20. M. Rahm, D. A. Roberts, J. B. Pendry, and D. R. Smith, "Transformation-optical design of adaptive beam bends and beam expanders," Opt. Express **16**(15), 11555–11567 (2008).
21. J. Huangfu, S. Xi, F. Kong, J. Zhang, H. Chen, D. Wang, B.-I. Wu, L. Ran, and J. A. Kong, "Application of coordinate transformation in bent waveguide," J. Appl. Phys. **104**(1), 014502 (2008).
22. D. A. Roberts, M. Rahm, J. B. Pendry, and D. R. Smith, "Transformation-optical design of sharp waveguide bends and corners," Appl. Phys. Lett. **93**(25), 251111 (2008).
23. P.-H. Tichit, S. N. Burokur, and A. de Lustrac, "Waveguide taper engineering using coordinate transformation technology," Opt. Express **18**(2), 767–772 (2010).
24. V. Ginis, P. Tassin, C. M. Soukoulis, and I. Veretennicoff, "Confining light in deep subwavelength electromagnetic cavities," Phys. Rev. B **82**(11), 113102 (2010).
25. V. Ginis, P. Tassin, J. Danckaert, C. M. Soukoulis, and I. Veretennicoff, "Creating electromagnetic cavities using transformation optics," New J. Phys. **14**(3), 033007 (2012).
26. Y. Lai, J. Ng, H. Chen, D. Han, J. Xiao, Z.-Q. Zhang, and C. T. Chan, "Illusion optics: the optical transformation of an object into another object," Phys. Rev. Lett. **102**(25), 253902 (2009).
27. W. H. Wee and J. B. Pendry, "Shrinking optical devices," New J. Phys. **11**(7), 073033 (2009).
28. W. Lu, Z. Lin, H. Chen, and C. T. Chan, "Transformation media based super focusing antenna," J. Phys. D Appl. Phys. **42**(21), 212002 (2009).
29. Y. Luo, J. Zhang, L. Ran, H. Chen, and J. A. Kong, "Controlling the emission of electromagnetic source," PIERS Online **4**(7), 795–800 (2008).
30. J. Allen, N. Kundtz, D. A. Roberts, S. A. Cummer, and D. R. Smith, "Electromagnetic source transformations using superellipse equations," Appl. Phys. Lett. **94**(19), 194101 (2009).
31. B. I. Popa, J. Allen, and S. A. Cummer, "Conformal array design with transformation electromagnetics," Appl. Phys. Lett. **94**(24), 244102 (2009).
32. P.-H. Tichit, S. N. Burokur, D. Germain, and A. de Lustrac, "Design and experimental demonstration of a high-directive emission with transformation optics," Phys. Rev. B **83**(15), 155108 (2011).
33. P.-H. Tichit, S. N. Burokur, D. Germain, and A. de Lustrac, "Coordinate transformation based ultra-directive emission," Electron. Lett. **47**(10), 580–582 (2011).
34. Z. H. Jiang, M. D. Gregory, and D. H. Werner, "Experimental demonstration of a broadband transformation optics lens for highly directive multibeam emission," Phys. Rev. B **84**(16), 165111 (2011).
35. P.-H. Tichit, S. N. Burokur, and A. de Lustrac, "Transformation media producing quasi-perfect isotropic emission," Opt. Express **19**(21), 20551–20556 (2011).

1. Introduction

In the telecommunications domain, there are actually growing interests in the miniaturization of devices, particularly for antennas in transport and aeronautical fields. In most cases it is the physics itself that limits the possibility of size reduction. The transformation optics (or coordinate transformation) concept [1–5], an innovative approach to design new class of electromagnetic devices, can prove its usefulness for miniaturization since it allows making a link between space, time and material. The main idea of coordinate transformation is to make an equivalence between Maxwell equations described in an initial coordinate system and these same equations described in another arbitrary transformed one. The result is a direct link between the permittivity and permeability of the material and the metric tensor of the transformed space containing the desired electromagnetic properties [6–8]. This method was first used by U. Leonhardt [1] and J. B. Pendry [2] to design an electromagnetic invisibility cloak in 2006 [9]. Since then, the invisibility cloak has been a subject of intensive studies [10] and later, other systems resulting from coordinate transformation have emerged. Thus, concentrators [11], rotators [12], lenses [13–16], artificial wormholes [17], waveguide bends and transitions [18–23], electromagnetic cavities [24,25], illusion systems [26,27] and antennas [28–35] have emerged. In most cases, the generated materials are inhomogeneous and anisotropic since the created virtual spaces make use of arbitrary coordinates. Devices generated by transformation optics can then be fabricated through the use of metamaterials, which are subwavelength engineered artificial structures that derive their properties from their structural geometry.

In this paper, transformation optics concept is applied to transform the signature of a radiating source. We show that a linear space compression followed by a space expansion, make the radiation pattern of a small aperture antenna appear like that of a large one. The material parameters generated from the transformation are discussed and the results are

#182364 - $15.00 USD Received 27 Dec 2012; revised 8 Feb 2013; accepted 11 Feb 2013; published 21 Feb 2013

validated by numerical simulations performed using sources of different shapes and lengths. We further show that the proposed transformation can also be applied to an array of miniaturized electromagnetic radiators.

2. Transformation formulations

To achieve the transformation of a small aperture source into a much larger one, we discretize the space around the latter radiating element into two different zones; a first zone which will make our source appear bigger than its real physical size and a second zone which ensures the impedance matching with the surrounding radiation environment. The operating principle is shown by the schematic in Fig. 1(a). In a space point of view, the technique consists in compressing a circular region of space of radius R_1/q_1 (with $q_1 < 1$), delimited by the red circle in Fig. 1(a)) in a region of radius R_1. In the studied transformation, our space is described by polar coordinates and the angular part of these coordinates remains unchanged. The second part of the transformation consists in an impedance matching with the surrounding space through an annular expansion zone defined between circular regions with radius R_1 and R_2, as illustrated in Fig. 1(b). This space expansion can be performed using three different transformations: a positive exponential transformation, a negative exponential transformation, and a linear one. We denote below and in the rest of the paper the two different zones by the index i, where $i = 1$ corresponds to the first zone and $i = 2$ to the second zone. The final virtual space describing our device is represented in Fig. 1(c). Figure 1(d) summarizes the different transformations considered. To secure the impedance and metric matching, continuity of our transformations is assured at the boundary of the first region (point A in Fig. 1(d)) and at the outer boundary of the device (point B in Fig. 1(d)).

Mathematically, the transformation in the different regions can be written as:

$$\begin{cases} r' = f_i(r,\theta) \\ \theta' = \theta \\ z' = z \end{cases} \tag{1}$$

The Jacobian matrix of the transformation is given in the cylindrical coordinate system as:

$$\overline{\overline{J_{cyl}}} = \begin{pmatrix} \frac{\partial r'}{\partial r} & \frac{\partial r'}{\partial \theta} & \frac{\partial r'}{\partial z} \\ \frac{\partial \theta'}{\partial r} & \frac{\partial \theta'}{\partial \theta} & \frac{\partial \theta'}{\partial z} \\ \frac{\partial z'}{\partial r} & \frac{\partial z'}{\partial \theta} & \frac{\partial z'}{\partial z} \end{pmatrix} = \begin{pmatrix} f_{i,r} & f_{i,\theta} & 0 \\ 0 & 1 & 0 \\ 0 & 0 & 1 \end{pmatrix} \tag{2}$$

where $f_{i,r}$ and $f_{i,\theta}$ represent the respective derivatives of f_i with respect to r and θ. To calculate permittivity and permeability tensors directly from the coordinate transformation in the cylindrical and orthogonal coordinates, we need to express the metric tensor in the initial and virtual spaces. The final Jacobian matrix needed for the permeability and permittivity tensors of our material is then given as:

$$\overline{\overline{J_i}} = \begin{pmatrix} f_{i,r} & \frac{f_{i,\theta}}{r} & 0 \\ 0 & \frac{r'}{r} & 0 \\ 0 & 0 & 1 \end{pmatrix} \tag{3}$$

#182364 - $15.00 USD Received 27 Dec 2012; revised 8 Feb 2013; accepted 11 Feb 2013; published 21 Feb 2013

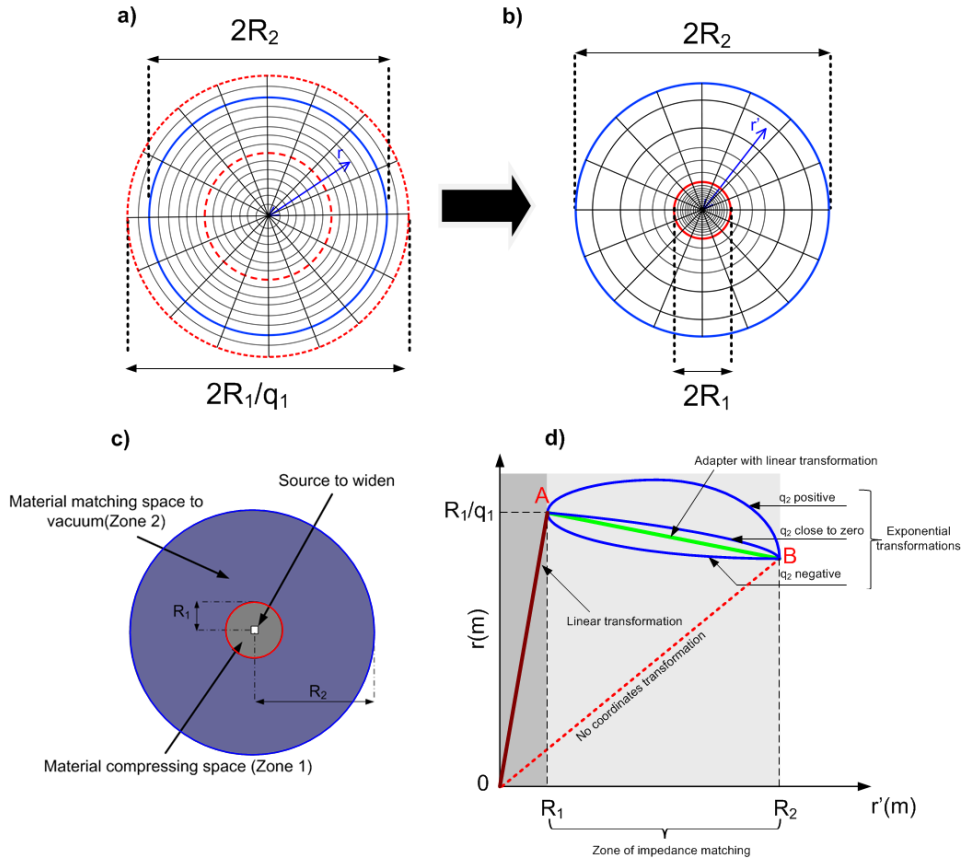

Fig. 1. Representation of the proposed coordinate transformation: (a) initial and (b) virtual space. (c) The region 1 of the material enlarges the aperture of the source whereas region 2 allows matching the impedance with that of the surrounding environment. (d) Operating principle of the transformation, which consists in firstly a compression of the central space ($0 < r' < R_1$) and secondly, an expansion to match the space metric ($R_1 < r' < R_2$). Continuity of the transformations is assured at the boundary of the compressed region (point A) and at the outer boundary of the device (point B).

The coefficient of our material can be written as $\overline{\overline{\psi_i}} = \frac{J_i J_i^T}{\det(J_i)}$ in the cylindrical coordinates. The material parameters obtained using the transformation in Eq. (1) are:

$$\begin{cases} (\psi_{rr})_i = \dfrac{r f_{i,r}}{r'} + \dfrac{f_{i,\theta}^2}{r r' f_{i,r}} \\ (\psi_{r\theta})_i = \dfrac{f_{i,\theta}}{r f_{i,r}} \\ (\psi_{\theta\theta})_i = \dfrac{r' f_{i,r}}{r} \\ (\psi_{zz})_i = \dfrac{r}{r' f_{i,r}} \end{cases} \quad (4)$$

These parameters are relatively simple for the transformation in the first zone since it leads to constant values. But the permittivity and permeability components have to be

#182364 - $15.00 USD Received 27 Dec 2012; revised 8 Feb 2013; accepted 11 Feb 2013; published 21 Feb 2013

expressed in the Cartesian coordinate system so as to have a perfect equivalence in Maxwell's equations and also to physically design our device. Using matrix relations between cylindrical and Cartesian coordinates, we have:

$$\overline{\overline{\varepsilon}} = \begin{pmatrix} \psi_{xx} & \psi_{xy} & 0 \\ \psi_{yx} & \psi_{yy} & 0 \\ 0 & 0 & \psi_{zz} \end{pmatrix} \varepsilon_0 \qquad \overline{\overline{\mu}} = \begin{pmatrix} \psi_{xx} & \psi_{xy} & 0 \\ \psi_{yx} & \psi_{yy} & 0 \\ 0 & 0 & \psi_{zz} \end{pmatrix} \mu_0$$

$$\text{with} \begin{cases} \psi_{xx} = \psi_{rr}\cos^2(\theta) + \psi_{\theta\theta}\sin^2(\theta) - \psi_{r\theta}\sin(2\theta) \\ \psi_{xy} = \psi_{yx} = (\psi_{rr} - \psi_{\theta\theta})\sin(\theta)\cos(\theta) + \psi_{r\theta}\cos(2\theta) \\ \psi_{yy} = \psi_{rr}\sin^2(\theta) + \psi_{\theta\theta}\cos^2(\theta) + \psi_{r\theta}\sin(2\theta) \end{cases} \tag{5}$$

The angular part in the coordinate transformation described above allows obtaining more general and adjustable parameters for a possible physical realization of the device. However, in the present study, we consider $f_{i,\theta} = 0$ to simplify the calculations. To apply our proposed coordinate transformation, we consider a radial compression of the space in region 1. This leads to a material with high permittivity and permeability tensors. For the transformation, we choose $r' = f_1(r) = q_1 r$ with q_1 being a coefficient lower than 1. The physical meaning of the factor q_1 is the compression factor applied in the central region. This factor has a transition value which can be defined as $q_0 = R_1 / R_2$ where the material of the matching zone (region 2 in Fig. 1(c)) switch from a right-handed (positive refractive index) to a left-handed (negative refractive index) material. Indeed when $q_1 < q_0$ the material presents a negative index and the final apparent size of the source can be larger than $2R_2$. Now if this embedded source has a small aperture, much smaller than the wavelength, then after transformation this antenna will behave like one with a large aperture, typically q_1 times larger and potentially much greater than the wavelength. A small aperture antenna is well known to radiate isotropically. The same antenna embedded in the material defined by Eq. (5) will present a directive radiation and therefore electrically appear as if its size is larger than the working wavelength. Moreover, we can obtain the radiation of a conventional array of antennas using much smaller dimensions for the latter array embedded in zone 1. To assure a good impedance matching for the radiated fields, a matching zone (region 2) is added around region 1. To design this zone, we consider three different possible transformations that match the space from R_1 to R_2. The first studied transformation for this matching region is a linear one that takes the form $r' = f_2(r) = \frac{1}{\alpha}\left[r + R_2(\alpha - 1)\right]$ whereas the two other transformations have logarithmic forms that can be expressed as $r' = f_2(r) = \frac{1}{q_2}\ln\left(\frac{r-d}{p}\right)$ where $d = R_2 - pe^{q_2 R_2}$ and $p = \frac{R_2 - q_1 R_1}{e^{q_2 R_2} - e^{q_1 R_1}}$ are constant values. In these two cases, the inverse transformation defining r from r' has an exponential form defined by: $F_2(r') = d + pe^{q_2 r}$. This exponential transformation can be characterized by the factor q_2 that indicates the shape of the progressive metric matching to vacuum ($\overline{\overline{g}} = \overline{\overline{I}}$), as illustrated in Fig. 1(d). A small value of q_1 indicates a high compression of the space in the first region. To compensate this high compression, the transformation in the second region gives negative electromagnetic parameters due to the relative positions of points A and B (Fig. 1(d)), as presented in Fig. 2. In such case, the wave propagates with a backward phase in this region. Figure 2 shows the variations of the different components of the permittivity and permeability tensors for the matching region 2. For the linear transformation, the minimum and maximum of the material parameters depend

#182364 - $15.00 USD Received 27 Dec 2012; revised 8 Feb 2013; accepted 11 Feb 2013; published 21 Feb 2013

on the geometrical properties of the problem and thus they depend only on α and γ which are given by:

$$\alpha = \frac{R_2 - R_1 / q_1}{R_2 - R_1} \text{ and } \gamma = 1 + \frac{R_2 (1-\alpha)}{R_1 \alpha} \tag{6}$$

where q_1 is defined on]0, 1]. α is therefore defined on]-∞,1] and vanishes at $q_1 = q_0$. Thus, γ is a function of α and is larger than 1 for $q_1 > q_0$ and is negative for $q_1 < q_0$. In this last case such a medium is a left-handed material.

We can note that the trends of the permittivity and permeability values in the Cartesian coordinates are quite similar for both linear and exponential transformation. The values depend only on R_1, R_2, q_1 and q_2 for the linear transformation. For the case of the exponential transformation in region 2, the parameters considered are $q_1 = 1/16$, $q_2 = 15$, $R_1 = 5$ mm and $R_2 = 45$ mm and as it can be observed, the calculated components ψ_{xx}, ψ_{yy} and ψ_{zz} are always negative.

#182364 - $15.00 USD Received 27 Dec 2012; revised 8 Feb 2013; accepted 11 Feb 2013; published 21 Feb 2013

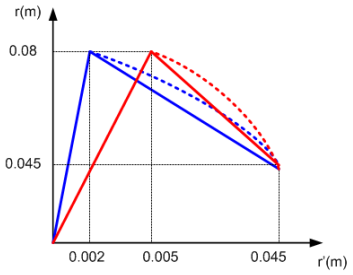

(a)

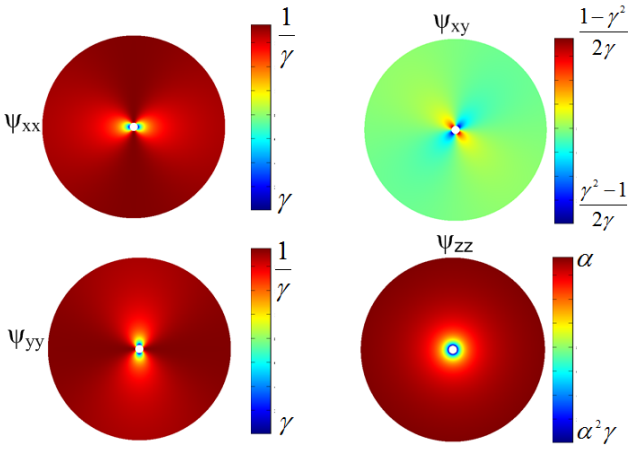

(b) Linear transformation

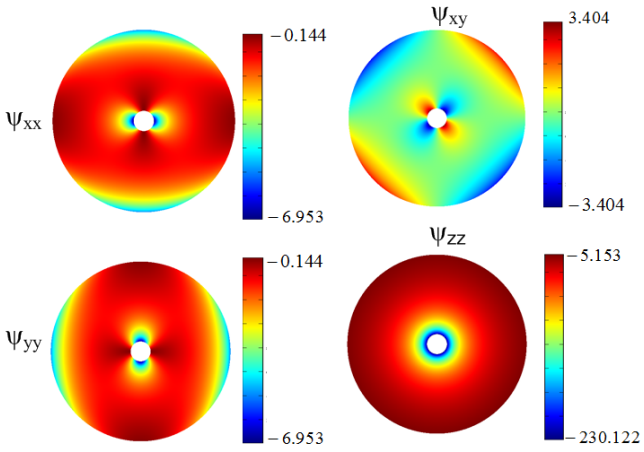

(c) Exponential transformation

Fig. 2. (a) Representation of the transformations in regions 1 and 2. The blue and red traces correspond respectively to q_1 = 1/40 and q_1 = 1/16 and the continuous and dashed traces correspond respectively to a linear and exponential transformations. (b)–(c) Variation of the components in Cartesian coordinates of the matching region 2. The permittivity and permeability are respectively plotted for the linear transformation with q_1 = 1/40, R_1 = 2 mm (continuous blue traces case) and for the exponential transformation with q_1 = 1/16, q_2 = 15 and R_1 = 5 mm (continuous and dashed red traces case).

#182364 - $15.00 USD Received 27 Dec 2012; revised 8 Feb 2013; accepted 11 Feb 2013; published 21 Feb 2013

3. Numerical validation

In order to validate the proposed concept, we use the commercial software Comsol MULTIPHYSICS to perform numerical simulations of the different transformation cases presented above. All the simulations are run in the microwave domain at 10 GHz. The validation of our design is performed in a two-dimensional configuration in a transverse electric mode (TEz) (E parallel to the *z*-axis). Different current sources perpendicular to the *xy* plane are used as radiating elements in order to show that our transformation can be applied to any type of source embedded in the region 1. Continuity and matched conditions are applied respectively to the boundary of zone 1 and zone 2.

To verify our design, we fix R_1 = 2 mm and R_2 = 45 mm. The results obtained from linear transformations both in region 1 and 2, as defined by the continuous blue trace in Fig. 2(a), are presented in Fig. 3. In Fig. 3(a), the electric field distribution of a current source radiating in free space is plotted. The source is supposed to have a width d = 80 mm (2.7λ at 10 GHz). For such a large size, the radiation is equivalent to that of an array of several elements and therefore, the radiated field is directive. Figure 3(b) shows a similar source but with a much smaller size d = 2 mm (λ/15 at 10 GHz) embedded in the metamaterial shell having a compression factor q_1 = 1/40. In this scenario, a radiation pattern similar to the large aperture source is observed, demonstrating that small aperture antennas inserted in the proposed material shell present the same electromagnetic behavior as much larger aperture antennas in free space. However, this same miniature source will radiate in an isotropic manner in free space (Fig. 3(c)). The same observations can be made when replacing the linear current source by a crossed-type one, as illustrated in Figs. 3(d)-3(f).

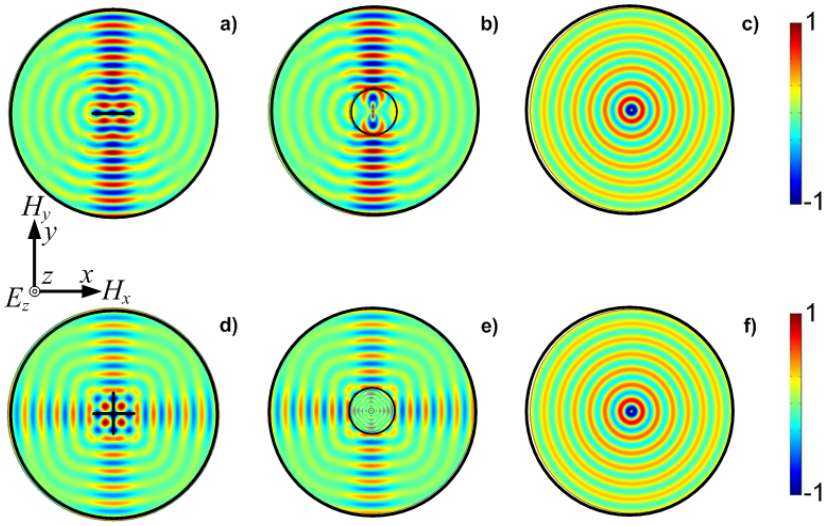

Fig. 3. Electric field distribution at 10 GHz of a linear source: (a) with dimension d = 80 mm radiating in free space, (b) with dimension d = 2 mm embedded in a metamaterial shell, and (c) with dimension d = 2 mm radiating in free space. Electric field distribution at 10 GHz of a crossed-type source: (d) with dimension d = 80 mm radiating in free space, (e) with dimension d = 2 mm embedded in a metamaterial shell, and (f) with dimension d = 2 mm radiating in free space. The metamaterial shell is defined by a double linear transformation where R_1 = 2 mm, R_2 = 45 mm and q_1 = 1/40.

In Figs. 4(a)-4(c), the linear transformation is followed by an exponential one with q_2 = 15 in region 2 and the compression factor in region 1 is decreased to q_1 = 1/40. The transformation is defined by the dashed blue trace in Fig. 2(a). The small size linear current source with d = λ/15 is embedded in the metamaterial shell defined by the proposed coordinate transformation. A directive emission is observed as in the previous case and as illustrated in the enlarged view of Fig. 4(b), we can clearly note the exponential form of the

#182364 - $15.00 USD Received 27 Dec 2012; revised 8 Feb 2013; accepted 11 Feb 2013; published 21 Feb 2013

radiated field. We can also observe the perfect impedance matching between the regions 1 and 2 and between the region 2 and free space. This is clearly confirmed by the continuity of the electric field norm at the interface $r = R_1$ and by the absence of stationary waves in region 2 in Fig. 4(c).

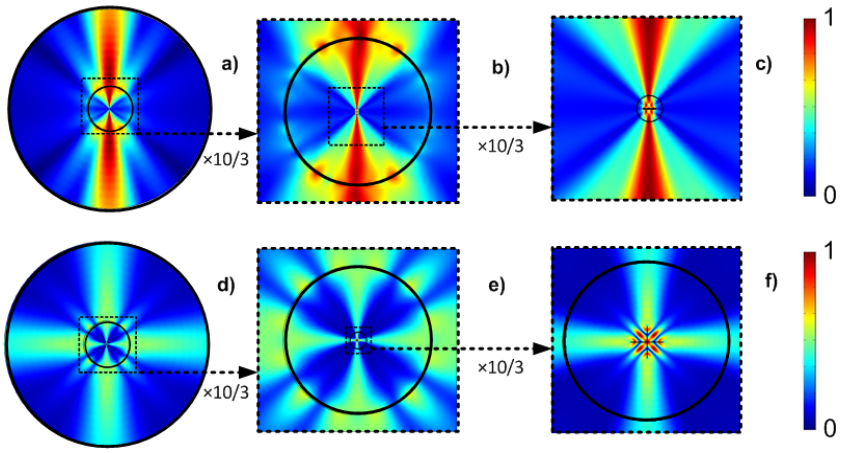

Fig. 4. (a)-(c) Norm of the electric field of a line source with dimension d = 2 mm. The metamaterial shell is defined by a linear transformation with q_1 = 1/40 followed by an exponential one with q_2 = 15 where R_1 = 2 mm and R_2 = 45 mm. (d)-(f) Norm of the electric field of a crossed-type source with dimension d = 2 mm. The metamaterial shell is defined by a linear transformation with q_1 = 1/16 followed by an exponential one with q_2 = 15 where R_1 = 5 mm and R_2 = 45 mm.

In Figs. 4(d)-4(f), the material in region 1 is defined by q_1 = 1/16 and in region 2, the material is defined by an exponential transformation with q_2 = 15. This transformation corresponds to the dashed red trace of Fig. 2(a) and the crossed-type source is embedded in the metamaterial shell. In this case also, a bidirectional directive beam can be observed even if the size of the source is very small compared to the working wavelength. In each case, the small aperture size of the radiating element has been transformed into a larger one: 40 times for the linear source and 16 times for the crossed-type source.

In the absence of the matching region, there is a high impedance mismatch at the boundary of the region 1 and all the energy emitted by the source is reflected at the boundary and confined in this latter region. This phenomenon is illustrated in Fig. 5 by the norm of the electric field. Stationary waves appear in the structure due to reflection at $r = R_1$.

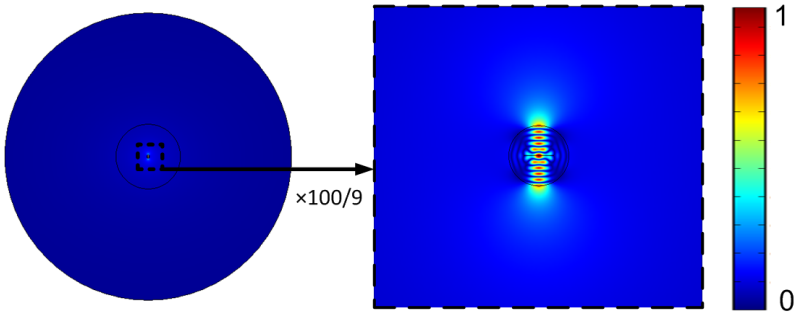

Fig. 5. Norm of the electric field of a line source with dimension d = 2 mm. The metamaterial shell is defined by only a compression region presenting a linear transformation with q_1 = 1/40. No matching region is used in this case.

The above results show that we are indeed able to hide the physical appearance of radiating sources by miniaturizing their physical dimensions without altering their radiation

#182364 - $15.00 USD Received 27 Dec 2012; revised 8 Feb 2013; accepted 11 Feb 2013; published 21 Feb 2013

diagrams. Furthermore, we show that our transformation still holds for an array of small antennas. We have simulated an array of three sources of length L = 12.5 mm, spaced by a distance a = 5 mm and with a 30° phase shift between each element. These sources radiate in vacuum and as illustrated in Fig. 6(a), we observe a radiated beam pointing in an off-normal direction due to the phase shift applied between the different elements of the array. When the dimensions of these antennas are reduced by a factor of 25 (q_1 = 1/25) the dimensions of the array become smaller compared to the wavelength and the radiated field becomes isotropic as shown in Fig. 6(b). By embedding the small sources in a material defined from the double linear transformation, we are able to recover the beam steering of the source array as shown in Fig. 6(c). This last example confirms the ability of our transformation to change the electromagnetic appearance of a group of radiators. Figures 6(d) and 6(e) show that in both cases, with and without transformed material, the impedance matching between the metamaterial shell and free space is perfect.

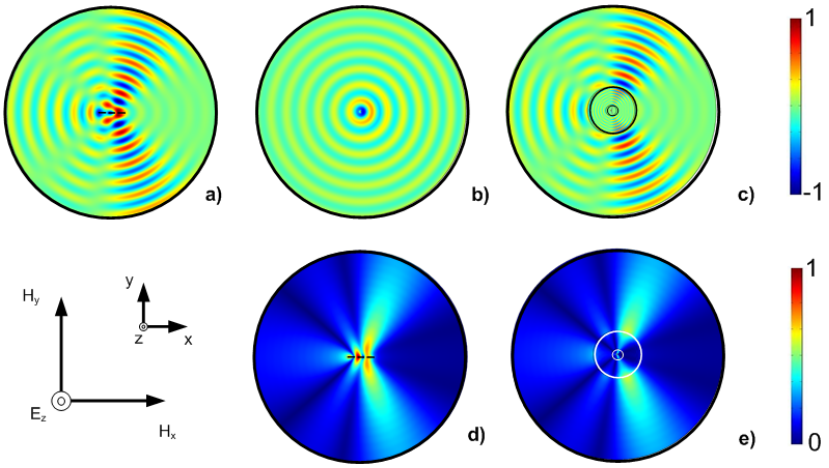

Fig. 6. 3 sources with length L = 12.5 mm spaced by a distance a = 5 mm and with a 30° phase shift between each element radiate in free space (a, d) at 10 GHz (z-components of the electric field). When all the dimensions are reduced by a factor of 25 (L = 0.5 mm and a = 0.2 mm) the electric field distribution (z-component) in free space is represented in (b). Embedding the miniaturized sources in the metamaterial shell defined by a double linear transformation leads to a similar radiation pattern as the original sized sources as shown in (c) with perfect matching to free space (e).

4. Conclusion

This work points out the use of transformation electromagnetics concept to design an artificial shell which allows hiding the physical appearance of electromagnetic sources by miniaturizing them. The latter concept makes use of two transformations; the first one to compress space and the second one to expand it. Numerical simulations have confirmed the operating principle of the transformations on sources of different geometries. We have shown that a very small source can emit a directive radiation comparable to an antenna with a large aperture. Furthermore, the concept has also been applied to an array of miniaturized radiating elements which is able to show an off-normal directive beam direction. The proposed idea constitutes an important step towards miniaturized devices in order to achieve performances that have been till now possible only with large physical devices. We can also imagine that such a device can be benefit in the design of headphones with a sound fidelity comparable to classical stereo speaker. High efficiency low profile field concentrators can also be imagined for energy harvesting.

#182364 - $15.00 USD Received 27 Dec 2012; revised 8 Feb 2013; accepted 11 Feb 2013; published 21 Feb 2013

Annexe 3.7

P.-H. Tichit, S. N. Burokur, C.-W. Qiu, A. de Lustrac

« Experimental verification of isotropic radiation from a coherent dipole source via electric-field-driven LC resonator metamaterials »

Physical Review Letters, vol. 111, no. 13 (133901), Septembre 2013

Experimental Verification of Isotropic Radiation from a Coherent Dipole Source via Electric-Field-Driven *LC* Resonator Metamaterials

Paul-Henri Tichit,[1] Shah Nawaz Burokur,[1,2] Cheng-Wei Qiu,[3] and André de Lustrac[1,2]
[1]*IEF, CNRS, UMR 8622, University Paris-Sud, 91405 Orsay Cedex, France*
[2]*University Paris-Ouest, 92410 Ville d'Avray, France*
[3]*Department of Electrical and Computer Engineering, National University of Singapore, 4 Engineering Drive 3, Singapore 117576, Singapore*
(Received 2 May 2013; revised manuscript received 25 July 2013; published 24 September 2013)

It has long been conjectured that isotropic radiation by a simple coherent source is impossible due to changes in polarization. Though hypothetical, the isotropic source is usually taken as the reference for determining a radiator's gain and directivity. Here, we demonstrate both theoretically and experimentally that an isotropic radiator can be made of a simple and finite source surrounded by electric-field-driven *LC* resonator metamaterials designed by space manipulation. As a proof-of-concept demonstration, we show the first isotropic source with omnidirectional radiation from a dipole source (applicable to all distributed sources), which can open up several possibilities in axion electrodynamics, optical illusion, novel transformation-optic devices, wireless communication, and antenna engineering. Owing to the electric-field-driven *LC* resonator realization scheme, this principle can be readily applied to higher frequency regimes where magnetism is usually not present.

DOI: 10.1103/PhysRevLett.111.133901 PACS numbers: 42.70.Qs, 41.20.Jb, 42.79.Ry

Although innovative electromagnetic notions continue to captivate minds [1–7], the antenna [8] has always been an indispensable source of light or radiation and important part of wireless communication systems that are widespread in laboratories and industries [9]. Brouwer's theorem [10] proves that a simple and finite source cannot have an isotropic radiation [11,12] pattern due to the obligation of polarization change for a simple and finite source. In his article, Brouwer demonstrated that no vector function can be continuous and tangent everywhere on the boundary of a sphere. As a consequence, there is a point $(r = R, \theta_0, \psi_0)$ on the sphere where all continuous vector functions have to be zero. Since the Poynting vector is defined by the vector product of the electric and magnetic fields, this prevents it from being perpendicular and constant everywhere on the boundary of a sphere and, therefore, isotropic emission. If isotropic radiation is obtained, the solution for Helmholtz's equation will have an infinitesimal point source of perfect symmetry in all directions. If not, then there will always be an extension in geometry breaking three-dimensional (3D) spherical symmetry regardless of the sources involved.

This problem occurs to all sources in electromagnetics and optics, as long as Maxwell's equations are valid. Hence, the significance of making an actual coherent dipole source to be isotropic certainly goes beyond antenna community, e.g., manipulation of axion electrodyanimcs [13], optical illusion [14], wireless communication [15], etc. We selected the microwave dipole source because it is more accessible in daily life and convenient to perform a proof-of-concept experiment.

The source can create photons from their charge acceleration. In this connection, almost all sources including antenna systems can be regarded equivalent to dynamic dipoles or multipoles which possess accelerated charges oscillating around the equilibrium. These dipoles, which are spatiotemporally coherent sources, emit photons of identical phase and amplitude. Therefore, perfect 3D spherically isotropic symmetry cannot be obtained unless a number of incoherent sources with sophisticated control of amplitudes, phases, and relative spacing are used [8]. Therefore, the isotropic radiation by an actual dipole source has not been validated hitherto (intrinsically prohibited in classic topology), though it has long been conjectured and used in characterization. Although engineering solutions have been found to design radio-frequency identification antennas producing nearly omnidirectional radiation [13,14], this again poses the fundamental scientific challenge and, thereby, significant value to this work achieving isotropic radiator for a simple coherent dipole source. As for achieving omnidirectional radiation of a single dipole, recently, a radially anisotropic zero-index metamaterial (RAZIM) shell has been proposed to generate perfect isotropic radiation in a two-dimensional space [15] by confining all 2-D anisotropic modes while keeping the isotropic mode propagating through [16]. It is, thus, still challenging to enhance the power yield for the antenna radiation due to the confinement of all anisotropic modes.

The solution to this problem may be found in transformation optics [4,5]. We experimentally demonstrate the isotropic radiation from an actual dipole source for the first time. Interestingly, this method, inspired by transformation optics, can enable the control of electromagnetic fields and engineering of new devices such as the

invisibility cloak [1,6,7,17–23], wormholes [24], waveguide connections [25–29], and antennas [30–36], by producing proper permittivity and permeability parameters. These devices can be realized by electric metamaterial fabrication, which are engineered by subwavelength artificial structures that produce necessary material properties corresponding to the space manipulation. We will employ space manipulation for making a dipole behave as an isotropic radiator and realize this equivalence by speculated nonmagnetic materials by electric-type metamaterials, which may pave the way for higher frequency scaling and realization of better isotropy.

In this Letter, we will focus on the creation of isotropic emission by a simple dipole inserted in a material calculated by transformation optics. It is more accessible to realize a metamaterial with weak inhomogeneity and anisotropy in 3-D cylindrical coordinates and to virtually compress the embedded dipole via radial component of cylindrical coordinates. We will further show the practical 2-D demonstration of an isotropic dipole at microwaves frequencies by judiciously engineering metamaterials to control the emission in a maximal solid angle with impedance matched between the metamaterial and the vacuum. To experimentally validate our isotropic emission, near-field distribution is measured which is in good agreement with theoretical simulation. Indeed, if one particularly selects an infinitely short source, it is much closer to the ideal point source, and, therefore, the radiation is approximately isotropic. The perfect isotropy is gradually degraded when the source becomes longer than a singular point. It is, thus, worthwhile mentioning that we demonstrated the isotropic performance for a half-wavelength dipole antenna, which is supposed to have a well-defined ∞-shape radiation pattern.

As depicted by the ray tracing for Poynting vectors in Fig. 1, a directive antenna in Fig. 1(a) (a current source with extended length) emitting along $\pm 90°$ directions is transformed to be emitting isotropically along all directions in Fig. 1(c), when an appropriately designed metamaterial surrounds the extended source. The photorealistic ray tracing in Fig. 1(b) reveals that a pin-hole camera (receiver) placed in the center will see a landscape where the zones in the vicinity of $-90°$ and $+90°$ directions are more clearly resolved. Once metamaterial corresponding to the space transformation delimited by the blue circle in Fig. 1(c) is introduced and placed around the directive source, the entire panorama is more evenly captured by the central camera as shown in Fig. 1(d).

The outermost region is maintained throughout the process. We exponentially stretch all the space enclosed by the outermost boundary such that the center area is expanded more in comparison to the parts near the outer boundary of the region (limited by the diameter D). Thus, any source placed in the center region will function equivalently as another virtual source of much reduced dimension. If the

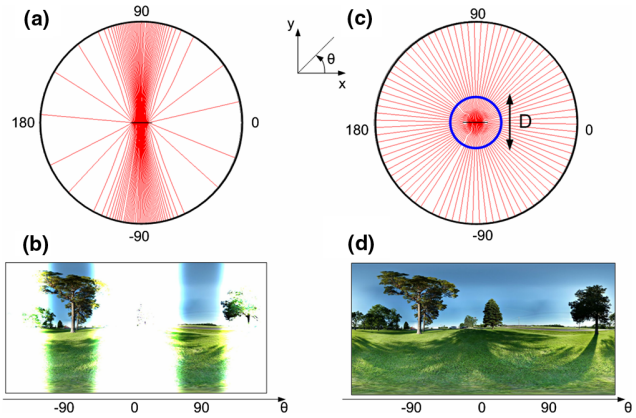

FIG. 1 (color online). A directive source emitting in the air as represented with the line of the Poynting vector (a) an equivalent receptor will see just two major part of a landscape. (b) An appropriate material is added in the central zone to create an isotropic radiation as represented with the Poynting vector (c). A receptor will see the entire landscape (d).

transformation is well manipulated, i.e., the expansion is complemented by the compression, perfect impedance matching at the boundary of the material can be achieved with no reflection.

Intuitively, the best transformation for isotropic radiation would have been to redistribute the angular component of the polar coordinates with a certain function $\theta' = g(r, \theta)$. The function g is able to make the source appear as a point by changing the direction of the light flow with an additional angular parameter in the transformation. Though it works with perfect theoretical permittivity and permeability parameters, the components are nondiagonal in polar coordinates. This transformation adversely results in metamaterials with stringently high values of permittivity and permeability which are difficult to realize, if not impossible. We have instead selected a radial transformation $r' = f(r, \theta)$ which leads to more plausible material parameters. It is noteworthy that this transformation optic method can approach near-perfect isotropy by significantly reducing the size of the physical dipole, though it may not be able to ideally reach the extreme equivalence of one point source considering the fabrication capability of metamaterials. The idea of the transformation is to reduce the size of the source such that it becomes a point source which is the only possible isotropic radiator. To do so, a space expansion is assured around the source, making its size appear very small with regard to the operating wavelength. This is then further covered by a compressed space in order to produce perfect impedance matching. Mathematically, the transformation has an exponential form and is given by [37]:

$$r' = \alpha(1 - e^{qr}), \qquad \theta' = \theta, \qquad z' = z, \tag{1}$$

with $\alpha = (D/2)(1/1 - \mathrm{e}^{(qD/2)})$, where α is a function of the dimension of our material. Both α and q are constants.

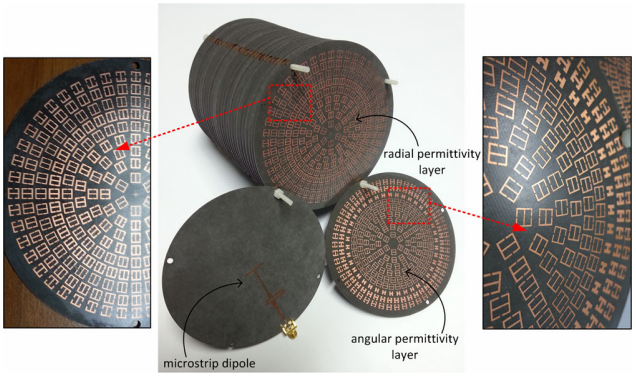

FIG. 2 (color online). Photography of the fabricated prototype consisting of alternating radial and angular electric permittivity metamaterial layers. In the experiment, a microstrip dipole antenna is used as the radiating source in the center of the stack.

Also, q must be negative for impedance matching and is the expansion factor of the stretched space. When q is high and close to zero, there is no change in the radiation pattern. On the contrary, a low q such as $q = -50$ leads to a nearly perfect isotropic radiation pattern. Interestingly, a full-parameter cloak has been suggested for one-directional invisibility [38] and it is challenging to design a full-parameter omnidirectional dipole hitherto. Therefore, the material derived from the rigorous transformation is still simplified due to fabrication constraints.

A dipole antenna operating at 10 GHz on a dielectric substrate (Fig. 2) is used as a radiating source along the y axis. Our surrounding material made of alternating layers of electric angular and radial metamaterial permittivity transforms the directive emission in the xy plane of the dipole into an isotropic one. Choosing a polarized electromagnetic field along the z direction fixes $\mu_{zz} = 1$, and we control $\varepsilon_{\theta\theta}$ and ε_{rr} only. The material is composed of nine different regions where radial and angular permittivities are not constant. We built the metamaterial from 30 layers of dielectric boards on which subwavelength resonant structures are printed. Fifteen layers contain artificial electric resonators [39] which assure radial permittivity. The remaining layers control angular permittivity. Each layer is divided into nine zones of metamaterial cells representing the inhomogeneous parameter distribution. The design geometries of these zones and their metamaterial cells has been provided in Supplemental Material [40]. The layers are stacked in an alternating manner, with a constant air spacing of 3.3 mm between neighboring layers. The overall dimensions of our antenna are $RH = 5$ cm $\times$ 12 cm, where R and H represent, respectively, the radius and the height of the antenna.

We present the metamaterial building blocks in Fig. 3(a) that meet the required parameters along radial and angular directions [shown in Fig. 3(c)]. The cell consists of two types of electric-field-driven LC resonators, as shown in Fig. 3(b). The metamaterial building block is not periodic, and two types of elementary resonators are optimized in one go since common parameters are shared. The distribution in Fig. 3(c) presents material parameters that we have discretized from an original continuous profile into nine regions of the metamaterial used for experimental validation. The imaginary parts (shown in the Supplemental Material [40] Fig. S3) of the material parameters are very low, suggesting negligible losses in the transformation medium.

The simulated cell is presented in Fig. 3(b). The permittivities ε_{rr} and $\varepsilon_{\theta\theta}$ can be achieved in a composite electric-field-driven LC resonator (ELC), thus providing electric responses that can be tailored. Taking the layout constraints under consideration, we chose a rectangular unit cell with dimensions $L_r = 5$ mm except for the first zone where we set $L_r = 20/3$ mm. We choose $L_\theta = (\pi/NL_r)[R_n^2 - R_{n-1}^2]$, where N represents the number of patterns in the nth zone and R_n is the radius of the nth zone. The desired ε_{rr} and $\varepsilon_{\theta\theta}$ were retrieved from S parameters by tuning geometric parameters of the resonators as

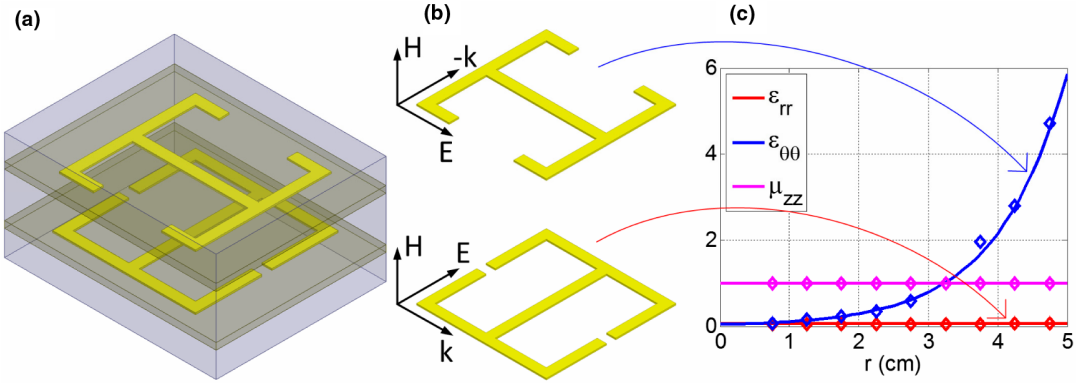

FIG. 3 (color online). (a) Metamaterial unit cell. (b) Each cell is composed of two electric-field-driven LC resonators enabling two varying parameters ε_{rr} and $\varepsilon_{\theta\theta}$. (c) The parameters from simplified transformation: theoretical values (continuous lines) and retrieved values based on the metamaterial cells (markers). It shows that $\varepsilon_{\theta\theta}$ ranges from 0.07 to 4.71 while ε_{rr} varies from 0.05 to 0.07.

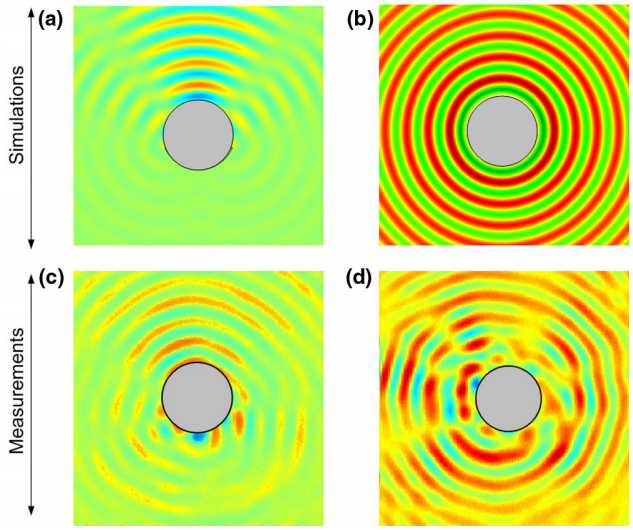

FIG. 4 (color online). Near-field scanning experiment in comparison with simulations. Magnitude of the electric field for the dipole source in simulation (a) and in measurement (c). Magnitude of the electric field of the dipole source and with the material defined with transformation optics in simulation (b) and in measurement (d). The mappings are shown at 10.8 GHz.

illustrated in Fig. 3(b). The discrete set of simulations and extractions are interpolated to obtain intermittent values of the geometric parameters that yield the material properties in Fig. 3(c). We observe that ε_{rr} takes on values close to zero. This is a consequence of setting q to -50 to achieve near-perfect isotropic emission in the xy plane. Impedance matching is assured in the proposed implementation. The operating frequency is selected set to approximately 10 GHz. This ensures $\lambda/L_r > 6$, where λ is the wavelength in free space. The design parameters of the unit cells and their retrieved parameters have been listed in the tables in Supplemental Material [40].

We present in Fig. 4(a) the theoretical result of the z component of electric field emanating from an ideal dipole antenna. When the dipole is surrounded with the metamaterial, the omnidirectional radiation can be obtained. This is presented in Fig. 4(b). The experimental verifications have been unambiguously demonstrated in Fig. 4(c) [measured radiation of Fig. 4(a)] and 4(d) [measured radiation of Fig. 4(b), respectively. An isotropic emission from an actual dipole antenna was thereby realized at originally a nonisotropic plane and measured by the near-field mapping of the antenna's radiation. It reveals that the directive radiation can be metamorphosed to be isotropic by the proposed metamaterials. The experimental setup was employed to probe the near field of the antenna's radiation. The E field is scanned by a field-sensing monopole probe connected to the network analyzer by a coaxial cable. The probe was mounted on two orthogonal linear translation stages (computer-controlled Newport MM4006), so that the probe could be translated with respect to the radiation region of the antenna. By stepping the field sensor in small increments and recording the field amplitude and phase at every step, a full 2-D spatial field map of the microwave near-field pattern can be acquired in the free-space radiation region. The total scanning area covers 400×400 mm^2 with a step resolution of 2 mm in lateral dimensions. Microwave absorbers are applied around the measurement stage in order to suppress undesired scattered radiations at the boundaries.

In this Letter, we have designed, fabricated, and demonstrated an almost isotropically emitting dipole source verified in the microwave regime, the principle of which is scalable in all frequencies of light especially for the currently used metmatateriall that does not rely on magnetic response. An anisotropic nonmagnetic metamaterial is realized by the ELC model, and its electric parameters are finely adjusted to meet the required material in the physical space which is manipulated by a particular radial transformation function to achieve omnidirectional emission in both xy and yz planes. Our result, verified by experimental measurements, paves the way for manipulating emission characteristics of various sources, fabricating nonmagnetic metamaterials for optical applications and enabling unprecedented applications in a wide spectrum of waves.

We thank Prof. Shuang Zhang in University of Birmingham for stimulating discussions and comments. We thank Eric Hendrix and Ahmed Mehmood for language editing, and grateful for the assistance from Alireza Akbarzadeh in Fig. 1. The authors acknowledge the support from French-UK project MIMICRA No. B0883 GEM1 ERG. C. W. Q. acknowledges the partial financial support from TDSI/11-004/1A from Temasek Defence Systems Institute.

[1] W. Cai, U. K. Chettiar, A. V. Kildishev, and V. M. Shalaev, Nat. Photonics **1**, 224 (2007).
[2] D. A. Genov, S. Zhang, and X. Zhang, Nat. Phys. **5**, 687 (2009).
[3] M. Rahm, S. A. Cummer, D. Schurig, J. B. Pendry, and D. R. Smith, Phys. Rev. Lett. **100**, 063903 (2008).
[4] U. Leonhardt, Science **312**, 1777 (2006).
[5] J. B. Pendry, D. Schurig, and D. R. Smith, Science **312**, 1780 (2006).
[6] D. Schurig, J. J. Mock, B. J. Justice, S. A. Cummer, J. B. Pendry, A. F. Starr, and D. R. Smith, Science **314**, 977 (2006).
[7] R. Liu, C. Ji, J. J. Mock, J. Y. Chin, T. J. Cui, and D. R. Smith, Science **323**, 366 (2009).
[8] C. A. Balanis, *Antenna Theory* (Wiley, New York, 1997).
[9] D. Roddy and J. Coolen, *Electronic Communications* (Prentice Hall, New York, 1999).
[10] L. E. J. Brouwer, KNAW Proc. **11**, 850 (1909).
[11] H. F. Mathis, Proc. IRE **39**, 970 (1951).
[12] W. K. Saunders, in *On the Unity Gain Antenna*, edited by E. C. Jordan, Electromagnetic Theory and Antennas (Macmillan, New York, 1963), Part 2, p. 1125.

[13] F. Wilczek, Phys. Rev. Lett. **58**, 1799 (1987).
[14] Y. Lai, J. Ng, H. Y. Chen, D. Z. Han, J. J. Xiao, Z.-Q. Zhang, and C. T. Chan, Phys. Rev. Lett. **102**, 253902 (2009); W. X. Jiang and T. J. Cui, Phys. Rev. E **83**, 026601 (2011).
[15] J. Soric, S. Maci, N. Engheta, and A. Alu, IEEE Trans. Antennas Propag. **61**, 33 (2013).
[16] Y. Kim, Microw. Opt. Technol. Lett. **55**, 375 (2013).
[17] S. L. Chen, K. H. Lin, and R. Mittra, Electron. Lett. **45**, 923 (2009).
[18] Q. Cheng, W. X. Jiang, and T. J. Cui, Phys. Rev. Lett. **108**, 213903 (2012).
[19] Y. Yuan, N. Wang, and J. H. Lim, Europhys. Lett. **100**, 34 005 (2012).
[20] W. Cai, U. K. Chettiar, A. V. Kildishev, V. M. Shalaev, and G. W. Milton, Appl. Phys. Lett. **91**, 111105 (2007).
[21] J. Li and J. B. Pendry, Phys. Rev. Lett. **101**, 203901 (2008).
[22] L. H. Gabrielli, J. Cardenas, C. B. Poitras, and M. Lipson, Nat. Photonics **3**, 461 (2009).
[23] U. Leonhardt and T. Tyc, Science **323**, 110 (2009).
[24] J. Valentine, J. Li, T. Zentgraf, G. Bartal, and X. Zhang, Nat. Mater. **8**, 568 (2009).
[25] T. Ergin, N. Stenger, P. Brenner, J. B. Pendry, and M. Wegener, Science **328**, 337 (2010).
[26] M. W. McCall, A. Favaro, P. Kinsler, and A. A. Boardman, J. Opt. **13**, 024003 (2011).
[27] A. Greenleaf, Y. Kurylev, M. Lassas, and G. Uhlmann, Phys. Rev. Lett. **99**, 183901 (2007).
[28] D. H. Kwon and D. H. Werner, New J. Phys. **10**, 115023 (2008).
[29] M. Rahm, D. A. Roberts, J. B. Pendry, and D. R. Smith, Opt. Express **16**, 11 555 (2008).
[30] D. A. Roberts, M. Rahm, J. B. Pendry, and D. R. Smith, Appl. Phys. Lett. **93**, 251111 (2008).
[31] J. Huangfu, S. Xi, F. Kong, J. Zhang, H. Chen, D. Wang, B.-I. Wu, L. Ran, and J. A. Kong, J. Appl. Phys. **104**, 014502 (2008).
[32] P. H. Tichit, S. N. Burokur, and A. de Lustrac, Opt. Express **18**, 767 (2010).
[33] U. Leonhardt and T. Tyc, New J. Phys. **10**, 115026 (2008).
[34] Y. Luo, J. Zhang, L. Ran, H. Chen, and J. A. Kong, IEEE Antennas Wireless Propagat. Lett. **7**, 509 (2008).
[35] F. Kong, B.-I. Wu, J. A. Kong, J. Huangfu, S. Xi, and H. Chen, Appl. Phys. Lett. **91**, 253509 (2007).
[36] P. H. Tichit, S. N. Burokur, D. Germain, and A. de Lustrac, Phys. Rev. B **83**, 155108 (2011).
[37] J. Allen, N. Kundtz, D. A. Roberts, S. A. Cummer, and D. R. Smith, Appl. Phys. Lett. **94**, 194101 (2009).
[38] C. Garcia-Meca, A. Martinez, and U. Leonhardt, Opt. Express **19**, 23 743 (2011).
[39] D.-H. Kwon, IEEE Antennas Wireless Propagat. Lett. **11**, 1125 (2012).
[40] See Supplemental Material at http://link.aps.org/supplemental/10.1103/PhysRevLett.111.133901 for detailed design of the ELC metamaterial cells and effective parameter extraction.

Annexe 3.8

P.-H. Tichit, S. N. Burokur, A. de Lustrac

« Spiral-like multi-beam emission via transformation electromagnetics »

Journal of Applied Physics, accepted December 2013

Spiral-like multi-beam emission via transformation electromagnetics

Paul-Henri Tichit,[1] Shah Nawaz Burokur,[1,2] and André de Lustrac[1,2]

Affiliations: [1]IEF, Univ. Paris-Sud, CNRS, UMR 8622, 91405 Orsay Cedex, France.

[2]Univ. Paris-Ouest, 92410 Ville d'Avray, France.

ABSTRACT: Transformation optics offers an unconventional approach for the design of novel radiating devices. Here we propose an electromagnetic metamaterial able to split an isotropic radiation into multiple directive beams. By applying transformations that modify distance and angles, we show how the multiple directive beams can be steered at will. We describe transformation of the metric space and the calculation of the material parameters. Different transformations are proposed for a possible physical realization through the use of engineered artificial metamaterials. Full wave simulations are performed to validate the proposed approach. The idea paves the way to interesting applications in various domains in microwave and optical regimes.

Electronic mail: paul-henri.tichit@u-psud.fr, shah-nawaz.burokur@u-psud.fr, andre.de-lustrac@u-psud.fr

INTRODUCTION

In the telecommunications domain, there are actually growing interests in the miniaturization of devices, particularly for antennas in transport and aeronautical fields. We therefore need to couple miniaturization with the design of smart multi-function antennas so as to reduce the growing number of antenna systems in the environment. In most cases it is the physics itself that limits the possibility of size reduction and the physical realization, justifying the exploration of innovative ways to overcome such limitations. The transformation electromagnetics (or coordinate transformation) concept [1-5], an innovative approach to design new class of electromagnetic devices, can prove its usefulness for miniaturization since it allows making a link between space, time and material. In a mathematical point of view, this tool consists in generating a new transformed space from an initial one where solutions of Maxwell's equations are known. The result is a direct link between the permittivity and permeability of the material and the metric tensor of the transformed space containing the desired electromagnetic properties [6-8]. This method was first used by U. Leonhardt [1] and J. B. Pendry [2] to design an electromagnetic invisibility cloak in 2006 [9]. Since then, the invisibility cloak has been a subject of intensive studies [10] and later, other systems resulting from coordinate transformation have emerged. Thus, concentrators [11], rotators [12], lenses [13-16], artificial wormholes [17], waveguide bends and transitions [18-23], electromagnetic cavities [24-25], illusion systems [26-27] and antennas [28-36] have emerged. Recently, transformation optics concept has been applied to transform the signature of a radiating source [37]. We have shown that a linear space compression followed by a space expansion, makes the radiation pattern of a small aperture antenna appear like that of a large one. By the use of a metamaterial shell, the apparent size of a small source presenting an isotropic radiation was transformed into a larger one with a directive radiation. In most cases, the generated materials are inhomogeneous and anisotropic since the created virtual spaces make use of arbitrary coordinates.

Devices generated by transformation optics can then be fabricated through the use of metamaterials, which are subwavelength engineered artificial structures that derive their properties from their structural geometry.

In this present paper, we firstly extend the concept proposed in [37] to the transformation of a small antenna emitting an isotropic radiation into one emitting two directive beams that can be steered. We further propose to create multiple directive beams from an isotropic radiation by applying a transformation that decomposes the initial space into multiple segmented ones. We demonstrate that adjusting the transformation enables to control the number and the angular direction of the radiated beams. The material parameters generated from the transformation are discussed and the results are validated by numerical simulations performed using finite element method based Comsol MULTIPHYSICS software.

TRANSFORMATION FORMULATIONS

We consider a radiating source with an aperture much smaller than the wavelength, therefore isotropic in the xOy plane. To achieve the transformation of this small aperture source into two much larger ones that are steered, we discretize the space around the latter radiating element into two different regions; a first zone which will make our source appear bigger than its real physical size and radiate a directive beam and a second zone which will split the directive beam into two steered beams. The operating principle is shown by the schematic in Fig. 1. In the first zone illustrated by the circular region of radius $r = R_1/q_1$ [Fig. 1(a)], our space is described by polar coordinates and the angular part of these coordinates remains unchanged. A purely high permittivity dielectric medium can be used for this zone to increase the apparent electromagnetic size of the antenna producing a directive emission. In the second zone defined between circular regions with radius R_1/q_1 and R_2, the transformation consists firstly in an impedance matching with the

surrounding space by space expansion and secondly a transformation of the angular part in function of the radial part which assures perfect impedance matching at some specific locations on the external material boundary [Fig. 1(b)]. Figs. 1(c) and 1(d) present the transformations used respectively in the two regions. The radial part transformation shown in Fig. 1(c) is linear in both regions. However, the angular part transformation in Fig. 1(d) shows no transformation in region 1, since only the radial part was considered for the transformation in this region. The angular part transformation in region 2 can be performed using three different transformations: a positive exponential transformation, a negative exponential transformation, and a linear one. Two free parameters q_1 and q_2 allows adjusting electromagnetic achievable parameters of the metamaterials for realization. We denote below and in the rest of the paper the two different zones by the index i, where $i = 1$ corresponds to the first zone and $i = 2$ to the second zone.

In a space point of view, the virtual space which assures the properties of our material has been designed such that the angular lines are curved in function of the position in the space (red trace in Fig. 1(b)) but also the radial lines which are extended or compressed (green trace in Fig. 1(b)). The boundary material is fixed and has a radius R_2 represented by the dark blue line.

Mathematically, the transformation in the different regions can be written as:

$$\begin{cases} r' = f_i(r) \\ \theta' = g_i(r,\theta) \\ z' = z \end{cases} \tag{1}$$

The Jacobian matrix of the transformation is given in the cylindrical coordinate system as:

$$\overline{\overline{J_{cyl}}} = \begin{pmatrix} \frac{\partial r'}{\partial r} & \frac{\partial r'}{\partial \theta} & \frac{\partial r'}{\partial z} \\ \frac{\partial \theta'}{\partial r} & \frac{\partial \theta'}{\partial \theta} & \frac{\partial \theta'}{\partial z} \\ \frac{\partial z'}{\partial r} & \frac{\partial z'}{\partial \theta} & \frac{\partial z'}{\partial z} \end{pmatrix} = \begin{pmatrix} f_{i,r} & 0 & 0 \\ g_{i,r} & g_{i,\theta} & 0 \\ 0 & 0 & 1 \end{pmatrix} \tag{2}$$

where $f_{i,r}$, $g_{i,r}$ and $g_{i,\theta}$ represent the respective derivatives of f_i with respect to r and g_i with respect to r and θ. To calculate permittivity and permeability tensors directly from the coordinate transformation in the cylindrical and orthogonal coordinates, we need to express the metric tensor in the initial and virtual spaces. The final Jacobian matrix needed for the permeability and permittivity tensors of our material is then given as:

$$\overline{\overline{J}}_i = \begin{pmatrix} f_{i,r} & 0 & 0 \\ r' g_{i,r} & \dfrac{r'}{r} g_{i,\theta} & 0 \\ 0 & 0 & 1 \end{pmatrix} \tag{3}$$

The coefficient of our material can be written as $\overline{\overline{\psi}}_i = \dfrac{J_i J_i^T}{\det(J_i)}$ in the cylindrical coordinates. The material parameters obtained using the transformation in Eq. (1) are:

$$\begin{cases} (\psi_{rr})_i = \dfrac{r f_{i,r}}{r' g_{i,\theta}} \\ (\psi_{r\theta})_i = \dfrac{r g_{i,r}}{g_{i,\theta}} \\ (\psi_{\theta\theta})_i = \dfrac{r r' g_{i,r}^2 + \dfrac{r'}{r} g_{i,\theta}^2}{g_{i,\theta} f_{i,r}} \\ (\psi_{zz})_i = \dfrac{r}{r' g_{i,\theta} f_{i,r}} \end{cases} \tag{4}$$

These parameters are relatively simple for the transformation in the first zone since it leads to constant values. But the permittivity and permeability components have to be expressed in the Cartesian coordinate system so as to have a perfect equivalence in Maxwell's equations and also to physically design our device. Using matrix relations between cylindrical and Cartesian coordinates, we have:

$$\overline{\overline{\varepsilon}} = \begin{pmatrix} \psi_{xx} & \psi_{xy} & 0 \\ \psi_{yx} & \psi_{yy} & 0 \\ 0 & 0 & \psi_{zz} \end{pmatrix} \varepsilon_0 \qquad \overline{\overline{\mu}} = \begin{pmatrix} \psi_{xx} & \psi_{xy} & 0 \\ \psi_{yx} & \psi_{yy} & 0 \\ 0 & 0 & \psi_{zz} \end{pmatrix} \mu_0$$

$$\text{with } \begin{cases} \psi_{xx} = \psi_{rr}\cos^2(\theta) + \psi_{\theta\theta}\sin^2(\theta) - \psi_{r\theta}\sin(2\theta) \\ \psi_{xy} = \psi_{yx} = (\psi_{rr} - \psi_{\theta\theta})\sin(\theta)\cos(\theta) + \psi_{r\theta}\cos(2\theta) \\ \psi_{yy} = \psi_{rr}\sin^2(\theta) + \psi_{\theta\theta}\cos^2(\theta) + \psi_{r\theta}\sin(2\theta) \end{cases} \quad (5)$$

To apply our proposed coordinate transformation, we have considered a radial compression of the space in region 1. This leads to a material with high permittivity and permeability tensors. For the transformation, we choose $r' = f_1(r) = q_1 r$ with q_1 being a coefficient lower than 1. The physical meaning of the factor q_1 is the compression factor applied in the central region. This factor has a transition value which can be defined as $q_0 = R_1 / R_2$ where the material of the matching zone (region 2 in Fig. 1(d)) switch from a right-handed (positive refractive index) to a left-handed (negative refractive index) material. Indeed when $q_1 < q_0$ the material presents a negative index and the final apparent size of the source can be larger than $2R_2$. Now if this embedded source has a small aperture, much smaller than the wavelength, then after transformation this antenna will behave like one with a large aperture, typically q_1 times larger and potentially much greater than the wavelength. A small aperture antenna is well known to radiate in an isotropic manner. The same antenna embedded in the material defined by Eq. (5) will present a directive radiation and therefore electrically appear as if its size is larger than the working wavelength.

To assure a good impedance matching for the radiated fields and create multiple steered beams, a second zone (region 2) is added around region 1. To design this zone, we perform a transformation on both the radial and the angular parts. The transformation on the radial part is always a linear transformation and takes the form:

$$r' = f_2(r) = \frac{q_1(R_2 - R_1)r + R_1 R_2(q_1 - 1)}{q_1 R_2 - R_1} \quad (6)$$

However, the angular part transformation can be of two different types in order to divide the space into different segments and to steer the beam in each segment. The first studied transformation is a linear one that takes the form:

$$\theta' = g_2(r,\theta) = \frac{\theta}{1+N/2} + \alpha\left(\frac{r-R_1}{R_2-R_1}\right) \tag{7}$$

The other transformation have an exponential form that can be expressed as:

$$\theta' = g_2(r,\theta) = \frac{\theta}{1+N/2} + \alpha\left(\frac{e^{q_2(r-R_1)}-1}{e^{q_2(R_2-R_1)}-1}\right) \tag{8}$$

The parameter α is an angle which can be viewed as the output angle of the transformed material. It is introduced in the transformation in order to rotate the beam in the material. The transformations used are general and to validate the possibility of theses transformations, we need to consider different cases. The denominator $1+N/2$ of the function θ' have to be an integer meaning that N can only take 0 or positive even values. For example when $N = 0$, there is no multi-beam creation due to non-segmentation of the space.

To calculate the components of the electromagnetic tensors ψ_{ij} for linear transformation in both regions 1 and 2, the parameters considered are $R_1 = 5$ mm, $R_2 = 50$ mm, $q_1 = 1/7$, $N = 0$, $\alpha = 80°$. The frequency is set to 20 GHz and Fig. 2 shows the variation of the different components of the permittivity and permeability tensors. The components ε_{xx}, ε_{yy} and ε_{zz} are always positive but can be negative if the source appearance become larger. Only the non-diagonal term ε_{xy} takes both positive and negative values.

NUMERICAL VALIDATION OF THE BEAM STEERING DEVICE

In order to validate the proposed beam steering concept, we use the commercial software Comsol MULTIPHYSICS to perform numerical simulations of the different transformation cases

presented above. All the simulations are run in the microwave domain at 20 GHz. The validation of our design is performed in a two-dimensional configuration in a transverse electric mode (TEz) (E parallel to the *z*-axis). A current source of dimension d = 4 mm placed perpendicular to the *xy* plane is used as a radiating element. Continuity and matched conditions are applied respectively to the boundary of zone 1 and zone 2.

To verify our design, we fix R_1 = 5 mm and R_2 = 50 mm. The results obtained from linear transformations in both regions 1 and 2 with the material parameters of Fig. 2 are presented in Fig. 3. Since the size of the source is much smaller than the operating wavelength (λ_0 = 1.5 cm at 20 GHz), the radiation is isotropic in the *xy* plane, as shown in Fig. 3(a) for free space as surrounding medium. The electric field (Ez-component) distribution of the same linear source placed in both materials calculated by the transformations having parameters N = 0, α = 80° and q_1=1/7 is presented in Fig. 3(b). The radiating field is equivalent to a new source with dimension d/q_1=2.8 cm producing a 130° beam steering.

As stated earlier, the transformation in the second region allows creating multi-beams and steering them. The parameter N enables to vary the number of the radiated beams. However in Fig. 3, N is considered to be zero. Therefore, we should not be in presence of multi-beam. Such a scenario of two steered directive beams is the result of firstly the compression region 1 where the source appears as a large aperture radiator with two opposite directive beams as previously reported in [36], and secondly to the rotations in region 2 which enables to steer the beams. Figs. 3(c) and 3(d) show the norm of the total electric field in such configuration.

If we consider N different from zero, the device does not work properly since the two directive beams emanating from region 1 are not channeled properly into the different space segments. Therefore for $N \neq 0$, we need to have an isotropic beam emanating from region 1 in order to input the different space segments. Such a configuration is detailed in the next section.

SPIRAL-LIKE EMISSION OF MULTIPLE DIRECTIVE BEAMS

As stated, when considering $N \neq 0$, there must be no space compression in region 1. Fig. 4 shows the variation of the tensor for the exponential transformation case in region 2 and when N is different from zero, so as to be in a multi-beam configuration. The parameters are $q_1 = 1$, $q_2 = -30$, $N = 2$, $\alpha = 300°$.

In Fig. 5, the linear transformation of the radial part in region 2 is followed by an exponential one with N different from zero, $q_2 = -30$ and $\alpha = 300°$, corresponding to the material parameters presented in Fig. 4. Figs. 5(a)-(b) show the electric field distribution in the proposed device for $N = 2$. Two steered beams can be clearly observed.

The cases for $N = 4$ and $N = 6$ are respectively shown in Figs. 5 (e)-(f) and Figs. 5(g)-(h) respectively. In each case, the electromagnetic field is rotated in the material as shown in Figs. 5(c)-(d). When α increases, the radiation tends to be more and more tangential to the surface of the material, and the interferences observed in Fig. 5(g) between the emitted beams decrease in Fig. 5(h).

CONCLUSION

This work points out the use of transformation electromagnetics concept to design an artificial shell which allows creating multiple directive beams. The latter concept makes use of two transformations; the first one to compress space and the second one to divide and rotate it. Numerical simulations have confirmed the operating principle of the transformations. We have firstly shown that a very small source can emit two directive beams comparable to an antenna with a large aperture. These directive beams can then be steered in a desired direction. Furthermore, the concept has also been applied to create more than two directive steered beams. In this case, space

has to be divided into different segments so to channel directive beams from an isotropic source. For a possible future prototype fabrication, choosing a polarization in a fixed direction of the electromagnetic field will lead after the parameters reduction procedure to two variations of permittivity or permeability in a spiral-like eigen-base, which can be achieved by common metamaterial structures. This study shows the great possibilities that transformation electromagnetics can offer for the design and synthesis of new devices in both microwave and optical wavelength regimes.

References

1. J. B. Pendry and S. A. Ramakrishna, "Focusing light using negative refraction," J. Phys.: Condens. Matter **15**, 6345 (2003).
2. S. Guenneau, B. Gralak, and J. B. Pendry, "Perfect corner reflector," Opt. Lett. 30, 1204 (2005).
3. U. Leonhardt, "Optical conformal mapping," Science **312**, 1777 (2006).
4. J. B. Pendry, D. Schurig, and D. R. Smith, "Controlling electromagnetic fields," Science **312**, 1780 (2006).
5. D. Schurig, J. B. Pendry, and D. R. Smith, "Calculation of material properties and ray tracing in transformation media," Opt. Express **14**, 9794 (2006).
6. U. Leonhardt and T. G. Philbin, "General relativity in electrical engineering," New J. Phys. **8**, 247 (2006).
7. R. A. Crudo and J. G. O'Brien, "Metric approach to transformation optics," Phys. Rev. A **80**, 033824 (2009).
8. U. Leonhardt and T. G. Philbin, "Transformation optics and the geometry of light," Prog. Opt. **53**, 69 (2009).
9. D. Schurig, J. J. Mock, B. J. Justice, S. A. Cummer, J. B. Pendry, A. F. Starr, and D. R. Smith, "Metamaterial electromagnetic cloak at microwave frequencies," Science **314**, 977 (2006).
10. F. Zolla, S. Guenneau, A. Nicolet, and J. B. Pendry, "Electromagnetic analysis of cylindrical invisibility cloaks and mirage effect," Opt. Lett. **32**, 1069 (2007).
11. M. Rahm, D. Schurig, D. A. Roberts, S. A. Cummer, D. R. Smith, and J. B. Pendry, "Design of electromagnetic cloaks and concentrators using form-invariant coordinate transformations of Maxwell's equations," Photon. Nanostruct.: Fundam. Appl. **6**, 87 (2008).

12. H. Chen, B. Hou, S. Chen, X. Ao, W. Wen, and C. T. Chan, "Design and experimental realization of a broadband transformation media field rotator at microwave frequencies," Phys. Rev. Lett. **102**, 183903 (2009).
13. D.-H. Kwon and D. H. Werner, "Transformation optical designs for wave collimators, flat lenses and right-angle bends," New J. Phys. **10**, 115023 (2008).
14. M. Tsang and D. Psaltis, "Magnifying perfect lens and superlens design by coordinate transformation," Phys. Rev. B **77**, 035122 (2008).
15. N. Kundtz and D. R. Smith, "Extreme-angle broadband metamaterial lens," Nat. Mater. **9**, 129-132 (2010).
16. D. A. Roberts, N. Kundtz, and D. R. Smith, "Optical lens compression via transformation optics," Opt. Express **17**, 16535 (2009).
17. A. Greenleaf, Y. Kurylev, M. Lassas, and G. Uhlmann, "Electromagnetic wormholes and virtual magnetic monopoles from metamaterials," Phys. Rev. Lett. **99**, 183901 (2007).
18. A. Nicolet, F. Zolla and S. Guenneau, "A finite element modelling for twisted electromagnetic waveguides," Eur. J. Phys. Appl. Phys. **28**, 153 (2004).
19. M. Rahm, S. A. Cummer, D. Schurig, J. B. Pendry, and D. R. Smith, "Optical design of reflectionless complex media by finite embedded coordinate transformations," Phys. Rev. Lett. **100**, 063903 (2008).
20. M. Rahm, D. A. Roberts, J. B. Pendry, and D. R. Smith, "Transformation-optical design of adaptive beam bends and beam expanders," Opt. Express **16**, 11555 (2008).
21. J. Huangfu, S. Xi, F. Kong, J. Zhang, H. Chen, D. Wang, B.-I. Wu, L. Ran, and J. A. Kong, "Application of coordinate transformation in bent waveguide," J. Appl. Phys. **104**, 014502 (2008).

22. D. A. Roberts, M. Rahm, J. B. Pendry, and D. R. Smith, "Transformation-optical design of sharp waveguide bends and corners," Appl. Phys. Lett. **93**, 251111 (2009).
23. P.-H. Tichit, S. N. Burokur, and A. de Lustrac, "Waveguide taper engineering using coordinate transformation technology," Opt. Express **18**, 767 (2010).
24. V. Ginis, P. Tassin, C. M. Soukoulis, and I. Veretennicoff, "Confining light in deep subwavelength electromagnetic cavities," Phys. Rev. B **82**, 113102 (2010).
25. V. Ginis, P. Tassin, J. Danckaert, C. M. Soukoulis, and I. Veretennicoff, "Creating electromagnetic cavities using transformation optics," New J. Phys. **14**, 033007 (2012).
26. Y. Lai, J. Ng, H. Chen, D. Han, J. Xiao, Z.-Q. Zhang, and C. T. Chan, "Illusion optics: the optical transformation of an object into another object," Phys. Rev. Lett. **102**, 253902 (2009).
27. W. H. Wee and J. B. Pendry, "Shrinking optical devices," New J. Phys. **11**, 073033 (2009).
28. W. Lu, Z. Lin, H. Chen, and C. T. Chan, "Transformation media based super focusing antenna," J. Phys. D: Appl. Phys. **42**, 212002 (2009).
29. Y. Luo, J. Zhang, L. Ran, H. Chen, and J. A. Kong, "Controlling the emission of electromagnetic source," PIERS Online **4**, 795 (2008).
30. J. Allen, N. Kundtz, D. A. Roberts, S. A. Cummer, and D. R. Smith, "Electromagnetic source transformations using superellipse equations," Appl. Phys. Lett. **94**, 194101 (2009).
31. B. I. Popa, J. Allen, and S. A. Cummer, "Conformal array design with transformation electromagnetics," Appl. Phys. Lett. **94**, 244102 (2009).
32. P.-H. Tichit, S. N. Burokur, D. Germain, and A. de Lustrac, "Design and experimental demonstration of a high-directive emission with transformation optics," Phys. Rev. B **83**, 155108 (2011).
33. P.-H. Tichit, S. N. Burokur, D. Germain, and A. de Lustrac, "Coordinate transformation based ultra-directive emission," Elec. Lett. **47**, 580 (2011).

34. Z. H. Jiang, M. D. Gregory, and D. H. Werner, "Experimental demonstration of a broadband transformation optics lens for highly directive multibeam emission," Phys. Rev. B **84**, 165111 (2011).
35. P.-H. Tichit, S. N. Burokur, and A. de Lustrac, "Transformation media producing quasi-perfect isotropic emission," Opt. Express **19**, 20551 (2011).
36. P.-H. Tichit, S. N. Burokur, C.-W. Qiu, and A. de Lustrac, "Experimental verification of isotropic radiation from a coherent dipole source via electric-field-driven LC resonator metamaterials," Phys. Rev. Lett. **111**, 133901 (2013).
37. P.-H. Tichit, S. N. Burokur, and A. de Lustrac, "Reducing physical appearance of electromagnetic sources," Opt. Express **21**, 5053 (2013).

Figure captions

Figure 1: Representation of the proposed coordinate transformation: (a) initial space and (b) virtual space. The device is composed of 2 regions (green and blue) with radius R_1 and R_2. The first zone increases the apparent size of the source. The second zone allows creating several radiation beams and rotating them in a spiral way as indicated by the transformation of the red line. (c) The r-dependent linear transformation in the first zone. (d) The θ-dependent transformation in the second zone which can be linear or exponential (positive or negative).

Figure 2: Variation of the components in Cartesian coordinates of the region 2. The permittivity and permeability are respectively plotted for the linear transformation with $q_1 = 1/7$, $R_1 = 5$ mm, $R_2 = 50$ mm, $N = 0$ and $\alpha = 80°$.

Figure 3: Electric field distribution at 20 GHz of a linear source with dimension $d = 6$ mm: (a) radiating in free space, (b) embedded in a metamaterial shell defined by linear transformations having parameters $N = 0$, $\alpha = 80°$ and $q_1=1/7$. (c)-(d) Norm of the electric field.

Figure 4: Variation of the components in Cartesian coordinates of the region 2. The permittivity and permeability are respectively plotted for the exponential transformation with $q_1 = 1$, $q_2 = -30$, $R_1 = 5$ mm, $R_2 = 50$ mm, $N = 2$ and $\alpha = 300°$.

Figure 5: Electric field (z-component) distribution of a source with dimension $d = 4$ mm with material defined with $\alpha = 130°$ (a, c, e, g) and 300° (b, d, f, h) at 20 GHz. Multi-beam emission is shown for $N = 2$ (a, b), $N = 4$ (e, f), $N = 6$ (g, h). Electric field distribution for $q_1 = 1$, $\alpha = 130°$ and

300°, q_2 = -30: the electromagnetic field is rotated in the material as shown in the zooms presented in parts (c) and (d).

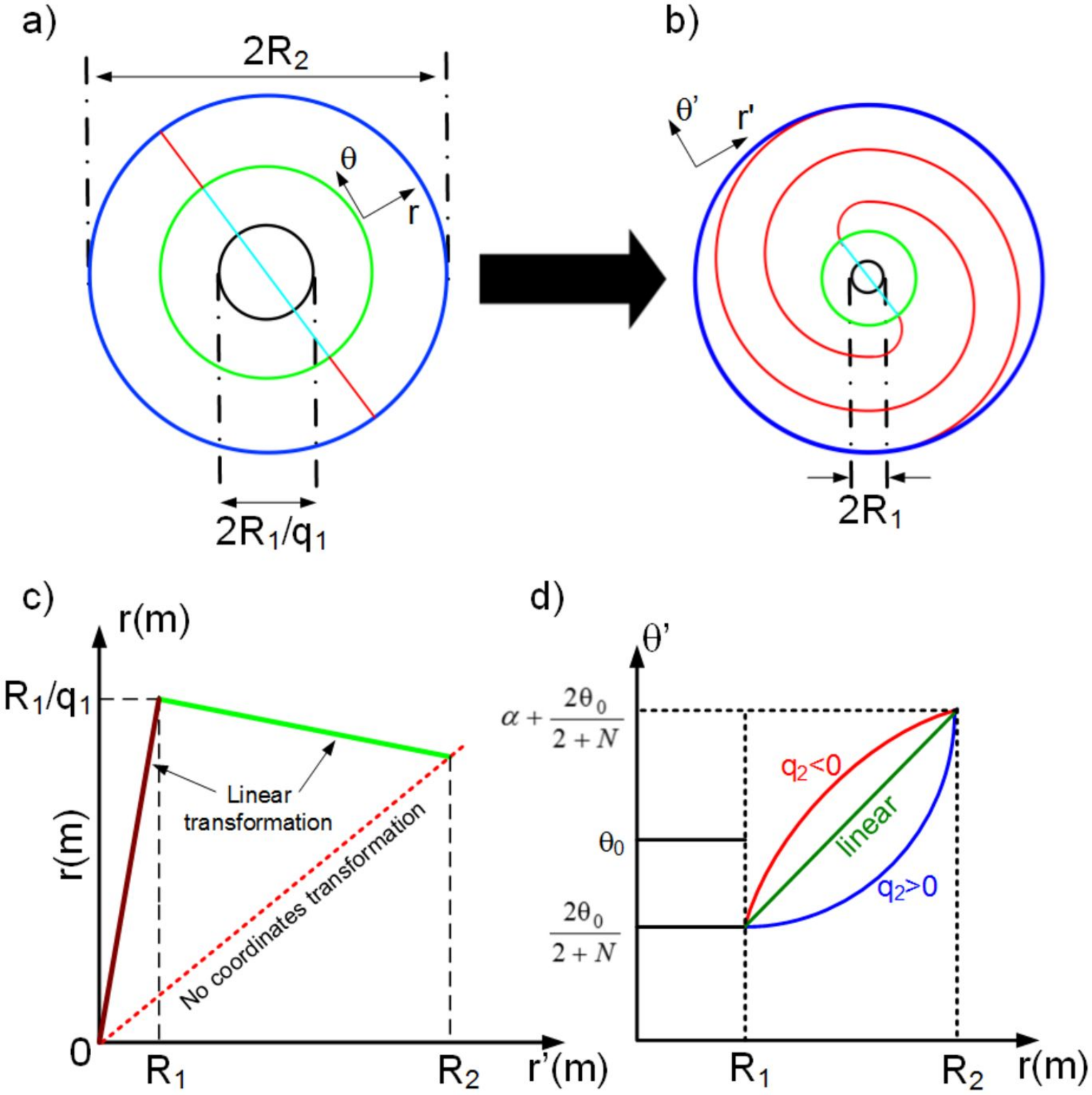
a)
2R2
θ
r
2R1/q1
b)
θ'
r'
2R1
c)
r(m)
R1/q1
r(m)
Linear
transformation
No coordinates transformation
0
R1
R2
r'(m)
d)
θ'
α + 2θ0/(2+N)
θ0
2θ0/(2+N)
q2<0
linear
q2>0
R1
R2
r(m)

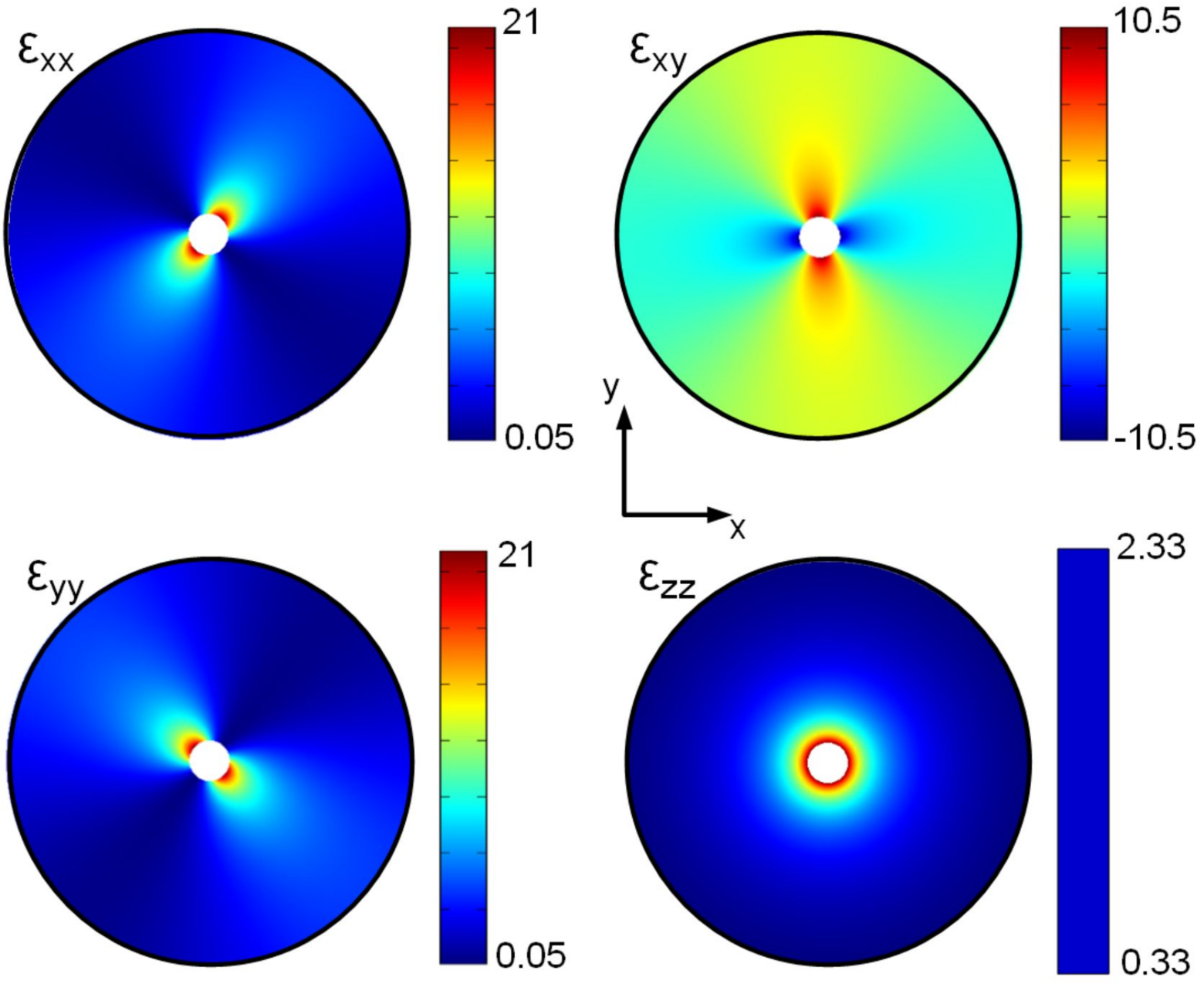
ε_{xx}
21
0.05
ε_{xy}
10.5
-10.5
y
x
ε_{yy}
21
0.05
ε_{zz}
2.33
0.33

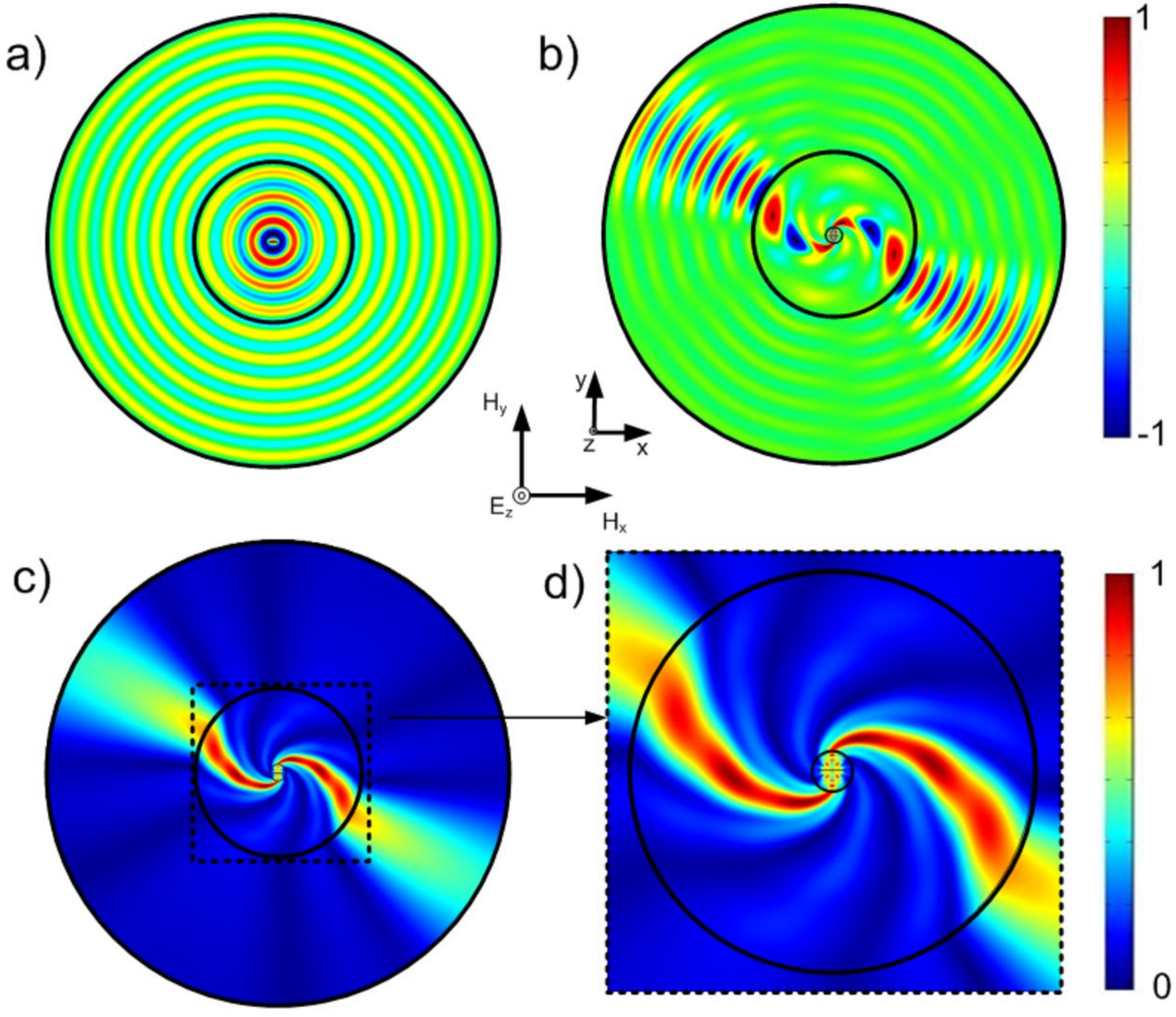
a)
b)
1
-1
y
z
x
H_y
E_z
H_x
c)
d)
1
0

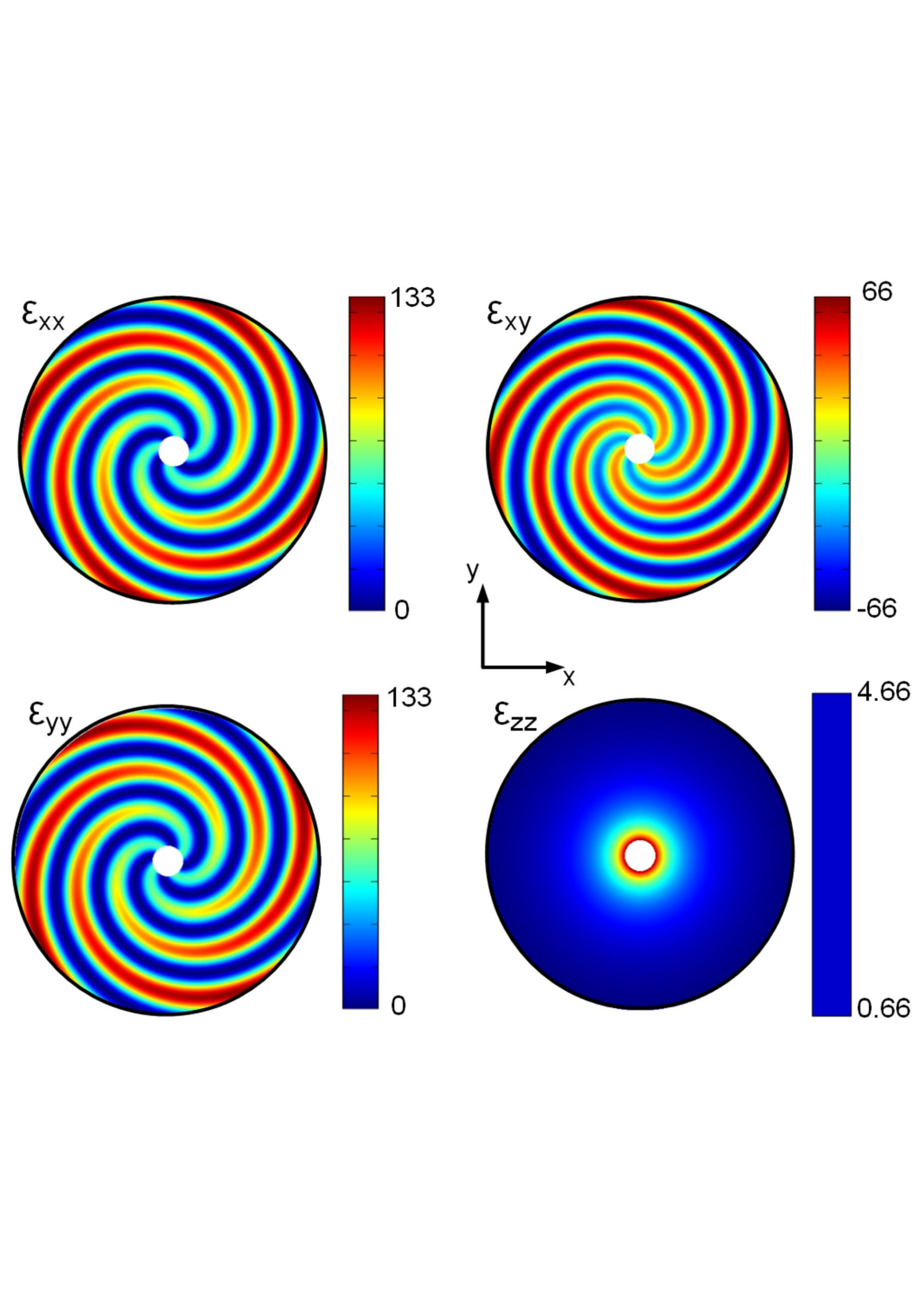
ε_{xx}
133
0
ε_{xy}
66
-66
y
x
ε_{yy}
133
0
ε_{zz}
4.66
0.66

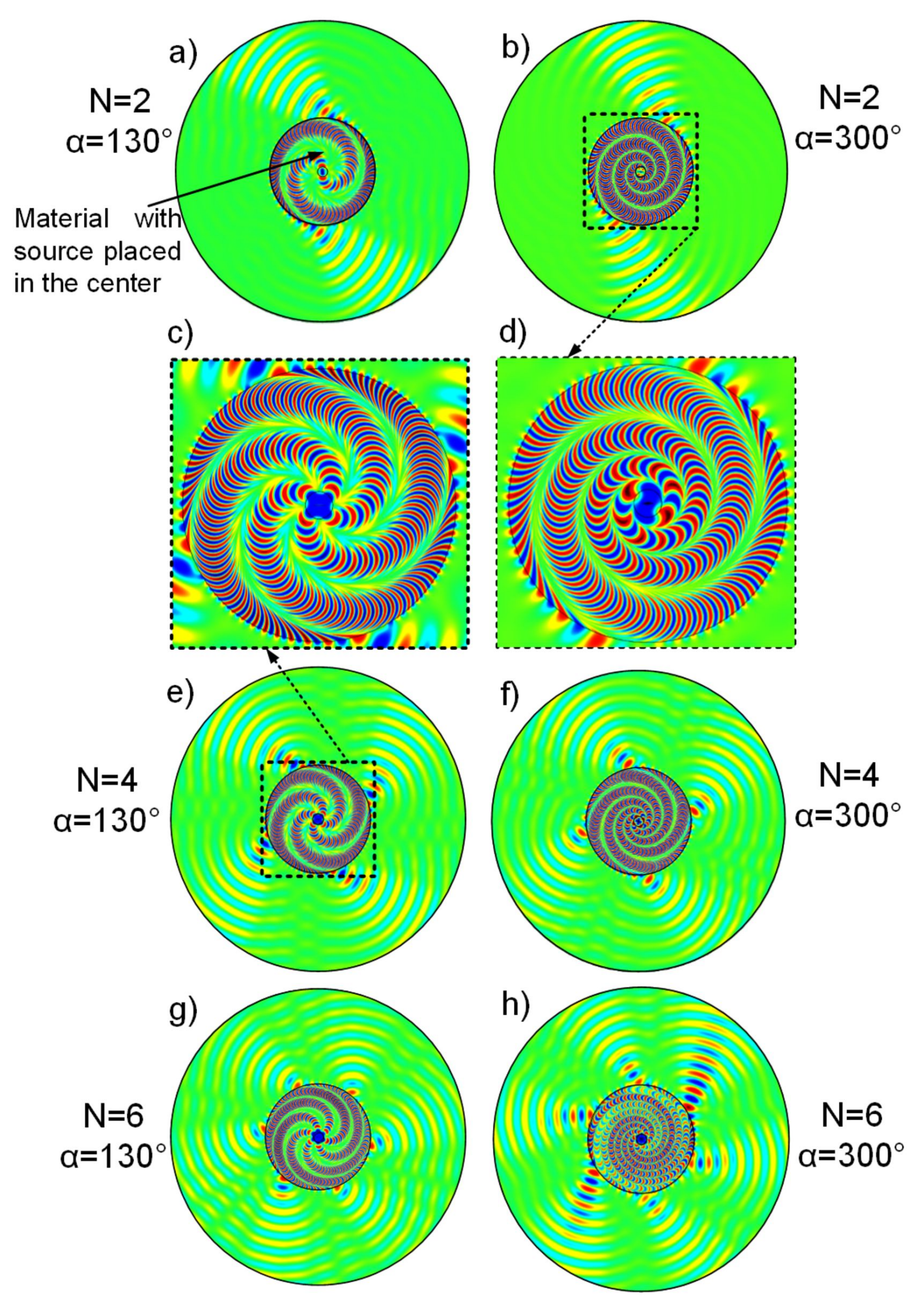
a)
N=2
α=130°
Material with source placed in the center
b)
N=2
α=300°
c)
d)
e)
N=4
α=130°
f)
N=4
α=300°
g)
N=6
α=130°
h)
N=6
α=300°

Annexe 3.9

A. de Lustrac, S. N. Burokur, P.-H. Tichit

« Transformation electromagnetics and non-standard devices »

Transformation Electromagnetics and Metamaterials : Fundamental Principles and Applications, edited by D. H. Werner and D.-H. Kwon, ISBN 978-1-4471-4995-8, Springer, 2014

Layout: T1 Standard SC | Book ID: 272865_1_En | Book ISBN: 978-1-4471-4995-8
Chapter No.: 14 | Date: 15-2-2013 | Page: 1/33

Chapter 14
Transformation Electromagnetics and Non-standard Devices

André de Lustrac, Shah Nawaz Burokur and Paul-Henri Tichit

14.1 Introduction

The concept of transformation electromagnetics originally introduced by Pendry [1] and Leonhardt [2] provides a method for designing new electromagnetic systems by controlling the permeability and permittivity distributions. It allows control over the path of electromagnetic waves in the structure in a manner unattainable with natural materials. However, the practical realization of these structures remains a challenge without the use of the extremely successful concept of metamaterials. The first example of this successful merging was the design and experimental characterization of an invisibility cloak in 2006 [3]. Later, other versions of cloaks have been proposed at microwave and optical frequencies. These invisibility cloaking structures [4–12] can serve as benchmark examples for the development of microwave and optical systems based on transformation electromagnetics. In recent years, the combination of transformation optics and metamaterials has led to non-standard electromagnetic systems. Proposals for new devices such as concentrators [13–15], electromagnetic wormholes [16, 17], transitions between waveguides and bends [18–23], and planar antennas [24] have been explored theoretically. Experiments and demonstrations of the space transformation of several devices have later been published [3, 6, 7, 9, 11, 12, 25, 26]. Indeed, practical implementation of transformation optics devices requires the design and use of anisotropic metamaterials with high accuracy as well as trade-offs between theoretical design and realization.

A. de Lustrac (✉) · S. N. Burokur · P.-H. Tichit
Institut d'Electronique Fondamentale, Univ Paris-Sud,
CNRS UMR 8622 91405 Orsay, France
e-mail: andre.de-lustrac@u-psud.fr

S. N. Burokur
e-mail: shah-nawaz.burokur@u-psud.fr

P.-H. Tichit
e-mail: paul-henri.tichit@u-psud.fr

D. H. Werner and D.-H. Kwon (eds.), *Transformation Electromagnetics and Metamaterials*, DOI: 10.1007/978-1-4471-4996-5_14,

Although the concept was well known for many years [27, 28], the introduction of transformation electromagnetics in 2006 has helped to bring back the correspondence between geometry and materials. In this way, the material can be considered as a new geometry, and information about the coordinate transformation is given by material properties. Based on the reinterpretation of the form-invariance of Maxwell's equations against coordinate transformation, arbitrary control of the electromagnetic field has become possible by introducing a specific coordinate transformation that maps an initial space into another one containing the imagined (or desired) properties. Among the classes of transformations in the literature, several possibilities are available for the design of electromagnetic structures. For example, continuous transformations were introduced by Pendry to realize the first invisibility cloak, which led to anisotropic and inhomogeneous permittivity and permeability tensors. Continuous transformations offer a substantial advantage in their generality of application. The contribution of these transformations was leveraged in many cases as cited above. In parallel, Leonhardt proposed the concept of conformal mappings [2] where transformations obey Fermat's principle and allow the design of devices through the use of isotropic dielectric media [20, 29–31]. The main drawback of these transformations is that their mathematical requirements are often too complex to realize the systems. Following this idea, quasiconformal transformations [6, 8, 9, 11, 12, 32] have emerged, where a slight deformation of the transformation minimizes the anisotropy of the material and allows an approximation of the device with an isotropic medium. Other theoretical works have appeared on space–time transformations [33–36], creating a link with cosmology and celestial mechanics [37–39]. Simultaneously, the concept of finite embedded transformations [13, 21, 22, 40–42] was introduced, which significantly added to design flexibility and enabled steering or focusing electromagnetic waves. Finally, source transformation techniques [43–46] have offered new opportunities for the design of active devices with a source distribution included in the transformed space.

The design stage is very important; first, because the theoretical values of electromagnetic parameters calculated by transformation optics are often too extreme to be practically realized. Therefore, a careful design should allow a simplification of these values. Moreover, in some cases, the permittivity and permeability tensors have non-diagonal terms that are difficult to implement. To facilitate the realization of structures, it is important to minimize or cancel these terms. In all cases, for a real device, the parameter values should be achievable with available electromagnetic metamaterials. Second, a practical implementation requires a discretization of the theoretical material. This discretization, which is often accompanied by performance degradation, must maintain the degradation to an acceptable level. A trade-off is necessary between the level of discretization and the degradation of structure performance due to this discretization. The space transformation technique can also be used to transform a singular profile of an isotropic material in a regular pattern into an equivalent anisotropic material, leading to a more easily realizable device. For example, dielectric singularities are points where the refractive index n tends toward infinity or zero and electromagnetic waves travel infinitely slow or infinitely fast. Such singularities cannot be realized in practice over a broad spectral range,

Layout: T1 Standard SC | Book ID: 272865_1_En | Book ISBN: 978-1-4471-4995-8
Chapter No.: 14 | Date: 15-2-2013 | Page: 3/33

but the index profile can be transformed into an anisotropic tensor of permittivity and permeability. For example, Ma et al. [47] have succeeded in implementing an omnidirectional retro-reflector through the transformation of a singularity in the index profile into a topological defect. Thus, bounded values of the permittivity and permeability components allowed the realization of the device.

After the discretization of a theoretical profile, the next metamaterial engineering step is to approach and implement the target device. Based on the electric and magnetic resonances, subwavelength metamaterial cells must be properly designed such that the effective electromagnetic parameters can reach desired values.

In the following sections, the transformation electromagnetics technique is applied to four systems: first, the case discussed is of a highly directive antenna by transforming an isotropic one. Then, the case of wave bending in a steerable antenna is addressed. Another antenna application concerning the transformation of a directive emission into an isotropic one is also discussed. Finally, a taper between two waveguides with different widths is proposed and it is shown how it is possible to connect them so as to have a transmission close to unity.

14.2 Highly Directive Antenna

This section deals with the design of a highly directive antenna based on the transformation of an isotropic source radiating in a cylindrical space into a directive antenna radiating in a rectangular space. This begins by deriving the permeability and permittivity tensors of a metamaterial capable of transforming the isotropic source into a compact highly directive antenna in the microwave domain. The aim is to show how a judiciously engineered metamaterial allows the direction of emission of a source to be controlled in order to collect all the energy in a small angular domain around the surface normal, with good impedance matching between the radiating source and the material obtained by transformation optics.

14.2.1 Theoretical Formulation

For the theoretical formulation of the highly directive emission, consider a line source radiating in a cylindrical vacuum space (Fig. 14.1). The line source is placed along the cylindrical axis. Wavefronts represented by cylinders at $r =$ constants and polar coordinates (r, θ) are appropriate to describe such a problem. To transform the cylindrical space, a physical one where lines $\theta =$ constant become horizontal is generated, as illustrated by the schematic principle in Fig. 14.1. Each colored circle of the cylindrical space becomes a vertical line having the same color in the rectangular space, whereas each radial

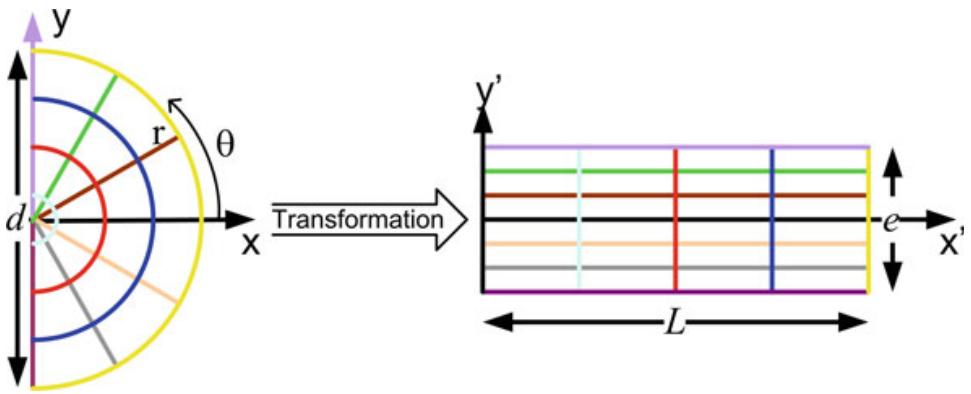

Fig. 14.1 Representation of the transformation of the initial space into the desired space. Each radius line of the cylindrical space is transformed into a horizontal line of the right rectangular space. Each circular line is transformed into a vertical one. Reprinted with permission from Journal of Applied Physics, 2009. 105(10) 104912. Copyright 2009, American Institute of Physics

line becomes a horizontal one. Finally, the right half cylinder of diameter d is transformed into a rectangular region with width e and length L. The line source in the center of the cylinder becomes the left black vertical radiating surface in the rectangular space. The transformation can then be expressed as:

$$\begin{cases} x' = \frac{2L}{d}\sqrt{x^2+y^2} \\ y' = \frac{e}{\pi}\tan^{-1}\left(\frac{y}{x}\right) \\ z' = z \end{cases} \quad \text{with} \quad -\frac{\pi}{2} \le \tan^{-1}\left(\frac{y}{x}\right) \le \frac{\pi}{2} \tag{14.1}$$

where x', y', and z' are the coordinates in the transformed rectangular space and x, y, and z are those in the initial cylindrical space. Free space is assumed in the cylinder, with isotropic permeability and permittivity tensors ε_0 and μ_0. The following transformations are used to obtain the material parameters of the rectangular space:

$$\varepsilon^{i'j'} = \frac{J_i^{i'} J_j^{j'} \varepsilon_0 \delta^{ij}}{\det(J)} \text{ and } \mu^{i'j'} = \frac{J_i^{i'} J_j^{j'} \mu_0 \delta^{ij}}{\det(J)} \text{ with } J_\alpha^{\alpha'} = \frac{\partial x'^\alpha}{\partial x^\alpha} \tag{14.2}$$

where $J_\alpha^{\alpha'}$ and δ^{ij} are respectively the Jacobian transformation matrix of the transformation of (14.1) and the Kronecker symbol. The Jacobian matrix between the transformed and the original coordinates has four nonzero parameters which depend on the distance from the origin. J_{xx}, J_{yy}, J_{xy} are assumed to be z-independent with $J_{zz} = 1$. The divergence of J_{yy} can be explained by the non-bijection of the initial coordinates y-lines transformation. The inverse transformation is obtained from the initial transformation (14.1) and derived by a substitution method, enabling the metamaterial design which leads to anisotropic permittivity and permeability tensors. Both electromagnetic parameters μ and ε have the same behavior. Also, note that the equality of permittivity and permeability tensors implies a perfect impedance match with no reflection at the interface with vacuum.

By substituting the new coordinate system in the tensor components, and after some simplifications, the following material parameters are derived:

$$\overline{\overline{\varepsilon}} = \begin{pmatrix} \varepsilon_{xx}(x', y') & 0 & 0 \\ 0 & \varepsilon_{yy}(x', y') & 0 \\ 0 & 0 & \varepsilon_{zz}(x', y') \end{pmatrix} \varepsilon_0$$
$$\overline{\overline{\mu}} = \begin{pmatrix} \mu_{xx}(x', y') & 0 & 0 \\ 0 & \mu_{yy}(x', y') & 0 \\ 0 & 0 & \mu_{zz}(x', y') \end{pmatrix} \mu_0 \tag{14.3}$$

where

$$\varepsilon_{xx}(x', y') = \mu_{xx}(x', y') = \frac{\pi}{e}x' \quad \varepsilon_{yy}(x', y') = \mu_{yy}(x', y') = \frac{1}{\varepsilon_{xx}(x', y')}$$

$$\varepsilon_{zz} = \mu_{zz} = \frac{d^2\pi}{4eL^2}x'. \tag{14.4}$$

The appropriate choice of the transformation thus assures an absence of non-diagonal components, giving rise to a practical implementation of the device using metamaterials. Figure 14.2 shows the variation of the permittivity tensor components in the transformed rectangular space. The different geometrical dimensions of the initial and transformed space are respectively $d = 15$ cm, $e = 15$ cm, and $L = 5$ cm. Note that the three components of the permittivity depend only on the coordinate x'. This is due to the invariance of the initial space with θ with respect to the distance from the source in the cylindrical space. This distance is represented by x' in the transformed rectangular space.

The divergence of ε_{yy} near $x' = 0$ creates an "electromagnetic wall" with ε_{yy} tending toward infinity on the left side of the rectangular area. This left side also corresponds to the radiating source transformed from the center line source of the cylindrical space. Note the simplicity of the ε_{xx} and ε_{zz} terms that present only a linear variation.

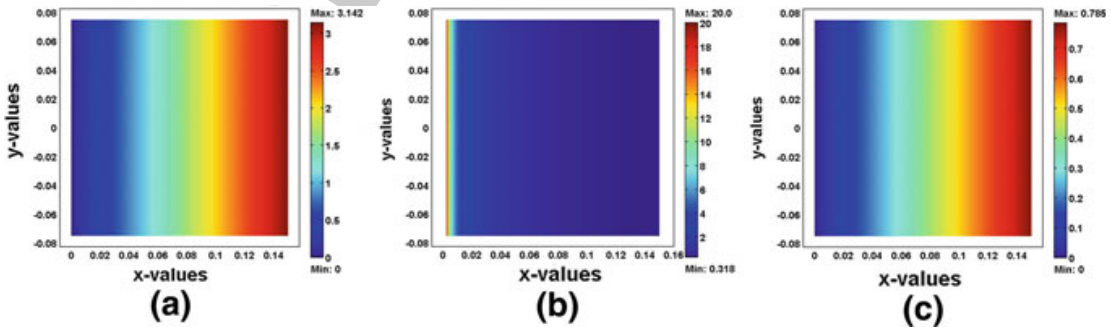

Fig. 14. 2 Variation of the permittivity tensor components: **a** ε_{xx}, **b** ε_{yy}, and **c** ε_{zz}. Reprinted with permission from Journal of Applied Physics, 2009. 105(10) 104912. Copyright 2009, American Institute of Physics

Layout: T1 Standard SC | Book ID: 272865_1_En | Book ISBN: 978-1-4471-4995-8
Chapter No.: 14 | Date: 15-2-2013 | Page: 6/33

In the transformed rectangular space the confinement of the electromagnetic field can be controlled and increased by the different parameters d, e, and L, and particularly by the ratio $d/2L$. After the transformation, the electromagnetic energy enclosed in the half cylindrical space is confined in the rectangular space. To characterize the emission directivity realized by the radiating source in the rectangular space, the most important parameter is the ratio between the width e of the aperture and the square of the wavelength λ^2 since the maximum directivity of an antenna is given by:

$$D_{\max} = \frac{4\pi A_{\text{eff}}}{\lambda^2} \text{ where } A_{\text{eff}} = \frac{\left|\int_A \int E_a(r)\mathrm{d}S\right|^2}{\int_A |E_a(r)|^2 \mathrm{d}S} \tag{14.5}$$

where A_{eff} is the effective aperture of the antenna and depends on the width e and on the field distribution $E_a(r)$.

14.2.2 Numerical Simulations

Finite Element Method (FEM)-based numerical simulations with Comsol Multiphysics are used to design this transformed directive antenna. As the line source of the right half-cylindrical space becomes a radiating plane in the transformed rectangular space, an excitation is inserted at the left side of the rectangular space as shown in Fig. 14.3a. This space is delimited by metallic boundaries on the upper and lower sides and at the left side of the rectangular space representing the metamaterial having dimensions 15×5 cm. The radiating properties of the antenna are calculated and presented in Fig. 14.3.

Three operating frequencies have been considered here; 5, 10, and 40 GHz, corresponding respectively to $e/\lambda = 2.5$, 5 and 20. A directive emission can be observed as illustrated by the magnetic field radiations of the antenna for a TM

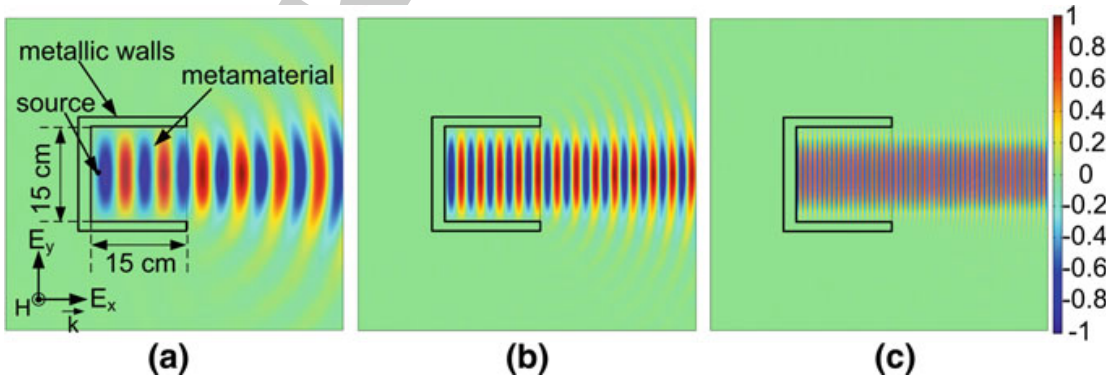

Fig. 14.3 Magnetic field distribution for a TM wave polarization at (**a**) 5 GHz, (**b**) 10 GHz, and (**c**) 40 GHz. Reprinted with permission from Journal of Applied Physics, 2009. 105(10) 104912. Copyright 2009, American Institute of Physics

Layout: T1 Standard SC | Book ID: 272865_1_En | Book ISBN: 978-1-4471-4995-8
Chapter No.: 14 | Date: 15-2-2013 | Page: 7/33

wave polarization. A very high directivity is noted and can be calculated using the expression given in [48]:

$$D = \frac{4,1253}{(\theta_1 \theta_2)} \tag{14.6}$$

where θ_1 and θ_2 are respectively the half-power beamwidths (in degrees) for the H-plane and E-plane patterns. Here, assume $\theta_1 = \theta_2$. Then for a half-power beamwidth of 13.5° at 10 GHz a directivity of 23.6 dB is obtained, implying a ratio $e/\lambda = 5$. This directivity is comparable with that of a parabolic reflector antenna of the same size [48] and is greater than that of a wideband [2–18 GHz] dual polarized FLANN® horn antenna where the directivity varies from 10 to 23 dB.

The far-field radiation patterns of the antenna are calculated at different frequencies to assess the variation of the directivity. The dimensions of the rectangular box remain the same as above ($e = 15$ cm and $L = 5$ cm). Figure 14.4a shows the radiation patterns for the cases $e/\lambda = 2.5$ (5 GHz), 5 (10 GHz), and 20 (40 GHz). The directivity strongly increases as the frequency increases. It goes from 23.6 dB at 5 GHz to 29.5 dB at 10 GHz and 42 dB at 40 GHz. The directivity enhancement is illustrated by the evolution of the half-power beamwidth versus frequency in Fig. 14.4b.

14.2.3 Parameter Reduction and Discrete Metamaterial Layers

The metamaterial calculated above shows coordinate-dependent electromagnetic parameters following (14.4). This dependency is identical for the permittivity and permeability, allowing an exact impedance matching with vacuum. It is proposed

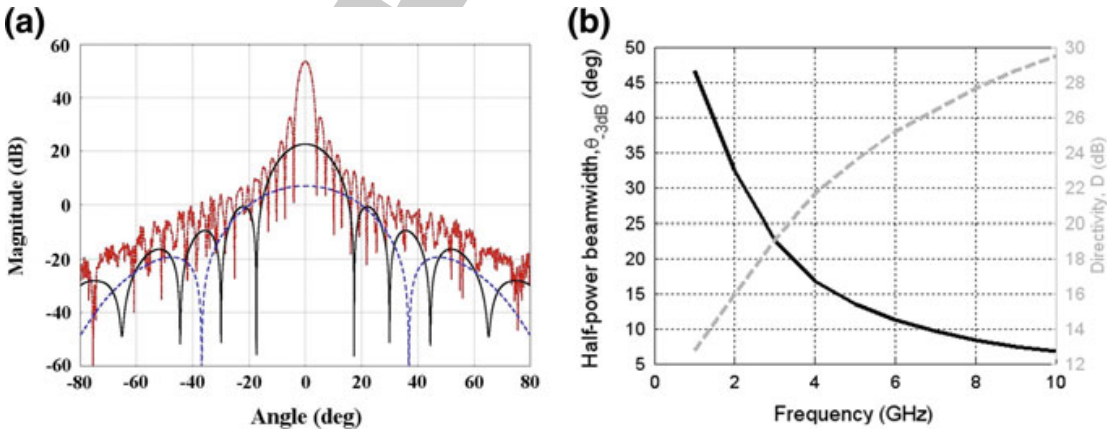

Fig. 14.4 **a** Far-field radiation patterns at 5 GHz (*dashed*), 10 GHz (*continuous*), and 40 GHz (*dashed-dotted*). **b** Half-power beamwidth (*continuous*) and directivity (*dashed*) versus frequency. Reprinted with permission from Journal of Applied Physics, 2009. 105(10) 104912. Copyright 2009, American Institute of Physics

Layout: T1 Standard SC | Book ID: 272865_1_En | Book ISBN: 978-1-4471-4995-8
Chapter No.: 14 | Date: 15-2-2013 | Page: 8/33

to simplify the calculated parameters of the highly directive antenna for a realistic experimental realization from achievable metamaterial structures. Choosing plane wave solutions for the electric field and magnetic field, with a wave vector $\boldsymbol{k}$ in the x–y plane, and a TM or a TE polarization with respectively the magnetic or electric field polarized along the z-axis, a dispersion equation is obtained:

$$\det(F) = 0 \tag{14.7}$$

with

$$F = \begin{pmatrix} \varepsilon_{xx} - \frac{k_y^2}{\mu_{zz}} & \frac{-k_x k_y}{\mu_{zz}} & 0 \\ \frac{-k_x k_y}{\mu_{zz}} & \varepsilon_{yy} - \frac{k_x^2}{\mu_{zz}} & 0 \\ 0 & 0 & \varepsilon_{zz} - \frac{k_x^2}{\mu_{yy}} - \frac{k_y^2}{\mu_{xx}} \end{pmatrix}. \tag{14.8}$$

The determinant of this equation must be equal to zero. Solving it, one equation is obtained for each polarization. In the TE polarization this equation can be written as

$$\epsilon_{zz} = \frac{k_x^2}{\mu_{yy}} + \frac{k_y^2}{\mu_{xx}} \tag{14.9}$$

whereas in the TM polarization, it becomes:

$$\mu_{zz} = \frac{k_x^2}{\epsilon_{yy}} + \frac{k_y^2}{\epsilon_{xx}}. \tag{14.10}$$

For a possible realization, the dimensions of the semi-cylindrical space must be set so that $d^2/4L^2 = 4$ in order to obtain achievable values for the electromagnetic parameters. An additional simplification arises from the choice of the polarization of the emitted wave. Here, consider a polarized electromagnetic wave with an electric field pointing in the z-direction, which allows for modifying the dispersion equation in order to simplify the electromagnetic parameters without changing Maxwell's equations and propagation in the structure. To obtain these electromagnetic parameters values that are suitable for the manufacturing technology, the same method is used as proposed in [3]. The dispersion equation is multiplied by $xx\psi$ and the metamaterial is thus simply described by:

$$\begin{cases} \mu_{xx} = 1 \\ \mu_{yy} = \frac{1}{\varepsilon_{xx}^2} \\ \varepsilon_{zz} = 4\varepsilon_{xx}^2 \end{cases}. \tag{14.11}$$

Equation (14.11) describes the material parameters that can be achieved with existing metamaterial structures, for example, split ring resonators (SRR) [49] and electric-LC (ELC) resonators [50].

Layout: T1 Standard SC | Book ID: 272865_1_En | Book ISBN: 978-1-4471-4995-8
Chapter No.: 14 | Date: 15-2-2013 | Page: 9/33

The penalty of the above reduction is an imperfect impedance match at the outer boundary of the metamaterial at $Z = \sqrt{\frac{\mu_{yy}}{\varepsilon_{zz}}}(x = L) = \frac{9}{2\pi^2}$ with $L = 5$ cm and $d = 15$ cm. Thus, the transmission at the outer boundary is calculated classically with$T = \frac{4Z}{(1+Z)^2} = 0.85$ which assures a high level of radiated electromagnetic field. Further simplification consists in discretizing the desired variation of the parameters μ_{yy} and ε_{zz} to secure a practical realization that produces experimental performances close to theory.

Figure 14.5a shows the schematic structure of the directive emission antenna. A microstrip patch antenna on a dielectric substrate constitutes the radiating source. A surrounding material made of alternating electric metamaterial and magnetic metamaterial layers transforms the isotropic emission of the patch antenna into a directive one. The material is composed of five different regions where permittivity and permeability vary according to the profile of Fig. 14.5c.

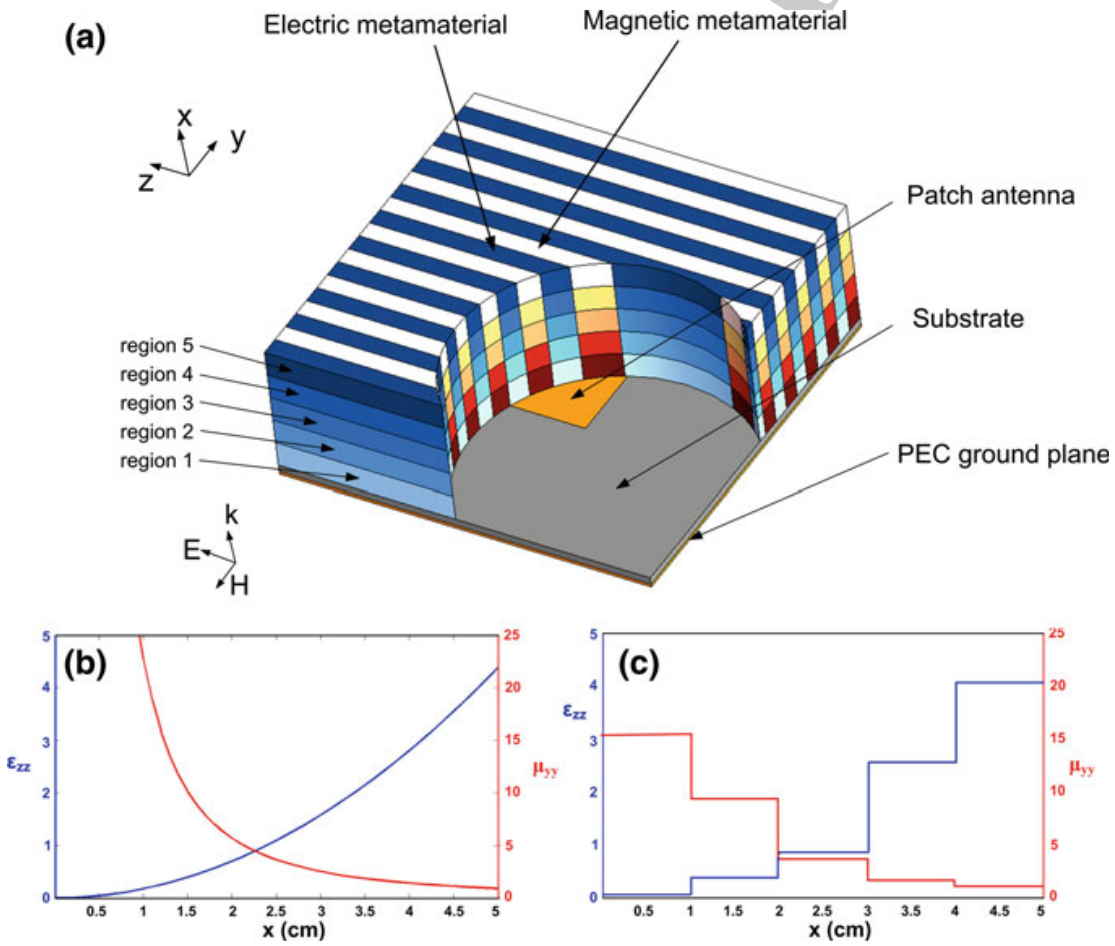

Fig. 14.5 **a** Schematic structure of the proposed antenna with a cylindrical cut to show the internal structure of the material and the radiating source. This source is a microstrip patch antenna on a dielectric substrate. The metamaterial is composed of alternating permittivity and permeability vertical layers. Each layer is made of five different material regions (*pale color* near the patch to *dark color* in the *x*-direction). **b** Theoretical material parameters given by relation (14.11). **c** Discrete values of material parameters used in experimental realization

Layout: T1 Standard SC | Book ID: 272865_1_En | Book ISBN: 978-1-4471-4995-8
Chapter No.: 14 | Date: 15-2-2013 | Page: 10/33

The corresponding reduced magnetic and electric properties of the metamaterial obtained from transformation optics are presented in Fig. 14.5b and c. The distribution of the theoretical material parameters satisfying relation (14.11) is shown in Fig. 14.5b. The distribution in Fig. 14.5c presents the discrete values corresponding to the five regions of the metamaterial used for the experimental validation. To implement the material specifications in Eq. (14.11) using metamaterials, one must choose the overall dimensions, design the appropriate unit cells, and specify their layout. For this implementation, the metamaterial unit cell is not periodic. It is advantageous to optimize the three design elements all at once since common parameters are shared. Equation (14.11) shows that the desired ultra-directive emission will have constant μ_{xx}, with ε_{zz} and μ_{yy} varying longitudinally throughout the structure. The axial permittivity ε_{zz} and permeability μ_{yy} show values ranging from 0.12 to 4.15 and from 1.58 to 15.3, respectively.

As shown by the schematic structure of the antenna in Fig. 14.5a, a square copper patch is printed on a 0.787 mm thick low-loss dielectric substrate (Rogers RT/Duroid 5870™ with 17.5 μm copper cladding, $\varepsilon_r = 2.33$ and $\tan\delta = 0.0012$) and used as the feed source. The metamaterial covers completely the patch feed source to capture the emanating isotropic radiation and transform it into a directive pattern. The metamaterial is a discrete structure composed of alternating layers with anisotropic permeability and permittivity. Figure 14.6 shows photography of the fabricated antenna device. The bulk metamaterial was built from 56 layers of dielectric boards on which subwavelength resonant structures are printed. 28 layers contain artificial magnetic resonators and 28 electric ones. Each layer is made of five regions of metamaterials corresponding to the discretized values of Fig. 14.5c. The layers are mounted two-by-two with a constant air spacing of 2.2 mm between each, in order to best represent the permeability and permittivity characteristics in the different regions. Overall dimensions of the antenna are 15 × 15 × 5 cm.

The details of the metamaterial cells are illustrated in Fig. 14.6. The left and right inserts show the designs of the resonators used in the magnetic (right) and electric (left) metamaterial layers. The layers are divided into five regions in the direction of wave propagation. Each region is composed of three rows of resonators with identical geometry and dimensions. Different resonators are used for electric and magnetic layers. Their schematic drawings are depicted at the bottom of Fig. 14.6.

The permeability (μ_{yy}) and permittivity (ε_{zz}) parameter sets plotted in Fig. 14.5c can be respectively achieved in a composite metamaterial containing SRRs and ELCs, known to provide respectively a magnetic response and an electric response that can be tailored (Fig. 14.6). Because of layout constraints, a rectangular unit cell with dimensions $p_x = p_z = 10/3$ mm was chosen for both resonators. The layout consisted of five regions, each of which was three unit cells long (10 mm). The desired ε_{zz} and μ_{yy} were obtained by tuning the resonators' geometric parameters. Using the Ansoft HFSS commercial full-wave finite element simulation software, a series of scattering (S) parameter simulations were performed for the SRR and ELC unit cells separately over a discrete set of the geometric parameters covering the range of interest. A normally incident wave

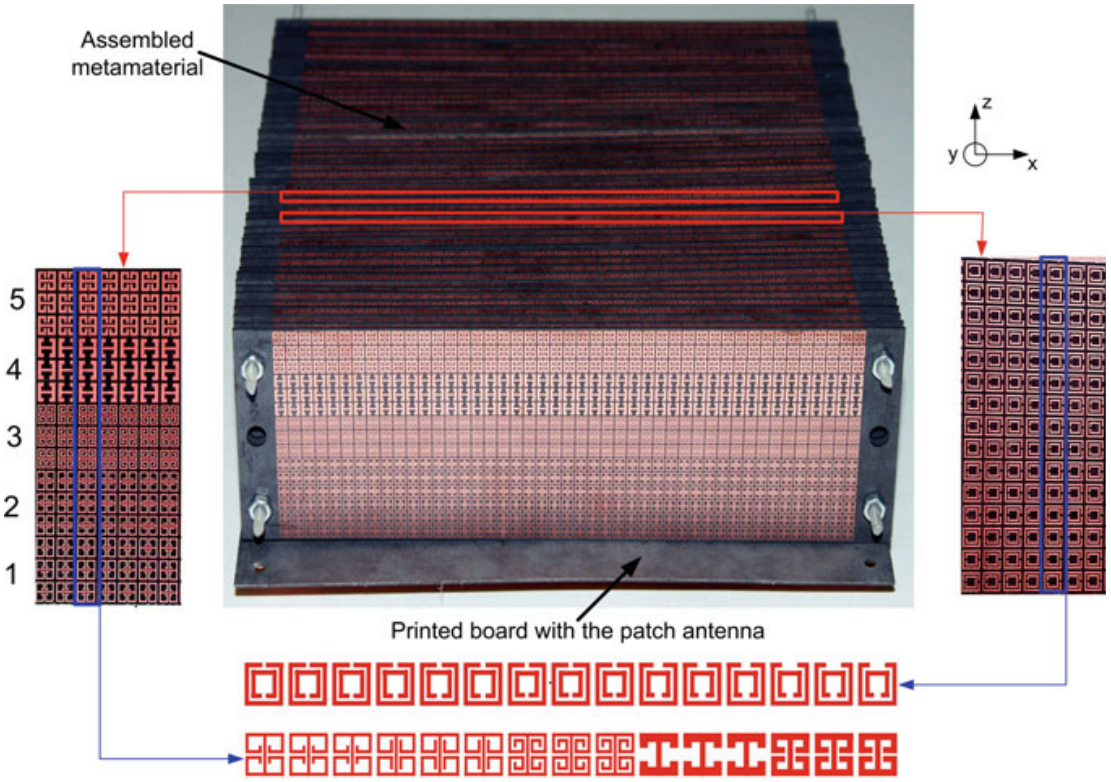

Fig. 14.6 Structure of the antenna: each magnetic and dielectric layer of the metamaterial is divided into five regions to assure the desired variations of electromagnetic parameters along wave propagation direction. The dimensions of the antenna are 15 × 15 × 5 cm. The operating frequency is 10.6 GHz. *Left* and *right* inserts show details of the resonators used in the magnetic (*right*) and electric (*left*) metamaterial layers. Each level is made of three rows of identical resonators

impinging on the unit cell is considered for simulations. Electric and magnetic symmetry planes are applied on the unit cell respectively for the faces normal to the electric and magnetic field vector. By calculating the unit cells separately, there is very low coupling between neighboring ELCs and SRRs. The influence of this coupling is even lower when the electric and magnetic layers are mounted two-by-two. A standard retrieval procedure was then performed to obtain the effective material properties ε_{zz} and μ_{yy} from the *S*-parameters [51]. The discrete set of simulations and extractions was interpolated to obtain the particular values of the geometric parameters that yielded the desired material properties plotted in Fig. 14.5c. Simulations were also performed using Comsol Multiphysics to assure the functionality of the metamaterial. An operating frequency around 10 GHz was chosen, which yields a reasonable effective medium parameter $\lambda/p_x > 10$, where λ is the free-space wavelength.

In the designs presented in Figs. 14.5 and 14.6, the SRRs and ELCs are used to realize the continuous-material properties required by the directive antenna. To illustrate the equivalence between continuous materials and the actual combination of SRR and ELC metamaterials, simulations were performed of the ideal antenna composed of continuous materials and the experimental antenna composed of SRR

and ELC metamaterials, simultaneously and their electromagnetic properties compared. However, full-wave simulation of the experimental antenna is impossible using current computer resources owing to the extremely large memory and computer time required. Instead, full-wave simulations were done using the equivalent discrete material with parameters as shown in Fig. 14.5c. The full-wave simulations have been performed using the finite element method-based commercial software Comsol Multiphysics. Also, the simulations have been made in a 2D configuration using the RF module in a transverse electric (TE) wave propagation mode. A surface current with similar dimensions to the patch feed is used to model the source. The diagram pattern of the antenna is plotted by inserting matched boundaries with far-field conditions. For the metamaterial, values of permittivity and permeability shown in Fig. 14.5 have been introduced in each of the five layers. Figure 14.7 shows simulation results of the electric field emanating from the antenna in both the continuous and discrete material cases. Excellent qualitative agreement is observed from the simulations, indicating that the SRR-ELC combination presents nearly the same electromagnetic parameters as the continuous material. As observed, the intensity of emitted radiation decreases rapidly since the source transformation operates only in the x–y plane.

14.2.4 Experimental Measurement of the Ultra-Directive Antenna

To validate the directive emission device performance, two experimental systems are set up to measure the radiated field. The first method consists in measuring the far-field radiation patterns of the antenna in an anechoic chamber. Figure 14.8a

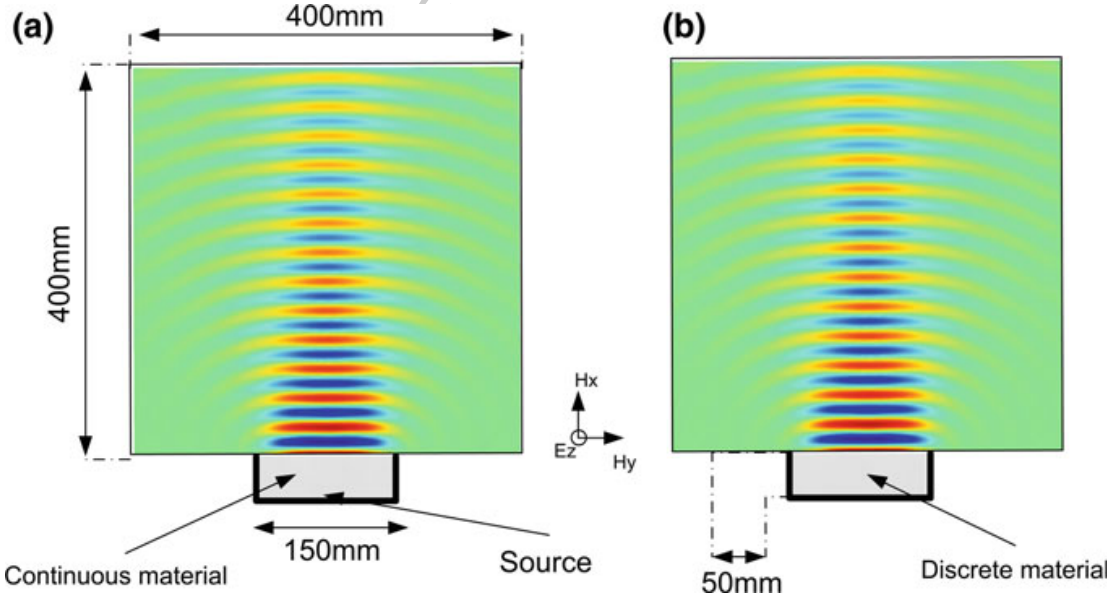

Fig. 14.7 Full-wave finite element simulations of electric fields emitted by the metamaterial antenna. Calculations are performed using the continuous and discrete materials in a 2D configuration using a line source as excitation. **a** Continuous material. **b** Discrete material

Layout: T1 Standard SC | Book ID: 272865_1_En | Book ISBN: 978-1-4471-4995-8
Chapter No.: 14 | Date: 15-2-2013 | Page: 13/33

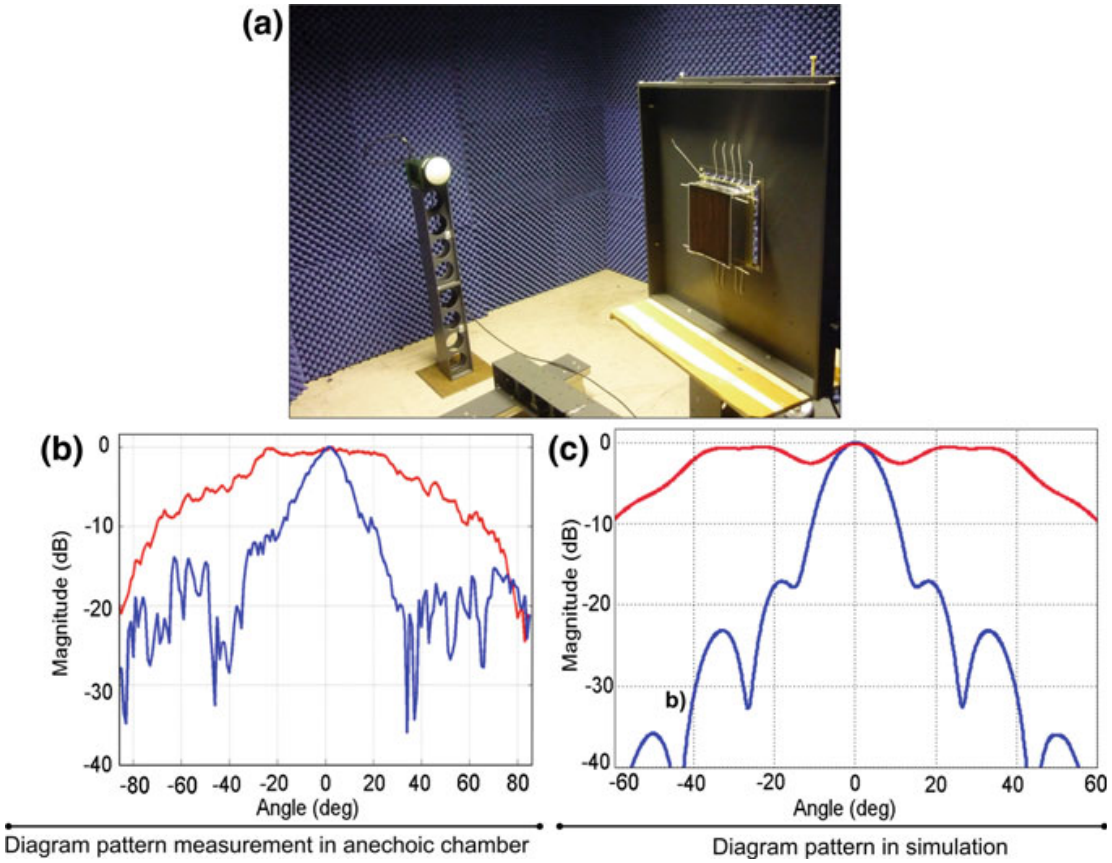

Fig. 14.8 Far-field measurement in an anechoic chamber. **a** Experimental setup. **b** Measurements. **c** Simulations. Radiation patterns of the metamaterial antenna (*blue trace*) and of the feeding microstrip patch antenna alone (*red trace*) are presented at 10.6 GHz

shows the far-field measurement system. In such an emission-reception setup, the fabricated metamaterial antenna is used as an emitter and a wideband (2–18 GHz) dual-polarized horn antenna is used as the receiver to measure the radiated power level of the radiating antenna. The measurements are performed for computer-controlled elevation angle varying from −90° to +90°. The microwave source is a vector network analyzer (Agilent 8722 ES) that was also used for detection. The feeding port is connected to the metamaterial antenna by means of a coaxial cable, whereas the detecting port is connected to the horn antenna also by means of a coaxial cable. The measured far-field radiation pattern in the E-plane (plane containing E and k vectors) is presented in Fig. 14.8b.

The antenna presents maximum radiated power at 10.6 GHz with a directive main beam and low parasitic secondary lobes, under −15 dB. The main lobe presents a 13° half-power beamwidth in the E-plane (*x*–*y* plane). This narrow beamwidth is less than that of a parabolic reflector antenna having similar dimensions (diameter equal to 15 cm), where the half-power beamwidth is around 16°. Measurements are found to be consistent with the predicted radiation patterns shown in Fig. 14.8c.

The second experimental setup (Fig. 14.9a) was intended to measure the antenna's near-field microwave radiation. The E-field is scanned by a field-sensing

Layout: T1 Standard SC | Book ID: 272865_1_En | Book ISBN: 978-1-4471-4995-8
Chapter No.: 14 | Date: 15-2-2013 | Page: 14/33

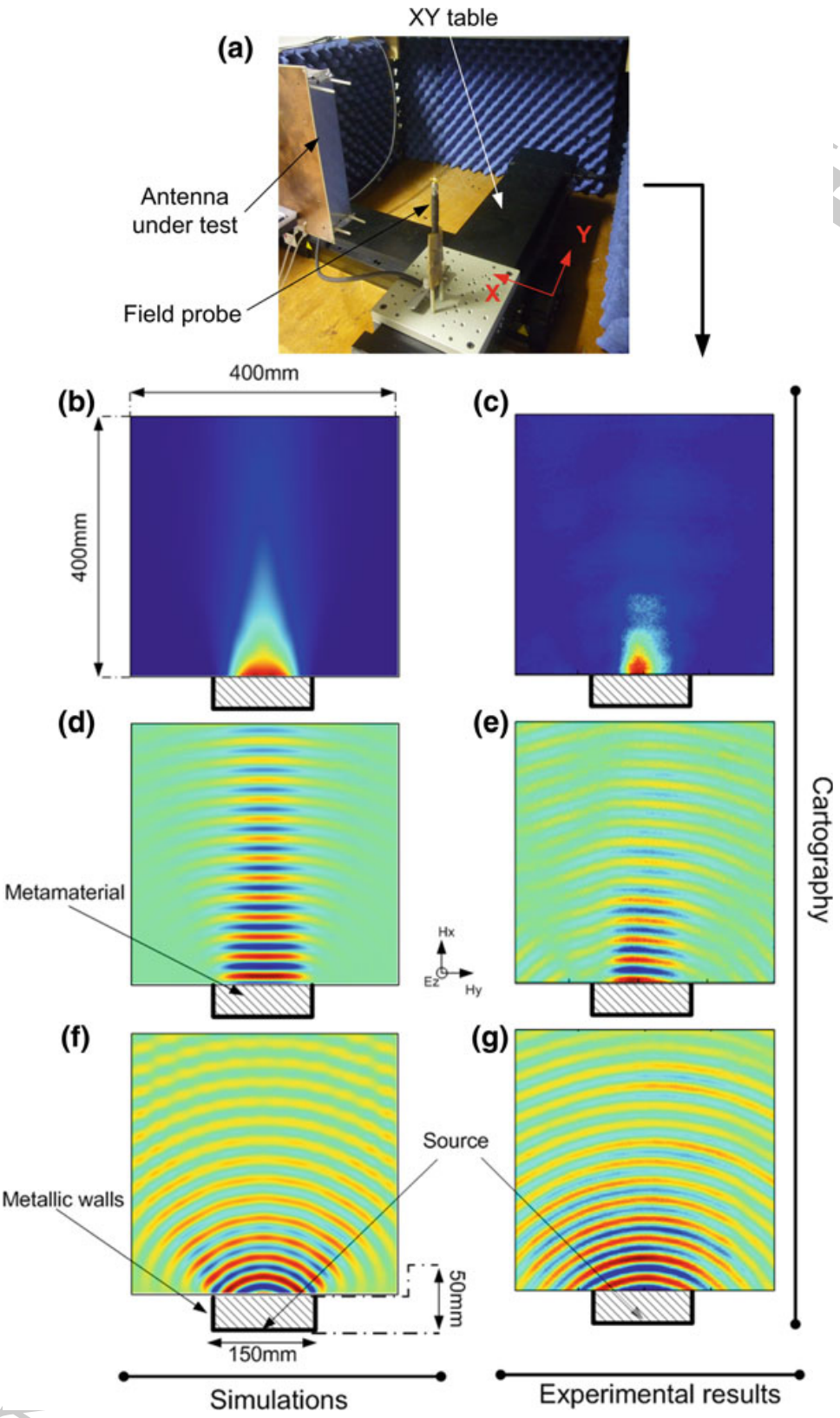

Fig. 14.9 Near-field scanning experiment in comparison with simulations. **a** Experimental setup system. **b** Magnitude of the predicted Poynting vector. **c** Magnitude of the experimental Poynting vector. **d** Magnitude of the predicted near field. **e** Mapping of the near field. **f** Magnitude of the excitation source's predicted near field. **g** Mapping of the excitation source's near field. The mappings are shown at 10.6 GHz

Layout: T1 Standard SC | Book ID: 272865_1_En | Book ISBN: 978-1-4471-4995-8
Chapter No.: 14 | Date: 15-2-2013 | Page: 15/33

monopole probe connected to the network analyzer by a coaxial cable. The probe was mounted on two orthogonal linear translation stages (computer-controlled Newport MM4006), so that the probe could be translated with respect to the radiation region of the antenna. By stepping the field sensor in small increments and recording the field amplitude and phase at every step, a full 2D spatial field map of the microwave near-field pattern could be acquired in the free-space radiation region.

The total scanning area covers 400 × 400 mm^2 with a lateral step resolution of 2 mm in the dimensions shown by red arrows in Fig. 14.9a. Microwave absorbers are applied around the measurement stage in order to suppress undesired scattered radiations at the boundaries. Figure 14.9 shows the comparison between simulations and experimental results. In Fig. 14.9b, the magnitude of the numerical Poynting vector interpreted as an energy flux for the electromagnetic radiation is plotted for the device and compared to measurements in Fig. 14.9c. As stated earlier, the emission decreases rapidly since only the x–y plane has been considered for the source transformation procedure. A clear directive emission is radiated by the antenna as presented by the numerical simulation in Fig. 14.9d and measurement presented in Fig. 14.9e for the electric near-field mapping of the antenna's radiation. Also, when compared to the radiation of the patch feed alone shown in Fig. 14.9f and g, the narrow beam profile of the proposed device can be seen.

14.3 Azimuthal Antenna

Following the previous example, a two-dimensional coordinate transformation is now proposed which transforms the vertical radiation of a directive plane source into a directive azimuthal emission.

14.3.1 Design Concept

Consider a source radiating in a rectangular space. In theory, the radiation emitted from this source can be transformed into an azimuthal pattern using transformation optics. The transformation procedure is denoted F(x',y') and consists of bending the radiation. Figure 14.10 shows the operating principle of this rotational coordinate transformation. Mathematically, F(x',y') can be expressed as:

$$\begin{cases} x' = ax\cos(by) \\ y' = ax\sin(by) \\ z' = z \end{cases} \tag{14.12}$$

where x', y', and z' are the coordinates in the bent space, and x, y, and z are those in the initial rectangular space. The initial space is assumed to be free space. L_2, L_1,

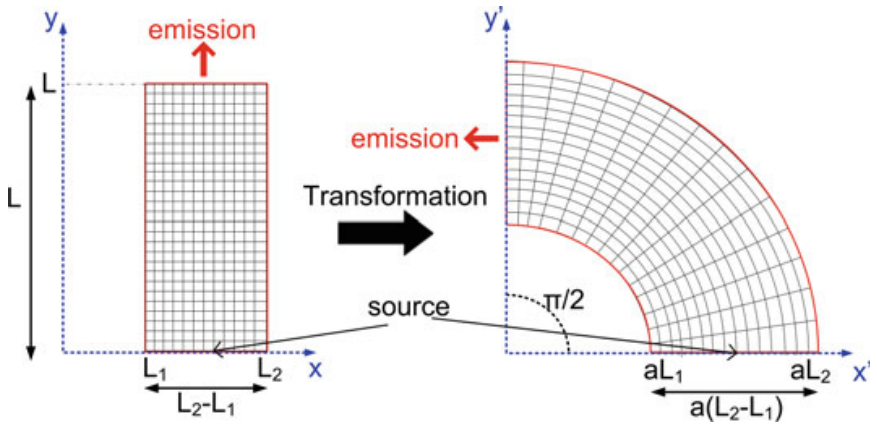

Fig. 14.10 Schematic principle of the 2D rotational coordinate transformation. The emission in a rectangular space is transformed into an azimuthal one

and L are, respectively, the width and the length of the rectangular space. The rotational transformation of Fig. 14.10 is defined by parameter a considered as an "expansion" parameter and parameter b which controls the rotation angle of the transformation F(x',y'). By substituting the new coordinate system in the tensor components, and after some simplifications, the material parameters are derived. After diagonalization, calculations lead to permeability and permittivity tensors given in the diagonal base by:

$$\bar{\bar{\varepsilon}} = \begin{pmatrix} \psi_{rr} & 0 & 0 \\ 0 & \psi_{\theta\theta} & 0 \\ 0 & 0 & \psi_{zz} \end{pmatrix} \varepsilon_0 \qquad \bar{\bar{\mu}} = \begin{pmatrix} \psi_{rr} & 0 & 0 \\ 0 & \psi_{\theta\theta} & 0 \\ 0 & 0 & \psi_{zz} \end{pmatrix} \mu_0$$

$$\text{with } \psi_{rr} = \frac{a}{br};\ \psi_{\theta\theta} = \frac{a}{b} r;\ \psi_{zz} = \frac{1}{abr} \qquad (14.13)$$

14.3.2 Numerical Simulations

The transformation formulation is implemented using the finite element-based commercial solver Comsol Multiphysics. Figure 14.11 shows the comparison of a 2D simulation between a planar source made of current lines in the y–z plane above a limited metallic ground plane (Fig. 14.11a) and the same source surrounded by a metamaterial defined by Eq. (14.13) (Fig. 14.11b). Figure 14.11c and d show, respectively, the far-field patterns of the plane source without and with the metamaterial structure. The left shift of the peak corresponds to a rotation of 76° of the emitted radiation.

For the fabrication of the physical prototype, the calculated material parameters are simplified through a parameter reduction procedure. Then, the polarization of the electromagnetic field is set such that the magnetic field is along the z-direction.

Layout: T1 Standard SC | Book ID: 272865_1_En | Book ISBN: 978-1-4471-4995-8
Chapter No.: 14 | Date: 15-2-2013 | Page: 17/33

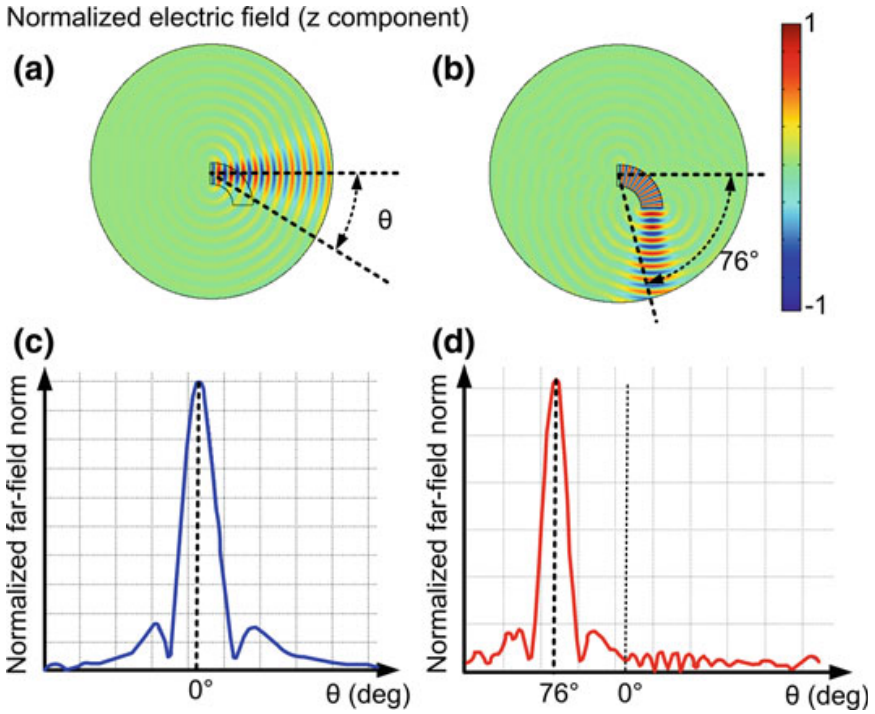

Fig. 14.11 **a–b** Calculated emission of a plane current source above a limited metallic ground plane without and with the metamaterial structure. **c–d** Calculated normalized far field of the antenna without and with metamaterial. A 76° rotation of the radiation is clearly observed

In this case, the relevant electromagnetic parameters are μ_{zz}, $\varepsilon_{\theta\theta}$, and ε_{rr}. The terms $\varepsilon_{\theta\theta}$ and μ_{zz} are held constant, leaving the new set of coordinates given by (14.14):

$$\varepsilon_{rr} = \frac{\left(\frac{1}{br}\right)^2}{1.7};\ \varepsilon_{\theta\theta} = 2.8;\ \mu_{zz} = 1.7 \tag{14.14}$$

Setting the physical parameter $b = 6$ allows an optimization of the material parameter ε_{rr}. The profile of the different parameters is presented in Fig. 14.12a. The fabricated prototype is composed of 30 identical layers where each layer is divided into 10 unit cells as illustrated by the single layer in Fig. 14.12b. For the discretization of the material parameters, meta-atoms producing electric resonances are designed on the 0.787 mm thick low loss (tan $\delta = 0.0013$) RO3003^{TM} dielectric substrate. 5 mm rectangular unit cells were chosen for the resonators. The desired ε_{zz} and μ_{yy} were obtained by tuning the resonators' geometric parameters. The 10 cells presented in Fig. 14.12c are designed to constitute the discrete variation of ε_{rr}. Table 14.1 summarizes the corresponding electromagnetic parameters of the cells. The cells are composed of SRRs and ELCs to secure μ_{zz} and ε_{rr}, respectively. $\varepsilon_{\theta\theta}$ is produced by a host medium, which is a commercially available resin.

For numerical verification of the proposed device performance, a microstrip patch antenna presenting a quasi-omnidirectional radiation pattern is used as the feed source of the metamaterial antenna. This patch source is optimized for a 10 GHz operation. A 3D simulation of the patch antenna and the layered metamaterial is

Layout: T1 Standard SC | Book ID: 272865_1_En | Book ISBN: 978-1-4471-4995-8
Chapter No.: 14 | Date: 15-2-2013 | Page: 18/33

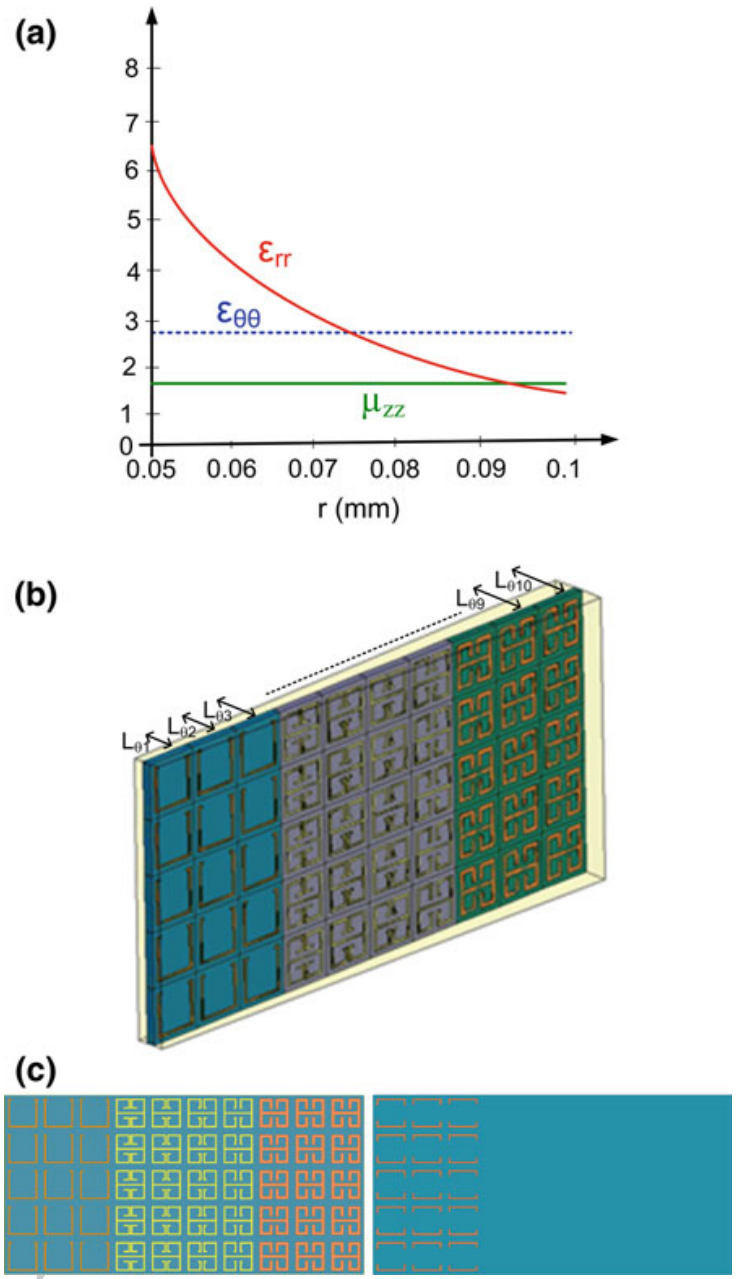

Fig. 14.12 **a** Profile of the material parameters. **b** Single metamaterial layer composed of 10 unit cells providing the material parameters necessary for the coordinate transformation. **c** Front and rear views of the metamaterial cells

performed using HFSS as illustrated in Fig. 14.13a. Figure 14.13b shows the calculated energy distribution in the middle plane of the layered metamaterial structure. Note that the latter structure first transforms the quasi-omnidirectional radiation of the patch source into a directive pattern and also maintains this highly directive emission after the 76° rotation.

14.3.3 Experimental Measurements

To validate experimentally the azimuthal directive emission, the device shown in Fig. 14.14a is fabricated. A microstrip square patch antenna printed on a 1 mm

Table 14.1 Electromagnetic parameters μ_{zz}, and ε_{rr} for the 10 cells of the metamaterial layers

Layer	r_i (mm)	$L_{\theta i}$ (mm)	μ_{zz}	ε_{rr}
1	52.5	2.75	1.7	5.8
2	57.5	3.01	1.7	4.842
3	62.5	3.27	1.7	4.096
4	67.5	3.53	1.7	3.504
5	72.5	3.8	1.7	3.04
6	77.5	4.06	1.7	2.664
7	82.5	4.32	1.7	2.35
8	87.5	4.58	1.7	2.09
9	92.5	4.84	1.7	1.87
10	97.5	5.1	1.7	1.68

The length L_θ of each cell is given as a function of its position along the layer

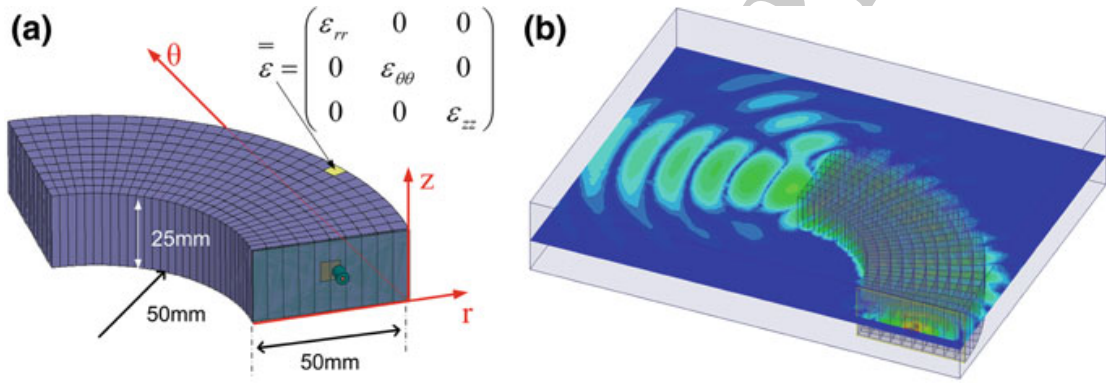

Fig. 14.13 **a** Simulated design consisting of 30 metamaterial layers each composed of 10 cells. **b** Calculated energy distribution at 10 GHz

thick epoxy dielectric substrate ($\varepsilon_r = 3.9$ and $\tan\delta = 0.02$) is used as the radiating source. The metamaterial is a discrete structure composed of 10 different regions where permittivity and permeability vary according to Eq. (14.14) and to the values of Table 14.1. The bulk metamaterial is assembled using 30 layers of RO3003^{TM} dielectric boards on which subwavelength resonant structures are printed. The layers are mounted one-by-one in a molded matrix with a constant angle of 3° between each. A commercially available liquid resin is then poured into the mold. This resin constitutes the host medium and is an important design parameter closely linked to $\varepsilon_{\theta\theta}$. Its measured permittivity is close to 2.8. The mold is removed after solidification of the resin.

S_{11} parameter measurements are first performed on the fabricated prototype. The measured S_{11} parameter of the metamaterial antenna is compared with the HFSS-simulated one in Fig. 14.14b. A good agreement can be observed and return losses reaching 18 dB is observed experimentally at 10.3 GHz compared to 15 dB calculated. This quantity is further compared with that of the feeding patch antenna alone. A better matching can be clearly observed for the metamaterial antenna.

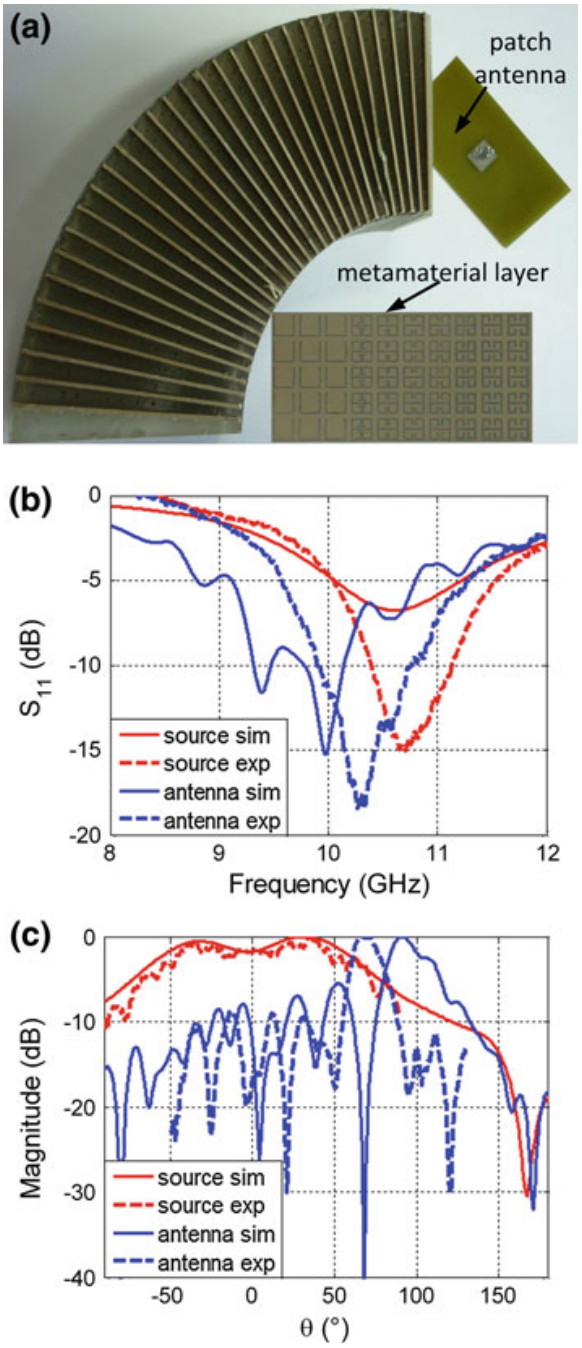

Fig. 14.14 **a** Photograph of the fabricated prototype. **b** Simulated and measured S_{11} parameter of the patch source alone and the metamaterial antenna. **c** Far-field E-plane radiation patterns of the patch source alone and of the metamaterial antenna

The E-plane far-field radiation pattern of the metamaterial antenna is measured in an anechoic chamber. Measurements are performed for the computer-controlled elevation angle varying from −90° to +90°. The measured far-field radiation pattern is presented for the metamaterial device (Fig. 14.14c). From the experiments, it is clearly observed that the transformation of the omnidirectional far-field radiation of the patch antenna into a directive one which is further bent at an angle of 66°, which is consistent with the 76° predicted by numerical simulations. The difference in bending angle is due to the fabrication tolerances of the meta-atoms providing the gradient radial permittivity and to the positioning of the patch source.

Layout: T1 Standard SC | Book ID: 272865_1_En | Book ISBN: 978-1-4471-4995-8
Chapter No.: 14 | Date: 15-2-2013 | Page: 21/33

14.4 Isotropic Antenna

In contrast to the first example where a quasi-isotropic emission was transformed into a directive one, here it is described how a coordinate transformation can be applied to transform directive emissions into isotropic ones. It will also be seen how transformation electromagnetics can modify the apparent (electromagnetic) size of a physical object.

14.4.1 Theoretical Design

An intuitive schematic principle to illustrate the proposed method is presented in Fig. 14.15. Consider a source radiating in a circular space as shown in Fig. 14.15a where a circular region bounded by the blue circle around this source limits the radiation zone. Here, a "space stretching" technique is applied. The "space stretching" coordinate transformation consists in stretching exponentially the central zone of this delimited circular region represented by the red circle as illustrated in Fig. 14.15b.

However, a good impedance match must be preserved between the stretched space and the exterior vacuum. Thus, the expansion procedure is followed by a compression of the annular region formed between the red and blue circles so as to secure an impedance match with free space. Figure 14.15c summarizes the exponential form of the coordinate transformation. The diameter of the transformed (generated metamaterial) circular medium is denoted D.

Mathematically this transformation is expressed as [52]:

$$\begin{cases} r' = \alpha(1 - e^{qr}) \\ \theta' = \theta \\ z' = z \end{cases} \quad \text{with } \alpha = \frac{D}{2}\frac{1}{1 - e^{\frac{qD}{2}}} \tag{14.15}$$

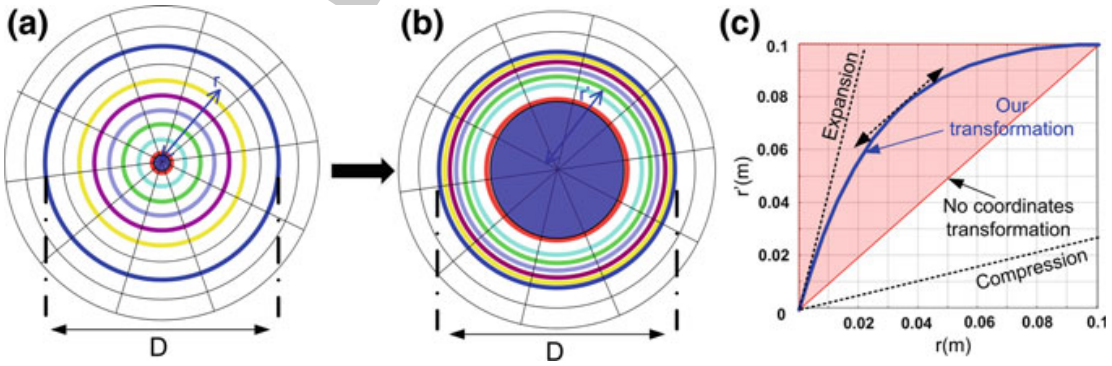

Fig. 14.15 **a** initial space, **b** transformed space, **c** the *blue curve* shows the transformation rule made of an expansion followed by a compression. Reprinted from [52]

where r', θ', and z' are the coordinates in the transformed cylindrical space, and r, θ, and z are those in the initial cylindrical space. In the initial space, free-space conditions are assumed with isotropic permittivity and permeability tensors ε_0 and μ_0. Parameter q (in m^{-1}) appearing in Eq. (14.15) must be negative in order to achieve the impedance matching condition. This parameter is an expansion factor which can be physically viewed as the degree of space expansion. A high (negative) value of q means high expansion whereas a low (negative) value of q means nearly zero expansion.

Calculations lead to permeability and permittivity tensors given in the diagonal base by:

$$\overline{\overline{\psi}} = \begin{pmatrix} \psi_{rr} & 0 & 0 \\ 0 & \psi_{\theta\theta} & 0 \\ 0 & 0 & \psi_{zz} \end{pmatrix} = \begin{pmatrix} \frac{qr(r'-\alpha)}{r'} & 0 & 0 \\ 0 & \frac{r'}{qr(r'-\alpha)} & 0 \\ 0 & 0 & \frac{r}{qr'(r'-\alpha)} \end{pmatrix}$$

with

$$r = \frac{\ln\left(1 - r'/\alpha\right)}{q} \tag{14.16}$$

The components in the Cartesian coordinate system are calculated and are as follows:

$$\begin{cases} \psi_{xx} = \psi_{rr}\cos^2(\theta) + \psi_{\theta\theta}\sin^2(\theta) \\ \psi_{xy} = \psi_{yx} = (\psi_{rr} - \psi_{\theta\theta})\sin(\theta)\cos(\theta) \\ \psi_{yy} = \psi_{rr}\sin^2(\theta) + \psi_{\theta\theta}\cos^2(\theta) \end{cases} \tag{14.17}$$

The ε and μ tensors components present the same behavior as given in Eq. (14.17).

Figure 14.16 shows the variation of the permittivity and permeability tensor components in the newly generated transformed space. The geometric dimension D is chosen to be 20 cm and parameter q is fixed to $-40\ \mathrm{m}^{-1}$. It can be noted that components ψ_{xx}, ψ_{yy}, and ψ_{zz} present variations and an extrema that are simple to realize with commonly used metamaterials by reducing their inhomogeneous dependence [26]. At the center of the transformed space, ε and μ present very low values ($\ll 1$). Consequently, light velocity and the corresponding wavelength are

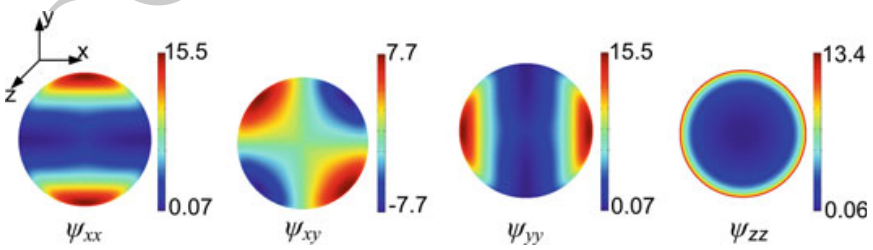

Fig. 14.16 Variation in the permeability and permittivity tensor components of the transformed space for $D = 20$ cm and $q = -40\ \mathrm{m}^{-1}$. Reprinted from [52]

Layout: T1 Standard SC | Book ID: 272865_1_En | Book ISBN: 978-1-4471-4995-8
Chapter No.: 14 | Date: 15-2-2013 | Page: 23/33

much higher than in vacuum. The width of the plane source then appears very small compared to wavelength and the source can then be regarded as a radiating wire, which is in fact an isotropic source. The merit of this transformation depends effectively on the expansion factor q value, and more generally, it can be applied to a wide range of electromagnetic objects, where the effective size can be reduced compared to a given wavelength.

By fixing the electric field directed along the z-axis and by adjusting the dispersion equation without changing propagation in the structure, the following reduced parameters can be obtained:

$$\begin{cases} \mu_{rr} = 1 \\ \mu_{\theta\theta} = \left(\frac{r'}{qr(r'-\alpha)}\right)^2 \\ \varepsilon_{zz} = \left(\frac{r}{r'}\right)^2 \end{cases} \tag{14.18}$$

In Eq. (14.18), the parameters present positive values (Fig. 14.17) which can be easily achieved first by discretizing their continuous profile and second by using metamaterial resonators where magnetic and electric responses can be tailored and controlled.

14.4.2 Numerical Verifications

Figure 14.18 presents simulations results of the source radiating in the initial circular space at an operating frequency of 4 GHz for several values of q. The current direction of the source is supposed to be along the z-axis. Simulations are performed in a TE mode with the electric field polarized along the z-direction. The surface-current source is considered to have a width of 10 cm, which is greater than the 7.5 cm wavelength at 4 GHz. Radiation boundary conditions are placed around the calculation domain in order to plot the radiation properties. Continuity of the field is assured in the interior boundaries. As stated previously and verified

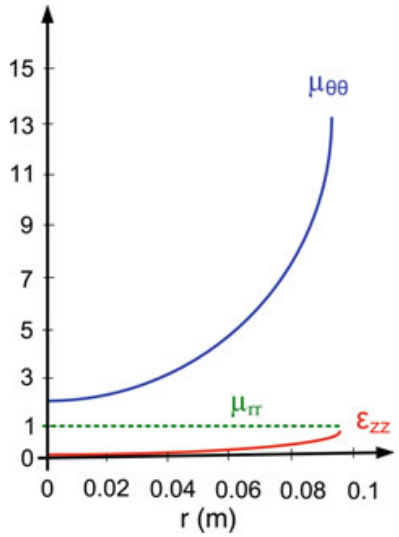

Fig. 14.17 Tailored permittivity and permeability values in a cylindrical configuration. Reprinted from [52]

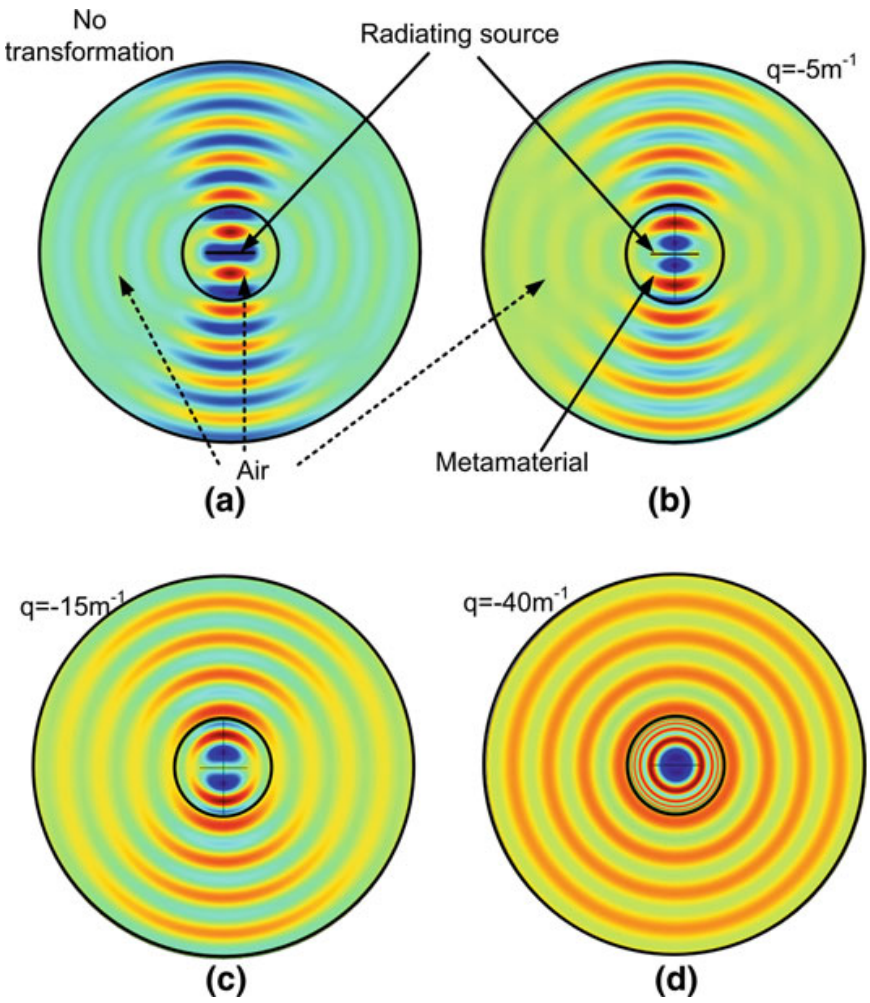

Fig. 14.18 Simulated electric field distribution for a TE wave polarization at 4 GHz. **a** A planar current source is used as the excitation for the transformation. The current direction is perpendicular to the plane of the figure. (**b–d**) Verification of the transformation for different values of expansion factor q. Reprinted from [52]

from the different electric field distribution patterns, a high negative value of q leads to a quasi-perfect isotropic emission since the space expansion is higher. This phenomenon can be clearly observed in Fig. 14.18d for $q = -40$ m^{-1}.

The calculated far-field patterns are shown in Fig. 14.19a. The source alone produces a directive emission, but when it is surrounded by the judiciously engineered coordinate-transformation-based metamaterial, an isotropic emission is produced. Figure 14.19b shows the influence of parameter q on the space expansion in the coordinate transformation. As q becomes highly negative, a greater space expansion is achieved.

To summarize, a directive radiating source with a size greater than the wavelength has been transformed into an isotropic one with a size is much smaller than the wavelength. This transformation is equivalent to reduce the apparent electromagnetic size of this source. With an opposite transformation the apparent size of the source would have increased. The practical implementation of both transformations is in progress.

Layout: T1 Standard SC | Book ID: 272865_1_En | Book ISBN: 978-1-4471-4995-8
Chapter No.: 14 | Date: 15-2-2013 | Page: 25/33

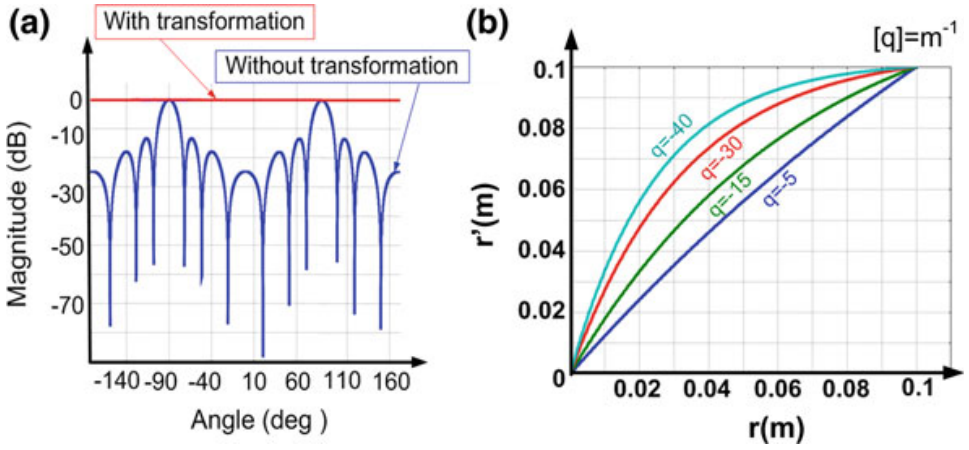

Fig. 14.19 **a** Far-field radiation pattern of the emission with ($q = -40$ m^{-1}) and without transformation. **b** Influence of the expansion parameter q on the proposed coordinate transformation. The emitted radiation is more and more isotropic as q tends to high negative values

14.5 Waveguide Taper

In this last section, the design of a taper is presented to control the flow of light between two waveguides of different cross sections. Three different transformation techniques are presented so as to achieve a reflection less taper between the two waveguides. This example shows the importance of the optimization of the analytical transformation between the initial space and the transformed one to obtain realizable values of electromagnetic parameters. The media obtained from these three methods presents complex anisotropic permittivity and permeability. However, using an exponential transformation leads to the design of a taper from a material with physically achievable material parameters. This application is primarily concerned with the optical frequency regime.

14.5.1 Transformation Formulations

Three different formulations are proposed below to achieve a low-reflection taper between two waveguides of different cross sections. Each waveguide is represented by black lines in its respective space given in Cartesian coordinates as depicted in Fig. 14.20. The aim is to connect the horizontal lines between the spaces to allow transmission of electromagnetic waves. Thus, in the geometric approximation, each ray of light in the first waveguide is guided into the second one by green lines representing the taper. For the first formulation, a linear transformation may be assumed by connecting the two spaces with straight lines as shown in Fig. 14.20a. The second formulation uses a parabolic transformation to achieve the connection (Fig. 14.20b). For the third one, an exponential transformation is defined as shown in Fig. 14.20c. In all three cases, the geometrical

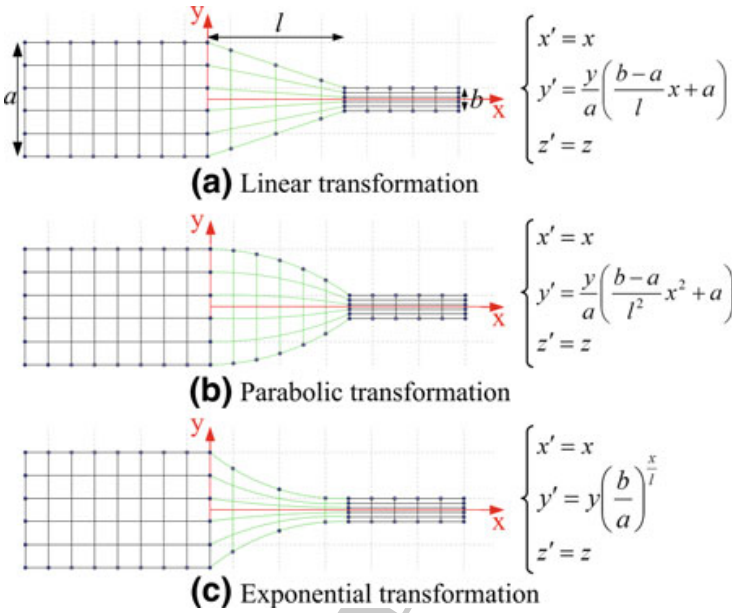

Fig. 14.20 Transformed tapers (*green lines*) between two waveguides (*black lines*) with different cross sections. **a** Linear, **b** parabolic, and **c** exponential transformation formulation. Reprinted from [23]

properties of the schema under analysis remain unchanged. The widths of the input and output waveguides are denoted a and b, respectively, and the length of the taper in all three cases is taken to be l. Mathematical expressions defining each formulation of the transformation approaches are given in Fig. 14.20. x', y' and z' are the coordinates in the transformed (new) space and x, y, and z are those in the initial space. As can be observed from the mathematical expressions, the different formulations depend on the geometric parameters (a, b, l).

Each transformation leads to a material with specific properties that can play the role of the desired taper. The transformation approach can be summarized into two main points. First, the Jacobian matrix of each transformation formulation is determined so as to obtain the properties of the "taper space".

The second step consists of calculating the new permittivity and permeability tensors in the coordinate system (x', y') so as to mimic the transformed space. At this point, a material has been designed with the specific desired physical properties. This material can then be described by the permeability and permittivity tensors $\overline{\overline{\varepsilon}} = \overline{\overline{\theta}}\varepsilon_0$ and $\overline{\overline{\mu}} = \overline{\overline{\theta}}\mu_0$. In order to simplify the different calculations, take $\frac{J_i^{i'} J_j^{j'} \delta^{ij}}{\det(J)} = \theta^{i'j'}$ with

$$\overline{\overline{\theta}} = \begin{pmatrix} \theta_{xx}(x') & \theta_{xy}(x', y') & 0 \\ \theta_{xy}(x', y') & \theta_{yy}(x', y') & 0 \\ 0 & 0 & \theta_{zz}(x') \end{pmatrix} \tag{14.19}$$

The component values of the $\overline{\overline{\theta}}$ tensor are given in Table 14.2 where a non-diagonal term (θ_{xy}) appears. This non-diagonal term is necessary to guide electromagnetic waves in the x–y plane as the case for this taper.

Table 14.2 Components values of $\overline{\overline{\theta}}$ tensor for the three transformations

	$\theta_{xx}(x') = \theta_{zz}(x')$	$\theta_{xy}(x', y')$	$\theta_{yy}(x', y')$
Linear transformation	$\frac{al}{a(l-x')+bx'}$	$\theta_{xx}^2 \frac{b-a}{al} y'$	$\frac{1}{\theta_{xx}} + \frac{\theta_{xy}^2}{\theta_{xx}}$
Parabolic transformation	$\frac{al^2}{(al^2-ax'^2+bx'^2)}$	$\frac{2\theta_{xx}^2(b-a)x'y'}{al^2}$	$\frac{1}{\theta_{xx}} + \frac{\theta_{xy}^2}{\theta_{xx}}$
Exponential transformation	$\left(\frac{b}{a}\right)^{-\frac{x'}{l}}$	$\frac{\theta_{xx}y' \ln\left(\frac{b}{a}\right)}{l}$	$\frac{1}{\theta_{xx}} + \frac{\theta_{xy}^2}{\theta_{xx}}$

14.5.2 Simulations and Results

To verify the results expressed in the previous section, the finite element-based commercial software Comsol MULTIPHYSICS is used to design the described waveguide taper. Two-dimensional simulations are performed for the validation of the proposed material parameters. Port boundaries are used to excite the first and third transverse electric (TE_1 and TE_3) modes of the input waveguide with the E-field directed along the z-axis to verify the conservation of modes through the taper. The waveguides boundaries are assumed to be Perfect Electric Conductors (PECs) and matched boundaries conditions are applied to the taper. Verifications are done in the microwave domain for a possible future physical prototype based on metamaterials.

The waveguide widths are chosen to be $a = 10$ cm and $b = 2$ cm with 1.5 and 7.5 GHz cutoff frequencies, respectively. The length of the taper is chosen as $l = 5$ cm, thus allowing the generation of the entire spatial dependence of the material parameters $\theta_{xx}(x')$, $\theta_{zz}(x')$, $\theta_{xy}(x',y')$, and $\theta_{yy}(x',y')$ as shown in Fig. 14.21. These distributions are plotted from the expressions given in Table 14.2. Values of permittivity and permeability presented in Fig. 14.21 account for the control of the electromagnetic field in the taper and the conservation of the propagating modes from waveguide 1 to waveguide 2. Although the same spatial distribution profile can be observed for the three different formulations, the parameter values are completely different. For the linear and parabolic transformations, values of μ_{yy} are too high to be physically achievable with existing metamaterials. However, it is clear that the exponential transformation leads to values more easily achievable with metamaterials. Moreover, the physical realization of such a metamaterial taper will be facilitated by the slow variation of the material parameters, implying a gradual variation in the geometric parameters of metamaterial inclusions. Note that the components are calculated in the Cartesian system and obey the following dispersion relation in the TE mode:

$$\varepsilon_{zz}\left(\mu_{xy}^2 - \mu_{xx}\mu_{yy}\right) + \mu_{xx}k_x^2 + k_y\left(\mu_{yy}k_y - 2\mu_{xy}k_x\right) = 0 \qquad (14.20)$$

This equation is obtained from the propagation equation and describes the control of electromagnetic waves in the material. This relation is also important for a future reduction of parameters, which can be done by simplifying the non-diagonal parameter θ_{xy} to a closed interval near zero when choosing the

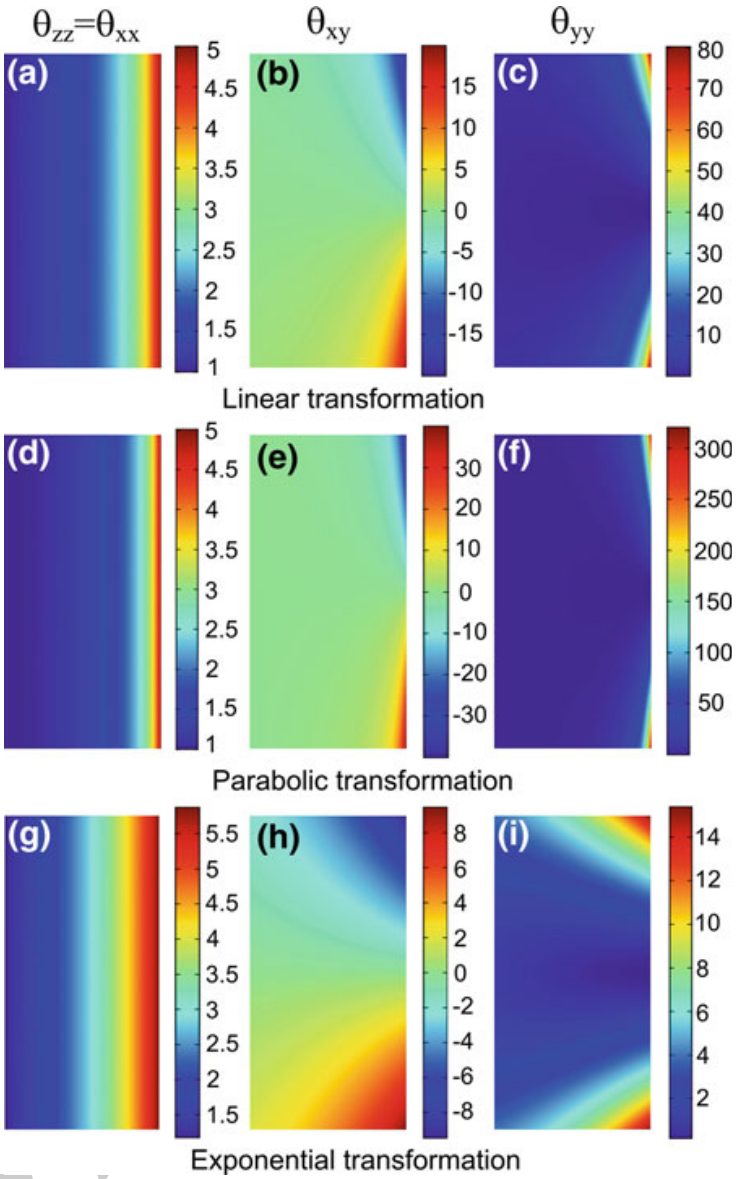

Fig. 14.21 Components of the permittivity and permeability tensors $\overline{\overline{\theta}}$ for the three transformations with $a = 10$ cm, $b = 2$ cm, and $l = 5$ cm. Reprinted from [23]

appropriate length of the taper. For example, by bounding the non-diagonal term of the exponential formulation in Table 14.2, the condition $l > \frac{a^2}{b}\frac{\left|\ln\left(\frac{b}{a}\right)\right|}{2\Delta}$ leads to $-\Delta < \mu_{xy} < \Delta$ where Δ can be very close to zero.

Simulation results for the E-field distribution of the structure under study for all three transformations are presented in Fig. 14.22. The distributions in the tapered waveguides are compared to a non-tapered case at 10 and 30 GHz for the fundamental (TE_1) excitation mode and at 30 GHz for the third (TE_3) excitation mode. Concerning the non-tapered junction waveguides, phase distortions may be observed due to reflections at the junction from the larger waveguide to the smaller one (Fig. 14.22a–c). These distortions become more severe at higher frequencies (30 GHz). However, simulations performed on the tapered waveguides (Fig. 14.22d–l) illustrate that electromagnetic waves are properly guided from one waveguide to the other without any impact on the guided mode when the transformed medium is embedded between the two waveguides.

Layout: T1 Standard SC | Book ID: 272865_1_En | Book ISBN: 978-1-4471-4995-8
Chapter No.: 14 | Date: 15-2-2013 | Page: 29/33

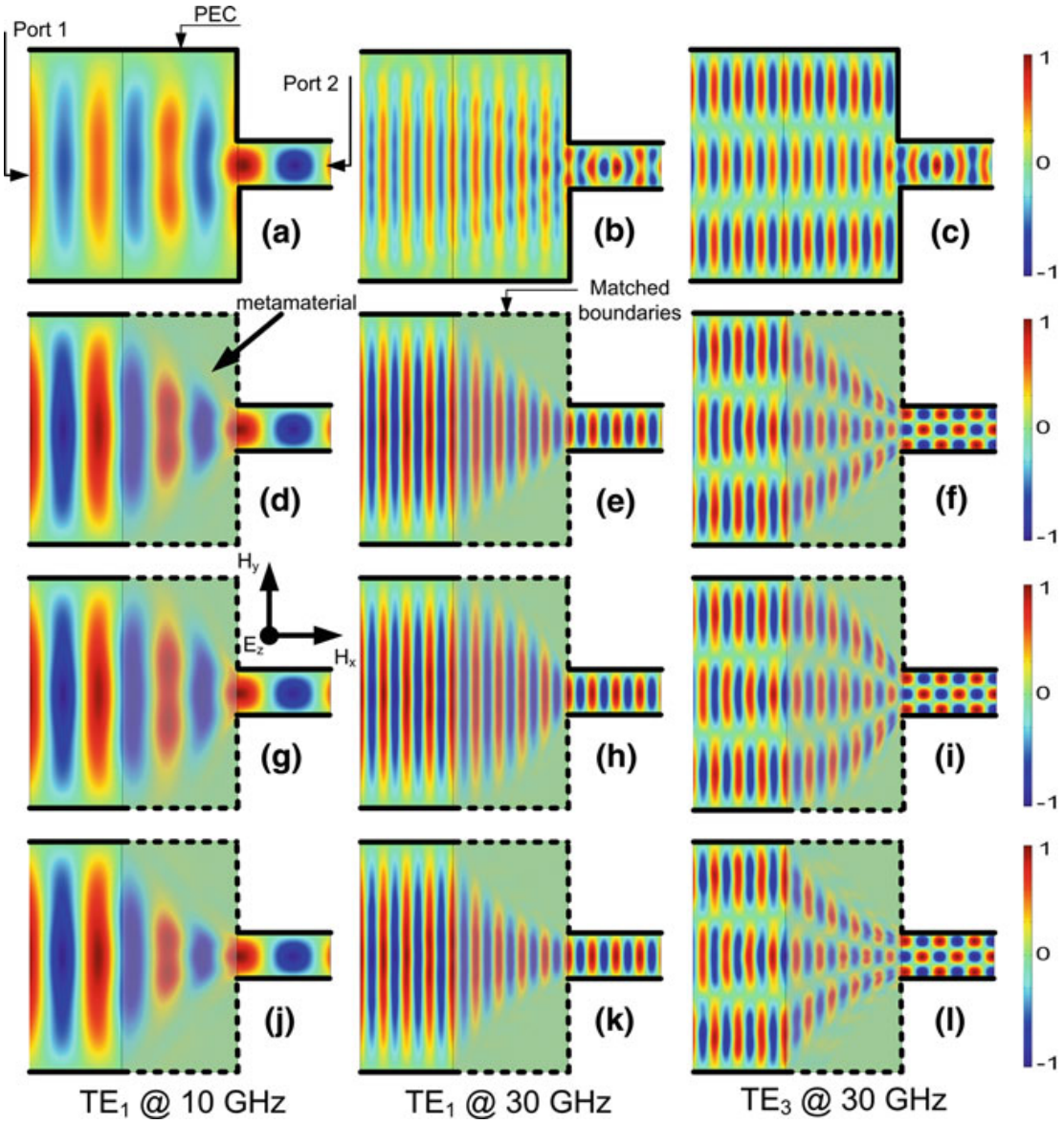

Fig. 14.22 Normalized E-field distribution for TE polarization. **a–c** Non-tapered junction waveguides. **d–f** Tapered junction waveguides with linear transformation. **g–i** Tapered junction waveguides with parabolic transformation. **j–l** Tapered junction waveguides with exponential transformation. Reprinted from [23]

The difference in the transformation formulations indicates a change in the path of electromagnetic waves in the tapered section, highlighted by the shaded gray area in Fig. 14.22. Increasing the frequency improves the transmission between the two waveguides through the tapered section. This phenomenon can be observed when the E-field distributions are compared at 10 and 30 GHz. At 10 GHz, a slight impedance mismatch between the taper output and the small waveguide input can be observed. This phenomenon decreases at higher frequencies, as illustrated for 30 GHz. It is due to the general rule of coordinate transformations when compressing or expanding space.

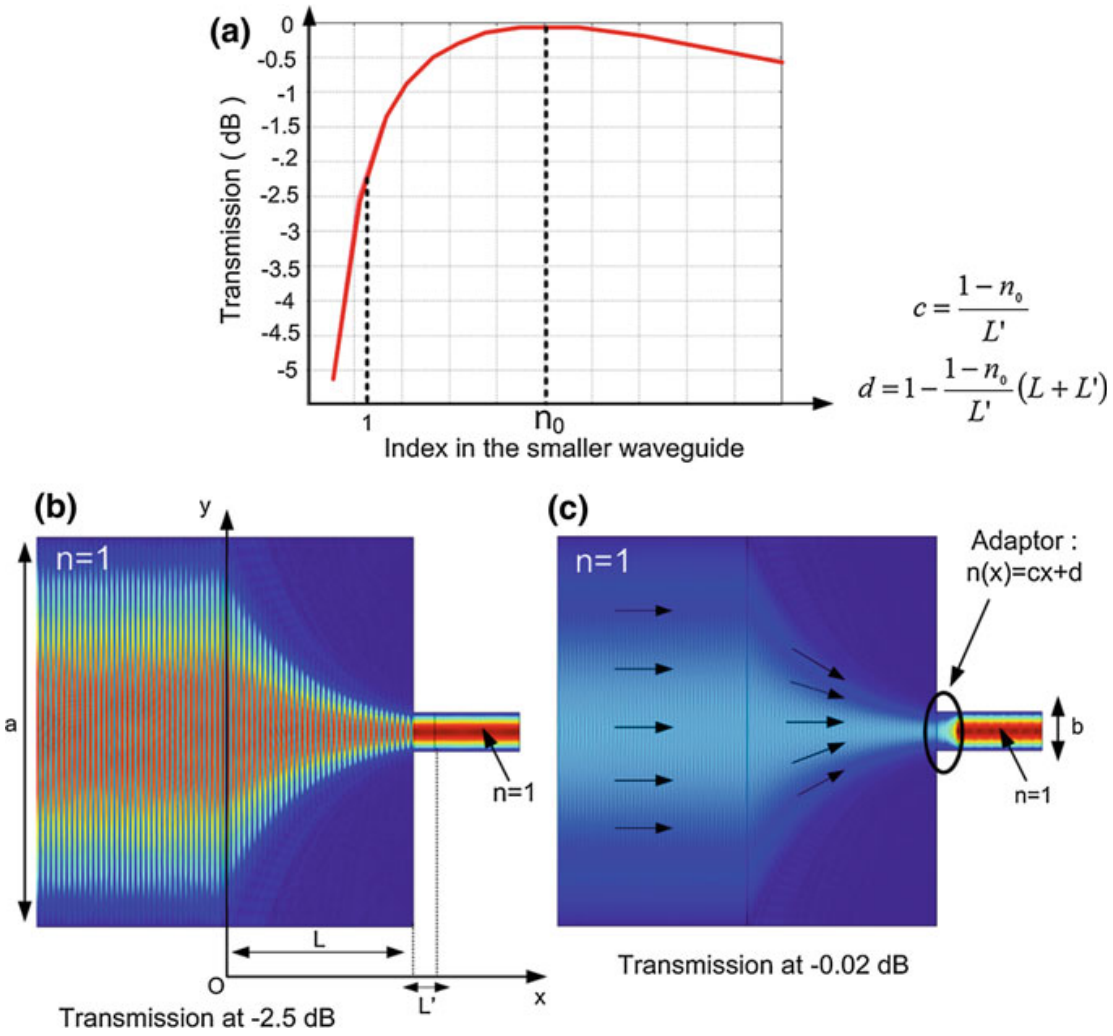

Fig. 14.23 Evolution of the transmission according to the index in the smaller waveguide. Maximum transmission is ensured for n_0. An adaptor is calculated for total transmission between the two waveguides filled with vacuum

To cancel all the reflections and to have a total transmission, it is possible, for example, to create an isotropic gradient index in the second guide. This gradient can be created by choosing a conformal transformation, with a transformation on the x component. Figure 14.23a illustrates the evolution of the transmission coefficient with the index in the small waveguide. Figure 14.23a and b highlights standing waves in the transformation-based material and the large waveguide due to reflections at the entrance of the small waveguide. So, to ensure a quasi-total transmission a material with a gradient index is introduced following the x-axis as presented in Fig. 14.23c. All the energy is then transferred to the smaller waveguide. The conservation of the energy flow allows us to understand the higher amplitude in the smaller waveguide by a factor $\sqrt{(a/b)}$. Indeed, by denoting π as the norm of the Poynting vector, the relationship is $\pi_1 a = \pi_2 b$; since π is proportional to E^2 in vacuum, the field ratio is equal to $\sqrt{(a/b)}$.

To summarize, compared to an abrupt (non-tapered) junction where phase distortions appear, transformation optics helps to properly guide electromagnetic

Layout: T1 Standard SC | Book ID: 272865_1_En | Book ISBN: 978-1-4471-4995-8
Chapter No.: 14 | Date: 15-2-2013 | Page: 31/33

waves from one waveguide to another without any impact on the guided propagating modes. The implementation of this taper on silicon and glass at 1.5 μm is in progress [53, 54].

14.6 Conclusion

In this chapter, the coordinate transformation theory has been presented as applied to the design of non-standard electromagnetic devices. The coordinate transformation technique does not present any theoretical limit in the design concept, and applications can be scaled to any frequency regime. The ideas of applications can then be extremely varied. The only limit is technological, mainly due to the practical values of electromagnetic parameters achievable with metamaterials. Here, three antenna applications have been proposed in the microwave domain through the use of metamaterials, as well as an optical waveguide taper. The two antenna examples have been practically realized using metamaterials. These metamaterials are periodic structures composed of subwavelength metallic inclusions in a host dielectric matrix. The difficulty in the design of such metamaterials resides in the engineering of the proper inclusions for electric and magnetic resonances. The permittivity and permeability tensors generated by coordinate transformation are often inhomogeneous and anisotropic and it is thus necessary to reduce and discretize these parameters by controlling the dispersion relation of the structure. Thus, a careful choice will make it possible to find an inexpensive and easily realizable material. The drawback of this simplification will then be an impedance mismatch. However, this impedance mismatch can be controlled by an optimization of the parameter simplification.

Acknowledgments The authors thank D. Germain, A. Sellier, X. Wu, and S. Kirouane for their help in the realization and characterization of the prototypes in this study. They also thank the French National Research Agency for its financial support through the METAPHORT, METAVEST, and METAPHOTONIQUE projects.

References

1. Pendry JB, Schurig D, Smith DR (2006) Controlling electromagnetic fields. Science 312:1780–1782
2. Leonhardt U (2006) Optical conformal mapping. Science 312:1777–1780
3. Schurig D, Mock JJ, Justice BJ et al (2006) Metamaterial electromagnetic cloak at microwave frequencies. Science 314:977–980
4. Cai W, Chettiar UK, Kildishev AV et al (2007) Optical cloaking with metamaterials. Nat Photon 1:224–227
5. Kanté B, de Lustrac A, Lourtioz JM et al (2008) Infrared cloaking based on the electric response of split ring resonators. Opt Express 16:9191–9198
6. Gabrielli LH, Cardenas J, Poitras CB et al (2009) Silicon nanostructure cloak operating at optical frequencies. Nat Photon 3:461–463

Layout: T1 Standard SC | Book ID: 272865_1_En | Book ISBN: 978-1-4471-4995-8
Chapter No.: 14 | Date: 15-2-2013 | Page: 32/33

7. Kanté B, Germain D, de Lustrac A (2009) Experimental demonstration of a nonmagnetic metamaterial cloak at microwave frequencies. Phys Rev B 80:201104
8. Valentine J, Li J, Zentgraf T et al (2009) An optical cloak made of dielectrics. Nat Mater 8:568–571
9. Ergin T, Stenger N, Brenner P et al (2010) Three-dimensional invisibility cloak at optical wavelengths. Science 328:337–339
10. Leonhardt U, Tyc T (2009) Broadband invisibility by non-Euclidean cloaking. Science 323:110–112
11. Li J, Pendry JB (2008) Hiding under the carpet: a new strategy for cloaking. Phys Rev Lett 101:203901
12. Liu R, Ji C, Mock JJ et al (2009) Broadband ground-plane cloak. Science 323:366–369
13. Jiang WX, Cui TJ, Qiang C, Chin JY, Yang XM, Liu R, Smith DR (2008) Design of arbitrarily shaped concentrators based on conformally optical transformation of nonuniform rational B-spline surfaces. Appl Phys Lett 92:264101
14. Luo Y, Chen H, Zhang J, Ran L, Kong JA (2008) Design and analytical full-wave validation of the invisibility cloaks, concentrators, and field rotators created with a general class of transformations. Phys Rev B 77:125127
15. Rahm M, Schurig D, Roberts DA, Cummer SA, Smith DR, Pendry JB (2008) Design of electromagnetic cloaks and concentrators using form-invariant coordinate transformations of Maxwell's equations. Photon Nanostruct Fundam Appl 6:87–95
16. Greenleaf A, Kurylev Y, Lassas M, Uhlmann G (2007) Electromagnetic wormholes and virtual magnetic monopoles from metamaterials. Phys Rev Lett 99:183901
17. Zhang J, Luo Y, Chen H, Huangfu J, Wu BI, Ran L, Kong JA (2009) Guiding waves through an invisible tunnel. Opt Express 17:6203–6208
18. Huangfu J, Xi S, Kong F, Zhang J, Chen H, Wang D, Wu BI, Ran L, Kong JA (2008) Application of coordinate transformation in bent waveguides. J Appl Phys 104:014502
19. Kwon DH, Werner DH (2008) Transformation optical designs for wave collimators, flat lenses and right-angle bends. New J Phys 10:115023
20. Landy NI, Padilla WJ (2009) Guiding light with conformal transformations. Opt Express 17:14872–14879
21. Rahm M, Roberts DA, Pendry JB, Smith DR (2008) Transformation-optical design of adaptive beam bends and beam expanders. Opt Express 16:11555–11567
22. Roberts DA, Rahm M, Pendry JB, Smith DR (2009) Transformation-optical design of sharp waveguide bends and corners. Appl Phys Lett 93:251111
23. Tichit PH, Burokur SN, de Lustrac A (2010) Waveguide taper engineering using coordinate transformation technology. Opt Express 18:767–772
24. Kong F, Wu BI, Kong JA, Huangfu J, Xi S (2007) Planar focusing antenna design by using coordinate transformation technology. Appl Phys Lett 91:253509
25. Chen H, Hou B, Chen S, Ao X, Wen W, Chan CT (2009) Design and experimental realization of a broadband transformation media field rotator at microwave frequencies. Phys Rev Lett 102:183903
26. Tichit PH, Burokur SN, Germain D, de Lustrac A (2011) Design and experimental demonstration of a high-directive emission with transformation optics. Phys Rev B 83:155108
27. Tamm IY (1924) Electrodynamics of an anisotropic medium in the special case of relativity. J Russ Phys Chem Soc 56:248
28. Plebanski J (1960) Electromagnetic waves in gravitational fields. Phys Rev 118:1396–1408
29. Han T, Qiu CW (2010) Isotropic nonmagnetic flat cloaks degenerated from homogeneous anisotropic trapeziform cloaks. Opt Express 18:13038–13043
30. Schmiele M, Varma VS, Rockstuhl C, Lederer F (2010) Designing optical elements from isotropic materials by using transformation optics. Phys Rev A 81:33837
31. Turpin JP, Massoud AT, Jiang ZH, Werner PL, Werner DH (2010) Conformal mappings to achieve simple material parameters for transformation optics devices. Opt Express 18:244–252

786 32. Chang Z, Zhou X, Hu J, Hu G (2010) Design method for quasi-isotropic transformation
787 materials based on inverse Laplace's equation with sliding boundaries. Opt Express
788 18:6089–6096
789 33. Leonhardt U (2000) Space-time geometry of quantum dielectrics. Phys Rev A 62:012111
790 34. Bergamin L (2008) Generalized transformation optics from triple spacetime metamaterials.
791 Phys Rev A 78:43825
792 35. Thompson RT, Cummer SA, Frauendiener J (2011) A completely covariant approach to
793 transformation optics. J Opt 13:024008
794 36. Crudo RA, O'Brien JG (2009) Metric approach to transformation optics. Phys Rev A
795 80:033824
796 37. Cheng Q, Cui TJ, Jiang WX, Cai BG (2010) An omnidirectional electromagnetic absorber
797 made of metamaterials. New J Phys 12:063006
798 38. Narimanov EE, Kildishev AV (2009) Optical black hole: Broadband omnidirectional light
799 absorber. Appl Phys Lett 95:041106
800 39. Genov DA, Zhang S, Zhang X (2009) Mimicking celestial mechanics in metamaterials. Nat
801 Phys 5:687–692
802 40. Jiang WX, Cui TJ, Ma HF, Zhou XY, Cheng Q (2008) Cylindrical-to-plane-wave conversion
803 via embedded optical transformation. Appl Phys Lett 92:261903
804 41. Kundtz N, Smith DR (2009) Extreme-angle broadband metamaterial lens. Nat Mater
805 9:129–132
806 42. Rahm M, Cummer SA, Schurig D, Pendry JB, Smith DR (2008) Optical design of
807 reflectionless complex media by finite embedded coordinate transformations. Phys Rev Lett
808 100:63903
809 43. Luo Y, Zhang J, Ran L, Chen H, Kong JA (2008) Controlling the emission of electromagnetic
810 source. PIERS Online 4:795–800
811 44. Luo Y, Zhang J, Ran L, Chen H, Kong JA (2008) New concept conformal antennas utilizing
812 metamaterial and transformation optics. IEEE Antennas Wireless Propag Lett 7:509–512
813 45. Popa BI, Allen J, Cummer SA (2009) Conformal array design with transformation
814 electromagnetics. Appl Phys Lett 94:244102
815 46. Allen J, Kundtz N, Roberts DA, Cummer SA, Smith DR (2009) Electromagnetic source
816 transformations using superellipse equations. Appl Phys Lett 94:194101
817 47. Ma YG, Ong CK, Tyc T, Leonhardt U (2009) An omnidirectional retroreflector based on the
818 transmutation of dielectric singularities. Nat Mater 8:639–642
819 48. Balanis CA (1997) Antenna theory: analysis and design, 2nd edn. Wiley, New York
820 49. Pendry JB, Holden AJ, Robbins DJ, Stewart WJ (1999) Magnetism from conductors and
821 enhanced nonlinear phenomena. IEEE Trans Microwave Theory Tech 47:2075–2084
822 50. Schurig D, Mock JJ, Smith DR (2006) Electric-field-coupled resonators for negative
823 permittivity metamaterials. Appl Phys Lett 88:041109
824 51. Nicholson AM, Ross GF (1970) Measurement of the intrinsic properties of materials by time-
825 domain techniques. IEEE Trans Instrum Meas 19:377–382
826 52. Tichit PH, Burokur SN, de Lustrac A (2011) Transformation media producing quasi-perfect
827 isotropic emission. Opt Express 19:20551–20556
828 53. Ghasemi R, Tichit PH, Degiron A, Lupu A, de Lustrac A (2010) Efficient control of a 3D
829 optical mode using a thin sheet of transformation optical medium. Opt Express
830 18:20305–20312
831 54. Lupu A, Dubrovina N, Ghasemi R, Degiron A, de Lustrac A (2011) Metal-dielectric
832 metamaterials for guided wave silicon photonics. Opt Express 19:24746–24761

Annexe 4 : Principaux travaux relatifs au chapitre 4

Annexe 4.1

A. Dhouibi, S. N. Burokur, A. de Lustrac, A. Priou

« Compact metamaterial-based substrate-integrated luneburg lens antenna »

IEEE Antennas and Wireless Propagation Letters, vol. 11, pp. 1504-1507, 2012

Compact Metamaterial-Based Substrate-Integrated Luneburg Lens Antenna

Abdallah Dhouibi, Shah Nawaz Burokur, André de Lustrac, *Member, IEEE*, and Alain Priou, *Senior Member, IEEE*

***Abstract*—A compact and small electric-size aperture directive broadband Luneburg lens antenna is presented. The substrate-integrated lens antenna is based on embedding a Vivaldi antenna source inside a parallel-plate waveguide to illuminate a Luneburg lens operating in X-band. The focusing condition of the lens, requiring a gradient refractive index, is achieved through the use of complementary nonresonant metamaterial structures. Numerical simulations are performed to determine the suitable unit cells geometry with respect to the wave launcher inserted into the parallel-plate waveguide. A prototype fabricated using standard printed circuit board techniques has been measured in an anechoic chamber. The electric field distribution inside the antenna system has also been explored using a two-dimensional near-field microwave scanning setup. A good qualitative agreement is observed between simulations and experiments. It has been shown from both far- and near-field measurements that the proposed planar antenna presents good focusing properties.**

***Index Terms*—Gradient index materials, Luneburg lens antenna, parallel-plate waveguide, Substrate-integrated.**

I. Introduction

DUE TO their peculiar abilities to control and manipulate light, gradient index (GRIN) media [1] have been widely used to realize several microwave devices since at least Maxwell's time [2]. Up to now, there is an ongoing effort to achieve more general gradient parameter distributions suitable to growing new fields of applications based on novel class coordinate transformation devices [3], [4] like invisibility cloaks [5], Luneburg lenses [6], and antennas [7]–[9]. Metamaterials have interesting physical properties that are well suited to realize such structures. GRIN lenses have been proposed as alternatives to conventional dielectric ones, where refractive index is varied throughout the lens instead of relying on the interfaces of the dielectric material to control light flow. It has been shown lately that a planar medium composed of metallic inclusions on a printed circuit board can satisfy the refractive index profile of a Luneburg lens [10], [11] given by the relation $n(r) = \sqrt{2 - (r/R)^2}$ $(0 \leq r \leq R)$ [12], where R is the radius of the lens and r is the distance from any point to the lens center. It has been reported that a point source on the surface of such planar 2-D lenses is transformed into a collimated beam on its diametrically opposite side. Experimental validation of such lenses was generally done by using horn antennas or coaxial-to-waveguide transitions as primary source to illuminate the lens. Such feed methods cause an increase in the profile of the Luneburg lens by the voluminous size of the feeding structure, making in-board integration of such devices very difficult. Also, the spherical locus of focal points of such lenses is inherently unsuitable for receiver arrays, which are generally planar. Later, the continuous refractive index variation of a Luneburg lens antenna, with an aperture size of 12.4 λ_0 (λ_0 is the free-space wavelength) has also been achieved by meandering crossed microstrip lines and varying their widths around 13 GHz [13]. In the latter antenna, a 10-cm-thick circular flare was added to the lens by soldering thin copper-clad laminates to its edge. Although their efficiencies are good, these previously proposed designs remain bulky and difficult to integrate in radio systems where low profile is desired.

In this letter, we focus our attention on the combination of a compact planar feeding structure with a substrate-integrated GRIN material assimilating a small electric size Luneburg lens. The design of the planar broadband Luneburg lens antenna using a Vivaldi antenna as feed is detailed. The antenna dimensions are 130×190 mm^2 with a total height of 11 mm and operation in a quasi-TEM mode in the [8–12 GHz] frequency band. The gradient index of the Luneburg lens is achieved through a two-dimensional array of waveguided units of complementary closed-ring (CCR) resonators [14]. The proposed lens antenna system is excited by an integrated Vivaldi primary source, which is fed by a tapered microstrip transmission line. The proposed antenna configuration is compact and lightweight and presents broadband features. Furthermore, the use of a planar feed in the overall low-profile lens antenna suggests a good matching to the spherical locus of focal points and an easy integration into in-board systems incorporating active devices.

II. Lens Design

The metamaterial-based Luneburg lens of radius $R = 56$ mm is designed for an 8–12-GHz frequency band operation. A nonresonant electric complementary closed-ring resonator is used as the basic unit cell of the artificial medium representing the Luneburg lens. As illustrated in Fig. 1, the closed-ring resonator patterns are etched on the copper-cladding of a Rogers RT/duroid 5880 material, with a relative permittivity of 2.2, a thickness of 0.4 mm, and a loss tangent of 0.0009. In our experiments, the metamaterial planar slab is inserted in a

Manuscript received August 27, 2012; accepted December 03, 2012. Date of publication December 11, 2012; date of current version January 03, 2013. This work was supported by the EADS Company Foundation through the METAQOPT project under Contract No. 090-AO09-1006. The work of A. Dhouibi was supported by the EADS Company Foundation under a Ph.D. scholarship.

A. Dhouibi and A. Priou are with LEME, EA 4416, Université Paris Ouest, 92410 Ville d'Avray, France.

S. N. Burokur and A. de Lustrac are with IEF, CNRS, UMR 8622, Université. Paris-Sud, 91405 Orsay cedex, France, and also with Université Paris Ouest, 92410 Ville d'Avray, France (e-mail: shah-nawaz.burokur@u-psud.fr).

Color versions of one or more of the figures in this letter are available online at http://ieeexplore.ieee.org.

Digital Object Identifier 10.1109/LAWP.2012.2233191

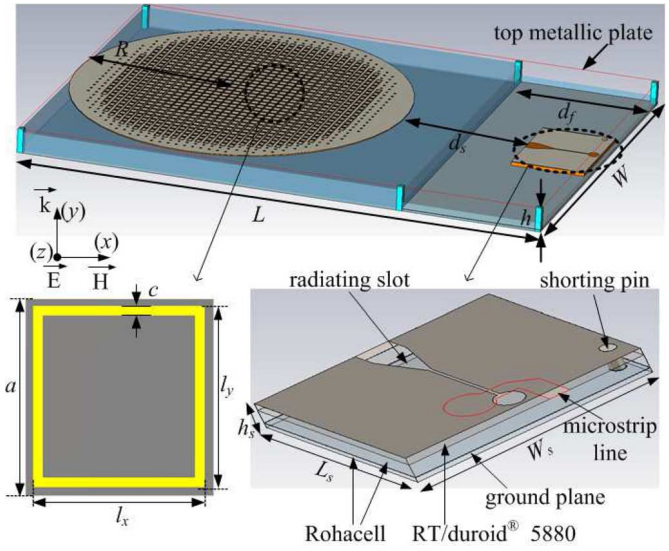

Fig. 1. Luneburg lens antenna composed of a planar metamaterial-based lens and a Vivaldi antenna feed placed in a quasi-TEM parallel-plate waveguide. In the CCR cell: $a = 3.333$ mm, $c = 0.3$ mm, and l_x and l_y are variable parameters. In the Vivaldi feed: $L_s = 26.5$ mm, $W_s = 35$ mm, and $h_s = 5.2$ mm. In the whole antenna system: $L = 190$ mm, $W = 130$ mm, $h = 11$ mm, $d_f = 50$ mm, $d_s = 51.5$ mm, and $R = 56$ mm.

TABLE I
DIMENSIONS OF THE CCR CELLS AND THEIR EFFECTIVE INDEX AT 10 GHZ IN THE DIFFERENT DISCRETIZED ZONES OF THE LUNEBURG LENS

Zone	l_x (mm)	l_y (mm)	n_{eff}
1	0.8	0.8	1.01
2	2	2.6	1.09
3	2.3	2.6	1.14
4	2.6	2.8	1.22
5	2.8	2.8	1.30
6	2.9	2.8	1.33
7	2.9	2.9	1.36

quasi-TEM waveguide consisting of two parallel copper plates having dimensions 130×190 mm^2 ($5.2\lambda_0 \times 7.6\lambda_0$ at 12 GHz) and spaced by 11 mm. As shown in Fig. 1, the sample is placed on a Rohacell foam spacer, with a relative permittivity close to 1, to fill up the space between the substrate and the bottom metallic plate. The gap between the patterned circuit board and the top copper plate of the waveguide is kept as 1 mm. To obtain the desired effective permittivity and permeability of the CCR units, the properties are characterized numerically using the finite-difference time-domain (FDTD) Maxwell's equations solver of CST Microwave Studio Suite. The electromagnetic parameters are retrieved using the simulated S-parameters as proposed by the inversion method described in [15]. The variation of the refractive index from the center to the border of the lens consists in changing the CCR geometrical dimensions l_x and l_y, as illustrated in Table I, while keeping the lattice period a fixed to 3.333 mm. In our design, the Luneburg lens was discretized into seven concentric regions, where each region composed of two cells corresponds to a specific refractive index. Hence, the effective refractive index can be varied from 1.01 to 1.36. The waveguided metamaterials are utilized in their nonresonant frequency regime such that they present

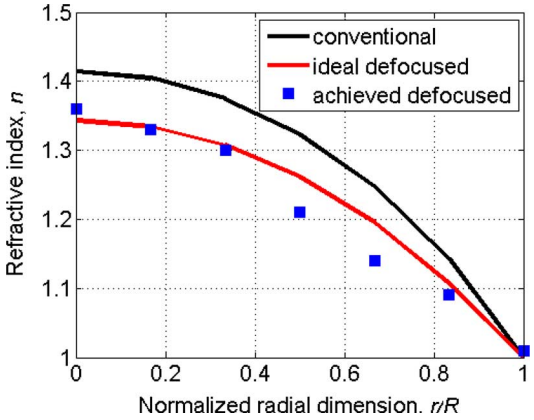

Fig. 2. Refractive index profiles of the conventional, ideal defocused, and our achieved defocused Luneburg lens.

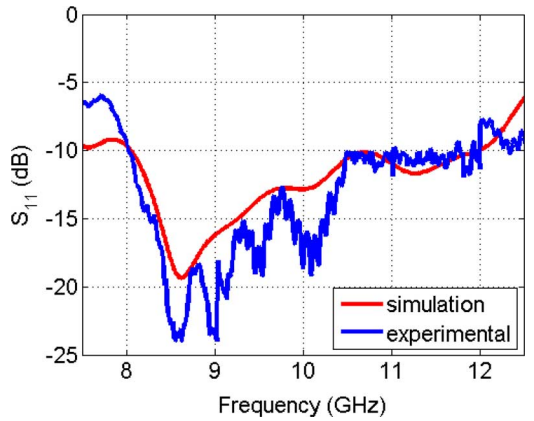

Fig. 3. S_{11} coefficients of the Luneburg lens antenna.

broadband material properties. Indeed for frequencies well below resonance, the index exhibits only a slight variation and losses are found to be negligible.

III. FEEDING STRUCTURE DESIGN

A microstrip-fed Vivaldi antenna [16] is inserted in the parallel-plate waveguide containing the metamaterial-based Luneburg lens to act as primary feed. It is composed of a tapered slot made from the top copper sheet of a 1.6-mm-thick Rogers RT/duroid 5880 dielectric substrate. The slot is then excited by a microstrip line printed on the bottom layer of the substrate together with a radial stub, as illustrated in Fig. 1. The Vivaldi antenna is placed upon two layers of Rohacell foam separated by a thin metallic sheet and fixed to the bottom plate of the parallel-plate TEM waveguide. The radial stub feeding the Vivaldi antenna is shielded to avoid having an undesirable point source resulting from the microstrip line and also to ensure low spurious radiation and hence low cross-polarization levels. To do so, a shorted pin is inserted between the slot radiating plane and the metallic sheet separating the two Rohacell layers in order to act as a stopband filter for TEM waves that may radiate under the feed antenna, and it serves also as an extension of the microstrip feed ground plane. The presented feeding antenna is a close approximation of a point source. In our design, it has been numerically found that the phase center

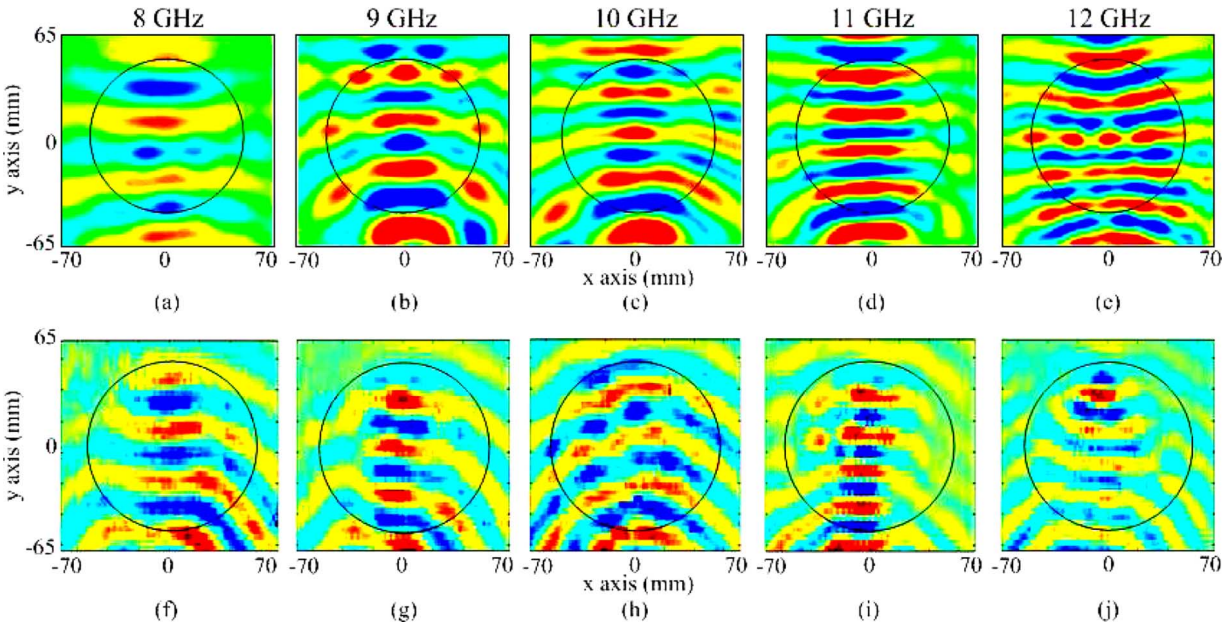

Fig. 4. Electric near-field distribution of the Luneburg lens antenna inside the quasi-TEM waveguide. (a)–(e) Simulations. (f)–(j) Experiments.

of such a structure is located at a distance of 8 mm from the lens periphery. Thus, a defocused Luneburg lens is designed in accordance to [17]. As illustrated in Fig. 2, the realized index profile obtained from the CCR cells agrees qualitatively with that of an ideal defocused Luneburg lens. We shall note that only the dominant TEM mode can be supported in the designed waveguide. The electric field is always parallel to the z-axis and perpendicular to the CCR plane. A semi-rigid coaxial cable is used to connect the antenna to the measurement instrumentation via an SMA connector. The measured and simulated return losses of the whole Luneburg lens antenna are shown in Fig. 3. The proposed structure provides a return loss greater than 10 dB over the X-band frequency range.

IV. Experimental Results

The electric field map directly above the lens is probed over a number of frequencies throughout the X-band inside the planar waveguide. A near-field microwave scanning apparatus (2-D mapper) is fitted to the antenna and configured to provide data as reported in [18]. The lower copper plate of the fabricated antenna system containing the lens and the feed structure is kept fixed in our experiment. An SMA connector used as probe is fixed at a point on the upper movable plate of the scanning apparatus and is connected via a coaxial cable to the computerized motor so as to scan a surface of 200×200 mm^2. The probe is connected to one port of an Agilent 8722ES vector network analyzer, and the feed line of the Vivaldi antenna is connected to the other port. The distance between the top and bottom plate is kept fixed to 11 mm, which corresponds to the designed two-dimensional waveguided CCR units, and the gap between the patterned circuit board and the top PEC plate of the waveguide is kept as 1 mm. We shall note that in this near-field measurement system, the plate supporting the probe is larger than 130×190 mm^2, so that we can assure parallel-plate TEM waveguide configuration when the scanning procedure is running. The dominant TEM mode is formed between the bottom plate of the 2-D mapper and the CCR metallic plane without any use of metallic ramp in front of the lens. The incident waves radiated by the Vivaldi antenna pass through the metamaterial region with low reflections. Only an 11-mm-thick rectangular absorber was placed at the edges of the top metallic plate in order to decrease the effect of the waveguide to air impedance mismatch.

The electric field mapping inside the antenna system is depicted in Fig. 4 for different frequencies. An overall good qualitative agreement can be observed between simulations and measurements. Fields near the Vivaldi feed are so strong that the field distribution in the other region cannot be displayed clearly. Hence the field around the feed is not scanned. The low insertion loss between the Vivaldi antenna and the Luneburg lens can be estimated by comparing the intensity of the color map corresponding to the wave at the entrance and the exit of the Luneburg lens. Any loss of intensity observed in these data is more likely due to the effects of diffraction and the spreading of the beam rather than insertion losses. As illustrated, after passing through the lens, the circular wave fronts are flattened, and the cylindrical waves are transformed into quasi-plane waves on the opposite side of the lens, demonstrating a highly directive radiation. The simulated and measured near-field distributions agree very well except at 12 GHz. The difference in the field distributions is attributed to two factors. First, simulations have been performed with a lens of radius of 49 mm, with a region thickness of 7 mm taking into account two square cells. The different regions are then composed of concentric cylinders representing the effective material parameters. On the counterpart, the CCR designed lens has a radius of 56 mm. The difference in radius is due to the metallic part left around the CCR cells so as to ensure the circular shape of the lens. From the numerical simulations, the feed phase center assimilating the point source is effectively seen to be located at an approximate distance of 8 mm from the periphery of the lens. Second, it is quite difficult to have exactly a 1-mm-thick Rohacell

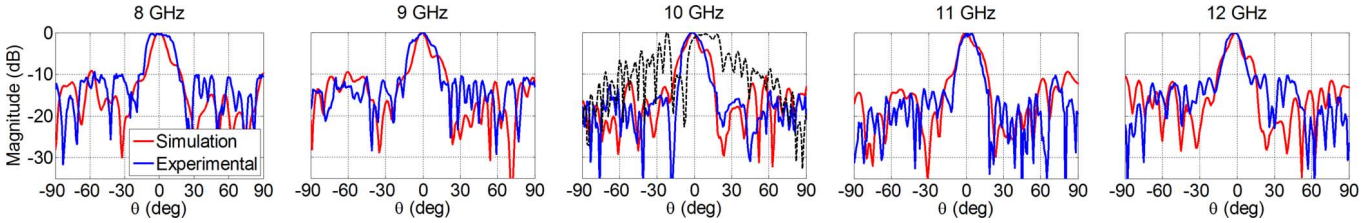

Fig. 5. Simulated and measured far-field radiation patterns of the lens antenna.

foam to assure the 1-mm gap between the GRIN material and top metallic surface of the 2-D mapper. This leads to a slight change of the desired effective parameters, causing deleterious effects on the measured field distributions around the lens. Nevertheless, the focusing phenomenon is clearly observed for all tested frequencies.

To further investigate the directive behavior of the integrated lens antenna as receiver, far-field radiation patterns have been measured in a full anechoic chamber. Unlike the measurement setup for the 2-D electric field mapping in which a large movable metallic plate has been used for scanning, here the two parallel plates forming the quasi-TEM waveguide have similar lateral dimensions 130×190 mm^2. The simulated and measured radiations patterns are presented in Fig. 5. A highly directive emission is observed at all tested frequencies. The sidelobes are below -10 dB for the measured data. However, small disparities with the simulated results are observed around the sidelobes. This is attributed to field leakage in the experimental setup; microwave absorber materials have been added on both sides of the waveguide to improve the enclosure of the point source generated by the Vivaldi antenna. A slight asymmetry appears in the sidelobes due to the offset of the microstrip line feeding the Vivaldi antenna. To clearly illustrate the lens effect on the Vivaldi antenna and to validate the performance of such an integrated Luneburg lens antenna, measurement performed at 10 GHz without the lens in the TEM waveguide is also plotted (black trace) in Fig. 5. The lens renders the beam more directive and lowers the level of the parasitic lobes.

The estimated directivity of the proposed lens antenna is found to lie between 13.5 and 16 dBi in the [8–12 GHz] frequency band. Compared to an ideal aperture having a similar physical surface as the Luneburg lens where directivity lies between 18.3 and 21.8 dBi, our proposed lens antenna presents overall good performances to be used in new antenna communication systems.

V. Conclusion

In this letter, we have presented a compact and substrate-integrated planar Luneburg lens antenna. The metamaterial-based lens is excited by a Vivaldi source and operates in a quasi-TEM parallel-plate waveguide. The lens antenna exhibits a wideband operation from 8 to 12 GHz and good performances and can be easily associated with a radio front end due to its low profile.

References

[1] D. R. Smith, J. J. Mock, A. F. Starr, and D. Schuring, "Gradient index metamaterials," *Phys. Rev. E*, vol. 71, no. 3, p. 036609, Mar. 2005.
[2] C. A. Swainson, "Problems," *Cambridge Dublin Math. J.*, vol. 8, pp. 188–189, 1854, (alias J. C. Maxwell).
[3] J. B. Pendry, D. Schurig, and D. R. Smith, "Controlling electromagnetic fields," *Science*, vol. 312, no. 5781, pp. 1780–1782, Jun. 2006.
[4] U. Leonhardt, "Optical conformal mapping," *Science*, vol. 312, no. 5781, pp. 1777–1780, Jun. 2006.
[5] D. Schurig, J. J. Mock, B. J. Justice, S. A. Cummer, J. B. Pendry, A. F. Starr, and D. R. Smith, "Metamaterial electromagnetic cloak at microwave frequencies," *Science*, vol. 314, no. 5801, pp. 977–980, Oct. 2006.
[6] N. Kundtz and D. R. Smith, "Extreme-angle broadband metamaterial lens," *Nature Mater.*, vol. 9, no. 2, pp. 129–132, Feb. 2010.
[7] P.-H. Tichit, S. N. Burokur, D. Germain, and A. de Lustrac, "Design and experimental demonstration of a high-directive emission with transformation optics," *Phys. Rev. B*, vol. 83, no. 15, p. 155108, Apr. 2011.
[8] Z. H. Jiang, M. D. Gregory, and D. H. Werner, "Experimental demonstration of a broadband transformation optics lens for highly directive multibeam emission," *Phys. Rev. B*, vol. 84, no. 16, p. 165111, Oct. 2011.
[9] P.-H. Tichit, S. N. Burokur, and A. de Lustrac, "Transformation media producing quasi-perfect isotropic emission," *Opt. Express*, vol. 19, no. 21, pp. 20551–20556, Oct. 2011.
[10] H. F. Ma, X. Chen, X. M. Yang, H. S. Xu, Q. Cheng, and T. J. Cui, "A broadband metamaterial cylindrical lens antenna," *Chinese Sci. Bull.*, vol. 55, no. 19, pp. 2066–2070, Jul. 2010.
[11] Q. Cheng, H. F. Ma, and T. J. Cui, "Broadband planar Luneburg lens based on complementary metamaterials," *Appl. Phys. Lett.*, vol. 95, no. 18, p. 181901, Nov. 2009.
[12] R. K. Luneburg, *Mathematical Theory of Optics*. Providence, RI: Brown Univ. Press., 1944.
[13] C. Pfeiffer and A. Grbic, "A printed, broadband Luneburg lens antenna," *IEEE Trans. Antennas Propag.*, vol. 58, no. 9, pp. 3055–3059, Sep. 2010.
[14] R. Liu, Q. Cheng, J. Y. Chin, J. J. Mock, T. J. Cui, and D. R. Smith, "Broadband gradient index microwave quasi-optical elements based on non-resonant metamaterials," *Opt. Express*, vol. 17, no. 23, pp. 21030–21041, Nov. 2009.
[15] D. R. Smith, S. Schultz, P. Markos, and C. M. Soukoulis, "Determination of effective permittivity and permeability of metamaterials from reflection and transmission coefficients," *Phys. Rev. B.*, vol. 65, no. 19, p. 195104, May 2002.
[16] K. S. Yngvesson, D. H. Schaubert, T. L. Korzeniowski, E. L. Kollberg, T. Thungren, and J. F. Johansson, "Endfire tapered slot antennas on dielectric substrates," *IEEE Trans. Antennas Propag.*, vol. AP-33, no. 12, pp. 1392–1400, Dec. 1985.
[17] D. K. Cheng, "Modified Luneberg lens for defocused source," *IRE Trans. Antennas Propag.*, vol. AP-8, no. 1, pp. 110–111, Jan. 1960.
[18] B. J. Justice, J. J. Mock, L. Guo, A. Degiron, D. Schurig, and D. R. Smith, "Spatial mapping of the internal and external electromagnetic fields of negative index metamaterials," *Opt. Express*, vol. 14, no. 19, pp. 8694–8705, Sep. 2006.

Annexe 4.2

A. Dhouibi, S. N. Burokur, A. de Lustrac, A. Priou

« Métamatériaux à gradient d'indice pour les antennes-lentilles large-bande »

Revue de l'Électricité et de l'Électronique, no. 4, pp. 63-67, 2013

Métamatériaux à gradient d'indice pour les antennes-lentilles large-bande

Abdallah Dhouibi[1], Shah Nawaz Burokur[2,3], André de Lustrac[2,3], Alain Priou[1]
LEME, Université Paris Ouest[1], IEF, Université Paris-Sud, CNRS, UMR 862[2], Université Paris-Ouest[3]

Introduction

Les avancées dans les études des interactions onde-matière nous permettent aujourd'hui d'envisager la conception de nouveaux types de dispositifs antennaires basés sur le contrôle des paramètres électromagnétiques des métamatériaux. De nombreuses études et expériences ont été menées ces dernières années [1] sur les structures à gradient d'indice (GRIN). L'utilisation de telles structures permet principalement de focaliser les ondes radio par l'utilisation de structures sphériques ou hémisphériques à saut d'indice. Des travaux récents ont été menés sur de telles lentilles et notamment sur leurs analyses électromagnétiques pour les présenter comme des alternatives aux lentilles diélectriques conventionnelles. En effet, au lieu de contrôler le trajet de l'onde à l'interface entre deux diélectriques différents, on le fait par le gradient d'indice dans une structure à métamatériaux. Dans ce papier, nous étudions deux lentilles : la lentille de Luneburg [2] et la demi-lentille Maxwell fish-eye (HMFE) [3]. Ces deux lentilles sont capables de transformer une onde cylindrique incidente en une one plane et ainsi de produire un faisceau directif. Des lentilles à gradient d'indice obtenu par l'utilisation de métamatériaux ont été présentées dans la littérature [4, 5]. Leurs validations expérimentales ont été faites soit en utilisant des antennes cornets ou des transitions coaxial-guide pour illuminer les lentilles, ce qui augmente considérablement l'encombrement des antennes-lentilles et rendent donc ces antennes difficilement intégrables.

Notre travail consiste à nous focaliser sur l'association d'une source planaire compacte avec des lentilles à gradient d'indice. Nous proposons ainsi la réalisation de deux systèmes antennaires directifs, compacts et plats composés d'une source imprimée et d'une lentille à gradient d'indice planaire. Ces antennes fonctionnent sur une large-bande de fréquences et peuvent être facilement intégrées dans des systèmes de communications RF.

Métamatériaux à gradient d'indice large-bande

Le gradient d'indice nécessaire à la réalisation des deux lentilles (Luneburg et HMFE) qui opèrent dans la bande 8 – 12 GHz est obtenu par l'utilisation de structures à métamatériaux. Dans notre cas, on utilise des Complementary Closed Rings « CCR », qui sont des fentes annulaires rectangulaires faites dans un plan métallique posé un substrat diélectrique de type Rogers RT/Duroid® 5880 ayant une permittivité relative $\varepsilon_r = 2{,}2$ et des pertes tangentielles (tan δ) de l'ordre de 0,0009 (figure 1(a)) [6]. Ce méta-atome fonctionne dans une configuration de guide d'ondes quasi-TEM et présente une résonance magnétique quand le champ électrique E est normal au plan de la cellule. Les propriétés de la cellule sont caractérisées avec le logiciel commercial CST Microwave Studio. En simulation, les ports d'excitation sont placés loin du résonateur afin d'assurer une excitation par une onde plane et d'éviter un couplage avec le champ proche.

ABSTRACT

Gradient index lenses are proposed to transform a cylindrical wave into a plane wave. The lenses are designed from metamaterials engineering on a wide frequency band. A suitable X-band frequency primary feeding source is used to illuminate the lenses. The lens-antennas systems fabricated using conventional printed circuit board technology are low profile and present small footprints. In terms of performances, a directive emission is obtained in the H-plane. A qualitatively good agreement is observed between the measurements performed on the fabricated antennas and numerical simulations.

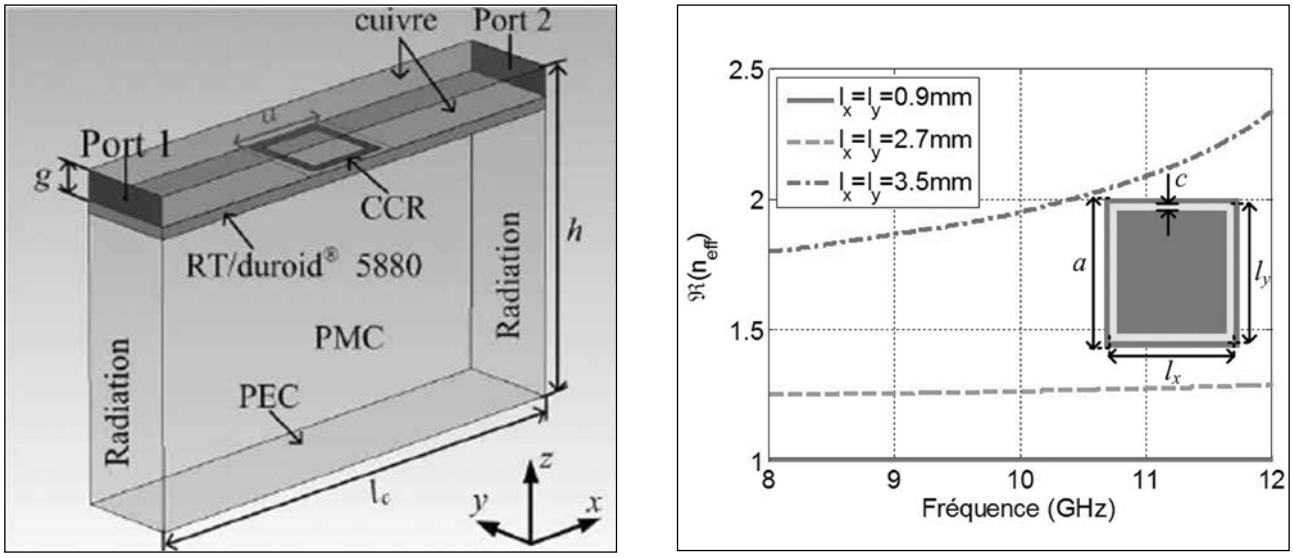

(a) (b)

Figure 1 : (a) Cellule de métamatériau utilisée en simulation pour le gradient d'indice. (b) Partie réelle de l'indice obtenu pour différentes dimensions de la cellule. Les dimensions géométriques sont : g = 1 mm, h = 11 mm, a = 3,6 mm et c = 0,3 mm.

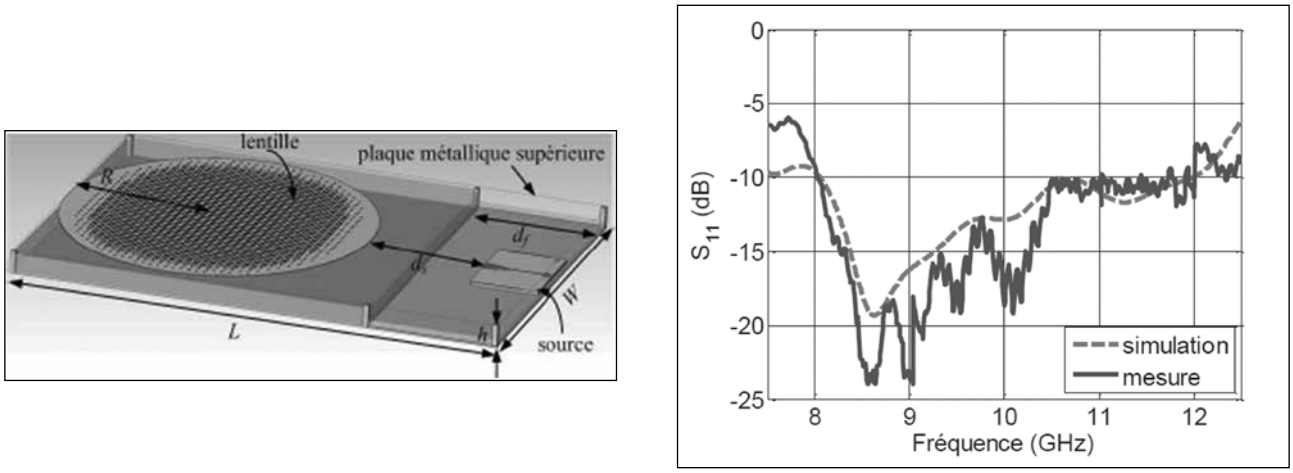

(a) (b)

Figure 2 : (a) Configuration des antennes-lentilles où L = 190 mm, W = 130 mm, h = 11 mm, d_f = 51,5 mm, d_s = 51,5 mm et R = 56 mm. (b) Adaptation des antennes proposées.

Cependant pour l'extraction des paramètres effectifs suivant la méthode proposée dans [7], des plans de référence sont choisis de sorte que la période a de la cellule est égale à 3,6 mm. Ce méta-atome est utilisé à des fréquences beaucoup plus basses que sa fréquence de résonance ; ce qui permet d'assurer une valeur constante de l'indice de réfraction dans la bande utile de l'antenne, comme illustré sur la figure 1(b).

Antennes-lentilles

La lentille est conçue par une texturation de cellules CCR de différentes dimensions qui produisent le gradient d'indice nécessaire. Elle est ensuite insérée entre deux plaques métalliques parallèles (guide d'ondes quasi-TEM) de dimensions 130 x 190 mm^2 et espacées de h = 11 mm. La lentille est fixée sur un support en mousse de type Rohacell ayant une permittivité proche de l'unité. Pour générer un point source à la périphérie de la lentille, une antenne planaire de type Vivaldi est insérée entre les deux plaques métalliques jouant le rôle du guide d'ondes quasi-TEM (figure 2(a)). Cette source Vivaldi est une très bonne approximation d'une source ponctuelle à la périphérie de la lentille mais son centre de phase se trouve à 8 mm de la périphérie. On se retrouve donc dans le cas d'une lentille défocalisée et le gradient d'indice de la lentille est légèrement différent de celui excité par une source ponctuelle [8]. La figure 2(b) présente l'adaptation simulée et mesurée de l'antenne-lentille. L'insertion

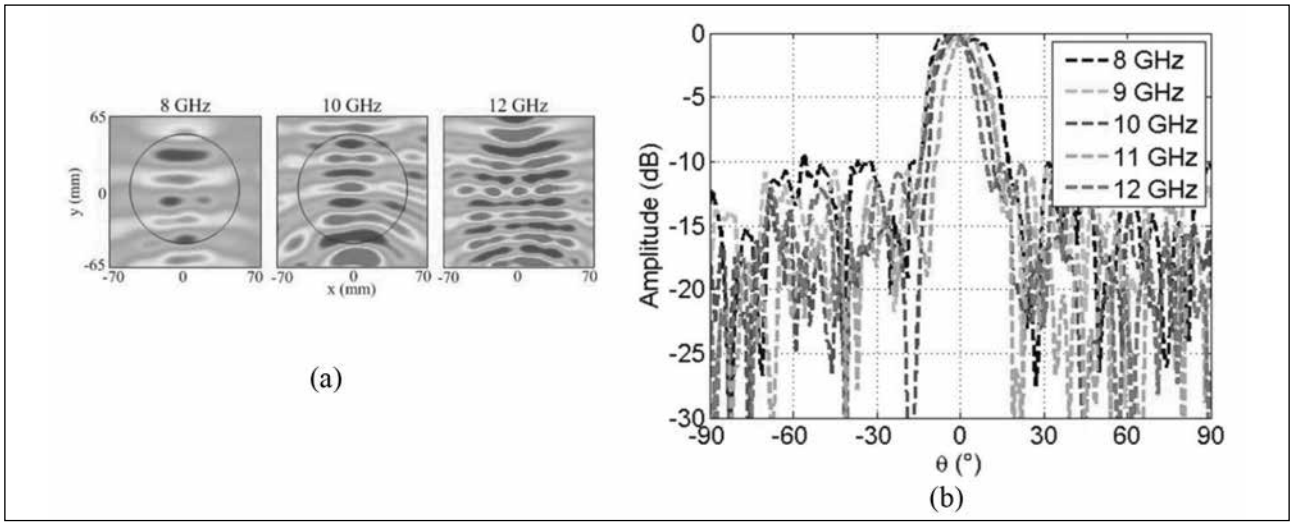

Figure 3 : (a) Cartographie du champ électrique dans l'antenne-lentille Luneburg. (b) Diagrammes de rayonnement de l'antenne-lentille Luneburg.

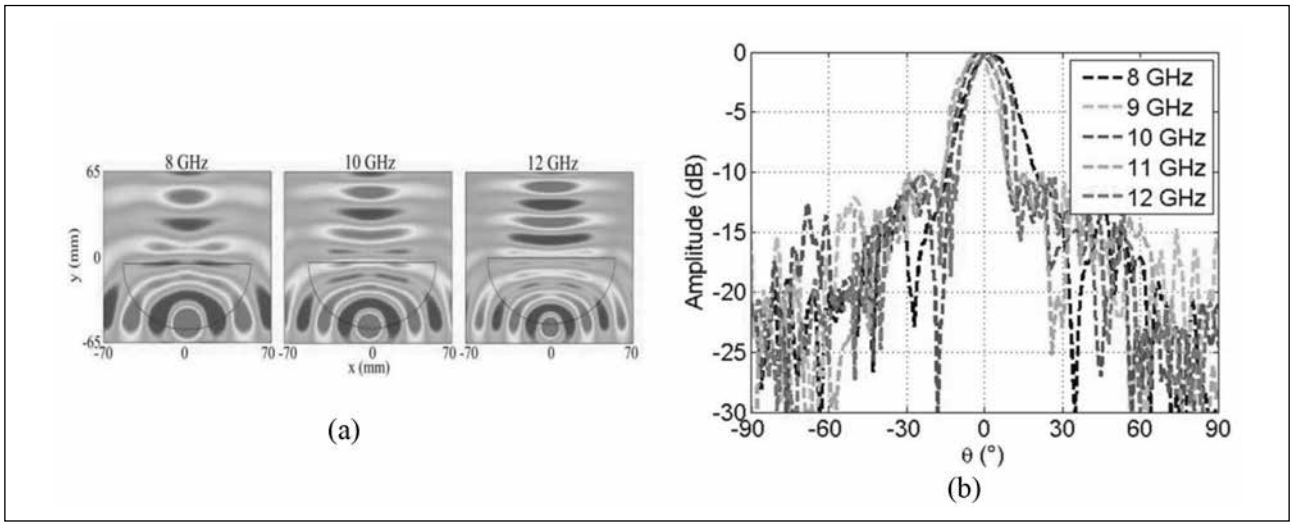

Figure 4 : (a) Cartographie du champ électrique dans l'antenne-lentille HMFE. (b) Diagrammes de rayonnement de l'antenne-lentille HMFE.

des métamatériaux représentant la lentille n'a que très peu d'influence sur l'adaptation de la source Vivaldi seule dans le guide Quasi-TEM.

Lentille de Luneburg

La cartographie du champ électrique à la surface de la lentille de Luneburg entre les plaques parallèles est présentée sur la figure 3(a). Les simulations numériques ont été faites avec des couches concentriques de permittivités représentant les indices des matériaux effectifs calculés qui varient de 1,01 sur la périphérie à 1,36 au centre de la lentille. Les fronts d'ondes incidents émis par la source Vivaldi traversent la lentille avec très peu de réflexions et se transforment en ondes quasi planes sur le côté opposé de la lentille. Des mesures faites en chambre anéchoïque sur cette antenne-lentille montrent des diagrammes très directifs dans le plan H sur toute la bande de fréquences 8– 12 GHz (figure 3(b)). Les lobes secondaires montrent des niveaux raisonnables (< -10 dB). La légère asymétrie qui apparaît dans les lobes secondaires est principalement due à l'asymétrie dans l'excitation de la source Vivaldi. La directivité estimée de cette antenne-lentille Luneburg varie de 13,5 à 16 dBi dans la bande de fréquences 8 – 12 GHz.

Lentille HMFE

L'indice effectif des CCR constituant la lentille HMFE varie de 1,01 sur la périphérie circulaire à 2 sur le côté plat. La distribution du champ électrique à la surface de la lentille HMFE intégrée dans le guide Quasi-TEM est présentée sur la figure 4(a). Comme dans le cas de la lentille de Luneburg, les fronts d'ondes

incidents circulaires émis par la source Vivaldi traversent la lentille avec très peu de réflexions et se transforment en ondes quasi planes sur le côté plan de la lentille [9]. Une émission directive est donc obtenue dans toute la bande de fréquences. Des mesures faites sur ce système antennaire montrent des diagrammes très directifs dans le plan H sur toute la bande de fréquences 8 – 12 GHz (figure 4(b)). La directivité de l'antenne-lentille est de 15,5 dBi en moyenne sur toute la bande.

Conclusion

Cette étude montre l'intérêt des métamatériaux dans le domaine des antennes. En effet, nous avons présenté la mise en œuvre de deux antennes-lentilles planaires large-bande fonctionnant sur la toute la bande X. Cette réalisation a été rendue possible en utilisant des métamatériaux complémentaires de type CCR pouvant produire des valeurs d'indice stable sur une large bande de fréquences et aussi en utilisant une source planaire pour diminuer l'encombrement du système. La cartographie du champ électrique à la surface des lentilles montre une transformation des ondes cylindriques en ondes quasi planes et donc une émission directive. Les mesures en champ lointain effectuées sur ces antennes montrent un rayonnement directif dans le plan H sur la bande de fréquences 8 – 12 GHz.

Rappels sur les lentilles à gradient d'indice

L'idée de réaliser des lentilles à gradient d'indice, dans lesquelles l'indice de réfraction varie à l'intérieur de la lentille, n'est pas nouvelle. En 1854, **James Clerk Maxwell**, en réponse à un problème de l'Irish Academy, montre qu'une lentille sphérique de rayon R dont l'indice varie en fonction de la distance au centre selon la formule : $n(r)=\frac{2}{1+\left(\frac{r}{R}\right)^2}$ a la propriété de permettre la convergence parfaite de tout rayon issu d'un point A de la sphère vers un point B diamétralement opposé (figure 1). C'est ce qu'on appelle une lentille fish-eye (MFE : Maxwell fish-eye).

Le problème peut évidemment être généralisé en recherchant le profil d'indice permettant la convergence parfaite d'un point A quelconque vers un Point B quelconque, pour une lentille de forme quelconque. Ce type de problème n'admet pas une solution unique.

En 1944, **Rudolf Luneburg** a proposé une famille de solutions et en particulier le profil, dit profil de Luneburg, permettant d'assurer la convergence entre un point situé sur une lentille sphérique et un foyer renvoyé à l'infini (figure 1-2) :

$$n(r)=\sqrt{2-\left(\frac{r}{R}\right)^2}$$

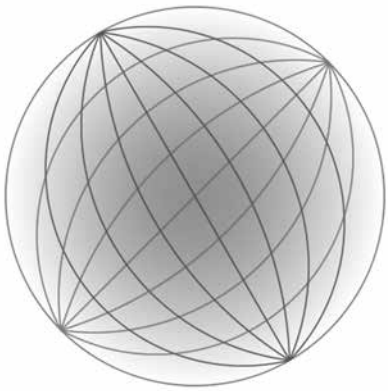

Figure 1-1 : Profil de Maxwell appliqué à une lentille sphérique fish-eye.

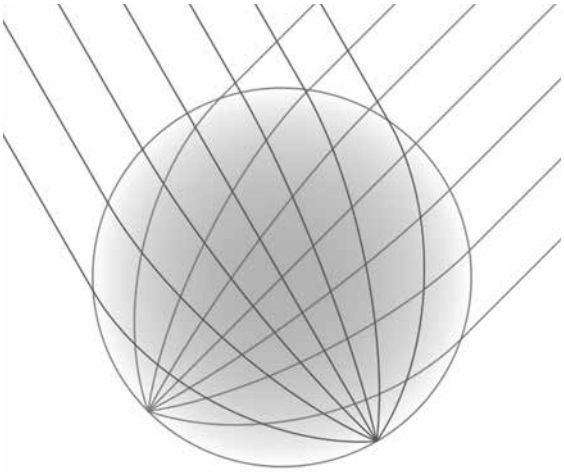

Figure 1-2 : Profil de Luneburg appliqué à une lentille sphérique. Source : Wikipedia.

D'autres profils ont été proposés, notamment le profil de **Wood** permettant de réaliser des lentilles à faces parallèles (1905) ainsi que les solutions de **Samuel Morgan** de Bell Telephone Labs qui généralisent celles de Luneburg (1958).

La plupart des systèmes de communications par satellite nécessite des systèmes antennaires multifaisceaux qui opèrent en fréquences millimétriques. Ceci est le facteur principal du récent regain d'intérêt pour les lentilles focalisantes basées sur le principe de Luneburg. L'avantage de ces structures réside en leur capacité à former une multitude de faisceaux qui peuvent pointer simultanément et/ou séparément dans des directions quelconques de l'espace et ce sur une large bande de fréquences. Depuis les années 50, les concepteurs d'antennes ont largement utilisé ce principe pour réaliser une variété d'applications radiofréquences, notamment pour concevoir des balises radar à hautes performances.

Une équipe de recherche de l'Institut d'Electronique et des Télécommunications de Rennes a récemment montré que la lentille MFE, telle qu'elle a été présentée par Maxwell, peut être utilisée pour des applications d'antennes directives. En effet, les auteurs ont proposé de n'utiliser que la moitié de la lentille diélectrique afin de faire ressortir une onde plane. Cette demi-lentille MFE a donc été appelée Half Maxwell fish-eye (HMFE) (figure 1-3).

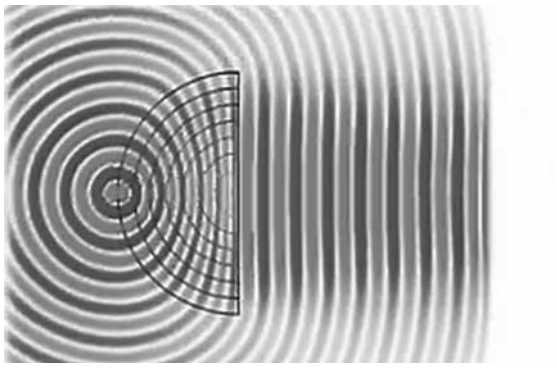

Figure 1-3 : Propagation des ondes dans une lentille HMFE.

La réalisation pratique des lentilles à gradient d'indices a été rendue possible dans le domaine des ondes électromagnétiques grâce aux propriétés des métamatériaux.

Références

[1] R. Liu, Q. Cheng, J. Y. Chin, J. J. Mock, T. J. Cui & D. R. Smith, "*Broadband Gradient Index Microwave Quasi-Optical Elements Based on Non-Resonant Metamaterials*", Opt. Express, vol. 17, no. 23, pp. 21030-21041, Nov. 2009.

[2] R. K. Luneburg, "*Mathematical Theory of Optics. Providence*", RI: Brown Univ. Press, 1944.

[3] B. Fuchs, O. Lafond, S. Rondineau & M. Himdi, "*Design and Characterization of Half Maxwell Fish-Eye Lens Antennas in Millimeter Waves*", IEEE Trans. Microw. Theory Tech., vol. 54, no. 6, pp. 2292-2300, June 2006.

[4] Q. Cheng, H. F. Ma & T. J. Cui, "*Broadband Planar Luneburg Lens Based on Complementary Metamaterial*", Appl. Phys. Lett., vol. 95, no. 18, 181901, Nov. 2009.

[5] Z. L. Mei, J. Bai, T. M. Niu & T. J. Cui, "*A Half Maxwell Fish-Eye Lens Antenna Based on Gradient-Index Metamaterials*", IEEE Trans. Antennas Propag., vol. 60, no. 1, pp. 398-401, Jan. 2012.

[6] A. Dhouibi, S. N. Burokur, A. de Lustrac & A. Priou, "*Compact Metamaterial-Based Substrate-Integrated Luneburg Lens Antenna*", IEEE Antennas Wireless Propag. Lett., vol. 11, pp. 1504-1507, 2012.

[7] D. R. Smith, S. Schultz, P. Markos & C. M. Soukoulis, "*Determination of Effective Permittivity and Permeability of Metamaterials from Reflection and Transmission Coefficients*", Phys. Rev. B., vol. 65, no. 19, 195104, May 2002.

[8] D. K. Cheng, "*Modified Luneberg Lens for Defocused Source*", IRE Trans. Antennas Propag., vol. 8, no. 1, pp. 110-111, Jan. 1960.

[9] A. Dhouibi, S. N. Burokur, A. de Lustrac & A. Priou, "*Low-Profile Substrate-Integrated Lens Antenna Using Metamaterials*", IEEE Antennas Wireless Propag. Lett., vol. 12, pp. 43-46, 2013.

LES AUTEURS

Abdallah Dhouibi est ingénieur diplômé de l'Ecole Polytechnique de l'Université de Nantes (2009). Il effectue une thèse financée par la fondation EADS au Laboratoire Energétique Mécanique Electromagnétisme (LEME) de l'Université Paris-Ouest Nanterre-La Défense sur le développement de métamatériaux et leurs applications aux antennes.

Alain Priou est professeur CE2, DR en électronique et électromagnétisme à l'Université Paris Ouest Nanterre la Défense, site de Ville d'Avray. Il est membre senior de la SEE, life senior member des IEEE MTT et APS, life fellow member de l'académie d'électromagnétisme du MIT. Il a été directeur adjoint du département de micro-ondes de l'ONERA-CERT de Toulouse jusqu'en 1998, puis responsable de la technologie radar à la DGA/DRET et STTS jusqu'en 2007 et enfin directeur du groupe d'Electromagnétisme Appliqué (GEA) devenu groupe Ondes Matériaux et Systèmes du Laboratoire Energie, de Mécanique et d'Electromagnétisme (LEME-OMS) jusqu'en 2012. Il est à présent professeur émérite de l'université Paris-Ouest Nanterre la Défense, professeur Invité du Nankin université des sciences et technologies et d'autres universités. Il est président de la Com B de l'URSI France et du groupe de travail emploi-formation-recherche du pôle aéronautique ASTECH Paris Ile de France

Annexe 4.3

A. Dhouibi, S. N. Burokur, A. de Lustrac, A. Priou

« Metamaterial-based half Maxwell fish-eye lens for broadband directive emissions »

Applied Physics Letters, vol. 102, no. 2 (024102), January 2013.

Metamaterial-based half Maxwell fish-eye lens for broadband directive emissions

Abdallah Dhouibi,[1,a)] Shah Nawaz Burokur,[2,3,b)] André de Lustrac,[2,3] and Alain Priou[1]
[1]*LEME, EA 4416, Université Paris-Ouest, 92410 Ville d'Avray, France*
[2]*IEF, CNRS, UMR 8622, Université Paris-Sud, 91405 Orsay Cedex, France*
[3]*UFR SITEC, Université Paris-Ouest, 92410 Ville d'Avray, France*

(Received 30 July 2012; accepted 28 December 2012; published online 16 January 2013)

The broadband directive emission from a metamaterial surface is numerically and experimentally reported. The metasurface, composed of non-resonant complementary closed ring structures, is designed to obey the refractive index of a half Maxwell fish-eye lens. A planar microstrip Vivaldi antenna is used as transverse magnetic polarized wave launcher for the lens. A prototype of the lens associated with its feed structure has been fabricated using standard lithography techniques. To experimentally demonstrate the broadband focusing properties and directive emissions, both the far-field radiation patterns and the near-field distributions have been measured. Measurements agree quantitatively and qualitatively with theoretical simulations. © *2013 American Institute of Physics*. [http://dx.doi.org/10.1063/1.4776662]

Metamaterials are artificial materials typically fabricated via suitable periodic arrangement of micro-structured metallic or dielectric inclusions. Due to their unusual electromagnetic properties,[1] these microstrutured metamaterials have made relevant a wide array of interesting applications particularly since the introduction of the transformation optics concept.[2,3] Devices such as invisibility cloaks,[4–6] directive[7] and omnidirectional[8] antennas, Luneberg[9] and Eaton[10] lenses, and waveguide tapers[11] have then been proposed. These devices are generally implemented using materials presenting permittivity and/or permeability gradients, which can be provided by metamaterial engineering. In recent few years, gradient index (GRIN) lenses have been proposed as alternatives to conventional dielectric ones, where refractive index is varied throughout the lens instead of relying on the interfaces of the dielectric material to control light flow. As such, GRIN materials[12] have shown their utility in designing a variety of microwave applications. The attractive performances of lens antennas[13] for Radio Frequency (RF) communications have been highlighted. Collimating lenses have aroused this wide interest because of their interesting electromagnetic properties. Indeed, such structures allow converging or diverging light to ensure directional emissions.

Like the Luneburg lens,[14] the Maxwell fish-eye (MFE) lens[15] is a spherical GRIN device. It is able to focus each point on the lens surface to a diametrically opposite point, such that a spherical wave at the surface of the lens is converted into a local plane wave at the center of the lens and reemerges as a spherical wave at the surface on the opposite side. In 2006, Fuchs *et al.*[16] proposed to use only half of the lens referred to as the half Maxwell fish-eye (HMFE) so as to transform a point source on the spherical surface into a plane wave and therefore to produce a highly directive emission. The refractive index of the lens varies from 1 to 2 inside a semi-circular geometry and obeys the spatial position function, $n(r) = \frac{n_0}{1+\left(\frac{r}{R}\right)^2}$, where n_0 represents the refractive index at the center of the lens, R is the radius of the lens, and r represents the distance from the center of the lens.

Experimental validation of such GRIN lenses showing good efficiencies has been reported recently.[17–22] For example, a three-dimensional (3D) version of the two-dimensional (2D) flattened Luneburg lens of Ref. 9 has been experimentally demonstrated.[20]

In this letter, we design a (2D) planar and electrically compact HMFE lens operating in the [8 GHz–12 GHz] frequency band, using GRIN metamaterials. The gradient index of the lens is achieved through a two-dimensional array of waveguided units of complementary closed ring (CCR) resonators.[23] We focus our attention on the combination of a planar transverse magnetic (TM) polarized waves launcher to feed the lens in a parallel-plate waveguide configuration. Furthermore, the use of a planar feed in the overall low profile lens antenna suggests a good matching to the spherical locus of focal points and facilitates the integration into RF communication systems. Reported experimental near-field distributions and far-field radiation patterns demonstrate broadband focusing properties and directive emissions.

A broadband metamaterial-based HMFE lens of radius $R = 56$ mm is designed for an 8 GHz to 12 GHz frequency band operation. A non-resonant electric CCR structure is used as the basic unit cell of the artificial medium representing the lens. As illustrated in Fig. 1, the closed ring resonators are etched on the copper-cladding of a 0.4 mm thick Rogers RT/duroid® 5880 substrate ($\varepsilon_r = 2.2$ and $\tan\delta = 0.0009$). In our experiments, the metamaterial planar slab is inserted in a quasi-transverse electromagnetic (TEM) waveguide consisting of two parallel copper plates having dimensions $L = 190$ mm, $W = 130$ mm, and spaced by $h = 11$ mm. As shown in Fig. 1, the GRIN slab is placed on a Rohacell® foam spacer, with a relative permittivity close to 1, to fill up the space between the substrate and the bottom metallic plate. The gap g between the patterned circuit board and the top copper plate of the waveguide is kept as 1 mm. To obtain the desired effective permittivity and permeability of the CCR units, the

[a)]Electronic mail: a.dhouibi@u-paris10.fr.
[b)]Electronic mail: shah-nawaz.burokur@u-psud.fr.

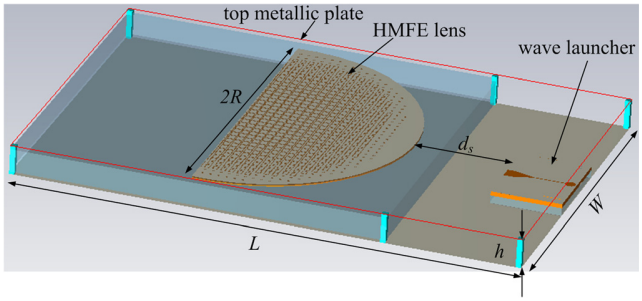

FIG. 1. Schematic view of the lens antenna composed of a planar metamaterial-based lens and a Vivaldi-type antenna feed placed in a quasi-TEM parallel-plate waveguide. The geometrical dimensions are $L = 190$ mm, $W = 130$ mm, $h = 11$ mm, $d_s = 51.5$ mm, and $R = 56$ mm.

properties are characterized numerically using the Maxwell's equations solver of CST Microwave Studio Suite. Fig. 2(a) shows the simulation setup used to retrieve the effective constitutive parameters of the CCR cells. The polarization of the incident TEM wave is constrained by the use of perfect magnetic conducting (PMC) boundaries on the sides of the computational domain. Radiation boundaries are assigned below the ports, as shown in the figure. The two ports are positioned far away from the CCR structure to avoid near-field cross coupling between the ports and the CCR; however, the phase reference planes for the retrieval are chosen such that the period a of the unit cell is 3.6 mm.

Fig. 2(b) shows the typical reflection and transmission responses of the CCR structure, which is a magnetic resonator presenting a Lorentz-like resonance. The electromagnetic parameters are retrieved using the simulated S-parameters as proposed by the inversion method described in Ref. 24. The waveguided CCR metamaterials are utilized in their non-resonant frequency regime such that they present broadband material properties in the 8-12 GHz band (Fig. 2(c)). Indeed for frequencies well below resonance, the index exhibits only a slight variation and losses are found to be negligible. The variation of the refractive index from the center to the border of the lens consists in changing the CCR geometrical dimensions l_x and l_y, as illustrated in Table I, while keeping the lattice period a fixed to 3.6 mm. Due to the square profile of the CCR structure, the HMFE lens was discretized into seven concentric semi-circular regions, where each region corresponds to a specific refractive index. In order to create a point source at the periphery of the lens, a microstrip fed Vivaldi-type antenna is inserted in the parallel-plate waveguide containing the metamaterial-based HMFE lens. The distance d_s is optimized such that the phase center of the Vivaldi feed is situated at the lens periphery. Such a feed acts as a TM-polarized wave launcher inside the parallel plate waveguide. The feeding structure is designed to provide an electric field always parallel to the z-axis and perpendicular to the CCR plane and the dominant TEM mode supported in the designed waveguide can be assimilated to plane waves inside the planar waveguide.

The electric field map directly above the lens is probed over a number of frequencies throughout the X-band inside the quasi-TEM waveguide. A near field microwave scanning apparatus (2D mapper) is fitted to the lens and configured to

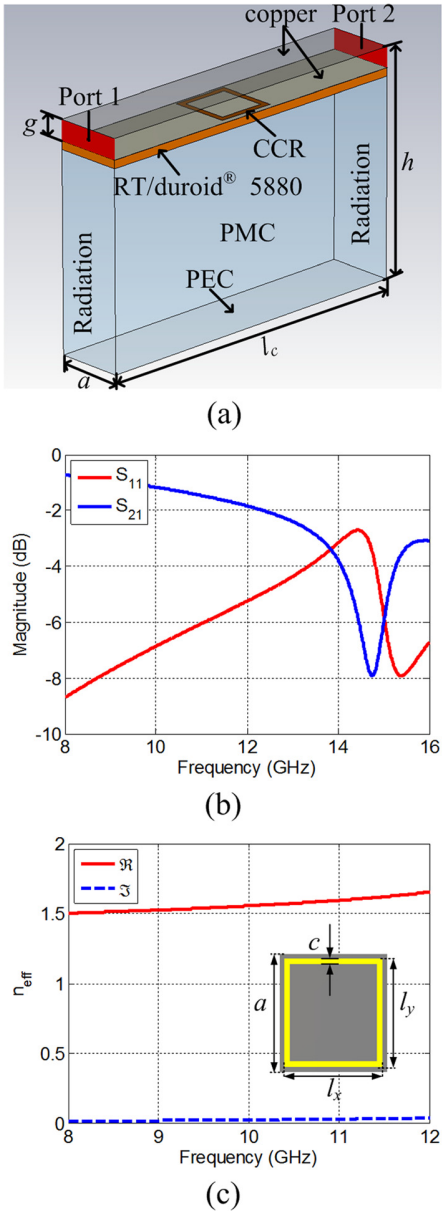

FIG. 2. (a) Simulation setup used to retrieve the effective constitutive parameters of the CCR cells. (b) Reflection and transmission responses of a typical CCR structure with $l_x = l_y = 3.3$ mm, which is used in the non-resonant frequency regime such that it presents broadband features in the 8-12 GHz band (less than 10% variation over the whole band). (c) Extracted effective index of the CCR structure. The geometrical dimensions are $l_c = 18.5$ mm, $h = 11$ mm, $g = 1$ mm, $a = 3.6$ mm, and $c = 0.3$ mm.

TABLE I. Dimensions of the CCR cells and their effective index in the different discretized zones of the HMFE lens.

Zone	l_x (mm)	l_y (mm)	n_{eff}
1	0.9	0.9	1.01
2	2.2	2.2	1.12
3	2.5	2.5	1.18
4	2.7	2.7	1.27
5	2.9	2.9	1.4
6	3.3	3.3	1.56
7	3.5	3.5	2.0

provide data as reported in Ref. 25. The lower copper plate of the fabricated waveguide containing the lens and the feed structure is kept fixed in our experiment. A coaxial RF connector used as probe is fixed at a point on the upper movable plate of the scanning apparatus and is connected via a coaxial cable to the computerized motor so as to scan a surface of 200 mm × 200 mm. The probe is connected to one port of an Agilent 8722ES vector network analyzer, and the Vivaldi feed antenna is connected to the other port. The distance between the top and the bottom plate is kept fixed to 11 mm which corresponds to the designed two-dimensional waveguided CCR units and the gap between the patterned circuit board and the top PEC plate of the waveguide is kept as 1 mm. We shall note that in this near-field measurement system, the plate supporting the probe is larger than 130 mm × 190 mm, so that we assure parallel-plate waveguide configuration when the scanning procedure is running. The dominant TEM mode is formed between the bottom plate of the 2D mapper and the CCR metallic plane. The incident waves radiated by the Vivaldi antenna pass through the metamaterial region with low reflections as shown by the near field measurements. An 11 mm thick rectangular absorber was placed at the edges of the lower metallic plate in order to decrease the effect of the waveguide to air impedance mismatch and also to approximate magnetic boundary conditions. The electric field mapping inside the antenna system is depicted in Fig. 3 for different frequencies. Fields near the Vivaldi feed are so strong that the field distribution in the other region cannot be displayed clearly. Hence, the field around the feed has not been scanned. As illustrated, the radiation from the Vivaldi feed is transformed into plane waves on the opposite side of the lens. The low insertion loss between the Vivaldi antenna and the HMFE lens can be estimated by comparing the intensity of the color map corresponding to the wave at the entrance and the exit of the HMFE lens. Any loss of intensity observed in these data is more likely due to the effects of diffraction and the spreading of the beam rather than insertion losses. As illustrated, after passing through the lens, the cylindrical wave fronts are flattened and transformed into quasi-plane waves, demonstrating a highly directive radiation. Deleterious effects on the measured field distributions around the lens can be observed due to our modest and imperfect near-field scanning system. In the near-field mapping process, we can hardly have a fixed gap g of 1 mm between the top metallic plate and the GRIN lens when the latter plate is moving for probing the field distribution. This consequently leads to slight changes in the desired effective parameters of lens, therefore altering the transformation of cylindrical to plane waves. Nevertheless, the high directivity phenomenon is clearly observed for all tested frequencies. Compared to Refs. 19 and 22 where no critical air gap is needed to provide the effective parameters of the bulky metamaterials, our actual measured near-field cartography presents imperfections. However, these measurements are consistent with those presented in Ref. 18 for similar waveguided metamaterial configuration.

To further investigate the directive behavior of the integrated lens antenna, far-field radiation patterns have been measured in a full anechoic chamber. Unlike the measurement setup for the 2D electric field mapping in which a large

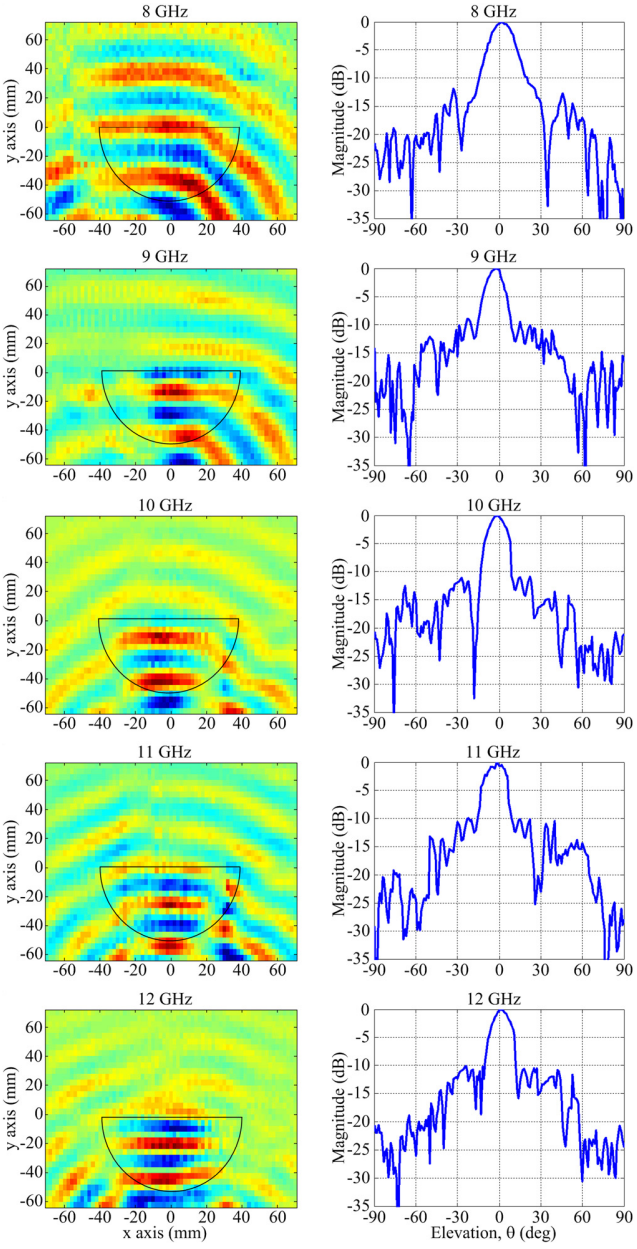

FIG. 3. Measured electric near-field distribution and H-plane (horizontal) far-field radiation patterns of the metamaterial-based lens antenna in the 8-12 GHz frequency band.

movable metallic plate has been used for scanning, here the two parallel plates forming the quasi-TEM waveguide have similar lateral dimensions 130 mm × 190 mm. The measured radiations patterns are presented in Fig. 3. A highly directive radiation lobe is observed at all tested frequencies. The measured side lobes are below −10 dB. The measured half-power beam width is less than 17° in the whole operating frequency band.

In summary, we have presented the experimental realization of a low profile and substrate-integrated planar HMFE lens. The metamaterial-based structure is excited by a Vivaldi source and configured to operate in a quasi-TEM parallel-plate waveguide. The scanning measurements of the electric field of the lens have demonstrated a directive emission, and the association between the feed structure and the

metamaterial-based lens has shown a broadband frequency operation from 8 GHz to 12 GHz.

This work was supported by the EADS Company Foundation through the METAQOPT project, Contract No. 090-AO09-1006. One of the authors (A.D.) would like to acknowledge support for his Ph.D. scholarship from EADS Company Foundation.

[1]V. G. Veselago, Sov. Phys. Usp. **10**, 509 (1968).
[2]J. B. Pendry, D. Schurig, and D. R. Smith, Science **312**, 1780 (2006).
[3]U. Leonhardt, Science **312**, 1777 (2006).
[4]D. Schurig, J. J. Mock, B. J. Justice, S. A. Cummer, J. B. Pendry, A. F. Starr, and D. R. Smith, Science **314**, 977 (2006).
[5]W. Cai, U. K. Chettiar, A. V. Kildishev, and V. M. Shalaev, Nat. Photonics **1**, 224 (2007).
[6]B. Kanté, A. de Lustrac, J.-M. Lourtioz, and S. N. Burokur, Opt. Express **16**, 9191 (2008).
[7]P.-H. Tichit, S. N. Burokur, D. Germain, and A. de Lustrac, Phys. Rev. B **83**, 155108 (2011).
[8]P.-H. Tichit, S. N. Burokur, and A. de Lustrac, Opt. Express **19**, 20551 (2011).
[9]N. Kundtz and D. R. Smith, Nature Mater. **9**, 129 (2010).
[10]Y. G. Ma, C. K. Ong, T. Tyc, and U. Leonhardt, Nature Mater. **8**, 639 (2009).
[11]P.-H. Tichit, S. N. Burokur, and A. de Lustrac, Opt. Express **18**, 767 (2010).
[12]D. R. Smith, J. J. Mock, A. F. Starr, and D. Schurig, Phys. Rev. E **71**, 036609 (2005).
[13]T. Driscoll, D. N. Basov, A. F. Starr, P. M. Rye, S. Nemat-Nasser, D. Schurig, and D. R. Smith, Appl. Phys. Lett. **88**, 081101 (2006).
[14]R. K. Luneburg, *Mathematical Theory of Optics* (Brown University Press, Providence, RI, 1944).
[15]J. C. Maxwell, "Solutions of Problems, Problem No. 2," Cambridge and Dublin Mathematical Journal **8**, 188 (1854).
[16]B. Fuchs, O. Lafond, S. Rondineau, and M. Himdi, IEEE Trans. Microwave Theory Tech. **54**, 2292 (2006).
[17]H. F. Ma, X. Chen, H. S. Xu, X. M. Yang, W. X. Jiang, and T. J. Cui, Appl. Phys. Lett. **95**, 094107 (2009).
[18]Q. Cheng, H. F. Ma, and T. J. Cui, Appl. Phys. Lett. **95**, 181901 (2009).
[19]H. F. Ma, X. Chen, X. M. Yang, H. S. Xu, Q. Cheng, and T. J. Cui, Chin. Sci. Bull. **55**, 2066 (2010).
[20]H. F. Ma and T. J. Cui, Nat. Commun. **1**, 124 (2010).
[21]X. Chen, H. F. Ma, X. Y. Zou, W. X. Jiang, and T. J. Cui, J. Appl. Phys. **110**, 044904 (2011).
[22]Z. L. Mei, J. Bai, T. M. Niu, and T. J. Cui, IEEE Trans. Antennas Propag. **60**, 398 (2012).
[23]R. Liu, Q. Cheng, J. Y. Chin, J. J. Mock, T. J. Cui, and D. R. Smith, Opt. Express **17**, 21030 (2009).
[24]D. R. Smith, S. Schultz, P. Markos, and C. M. Soukoulis, Phys. Rev. B **65**, 195104 (2002).
[25]B. J. Justice, J. J. Mock, L. Guo, A. Degiron, D. Schurig, and D. R. Smith, Opt. Express **14**, 8694 (2006).

Annexe 4.4

A. Dhouibi, S. N. Burokur, A. de Lustrac, A. Priou

« Low-profile substrate-integrated lens antenna using metamaterials »

IEEE Antennas and Wireless Propagation Letters, vol. 12, pp. 43-46, 2013.

Low-Profile Substrate-Integrated Lens Antenna Using Metamaterials

Abdallah Dhouibi, Shah Nawaz Burokur, André de Lustrac, *Member, IEEE*, and Alain Priou, *Senior Member, IEEE*

***Abstract*—A low-profile substrate-integrated lens antenna is designed using planar metamaterials for a broadband operation. The lens antenna is based on embedding a Vivaldi antenna source inside a parallel-plate waveguide to illuminate a half Maxwell fish-eye (HMFE) lens operating in X-band. The focusing condition of the lens, requiring a gradient refractive index is achieved through the use of complementary nonresonant metamaterial structures. Numerical simulations are performed to determine the suitable unit cells geometry with respect to the wave launcher inserted into the parallel-plate waveguide. The electric field distribution inside the antenna system has also been explored numerically. Far-field radiation patterns have been measured on a fabricated prototype in an anechoic chamber. It has been shown from both near- and far-field plots that the proposed planar antenna presents good focusing properties.**

***Index Terms*—Gradient index materials, lens antenna, parallel-plate waveguide, substrate-integrated.**

I. Introduction

METAMATERIALS are artificial materials typically fabricated via suitable periodic arrangement of microstructured metallic or dielectric inclusions. Due to their unusual electromagnetic properties, these microstructured metamaterials have made relevant a wide array of interesting applications. Devices such as invisibility cloaks [1], directive [2] and omnidirectional [3] antennas, Luneburg [4] and Eaton [5] lenses, and waveguide tapers [6] have then been proposed. These devices are generally implemented using materials presenting permittivity and/or permeability gradients, which can be provided by metamaterial technology. In recent years, gradient index (GRIN) lenses have been proposed as alternatives to conventional dielectric ones, where refractive index is varied throughout the lens instead of relying on the interfaces of the dielectric material to control light flow. Thus, GRIN materials [7] have shown their utility in designing a variety of microwave applications. The attractive performances of lens antennas [8] for radio frequency communications have been highlighted. Like the Luneburg lens [9], [10], the Maxwell fish-eye (MFE) lens [11] is also a spherical GRIN device. The MFE lens is able to focus each point on the lens surface to a diametrically opposite point. A spherical wave at the surface of the lens is converted into a local plane wave at the center of the lens and reemerges as a spherical wave at the surface on the opposite side. In 2006, Fuchs *et al.* [12] proposed to use only half of the lens, referred to as the half Maxwell fish-eye (HMFE), so as to transform a point source into a plane wave and therefore to produce a highly directive beam. The refractive index of the lens varies from 1 to 2 inside a semicircular geometry and obeys the spatial position function, $n(r) = n_0/(1 + (r/R)^2)$, where n_0 represents the refractive index at the center of the lens, R is the radius of the lens, and r is the distance from the center of the lens.

In this letter, we discuss the design of a substrate-integrated GRIN HMFE lens antenna in which a Vivaldi-type antenna is used as feed. The lens antenna is embedded inside a parallel-plate waveguide. The whole antenna dimensions are 130×190 mm^2 with a total height of 11 mm and operation in a quasi-TEM mode in the [8–12 GHz] frequency band. The gradient index of the HMFE lens is achieved through a two-dimensional array of waveguided units of complementary closed-ring (CCR) resonators. Similar lens antennas have been proposed in a parallel-plate waveguide configuration [13] and through the use of metamaterial-based Luneburg lenses [14], [15]. Compared to Rotman's parallel-plate microwave lens [16] and the two-dimensional Luneburg lens [17], here we use an integrated planar feed source. The proposed antenna configuration is low-profile and lightweight and presents broadband characteristics. Furthermore, the use of a planar feed in the overall low-profile lens antenna suggests a good matching to the semispherical surface and an easy integration into RF communication systems.

II. Metamaterial-Based Lens Design

The unit cell of the metamaterial structure considered to create the gradient index consists of a planar CCR resonator patterned in the copper cladding of a 0.4-mm-thick Rogers RT/Duroid 5880 dielectric substrate presenting relative permittivity, $\varepsilon_r = 2.2$, and loss tangent, $\tan\delta = 0.0009$. Such a complementary resonator operates in a quasi-TEM waveguide configuration as shown in Fig. 1(a) and exhibits a magnetic resonance when the E-field is aligned perpendicularly to its plane. To obtain the desired effective index of the CCR units, the properties are characterized numerically using Maxwell's equations solver of CST Microwave Studio Suite. The polarization of the incident TEM wave is constrained by the use of perfect magnetic conducting (PMC) boundaries on the sides of

Manuscript received October 30, 2012; revised December 06, 2012; accepted December 11, 2012. Date of publication January 01, 2013; date of current version March 12, 2013. This work was supported by the EADS Company Foundation under the METAQOPT project, Contract No. 090-AO09-1006. The work of A. Dhouibi was supported by the EADS Company Foundation under a Ph.D. scholarship.

A. Dhouibi and A. Priou are with the LEME, EA 4416, Université Paris Ouest, 92410 Ville d'Avray, France.

S. N. Burokur and A. de Lustrac are with the IEF, CNRS, UMR 8622, Université Paris-Sud, 91405 Orsay cedex, France, and also with the Université Paris Ouest, 92410 Ville d'Avray, France (e-mail: shah-nawaz.burokur@u-psud.fr).

Color versions of one or more of the figures in this letter are available online at http://ieeexplore.ieee.org.

Digital Object Identifier 10.1109/LAWP.2012.2237372

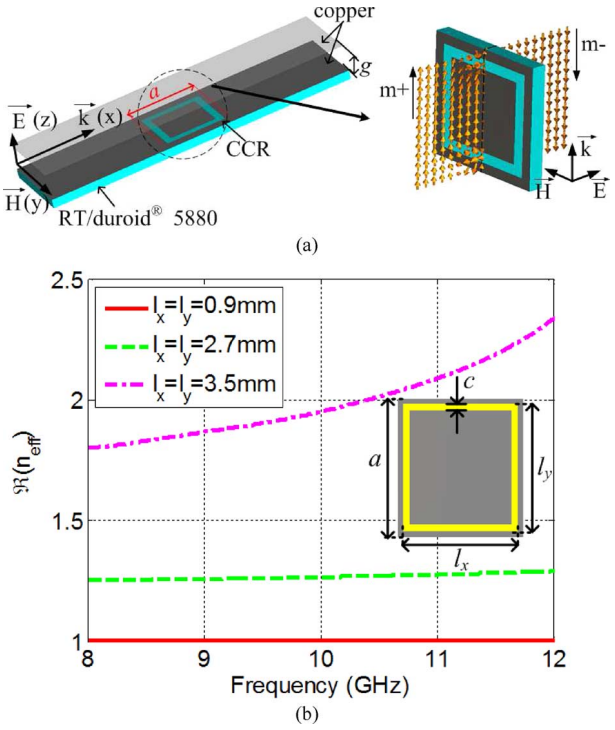

Fig. 1. (a) CCR resonator. (b) Extracted effective index for three different cells. The inset shows the CCR cell with: $g = 1$ mm, $a = 3.6$ mm, $c = 0.3$ mm, and l_x and l_y are variable parameters.

the computational domain in the xz-plane. The gap g between the patterned circuit board and the top copper plate of the waveguide is fixed to 1 mm. Radiation boundaries are assigned below the ports in the yz-plane. The two ports are positioned far away from the resonator structure to avoid near-field cross coupling between the ports and the CCR. However, the phase reference planes for the retrieval are chosen such that the period a of the CCR unit cell is kept as 3.6 mm.

The broadband metamaterial-based HMFE lens of radius $R = 56$ mm is designed for X-band operation. The nonresonant CCR structure is used as the basic unit cell of the lens. Due to the square profile of the CCR structure, the HFME lens is discretized into seven concentric quasi-semicircular regions. The first region corresponds to the cell with $l_x = l_y = 0.9$ mm, while the last one corresponds to $l_x = l_y = 3.5$ mm. Therefore, each region corresponds to a specific refractive index. The electromagnetic parameters are retrieved using the simulated S-parameters as proposed by the inversion method described in [18]. Fig. 1(b) shows the real part of the effective index (n_{eff}) for three different cell dimensions of the waveguided CCR metamaterials. They are utilized in their nonresonant frequency regime such that they present broadband material properties in the 8–12-GHz band. Indeed for frequencies well below resonance, the unit cell behaves as an effective medium. We can observe that the index present low dispersion except for the case $l_x = l_y = 3.5$ mm since resonance is around 14 GHz for $a = 3.6$ mm.

The metamaterial planar slab is inserted in a quasi-TEM waveguide consisting of two parallel copper plates having dimensions $L = 190$ mm, $W = 130$ mm and spaced by $h = 11$ mm. As shown in Fig. 2, the GRIN lens is composed

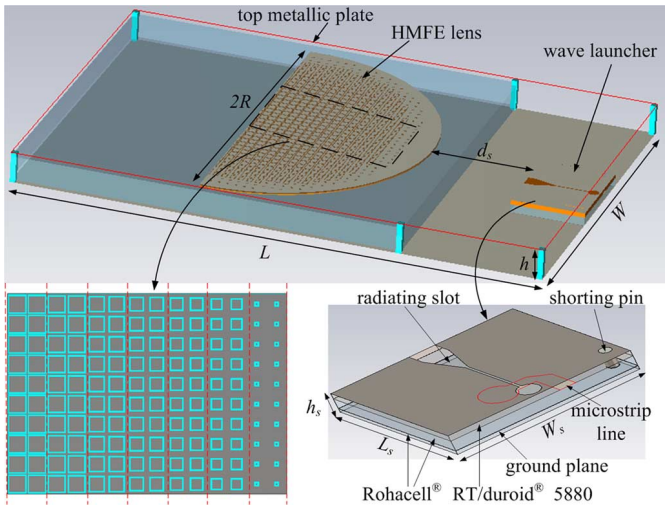

Fig. 2. HMFE lens antenna composed of a planar metamaterial-based lens and a Vivaldi antenna feed placed in a quasi-TEM parallel-plate waveguide. The dimensions of the feed are: $L_s = 26.5$ mm, $W_s = 35$ mm, and $h_s = 5.2$ mm. In the whole antenna system: $L = 190$ mm, $W = 130$ mm, $h = 11$ mm, $d_s = 51.5$ mm, and $R = 56$ mm.

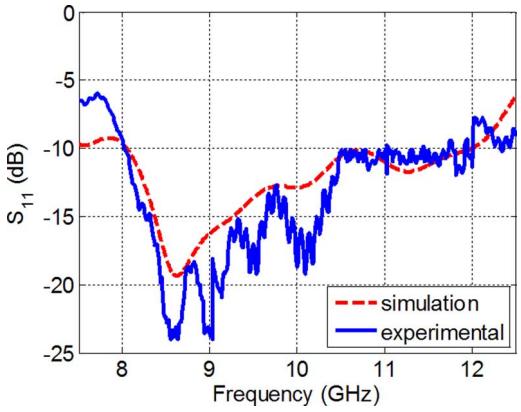

Fig. 3. S_{11} coefficients of the HMFE lens antenna.

of seven regions, each containing two CCR cells. The CCR dimensions l_x and l_y are different in each region in order to provide the gradient index necessary for the HMFE lens. The lens is placed on a Rohacell foam spacer, with a relative permittivity close to 1, to fill up the space between the substrate and the bottom metallic plate. The spacing between the lens and the top metallic plate is set to 1 mm as previously defined by the gap g in the simulation of the CCR unit cell.

III. Feeding Structure Design

In order to create a point source on the spherical surface of the lens, a microstrip-fed Vivaldi-type antenna [19] is inserted inside the parallel-plate waveguide. It has been designed to provide an electric field always parallel to the z-axis and perpendicular to the CCR plane. The Vivaldi feed is composed of a tapered slot made from the top copper sheet of a 1.6-mm-thick Rogers RT/duroid 5880 dielectric substrate. The slot is excited by a microstrip line printed on the bottom layer of the substrate together with a radial stub, as illustrated in Fig. 2. The feeding circuit of the Vivaldi antenna is composed of the orthogonal transition from the microstrip line to the input slotline of the

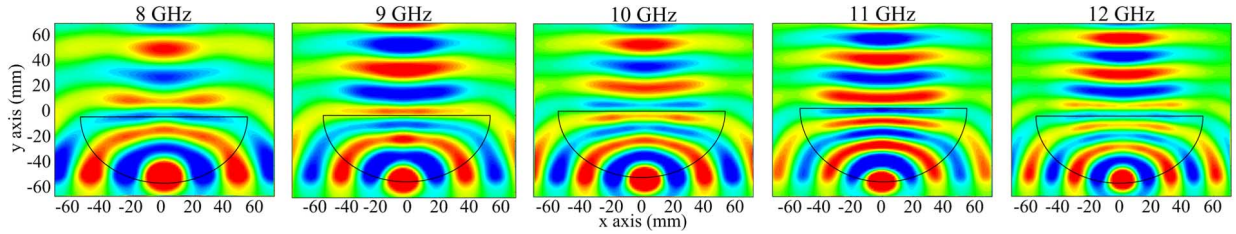

Fig. 4. Simulated near-field distribution of the lens antenna inside the parallel-plate waveguide at different frequencies.

Vivaldi radiating plane. It is a close approximation of a point source that is formed under the slot plane close to the HMFE lens periphery. Nevertheless, placing the feed structure in the parallel-plate waveguide causes parasitic radiations, and TEM waves are formed between the Vivaldi radiating plane and the bottom metallic plate of the waveguide. Such fields are unfavorable for the excitation of the HFME lens since a second undesirable point source can be created. In order to prevent such effects, the Vivaldi antenna is placed upon two layers of Rohacell foam separated by a thin metallic sheet and fixed to the bottom plate of the parallel-plate TEM waveguide. A metallic via is inserted between the slot radiating plane and the metallic sheet separating the two Rohacell layers. The radial stub feeding the Vivaldi antenna is thus shielded between two metallic planes that are short-circuited by the via acting as a stopband filter for TEM waves. Such a configuration allows to avoid having an undesirable point source resulting from the microstrip line and also to ensure low spurious radiation and hence low cross-polarization levels. The metallic via serves also as an extension of the microstrip feed ground plane and helps to improve the matching of the antenna. A semirigid coaxial cable is used to connect the antenna to the measurement instrumentation via an SMA connector. The measured and simulated return losses of the whole HMFE lens antenna are shown in Fig. 3. The proposed structure provides a return loss greater than 10 dB over the X-band frequency range.

IV. Results

The electric field map probed above the lens inside the planar waveguide is depicted in Fig. 4 for different frequencies. The simulations have been performed using concentric cylinders representing the effective material parameters and not with the CCR designed material. Perfectly matched layer (PML) absorbing boundaries are applied on the three lateral sides between the parallel plates except in the main radiation direction. Fields near the Vivaldi feed are so strong that the field distribution in the other region cannot be displayed clearly. Hence, the field around the feed is not shown in the plots. As illustrated, after passing through the lens, the circular wave fronts are flattened, and the cylindrical waves are transformed into quasi-plane waves. A directive emission is clearly observed for all tested frequencies.

To further investigate the directive behavior of the integrated lens antenna, far-field radiation patterns have been measured using a full anechoic chamber. The measured radiations patterns are presented in Fig. 5. A highly directive emission is observed at all tested frequencies in the H-plane. The sidelobes are below -10 dB for the measured data. A slight asymmetry appears in the sidelobes due to the offset of the microstrip line feeding the Vivaldi antenna. In the E-plane, a wide beam is radiated, resulting in a fan-shape beam of the lens antenna. The cross-polarization components reported in Fig. 5 show levels remaining below -19 dB over the whole [8–12 GHz] frequency band.

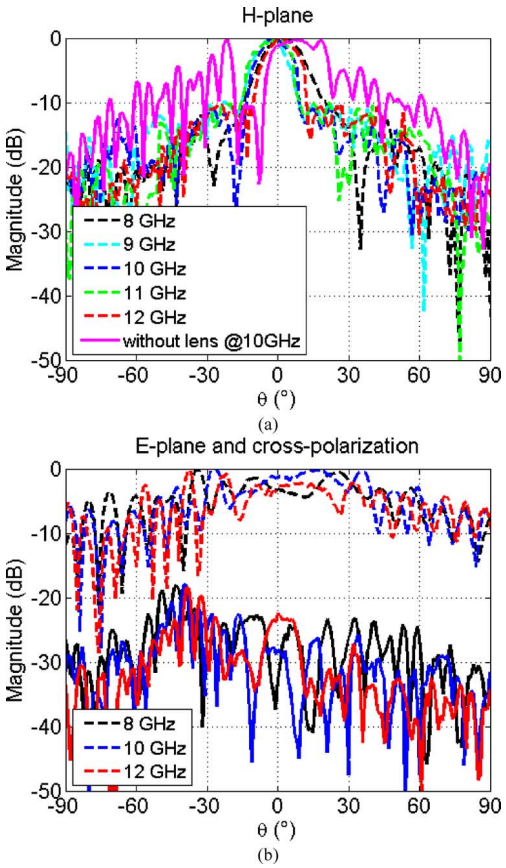

Fig. 5. Measured copolarization and cross-polarization components. (a) H-plane. (b) E-plane (- - -) and cross polarization (——).

To clearly illustrate the lens effect on the Vivaldi feed and to validate the performance of such an integrated lens antenna, measurement performed at 10 GHz in the H-plane without the lens in the TEM waveguide is also plotted [solid trace in Fig. 5(a)]. As it can be observed, the lens renders the beam more directive and lowers the level of the parasitic lobes.

The directivity of the proposed metamaterial-based lens antenna is depicted in Fig. 6. Compared to that of an ideal aperture having a similar physical surface as the HMFE lens, a lower directivity is observed in our case. However, the overall performances of the low-profile lens antenna suggest that it can be effectively used in communication antennas and sensor applications.

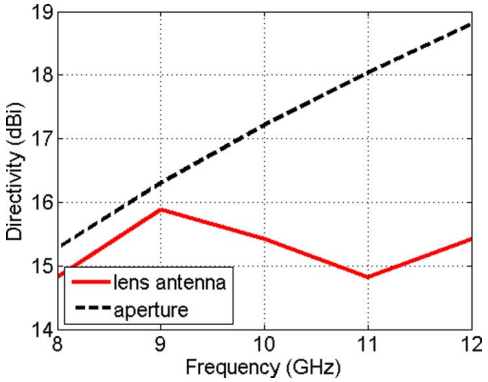

Fig. 6. Simulated directivity (at broadside) of the proposed lens antenna compared to that of an aperture having same physical surface as the HMFE lens.

V. Conclusion

In this letter, we have presented a low-profile and substrate-integrated planar HMFE lens antenna. The metamaterial-based lens is excited by a Vivaldi source and configured to operate in a quasi-TEM parallel-plate waveguide. The lens antenna has shown a wideband operation from 8 to 12 GHz. The conceived antenna system exhibits a good return loss and can be easily associated with a radio front end due to its low profile.

References

[1] D. Schurig, J. J. Mock, B. J. Justice, S. A. Cummer, J. B. Pendry, A. F. Starr, and D. R. Smith, "Metamaterial electromagnetic cloak at microwave frequencies," *Science*, vol. 314, no. 5801, pp. 977–980, Oct. 2006.

[2] P.-H. Tichit, S. N. Burokur, D. Germain, and A. de Lustrac, "Design and experimental demonstration of a high-directive emission with transformation optics," *Phys. Rev. B*, vol. 83, no. 15, p. 155108, Apr. 2011.

[3] P.-H. Tichit, S. N. Burokur, and A. de Lustrac, "Transformation media producing quasi-perfect isotropic emission," *Opt. Express*, vol. 19, no. 21, pp. 20551–20556, Oct. 2011.

[4] N. Kundtz and D. R. Smith, "Extreme-angle broadband metamaterial lens," *Nature Mater.*, vol. 9, no. 2, pp. 129–132, Feb. 2010.

[5] Y. G. Ma, C. K. Ong, T. Tyc, and U. Leonhardt, "An omnidirectional retroreflector based on the transmutation of dielectric singularities," *Nature Mater.*, vol. 8, no. 8, pp. 639–642, Aug. 2009.

[6] P.-H. Tichit, S. N. Burokur, and A. de Lustrac, "Waveguide taper engineering using coordinate transformation technology," *Opt. Express*, vol. 18, no. 2, pp. 767–772, Jan. 2010.

[7] D. R. Smith, J. J. Mock, A. F. Starr, and D. Schurig, "Gradient index metamaterials," *Phys. Rev. E*, vol. 71, no. 3, p. 036609, Mar. 2005.

[8] T. Driscoll, D. N. Basov, A. F. Starr, P. M. Rye, S. Nemat-Nasser, D. Schurig, and D. R. Smith, "Free-space microwave focusing by a negative-index gradient lens," *Appl. Phys. Lett.*, vol. 88, no. 8, p. 081101, Feb. 2006.

[9] R. K. Luneburg, *Mathematical Theory of Optics*. Providence, RI: Brown Univ. Press, 1944.

[10] C. H. Walter, "Surface-wave luneberg lens antennas," *IRE Trans. Antennas Propag.*, vol. AP-8, no. 5, pp. 508–515, Sep. 1960.

[11] J. C. Maxwell, ""Solutions of problems," problem no. 2," *Cambridge Dublin Math. J.*, vol. 8, pp. 188–195, 1854.

[12] B. Fuchs, O. Lafond, S. Rondineau, and M. Himdi, "Design and characterization of half Maxwell fish-eye lens antennas in millimeter waves," *IEEE Trans. Microw. Theory Tech.*, vol. 54, no. 6, pp. 2292–2300, Jun. 2006.

[13] C. Pfeiffer and A. Grbic, "A printed, broadband luneburg lens antenna," *IEEE Trans. Antennas Propag.*, vol. 58, no. 9, pp. 3055–3059, Sep. 2010.

[14] S. Maci, G. Minatti, M. Casaletti, and M. Bosiljevac, "Metasurfing: Addressing waves on impenetrable metasurfaces," *IEEE Antennas Wireless Propag. Lett.*, vol. 10, pp. 1499–1502, 2011.

[15] H. Gao, B. Zhang, S. G. Johnson, and G. Barbastathis, "Design of thin-film photonic metamaterial lüneburg lens using analytical approach," *Opt. Express*, vol. 20, no. 2, pp. 1617–1628, Jan. 2012.

[16] W. Rotman and R. F. Turner, "Wide-angle microwave lens for line source applications," *IEEE Trans. Antennas Propag.*, vol. AP-11, no. 6, pp. 623–632, Nov. 1963.

[17] G. D. M. Peeler and D. H. Archer, "A two-dimensional microwave luneberg lens," *IRE Trans. Antennas Propag.*, vol. AP-1, no. 1, pp. 12–23, Jul. 1953.

[18] D. R. Smith, S. Schultz, P. Markos, and C. M. Soukoulis, "Determination of effective permittivity and permeability of metamaterials from reflection and transmission coefficients," *Phys. Rev. B.*, vol. 65, no. 19, p. 195104, May 2002.

[19] K. S. Yngvesson, D. H. Schaubert, T. L. Korzeniowski, E. L. Kollberg, T. Thungren, and J. F. Johansson, "Endfire tapered slot antennas on dielectric substrates," *IEEE Trans. Antennas Propag.*, vol. AP-33, no. 12, pp. 1392–1400, Dec. 1985.